

International Workshop on Low-Frequency Propagation and Noise

Volume 1

Woods Hole, Massachusetts
14-19 October, 1974

1977



Sponsored by CNO (OP-095)
Supported by CNR

Coordinated at the
Maury Center for Ocean Science
Department of the Navy
Washington, D.C.

DATA LIBRARY & ARCHIVES
Woods Hole Oceanographic Institution

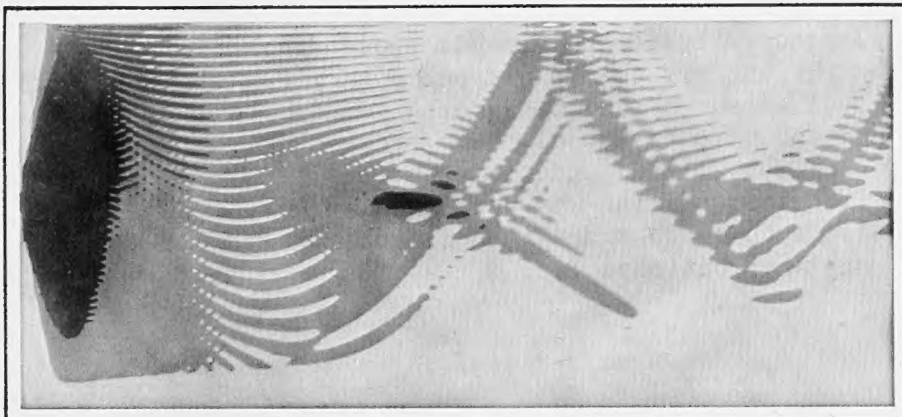


International Workshop on Low-Frequency Propagation and Noise

Volume 1

Woods Hole, Massachusetts

14-19 October, 1974



Sponsored by CNO (OP-095)

Supported by CNR

**Coordinated at the
Maury Center for Ocean Science
Department of the Navy
Washington, D.C.**

WHOI
DOCUMENT
COLLECTION

ACKNOWLEDGEMENTS

These proceedings record the first plenary session of the International Workshop on Low Frequency Propagation and Noise, sponsored by the Director, Antisubmarine Warfare Programs of the U. S. Navy Chief of Naval Operations staff. Scientists from six nations--Australia, Canada, New Zealand, Norway, the United Kingdom, and the United States--participated. The Workshop was conducted by the Chief of Naval Research. The executing agency was the Maury Center for Ocean Science; Director, Dr. J. B. Hersey. Commander A. G. Brookes, Jr., USN, coordinated the conduct of the symposium which was held at the Woods Hole Oceanographic Institution, Quisset Campus, Woods Hole, Massachusetts. The Office of Naval Research is indebted to the Institution for its excellent hosting of this meeting and in particular to Mr. Charles S. Innis for his conspicuous efficiency and skill in making all local arrangements. All participants in the Workshop made substantial contributions either by preparing the papers listed in the Table of Contents or by chairing various sessions. These proceedings were recorded in detail by Ace Federal Reporters, Inc. The completeness and quality with which the proceedings were recorded are much appreciated and have made possible the level of detail these proceedings contain. The proceedings were edited primarily by the authors themselves and by Mr. F. P. Diemer in the Office of Naval Research and Commander A. G. Brookes, Jr., USN. The final editing and preparation of these proceedings were performed by Science Applications, Inc., under contract to the Office of Naval Research. Technical editing was performed by Drs. J. Czika, J. S. Hanna, and R. C. Cavanagh under the direction of C. W. Spofford, all of Science Applications, Inc.

The illustration on the title page displays iso-loss contours in range and depth generated by the Parabolic Equation Model of Dr. F.D. Tappert. Regions of heaviest shading correspond to losses of less than 80 dB re 1 yard, lighter shading to losses between 80 and 90 dB, and lightest shading to losses greater than 90 dB. The calculation is for a constant (pressure) gradient sound-speed profile in water 16,000-feet deep overlying a highly absorbing bottom. The source is at a depth of 8,000 feet, the acoustic frequency is 50 Hertz, and the maximum range is 50 nautical miles.

Details on the technique and more examples are contained in Dr. Tappert's paper entitled "Selected Applications of the Parabolic-Equation Method in Underwater Acoustics" found in Volume I of these Proceedings.

Title page was designed by Frank Varcolik, SAI.

PREFACE

The International Workshop on Low-Frequency Propagation and Noise was held at the Woods Hole Oceanographic Institution, Woods Hole, Massachusetts, from October 15 to 19, 1974. These Proceedings consist of either author-supplied texts or edited versions of the oral presentations and edited condensations of the discussions. In the edited sections, the editors have made every effort to render faithfully the essential content of the oral presentation or discussion.

These Proceedings are presented in two volumes, each consisting of 2 days of presented papers. Several of the original presentations have been superceded by a published version, which the authors also have submitted for publication here. In these cases, with the permission of the authors and the publishers, the published articles are reproduced here in facsimile. The presentations so rendered are the following:

- i) Dr. Weinberg's paper appeared as NUSC Technical Report 4867.
- ii) The presentation of Drs. Flatté and Munk contained some of the information presented in the three articles published in the *Journal of the Acoustical Society of America*.
- iii) Dr. Raisbeck's paper appeared in the *U. S. Navy Journal of Underwater Acoustics*.

INTERNATIONAL WORKSHOP
ON LOW-FREQUENCY PROPAGATION AND NOISE

VOLUME I

TABLE OF CONTENTS

	<u>Page</u>
I. ENVIRONMENTAL MEASUREMENTS (<i>J. B. Hersey, Session Chairman</i>)	
INTRODUCTION, <i>Dr. J. B. Hersey</i>	1
TIME VARIATIONS OF SOUND SPEED OVER LONG PATHS IN THE OCEAN, <i>G. R. Hamilton</i>	7
THE ACOUSTIC OUTPUT OF EXPLOSIVE CHARGES, <i>Ermine A. Christian</i>	31
EXPLOSIVE SOUND-SOURCE STANDARDS, <i>M. S. Weinstein</i>	61
APPLICATION OF RAY THEORY TO LOW-FREQUENCY PROPAGATION, <i>Henry Weinberg</i>	93
II. PROPAGATION THEORY (<i>R. R. Goodman, Session Chairman</i>)	
NORMAL MODES IN OCEAN ACOUSTICS, <i>D. C. Stickler</i>	125
SELECTED APPLICATIONS OF THE PARABOLIC-EQUATION METHOD IN UNDERWATER ACOUSTICS, <i>Frederick Tappert</i>	155
CALCULATION OF THE EFFECT OF INTERNAL WAVES ON OCEANIC SOUND TRANSMISSION, <i>Stanley M. Flatté and Frederick D. Tappert</i>	201
SOUND PROPAGATION THROUGH A FLUCTUATING STRATIFIED OCEAN: THEORY AND OBSERVATION, <i>W. H. Munk and F. Zachariasen</i> . .	211
INTERPRETATION OF MULTIPATH SCINTILLATIONS ELEUTHERA TO BERMUDA IN TERMS OF INTERNAL WAVES AND TIDES, <i>Freeman Dyson, W. H. Munk and B. Zetler</i>	233

VOLUME I

TABLE OF CONTENTS (Cont'd)

	<u>Page</u>
III. EFFECTS OF BOUNDARIES (<i>M. Schulkin, Session Chairman</i>)	
ACOUSTIC PROPERTIES OF THE SEA FLOOR, <i>John Ewing</i>	249
THE EFFECT OF ROUGH INTERFACES ON SIGNALS THAT PENETRATE THE BOTTOM, <i>C. W. Horton, Sr.</i>	275
BOTTOM PROPERTIES FOR LONG-RANGE PROPAGATION PREDICTION, <i>Aubrey L. Anderson</i>	297
FORWARD SCATTERED LOW-FREQUENCY SOUND, <i>W. I. Roderick</i> . . .	325
IV. SIGNAL CHARACTERISTICS (<i>T. G. Birdsall, Session Chairman</i>)	
COHERENCE, <i>Theodore G. Birdsall</i>	357
FLUCTUATIONS: AN OVERVIEW, <i>Ira Dyer</i>	365
SOUND PROPAGATION IN A RANDOM MEDIUM, <i>Robert H. Mellen</i> . . .	387
PHASE FLUCTUATIONS, COHERENCE AND INTERNAL WAVES, <i>R. C. Spindel</i>	423
FIXED-SYSTEM MEASUREMENTS OF TIME-VARYING MULTIPATH AND DOPPLER SPREADING, <i>H. A. DeFerrari</i>	465
DESIGN OF TRANSMISSION LOSS EXPERIMENTS, <i>J. S. Hanna</i>	509

INTERNATIONAL WORKSHOP
ON LOW-FREQUENCY PROPAGATION AND NOISE

VOLUME II

TABLE OF CONTENTS

	<u>Page</u>
V. SPECIAL EFFECTS (<i>R. H. Nichols, Session Chairman</i>)	
SURFACE DECOUPLING EFFECTS, <i>M. A. Pedersen, D. F. Gordon, and D. White</i>	559
A THEORETICAL APPROACH TO THE PREDICTION OF SIGNAL FLUCTUATIONS DUE TO ROUGH-SURFACE SCATTERING, <i>F. M. Labianca and E. Y. Harper</i>	583
SOFAR PROPAGATION OF WIDE-BAND SIGNALS TO LONG RANGES, <i>R. P. Porter</i>	633
CONVERGENCE ZONE DEPENDENCE ON FREQUENCY, <i>R. M. Fitzgerald</i>	667
VI. GEOGRAPHIC EFFECTS (<i>E. E. Hays, Session Chairman</i>)	
LOW-FREQUENCY PROPAGATION IN THE ICE-COVERED ARCTIC OCEAN, <i>Henry W. Kutschale</i>	683
ARCTIC ENVIRONMENTAL LF ACOUSTICS MEASUREMENTS, MODELS AND PLANS, <i>Beaumont M. Buck</i>	725
ENVIRONMENTAL FACTORS AFFECTING LOW-FREQUENCY PROPAGATION IN THE OCEAN, <i>David G. Browning</i>	769

VOLUME II

TABLE OF CONTENTS (Cont'd)

	<u>Page</u>
VII. NOISE MECHANISMS (<i>I. Dyer, Session Chairman</i>)	
AMBIENT-NOISE MODELS, <i>R. C. Cavanagh</i>	801
GEOGRAPHICAL VARIATION OF AMBIENT NOISE IN THE OCEAN FOR THE FREQUENCY RANGE FROM 1 HERTZ TO 5 KILOHERTZ, <i>Robert L. Martin and Anthony J. Perrone</i>	817
STATISTICAL ANALYSIS OF SHIP-GENERATED NOISE, <i>S. C. Daubin</i>	843
VIII. NOISE MEASUREMENTS (<i>W. A. Von Winkle, Session Chairman</i>)	
VERTICAL NOISE DISTRIBUTION, <i>V. C. Anderson</i>	859
DIRECTIONAL NOISE AMBIGUITY RESOLUTION WITH LINEAR ARRAYS, <i>Gordon Raisbeck</i>	887

LOW-FREQUENCY PROPAGATION AND NOISE WORKSHOP

INTRODUCTION

Dr. J. B. Hersey
Office of Naval Research

It is a great pleasure to welcome members of the Low-Frequency Propagation and Noise Workshop to this, its first meeting. This international workshop is sponsored by the Director of Antisubmarine Warfare of the staff of the U. S. Chief of Naval Operations. It recognizes the growing cooperation among the participating nations in application of low-frequency underwater acoustic systems in ASW. Also, it is closely related to a series of workshops sponsored by various elements of the U. S. Navy oceanography and undersea warfare community. The broad purpose of the U. S. workshops is to support progress toward solving the priority problems of the U. S. Navy in undersea warfare and other concerns of the Navy where the oceans are influential.

The objective of this workshop is to assess our understanding of low-frequency ocean acoustics and to identify and prioritize what programs of investigation should be emphasized in the next 5 to 10 years. It is intended that our final product will be proceedings of this meeting and a planning guide that can be a useful and influential instrument for all nations here convened.

The general approach is first to hear reviews of as comprehensive a series of topics as possible during the next 4 days. Most of the talks are intended strictly to provide a basis for assessing our understanding and knowledge of this field. The remaining few talks present viewpoints that are thought to be of special interest because they represent new departures. We have tried to order the program so that

there will be ample opportunity for discussion, all of which will be recorded. On Saturday morning, we will make decisions on a structure of small working groups that will be responsible in the next 6 months for preparing a written assessment and recommendations for future programs of investigation. My office will make every effort to speed the availability of the proceedings of this meeting to its members so that all the material presented and discussed here will be available to the working groups. These proceedings will also be published and suitably distributed.

I earnestly hope that all members of the workshop will participate to some degree in the main work of the workshop — that of the next 6 months. You have received as part of your registration package two questionnaires. One is to be filled out and handed to CDR Brookes this morning. It will serve as the basis for the first cut at organizing the working groups. The second, intended as a guide to the Steering Committee, is to be filled out no earlier than Thursday afternoon so as to be available for the meeting of the Steering Committee Thursday evening. You will notice that it gives you an opportunity to change your mind about the first questionnaire. It also gives you an opportunity to comment on any aspect of the objective of the workshop, its content so far, and what you think should be done by the time the workshop is disbanded. Please use it generously.

The final plenary session of the workshop is now planned for May 1975, either in San Francisco, Monterey, or San Diego. Its objective will be to hear, discuss, and make provision for rewriting, editing, and publishing the planning guide. It is envisioned that talks will be presented describing the content of the several chapters as determined by the working groups. Further, a major part of this session will consist of discussion of this material, which should be

available to all members of the workshop well before the meeting. A small editorial staff will be responsible for final editing, production, and distribution of the planning guide. A record will be kept of the discussions at the second plenary session, but no useful decision can be made at present about its publication.

So much for generalities. In the next 4 days we will be reviewing some things old and some things new that represent our partial understanding of the characteristic behavior of low-frequency sound waves in and below the oceans. Low frequency here means the range from 1 to 1,000 Hertz. A quite arbitrary range which, unfortunately perhaps, includes at low frequencies the Airy wave of the deep ocean basins and at high frequencies phenomena that are sensitive to rather fine details of water structure and ocean floor topography. The past emphasis in research and applications is most uneven. Major U.S. emphasis has been on the spectral region from 20 to 150 Hz with some far less intense emphasis on the region from 150 to 1,000 Hz. Only in the past 3 or 4 years have we attempted anything significant below 20 Hz. Thus, we will find - if we look - that there is great unevenness in our information throughout this spectrum. In some areas of interpretation, there is great scope for speculation, because there is so little hard data; whereas in others we have so much information that the knowledgeable interpreter may feel tongue-tied. In the next 6 months — and a lot longer — we should look at the spectrum encompassing both extremes in order to learn what is going on in the ocean, thus solving many of the practical problems of warfare there — and other marine concerns of mankind as well.

All nations represented here use their knowledge of ocean acoustics more or less intensely for some or all of the following purposes:

- 1) To forecast the performance of existing sonars over the next few hours, tomorrow, next week, next year, and so on
- 2) To analyze operations or operational exercises as a means of improving system performance
- 3) To analyze the results of acoustic intelligence
- 4) To assist in force level trade-off studies
- 5) To assist in the identification and selection of new systems design options
- 6) To assist in the entire development process after options have been selected for development.

In formulating objectives within the framework of these purposes, we are driven by scientific or technical opportunities and constraints in the face of the potential enemy's capabilities and characteristics.

Our investigations can be programmed either to provide a technology base on which new analysis tools or new sonar systems can be developed or they can help develop a needed capability. The U.S. Defense Department has long subdivided these efforts by names such as research, exploratory development, advanced and engineering development, and so on.

The non-U.S. participants will inevitably hear American participants refer to these activities by their number, the budget sub-elements 6.1, 6.2, 6.3, and so on. In principle, I believe this workshop to be concerned with 6.1, 6.2, 6.3, 6.4, and 6.6. In practice we hear little of 6.6, and so far as I am aware, have no programs whatever in 6.4. For the remainder, I find it easier to divide our concerns into 6.1, 6.2, and 6.3 as follows. In 6.1, we should study acoustic and oceanic processes and how they interact. In 6.2,

HERSEY: INTRODUCTION TO LOW-FREQUENCY PROPAGATION AND NOISE WORKSHOP

we should examine how the resulting understanding of ocean acoustics can be applied in the framework of the broad purposes stated above. In 6.3, we determine as precisely as deemed necessary the significance of ocean acoustics in supplying a particular fleet service, analysis tool, or support for the development of a specific new sonar system. Again, all of these are a proper concern in this workshop.

In making our assessment of present understanding of low-frequency acoustics, significant confusion may result from the unevenness of our understanding. Acoustical theory has long been able to model complex processes for some simple configurations of the sound medium, and the question has been raised repeatedly whether much, if anything, remains to be done in basic acoustics. Nevertheless, the ocean, its surface, and its floor are so complex that these models are of limited practical use. The last 5 to 8 years have seen an intense effort in the U. S., mainly in 6.2 and 6.3 programs to develop models that would deal in practical and useful detail with the major complexities of the ocean and predict transmitted sound levels and noise. We have depended altogether on modern digital computing techniques and on comparisons with measurements. These modern methods are only now beginning to teach us when and where sweeping simplifications of the shape of the boundaries and the acoustical properties of the ocean are both useful and adequate. We shall be looking at some of these results. How should these computational methods be developed in the future?

We have done surprisingly few strict comparisons of acoustic measurements with model analysis based on simultaneously measured acoustic data and oceanic properties. The necessary impact of the few comparisons available has not had time to be fully felt and digested. Even so, important lessons are emerging. Nevertheless, we still don't now know how detailed a program of measurements is required. I hope that the workshop can help us chart a good course to answer the nagging question of: How much is enough?

TIME VARIATIONS OF SOUND SPEED OVER LONG PATHS IN THE OCEAN

G. R. Hamilton

Ocean Science and Technology Division

Technology Division

From 1961 to 1964 a series of precisely located and timed SOFAR charges were fired off Antigua to measure the transmission time stability of the sound channel axis arrival (i.e., the SOFAR signal cutoff) to MILS hydrophones at Eleuthera, Bermuda, the Canary Islands, Barbados, Ascension and Fernando de Noronha. The sound transmission speed was found to be stable for a few hours but it could not be predicted a week in advance. An application to the precise location of missile impacts using SOFAR signals, based on the dropping of SOFAR charges at the missile impact position within a few hours of missile launch, is described.

The most extensive measurement of sound-speed variations over long distances were made in a program in the early 60's called SCAVE, for Sound-Channel Axis Velocity Experiment. The locations of the experiment are shown in Figure 1. Results were published in the proceedings of the Naval Underwater Acoustics Symposia in 1962, 1963, and 1964.

The measurements were designed to make it possible to use SOFAR charges to determine the accurate impact position of Polaris missiles launched southeast into the Atlantic from Cape Kennedy, Florida. With a range of about 1600 miles, these missiles impacted in the open ocean east of the Caribbean. For this flight range, they could not be targeted to impact close to an island or coast line where shore-mounted radars or shore-connected bottom hydrophones could be used for determining impact position without overflying islands. Could SOFAR charges carried in the missile be used to accurately locate the impact position at a mid-ocean location? What impact position accuracy would SOFAR charge provide?

ATLANTIC MISSILE RANGE MISSILE IMPACT LOCATION SYSTEM



Figure 1. LOCATIONS OF SCAVE

Our initial ideas were to drop SOFAR charges over accurately located bottom hydrophones off Antigua, time the SOFAR arrivals 800 miles away at Bermuda, and basically use this experimental sound-speed measurement to calibrate sound velocimeters, in absolute terms, for the ocean conditions at 3000- to 4000-ft depth and 3°C. This was the only method we could conceive to obtain an absolute sound velocimeter calibration for these temperature and pressure conditions. For example, in 1962, when calibrating a sound velocimeter in the laboratory, there was an elusive one-foot-per-second difference in various tabulated values of sound speed for distilled water at surface temperatures and pressures.

In planning the experiment, we assumed that the axis sound speed at any open-ocean location would be stable. We would use this 800-mile travel-time measurement to calibrate the velocimeters in absolute terms based on multiple lowerings along the transmission path. Since SOFAR charges off Antigua could also be received on the MILS (Missile Impact Location System) sound-channel axis hydrophones at Eleuthera, at Fernando de Noronha off Brazil, at Barbados, and at Ascension, we recorded on these as well. Looking ahead, since our ultimate problem was to accurately locate a missile SOFAR charge in mid-Atlantic, a hydrophone was obviously needed in the northeast Atlantic to balance any unknown bias from the existing MILS hydrophones to the south and west. Such a hydrophone station was installed in the Canary Islands.

Figure 2 shows a typical SOFAR signal received over a Sargasso Sea transmission path. Typical, in that for a 900-mile transmission path the signal has a 9-second duration and terminates with a sharp cutoff. For this hydrophone buoyed up into the sound-channel axis,

HAMILTON: TIME VARIATIONS OF SOUND SPEED OVER LONG PATHS IN THE OCEAN

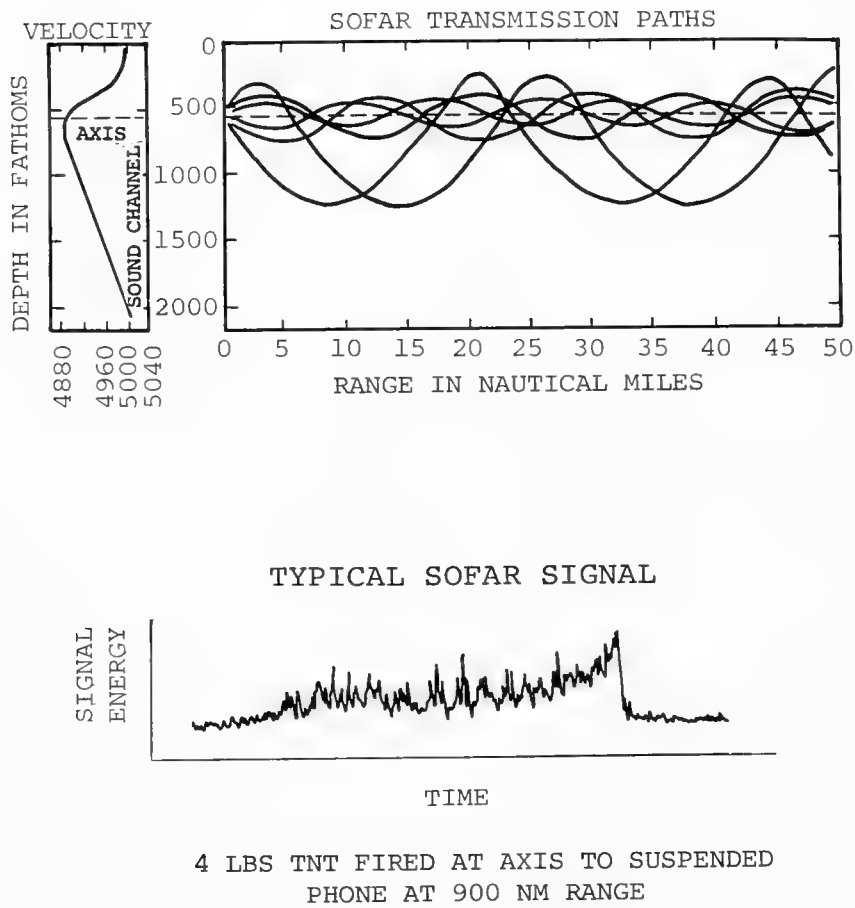


Figure 2. TYPICAL SOFAR SIGNAL OVER SARGASSO SEA TRANSMISSION PATH

the signal-amplitude cutoff is in excess of 30dB and occurs in about 0.02 seconds. The trace shown is a Sanborn direct-writing hot-pen recorder in the log-audio mode (i.e., the log of the rectified audio signal). The ray diagram shown is from the original Ewing and Worzel 1947 SOFAR paper. For this Sargasso Sea sound-speed profile with the Sargasso's 500m thick, near surface layer of 18°C water, the first arrivals of the SOFAR signal travel along paths that are near bottom grazing and through the 18°C near-surface water.

In Figure 3 is shown the bottom hydrophone array off Antigua over which SOFAR charges were dropped. The water is 3,000 fathoms deep. Three hydrophone signals are needed to locate and time an underwater explosion. With six hydrophones in this array, there is redundant data for greater system reliability and for greater time and position accuracy. One SOFAR charge could be located relative to another in the central area of this array with a precision of 30 feet. This shot-position precision on a transmission path of 1,000 miles to a fixed hydrophone means the error in the relative sound-speed measurement due to source-charge positioning errors is of the order of 0.04 feet per second.

In our SCAVE tests, and we ran about 25 or 28 of them, we chartered a small boat in Antigua as a SOFAR charge drop boat. This boat was the type of yacht you could charter for about \$2,000 a week. Normally a one-week charter was required to set up aboard, sail to the hydrophone area and drop SOFAR charges for two hours, return and offload. On one SCAVE, we dropped SOFAR charges every hour for 24 hours, and on another occasion every hour for eight days.

Figure 4 is a typical record for an overhead SOFAR signal on these bottom hydrophones, illustrating the S/N ratio and system frequency response that made the 30-ft shot-position precision possible.

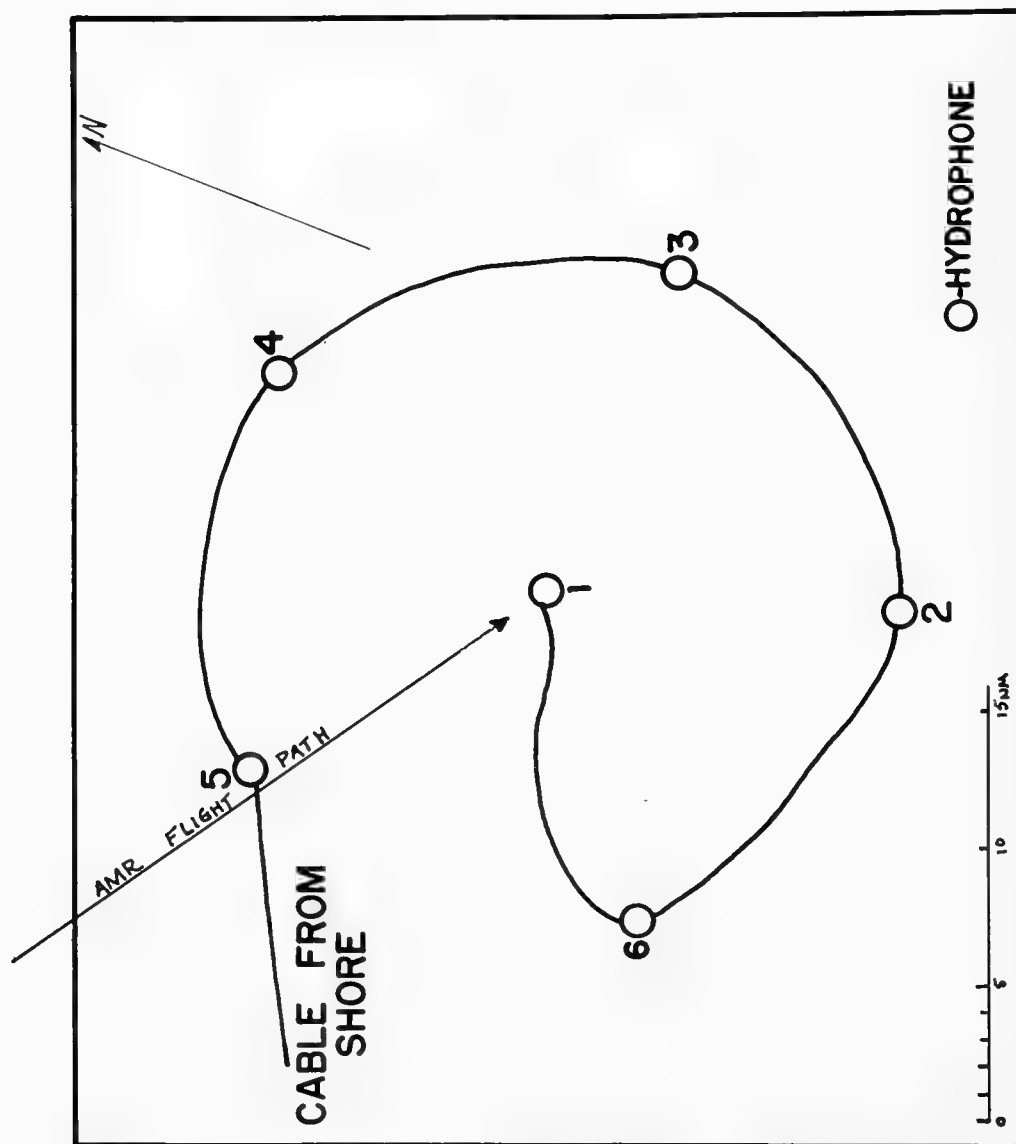


Figure 3. ANTIGUA PENTAGON ARRAY

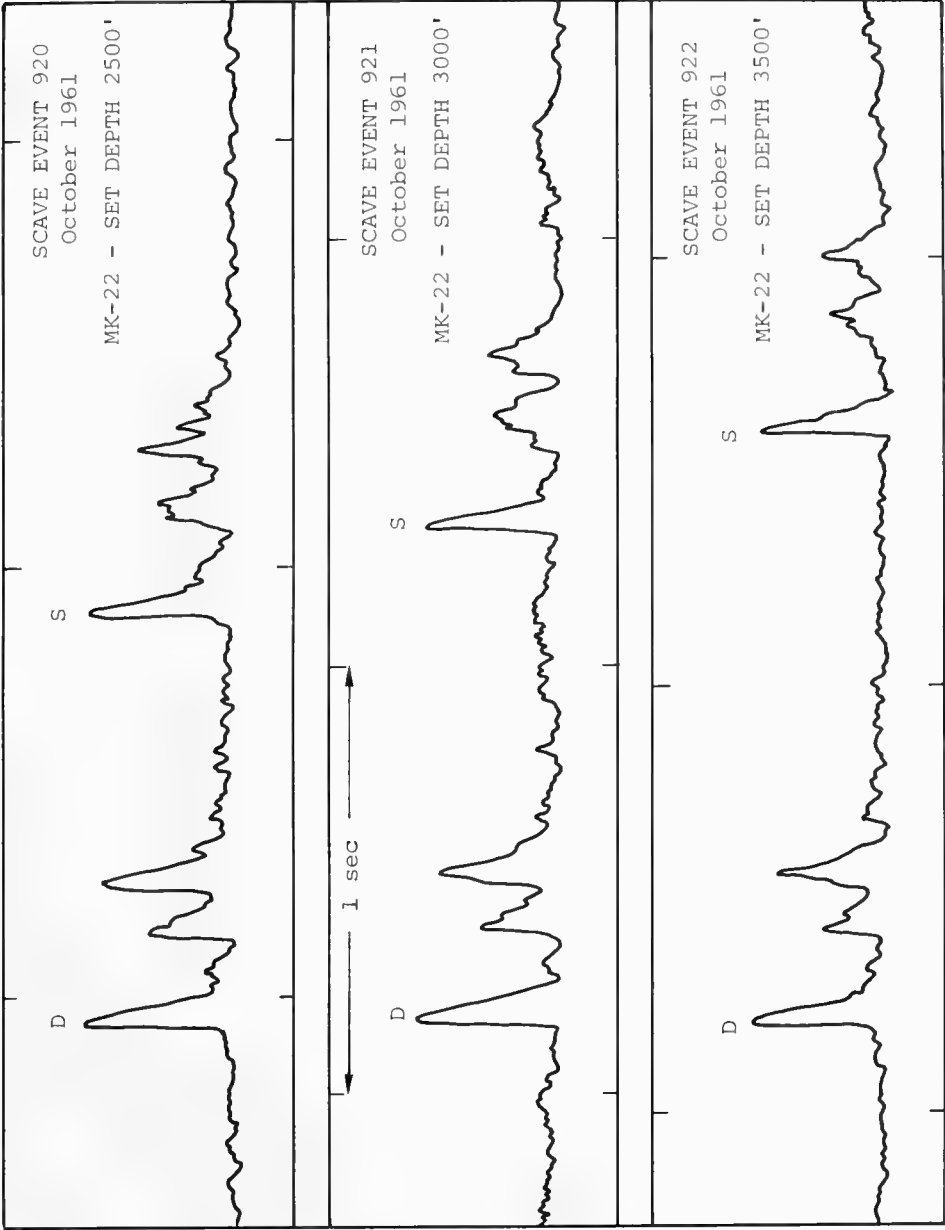


Figure 4. TYPICAL RECORD FOR OVERHEAD SOFAR SIGNALS

Again, this is a Sanborn recorder with log-audio recording. The vertical scale for each of the records covers 50 dB. Shown at the bottom is a one-second interval. Direct signals are marked with a D, surface reflections with an S. Rise times for these signals are less than 0.01 seconds. The two pulses following D and S are sub-bottom echoes.

In Figure 5 are shown the results of the first year's program. Primarily shown here are results for two phones at Bermuda and three at Eleuthera. The error bars indicate the full spread of the sound-speed data. There are two immediate conclusions. Obviously, the sound-channel axial speed was not constant. There are times when the speed remains constant for a month or two, but it can also change by 2 feet per second within a month. The second conclusion concerned the cause of the sound-speed variations. The month-to-month variations on the Bermuda and Eleuthera phones do not correlate. The inference therefore is that the cause of the speed variations is not a phenomenon at the source. Note also that speed variations at the two Bermuda phones track very nicely. Although these phones are about ten miles apart, the line between the "SOFAR Station bottom hydrophone" and the "BOA Spd" (Broad Ocean Area suspended) hydrophone continues directly to the Antigua hydrophone area. And so we inferred that whatever is causing the variations in the average sound-channel speed between Antigua and Bermuda is not some small-scale effect in the area of the receiving hydrophones.

For the three Eleuthera phones, the transmission paths to each of the individual phones are not identical, and the speed variations, although similar, don't track as accurately as those at Bermuda.

In Figure 6 are the SCAVE results for 2.5 years. At the top are three additional transmission paths, Ascension and Fernando de Noronha

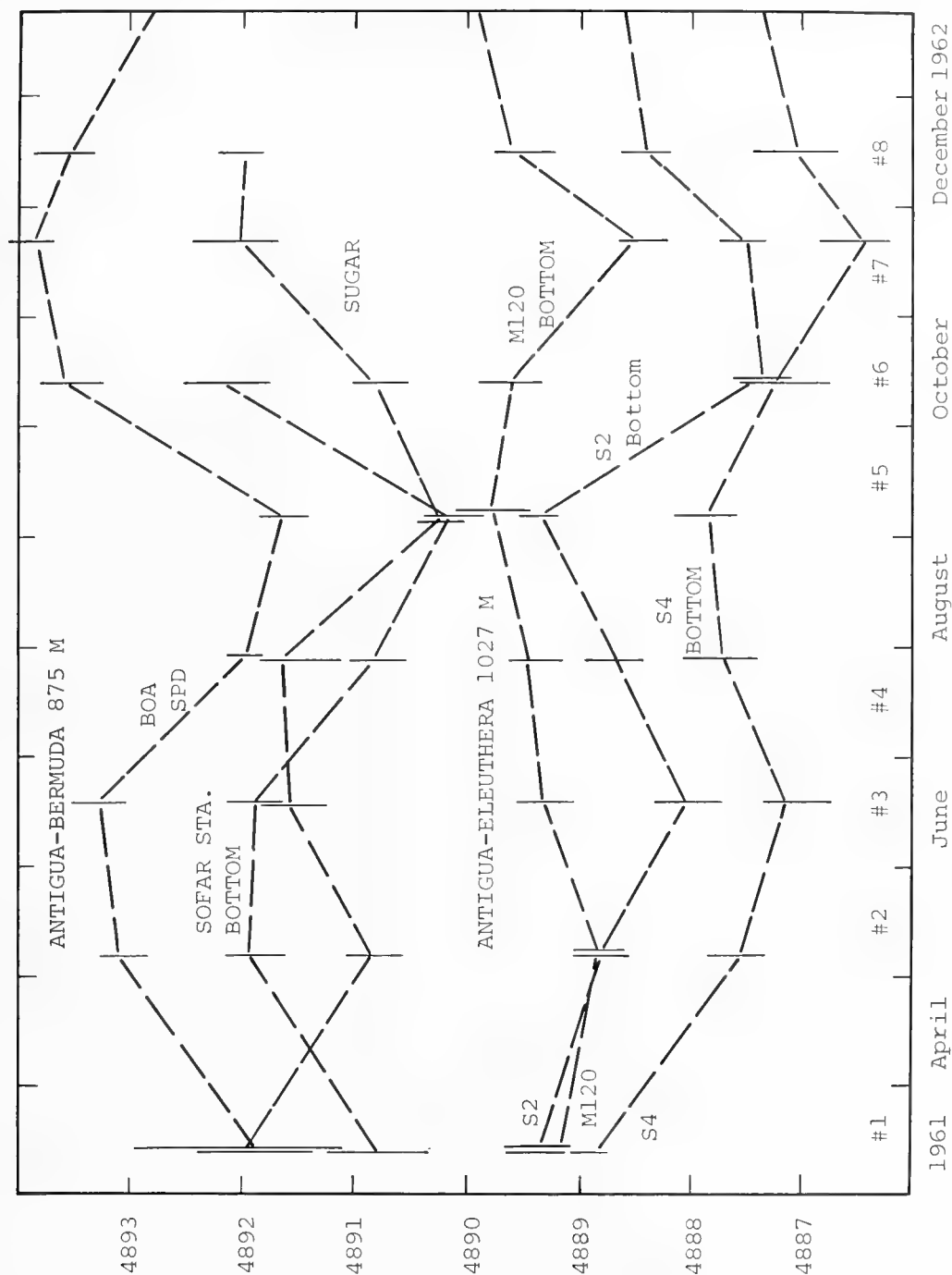


Figure 5. SUMMARY OF SOUND-CHANNEL AXIAL SPEED VARIATIONS FOR ONE YEAR

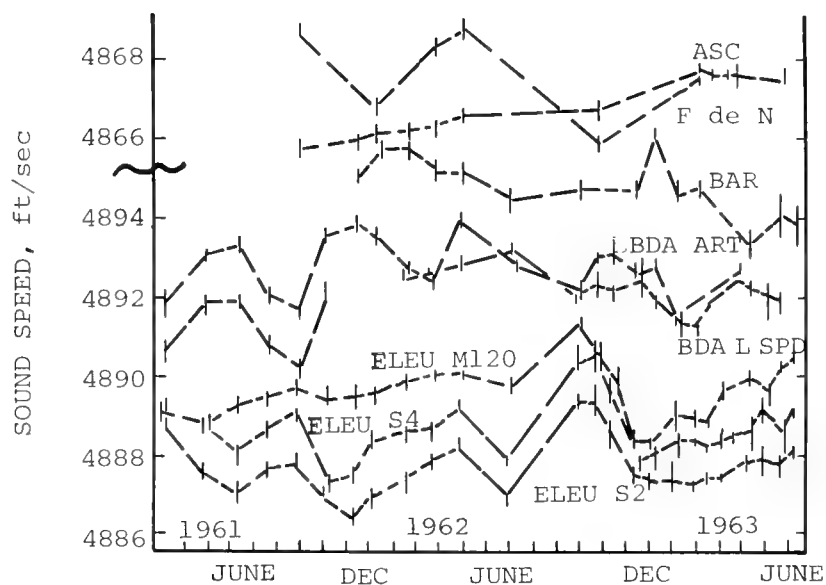


Figure 6. AXIS SPEED VARIATIONS (2.5 YEARS)

in the South Atlantic, and Barbados just 300 miles to the south of Antigua. The obvious conclusions we reached from this were that we couldn't predict the axis sound speed with the required accuracy for missile-splash location.

Note the long-term correlation between Eleuthera and Bermuda. For the first half of the program, there is a six-month cycle, rather well displayed, that occurs four months later at Eleuthera than Bermuda.

Shown in Figure 7 are the results of an eight-day SCAVE with signals at hourly intervals. The dots are the actual sound speeds measured. The dark line is a seven-point moving average. Although the sound-speeds change over this eight-day period, they change slowly. Hydrophones with closely adjacent transmission paths have similar changes. It was from these data that we developed a system for using SOFAR signals to provide accurate missile-impact location estimates.

Essentially we calibrated or measured the axis sound speed for each missile test for each receiving hydrophone. This was done by firing SOFAR charges in the missile-impact area over bottom transponders which had already been located. Ten SOFAR charges were fired before the test and ten after the test. An average measured SOFAR speed for each hydrophone was used for calculating the missile splash position.

In Figure 7, results from the Bermuda suspended phone for the first 3 days suggest a sound-speed variation with the period of a semi-diurnal tide. This Bermuda phone was at the 4000' sound-channel axis depth, but buoyed 5000' off the bottom. It was not unreasonable to suspect that this hydrophone moves back and forth with tidal currents at Bermuda. Without data on this hydrophone's movements, it is therefore impossible to state whether this is an actual sound-speed variation or an artifact of hydrophone motion. The hour-to-hour variations

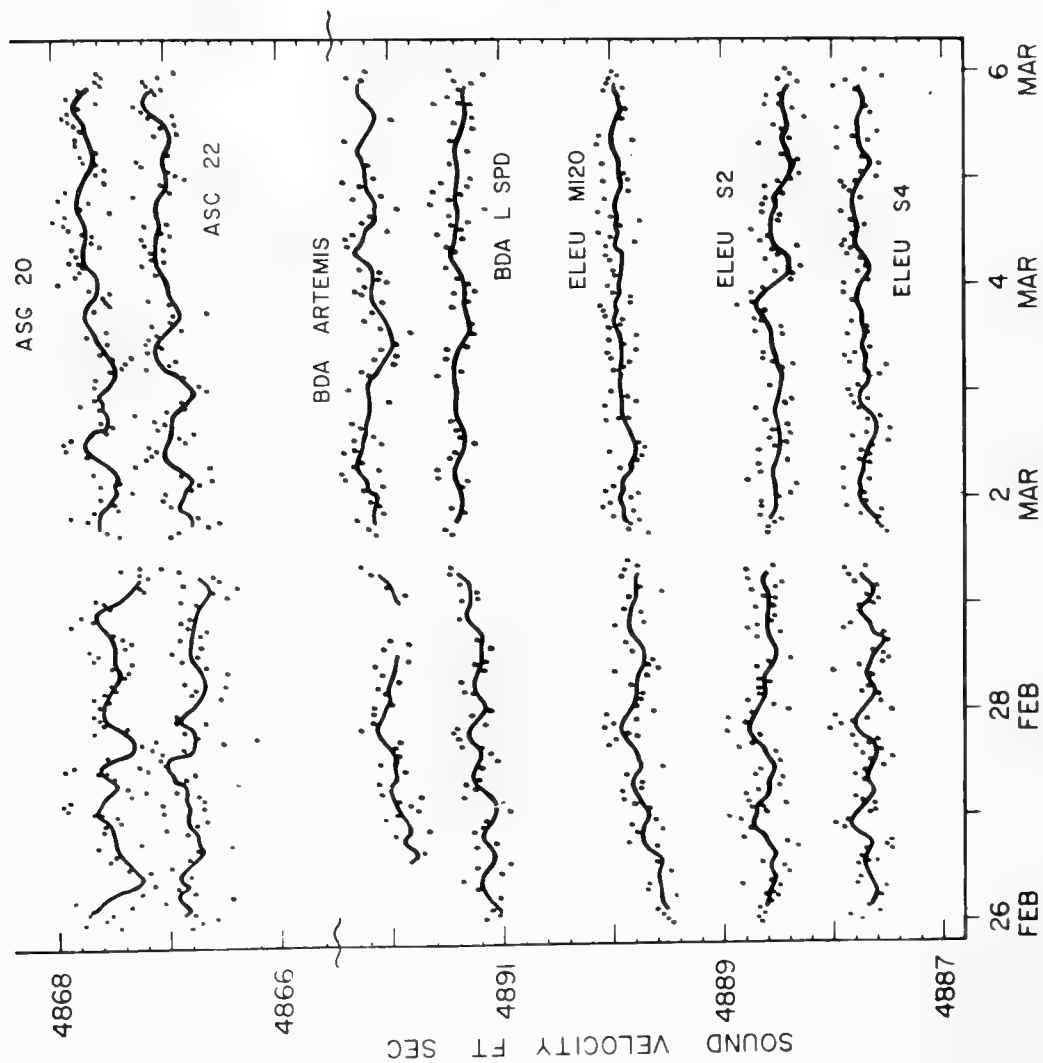


Figure 7. SOFAR AXIS SPEED VARIATIONS FROM ANTIGUA

here are of the order of 0.15 feet per second. The eight-day variation is about 0.4 feet per second.

Figure 8 data are from a series of SOFAR shots across the center of the Antigua hydrophone array on a NE-SW line to see if the axis sound speed to each hydrophone was sensitive to small changes in the source position. As shown, there is a small effect. Additional profiles would have been required to determine if this was a source-position or transmission-path effect.

Figure 9 is a record of the seawater temperature at the sound-channel axis off Eleuthera. The equivalent sound-speed variations are shown at the lower right. Shown are temperature variations in excess of 0.5°C corresponding to maximum sound-speed variations of five feet per second although more typical sound-speed variations are on the order of three feet per second.

Figure 9 also illustrates a rough comparison of the Figure 6 data for 1961, 1962, and 1963 Eleuthera hydrophone sound speeds with the seawater thermistor temperature readings. Speeds from Figure 6 are plotted as circles on Figure 9 with a vertical line drawn to the seawater temperature at that time. It is apparent that the correlation between the two is rather poor, indicating that the sound speed at the hydrophone is not the dominant factor controlling the average sound speed over this 1,000-mile transmission path.

Figure 10 is a series of sound-speed profiles in the area of the Antigua shot positions illustrating the extreme variability of the water masses in this area at axis depths. Two velocimeters calibrated to identical readings were used in this instrument package to increase the confidence that the small perturbations in the profile were real.

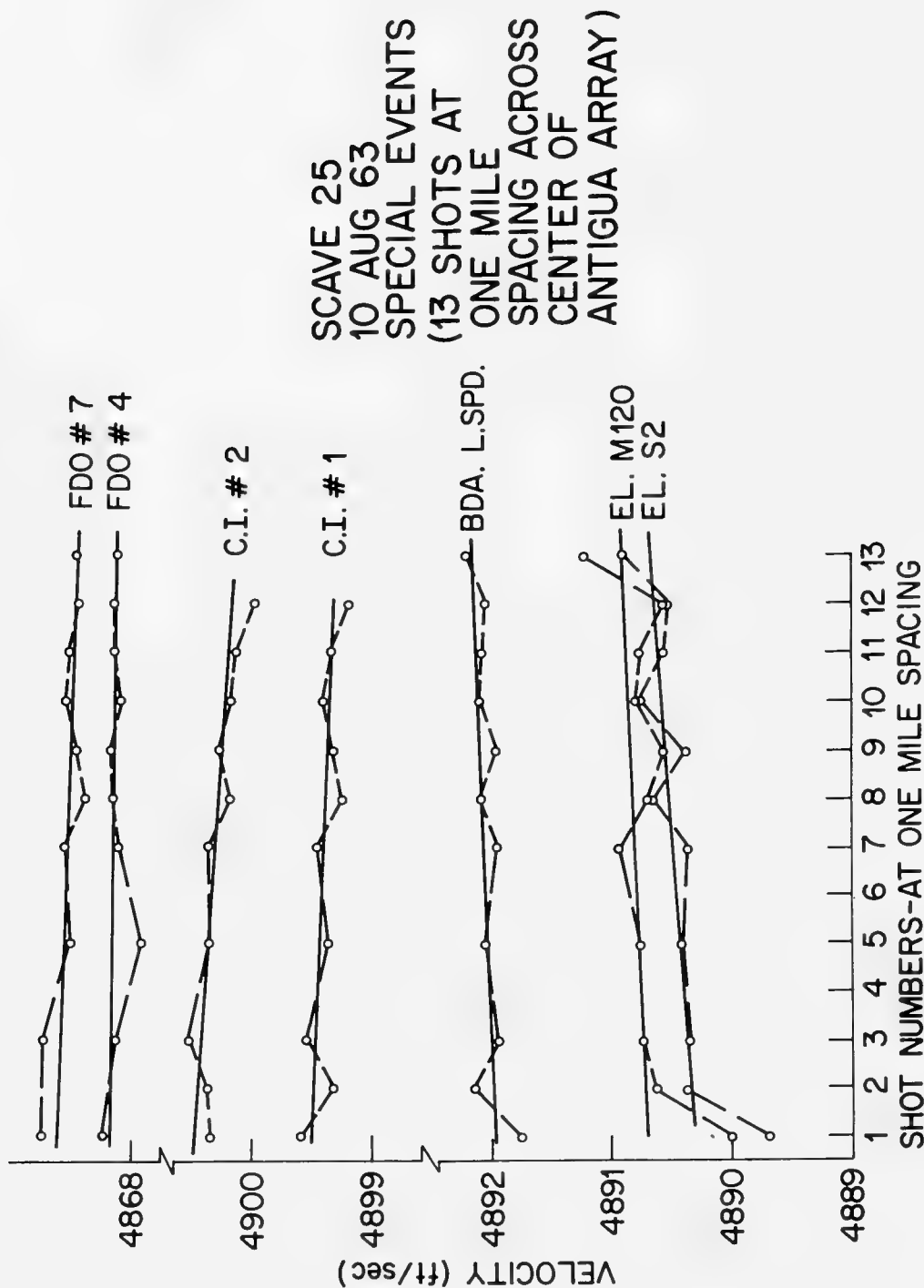


Figure 8. SENSITIVITY OF SOUND AXIS VELOCITY TO
SMALL CHANGES IN SOURCE POSITION

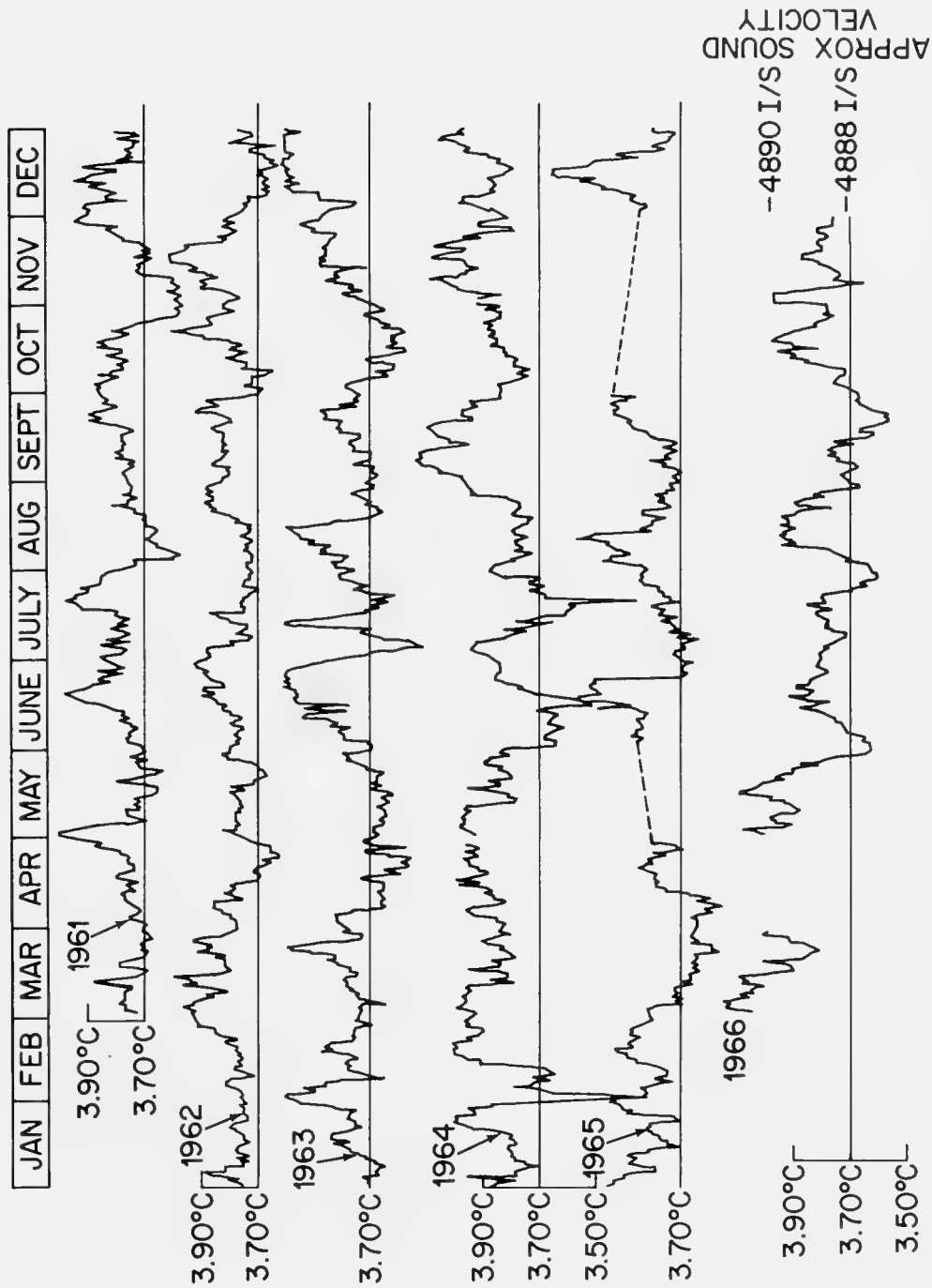


Figure 9. ELEUTHERA THERMISTOR READINGS 1961-66

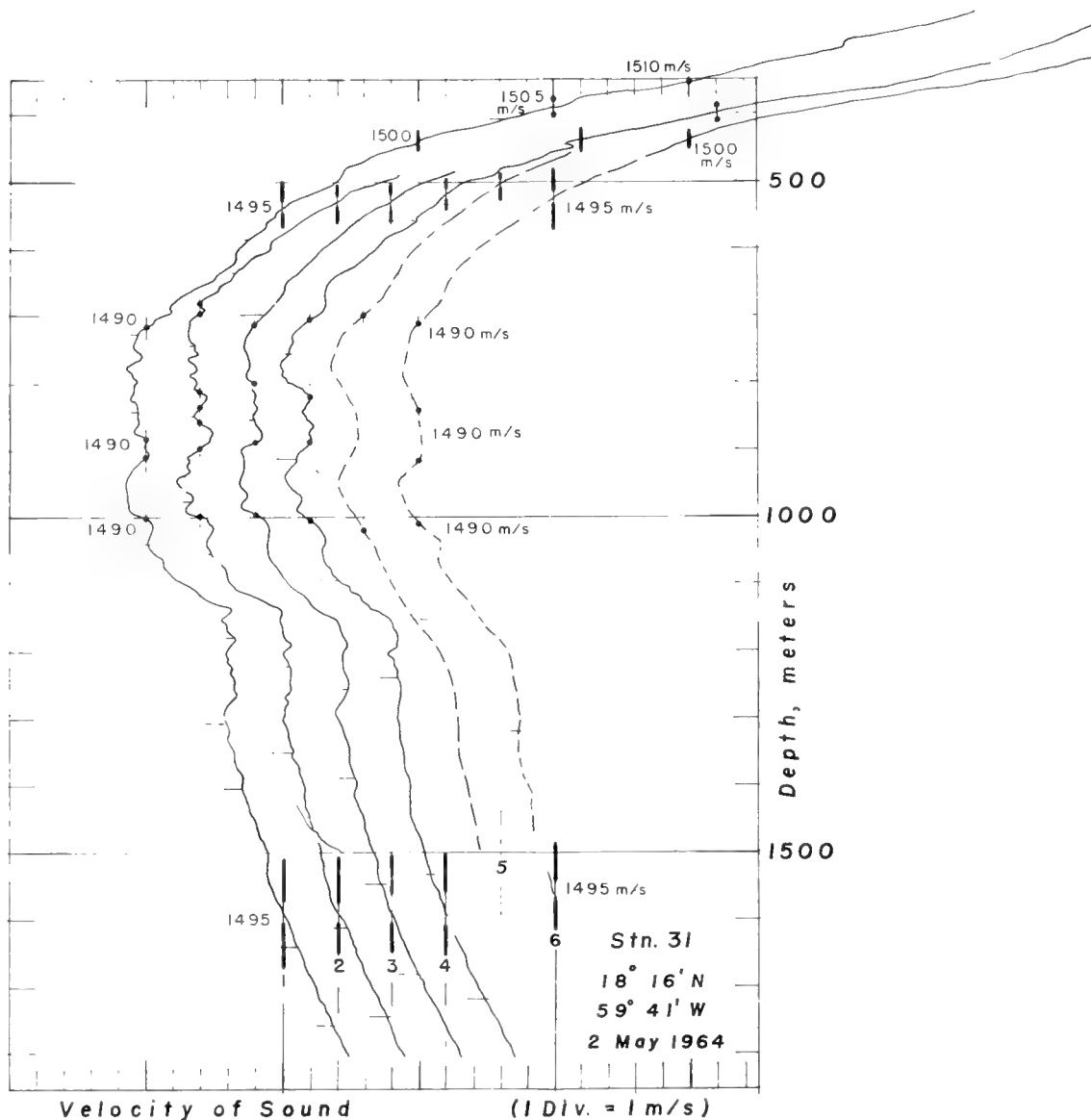


Figure 10. SERIES OF SOUND-SPEED PROFILES
ILLUSTRATING WATER-MASS VARIABILITY

Figure 11 is a series of SOFAR signals before and after a missile test as recorded at Bermuda. Shown are the scheduled detonation time, the detonation depth, the difference in the propagation speed from the average for the SOFAR timing tick marked, and the spread in range resulting from this timing tick. These SOFAR signals do not have the sharp, clean SOFAR cutoff of those fired over a flat bottom. Presumably, forward scatter from the rough mid-Atlantic Ridge topography degrades the cutoff for these signals.

Note that there is no variation in sound speed for the range of detonation depths shown. Actually, this is what you would expect for a SOFAR charge position east of Antigua. The average speed there at the sound-channel axis is of the order of 4875 feet per second. At Bermuda it's about 4890. So the axis is pinching down. This insensitivity of average axis sound speed to detonation depth was very convenient because the manufacturer making the SOFAR charges could never meet a depth spec on the SOFAR charge. We thought depth variations might cause speed variations and therefore wrote a 3 percent depth specification. The manufacturer could never meet it, but, as it turned out, it did not matter.

Summarizing the conclusions, 1) the sound channel axis speed was not stable; we couldn't predict it, and 2) neither the sound speed at the source nor the sound speed at the receiver seemed to control the average speed variation over these long transmission paths. The speed variations were apparently caused by what was happening in the water masses between the source and the receiver.

Received on Bermuda Lower Suspended from 1500 nm to SE

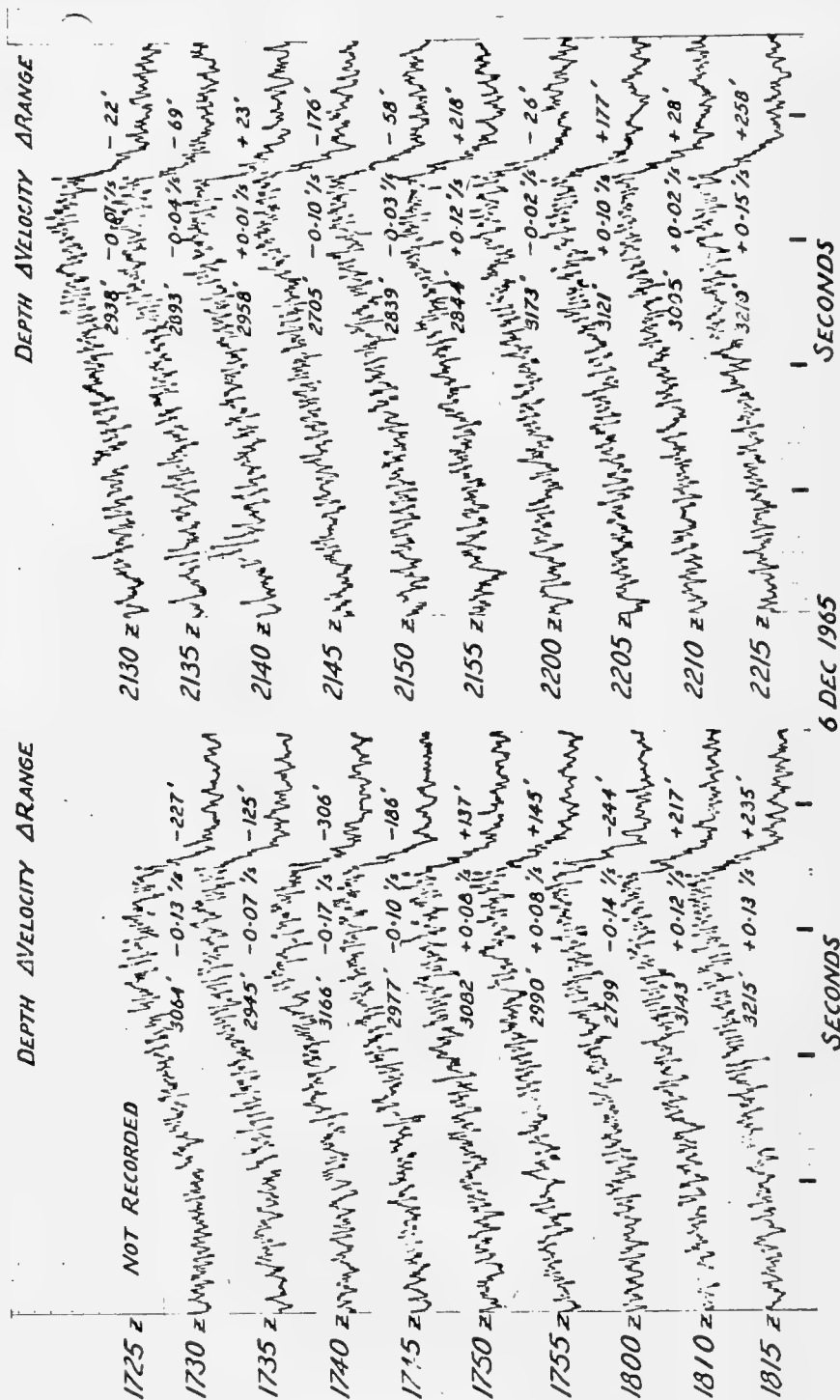


Figure 11. SERIES OF SOFAR SIGNALS BEFORE AND AFTER A MISSILE TEST

DISCUSSION

Dr. A. O. Sykes (Office of Naval Research): What do you read for the cutoff on the records in Figure 11?

Mr. Hamilton: You go through a learning cycle to determine what fits the data and gives nice results [laughter]. If the delta range is large in data such as this, the sources of error are few: 1) the shot boat position and the SOFAR detonation depth/time in the transponder array; 2) the SOFAR charge did not sink vertically; 3) the SOFAR signal cutoff timing; 4) something in the physics of sound transmission is not understood. It was never necessary to use either 2 or 4 to explain away inconsistent data.

Dr. D. C. Stickler (Applied Research Laboratory): Can you speculate about the origin of the six-month period in your sound-speed program?

Mr. Hamilton: There has been a recent series of papers by Jacobsen of RPI in JASA discussing ocean Rossby waves and their effect on acoustics. Rossby waves are similar to the 200nm diameter eddies seen by the Mid-Ocean Dynamics Experiment in 1974 between Bermuda and the Bahamas. That six-month variation is about the period of these eddies as they move westward a few kilometers per day.

Dr. Sykes: How far apart in time were the pre- and post-SOFAR shots used to calibrate the missile impact area? And how closely do the speeds correlate? Is it a matter of a day or so?

Mr. Hamilton: No, they were approximately two hours before and after missile impact.

Dr. Sykes: The reason for the question is I was trying to get an estimate from you of how close acoustic and sound-speed measurements should be made. That is, do you think a day apart is good enough? Or a week apart? Or really a few hours? Must they really be simultaneous?

Mr. Hamilton: You can see the individual variation from shot to shot in Figure 11. For this purpose the sound-speed measurement didn't seem to be very critical.

But remember we aren't talking about the rays that are going through the surface waters. We are talking about what is going along the axis. The seawater temperature at Eleuthera on Figure 9 shows no correlation with the average axis sound speed to a nearby hydrophone. The sound-speed measurement at a single site doesn't seem to be important.

The fact that variations in sound speed to the two Bermuda phones correlate so beautifully for transmission over exactly the same ocean transmission path in Figure 5 and that these do not correlate exactly to hydrophones on nearby paths for Eleuthera in Figures 5 and 6 leads me to believe that what is happening at the source is not very important.

So I am coming to the conclusion that at least for this measurement, the sound speed at either the source or the receiver is not important for the average horizontal propagation speed along the sound-channel axis.

Ms. E. A. Christian (Naval Ordnance Laboratory): It's no more important than the rest of the path?

Mr. Hamilton: Right.

Mr. M. A. Pedersen (Naval Undersea Center): I have several comments on this particular presentation. I have worked up a number of Pacific profiles for which the slowest arrival is not the axial arrival. It seems that the slowest arrival is associated with the steepness of the thermocline. That is, in one case I worked out the slowest ray formed was about a yard-per-second slower than the axial speed. And it corresponded to a ray which is turning around in the steep thermocline portion.

Mr. Hamilton: Figure D-1 shows a comparison of some typical profiles and their SOFAR signals. For the Sargasso Sea profile from the western North Atlantic, the slowest SOFAR arrival travels along the sound-channel axis. The resulting signal is in the lower left. In the typical Eastern Atlantic profile the Mediterranean outflow broadens the sound-speed minimum and increases its value, so the slowest arrival travels in the surface and bottom grazing ray paths. This SOFAR signal is on the lower right. In the Pacific profile, the SOFAR signal is shorter as shown in the middle bottom trace. It is actually quite similar to what a western North Atlantic SOFAR signal looks like if you eliminate the rays that penetrate the 18°C Sargasso water. In the Atlantic where you have the Sargasso water in the surface 500 meters, this high sound speed near surface water gives the early SOFAR arrivals in the lower left SOFAR signal.

I ran into the Eastern Atlantic SOFAR signals a few years ago. When I saw these signals, I assumed they were from surface shots and made some stupid statements to that effect. I then realized that the Eastern Atlantic was a different ocean entirely with this entirely different profile, that it just reverses the SOFAR signal completely from the classical one Dr. Worzel published, 25 years ago.

HAMILTON: TIME VARIATIONS OF SOUND SPEED OVER LONG PATHS IN THE OCEAN

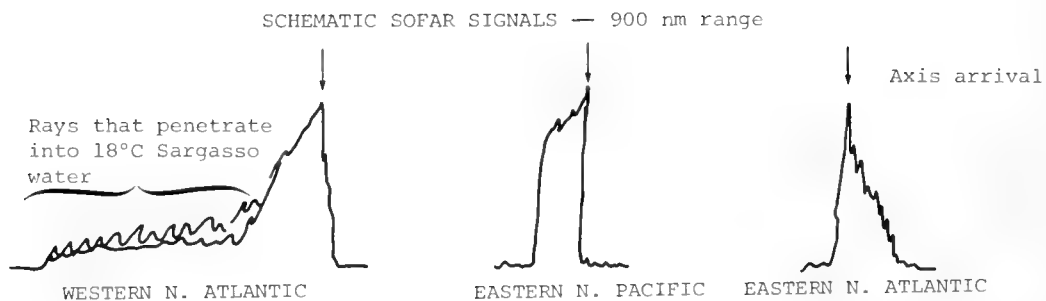
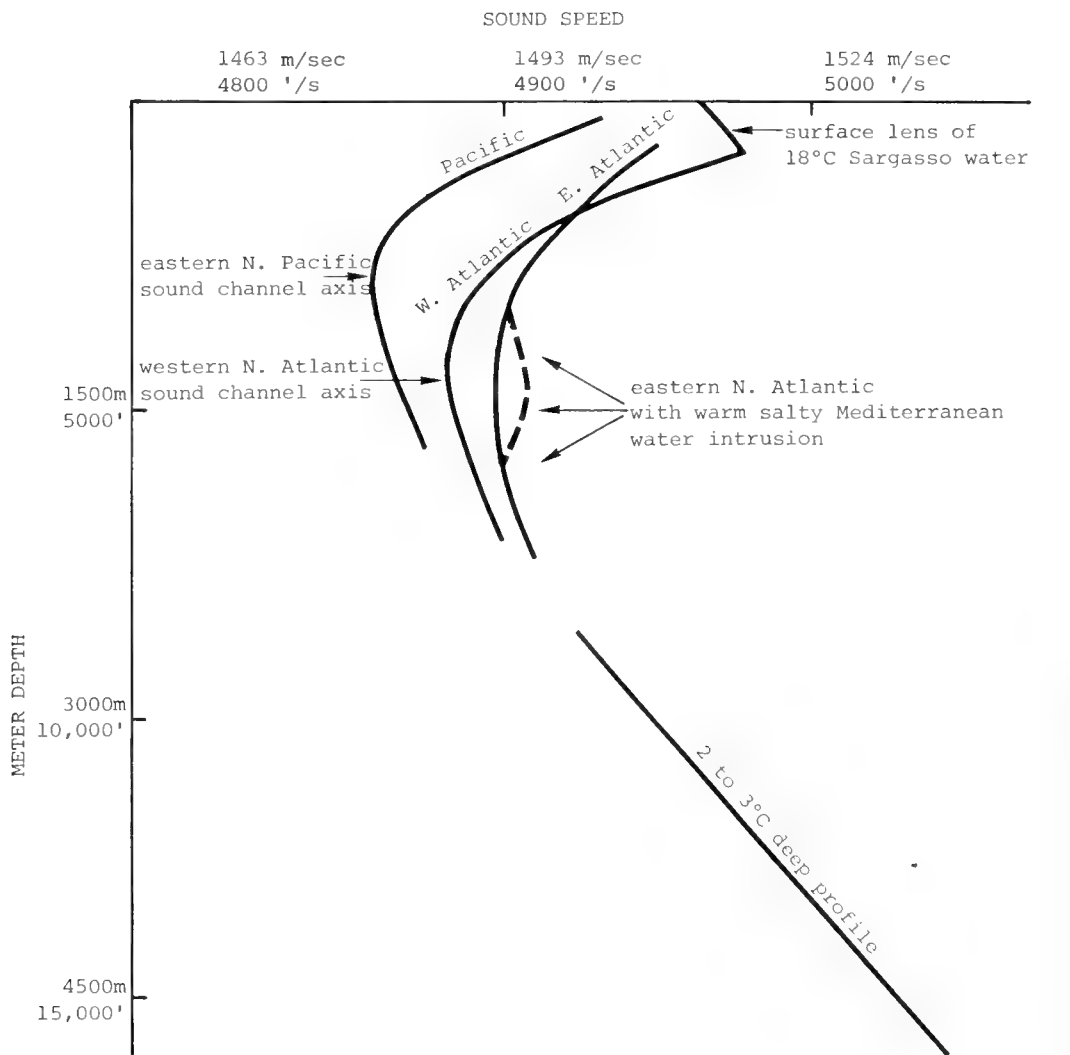


Figure D-1. SCHEMATIC SOUND SPEED PROFILES

Dr. R. P. Porter (Woods Hole Oceanographic Institution): Were you able to resolve any other arrivals besides the axial arrival? In other words, could you say there were specifically other paths that stood out that might have been rays that were going through water with a higher sound speed?

Mr. Hamilton: We occasionally would see it on the first group of arrivals when we had a suspended hydrophone. Within a group we would see the individual arrivals corresponding to the up- and down-going paths on both ends. These were apparent for the earliest orders, and then they start to get closer together, effectively overlapping.

Dr. Porter: Would you see this arrival structure then build up in the final arrival? In other words, could you analyze those shots in terms of the individual arrivals themselves prior to the axial arrival, because if you could do that, then you could possibly look at some of the average sound speeds through the remaining part of the water column.

Mr. Hamilton: Most of our work was at ranges like a thousand miles, and the cycling of the groups is about 30 miles, so we are talking about 30 of the groups building up into the final peak. We might see the first and the second, but after that it pretty much ran together. It didn't look to us at the time like an interesting problem to work on, and we didn't look at it.

Dr. W. B. Moseley (Naval Research Laboratory): In your data, the temperature variability at neither the source nor the receiver appears to directly correlate with the travel-time variability. However, if you were dealing with the same water mass type throughout the range, would you expect the statistics at either of the end points to correlate with the statistics of the arrival time?

In other words, could you simply measure statistics at the end points, or do you really need measurements throughout the entire path?

Mr. Hamilton: Are you asking whether one could take statistics at the source and at the receiver and compute the average transmission velocity?

Dr. Moseley: No, compute the statistics of the variability of the average travel velocity.

Mr. Hamilton: Yes. However, in this problem statistics don't help very much since the problem was: What is the actual range from the launch pad to the impact point expressed as a deterministic, accurate value? If the speed variation over that thousand-mile path were plus or minus a foot and a half per second, it would equate to a location uncertainty path of 1,800 feet. So we really weren't interested in the statistics. We had to have as accurate a value as we could at the time.

The Acoustic Output of Explosive Charges

Ermine A. Christian

White Oak Laboratory
Naval Surface Weapons Center
Silver Spring, Maryland

Although small explosive charges are widely used as sources for underwater acoustics studies, a number of unresolved questions exist concerning the proper source levels for use in data analysis. At the present time there is no generally accepted "standard" set of source levels, and deviations of 5 to 10 dB can be found among published values. Better information is needed to define a reference range beyond which finite amplitude effects are negligible. Spectral energy levels are sensitive to charge detonation depth, an experimental variable that typically is not controlled in acoustic experiments. These and other problem areas associated with explosion sources are reviewed with comments on their quantitative effects at low frequencies.

INTRODUCTION

I am well aware that the members of this acoustic community are not, in general, entranced with the beauties of explosions physics. It is a delightfully complex subject that is simply a pain in the neck to someone who wants a neat, simple source for underwater acoustics research work.

Unfortunately, in today's sophisticated world we are trying to do a number of rather closely controlled experiments. We are looking for subtle effects, small differences, and we are looking for detailed frequency dependencies rather than the broad-brush quantities that sufficed a decade ago. This means we can no longer gloss over inherent characteristics of the pressure waves generated by explosions, even though they may be uncomfortably complicated. So let me be a purist

for a few minutes and talk about an explosion wave as it really is, rather than as acousticians would like it to be.

Desirable attributes of sources for use in low-frequency acoustic work are much the same, whether the sources are CW transducers or are explosions. For use in the field it is desirable to have sources that are reliable, inexpensive, with a high energy output at the desired frequency range, and convenient and simple to operate under field test conditions. For use in data analysis, it is desirable to have known standard source levels, source level values that are compatible with the sonar equation, and values that are predictable within some specified decibel allowance in a narrow-band frequency. Explosion sources often come out ahead when considering field-use desirability, which is why they are used so widely for underwater acoustics research. But for the analysis end of the problem, explosions sometimes seem to be intractable. Today I will show you some of the reasons this is so.

For today's discussion, let me use values of bandwidths and frequency ranges and prediction errors that I have heard discussed within the past year as being desirable in acoustics research work. (It may be that during the course of this Workshop these values will be modified. If that is the case, I will only say that I hope all of them will increase, from the point of view of our ability to utilize available information today.) We would like source levels in 1/3-octave bands. And we want these levels to be predictable to within 1 dB, over the frequency range of 10 to 300 Hz. Here I purposely use the word "predictable," rather than "reproducible" to within 1 dB. Reproducibility is not the problem with the explosive compositions usually used in acoustics work. If you replicate the experiment — the charge type and depth, the measurement point, the recording and analysis

systems — you reproduce the pressure-wave output within a few per-cent.* Predictability, however, is another matter.

Given these quantitative constraints — source levels predictable within 1 dB in 1/3-octave bands over the frequency range 10 to 300 Hz — we are in rather poor shape for analyzing data taken with explosion sources. We do not have known, standard source level values. We have problems with sonar equation compatibility. And we very definitely have problems with our 1 dB error allowance.

I don't think we need much discussion on the question of known, standard values. Everyone in this room who has used explosion sources is aware that among the published values in the literature, the in-house publications, and the backs-of-envelope working papers we all turn to, a wide assortment of source level values can be found. These values vary perhaps by 5 dB, perhaps more, depending upon the bandwidth of interest. In fact, the question is so wide open that I have wondered if data reduction sometimes follows the line of "when in doubt, blame the source level; and then look around until you find one you like better."

To mention a few of the many names that are familiar to source level seekers, we have Weston's (1960) benchmark paper that is still widely used. We have Stockhausen's (1964) data, measurements reported by Turner and Scrimger (1970), Maples and Thorp (1970), Buck (1974), and Christian (1965, 1967). Oh, there is no dearth of source level values. But they do not add up to our desired "known, standard

* With some of the more exotic explosive materials there are problems with reproducibility; the charge output may vary with charge size, with the formulation, or with the density. But these materials are not found among the standard acoustic sources.

values." It is true, of course, that the visible problem is not as great for the lowest frequencies of interest as it is for higher frequencies. Many of the above references do not look at the very low frequency end of the scale.

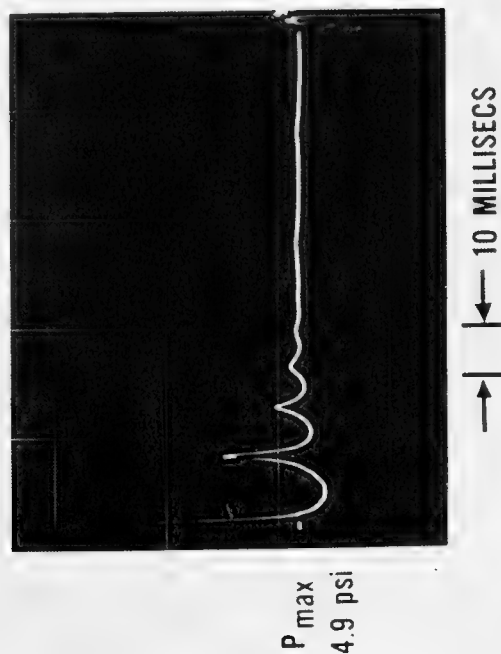
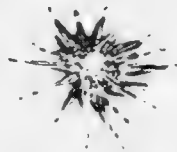
SONAR EQUATION COMPATIBILITY AND PREDICTABILITY

In order to examine the problems of sonar equation compatibility and predictability, we must face up to the nonlinear nature of explosion pressure waves. Before getting into that discussion, let us take a brief refresher look at the time and frequency domain functions in this explosion pressure field.

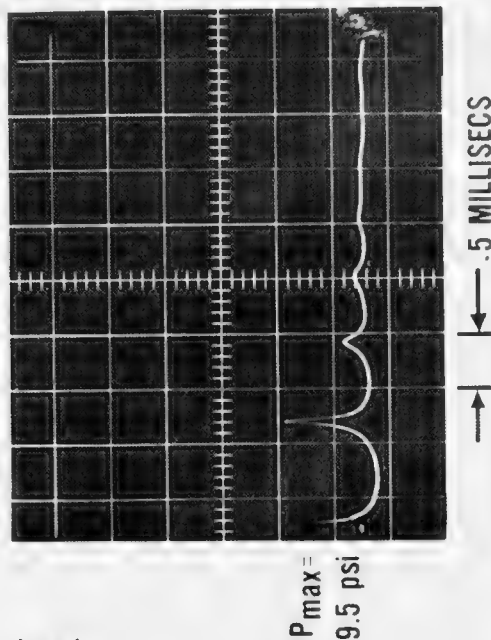
Figure 1 shows two typical pressure-time histories for underwater explosions, recorded with the special-purpose equipment designed for such measurements. The experimental setup is shown at the top of the figure. Charges were fired at depth and recorded at the surface above. The record on the left is from a 57-pound TNT charge detonated at 6,600-foot depth. That on the right is from an 8-pound TNT charge at 2,050-foot depth.

These pressure-wave records show the usual high-amplitude shock wave followed by the succession of pulses associated with the oscillating bubble of product gases. There are scaling laws for explosion pressure waves of this sort, in terms of explosive charge material, weight, and depth of detonation. Unfortunately (from the point of view of simplicity), these scaling laws contain different coefficients and exponents for different segments of the pressure wave; and therein lies the problem that you will hear more about later.

The frequency domain representation of an underwater explosion pressure wave, such as Figure 2, is also familiar. But in our everyday



57-POUND TNT CHARGE AT 6600 FOOT DEPTH



8 POUND TNT CHARGE AT 2050 FOOT DEPTH

Figure 1. PRESSURE-TIME RECORDINGS ABOVE DEEP EXPLOSIONS

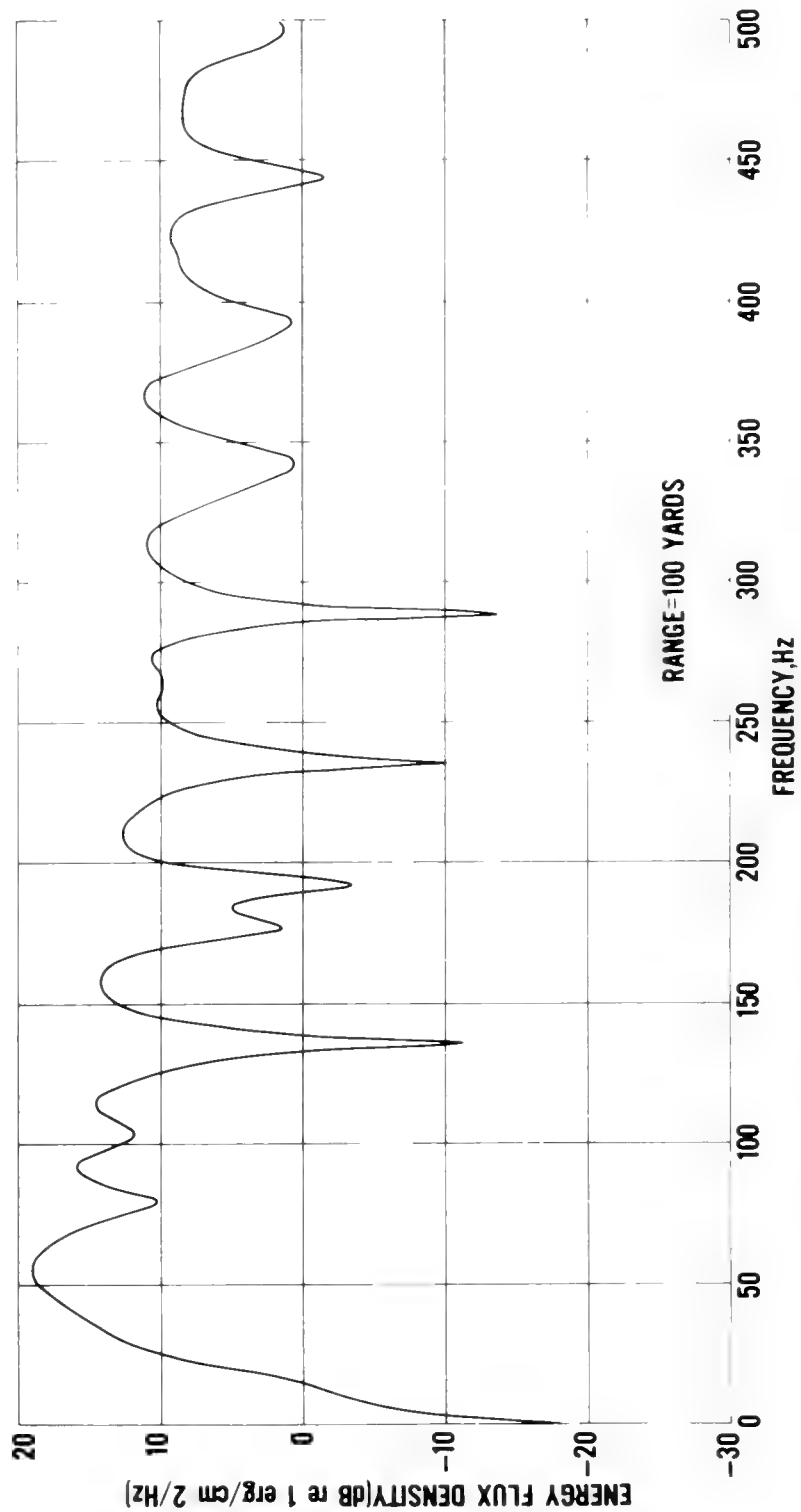


Figure 2. IDEALIZED SOURCE LEVEL --- 1.8 LB OF TNT AT 800-FT DEPTH

treatment of explosion data, where we usually study only narrow-band slices of the spectrum taken near selected frequencies, we may forget the oscillatory character of the spectral energy distribution. We find the highest spectral energy at the so-called "bubble fundamental frequency," which corresponds to the first bubble period spacing in the time function. We find minor irregularities in the spacings of the first several harmonics while the second and third bubble pulses are getting shaken out. And after a while, the pattern stabilizes, and we have a regularly spaced series of peaks and nulls. I must point out that true nulls are in the spectrum, even though they are not conspicuous at the higher frequencies in Figure 2. This is a computer-generated plot. The computational grid size used and the characteristics of the plotter control details of the picture. Lest you hope to find these oscillations smoothing out at long ranges, or start thinking of clever ways to clean up the source level curve by smoothing or filtering (e.g., Skretting and Leroy, 1971), let me show you one of Gordon Hamilton's sonagrams of signals recorded some 500 miles from explosions (Figure 3). The horizontal axis is time and the vertical axis is frequency (0 to 500 Hz). Those alternating light and dark horizontal bands corresponding to no-energy and high-energy show that neither distance nor manipulation can smooth out the true source spectrum.

Naturally we are going to have problems in fitting explosion source levels into the sonar equation, where quantities are added and subtracted in a comfortable linear fashion. The translation of "compatibility with the sonar equation" into more explicit prosaic terms is summarized in Figure 4. What we mean is that we wish there were no finite amplitude effects; no nonlinearities; no inherent change in wave shape or frequency distribution as the wave propagates outward, so that all observed changes could be ascribed to the medium.

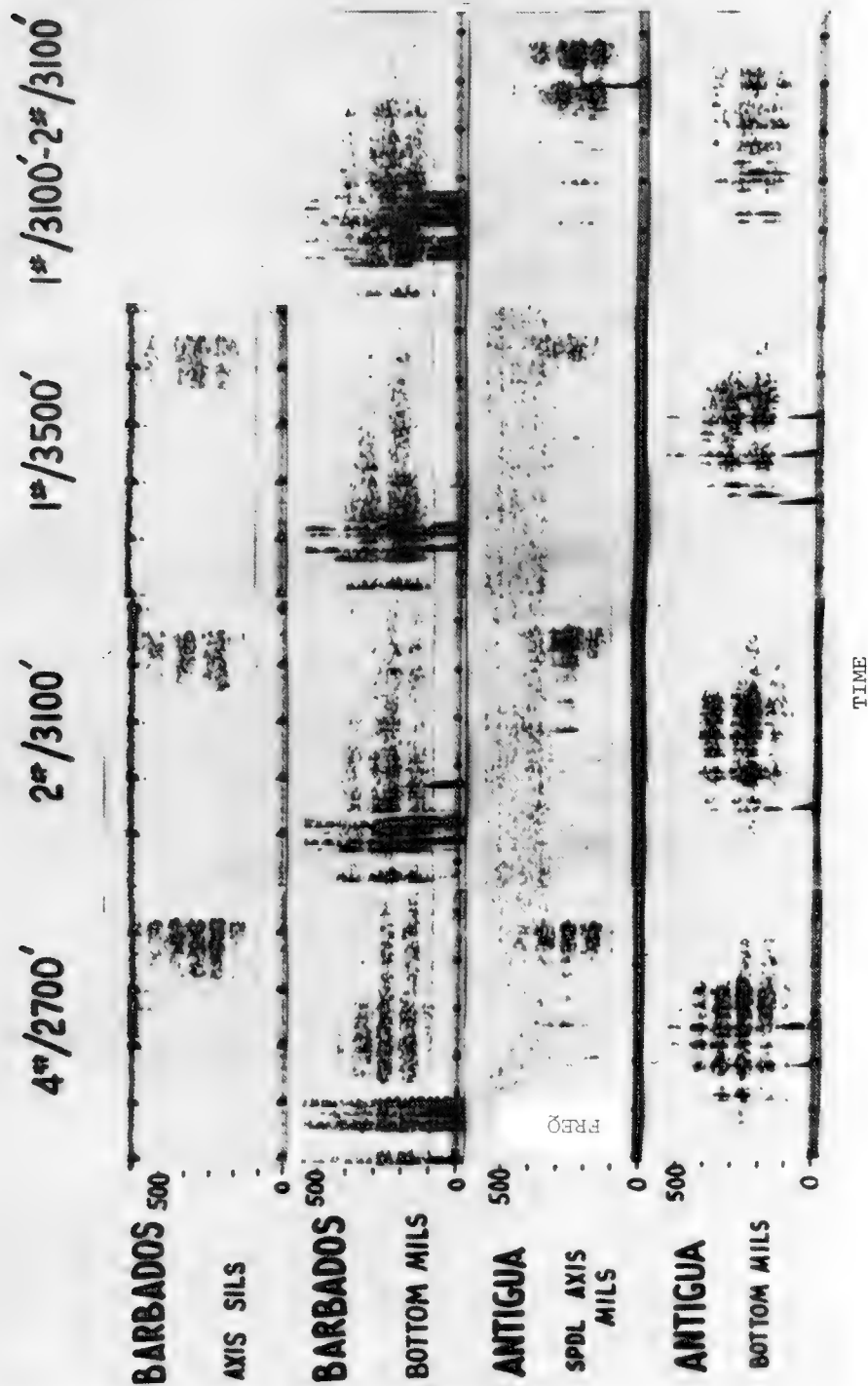


Figure 3. BUBBLE PULSE FREQUENCY — CLOSE SHOTS AT 500 NM

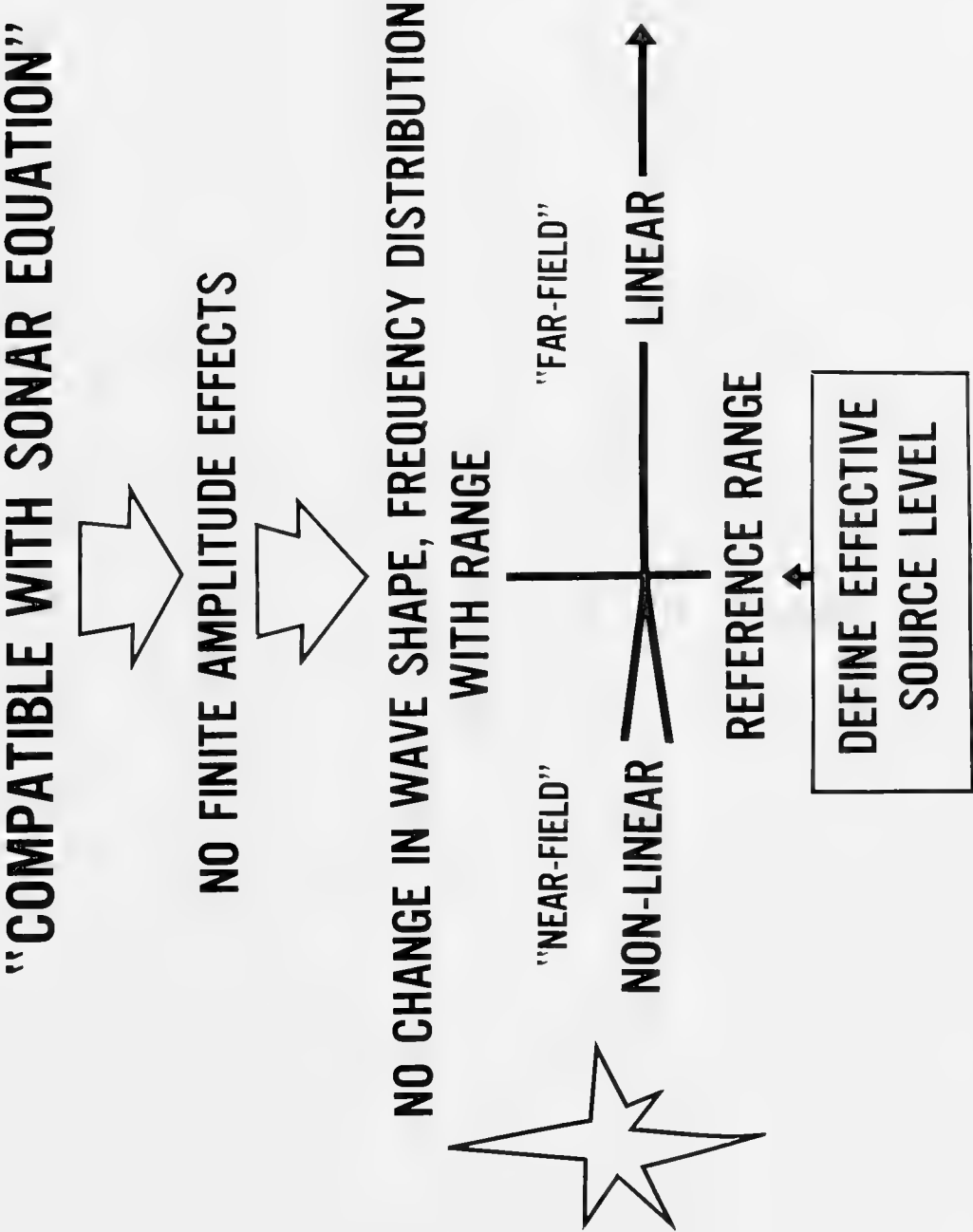


Figure 4. TRANSLATION OF "COMPATIBILITY WITH SONAR EQUATION"

The customary method of getting around the finite amplitude problem is indicated at the bottom of Figure 4. Just go a sufficient distance from the charge so that the nonlinear effects from that point on are negligible for the application of interest, call this a "reference range," and there define an effective source level which can then be used to examine the signals measured at greater ranges. This practice was initiated by Weston, who chose a 100-yard reference range. And for the fairly small charge weights and detonation depths that Weston was treating, most of the finite amplitude effects are, indeed, negligibly small beyond 100 yards range. Unfortunately, such quantities have a way of becoming gospel and being dissociated from the physical facts that led to their selection.

The 100-yard reference range by now has become a sort of junction through which source levels are shuttled at a rate of $20 \log R$. If you want to compare different measurements made at various ranges — a half mile, a mile or so — assume spherical spreading and extrapolate them to 100 yards. If you are enamored of the sonar equation's one-yard reference range, just add 40 dB to the source level. We rarely find experiments with data taken on a closely scaled grid that allow us to see the rate at which finite amplitude effects are varying, and to sort out all effects of the medium. So we often are trapped in the circuit of using our desired information to reduce available data to try to improve our desired information. We must break out of this circuit if we really want to know effective source levels within 1 dB for an assortment of charge weights, depths, and frequency bands.

The fact is that the appropriate reference range for defining effective source level is itself a function of the charge weight, the charge depth, and the frequency band of interest. I know of no

theoretical treatment that takes as input an explosive charge composition, weight, and depth and gives in return realistic, reliable pressure-time histories at any desired range. This problem has been worked on for many years, and we are coming closer than Kirkwood and Bethe might have hoped for. But we are still in an empirical world when trying to examine source levels parametrically.

Let me show you a sample of data that illustrates the kinds of wave-form changes we have to deal with. In Figure 5 some recorded pressure waves are sketched on the right, and the experimental arrangements used to record them is shown on the left. We lowered a small oscilloscope housed in a 30-inch diameter sphere down to about 14,000 feet. A tourmaline gage was suspended below the sphere, and 50-pound pentolite spheres were suspended some 200 to 1,000 feet below the gage. We also had pressure sensors near the surface above the charges.

In the pressure waves shown on the right of Figure 5, solid lines represent the data measured with the deep oscilloscope near the charge, and dashed lines represent the same pressure wave measured near the surface. The upper pair of curves are for a charge fired 190 feet below the deep gage; the lower pair are for a charge 935 feet below the gage. In both cases, the pressure waves for the deep (near-field) and shallow (far-field) recordings are plotted on scales in the same ratio as the stand-off ranges. In other words, had the waves propagated without changes of shape — simply decreased in amplitude at the acoustic rate of $1/R$ — the solid and dashed curves would coincide. The top set of curves, where measurements are compared for ranges of 190 and 13,690 feet, shows the well known shock-wave "finite amplitude effects" of a spreading profile and a peak pressure that decays more rapidly than $1/R$; it also shows that the same nonlinear behavior is followed in the first bubble pulse.

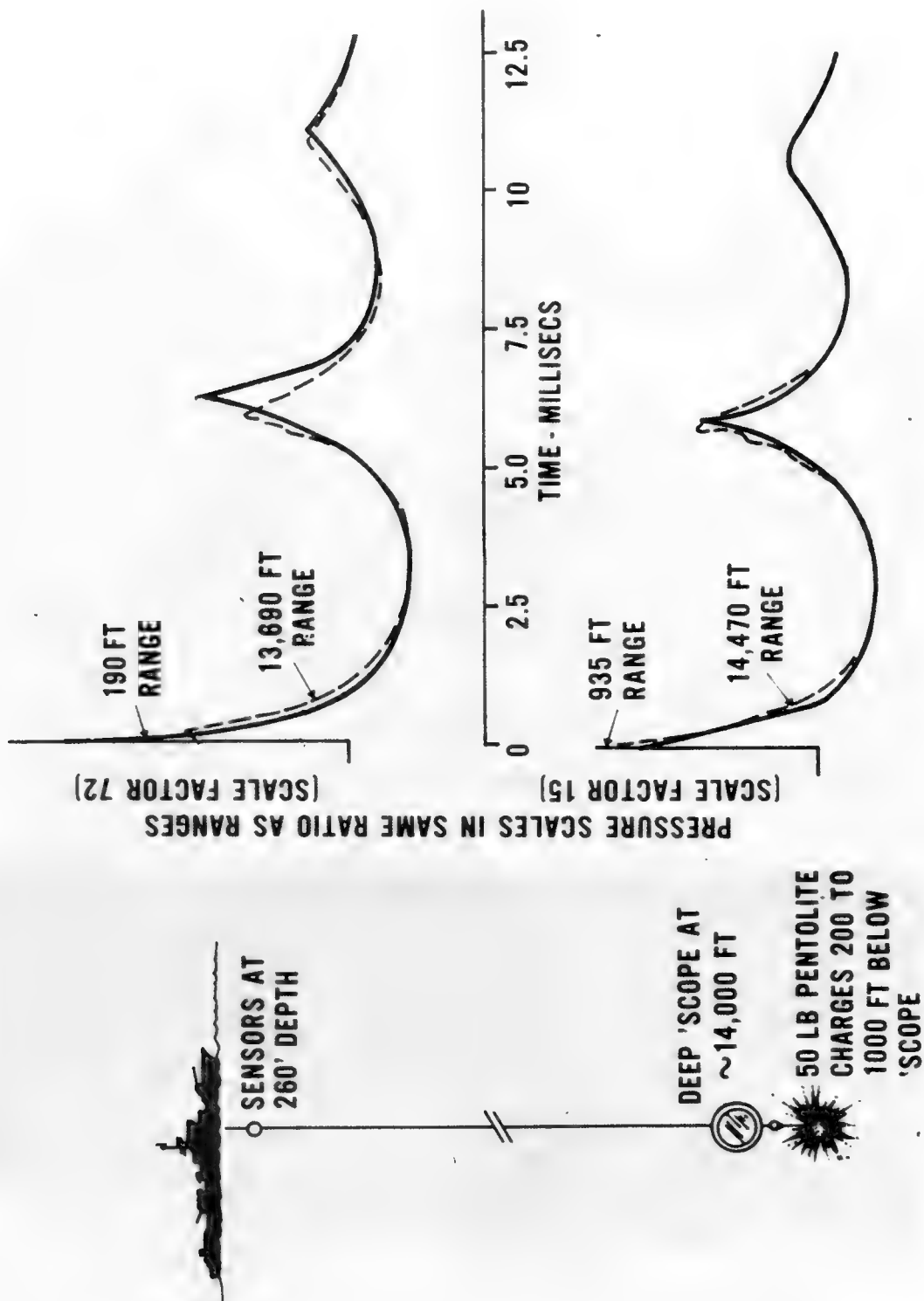


Figure 5. ILLUSTRATION OF PRESSURE WAVE EXPERIMENT

In the lower set of curves, where the close-in measurement was at a 935-foot standoff, the near-field and far-field curves are nearly coincident. This might suggest that perhaps 300 yards is a reasonable "reference range" for a 50-pound charge at 15,000 foot depth.

The quality of these few exploratory data is too poor, and the extent of them too limited, to give the kind of information on source level that we need. But they do show that we must re-examine the subject of reference ranges. This is not an academic question. I am convinced that the methods of extrapolating and interpolating among different sets of measurements contributes some of the variation found in reported source levels. And that the choice of reference range is important to the third and last of our desirable source attributes: predictability to within 1 dB in 1/3-octave bands.

FACTORS IN SOURCE LEVEL DETERMINATION

As noted earlier, we must still look primarily to empirical, rather than theoretical, methods of determining source levels. Even if we had an infinite, homogeneous ocean in which to work, source level determination would not be easy, because so many factors enter into the acquisition of the right number. The following list shows the major factors in more-or-less decreasing order of importance:

- CHARGE CHARACTERISTICS
 - Weight
 - Depth
 - Explosive Composition
 - Configuration
- MEASUREMENT RANGE (discussed above)
- RECORDING EQUIPMENT CHARACTERISTICS
- PROCESSING METHODS

Let me work up from the bottom of the list and give a few examples of the kinds of variation we have found influencing that desired 1 dB predictability in 1/3-octave bands.

Processing Methods. The most obvious source of differences from processing methods is, of course, the fact that some people use analog and others use digital processing. Even with digital processing, however, we have been surprised to find how easily some tenths of dB differences crop up. We recently made a joint study with another laboratory of selected data tapes — some we had recorded and some they had recorded. After overcoming the numerous communication problems involved in exploring our two "standard FFT programs" (and this took no small effort), we still found several computational details that introduced greater differences than one would expect. For example, simply changing the frequency interval of computation by a small amount introduced as much as 0.8 dB difference in the 1/3-octave band centered at 25 Hz on some of the records, but not on others. At 25 Hz, the 1/3-octave band is so narrow that the level is quite sensitive to small computational manipulations. This exercise reminded us again of how wary one must be of applying routine analyses without carefully examining their suitability for a particular spectral energy distribution.

Recording Equipment Characteristics. The importance of this factor is so well known that I will mention only one point that may be of interest. (We are speaking only of equipment that is fully calibrated, of course.) My example has to do with equipment overload. Overloading is familiar to underwater acousticians using explosion sources. One would like to think that in an overloaded recording the low-frequency content is still usable and that the signal has simply suffered high-frequency clipping. Figure 6 shows an analytical quick-look at this question, using an idealized

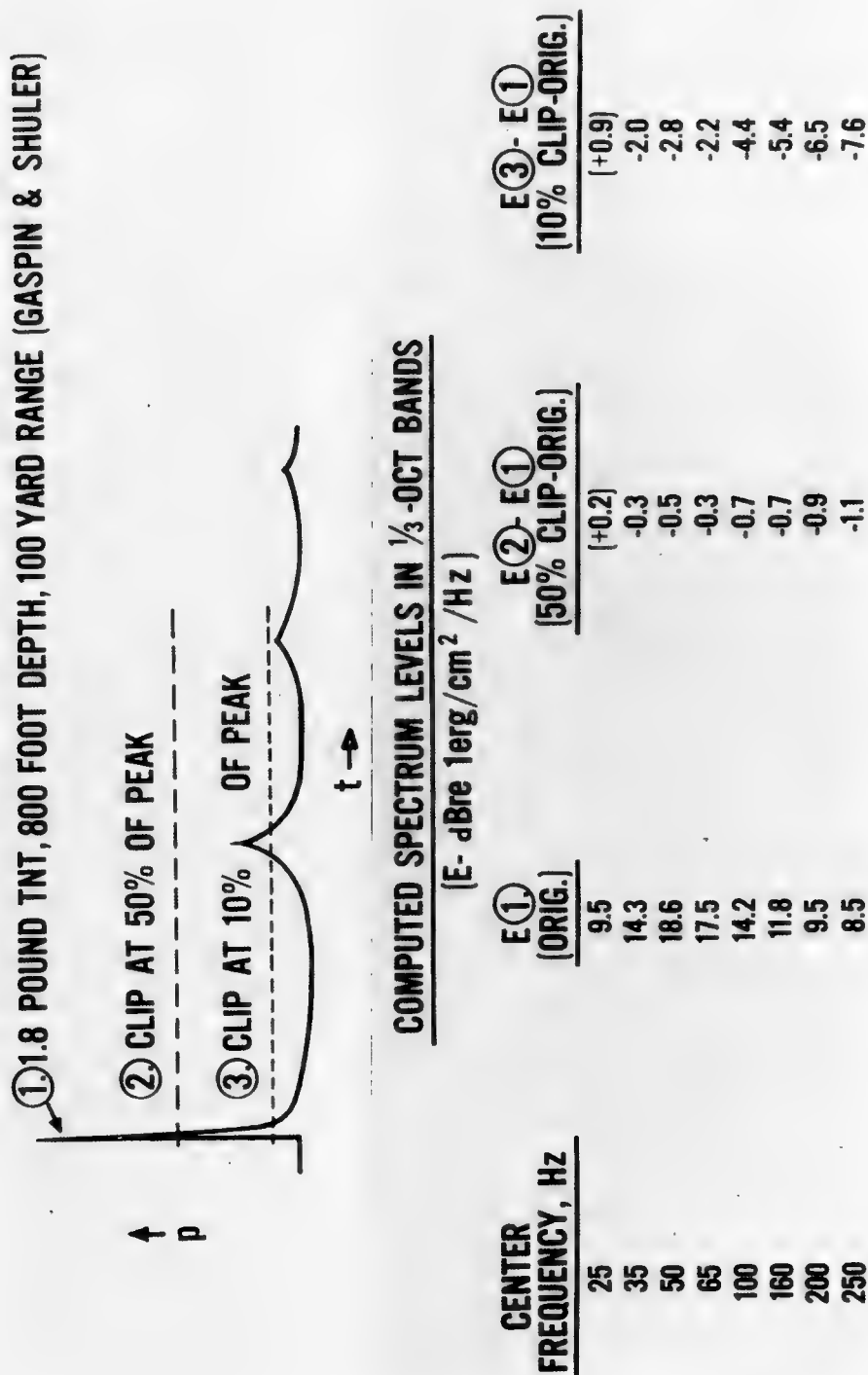


Figure 6. RECORDING EQUIPMENT OVERLOAD

pressure history for a 1.8-pound TNT charge at 800-foot depth. This curve (1) was "clipped" at 50 percent of the peak value (curve [2]), and again at 10 percent of the peak value (curve [3]) by the computer. We assumed the most amiable system imaginable, and calculated the spectrum levels in 1/3-octave bands for the two "clipped" records. The resultant decreases in levels at the low-frequency end of the spectrum are tabulated at the bottom of the figure.* When clipped at 50 percent of the peak — a matter of a few dB — the resultant error had reached 1 dB in the 250-Hz band. With a 10 percent of peak clipping, the error was twice our desired 1 dB even down at 35 Hz. Perhaps down at even lower frequency — one Hz or so — the 10 percent clipping would not matter. But I think clipped records have to be handled cautiously. And remember that the possible distortions imposed by a system without instantaneous recovery are not included in this example.

Charge Configuration. The variations in explosion pressure fields that we can achieve simply by distributing our explosive material in different configurations is a complex subject that I will not even try to touch on today. This discussion is limited to compact, consolidated, "point" charges that are omnidirectional. But if you want to modify your spectral energy distribution with a given weight of explosive, the quickest way is through charge configuration, and we know a fair amount about the subject.

Explosive Composition. We can accomplish some redistribution of spectral energy through choice of explosive composition. The bubble fundamental frequency is a function of the charge weight, the charge depth, and a material constant. The constants do not differ

* The positive values in parentheses for 25 Hz are spurious and mirror our failure to do a DC leveling when we clipped the wave.

appreciably for typical high-explosive material such as TNT, pentolite, and RDX. But they are changed significantly when aluminum is added to the explosive mixture. For example, HBX-3, which is a particular mixture of RDX, TNT, and aluminum, has a bubble period that is about 25 percent greater than the bubble period of TNT. Consequently, the bubble fundamental frequency, and the frequency spacings of subsequent peaks and nulls in the spectrum, are only about 80 percent as great as those of TNT. This is illustrated in Figure 7, where dashed and solid lines refer to HBX-3 and TNT, respectively. These curves are computed from simplified analytical representation of the pressure waves. The differences in 1/3-octave band spectrum levels of these two materials are tabulated on the right-hand side of the figure. At the lowest frequencies, while the curves are still increasing toward the first peak at the fundamental, the band level for HBX-3 is several dB higher than that of TNT. As one moves up in frequency, however, it becomes a game of catch-can, and which of the two materials has the higher energy level depends on the location of the particular frequency band. In any case, we expect serious trouble if we try to compare narrow-band data from two such different materials without accounting for their different source spectra.

Charge Weight and Depth. I would like to discuss these two important quantities together for a moment, to describe a method of source level prediction used by Gaspin and Shuler (1971). The technique involves first generating a quasi-theoretical pressure-time history, such as that shown in Figure 8, and then transforming to the frequency domain. The pressure-time curve is fitted through a series of points (indicated in Figure 8), the coordinates of which are derived from empirical functions as shown in Figure 9 (Slifko, 1967). The curve of Figure 9 allows one to estimate the amplitude of the first bubble pulse, P_B , for selected values of charge depth, Z_O ,

1.8-LB AT 800 FT DEPTH ,100 YD RANGE

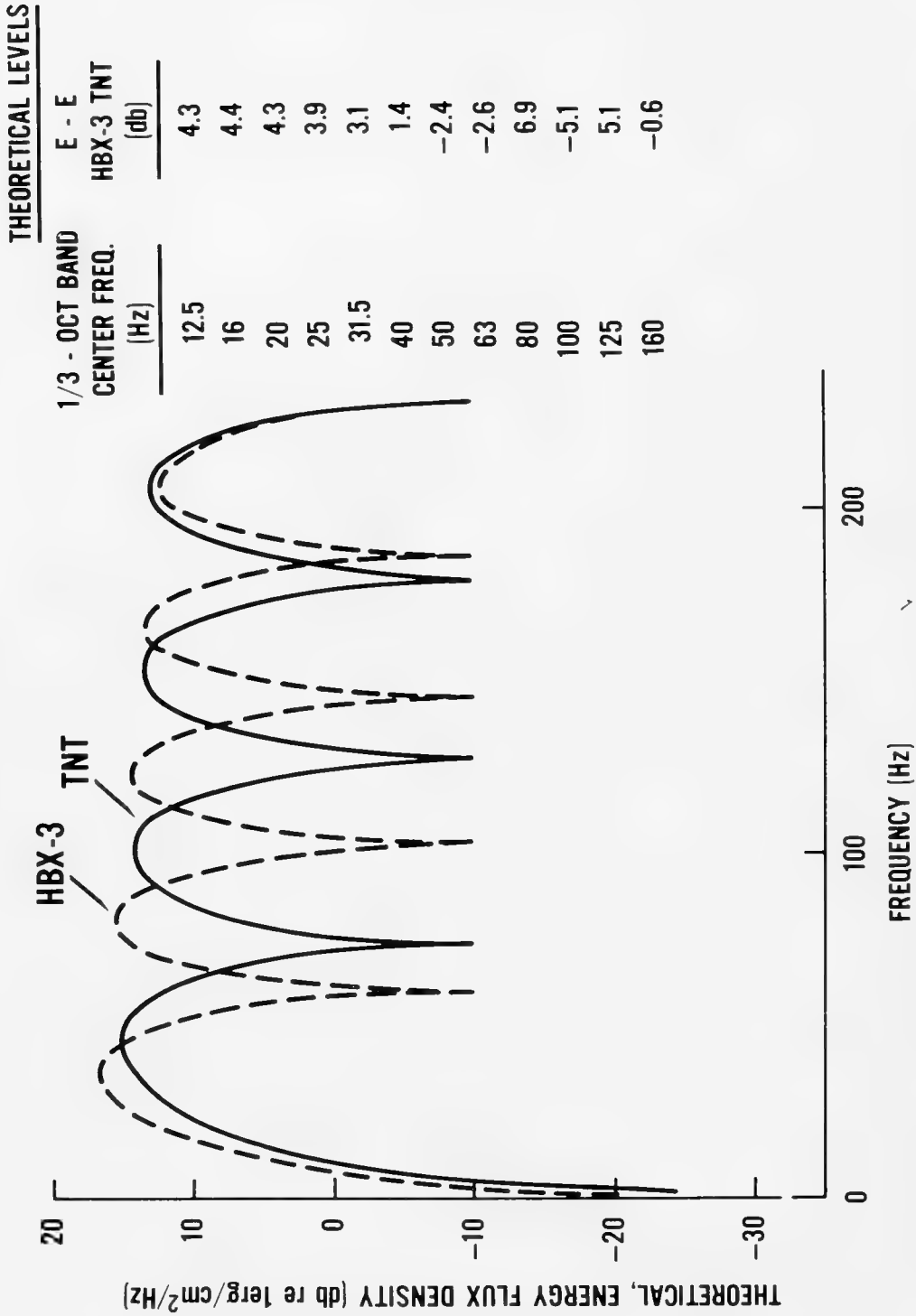


Figure 7. SPECTRA COMPARISON OF HBX-3 AND TNT EXPLOSIVES

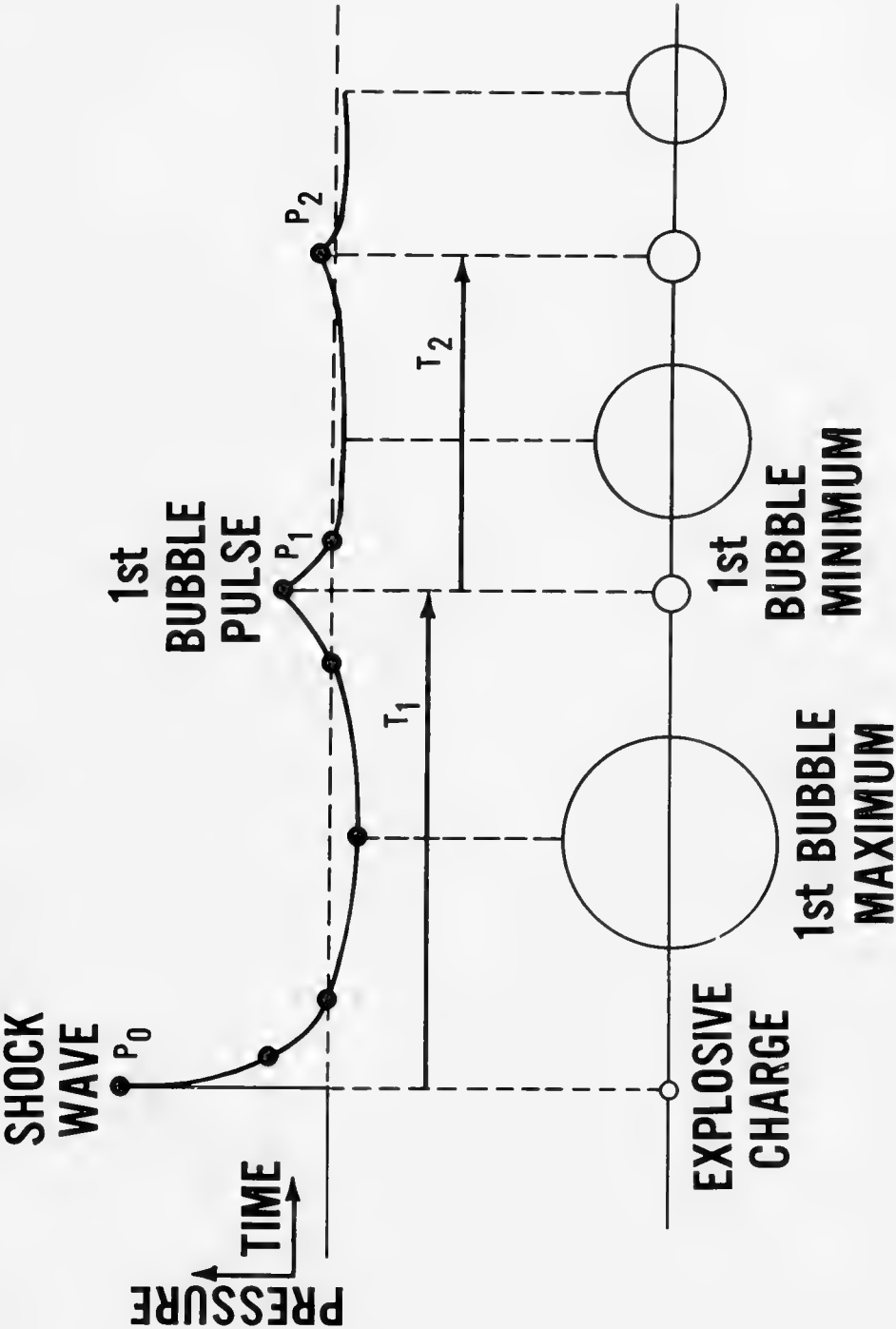


Figure 8. EXPLOSION BUBBLE AND PRESSURE-TIME HISTORY

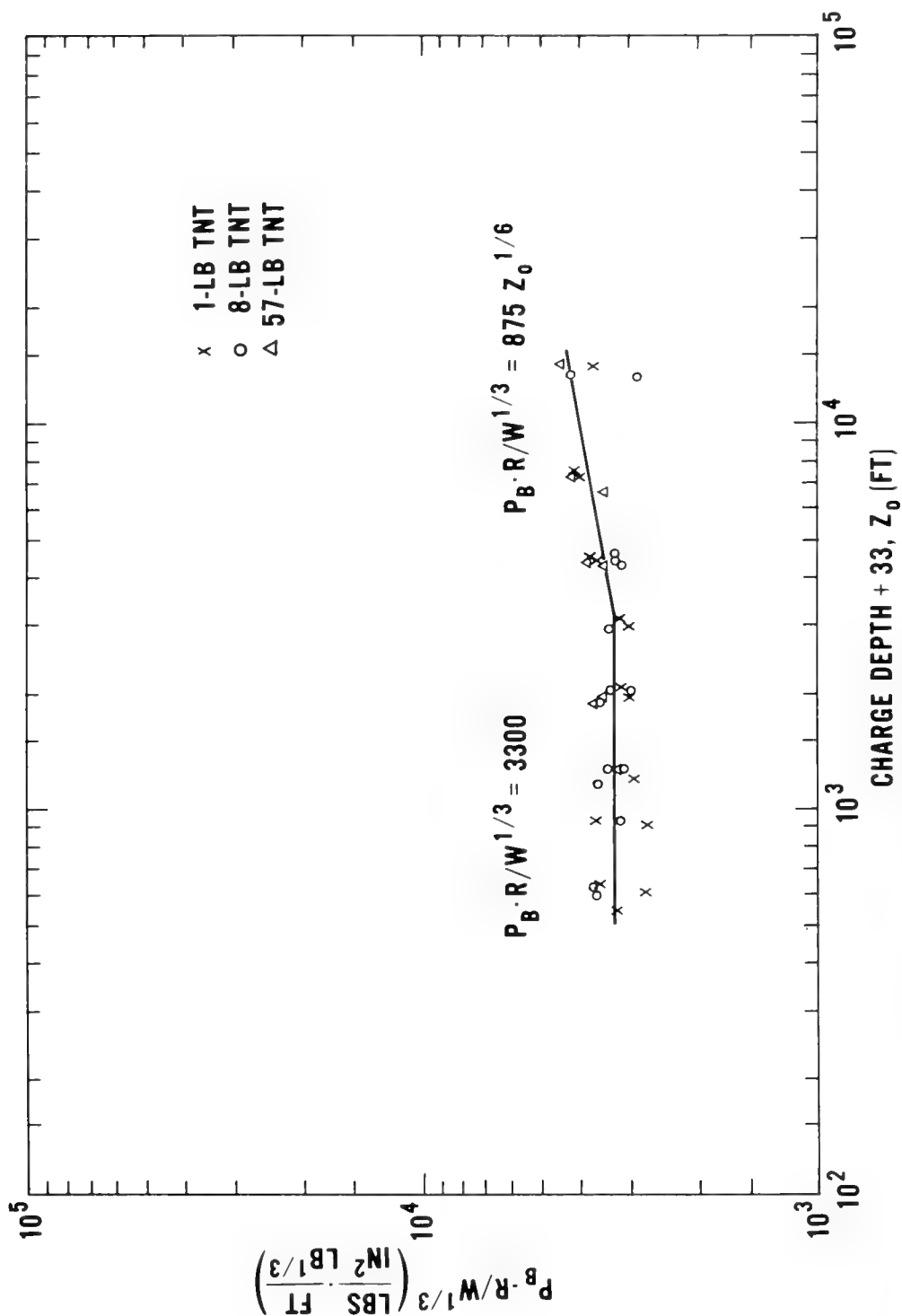


Figure 9. ESTIMATION OF FIRST BUBBLE PULSE AMPLITUDE

charge weight, W , and stand-off range, R . The Gaspin and Shuler model as it stands is a rather crude one and we need new data to remove some of its limitations. Nevertheless, in my opinion, the model provides the best source level estimates that are available, and it has been widely used.

Varying Charge Depth. In many experiments it is easier to control the weight of the explosive charge than to control its depth. This is especially true for acoustic research experiments, where free-fall charges are often dropped from moving ships or planes, and detonation depths depend on hydrostatic pressure devices or lengths of fuze. The SUS Mk-61 sound signal is such a charge. In Figure 10 are shown the Gaspin and Shuler (1971) theoretical spectra for 1.8 pounds of TNT — the Mk-61 loading — detonated at three depths, 700, 800, and 900 feet. These three curves indicate the range of source levels one might encounter with the Mk-61 SUS set at a nominal 800-foot burst depth. Although detonation depths might vary by only a few feet for charges drawn from the same lot, the MILSPEC standards are so written that mechanisms with variations of almost ± 100 feet about the nominal 800-foot depth might come within acceptable limits and be included in stock. The alternate shaded and unshaded frequency bands are the popular 1/3-octave bands. What these kinds of depth variations mean in terms of source level uncertainty is shown in Figure 11. The ordinate of Figure 11, ΔE , shows the dB error introduced when actual detonation depth deviates from the ideal 800-foot value. At high frequencies, where the 1/3-octave band encompasses a number of bubble harmonics, the errors fall within 1 dB of the norm. But down at low frequencies, where the measurement band width is narrow relative to the spectrum oscillation pattern, the errors are ± 3 dB. So much for the hope of predicting source levels to within 1 dB, unless the actual detonation depth is taken into account. Recent efforts along this line will be discussed by Dr. Weinstein.

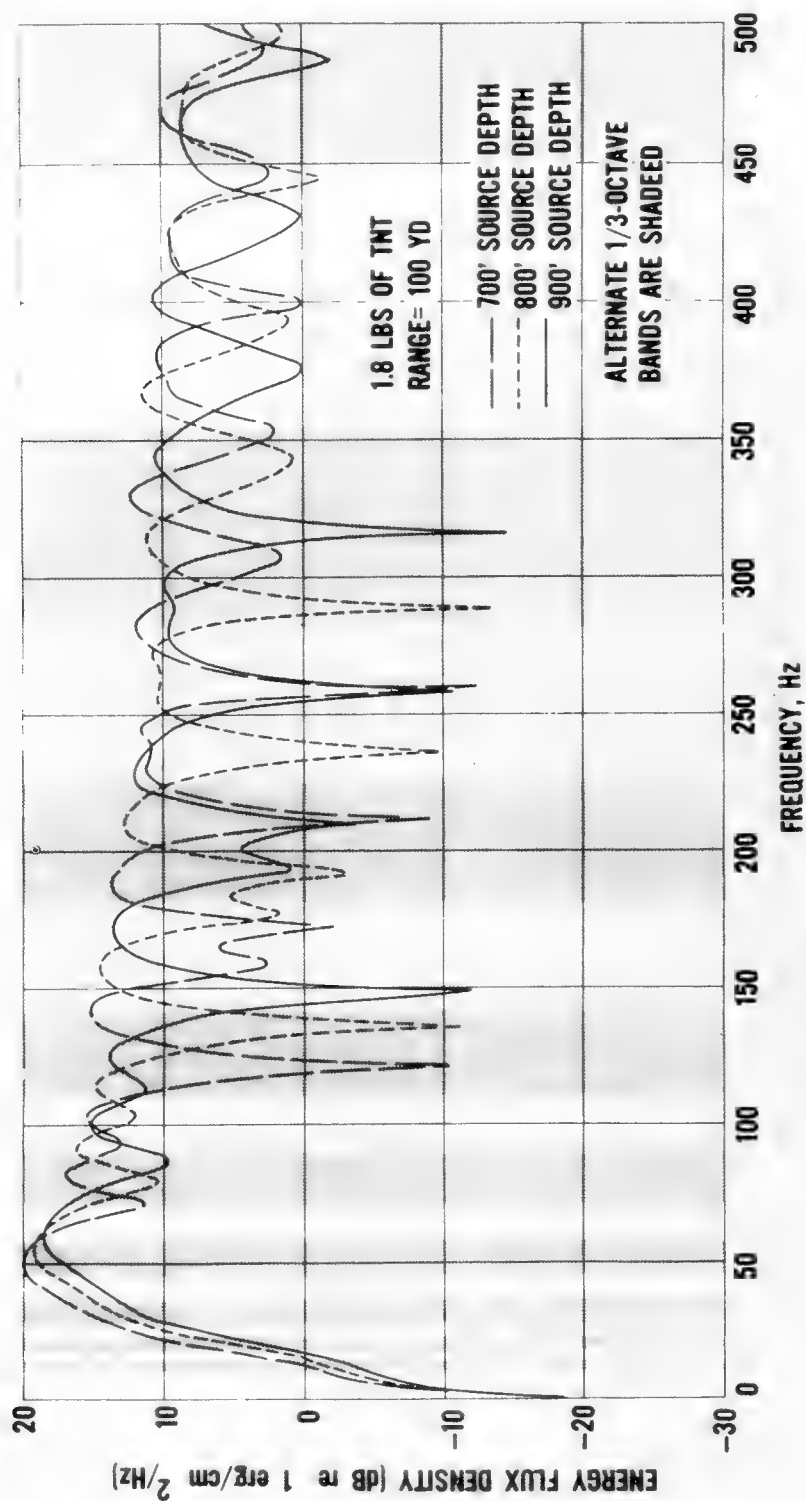


Figure 10. EFFECT OF SMALL VARIATIONS IN BURST DEPTH

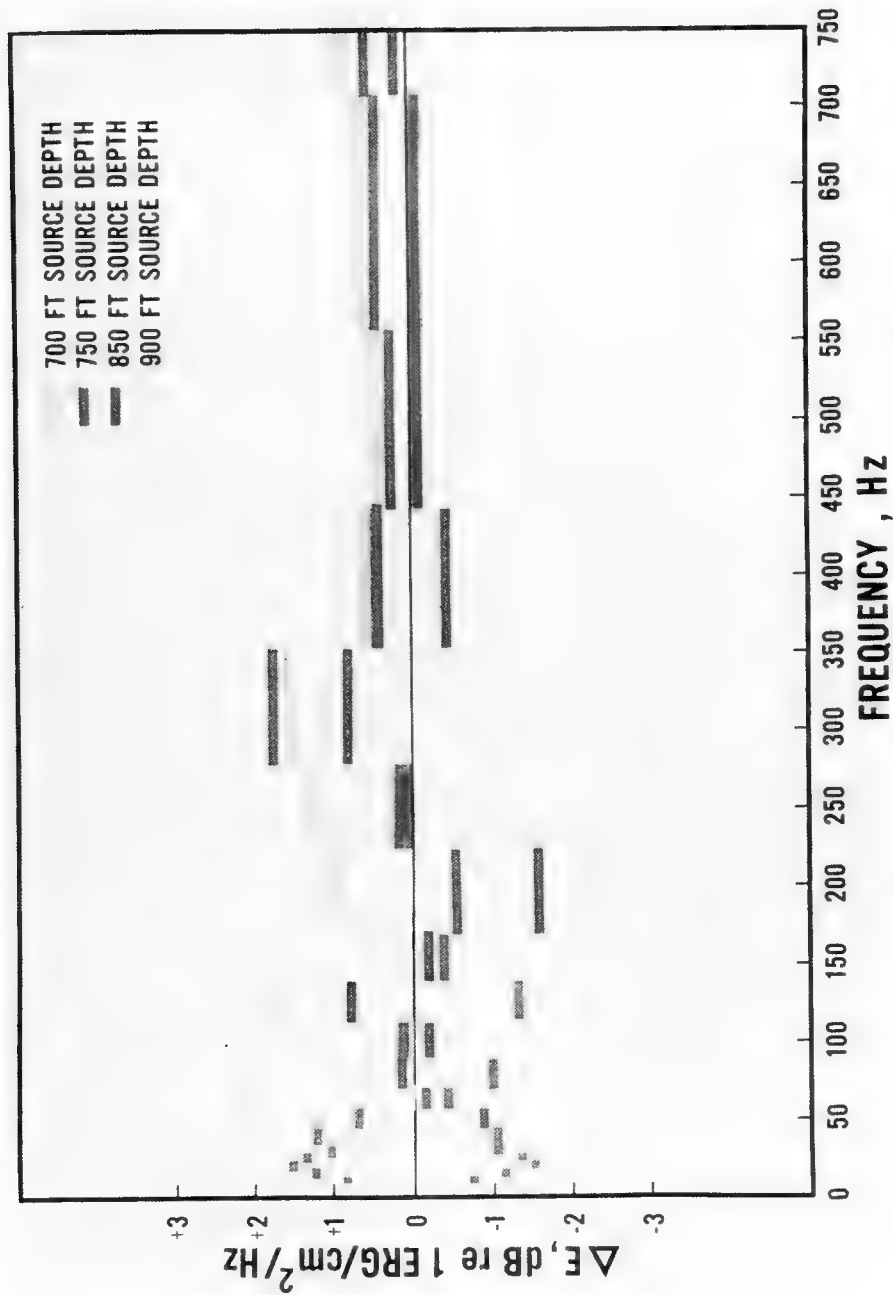


Figure 11. DEPTH VARIATION FOR AN 800-FT SOURCE, 1.8 LBS

$$\Delta E = E_d - E_{800}$$

Since I have gone to some lengths to emphasize the need for more and better data before we can solve source level problems, let me also mention a case where we will have to rely on processing techniques, even if we obtain perfect data. This is the shallow burst, where it is not possible to record the total output wave of the charge separate from the rarefaction wave that is reflected back into the water from the surface. For example, the first bubble period of the very popular Mk-61 SUS fired at 60 feet is about 120 milliseconds, and the entire train of explosion pulses that comprise the charge output lasts for several hundred milliseconds. There is no point in the water at which this pressure wave can be recorded faithfully, because the longest time interval between the direct and surface reflected waves that one can find is 24 milliseconds. This maximum interval occurs directly below the charge, as shown in Figure 12. The parabolic curves of Figure 12 are isopleths of the time of arrival of the reflected wave; values decrease rapidly as the gage location approaches the surface. (The cognomen "surface cut-off time, t_s " of Figure 12 is the explosions research community's jargon for the time separation between the shock front and the surface-reflected wave.) Whether one unscrambles the two signals by deconvolution in the frequency domain, as suggested by Hovem (1970) and by Hanna and Parkins (1974), or by extrapolating time domain functions, as done by Gaspin and Shuler (1971), some sort of special processing must be applied to obtain source levels. Figure 13 illustrates the degree of spectrum distortion introduced by the reflected pulse if it arrives well beyond the direct wave (top pair of curves), hard on the heels of the direct wave (center pair), or in the midst of the direct wave (bottom pair).

I have now completed my long list of reasons why it will always be difficult — if, indeed, possible — to predict explosion source levels in 1/3-octave bands to within 1 dB at low frequencies. Many

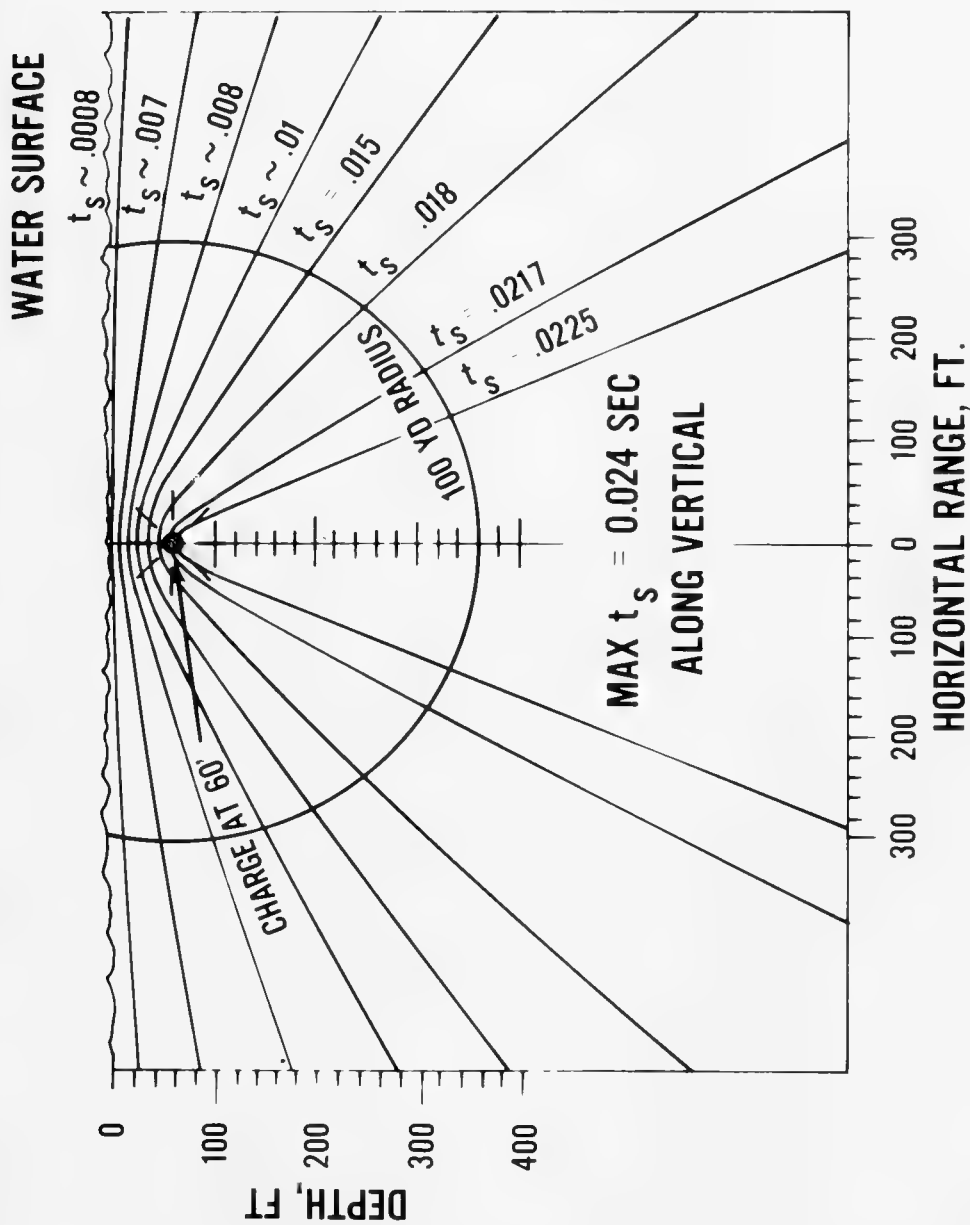


Figure 12. CONTOURS OF CONSTANT SURFACED CUT-OFF TIME, t_s FOR CHARGE AT 60-FT DEPTH

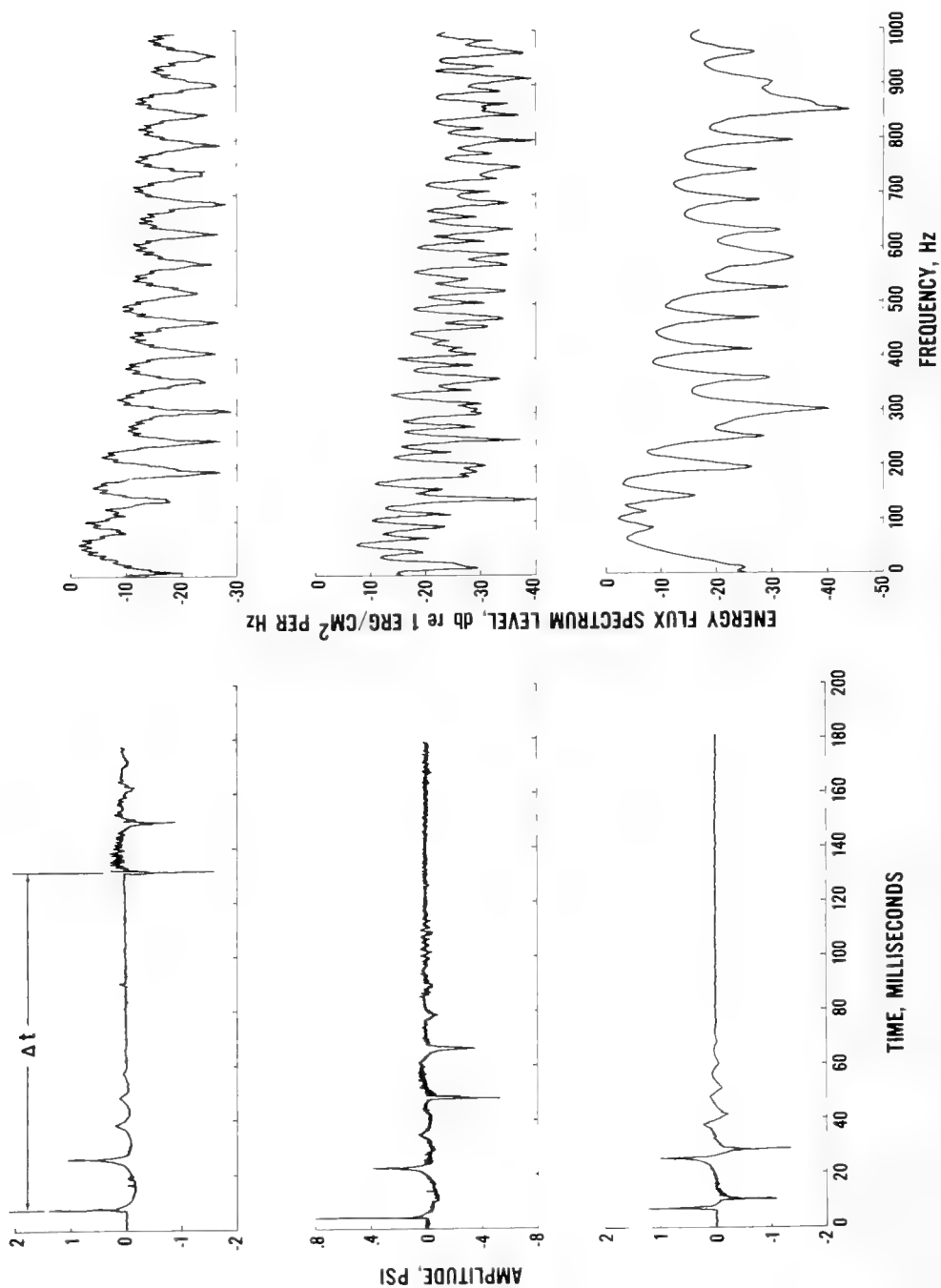


Figure 13. ILLUSTRATION OF SPECTRUM DISTORTION

of the problems can be removed if we want to pay the price: if we want to set stringent limits on SUS charge detonation depth tolerances, for example, or require high quality on-site measurement of charge output for each shot in a series. But such prices are high. I would like to suggest that there may be a better way out, a way that will involve some possibly painful changes over the short term, but will pay off handsomely over the long term. Why not work toward a sensible matching of explosion sources and processing methods? Does a SUS charge always have to be matched to 1/3-octave bands?

An explosion has an "inherent bandwidth," as it were, in its bubble fundamental. If analysis bandwidths were selected to be at least two or three times as wide as the bubble harmonics, much of the variability I have been discussing will be washed out. On the other hand, if the practical acoustics problem being attacked includes an important fixed recording bandwidth which is controlling, then perhaps we should design a charge to match the problem, not just pick the one that comes easily to hand. In short, I am suggesting we should try Figure 14.

To summarize: if explosion source levels in 1/3-octave (or narrower) bands must be predicted to within 1 dB over the frequency range of 10 to 300 Hz, then:

- 1) Our present state of knowledge is not adequate.
- 2) We must acquire new data with controlled experiments.
- 3) We must improve our source level models.
- 4) Recording and processing methods must be re-examined.
- 5) Shallow sources need special attention.

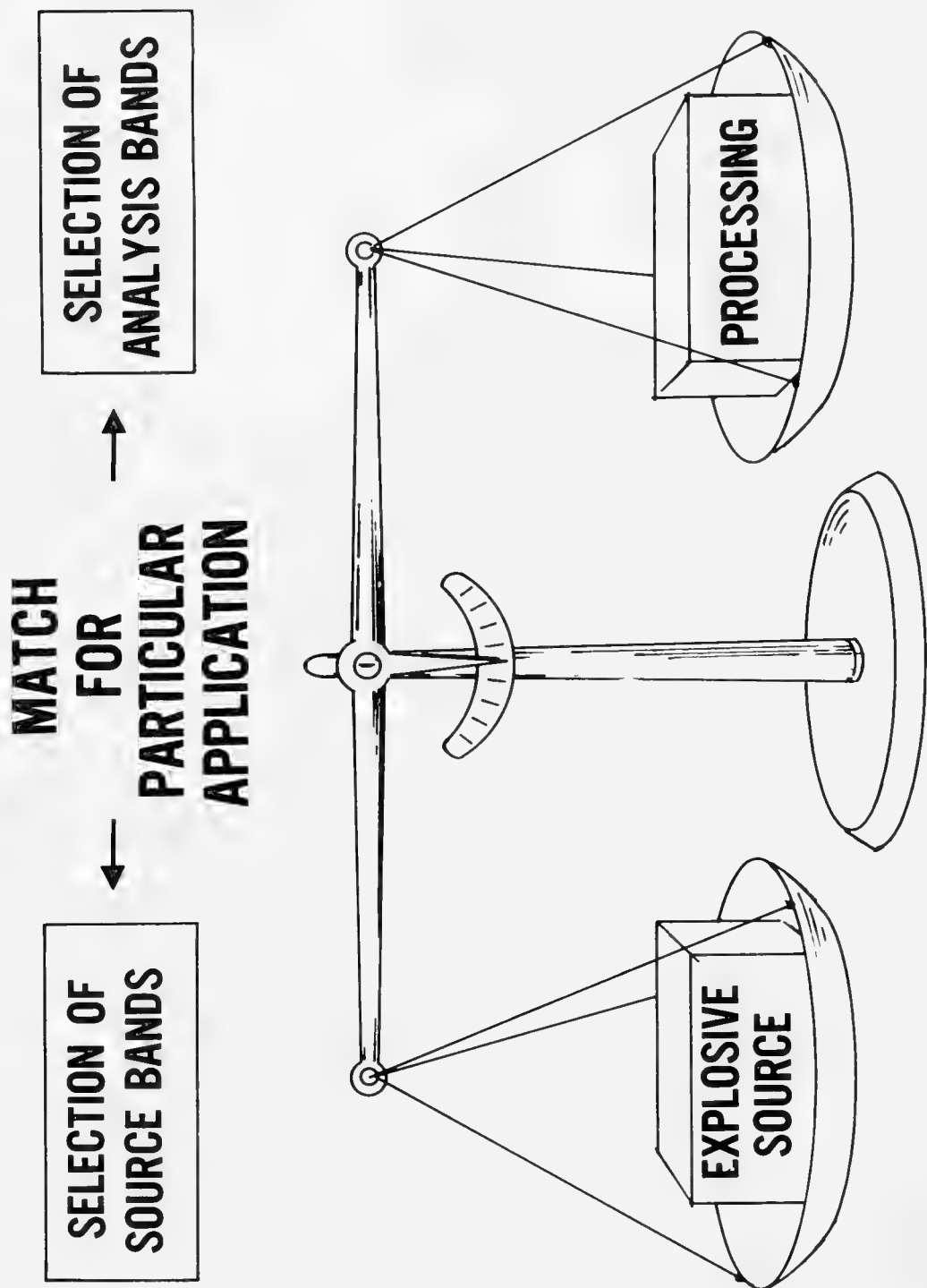


Figure 14. BALANCED CONSIDERATION

At the same time that we are working toward improving source level values as they are used today, we should also be considering the possibility of a brave new world in which explosion sources and analysis methods are matched for particular applications.

REFERENCES

- Buck, B. M., *J. Acoust. Soc. Am.*, 55:188-190(L), 1974.
- Christian, E. A., *J. Acoust. Soc. Am.*, 42:905-907(L), 1967.
- Christian, E. A., and M. Blaik, *J. Acoust. Soc. Am.*, 38:57-62, 1965.
- Gaspin, J. R., and V. K. Shuler, "Source levels of shallow underwater explosions," Naval Ordnance Laboratory Report No. 71-160, Oct. 1971.
- Hanna, J. S., and B. E. Parkins, *J. Acoust. Soc. Am.*, 56:378-386, 1974.
- Hovem, J. M., *J. Acoust. Soc. Am.*, 47:281-284, 1970.
- Maples, L. C., and W. H. Thorp, *J. Acoust. Soc. Am.*, 47 (part 1): 91(A), 1970.
- Skretting, A., and C. C. Leroy, *J. Acoust. Soc. Am.*, 49 (part 2): 276-282, 1971.
- Slifko, J. P., "Pressure pulse characteristics of deep explosions as functions of depth and range," Naval Ordnance Laboratory Report No. 67-87, Sept. 1967.
- Stockhausen, J. H., *J. Acoust. Soc. Am.*, 36:1220(L), 1964.
- Turner, R. G., and J. A. Scrimger, *J. Acoust. Soc. Am.*, 48 (part 2): 775-778(L), 1970.
- Weston, D. E., *Proc. Phys. Soc. (London)*, 77:233-249, 1960.

DISCUSSION

Dr. J. B. Hersey (Office of Naval Research): We have reviewed the way we make measurements and have had a very exciting discussion of what we do to ourselves or for ourselves when we use explosive charges.

In recent advanced development work in the United States, we have arrived at the same point that anyone does who tries to make practical, repeated, continuing application of methods which have evolved in an experimental atmosphere. We have no choice but to confirm our measurements in some way. We have to be sure. If the quantity is a varying quantity, we have to know why it is varying and how it is going to vary during the life of the application that we are addressing. This need frequently persists over many years. We, therefore, have to establish standardization procedures for the reliability of the techniques that we use. Dr. Marvin Weinstein has led a rather large group of people in taking a close look at some of these standardization problems.

EXPLOSIVE SOUND-SOURCE STANDARDS

M. S. Weinstein
Underwater Systems, Inc.
Silver Spring, Maryland

The desired accuracy of low-frequency transmission-loss calculations based on experimental data using explosive sound sources is plus or minus one decibel. Factors involved in determining transmission loss include uncertainties in source level, background noise, and processing procedures. Data are presented to illustrate the quantitative effect of these factors.

While the desired accuracy has not yet been universally achieved, errors may be minimized through the use of certain standards concerning source-level monitoring and data-processing procedures.

INTRODUCTION

The factors involved in propagation-loss determinations using explosive sources include:

- The desired accuracy
- The achievable accuracy, stressing the uncertainty in the source level, the effect of background noise, and processing procedures
- The information which should be included in technical reports to permit comparison of data obtained and published by different organizations.

DESIRED ACCURACY

The first point to consider is the desired accuracy. Our goal is about one decibel. This statement usually generates immediate concern, since it has yet to be achieved. There may be basic

problems, some of which have been touched on (Christian, these Proceedings). However, we shall examine some of the concepts which support 1 dB as a reasonable goal against which to gauge our performance.

Suppose we are considering the design of a surveillance system which will make detections at long range where the propagation loss follows cylindrical spreading. An uncertainty of ± 1 dB translates into an uncertainty in area coverage of about 50 percent; a not inconsiderable factor in estimating costs.

Suppose we wish to optimize the geographical location or depth of such a system. One might perform an experiment for simultaneous measurement of propagation loss at a number of sensor locations. We want to know the propagation loss difference to within one decibel for the same reason.

In a somewhat different context, fluctuations in propagation loss are of considerable interest. If true fluctuations have a standard deviation of about 3 dB, one cannot stand an uncertainty of more than about 1 dB before the results are significantly degraded.

Thus, the data needs indicate the desirability of obtaining propagation-loss data which are accurate to about one decibel.

SOURCE-LEVEL UNCERTAINTY

Consider the accuracies which can be achieved. First, the uncertainty in source level.

Figure 1 shows source levels in 1/3-octave bands for 1.8-pound charges detonated at 60 and 300 feet. These three data sets illustrate the range of values with which we are confronted. The spread

FREQUENCY (Hz)	NOL GASPIN & SHULER	BTL BUSCH	WESTON
60-FOOT DEPTH			
25	20.0	12.4	16.3
50	14.9	13.0	15.1
100	13.7	8.0	14.4
160	10.3	5.6	12.2
250	8.6	3.7	10.2
300-FOOT DEPTH			
25	20.7	15.8	18.1
50	15.7	11.8	15.3
100	13.3	8.7	13.8
160	11.5	6.7	12.1
250	9.1	5.0	10.2
ERGS/CM ² /HZ AT 100 YARDS			

Figure 1. SOURCE-LEVEL COMPARISONS

in source-level estimates is as high as 7.7 dB. The three data sets also have different spectral shapes.

The first data set consists of the detailed computation of Gaspin and Shuler (1971). Although based on experimental data, it does involve the extrapolation of the shock-wave impulse from measurements at deeper detonation depths. These extrapolated values are a good bit higher than those previously used.

The second data set is provided by Busch (1973) and corresponds to experimental measurements using MILS hydrophones. The system sensitivity is computed, and not measured. Additionally, corrections for surface reflections are made during processing, since the reflected signals arrive before the direct signal of shock wave and bubble pulses has died down.

The third data set is computed using the simplistic forms published by Weston (1960), which were based on the earlier experimental work of Arons and Yennie (1948).

Although the uncertainty in source level represented by the spread in these data sets is many times larger than our goal of ± 1 dB, the problem is recognized and it is reasonable to assume that the uncertainty in source level can be significantly reduced by performing carefully controlled experiments.

SOURCE-LEVEL FLUCTUATIONS

When measured data are compared to model computations, we would like the data to be free from random variations. To help satisfy this need, the source conditions should be identical from shot to shot. Fluctuation artifacts can arise from variations in shot depth which alter the spectral shape, principally by changing

the bubble-pulse period, and by variations in yield which change the total energy output.

Additionally, depth variation will alter the multipath propagation structure, introducing a third source of fluctuations which will be dependent on the environmental details.

During a recent experiment, SUS shots were monitored with a hull-mounted transducer on the drop vessel. The data were processed to determine the bubble-pulse period for approximately 700 shots each at 60- and 300-foot detonation depths.

Figure 2 shows the cumulative distribution for the 60-foot shots; the bubble-pulse period at the top, the detonation depth at the bottom, assuming that the yield was identical for all shots. The variation in yield expected from an examination of manufacturing procedures results in an uncertainty in detonation depth of about ± 2 feet. As is apparent, the detonation depth varies from 50 to 70 feet. About 90 percent of the data points lie between 54 and 60 feet. For this range of detonation depths the source-level variation in the 1/3-octave bands is about ± 1 dB.

Figure 3 shows similar results for the 300-foot shots with a data spread of 250 to 350 feet. About 90 percent of the data points lie between 270 and 320 feet, and source-level variations of about ± 1.5 dB can be expected.

For both detonation depths source-level variations directly attributable to variation in yield are estimated to be a fraction of a decibel.

These results suggest that source-level variations can be corrected to within a fraction of a decibel by monitoring the shots

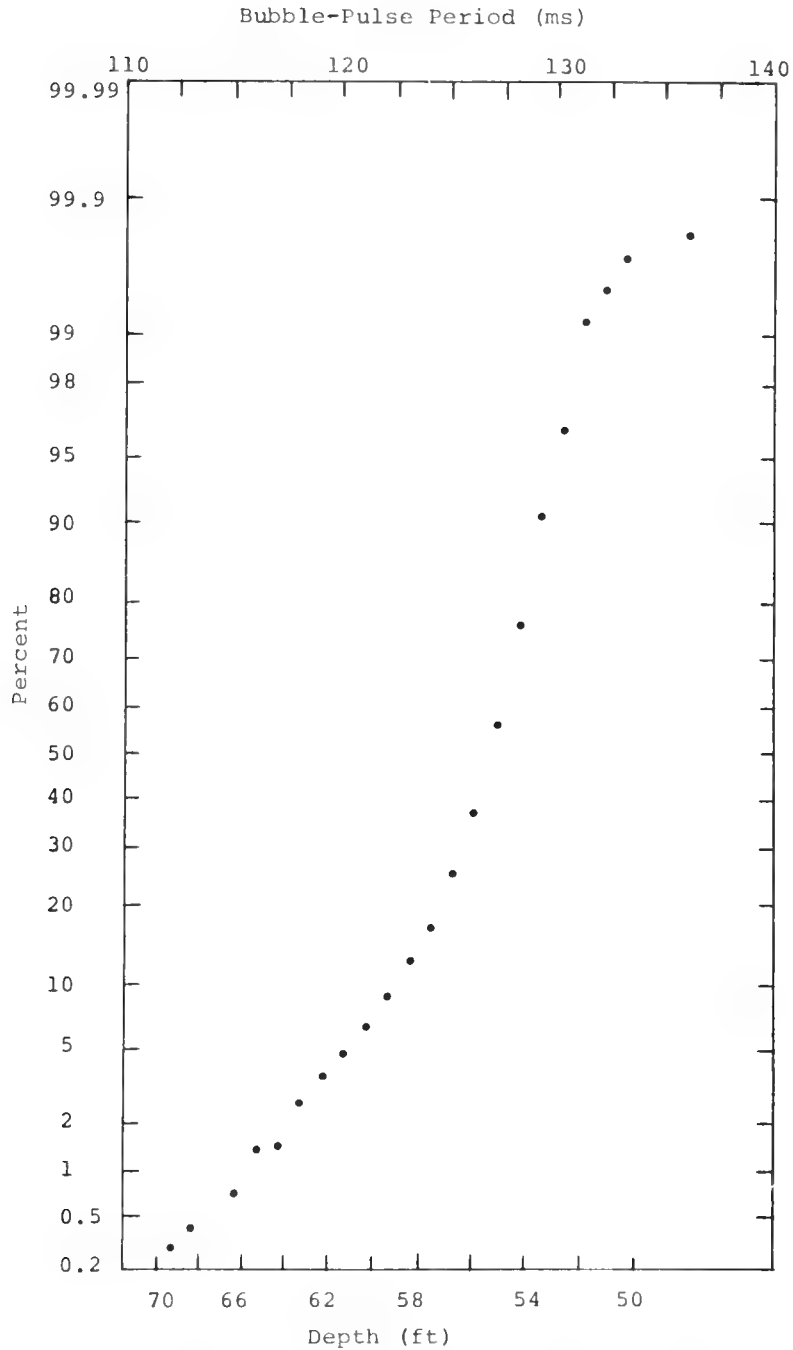


Figure 2. CUMULATIVE DISTRIBUTION OF BUBBLE-PULSE PERIOD AND DERIVED SHOT DEPTH FROM THE MK 61 (60 FEET) SUS CHARGES DROPPED BY THE USNS SILAS BENT. 654 SHOTS.

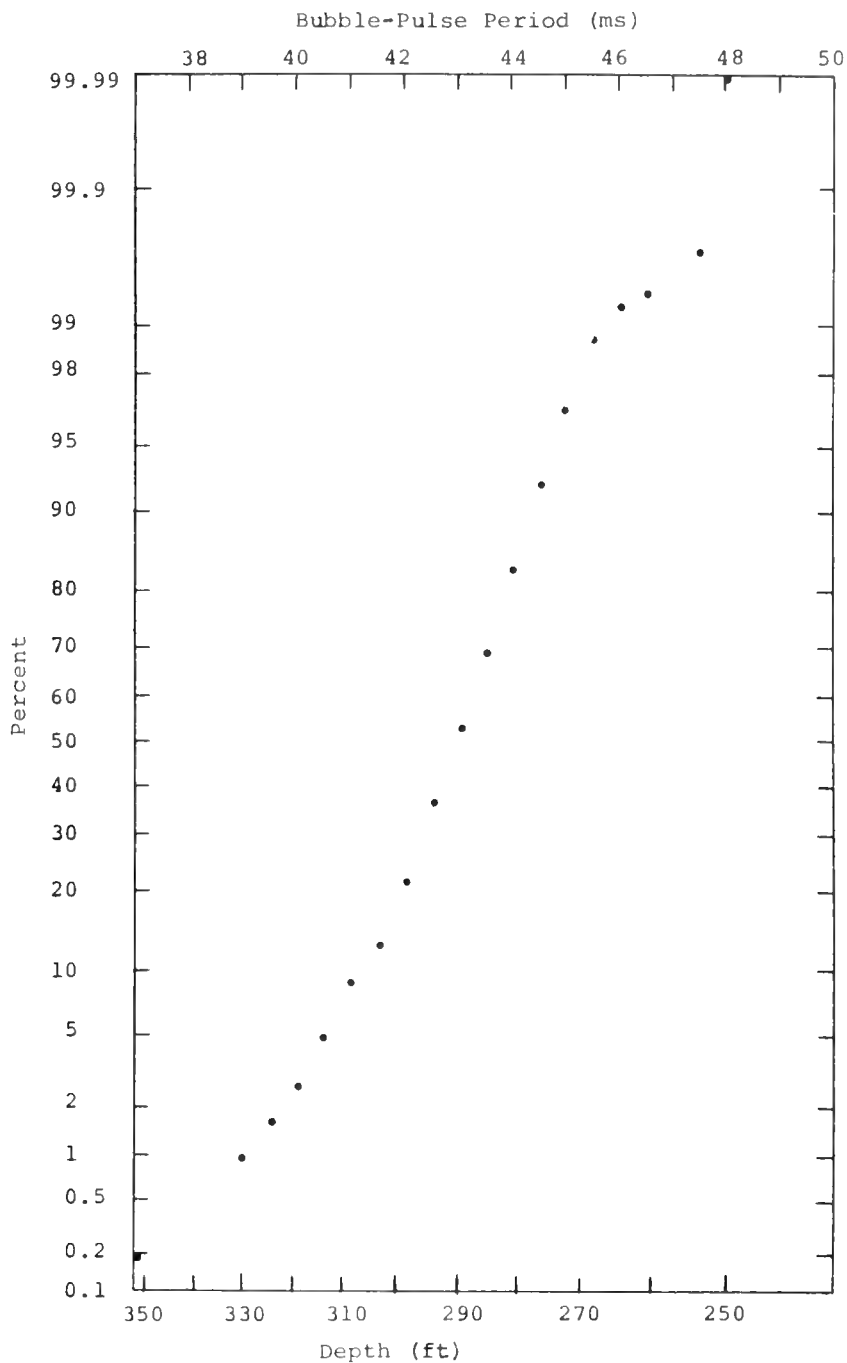


Figure 3. CUMULATIVE DISTRIBUTION OF BUBBLE-PULSE PERIOD AND DERIVED SHOT DEPTH FROM THE MK 82 (300 FEET) SUS CHARGES DROPPED BY THE USNS SILAS BENT. 655 SHOTS.

to determine the bubble-pulse period, provided we have either an experimentally determined data base, or a proven computational procedure, which permits us to relate depth variation to source-level variation in the processing bands of interest.

EFFECT OF NOISE

The second source of uncertainty is background noise. To determine propagation loss, one integrates the signal and noise over the signal arrival interval and subtracts out the noise from an estimate obtained by measurement prior to signal arrival. The time interval between the measurement of noise, and signal plus noise, is typically about one-half minute. If the noise varies over this time interval, an uncertainty will be introduced in the computed propagation loss. Ordinarily, by using only data with high signal-to-noise (S/N) ratios, perhaps 10 dB or more, this problem is minimal. However, in large-scale experiments employing many ships, thousands of shots, and automated remote recording systems, the problem may be more significant. If the S/N level is less than desired, quality assurance techniques must be applied to extract the good data and reject the poor data.

In Figure 4, the error in propagation loss is plotted as a function of S/N ratio for changes in noise level of ± 0.2 , ± 0.4 or ± 1.0 dB. As one would expect, the error increases as the signal-to-noise ratio decreases.

This problem was encountered in a recent experiment. The following figures illustrate the staged improvement in the quality of data as quality assurance procedures were applied.

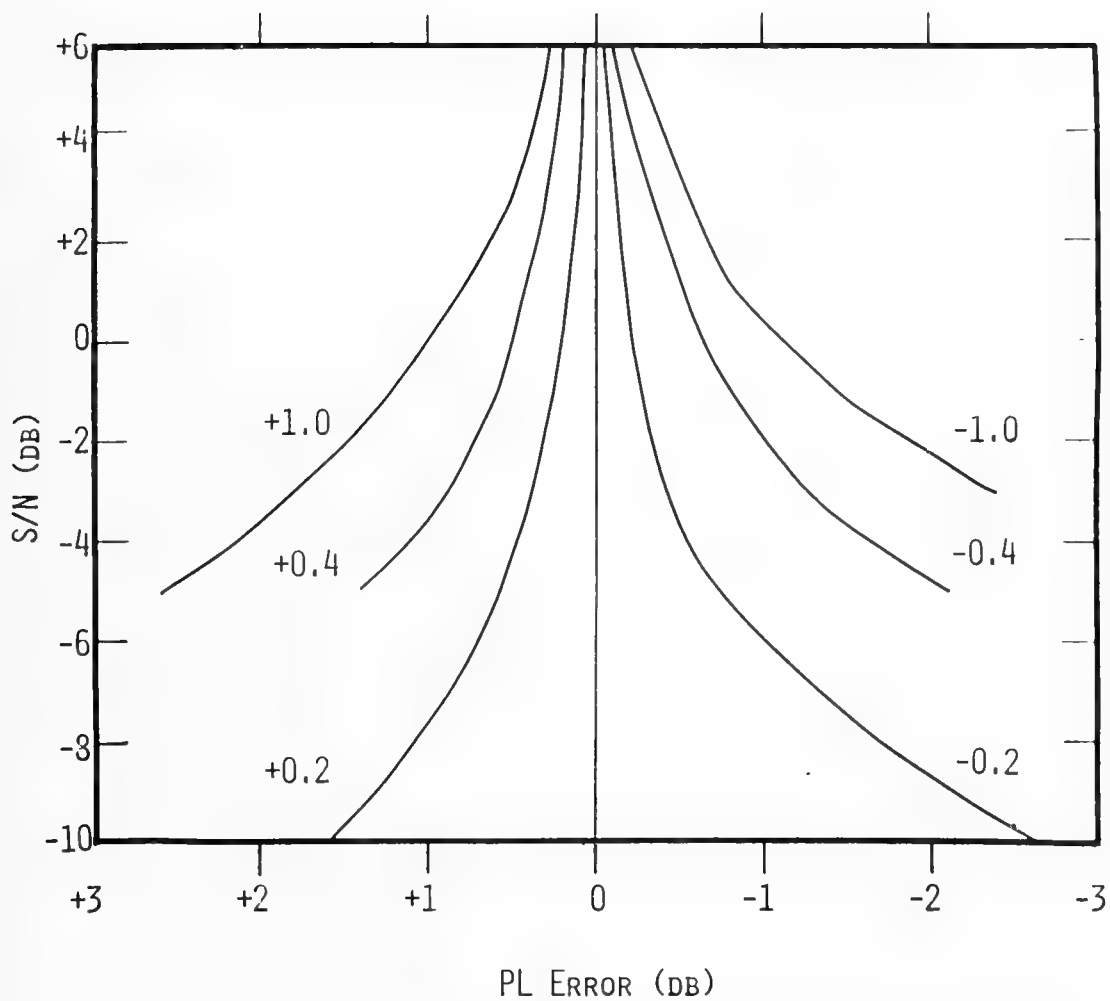


Figure 4. PROPAGATION LOSS ERROR AS A FUNCTION OF S/N FOR INDICATED CHANGES IN NOISE LEVEL

The central plot of Figure 5 shows the propagation-loss data. The ambient-noise levels which were received concurrent with the shots are plotted in the upper part of Figure 5 at the ranges of the shot. The resulting S/N ratio for each data point is shown in the lower set of data. S/N ratios as low as -10 dB had been accepted at this stage. Note that the background noise shows a large increase and that the propagation loss follows this change. Also note that the S/N ratio is poor over this entire region. What is happening is simply that following the noise measurement a noise burst coincidentally occurs at the approximate time that the SUS signal was expected, which is read as signal plus noise, so that, in effect, a noise fluctuation is mistaken for signal and an erroneous propagation loss is computed.

It is important to note that the processing system was fully automated. In a large experiment, the product of the number of hydrophones, shots and frequency bands of interest is of the order of 10^6 . Automation is essential to handle this quantity of data. The care and subjective experience which the scientist can apply when processing data by hand have to be converted to definitive algorithms for the computer to make a decision. This is not an easy task, particularly for those qualitative factors which the scientist does not verbalize but applies by gut feeling. If a 10-dB S/N ratio requirement were applied to this data set, nothing would be left.

Based on the preceding curves, we therefore decided to reject all data for which S/N was less than -3 dB, and plotted the remaining data with different symbols for S/N of -3 to 0 dB, 0 to +3 dB, and greater than +3 dB. The result is shown in Figure 6. Data rejected for poor S/N are shown along the bottom at the appropriate range.

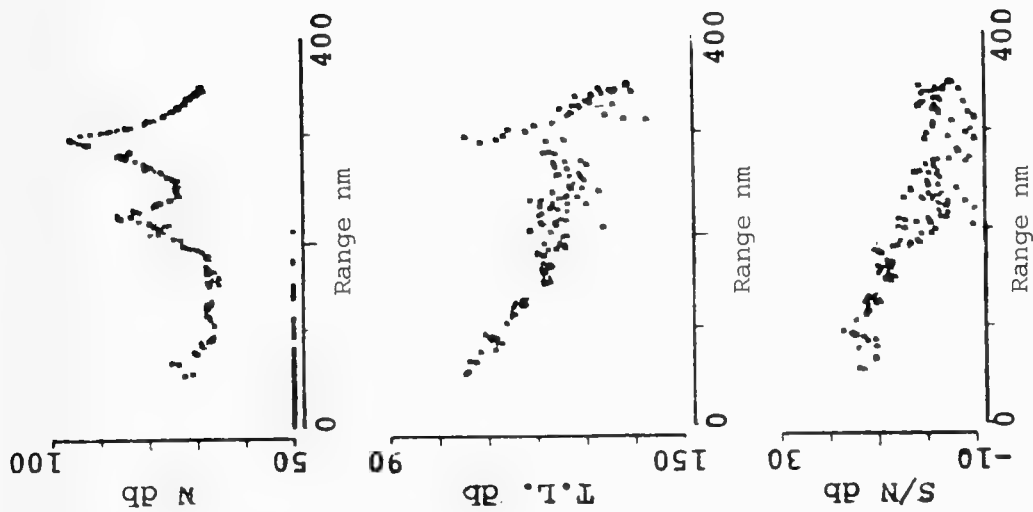


Figure 5. BENT C SOURCE 91M
RECEIVER

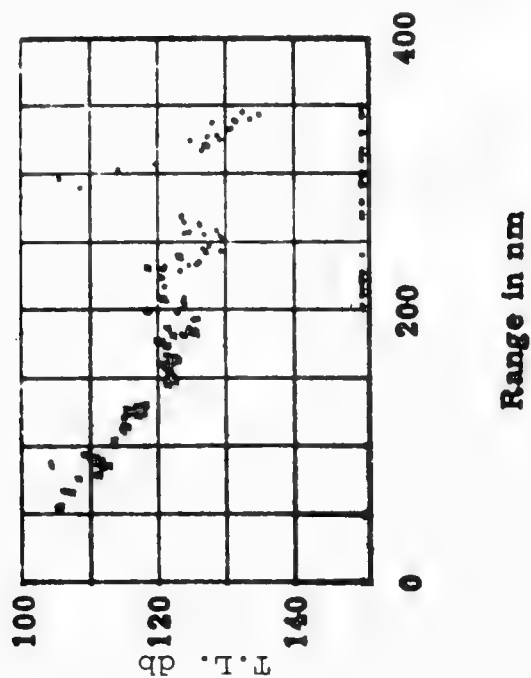


Figure 6. TRANSMISSION LOSS VERSUS RANGE
FOR SIGNAL-TO-NOISE RATIOS
LARGER THAN -3

These data have been cleansed considerably, but some artifacts are still present. The total number of data points which remain is considerably reduced so that other criteria can be applied.

It is known that the nulls and peaks in the source spectrum, resulting from the bubble pulse, are retained in the spectrum of signals at long range. Fortunately, narrow-band FFT processing was a part of the automated processing procedure, so that the spectra could be examined. The criteria applied was go/no-go. If the signal spectrum looked like a shot, the data point was accepted; if it did not, it was rejected.

Figure 7 shows the circled points that were rejected on the basis of the spectral criteria. The remaining data can now be relied upon. Further investigations of noise fluctuations permitted the establishment of estimated uncertainty bars in signal-to-noise bins. These exceeded our goal of ± 1 dB, exclusive of the uncertainty in source level.

Figure 8 shows the spectrum for signal plus noise on the left, and the noise alone at the right for a 300-foot shot at a high S/N ratio. Note that the signal plus noise shows pronounced scalloping with strong nulls spaced at about 25 Hz, consistent with the source spectrum expectation. The noise spectrum is totally different.

Figure 9 shows similar results for a lower S/N ratio. The signal-plus-noise spectrum is still good.

Figure 10 shows the results for a contaminated sample. Note that the signal-plus-noise spectrum does not show the null sequence, and is quite similar to the noise spectrum. This is a case where signal plus noise is dominated by a noise burst and this data point is therefore rejected.

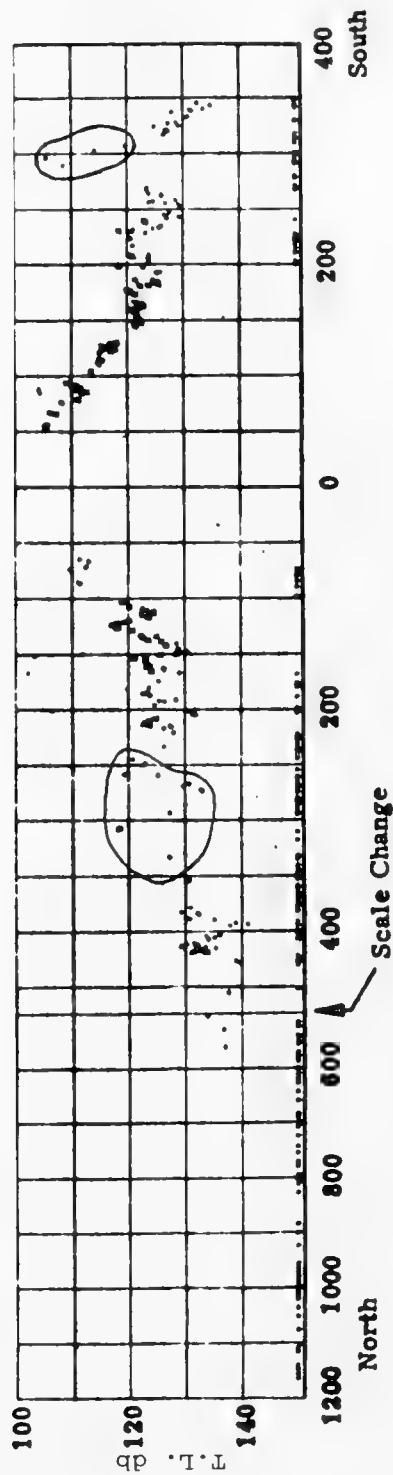


Figure 7. PROPAGATION LOSS NORTH AND SOUTH OF SITE C AT 50 HZ
FROM 91 M SOURCE TO A RECEIVER AT 5521 M

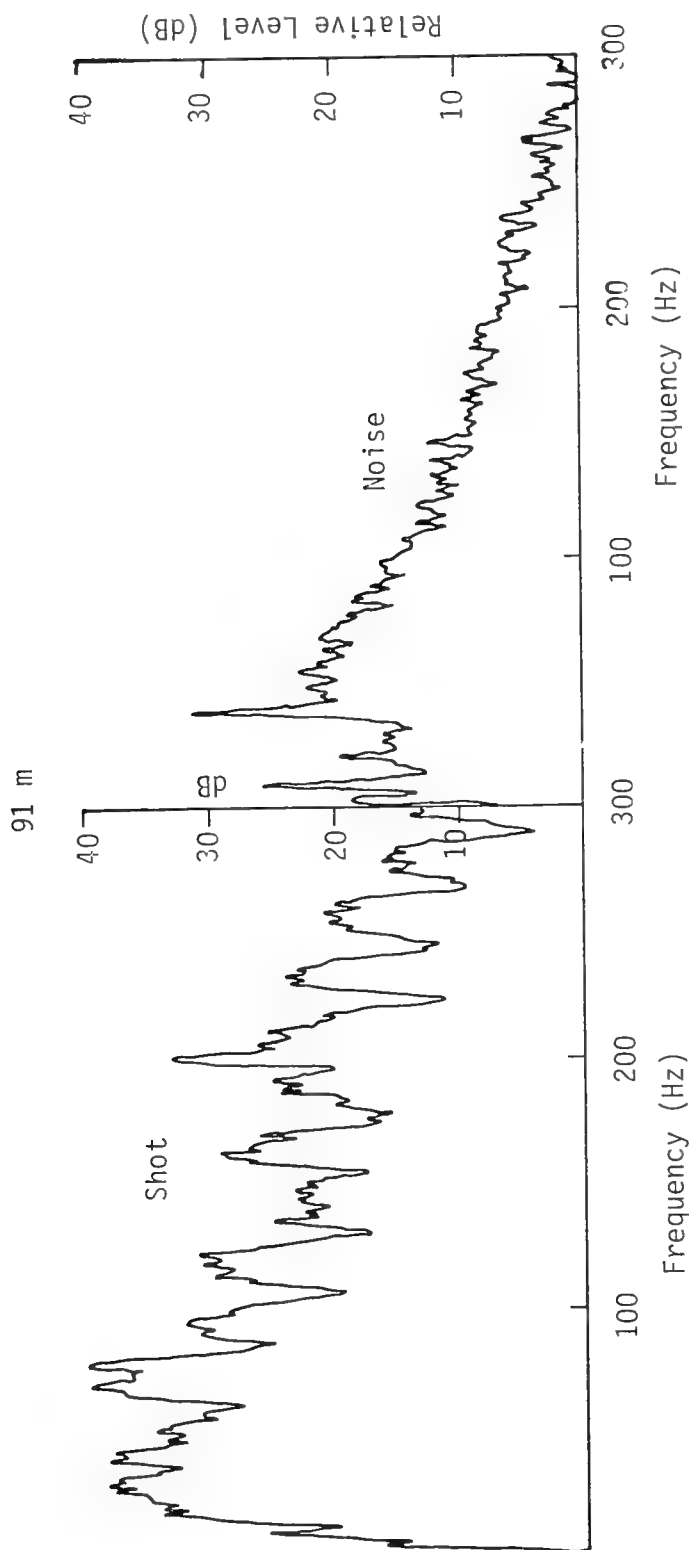


Figure 8. POWER SPECTRA OF SHOTS AND NOISE--HIGH SIGNAL-TO-NOISE RATIO

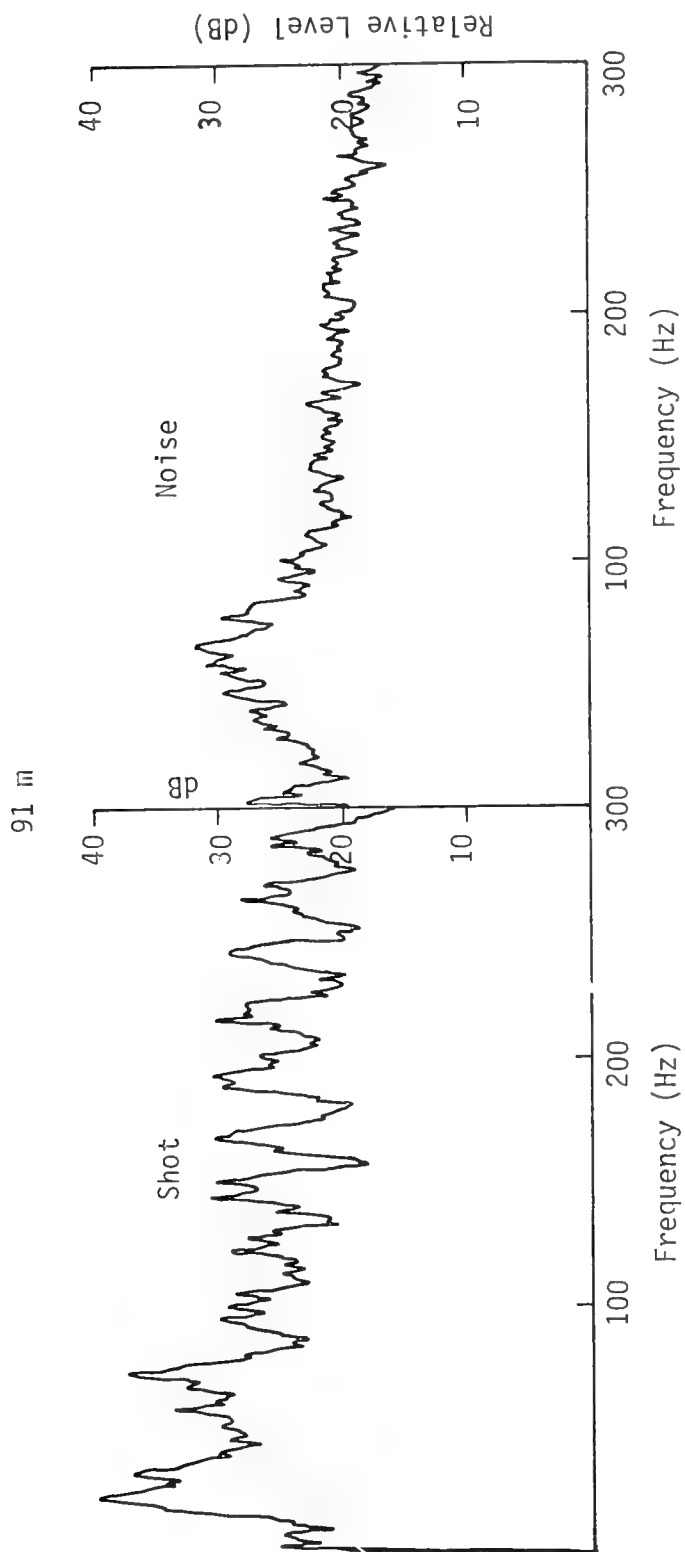


Figure 9. POWER SPECTRA OF SHOTS AND NOISE--POWER SIGNAL-TO-NOISE RATIO

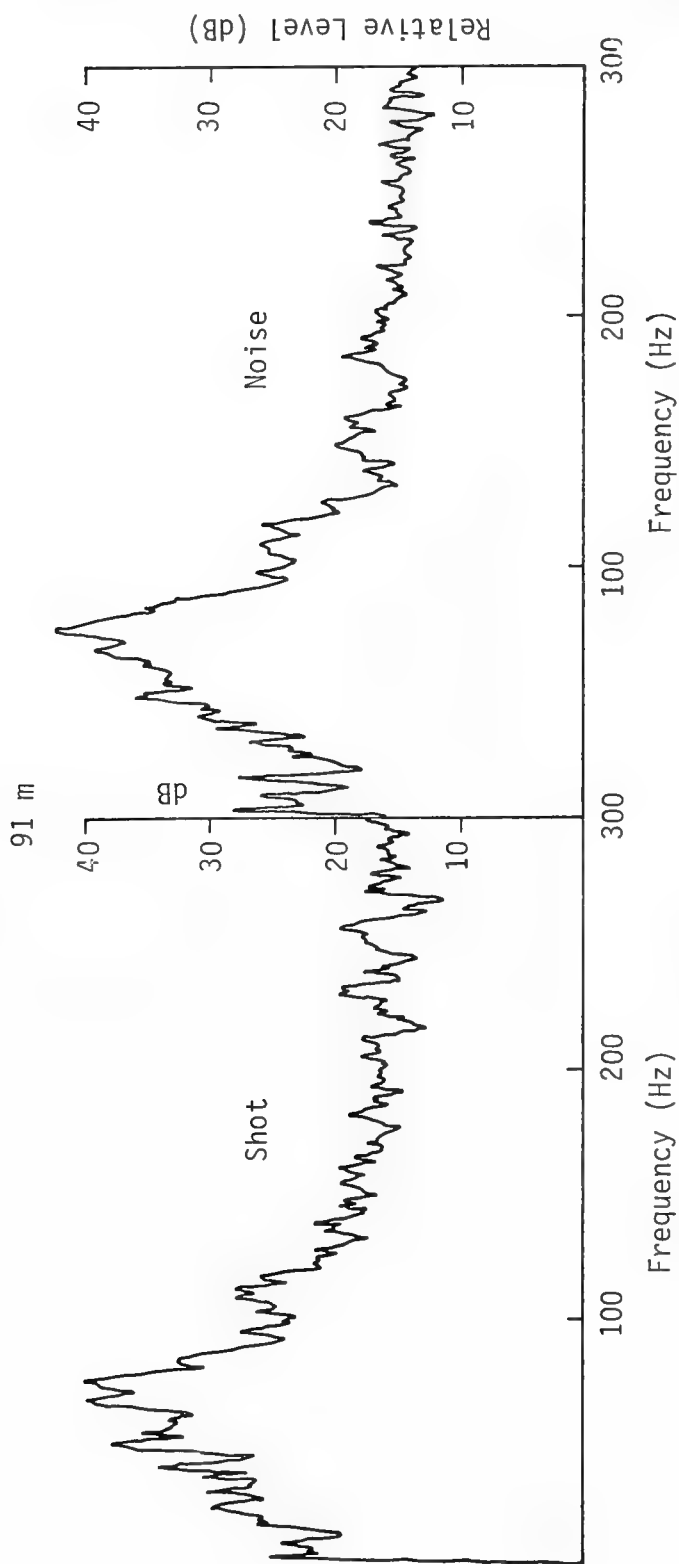


Figure 10. POWER SPECTRA OF SHOTS AND NOISE--POOR SIGNAL-TO-NOISE RATIO

PROCESSING PROCEDURES

Another source of uncertainty results from processing procedures. This is a broad subject in itself, which we touch upon only briefly.

Any processing system has an inherent limit on reproducibility which may stem from the tape-playback system, the processing equipment, or human factors. To illustrate the effect on propagation-loss measurements, assume a repeatability of ± 0.2 dB, uncorrelated for both the noise energy and the signal-plus-noise energy.

The uncertainty in propagation loss, as a function of the S/N ratio, is shown in Figure 11. For a signal-to-noise ratio of - 3 dB, the uncertainty is then + 1.0 to - 1.3 dB, about equal to the total accuracy goal. Also note that because of the asymmetry, a small fixed bias can be expected.

The results of a repeatability experiment using five 10-second noise samples from a direct-record ACODAC system are shown at the top of Figure 12. The operator exercised considerable care in tape handling to ensure proper lay up of the tape and drive-speed stabilization. The differences are plotted for 1/3-octave bands. Analog filters were used. The results range from + 1.0 to - 1.2 dB, with zero bias and a standard deviation of 0.36 dB. The lower curve shows similar results without care. Fast forward and reverse were used to find the data segment of interest. The results are considerably worse over the entire band, and get completely out of hand at the higher frequencies. This particular data set typifies the human-factors problem when direct record is used.

Repeatability measurements with an FFT processing system for the 50-Hz band yielded similar results; a bias shift of about 0.25 dB and a standard deviation of about 0.25 dB. However, the comparison

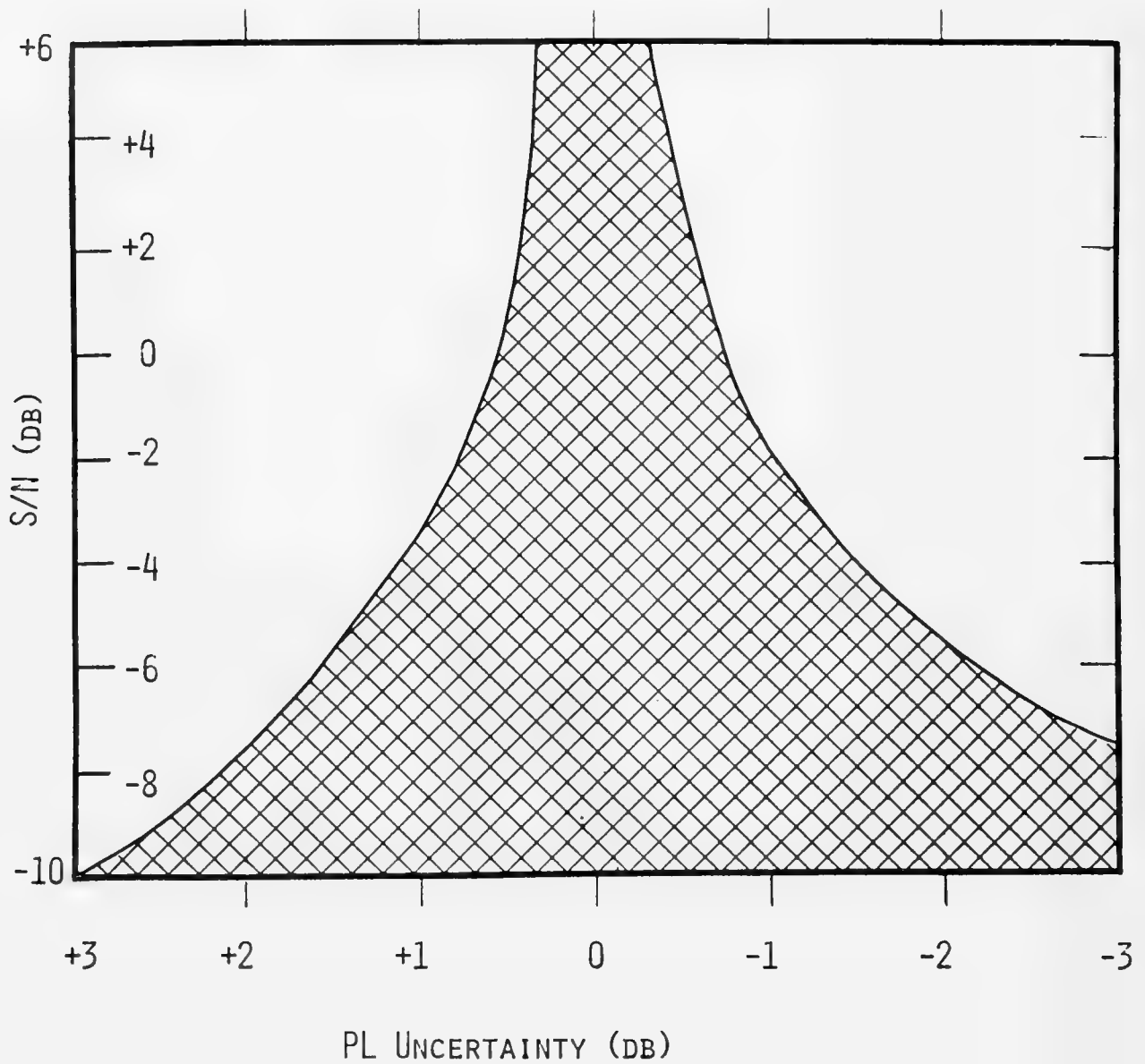


Figure 11. PROPAGATION LOSS AS A FUNCTION OF S/N FOR REPEATABILITY OF $+0.2$ dB IN NOISE AND SIGNAL-PLUS-NOISE MEASUREMENTS

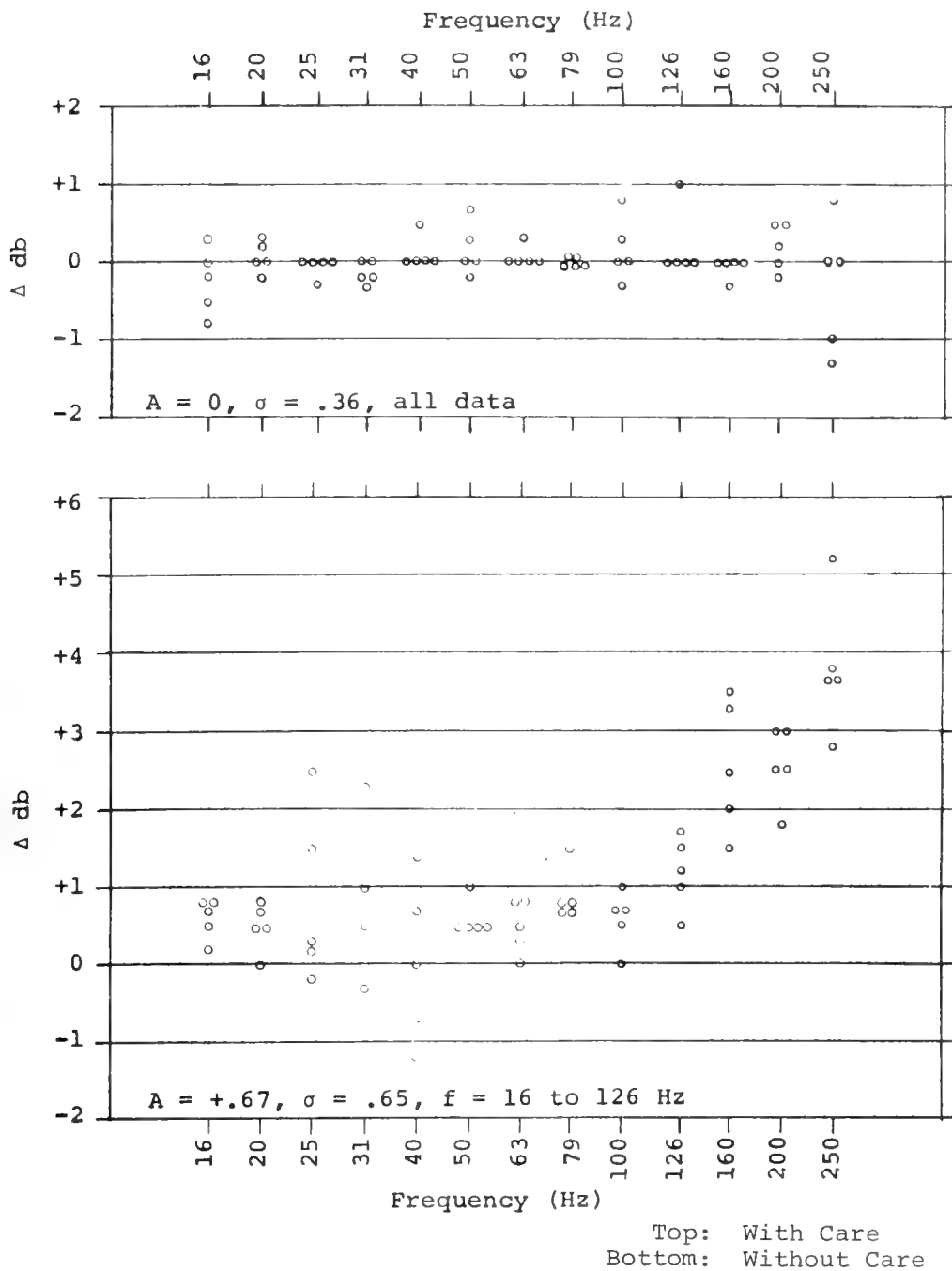


Figure 12. EXAMPLE OF PROCESSING DIFFERENCES
CONCERNING DATA TAPE HANDLING

of propagation loss with good S/N ratio was surprisingly good; essentially no bias and a standard deviation of 0.14 dB.

The automated systems used to process a large quantity of data are computer controlled but can employ either analog filtering or FFT processing. In the latter case, the FFT spectral levels are summed in the time domain to cover the total signal interval, and are summed in the frequency domain to construct square 1/3-octave or one-octave bands. A comparison of analog and FFT processing for noise, with everything else the same, yielded a bias of about 0.3 dB and a standard deviation of 0.8 dB in the 50-Hz 1/3-octave band. For propagation loss, again with good S/N ratio, there was essentially zero bias, and a standard deviation of about 0.5 dB.

Christian (these Proceedings) has pointed out that in processing one set of short-range recordings, the level changed by as much as 0.8 dB as the FFT bandwidth was changed. This observation is unexplained. There are a number of difficulties when we seek high accuracy. Concerning FFT processing, it appears that most of our knowledge is derived from consideration of long-duration Gaussian signals. Explosive signals do not satisfy this criterion. They consist of a series of short transients with deterministic spectral characteristics. Specifically, we must know how the broadband FFT levels depend upon:

- The bandwidth selected for processing
- The digitization rate
- The number of bits
- Whether Hanning is or is not used
- Whether coherent or incoherent summation in the time domain should be used.

It is illustrative to compare data processing results of different facilities. Each facility used a different duplicate of the original recording, either direct or FM, depending upon available equipment. Figure 13 compares about 100 shots for Systems (1) and (2). System (1) is fully digitized using FFT processing. System (2) uses analog 1/3-octave filters followed by digital processing. The comparison is for the 50-Hz band only, for three different hydrophones. Independent processing yielded biases from + 1.47 dB to + 2.13 dB, and standard deviations from 1.28 dB to 2.06 dB. One of the problems identified at this time was that the two facilities made independent and different determinations of signal duration. When these were made consistent and the data reprocessed, the bias was reduced to between + 0.95 and + 1.85 dB, and the standard deviation to between 1.05 and 1.52 dB.

To help identify the reasons for the observed differences, the tape recording used on System (2) was then processed with System (1). The additional improvement was a few tenths of a decibel, identifying the major source of the differences shown as resulting from differences in the processing systems.

A comparison between System (1) and another hybrid analog-digital system (System (3)) is shown in Figure 14. The agreement is somewhat better. These results, combined with the prior comparison of analog and FFT processing, with all else the same, suggest that the differences seen in the previous figure are not totally attributable to differences between analog and digital processing.

Figure 15 compares System (1) and a totally analog shot processor, System (4). It employs 1/4-octave rather than 1/3-octave filters. A simple 10-log bandwidth ratio correction was made.

HYDROPHONE	BIAS ORIG. RECOMP.	STD. DEVIATION ORIG. RECOMP.
#1	+2.13 +1.85	1.55 1.36
#3	+2.16 +0.95	2.06 1.52
#5	+1.47 +1.08	1.28 1.05

Figure 13. COMPARISON OF PROPAGATION-LOSS
DETERMINATIONS, SYSTEM 1 -
System 2

FREQUENCY	HYDROPHONE 1		HYDROPHONE 3		HYDROPHONE 5	
	BIAS	STD. DEVIATION	BIAS	STD. DEVIATIONS	BIAS	STD. DEVIATIONS
25 Hz	-.97	.61	+.50	.47	+.03	.74
50 Hz	-.24	.41	+.47	.51	-.15	.56
160 Hz	-.52	.39	+.39	.44	-.44	.57

Figure 14. COMPARISON OF PROPAGATION-LOSS DETERMINATIONS
SYSTEM 1 - SYSTEM 3

FREQUENCY	HYDROPHONE 3		HYDROPHONE 5	
	BIAS	STD. DEVIATION	BIAS	STD. DEVIATION
50Hz	+1.2	1.2	1.0	1.2
100Hz	0.0	1.2	0.8	0.6
200Hz	-0.6	1.5	0.6	1.4

Figure 15. COMPARISON OF PROPAGATION-LOSS DETERMINATIONS
SYSTEM 1 - SYSTEM 4

Summarizing the last three figures, we have propagation-loss uncertainties consisting of both biases and standard deviations as high as about 1.5 dB, which is not a particularly satisfying accuracy, especially since it does not include the uncertainty in source level.

DATA COMPARABILITY

Based on the investigations which have been conducted, it is clear that the source levels and processing bandwidths should be documented to permit data comparisons. Some indication of the quality assurance procedures used, or a best estimate of data accuracy is useful.

Ultimately, it appears desirable to develop standardized procedures for checking or adjusting processing systems. Some thought is currently being given to this in the LRAPP community using recorded transients to simulate explosive signals but constructed so that the spectral content can be computed by closed analytic forms.

REFERENCES

- Arons, A. B. and D. R. Yennie, "Energy Partition in Underwater Explosion Phenomena," *Rev. Mod. Phys.* 20, 519, 1948.
- Busch, J. M., "Spectra of Explosive Sound Sources: Mark 82 - Mod 0, Mark 64 - Mod 0, and No. 8 Vibro-Cap," Bell Laboratories, OSTP-12, November 12, 1973.
- Gaspin, J. B. and V. K. Shuler, "Source Levels of Shallow Underwater Explosions," Naval Ordnance Laboratory, NOLTR 71-160, November 13, 1971.
- Weston, D.E., "Underwater Explosions as Acoustic Sources," *Proc. Phys. Soc.* (London) 76, 233, 1960.

DISCUSSION

Dr. D. V. Wyllie (Weapons Research Establishment (WRE), Adelaide, South Australia): We are very interested in propagation-loss measurements using explosive charges as sound sources. We are also concerned with the difficulty in assigning a precise source level to these charges at frequencies around 20 Hz. Third-octave bands are unsuitable for use at these frequencies since they are too narrow and the resultant source level too uncertain. In our measurements we shall be employing octave bands. However, the source level still remains a problem.

Something we have considered is changing the pressure signature of the charge through the use of explosives other than TNT. There are groups within WRE interested in pursuing this approach.

Since the variation in level in narrow bands at low frequencies results from the interference between the radiation from the pressure and first-bubble pulse, the use of rocket propellant as the explosive could modify the pressure signature of the charge sufficiently to reduce level variations at low frequencies. The pressure signature can be modified by varying the burn rate of the explosive. The resulting explosive may be more useful at low frequencies. *Ms. Christian*, are you aware of previous work along these lines and would you like to comment on the approach?

Ms. E. A. Christian (Naval Surface Weapons Center): The fact is, yes, you certainly do have materials which have slower detonation (or burning) rates than typical HE materials. But the only way I have ever heard of for really eliminating this ungainly bubble pulse is through some mechanical method of breaking it up or venting it out. You can arrange to have a natural venting, as has been done by Woods Hole for many years; that is, you can fire the charge near the surface, shallow enough so that the bubble blows out and it isn't there to bother you.

However, when using very shallow charges, I think you have a serious source-level definition problem because you generate a directional pressure field that is highly sensitive to the exact firing depth. You no longer are really using the total charge output, so you no longer have the kind of source levels we are talking about. The best mechanical way of eliminating the bubble that I have heard about is a sort of iron maiden with a Swiss cheese skirt. You simply put the charge down into a big sphere with holes in it and this breaks up the bubble as it forms.

As far as eliminating the bubble pulse problem by varying your detonation rate in an explosive composition, I think the best you can do is redistribute your available energies somewhat; and you still come up with some sort of oscillation. What you are doing is transforming a solid mass of material into the same volume of gas in a very short time however much you slow down the detonation. Willy nilly, the gas is at a high pressure and temperature, it is going to expand rapidly, and then it is going to collapse. So I really can't see how you could eliminate the bubble pulse.

Dr. Wyllie: I wasn't talking about eliminating the bubble pulse, but rather the pressure pulse.

Ms. Christian: Well, in any case, it seems to me you are going to have a double pulse wave, even if you effectively cut off the top of your shock wave and have a slow-rising sinusoidal first pulse.

We have done a little work along those lines, not very much, using detonating black powder and an ARP propellant. We had problems of reproducibility with those materials. We found, for example, that with black powder you must have a very high containment to make the charge detonate reliably. And with the propellant indeed, you do cut off the top of the shock, but you still have the bubble. So if the

bubble is there oscillating, I would think you are still going to have an oscillatory spectrum.

Most likely you would cut off the level of the high-frequency end of your spectrum as you cut off the top of your sharp shock. So you have lost energy at the high-frequency end. You may not have lost as much energy at the low-frequency end as at the high, but possibly some is lost there as well. As I see it through my cloudy glasses, the problem is that so long as you have an oscillating bubble you don't have a white-noise spectrum, and I don't see how you can remedy this with chemical composition alone.

Dr. G. B. Morris (Scripps Institute of Oceanography): I believe the oil industry has had this problem of bubble pulses for several years and has in the past few years effected quite a number of solutions. One such system uses injections of high pressure steam, such that the steam condenses into water, eliminating the oscillating gaseous bubble. Other systems make use of what is known as a "sleeve exploder." A propane-oxygen mixture is injected into a perforated tube covered by a rubber sleeve. Upon detonation the sleeve contains the gaseous products which after full expansion are vented to the surface to prevent the bubble pulse.

Devices like these might get away from the bubble problem, although I suspect these devices give a lower energy output. The signal-to-noise ratios will be lower, and the resulting propagation measurements will be subjected to the signal-to-noise ratio problems discussed by Dr. Weinstein. What you have gained at one end by eliminating the bubble, you have lost at the other end by having a lower energy output source. However, it might be worthwhile examining the outputs of some of these sources.

Dr. M. Schulkin (Naval Oceanographic Office): What do you estimate is the high frequency cutoff for your oscillograms for those charges?

Ms. Christian: About 100 kHz. The response is flat up to about 100 kHz in oscilloscope readings.

Dr. Schulkin: We found that the peak pressure that you actually measure very much depended on the high-frequency response of the gage. For many systems used at sea, the tape recorder itself cuts off that peak.

Ms. Christian: Right. Actually, you can get within the typical reproducibility of the data points probably if your recordings are good up to about 20 kHz. You don't lose much in the peak pressure above that frequency. That is, you really can't see the very high-frequency spike above about 20 kHz. But if you cut off at, say, 5 kHz, you can be down 30 percent in the peak pressure. So all of those wave functions we use in the Gaspin and Shuler model require this extremely broad-band recording to give a true wave form.

Dr. Schulkin: I have seen records published where the peak and the first-bubble pulse have the same amplitude.

Ms. Christian: Oh sure, you will get to the point where the bubble peak pressure is higher than the shock if your cutoff frequency is sufficiently low. As a matter of fact, I think at an upper limit of about 500 Hz the bubble and shock are equal.

Mr. G. R. Hamilton (Office of Naval Research): What is the uniformity of our standard SUS from SUS to SUS if you detonate them all at the same depth? You talked about variations from variation in depth. What's the variation in source level if we fire them at precisely the same depth?

Dr. Weinstein: I have to honestly answer that we don't know. We don't have a set of data that would answer the question for us. We have been discussing means of finding out.

Mr. C. W. Spofford (Office of Naval Research): I have a comment for Dr. Weinstein. I am concerned with the measurements of transmission loss at low signal-to-noise ratios, especially when you might have many low signal-to-noise arrivals adding in the shot processor versus one larger arrival yielding the same total signal-to-noise ratio. The question is whether or not the accuracies of these two measurements are comparable. I think there may be less accuracy in the first measurement than the second, even when you appear to have 3 or 4 dB of signal-to-noise.

Dr. Weinstein: I think it goes the other way. If you have plus 3 dB signal-to-noise based on the total integration, and if you look at the peak of the individual arrivals and your multi-arrival structure to noise, your S/N would be a lot higher.

Mr. Spofford: I guess I'm concerned about losing arrivals down in the noise even though the final transmission loss appears to have adequate signal-to-noise. You may have lost the low amplitude arrivals in the noise.

Dr. Weinstein: The problem is we have noise and multiple arrivals. The signal-to-noise that I am talking about is what is obtained by doing a total integration over the multiple arrivals. You will obtain a lot lower signal-to-noise ratio than you would obtain if you were to define it based on the peak of one of your multi-path arrivals to noise background.

Dr. J. S. Hanna (Office of Naval Research): The question of signal-to-noise ratio that I believe Mr. Spofford was getting at is not the sort of thing that you get from looking at the peaks of those traces. He is interested in signal-to-noise ratio in a third-octave band around

some frequency. The question is what is the signal-to-noise ratio of each successive arrival? That's not directly inferrable from the broad-band pressure versus time history you showed.

You may have a very large signal-to-noise ratio based on peak amplitude but at some particular frequency have a very poor signal-to-noise ratio for that same arrival. So the point is, you may have some very marginal signal-to-noise ratios in that band arrival by arrival and yet have a total energy that is misleading.

Dr. Weinstein: Yes, I understand what you are saying. Why don't we consider the time series of the signal in a third-octave band already? If we were to look at a part of it, it would have a much higher signal-to-noise ratio than we would have for the total. Yes, there may be some arrival which we are not seeing which has a poor signal-to-noise ratio. But you have to recognize that we have time domain problems here. This harks back to the question of overloads in the system. Can you take an overloaded signal and make some estimate as to what the propagation loss level has to be at which you will overload? Well, the answer is you can't because the propagation loss depends upon the multistructure. The overload depends upon the individual peak.

Dr. S. C. Daubin (Rosenstiel School of Marine and Atmospheric Science, University of Miami): I want to ask a question related to Mr. Hamilton's question of variability from shot to shot at the same depth. Could you tell me what the manufacturing tolerance in a SUS is regarding the weight of the charge? Is it 1.8 pounds plus or minus what?

Dr. Weinstein: I don't remember the number precisely, but my recollection is it's going to be plus or minus a couple of tenths of a pound, something of that sort. But the problem doesn't lie in that tolerance. The problem lies in how the SUS is manufactured.

There can be as many as three pours for a single SUS with hardening and, therefore, layering between pours, so you have that additional problem.

APPLICATION OF RAY THEORY TO
LOW FREQUENCY PROPAGATION

Henry Weinberg

Naval Underwater Systems Center
New London Laboratory

Reprinted from NUSC Technical Report 4867, 18 December 1974.

ABSTRACT

The development of ray tracing techniques is reviewed, and then the effects of various sound-speed representations on the computed value of propagation loss are discussed. Since modified ray theories designed to treat caustics lose their effectiveness at the lower acoustic frequencies, an alternative approach for the horizontally stratified case is proposed. For oceans that are nearly horizontally stratified, the method of horizontal rays is applicable. Computed predictions are compared with measured data.

APPLICATION OF RAY THEORY TO LOW FREQUENCY PROPAGATION

INTRODUCTION

It is often said that ray theory is not applicable to low frequency propagation in the ocean. The purpose of this report is to demonstrate that this is not the case. If the word "ray" is allowed a more general meaning than that used in the classical sense, then ray tracing is indeed a useful means of modeling low frequency propagation.

Early ray tracing programs were primarily concerned with integrating the ray tracing equations of the next section accurately and efficiently. It is shown that the effect of sound-speed representations on the computed value of propagation loss is not as important as is currently believed. The most recent addition to practical ray tracing programs is the asymptotic treatment of caustics.

In the case of a horizontally stratified ocean, the integral representation may be expanded into a multipath series, each term of which corresponds to a particular ray type. Upon integrating, one obtains the acoustic pressure along the ray. It is important to note that this multipath expansion is exact. The accuracy of the final result depends on the method of solving the depth dependent wave equation and evaluating the ray type integrals.

For low frequency propagation in nearly horizontally stratified oceans, the method of horizontal rays is recommended. Here, the pressure is expressed as a summation of normal modes weighted by amplitudes satisfying horizontal ray tracing equations.

RAY TRACING EQUATIONS

Several years ago, the state of the art was described in Officer's¹ book on sound transmission. Then, ray tracing involved approximating the solution of the reduced wave equation for the acoustic pressure P

$$\nabla^2 P + \left(\frac{\omega}{c}\right)^2 P = 0$$

with the Wentzel-Kramers-Brillouin-Jeffreys (WKBJ) form

$$P = a \exp(i\omega T) .$$

The travel time T and amplitude a satisfy the eikonal equation

$$(\nabla T)^2 = c^{-2}$$

and the transport equation

$$\nabla \cdot a^2 \nabla T = 0 ,$$

respectively.

The eikonal equation may be solved by using the method of characteristics for first-order partial differential equations. Characteristic curves, better known as rays, are orthogonal to surfaces of constant time. They satisfy the ray tracing equations

$$\frac{d}{ds} \left(\frac{1}{c} \frac{dx}{ds} \right) = \frac{\partial}{\partial x} \frac{1}{c}$$

$$\frac{d}{ds} \left(\frac{1}{c} \frac{dy}{ds} \right) = \frac{\partial}{\partial y} \frac{1}{c}$$

$$\frac{d}{ds} \left(\frac{1}{c} \frac{dz}{ds} \right) = \frac{\partial}{\partial z} \frac{1}{c}$$

$$\frac{dT}{ds} = \frac{1}{c}$$

$$\left(\frac{dx}{ds} \right)^2 + \left(\frac{dy}{ds} \right)^2 + \left(\frac{dz}{ds} \right)^2 = 1 .$$

Once the rays have been found, the divergence theorem applied to the transport equation produces the geometrical spreading law for the pressure amplitude,

$$\frac{a}{a_0} = \left(\frac{c_0}{c} \frac{\delta \sigma}{\delta \sigma_0} \right)^{-1/2} ,$$

or for the equivalent plane wave intensity,

$$\frac{I}{I_0} = \left(\frac{\delta \sigma}{\delta \sigma_0} \right)^{-1} .$$

The subscript zero refers to a reference point (usually 1 yd away from a point source), and $\delta \sigma$ is the cross-sectional area of an infinitesimal ray tube. The intensity satisfies the conservation of energy law along a ray tube. It can be shown that pressure, on the other hand, satisfies the law of reciprocity.

In the case of a horizontally stratified ocean, that is, the sound speed and ocean boundaries are independent of both horizontal coordinates, the rays remain in a vertical plane and obey Snell's law,

$$\frac{1}{c} \frac{dr}{ds} = \text{constant} ,$$

where

$$r^2 = x^2 + y^2 .$$

SOUND SPEED REPRESENTATIONS

When ray theory was first implemented on digital computers, the primary concern was to integrate the ray tracing equations accurately and efficiently. Pedersen² motivated the design of many ray tracing programs by demonstrating the fact that discontinuities in the sound speed gradient could introduce anomalies in the computed value of geometrical spreading loss.

This effect is illustrated by fitting the sound speed profiles of figure 1 with piecewise linear,¹ piecewise quadratic,² and cubic spline³ representations. Differences are more readily seen in the sound speed gradients shown in this figure. The corresponding ray diagrams, figure 2, show that caustics due to discontinuities in the gradient of the piecewise linear fit disappear when smoother sound speed representations are employed. Propagation losses computed according to classical ray theory tend to accentuate this effect, but consider what would happen if a ray theory generalized to treat caustics correctly were used instead. Figure 3 indicates that the effect of different sound speed representations is insignificant providing that each representation accurately describes the input data to be fitted.

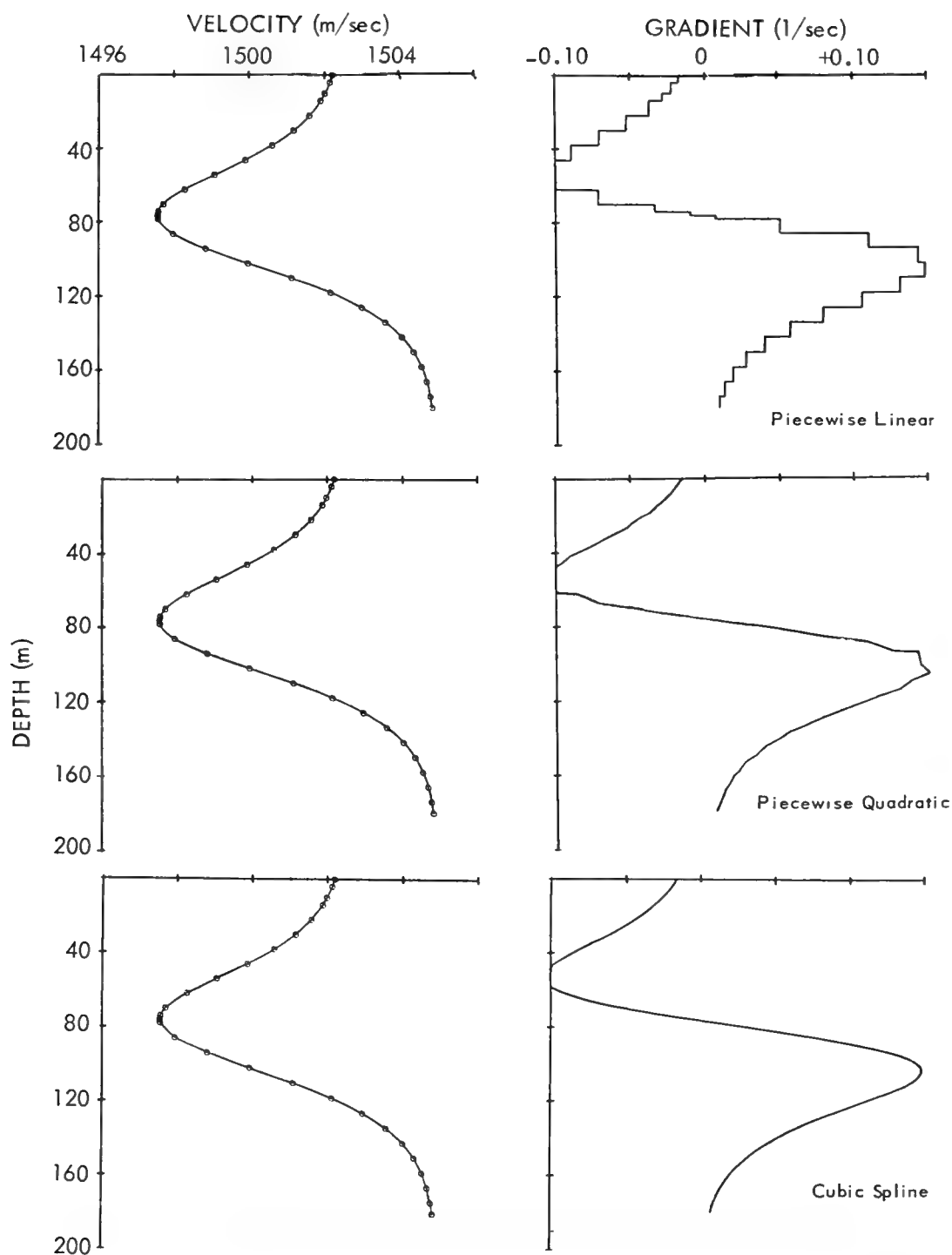


Figure 1. Comparison of Sound Speed Representations and Gradients

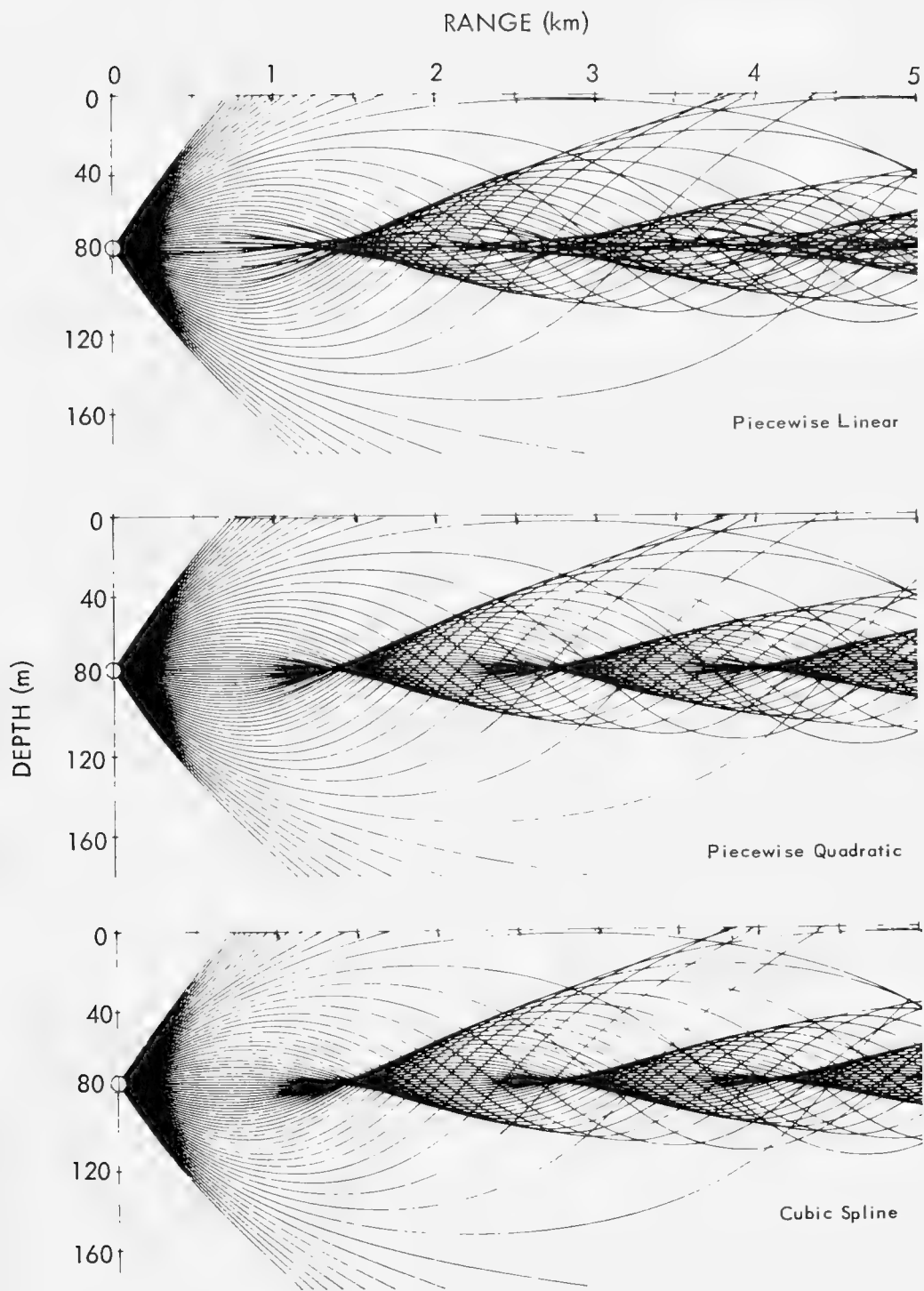


Figure 2. Comparison of Ray Diagrams for an Axial Source

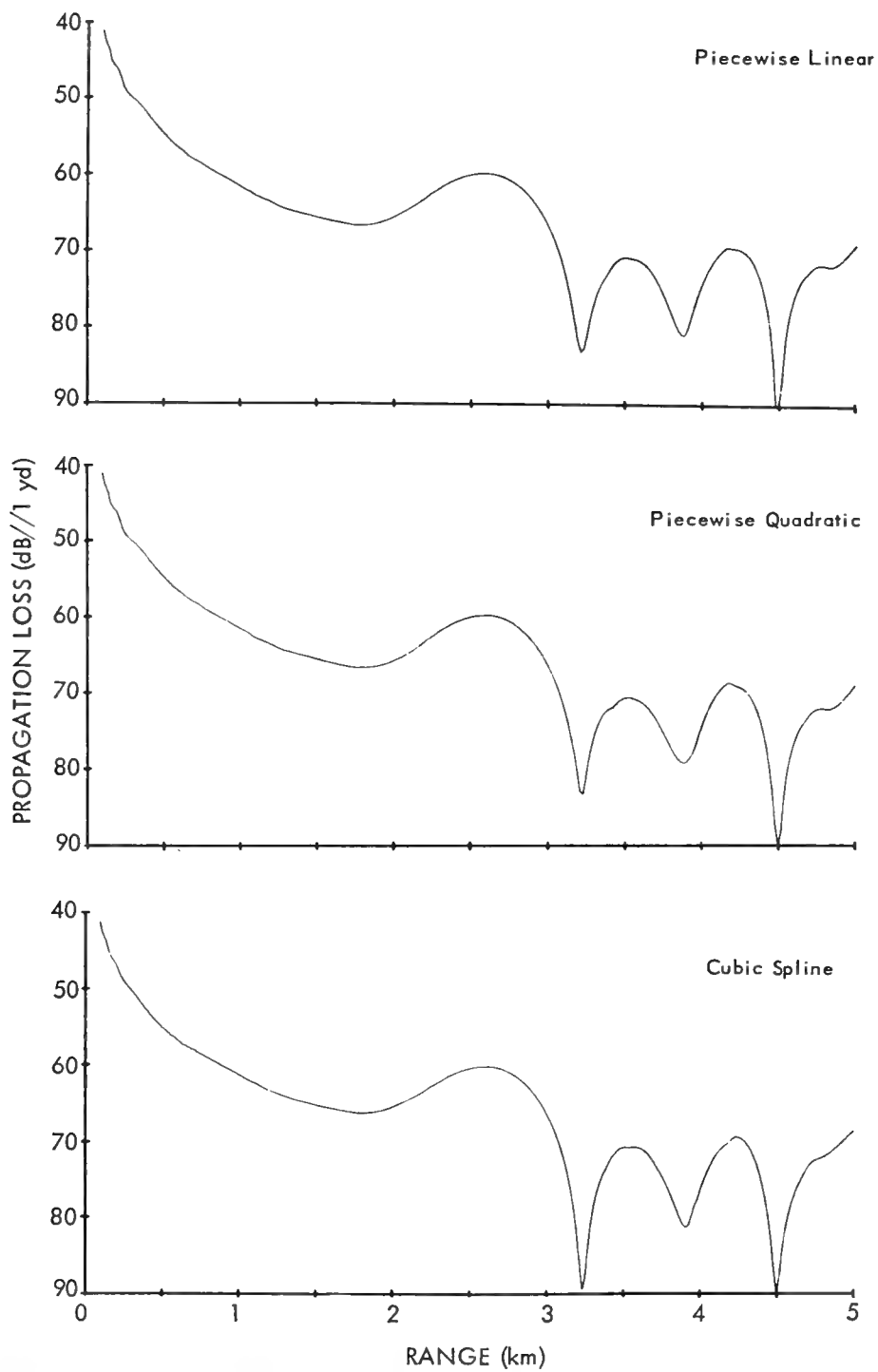


Figure 3. Comparison of 1-kHz Propagation Losses for a 40-m Receiver Depth

As far as ray diagrams and propagation losses computed according to classical ray theory are concerned, past experience indicates that cubic splines produce the best representations for analytic type sound speeds. However, as the input data become more irregular, the curve fitting procedure becomes more difficult to automate.⁴ A second disadvantage of cubic splines is that the corresponding ray tracing equations cannot be integrated in closed form, which is a process that can be accomplished with piecewise linear and quadratic fits.

Many of the statements made above are also true when the sound speed varies with one or more horizontal coordinates as well as depth. If, for example, the input data are fitted with triangular planes, the ray tracing equations may be integrated in closed form, but anomalies due to discontinuous gradients are possible.

ASYMPTOTIC TREATMENT OF CAUSTICS

In the last few years, significant advances in practical ray tracing techniques involved the treatment of caustics rather than improvements in curve fitting algorithms. The problem may be illustrated when the sound speed decreases inversely as the square root of depth, as shown in figure 4. We see that the ray diagram, figure 5, forms a well defined caustic.

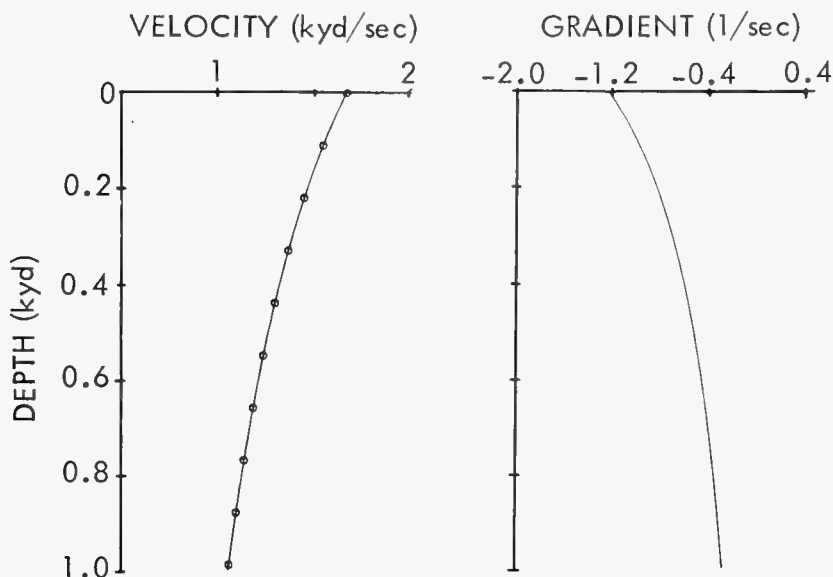


Figure 4. Sound Speed and Gradient Studied by Pedersen and Gordon

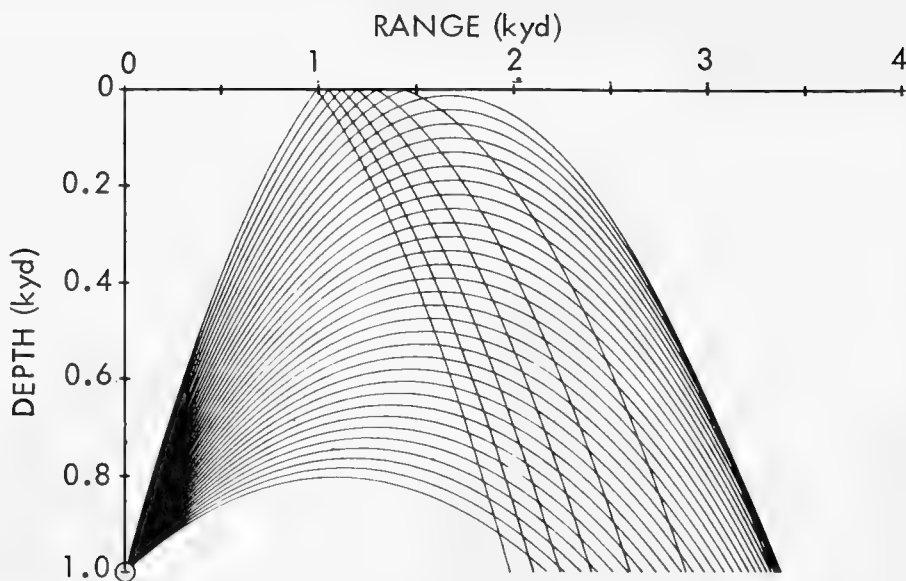


Figure 5. Ray Diagram for a 1-kyd Source Depth
Computed by Using the Sound Speed of Figure 4

Pedersen and Gordon⁵ compared the classical solution (solid line) with Brekhovskikh's⁶ modified ray theory (broken line) in figure 6. Classical ray theory predicts an infinite intensity at the caustic at 3159 yd and an infinite propagation loss in the shadow zone to the right of the caustic. Pedersen and Gordon explain that the abrupt change in loss at 3130 yd occurs at the ray that grazes the ocean surface. The modified ray theory did not apply to the left of this ray.

The above remark points out the difficulty of applying modified ray theories to the simplest of caustic geometries. Additional effects due to the ocean boundaries, cusped caustics, etc., prevent the theory from being applicable everywhere. One can program as many special cases as practical considerations suggest, but, more often, one uses classical and modified theories outside their domain of validity. Since caustic corrections are usually obtained by including additional terms of a high frequency expansion, errors increase as the frequency decreases.

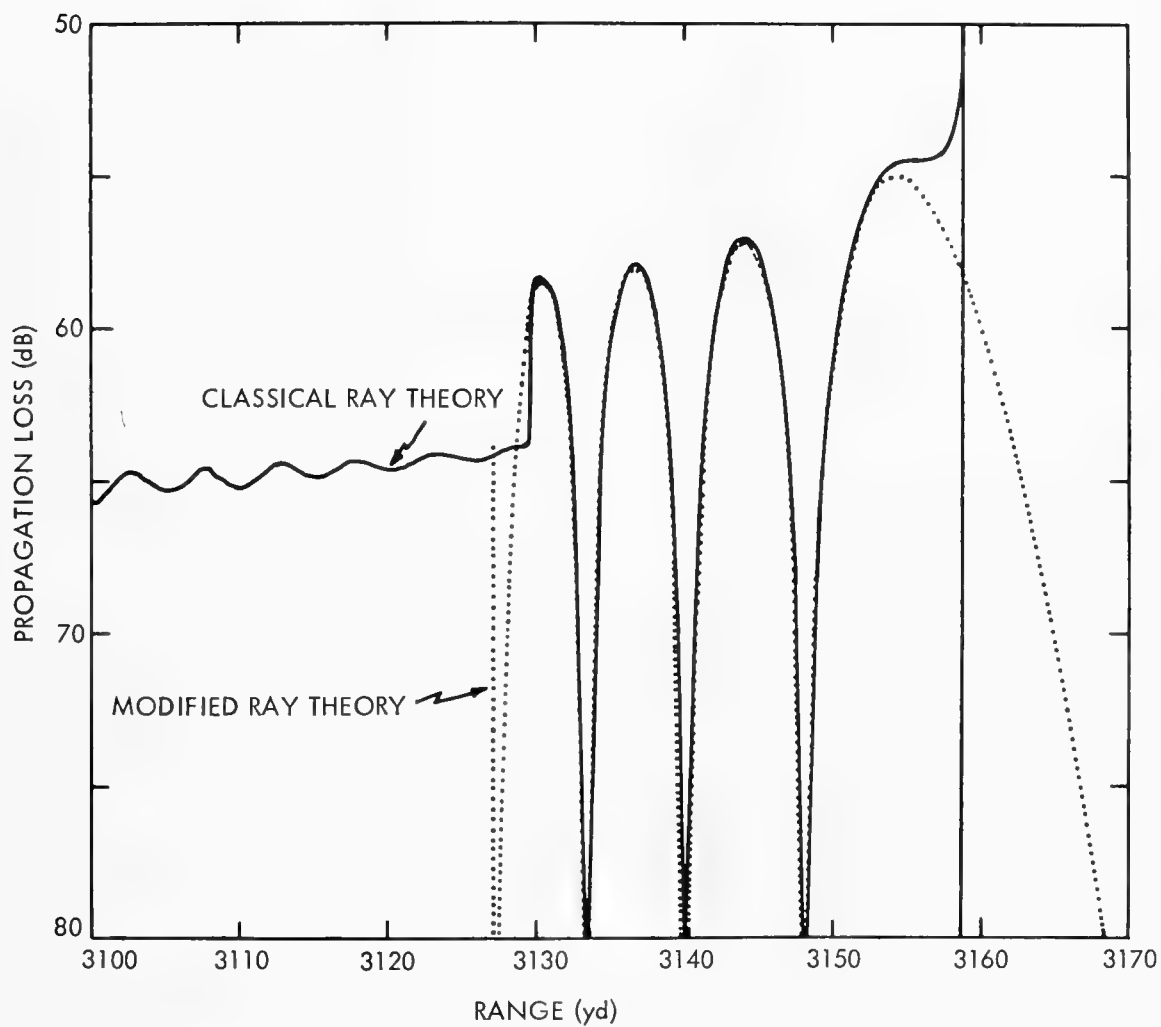


Figure 6. Comparison of 2-kHz Propagation Losses for a 0.8-kyd Receiver Depth Computed According to Classical and Modified Ray Theories (After Pedersen and Gordon, reference 5.)

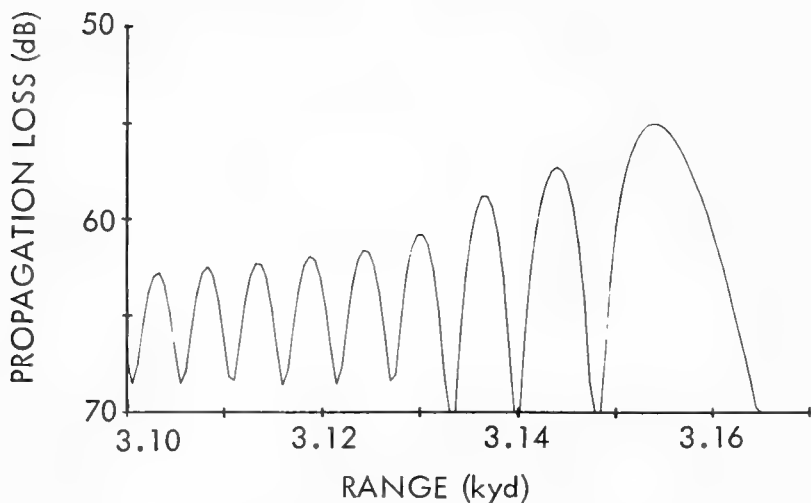


Figure 7. Propagation Loss for a 0.8-kyd Receiver Depth
Computed More Accurately Than That for Classical or
Modified Ray Theories

Consider what would happen if a theory generalized to treat caustics correctly were used instead. The result, figure 7, indicates that there is no discontinuity in propagation loss at the ray that grazes the ocean surface and also that classical ray theory appears to be more accurate to the right of the grazing ray than to the left. Consequently, modified ray techniques should be exercised with caution.

Spofford was one of the first to implement modified ray theory in a practical computer program. The procedure, based on the work of Ludwig,⁷ assumes that the reduced wave equation has an asymptotic solution of the form

$$P = \exp(i\omega T) \left\{ g \text{Ai}(\omega^{2/3} \rho) + \frac{h}{i\omega^{1/3}} \text{Ai}'(\omega^{2/3} \rho) \right\}$$

subject to the orthogonality condition

$$\nabla T \cdot \nabla \rho = 0 \quad ,$$

where Ai is the Airy function of the first kind, and T , ρ , g , and h are to be found. Upon substituting this ansatz into the reduced wave equation and comparing similar powers of frequency, one obtains

$$\begin{aligned} T &= (T_+ + T_-)/2 , \\ 2/3 \rho^{3/2} &= (T_+ - T_-)/2 , \\ g &= \rho^{1/4} (a_+ + a_-)/2 , \\ h &= \rho^{-1/4} (a_+ + a_-)/2 . \end{aligned}$$

As illustrated in figure 8, subscripts $+$ and $-$ refer to the two rays that touch and do not touch the caustic before reaching the field point, respectively. Therefore, all the quantities appearing in Ludwig's representation may be expressed in terms of the travel times T_{\pm} and amplitudes a_{\pm} of classical ray theory. Brekhovskikh's solution lacks the term involving the Airy function derivative, a term that is important away from the caustic. As a result, Ludwig's solution has a larger domain of validity.

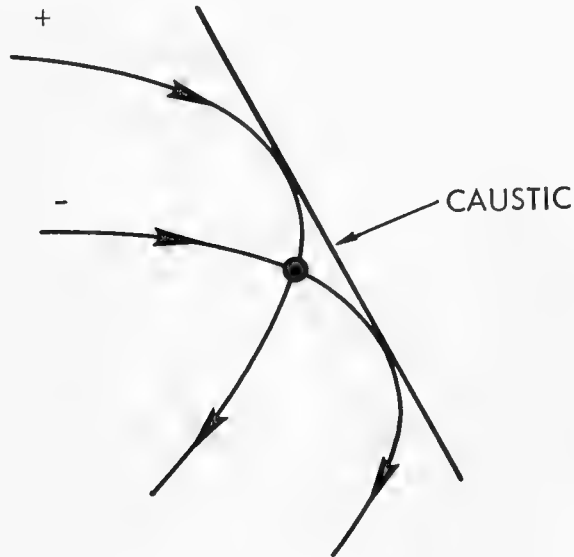


Figure 8. Classical Rays Used to Compute a Uniform Asymptotic Solution at a Caustic

LOW FREQUENCY PROPAGATION IN HORIZONTALLY STRATIFIED OCEANS

Most of the figures discussed before were produced by a computer program designed to model acoustic propagation in a horizontally stratified ocean. For mediums such as this, the acoustic pressure due to a unit point harmonic source situated at $(0, 0, z_S)$ has the integral representation

$$P(r, z, z_S; \omega) = \omega \int_0^\infty \omega \lambda J_0(\omega \lambda r) G(z, z_S; \lambda, \omega) d\lambda,$$

where the Green's function G satisfies the depth dependent wave equation

$$\left[\partial^2 / \partial z^2 + \omega^2 \left\{ c^{-2}(z) - \lambda^2 \right\} \right] G(z, z_S; \lambda, \omega) = -2\delta(z - z_S)$$

and suitable boundary conditions.

The method of solution used here, that is multipath expansion of the integral representation, is quite old, dating back nearly 40 years to Van der Pol and Bremmer.⁸ Following Leibiger and Lee,⁹ the Green's function is expressed in terms of two linearly independent solutions F_\pm of the homogeneous depth dependent equation. The solutions F_\pm are normalized so that their Wronskian equals $-2\omega i$. Upon expanding the denominator of G into a geometric series, the double summation

$$P(r, z, z_S; \omega) = \sum_{\nu=0}^{\infty} \sum_{n=1}^4 P_n^{(\nu)}(r, z, z_S; \omega)$$

is obtained. If $z < z_S$, one sees that

$$P_n^{(\nu)}(r, z, z_S; \omega) = \int_0^\infty i\omega J_0(\omega \lambda r) F_-(z; \lambda, \omega) F_+(z_S; \lambda, \omega) \gamma_{\text{sur}}^\nu(\lambda, \omega) \gamma_{\text{bot}}^\nu(\lambda, \omega) d\lambda,$$

where γ_{sur} and γ_{bot} are boundary reflection coefficients. Other terms of the series are similar, each integral representing a particular ray type. The first four are illustrated in figure 9. It is important to note that, so far, the solution is exact. The validity of the final result depends on the method of

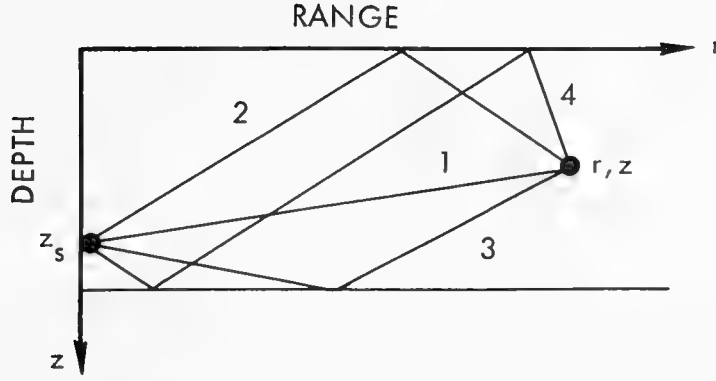


Figure 9. The Principal Ray Types

solving the depth dependent wave equation and evaluating the ray type integrals. If WKBJ and stationary phase techniques are used, respectively, the classical ray theoretic solution is obtained. Murphy¹⁰ replaced the WKBJ technique with a Weber function representation in order to treat the two-turning-point problem. Brekhovskikh replaced the method of stationary phase with an Airy integral modification in order to investigate caustics.

At present, our propagation model uses the following modified WKBJ expression to solve the depth dependent wave equation:

$$F_{\pm}(z; \lambda, \omega) = \pi^{1/2} \omega^{1/6} \exp \left\{ \pm i \omega Q(z_0, z_t; \lambda) \mp i \pi/4 \right\} \\ g(z; \lambda) \left(\text{Bi} \left\{ \omega^{2/3} \rho(z; \lambda) \right\} \pm i \text{Ai} \left\{ \omega^{2/3} \rho(z; \lambda) \right\} \right), \\ Q(z_0, z_t; \lambda) = \int_{z_0}^{z_t} \left\{ c^{-2}(\zeta) - \lambda^2 \right\}^{1/2} d\zeta, \\ \rho(z; \lambda) = - \left\{ \frac{3}{2} Q(z, z_t; \lambda) \right\}^{2/3}, \text{ and } g(z; \lambda) = \left| \frac{\partial \rho(z; \lambda)}{\partial z} \right|^{-1/2},$$

where

z_0 is a suitably chosen reference point

z_t is a turning point

Bi is the Airy function of the second kind.

Whenever $\omega^{2/3}\rho$ is a moderate to large negative number, F_{\pm} reduces to the usual WKBJ representation

$$F_{\pm}(z; \lambda, \omega) = \left\{ c^{-2}(z) - \lambda^2 \right\}^{-1/4} \exp \left\{ \pm i\omega Q(z_0, z; \lambda) \right\}.$$

Since this modified representation is inaccurate in the vicinity of double turning points, F_{\pm} are arbitrarily set to zero whenever they occur. Hopefully, this will only affect a small interval of integration and will not introduce significant errors in the final result. Murphy's technique offers an alternative procedure.

The method of evaluating the ray type integrals is based on the following:

1. Segment the interval of integration into suitably chosen subintervals.
2. Use stationary phase to evaluate subintegrals whenever possible.
3. Integrate the remaining cases numerically.

It was originally thought that the numerical integration, although lengthy when compared with stationary phase, would be invoked so infrequently that its contribution to the total computer running time would be inconsequential. So far, this has not been the case. Hopefully, the running time will be reduced eventually when the integration routine is made more efficient.

Since it is customary to give computer programs names so that they may be distinguished from others performing similar functions, the program used herein is called CONGRATS V, where CONGRATS is an acronym for Continuous Gradient Ray Tracing System. Actually, the completed program will predict the performance of active and passive sonar systems and is, therefore, more than just a propagation program. As shown in figures 1 through 3, CONGRATS V has the option to invoke several ray tracing procedures. The propagation losses were obtained by adding the multipath contributions coherently. CONGRATS V also produces a plot of propagation loss using power addition, in which case the phases of the individual contributors are neglected.

A COMPARISON OF PROPAGATION MODELS

At present, the state of the art of propagation modeling for stratified oceans may be illustrated by two figures compiled by E. Jensen of NUSC. (See figures 10a and 11a.) Both compare FFP,¹¹ FACT,¹² RAYMODE 9,¹³ and NISSM II¹⁴ computer predictions for 50-Hz propagation in the Pacific. The choice of programs included in the comparison was mainly of convenience, since each is available at NUSC, New London, and all but FACT were designed there.

Briefly, the Fast Field Program (FFP) utilizes Fast Fourier Transforms to evaluate the integral representation. The Fast Asymptotic Coherent Transmission Model (FACT) is a constant gradient ray tracing program incorporating sophisticated low frequency modifications. RAYMODE 9, the latest version of the series, uses ray theory to determine which intervals dominate the integral representation, but uses normal modes to compute the acoustic amplitude. The Navy Interim Surface Ship Model (NISSM) II is a continuous gradient ray tracing program designed to predict the performance of active sonar systems. All but FFP have the option to combine multipath contributions incoherently as well as coherently, and all but FFP use alternative procedures for surface duct propagation.

As a result, the first case (figure 10a), which is dominated by surface duct propagation, will show the greater variability. FACT is an order of magnitude faster than NISSM II and RAYMODE 9, while FFP is a good deal slower.

Upon adding CONGRATS V to the comparison (figure 10b) and invoking the coherent phase option, one sees good agreement with FFP. Had the incoherent phase option been invoked instead, CONGRATS V would have agreed with the others.

The second case, figure 11a is dominated by convergence zone propagation. The agreement is better than before although running times continue to differ by orders of magnitude.

Upon adding CONGRATS V to this comparison (figure 11b), one obtains reasonable agreement with FFP. It is unusual to find agreement among models that are based upon different theories and written by different programmers. Unfortunately, comparisons are not always this good. Hopefully, all discrepancies will soon be eliminated or at least accounted for.

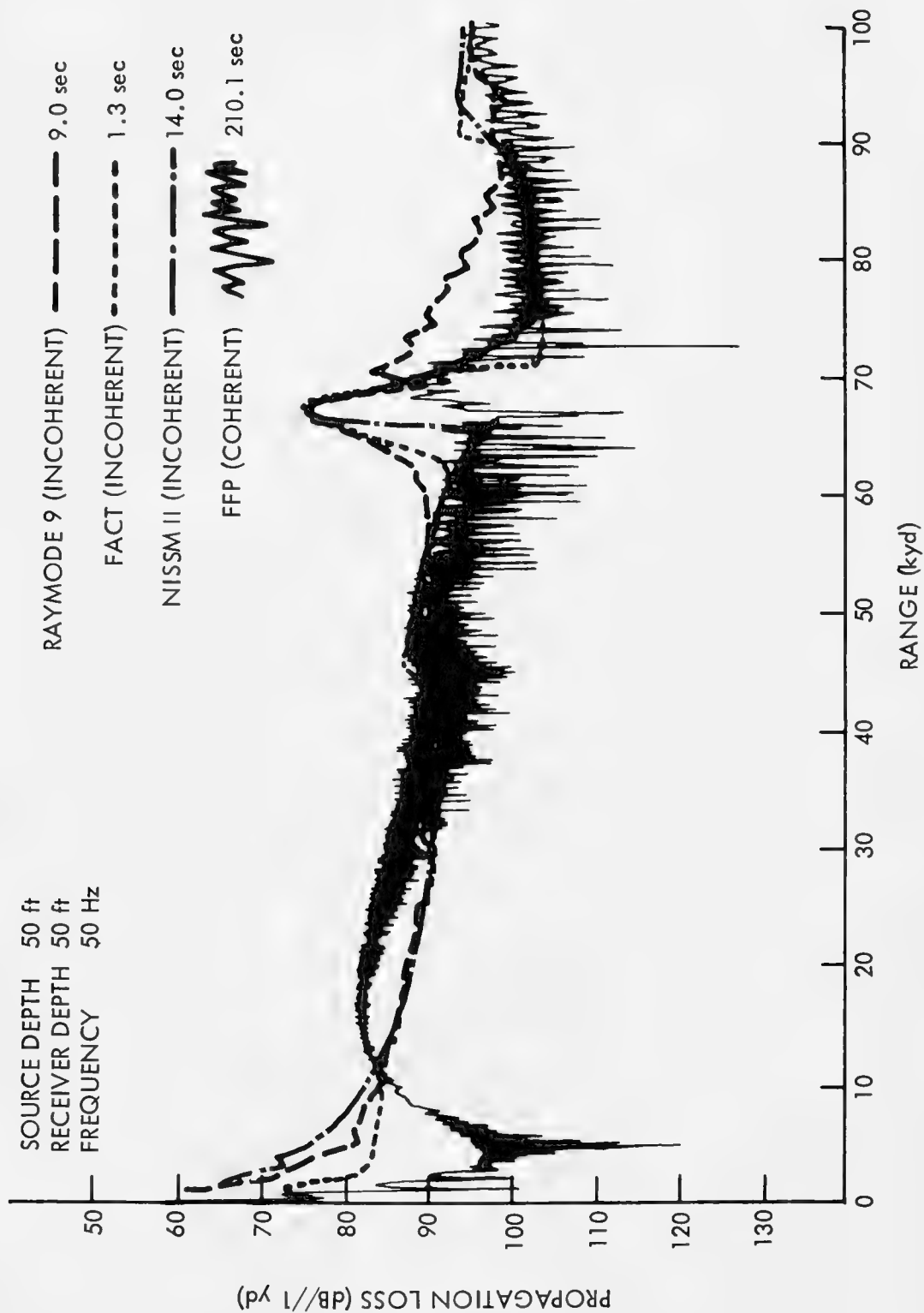


Figure 10a. Low Frequency Surface Duct Propagation for a Pacific Sound Speed Profile
 (From E. Jensen, of NUSC, unpublished data.)

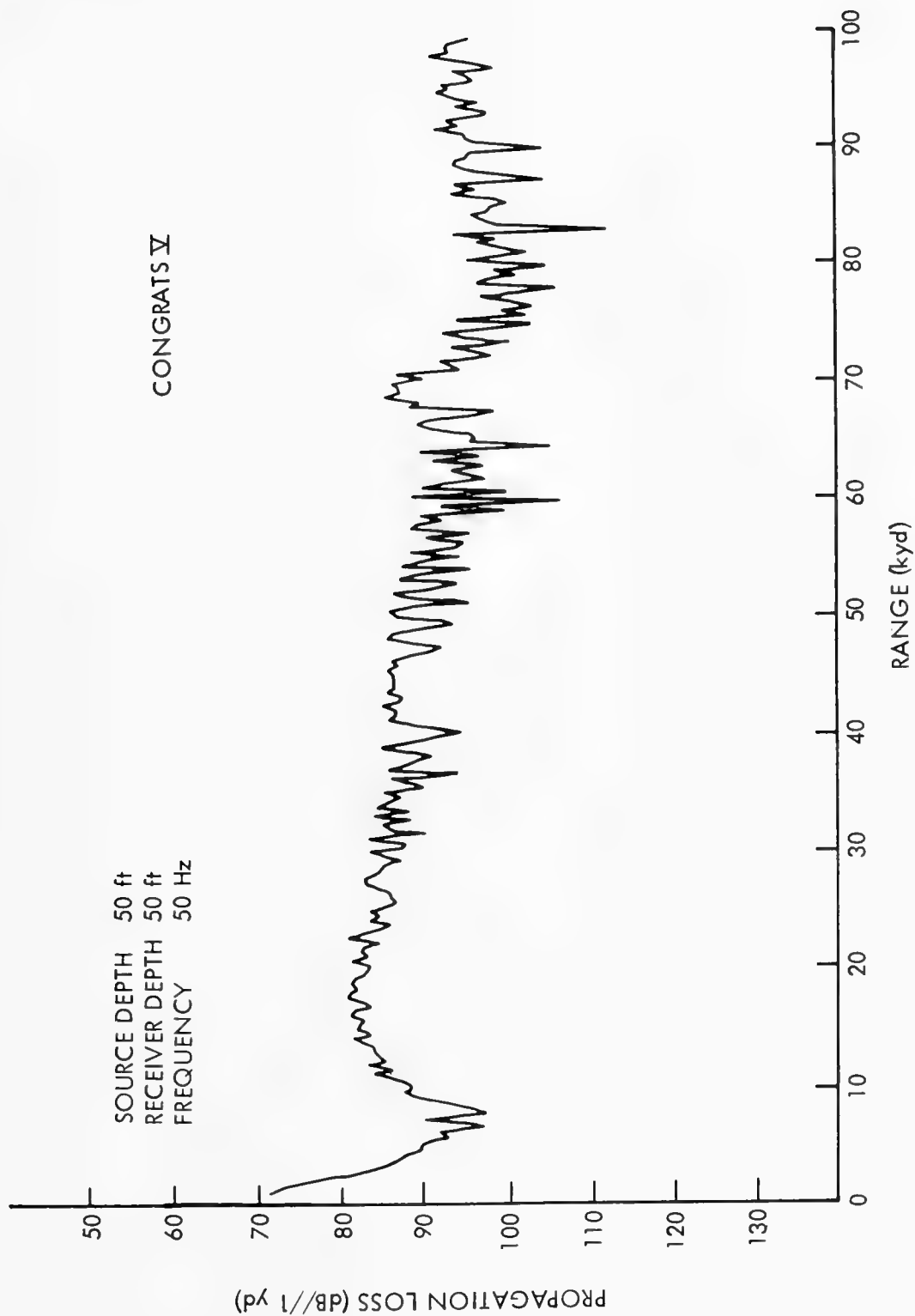


Figure 10b. CONGRATS V Low Frequency Surface Duct Propagation for a Pacific Sound Speed Profile

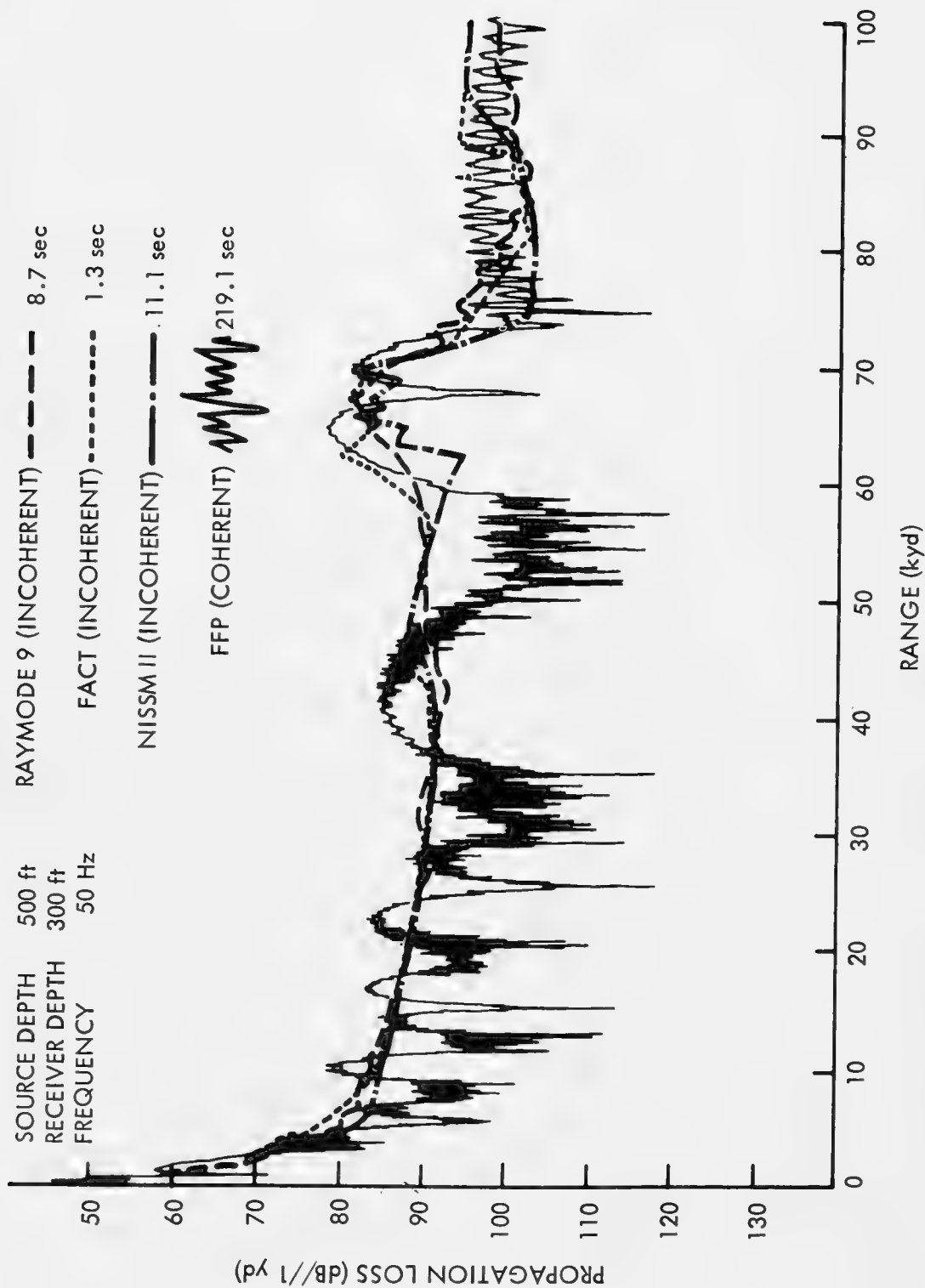


Figure 11a. Low Frequency Convergence Zone Propagation for a Pacific Sound Speed Profile
 (From E. Jensen, of NUSC, unpublished data.)

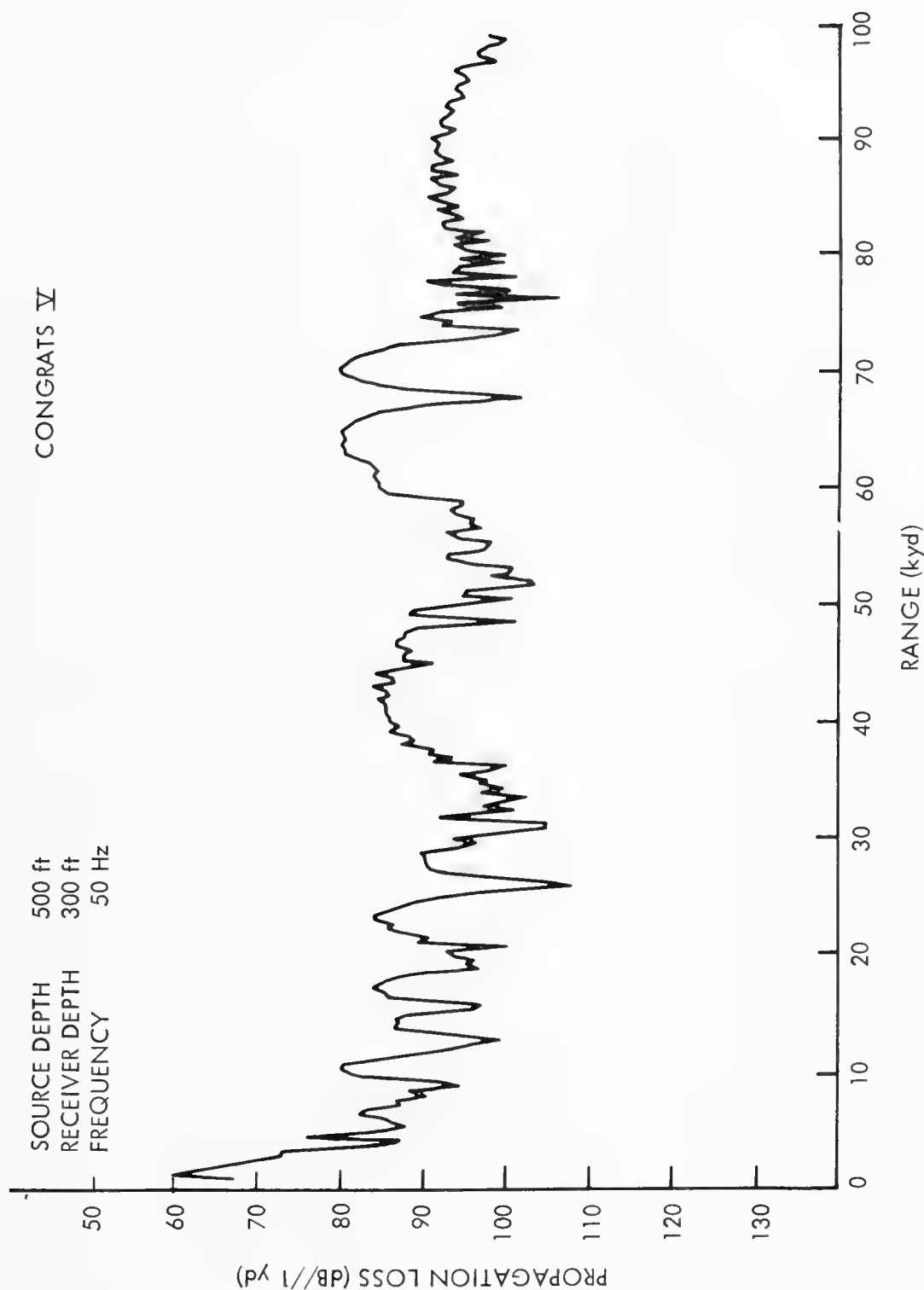


Figure 11b. CONGRATS V Low Frequency Convergence Zone Propagation for a Pacific Sound Speed Profile

HORIZONTAL RAY THEORY FOR NEARLY HORIZONTALLY STRATIFIED OCEANS

At long ranges or in shallow water, the effects of horizontal variations in the sound-speed or bottom characteristics are often large and not readily modeled by any of the techniques discussed previously. A nearly horizontally stratified ocean is one in which the horizontal variation is slow.

This rather vague notion is quantized by introducing a small parameter ϵ and assuming that the properties of the medium depend on the horizontal coordinates X, Y only through the combinations¹⁵

$$x = \epsilon X, \quad y = \epsilon Y.$$

This being so, let us seek solutions of the reduced wave equation in the form

$$P(x, y, z; \epsilon) \approx \exp \left\{ \theta(x, y)/i\epsilon \right\} \sum_{\nu=0}^{\infty} A_{\nu}(x, y, z) (i\epsilon)^{\nu}.$$

Each A_{ν} , in turn, is assumed to have the form

$$A_{\nu}(x, y, z) = \sum_{k=0}^{\infty} a_{\nu}^{(k)}(x, y) \psi_k(x, y, z),$$

where the ψ_k are orthonormal eigenfunctions of the depth dependent wave equation

$$\frac{\partial^2 \psi_k}{\partial z^2} + K^2(x, y, z) \psi_k = \lambda_k^2 \psi_k$$

subject to the appropriate boundary conditions.

Upon substituting our ansatz into the reduced wave equation and comparing similar powers of $i\epsilon$, one finds that the phase function, θ , satisfies the horizontally dependent eikonal equation

$$\left(\frac{\partial \theta}{\partial x} \right)^2 + \left(\frac{\partial \theta}{\partial y} \right)^2 = \lambda_p^2(x, y),$$

where λ_p is one of the eigenvalues, λ_k , computed above.

This equation, like the ordinary eikonal equation, may be solved by using ray tracing techniques. Note, however, that all depth dependence is missing. The pressure depends on depth only through the vertical eigenfunctions. It may also be shown that the leading amplitude, $a_p^{(0)}$, satisfies the conservation law

$$\lambda_p \left(a_p^{(0)} \right)^2 \delta \sigma = \text{constant}$$

along a horizontal ray tube.

A computer program based on the consideration above was written to proceed in two stages. The first determines the eigenvalues and normalized eigenfunctions at each point of a rectangular grid in the horizontal plane. Then, during the second part, a set of horizontal ray tracing equations is integrated for each eigenvalue, and the contributions of individual modes are combined to obtain the total field.

As in ordinary ray programs, only the leading term of the asymptotic expansion of each mode is found. The expansion then reduces to that derived by Pierce almost 10 years ago.¹⁶

The program predicted propagation loss along a 1500-nmi track extending northward from 27° 30'N, 157° 50'W to 52° 30'N, 157° 50'W. Eleven equidistant velocity-depth profiles obtained from the measured data displayed in figure 12 were entered into the computer program. Note that the SOFAR axis rises from a depth of 795 m at 27° 30'N to about 50 m at 52° 30'N. Lack of relevant data prevented the inclusion of any dependence of sound speed or bottom depth upon longitude.

Figure 13 displays propagation losses from dynamite charges detonated 500 ft below sea level along the track to a 2500-ft receiver depth situated at 27° 30'N. The top graph represents observational data, while the middle graph shows computed results. The two are superimposed in the bottom graph. The figure displays an interesting feature. The propagation loss decreases with increasing range beyond 42°N. This decrease may be explained by the fact that the receiver is only 124 ft away from the SOFAR axis, where the signal is strongly affected by the amplitude of the few lowest modes, as shown in figure 14. As the source ship moved north, the source approached the SOFAR axis causing the amplitude of these modes (figure 15) to increase to such an extent that eventually the loss due to horizontal spreading was overcome and the total propagation loss decreased.

The 10,800-ft receiver depth of figure 16 is well below the turning points of the first few modes, and so the signal there is dominated by the higher modes. The amplitudes of these modes are not greatly affected when the source approaches the SOFAR axis; therefore, for this receiver, cylindrical spreading dominates the entire track.

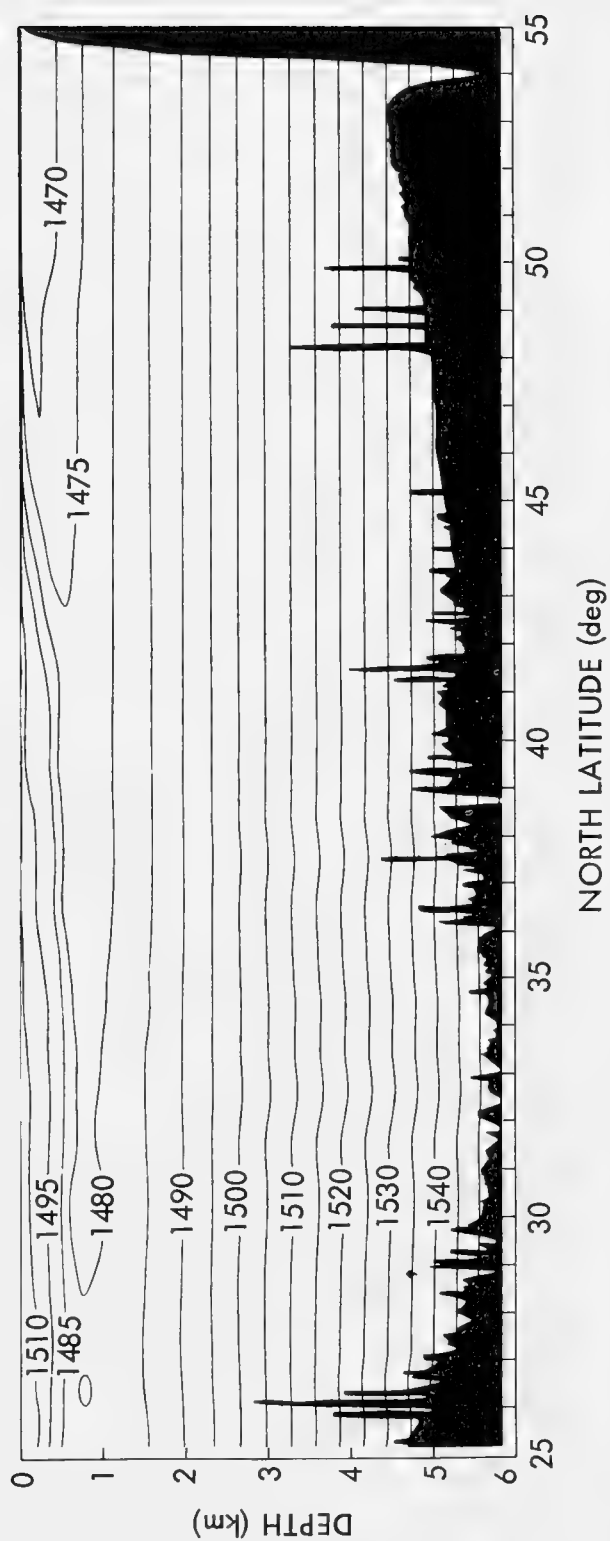


Figure 12. Contour of Sound Speed (m/sec) Along the Meridian 157° 50'W

FREQUENCY 31 Hz
SOURCE 500 ft
RECEIVER 2500 ft

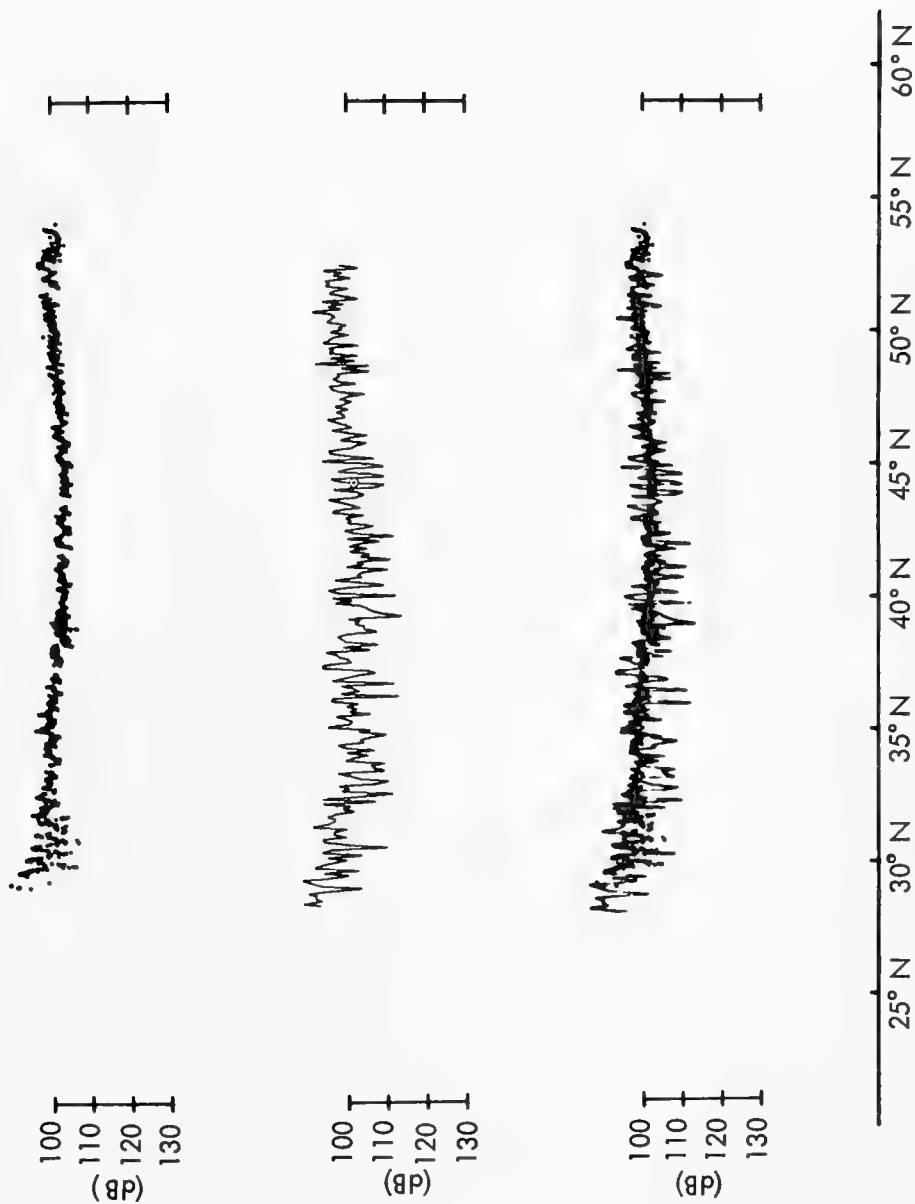


Figure 13. Propagation Loss versus Range for a 2500-ft Receiver Depth,
a 500-ft Source Depth, and a 31-Hz Frequency

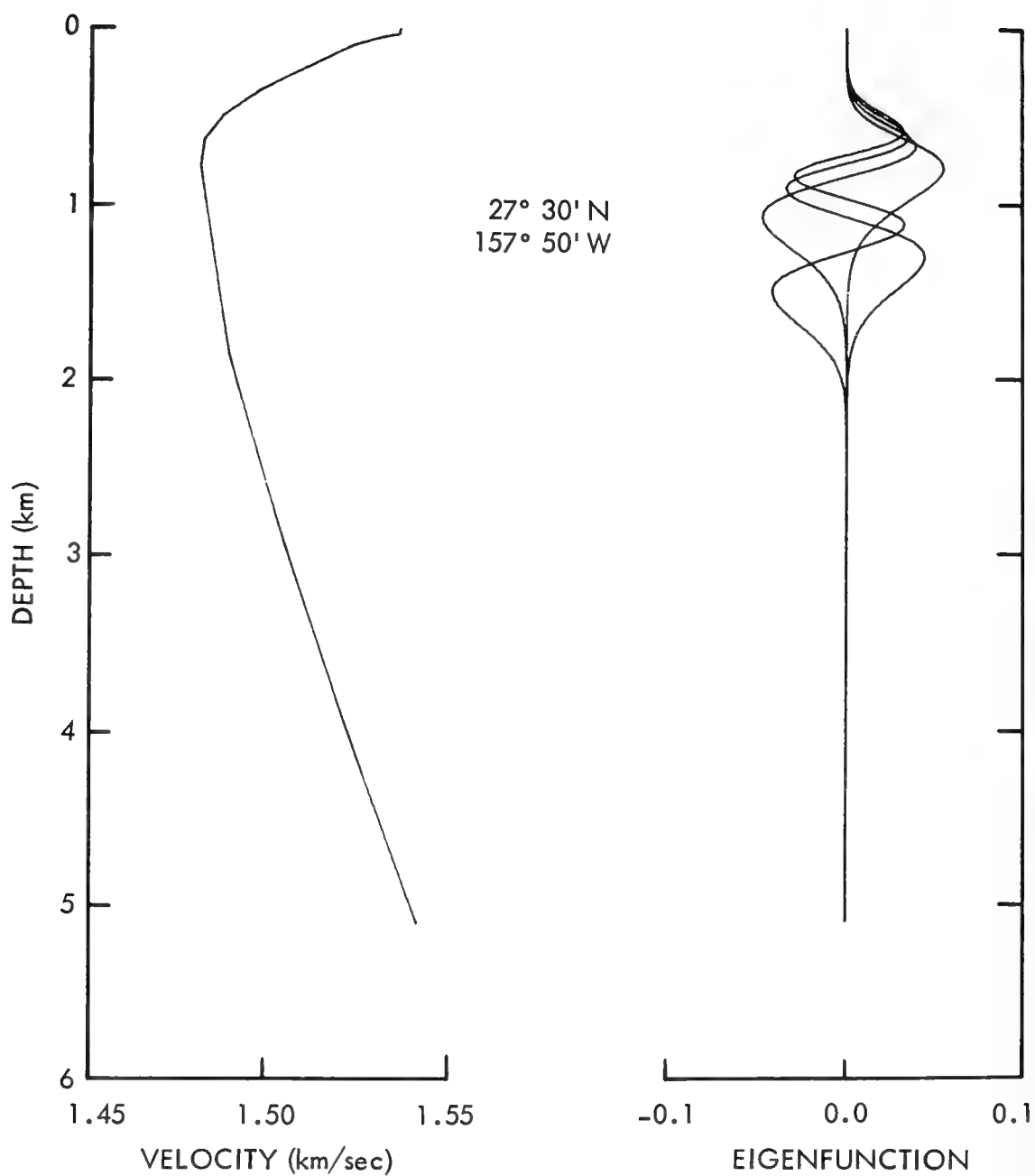


Figure 14. Sound Speed-Depth Profile at 27° 30'N, 157° 50'W and the Corresponding First Four Modes for a 31-Hz Frequency

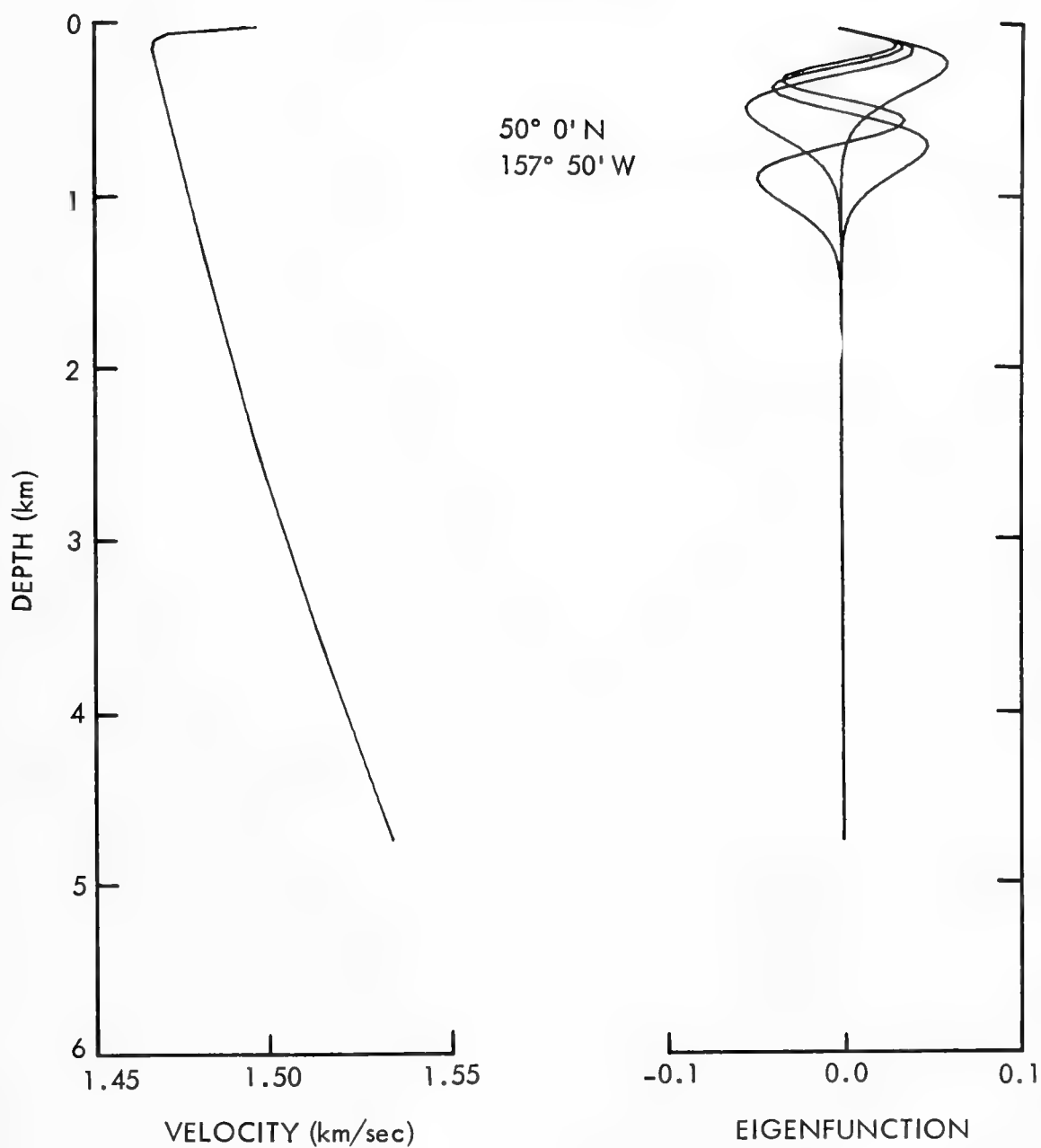


Figure 15. Sound Speed-Depth Profile at 50° 0'N, 157° 50'W and the Corresponding First Four Modes for a 31-Hz Frequency

FREQUENCY 31 Hz
SOURCE 500 ft
RECEIVER 10800 ft

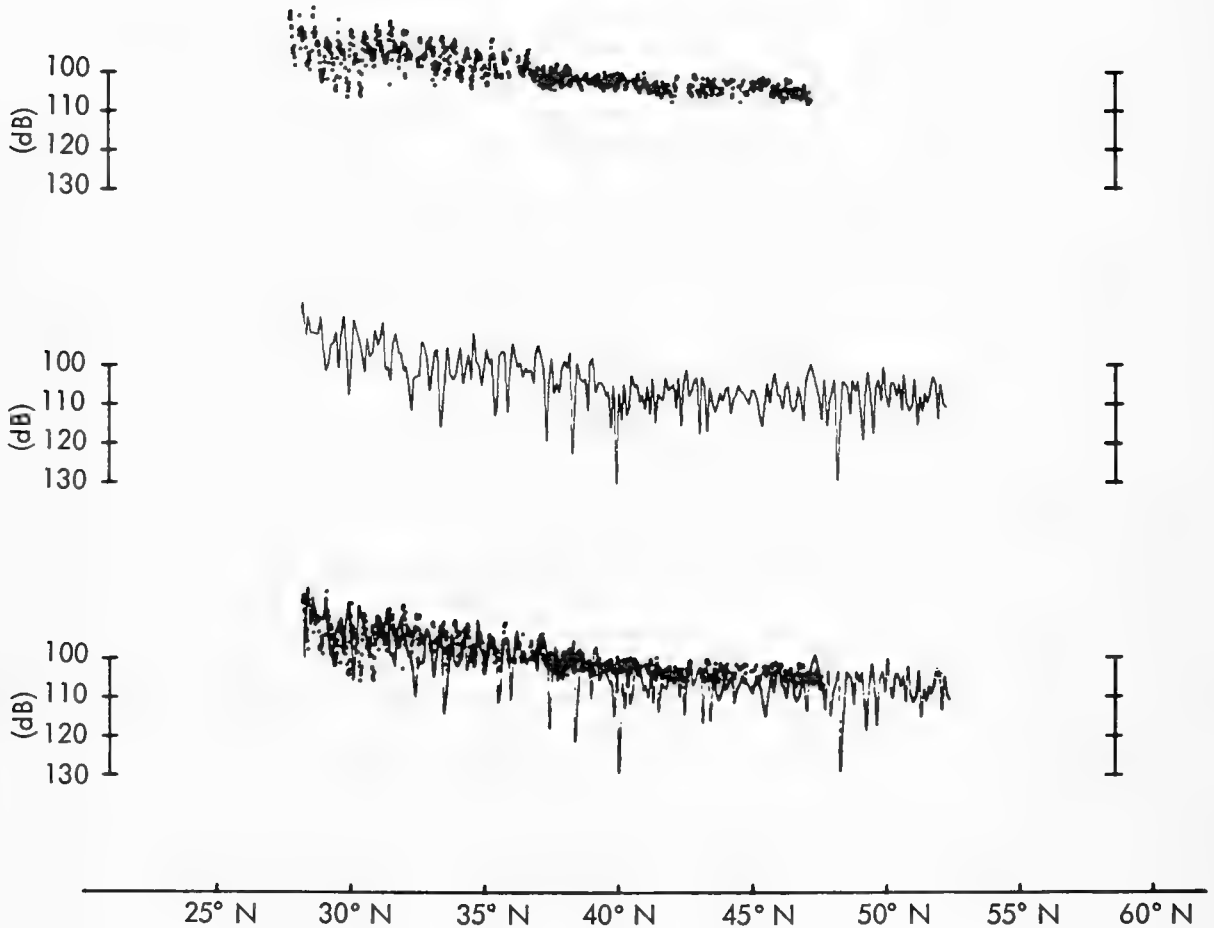


Figure 16. Propagation Loss versus Range for a 10,800-ft Receiver Depth, a 500-ft Source Depth, and a 31-Hz Frequency

SUMMARY

Contrary to popular belief, ray theory is an accurate and efficient means of investigating low frequency acoustic propagation in the ocean. Of course, in this report ray theory has not been used in its classical sense.

Several illustrative examples proved that it is possible to design a single propagation model that agrees with analytic solutions and measured data, as well as other computer programs. This effort is more difficult than one may realize, for once a computer program is tuned to the actual environmental conditions of a real ocean, it may be impossible to input data for which analytic solutions are known. The apparently simple task of comparing programs is in reality even more difficult than a comparison with analytic solutions. First, one must have access to the programs being compared. Second, the programs must treat the input data similarly. Finally, the programs must treat the output data similarly. For example, how is one to compare coherent phase propagation loss predictions with those of a random phase program?

Although all the computer models discussed above have been designed within the last few years, the theories upon which they are based are much older. Therefore, it is felt that improved computing facilities rather than improved acoustic theories have been responsible for improved prediction capabilities.

The future of ray theory may prove quite different. Application to unstratified media, random media, etc. is the next logical step, but these theories need more development before they can be implemented into practical prediction models.

REFERENCES

1. C. B. Officer, Introduction to the Theory of Sound Transmission, McGraw-Hill Book Company, New York, 1958.
2. M. A. Pedersen, "Acoustic Intensity Anomalies Introduced by Constant Velocity Gradients," Journal of the Acoustical Society of America, vol. 33, no. 4, April 1961, pp. 465-474.
3. C. B. Moler and L. P. Solomon, "Use of Splines and Numerical Integration in Geometrical Acoustics," Journal of the Acoustical Society of America, vol. 48, no. 3, September 1970, pp. 739-744.
4. A. K. Cline, "Scalar- and Planar-Valued Curve Fitting Using Splines Under Tension," Communications of the ACM, vol. 17, no. 4, April 1974, pp. 218-220.
5. M. A. Pedersen and D. F. Gordon, "Normal-Mode and Ray Theory Applied to Underwater Acoustic Conditions of Extreme Downward Refraction," Journal of the Acoustical Society of America, vol. 51, no. 1, January 1974, pp. 323-368.
6. L. Brekhovskikh, Waves in Layered Media, Academic Press, New York, 1960.
7. D. Ludwig, "Uniform Asymptotic Expansions at a Caustic," Communications on Pure and Applied Mathematics, vol. 19, no. 1, 1966, pp. 215-250.
8. B. Van der Pol and H. Bremmer, "The Diffraction of Electromagnetic Waves from an Electrical Point Source Round a Finitely Conducting Sphere, with Application to Radio Telegraphy and the Theory of the Rainbow," Philosophical Magazine, vol. 24, pt. 1, July 1937, pp. 141-176, and pt. 2, November 1937, pp. 825-864.
9. G. A. Leibiger and D. Lee, "Application of Normal Mode Theory to Convergence Zone Propagation," Vitro Laboratory Research Memorandum VL-8512-12-0, Vitro Laboratories, West Orange, New Jersey, 30 November 1968.
10. E. L. Murphy, "Modified Ray Theory for the Two-Turning-Point Problem," Journal of the Acoustical Society of America, vol. 47, no. 3, March 1970, pp. 899-908.
11. F. R. DiNapoli, Fast Field Program for Multilayered Media, NUSC Technical Report 4103, 26 August 1971.
12. Acoustic Environmental Support Detachment, "Fast Asymptotic Coherent Transmission (FACT) Model," Office of Naval Research, 1 April 1973.

13. G. A. Leibiger and D. Lee (This program has not yet been documented. See reference 9 for an earlier version.)
14. H. Weinberg, Navy Interim Surface Ship Model (NISSM) II, NUSC Technical Report 4527, 14 November 1973.
15. H. Weinberg and R. Burridge, "Horizontal Ray Theory for Ocean Acoustics," Journal of the Acoustical Society of America, vol. 55, no. 1, January 1974, pp. 63-79.
16. A. D. Pierce, "Extension of the Method of Normal Modes to Sound Propagation in an Almost-Stratified Medium," Journal of the Acoustical Society of America, vol. 37, no. 1, January 1965, pp. 19-27.

NORMAL MODES IN OCEAN ACOUSTICS

D. C. Stickler

Applied Research Laboratory
Pennsylvania State University

The utility of using normal-mode theory to explain acoustic phenomena when dealing with underwater acoustic problems has been established. Pekeris used it to predict the results of shallow-water transmission of explosive charges. This report discusses applications of normal-mode expansions and the role of the discrete and continuous spectrum, it provides a physical interpretation, describes the effect of both proper and improper or leaky modes, describes the differences arising from the branch-cut choices, and considers the effect of shear waves on the pressure field.

Several working computer programs based on normal-mode theory are compared both by a general description of their capabilities and by their specific treatment of the discrete and continuous spectral contributions.

BACKGROUND

During World War II C. L. Pekeris became the first to apply normal-mode theory to problems in underwater acoustics. Since that time this technique has been employed to explain various acoustic phenomena. The elementary model used by Pekeris will be used here to describe some of the properties of normal-mode expansions.

To apply normal-mode theory in underwater acoustics it is necessary to assume that the acoustic parameters depend on the depth coordinate alone. This means, in particular, that both the longitudinal and shear speeds and the density depend only on depth and that the ocean-surface and ocean-bottom interface are flat and orthogonal to the depth coordinate. Specifically, this excludes sound-speed profiles that depend upon either range or azimuth

and environments involving sloping bottoms. Perturbation techniques can be used to extend normal-mode theory to less restrictive environments.

Fortunately, in many areas this is an adequate model, and normal-mode theory has proved successful in explaining various acoustic phenomena. In those environments where this is not true, other methods must be employed. All these alternative methods involve approximations, some of which cannot be listed directly. The validity of some of these approximations can be tested by comparison with the "exact" normal-mode representation. These comparisons are certainly necessary, and they usually yield considerable insight into the nature of the approximations as well as suggest methods for improving them.

This paper has two points of focus: (1) the physical interpretation of the concept and techniques of normal-mode expansions, and (2) the description of those features of the expansion that are the result of the assumption that the depth coordinate is semi-infinite. Expanding slightly on this second point, consider the case of an acoustic wave guide of finite cross section with perfectly reflecting walls. The normal-mode expansion of the pressure field for this case consists of an infinite, discrete sum of normal modes. If one of these wave-guide walls is moved to infinity, then the normal-mode expansion must be modified, depending upon the behavior of the sound speed at infinity. Physically, this modification accounts for the energy that can now be propagated to infinity in this new direction. The principal effect on the normal-mode expansion is that, in general, the representation consists of a sum of trapped or proper modes plus an integral superposition of modes.

This feature depends on the nature of sound speed as the depth coordinate approaches infinity. If the sound speed is constant

as the depth coordinate becomes infinite, then the representation consists of a finite sum of "trapped" modes (there may be none) plus an integral superposition which can sometimes be approximated by a sum of "leaky" modes. If the sound speed approaches zero sufficiently rapidly as the depth coordinate approaches infinity, there are no trapped modes, only an integral superposition that, as above, can be approximated in some situations as a sum of leaky modes. Finally, if the square of the index of refraction approaches minus infinity as the depth coordinate approaches infinity, then no energy can be propagated to infinity, and the representation is an infinite sum of trapped modes.

Note that in the first two examples acoustic energy can be propagated to infinity. This is reflected in the fact that the continuous superposition of modes is present, while in the last it is not.

This paper attempts to develop a more precise meaning and to provide a physical interpretation for these terms. *The basic point is that the nature of the representation depends on how the sound-speed profile is terminated.* Furthermore, it should be pointed out that, while in some circumstances one termination is to be preferred over another, in general, each can be valid and useful.

This paper consists of two parts: a general description of normal-mode expansions, and a brief summary of some of the programs in underwater acoustics.

NORMAL-MODE THEORY

Integral Representation

A typical sound-speed profile in the ocean, shown in Figure 1, has the following special features: it shows the presence of shear in the bottom, and both the shear and sound-speed profiles in the bottom are terminated in isovelocity, constant-density half spaces. Some consequences of this choice for the termination of the sound profile will be discussed later.

The Hankel transform, chosen for the initial representation of the pressure field, is useful for two reasons: (1) This approach was used by Pekeris (1948), Ewing, Jardetsky and Press (1957), and Brekhovskikh (1960) and, hence, should be familiar to most workers in underwater acoustics. The alternative representation, based on Titchmarsh (1946) and described by Labianca in his paper on surface ducts (1973) is another possibility and, indeed, many of the subtle analytical properties are best discussed by that method; and (2) several points about proper or trapped modes, improper or leaky modes and branch cut integrals, and the physical interpretation of these terms, seem to fit best in the context of the Hankel transform.

The Hankel representation for the pressure field p at an observation point (r, z) due to a point harmonic source at $(0, z_0)$ is given by

$$p(r, z, z_0) = \int_{k=0}^{\infty} P(z, z_0, k) J_0(kr) k dk, \quad (1)$$

where J_0 is the zeroth order Bessel function of the first kind, and $P(z, z_0, k)$ is the transform of $p(r, z, z_0)$ with respect to r . This

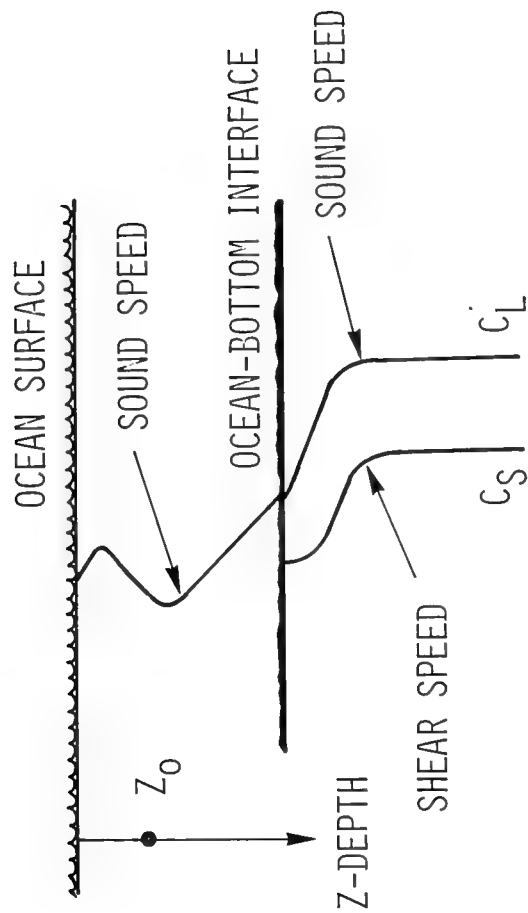


Figure 1. SOUND-SPEED PROFILE IN THE OCEAN

representation is a cylindrical superposition of waves, and the integration variable corresponds to the radial wave number.

The integration contour can be taken along the real k -axis if loss is introduced; if not, it can be taken just below the real axis. The transform $P(z, z_0, k)$ is determined by the sound-speed and density profiles, pressure-release condition at the ocean surface, continuity conditions at discontinuities in the acoustic properties, and a radiation condition. The determination of this function and the evaluation of this integral constitute the central practical problem in a normal-mode expansion. In a liquid region (with no shear) $P(z, z_0, k)$ satisfies

$$\rho(z) \frac{d}{dz} \left(\frac{1}{\rho(z)} \frac{dP}{dz} \right) + (k^2(z) - k^2)P = \frac{-1}{2\pi} \delta(z - z_0) \quad (2)$$

where $\rho(z)$ is the density and $k(z) = \omega/c(z)$. The presence of the 2π factor is due to the cylindrical symmetry.

A physical interpretation of the integration contour can be made in terms of incidence angles as shown in Figure 2. The polar transformation shown makes it possible to describe the pressure field as an integration over real and complex incidence angles or, alternatively, in terms of homogeneous and nonhomogeneous "plane" waves. The integration over $(0, k_1)$ in wavenumber space then corresponds to "real" incidence angles and the integration over (k_1, ∞) to nonreal incidence angles.

The discussion of normal-mode expansions is simplified by transforming Equation 1 so that the integration contour is infinite and the standing-wave component $J_0(kr)$ is replaced by an outward-going wave component $H_0^{(1)}(kr)$, the Hankel function. The representation is given in Equation 3 and the integration contour is shown in Figure 3. This technique is used by Brekhovskikh (1960).

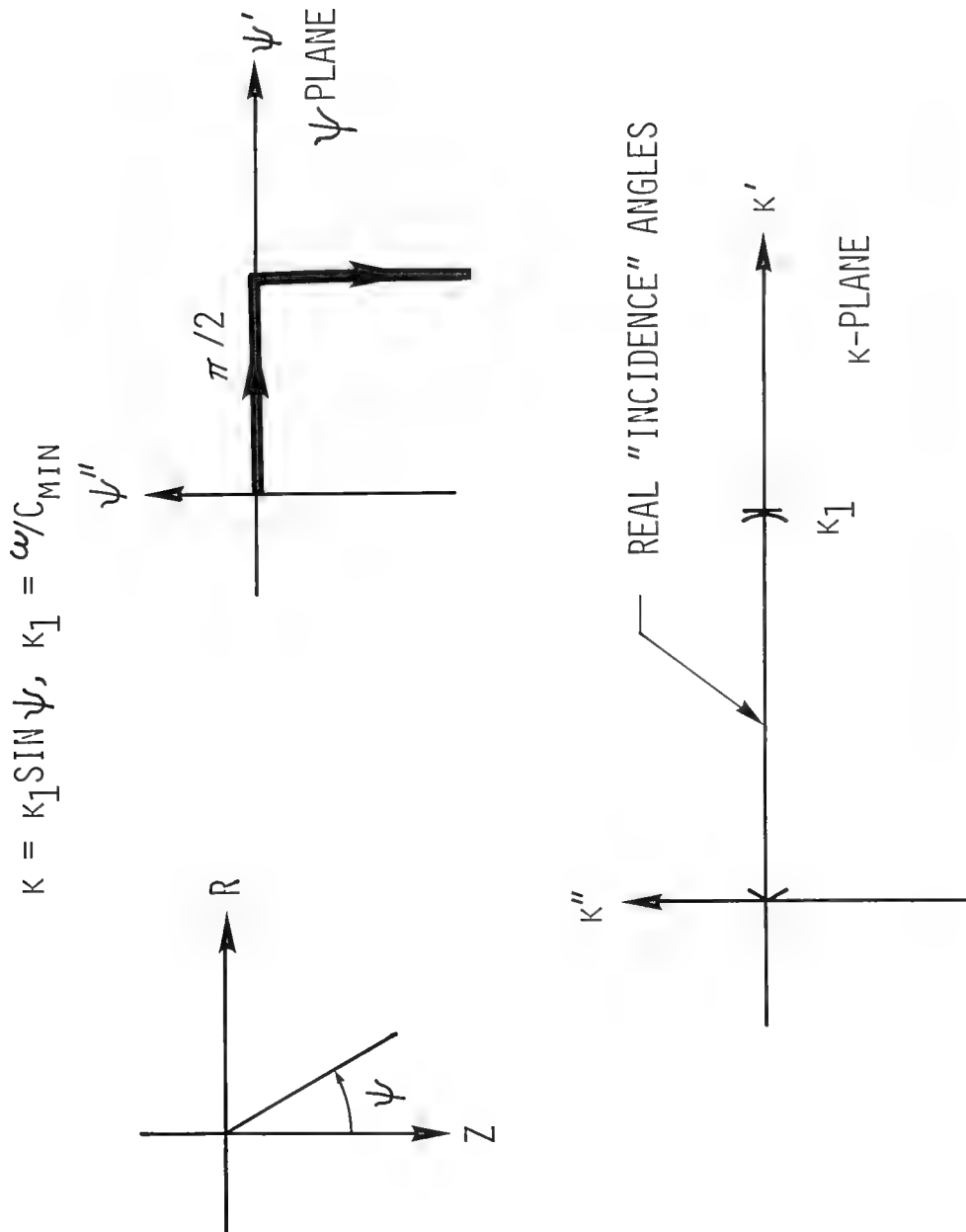


Figure 2. PHYSICAL INTERPRETATION OF INTEGRATION CONTOUR

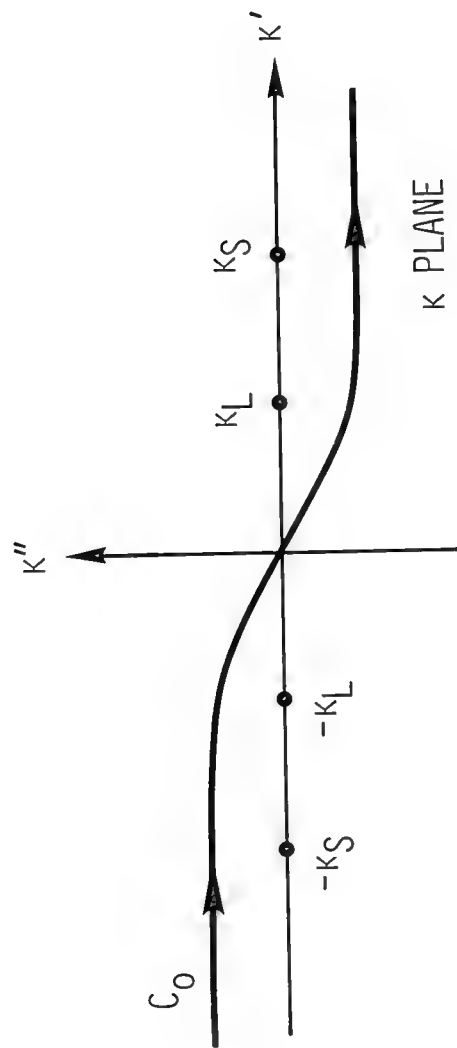


Figure 3. INTEGRATION CONTOUR AND BRANCH POINT LOCATIONS

$$p(r, z, z_o) = \frac{1}{2} \int_{C_o} P(z, z_o, k) H_o^{(1)}(kr) k dk. \quad (3)$$

The integral contains two factors $\sqrt{k_L^2 - k^2}$ and $\sqrt{k_s^2 - k^2}$ that introduce the branch point singularities in $P(z, z_o, k)$. Their presence is due to the isovelocity termination of the longitudinal and shear sound speeds.

Integral Evaluation

The evaluation of the integral in Equation 3 can be performed in several ways. To obtain a normal-mode expansion, however, it is necessary to identify the singularities of $P(z, z_o, k)$ as a function of k and to close the C_o integration contour around these singularities. For the class of sound-speed profiles described in Figure 1, the singularities of $P(z, z_o, k)$ are of two types, an infinity of poles plus two pairs of branch points.

In these ocean models the depth coordinate extends to infinity; therefore, the representation of the pressure field is always a finite sum of proper modes (which are defined below) plus a contribution of the continuous modes. For the profile described in Figure 1, the continuous modes are represented by an integration around the branch cuts mentioned above. For other terminations, this contribution can take a different form. This point will be discussed more completely below, but, roughly speaking, the continuous modes represent energy that does not remain ducted, and they will form part of the representation of the field when the sound-speed profile allows energy to be lost to infinity in the z direction. It is not a loss mechanism in the sense that acoustic energy is transformed to thermal energy but, rather, it represents acoustic energy radiated to infinity.

The residue contributions from the poles give rise to two types of modes: proper and improper. These will be described more completely below, after the role of the branch points has been discussed.

Physically, the outward going wave condition in the high speed sound layer gives rise to one pair of branch points. The other pair is due to the outward-going wave condition in the isovelocity shear layer. Each pair of branch points gives rise to a single branch-line-integral contribution to the field. Furthermore, the choice of the branch cut influences which modes or pole singularities contribute to the acoustic field. This point is now discussed.

To describe the differences arising from the choice of branch cut, it is convenient to examine the Pekeris model and to determine the differences in the representations that result from the two most common choices for the branch lines. The statements that will be made about this model apply, with little change, to the more general profile.

The Pekeris model, shown in Figure 4, consists of an isovelocity layer over a high-speed isovelocity half space. There is no shear in this model. The two common choices for the branch cuts are shown in the two lower figures. The EJP branch on the left is the branch cut chosen by Brekhovskikh; on the right is the branch cut chosen by Pekeris. First, I will discuss the representation arising from the EJP (Ewing, Jardetsky, Press) branch. The EJP branch is chosen such that on this sheet $\text{Im} \sqrt{k_L^2 - k^2} \geq 0$. The negative root occurs on the second sheet. This means the residue contribution from any pole on this sheet will eventually decay exponentially with depth and will represent a mode with finite energy. For this reason, these residue contributions are called proper modes.

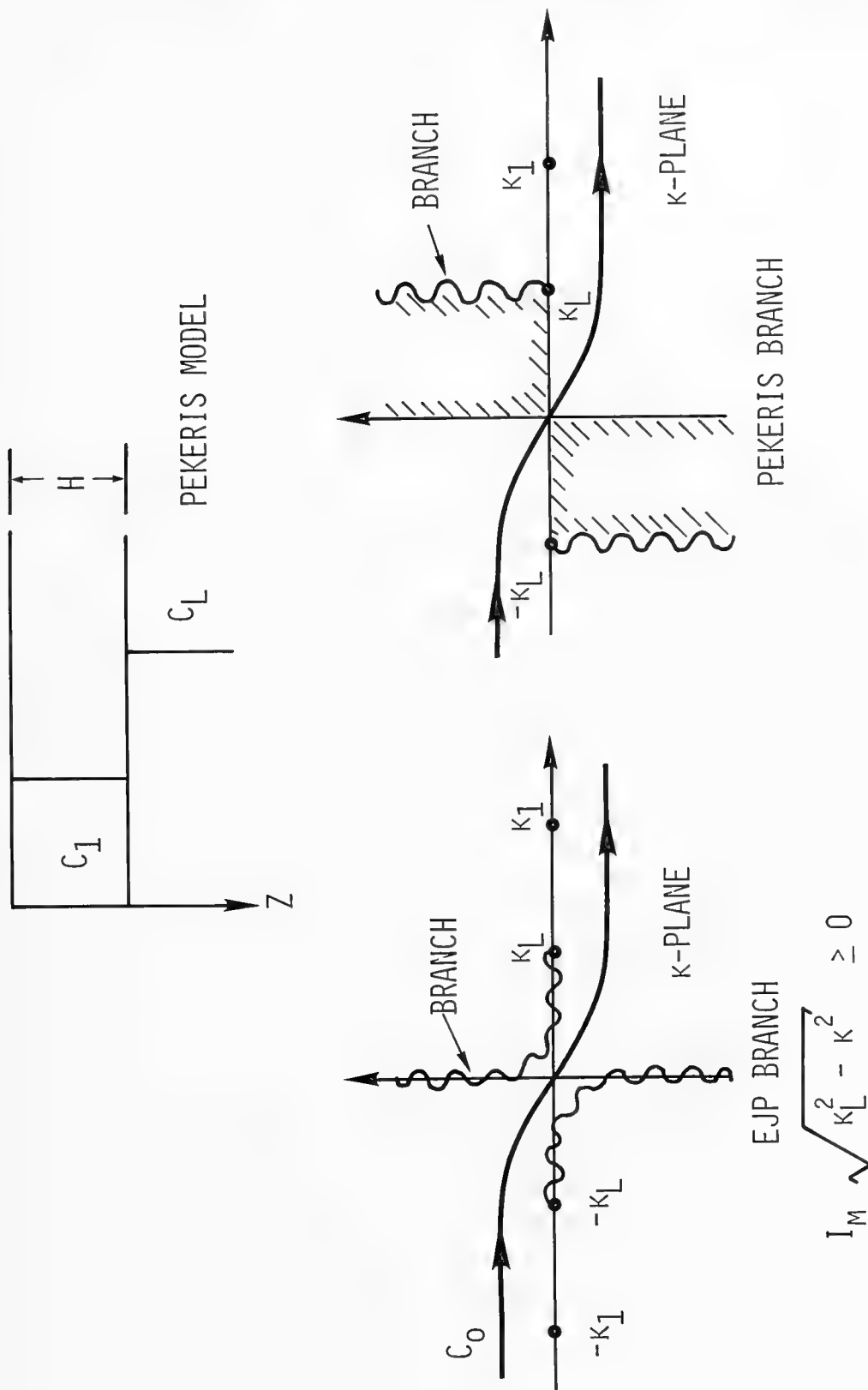


Figure 4. PEKERIS MODEL WITH TWO BRANCH CUT CHOICES

An analysis of the integrand for this model indicates only a finite number of such poles and that they lie between k_L and k_1 . This result can be anticipated physically and is not restricted to this elementary model. Since no loss mechanisms are present, we expect these proper wavenumbers to be real, to give rise to a standing wave field in the depth coordinate in the ocean layer, and eventually to decay with depth. This leads directly to the condition $k_L < k_n < k_1$. Note that these poles lie in the region of real incidence angles.

These proper roots have, in addition, the following properties and physical interpretations (see Figure 5): the phase velocity c_n satisfies $c_1 < c_n < c_L$; that is, the phase velocity in the radial direction is faster than that in the ocean layer and slower than that in the bottom.

These modes can also be thought of as being formed by a pair of plane waves traveling in the plus and minus z directions at an angle Ψ_n with respect to the z axis. This angle Ψ_n satisfies, through the simple polar transformation described earlier,

$$\Psi_n > \theta_c = \sin^{-1} c_1/c_L.$$

Recall, further, that for such an incidence angle, the plane-wave reflection coefficient has a modulus equal to one. That is, at these angles, no energy is transmitted into the bottom — all of the energy is trapped in the ocean layer and the fields must, therefore, decay with depth into the bottom. This is the origin of the term trapped mode.

Finally, the modes k_n near k_1 (i.e., c_n near c_1 or Ψ_n near $\pi/2$) correspond to the low-order modes, while those $k_n \approx k_L$ correspond to the high-order modes. The turning points for each of these trapped modes occur at the interface between the ocean and the bottom.

Finally, the representation for the EJP branch is given by the symbolic equation at the bottom of Figure 5: a finite sum of trapped or proper modes plus an integral around the EJP branch plus an integral around a semicircular contour at infinity. This latter integral can be shown for this branch to be arbitrarily small for all observation and source coordinates.

The representation arising from the Pekeris branch (see Figure 4) can be thought of as being formed by pushing the EJP branch to a vertical position. When this is done, some of what had been on the second sheet of the EJP branch is exposed. That is, in the unshaded region the condition $\text{Im } \sqrt{k_L^2 - k^2} < 0$. Any residue that arises from a pole in this shaded region will eventually grow exponentially with depth and, thus, will represent a mode with infinite energy. Such a mode will be called an improper mode.

An infinity of these improper poles has been found and the reason will be clear later. Some of the properties of these improper modes are shown in Figure 6. For these modes, the real part of k_n, k_n' , satisfies $k_n' < k_L$ and their phase velocity in the radial direction is greater than the phase velocity in the high-speed bottom. They are sometimes called fast waves. In addition, for the plane-wave incidence-angle analogy, $\psi_n' < \theta_c$. For such angles the reflection coefficient $|R| < 1$, and a plane-wave incident at such an angle will have some of its energy transmitted or leaked into the bottom. This is the origin of the term leaky mode.

These leaky modes not only eventually grow exponentially with depth and, hence, do not represent fields with finite energy, they also have another rather unphysical property: they decay exponentially with range. This decay suggests physically that some absorption mechanism rather than a radiation-type mechanism is present.

EJP BRANCH

FINITE NUMBER OF PROPER TRAPPED MODES

k_n = WAVE NUMBER

$k_L < k_n < k_1$

C_n = PHASE VELOCITY

$C_1 < C_n < C_L$

ψ_n = INCIDENCE ANGLE

$\psi_n > \theta_c = \sin^{-1} C_1 / C_L$

REPRESENTATION

$$p \sim \sum_{l=1}^n (\text{TRAPPED MODES}) + \int_{BR} (\text{EJP}) + \int_{\Sigma^\infty}$$

Figure 5. PHYSICAL PROPERTIES OF MODAL WAVENUMBER AND REPRESENTATION FOR EJP BRANCH CUT

The pressure field representation for the Pekeris branch is thus described by the symbolic equation at the bottom of Figure 6. For this choice the integration at the contour at infinity can be shown to be zero only if r is sufficiently large or z sufficiently shallow. This can present serious practical as well as theoretical problems. In addition, when the contribution of the integral at infinity is not zero, the sum of the trapped modes is divergent. When this representation is convergent, it can be used and, furthermore, when it does converge, we see that

$$\Sigma \text{ (leaky)} + \int_{\text{BR}} \text{Pekeris} = \int_{\text{BR}} \text{EJP}.$$

The foregoing analysis is, of course, not restricted to the Pekeris model. The simple plane-wave interpretations are model dependent, but the differences in representations due to the two choices of branch cut are not. There are two small differences:

- In the Pekeris model each mode has only one turning point and it occurs at the ocean-bottom interface. In a refracting ocean this is not the case. There may be more than one; however, as in the Pekeris model none can occur in the isovelocity half-space.
- The critical-angle concept depends on source location and the sound-speed profile, and it is defined by the grazing ray.

General Comments

In the next several paragraphs I will make several comments for general profiles, neglecting for the moment the effects of shear. It is convenient to return to a point discussed in the introduction, namely, the dependence of the representation on the termination of the sound-speed profile. If $c^2(z) \rightarrow 0$ sufficiently rapidly, then

PEKERIS BRANCH

PROPER MODES

INFINITY OF IMPROPER OR LEAKY MODES

$$k_n \text{ (COMPLEX)}$$

$$0 < k_n' < k_L$$

$$c_n' > c_L \text{ (FAST WAVE)}$$

$$\psi_n' < \theta_c$$

REPRESENTATION

$$p \sim \sum_l^n \text{ (TRAPPED)} + \sum_l^\infty \text{ (LEAKY)} + \int_{BR} (p) + \int_{\Sigma^\infty}$$

Figure 6. PHYSICAL PROPERTIES OF IMPROPER MODES, AND REPRESENTATION FOR PEKERIS BRANCH CUT

there are no proper or trapped modes; this has been pointed out by Labianca (1973) in his study of a surface-duct model. The result follows directly from a theorem by Titchmarsh (1946). In this case there is only a continuous superposition of modes. This integral can be evaluated, when the range is sufficiently large or the z sufficiently small, by summing the leaky modes — as has been done by Pedersen and Gordon (1965).

If $c^2 \rightarrow -\infty$ as $z \rightarrow \infty$, then it is clear that no energy can propagate to infinity in the z direction. For this termination, Titchmarsh (1946) has shown that there are only trapped modes. Such a termination has been used by Fitzgerald (private communication).

For the isovelocity termination, numerical examples show that the branch cut integrals can, in general, be expected to be important to a range of one water depth and sometimes more. Physically, they can be expected to be important when there is a constructive interference of the lateral wave and proper modes. This occurs for a set of modes near cut-off. An example will be presented later to illustrate this point.

When convergence is not a problem, one can ask, "When does a finite set of the leaky modes offer a good approximation to the EJP branch?" Numerical experience shows that this sum is not always a good approximation. This point will also be illustrated in a later example.

It can be established that the EJP branch decays roughly algebraically with range and faster than $1/\sqrt{r}$; thus, it is not surprising that the sum of leaky modes alone, which decay exponentially with range, is sometimes a poor approximation to the EJP branch. Returning to an earlier point, this also suggests why it takes an infinity of

these improper modes to approximate the algebraic decay associated with acoustic energy radiated to infinity.

Finally, it is interesting to bring the virtual-mode concept of Labianca (1973) into this framework. For the profile in Figure 1, the virtual-mode sum is obtained by an approximate integration of the EJP branch integral. This approximate integration accounts for the proximity of the leaky poles to the integrand of the branch line integral.

Effects of Shear

This section is concluded with the description of some of the effects that the presence of shear introduces into the representation for the pressure field. These effects are summarized in Figure 7 and, for completeness, the two corresponding cases neglecting shear are also included. These are at the top of Figure 7 with the case just considered being on the right. The case on the top left represents a case in which the "bottom" speed is less than water speed. It is not particularly useful since, in any model of the bottom, the sound speed eventually becomes greater than that in the water. However, for this case, there are no proper modes and, hence, the representation consists of either a single EJP-type branch integral or a Pekeris-type branch plus an infinite sum of improper modes. The convergence of the improper-mode sum can, again, be guaranteed only when z is sufficiently small or r is sufficiently large.

Continuing to the cases where shear is present, it is quite straightforward to show that only when c_s is larger than c_1 is it possible to have trapped modes. In the other two cases, one is either faced with the evaluation of the EJP branches or of the Pekeris branch and determination of the leaky-wave modes. The convergence of

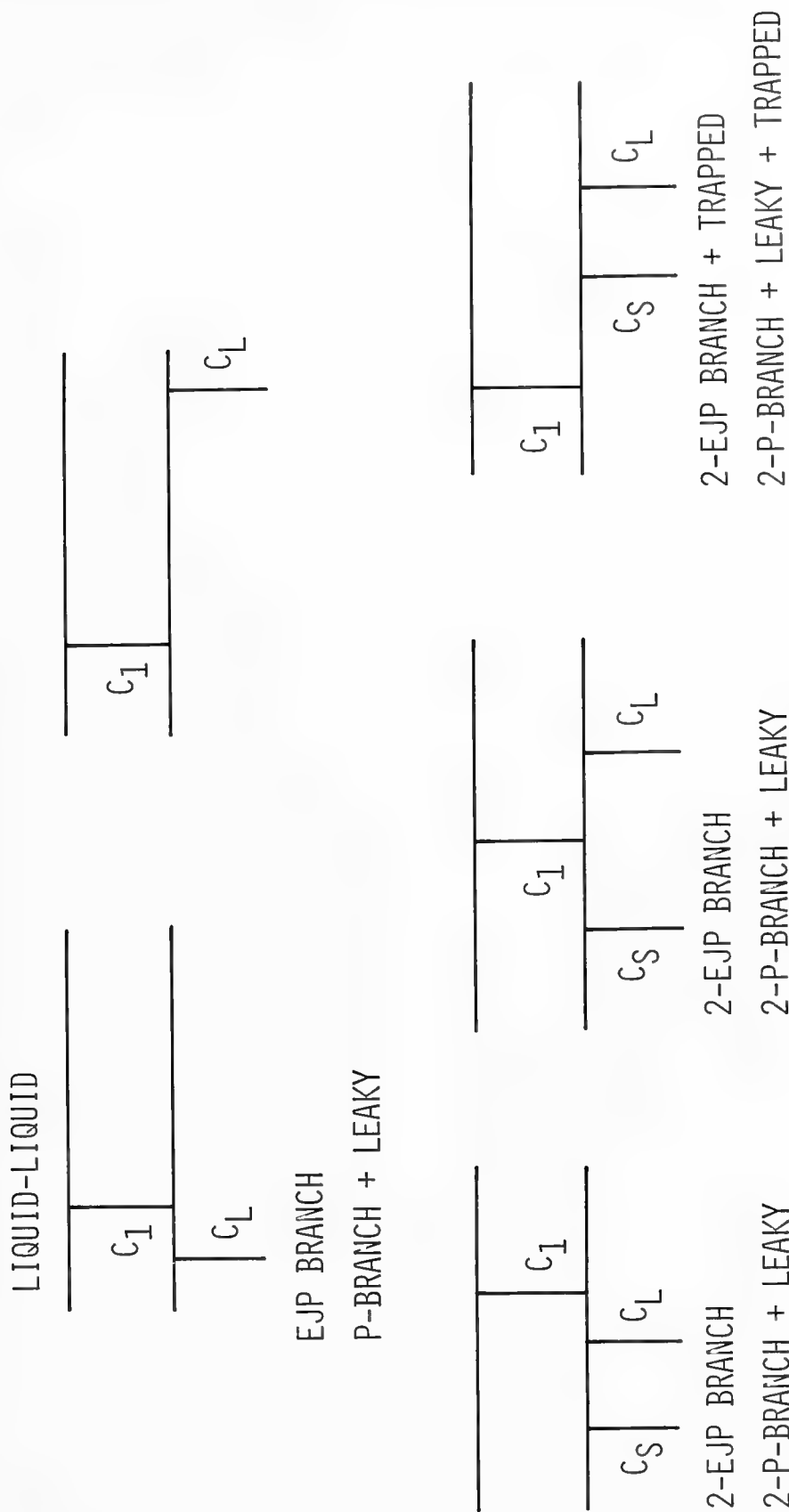


Figure 7. SUMMARY OF SHEAR EFFECTS

the leaky-wave modes still depends on the range and depth coordinate. When there is refraction in the model, the situation becomes more complicated. A discussion of the Stonely wave will not be given here (see Ewing, Jardetsky, and Press, 1957).

A hybrid representation is, of course, possible. For example, the diagram at the bottom center of Figure 7 might be chosen to model a sedimentary layer (i.e., the longitudinal sound speed higher than the water speed but with the shear speed slower than the water speed.) As remarked above, for this geometry there are no trapped modes; hence, one representation would consist of two EJP branch integrals. However, if one chose an EJP branch for the longitudinal speed and a Pekeris branch for the shear speed, then the representation would consist of an infinity of leaky shear modes plus a Pekeris-type branch and an EJP-type branch. Some care must be exercised in this approach because, while it may be possible to neglect the contribution of the Pekeris branch, we can expect the EJP branch to yield a contribution comparable to the sum of leaky shear modes.

BRIEF DESCRIPTION OF EXISTING NORMAL-MODE PROGRAMS

In this section, several working normal-mode programs are described.

The first group includes programs constructed by Cybulski, by Kanabis, by Blatstein and Uberall, as reported by Spofford (1973), and by Newman and Ingenito (1972). These programs all involve a numerical integration of Equation 2 beginning at the ocean-bottom interface and using the pressure-release condition at the ocean surface to determine the characteristic wavenumbers k_n and the wave functions $P(z, z_o, l_n)$. The proper modes are summed.

Bartberger (1973) uses the same numerical integration scheme, but he determines the proper as well as improper modes. He sums the proper modes plus a finite number of the improper modes.

Pedersen and Gordon (1965) consider a profile in which $c^2(z)$ approaches zero as $1/z$ and, hence, as mentioned above, is one in which there are no proper modes. They partition the sound speed in the upper portion of the sound-speed profile into layers such that the square of the index of refraction can be approximated by a straight line and the density by a constant. They determine and sum a finite number of improper modes.

Kutschale (1970) partitions the sound-speed profile into layers such that in each layer the sound speed and density can be approximated by a constant. He allows for shear in any layer. He determines and sums the proper modes and evaluates the EJP branch integrals.

Beisner (1974) uses a "shooting" technique to determine the proper modes and wavenumbers, and he sums the proper modes.

Deavenport and Beard (see Spofford, 1973) model the profile as an Epstein layer. The depth function can then be expressed in terms of hypergeometric functions. They determine and sum the proper modes.

Leiberger uses WKB techniques to determine the proper modes. This work is described briefly by Spofford (1973).

Fitzgerald (see Spofford, 1973) partitions the sound-speed profile in layers in the same manner as Pedersen and Gordon, but he terminates in a layer in which $c^2(z) \rightarrow -\infty$ as $z \rightarrow \infty$. He sums a finite number of the trapped modes.

Stickler (1975) partitions the sound speed into layers such that in each layer the sound speed can be approximated by a straight line

and the density by a constant. He sums the proper modes and evaluates the EJP branch integral.

Examples

In this section two comparisons are made; they are chosen to illustrate the importance of the continuous modal contribution. Consider the profile shown in Figure 8; it is of the type considered in Figure 1. It is very interesting because, at 50 Hz, there is only one proper mode, and it is quite near cut-off. In Figure 9, the transmission loss is shown at 50 Hz for a source at a depth of 20 feet and a receiver at 40 feet. The lower solid curve represents the contribution of the single proper mode. Blatstein's calculation (see Spofford, 1973) for this one proper mode is in good agreement. Bartberger (1973) has summed not only the one proper mode but several of the improper modes. However, for this case, it is seen that the leaky modes make virtually no contribution. Bartberger's calculation does not include the corresponding Pekeris-type branch. The upper solid curve is the sum of the one proper mode plus the EJP branch as calculated by Stickler (1975). The results of Kutschale (1970), who sums the proper modes and adds the EJP branch contribution, are seen to be in close agreement.

This calculation shows two interesting points: 1) The contribution of the continuous modes can be important to many water depths, and 2) the sum of the leaky modes is not always a good approximation to the EJP branch integral.

Figure 10 shows a plot of transmission loss for the same geometry except now the frequency is 100 Hz. There is still only one proper mode, the smooth lower curve. The upper solid curve shows the contribution of the proper plus the EJP branch contribution, and the dots

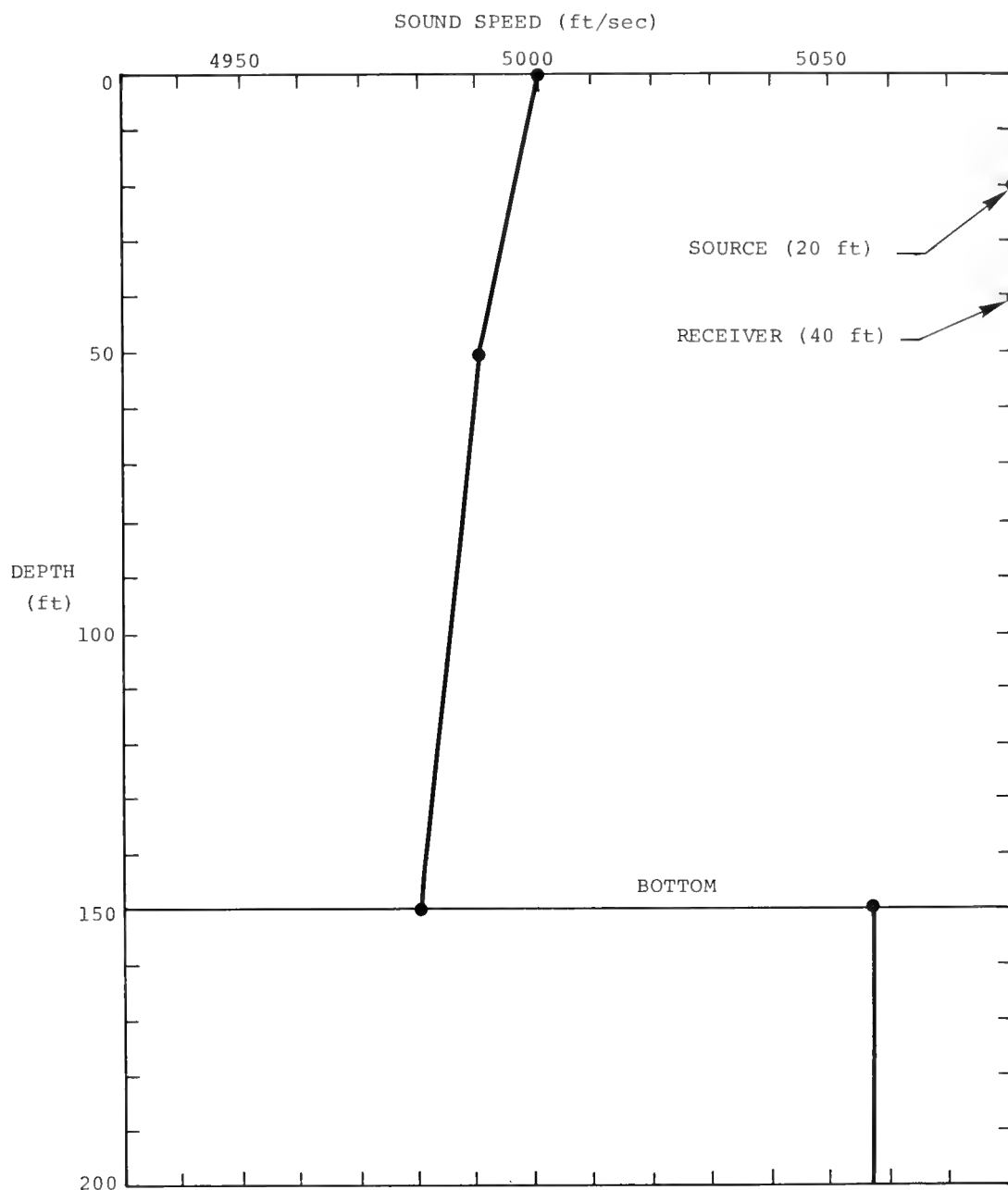


Figure 8. SOUND-SPEED PROFILE IN SHALLOW WATER

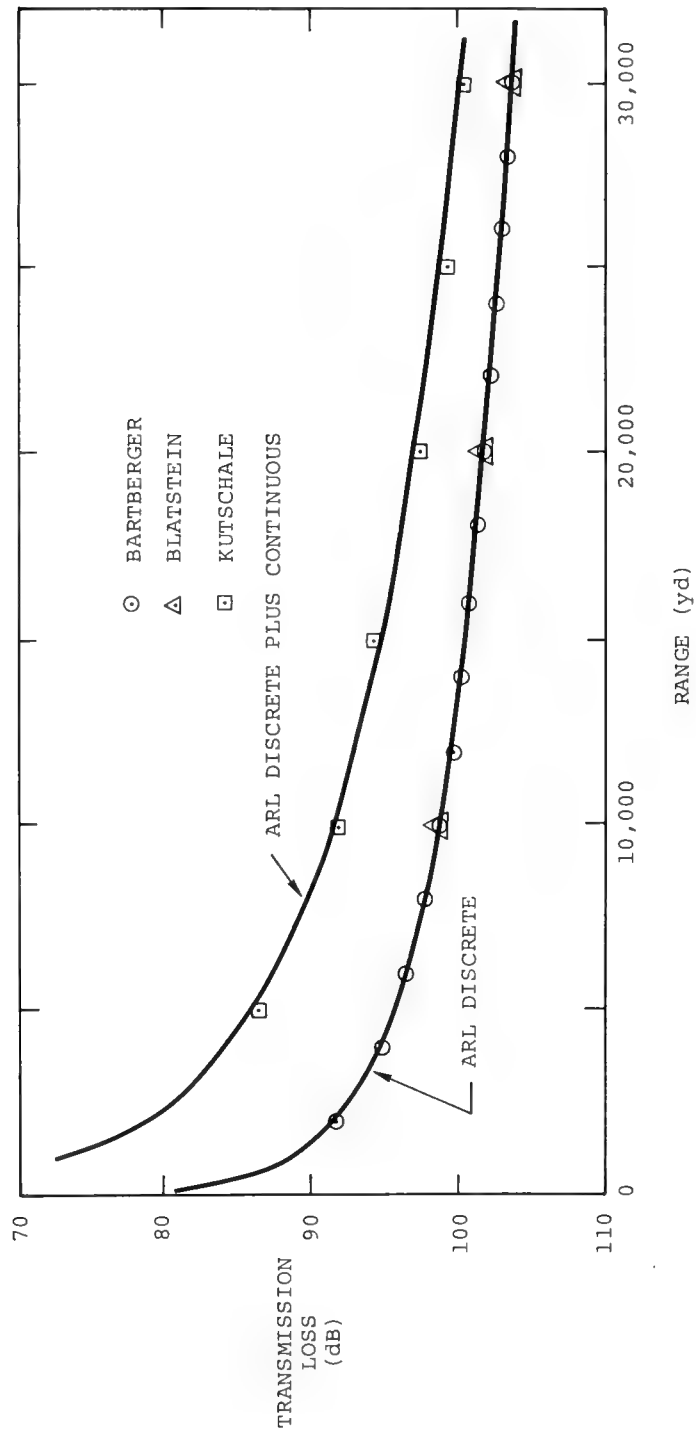


Figure 9. TRANSMISSION LOSS AT 50 Hz

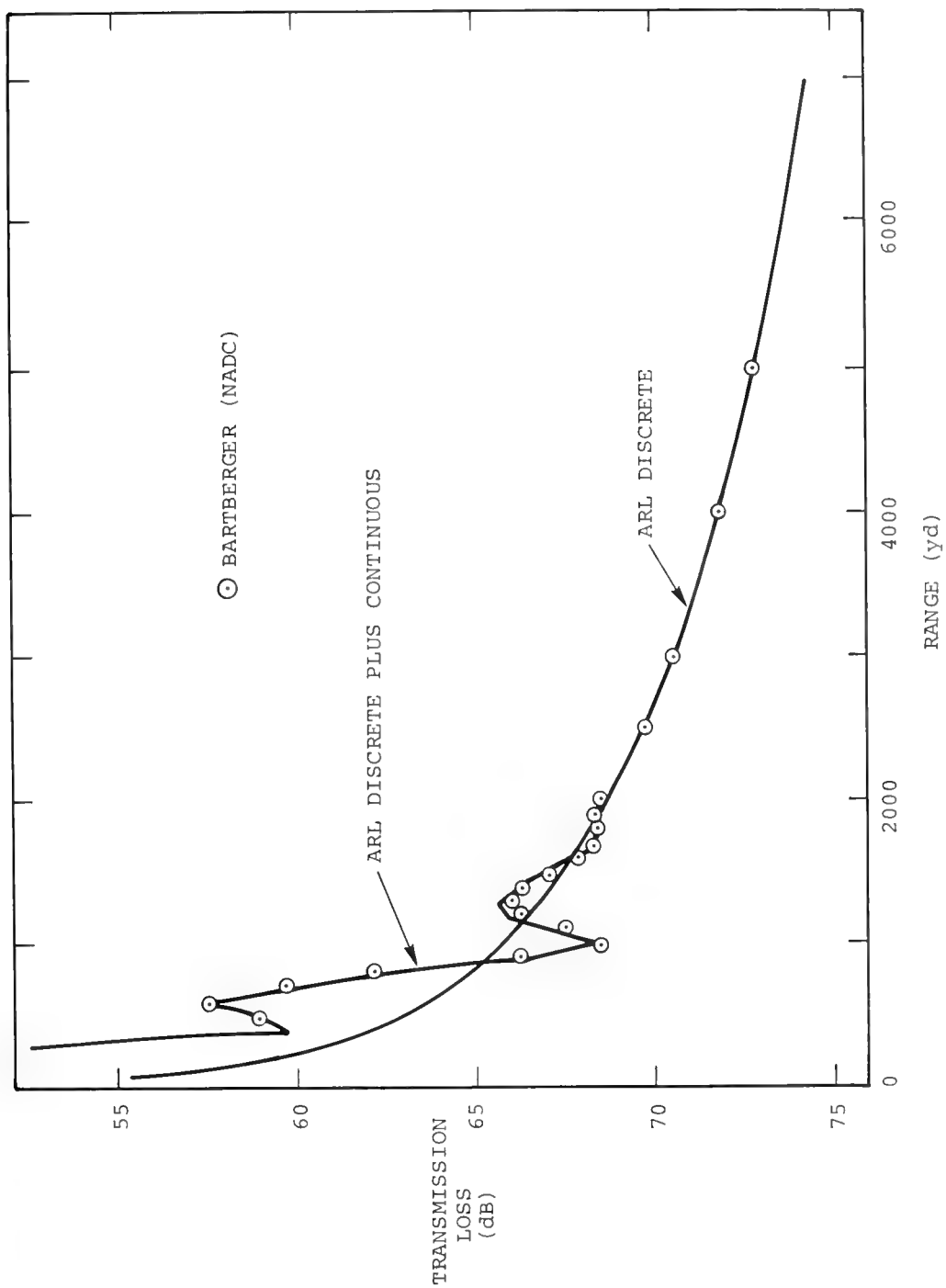


Figure 10. TRANSMISSION LOSS AT 100 HZ

indicate the sum of the proper plus a finite number of improper modes (neglecting the Pekeris branch). This example shows that sometimes the improper modes offer an excellent approximation to the EJP branch integral.

REFERENCES

- Bartberger, C., "Normal Mode Solutions and Computer Programs for Underwater Sound Propagation," Part I - Two-Layered and Three-Layered Programs, Report No. NADC-72001-AE; Part II - Program for Arbitrary Velocity Profiles, Report No. NADC-72002-AE, Naval Air Development Center, 4 April 1973.
- Beisner, H. M., "Numerical Calculation of Normal Modes for Underwater Sound Propagation" IBM J. Res. Develop., pp. 53-58, January 1974.
- Brekhovskikh, L. M., *Waves in Layered Media*, Academic Press, pp. 454-460, 1960.
- Ewing, W. M., W. S. Jardetsky, F. Press, *Elastic Waves in Layered Media*, McGraw-Hill, pp. 126-151, 1957.
- Kutschale, H. W., "The Integral Solution of the Sound Field in a Multilayered Liquid-Solid Half Space with Numerical Computations for Low-Frequency Propagation in the Arctic Ocean," Lamont-Doherty Geological Observatory, Tech. Report No. 1, 1970.
- Labianca, F. M., "Normal Modes, Virtual Modes, and Alternative Representations in the Theory of Surface Duct Sound Propagation," *J. Acoust. Soc. Am.* 53, pp. 1137-1157, 1973.
- Newman, A. V., F. Ingenito, et al., "A Normal Mode Computer Program for Calculating Sound Propagation in Shallow Water with Arbitrary Velocity Profile," Naval Research Laboratory, Washington, NRL Memorandum 2381, January 1972.
- Pedersen, M. A. and D. F. Gordon, "Normal-Mode Theory Applied to Short Range Propagation in an Underwater Acoustic Surface Duct," *J. Acoust. Soc. Am.* 34, pp. 105-118, 1965.

- Pekeris, D. L., "Theory of Propagation of Explosive Sound in Shallow Water," In: "Propagation of sound in the ocean," *Geological Soc. Amer. Memoir* 27:1-117, 1948.
- Stickler, D. C., "A Normal Mode Program with both Discrete and Branch Line Contributions," *J. Acoust. Soc. Am.* 57:856, 1975.
- Spofford, C. W., "A Synopsis of the AESD Workshop in Acoustic-Propagation Modeling by Non-Ray-Tracing Techniques," Acoustic Environmental Support Detachment, Tech Note, TN-73-05, November 1973.
- Titchmarsh, E. C., *Eigenfunction Expansions Associated with Second-Order Differential Equations*, ch. V, Oxford, 1946.

DISCUSSION

Dr. F. D. Tappert (New York University): Have you examined the question of what happens to these branch cuts when you make the parabolic approximation?

Dr. Stickler: Not directly, but I think that your restriction of parabolic method to low angles of incidence roughly corresponds to reflecting the integration around the branches. Physically that can be interpreted as integration over the faster phase velocities, which in turn correspond to the higher modes.

Dr. Tappert: The parabolic equation does have a continuous part to the spectrum and I wonder where it comes from? From the Helmholtz equation? It's not a proper mode so it must be either a branch-cut contribution or a leaky mode.

Dr. Stickler: You mean the spectrum of your parabolic operation has a continuous mode?

Dr. Tappert: Yes. It may be in the integration along the semicircular --

Dr. Stickler: I'm not sure there is a one-to-one correspondence. I don't know.

Dr. R. R. Goodman (Naval Research Laboratory): When doing these computations one should be aware that the experimentalists can put more than one hydrophone in the water and one can do some interesting space and time correlations to look at some of the realities of these various contributions. I think this is an important point because one can then begin to design an experiment to look for the types of things you are talking about.

Dr. F. M. Labianca (Bell Telephone Laboratories): I tend to agree that there is a continuous spectrum for the parabolic equation, but let me clarify one thing. Are you referring to the case where there is no range dependence in sound speed? In other words, where separation of variables applies?

Dr. Tappert: Yes.

Dr. Labianca: I agree there is a continuous spectrum in that case because the depth dependence is going to be exactly the same, you know, just straight separation of variables on the Helmholtz equation.

Mr. A. O. Sykes (Office of Naval Research): Would you clarify Figure 9 for me? There seem to be two groups of normal-mode models which give different results. Can you comment on that?

Dr. Stickler: Typically, it is, of course, much easier to only sum the modes that are involved. Carrying out the numerical integration for the branch-cut integral is a much more expensive proposition and so usually the branch-cut integrals are neglected or dismissed as not important at long range. Many times that is the case.

If I had used calculated or summed proper modes, then I would have made the prediction labelled "ARL discrete." Bartberger summed the proper and a finite number of the improper modes. They fell on the other curve.

When I added to the discrete contribution the contribution of the Ewing, Jardesky, Press type branch, then the transmission is given by the curve, "ARL discrete plus continuous."

Mr. Sykes: Is the point that some of the improper modes have a finite contribution which really should be included and so you think that the upper curve is the better estimate?

Dr. Stickler: Yes, the upper curve is a better estimate. Figure 9 illustrates several points. First, as I mentioned earlier, a sum of the improper modes is not always a good approximation to the Ewing, Jardesky, Press type branch. And it also illustrates that the Ewing, Jardesky, Press type branch cannot be neglected in some examples.

On the other hand, in Figure 10, which is the same case for 100 Hz, the proper plus a finite sum of the improper modes is an excellent approximation to the sum of the proper plus the Ewing, Jardeky, Press type branch.

Dr. Goodman: In this case you have only one proper mode. Isn't that right?

Dr. Stickler: This case only has one proper mode but it has, of course, an infinity of improper modes.

SELECTED APPLICATIONS OF THE PARABOLIC-EQUATION METHOD IN UNDERWATER ACOUSTICS

Frederick Tappert

Courant Institute of Mathematical Sciences
New York University

A review of the parabolic-equation method in underwater acoustics is presented. Applications of the parabolic-equation method discussed here include:

- Short-range (several hundred nm) calculations of transmission loss
- Calculations of transmission loss in environments with variable sound-speed profiles and bathymetry
- Calculations of fluctuating acoustic fields in a time-dependent fluctuating ocean using a model for a random internal-wave field superimposed on Munk's canonical profile.

The parabolic-equation method is also used as the starting point to derive theoretical expressions for fluctuations of acoustic fields in random oceans. Using the mathematical analogy with Schroedinger's wave equation, two such techniques are described: the first applies the wave kinetic equation approach to underwater acoustics; the second applies the Pauli master equation approach to the same problem.

Theoretical and numerical studies and comparisons to field data lead one to believe that the parabolic-wave equation adequately describes acoustic waves propagating in real oceans for frequencies between 5 and at least 500 Hz out to ranges of at least 10,000 nm.

BACKGROUND

Leontovich and Fock (1946), two Soviet scientists, were the first to approximate an elliptic reduced wave equation by a parabolic

wave equation in the mid-1940s in connection with tropospheric radio-wave propagation problems. Since then this method has been rather widely used in radio physics and ionospheric physics (Fock, 1965; Malyuzhinets, 1959; Barabanenkov, et al., 1971).

My first exposure to the parabolic-equation method was in work on radar systems involving the simulation of propagation of UHF radar pulses in a random ionosphere. My former colleague, Ron Hardin, and I developed computer codes based on the parabolic-equation method to simulate radar propagation.

When we became involved in underwater acoustics, it was natural for us to apply these same methods to the subject of low-frequency, long-range acoustic propagation in oceans. These applications turned out to be quite fruitful and a number of results have been presented prior to this workshop (Hardin and Tappert, 1973; Tappert and Judice, 1972; Tappert, 1974a; Hasegawa and Tappert, 1973, 1974). Progress has been rapid (Tappert and Hardin, 1973; Tappert, 1974b; Tappert and Hardin, 1974), and other workers have continued to develop and apply these methods (Spofford, 1974; McDaniel, 1974; Benthien, et al., 1974).

A key factor in the success of the parabolic-equation method is the numerical technique used to obtain the solution. The parabolic-wave equation is solved directly by the finite-difference split-up Fourier algorithm which makes use of Fast Fourier Transforms to achieve accuracy, efficiency, and unconditional stability. This yields a full-wave (all diffraction effects included), fully coupled (all mode-coupling effects included) solution for the acoustic field at all depths and ranges. Realistic ocean environments with depth- and range-dependent sound speed and volume loss, and layered

variable-depth bottom structure are readily included in the numerical calculations. Most recently, a randomly fluctuating (in depth, range, and time) component of the sound speed has been implemented without difficulty (Flatte and Tappert, 1974).

OUTLINE OF THE PARABOLIC-EQUATION METHOD

The starting point is the reduced elliptic wave equation for the pressure, p , given by Equation (1) in Figure 1, where r is the horizontal range, z is the depth, θ the azimuth angle, k_0 a reference wavenumber, and n the index of refraction.

Equation (2) relates k_0 to the reference sound speed, c_0 , and the angular frequency, ω , and n to the variable sound speed, c .

The basic idea behind the parabolic-equation method is expressed in Equation (3). The pressure is replaced by a slowly varying envelope function ψ and an outgoing wave represented by the Hankel function of zero order, $H_0^{(1)}$. Two approximations are then made: (1) that one is in the far field of the source (Equation 4), and (2) that the angles with respect to horizontal are small (Equation 5).

These lead to a parabolic wave equation for the slowly varying envelope function ψ , shown in Equation (6). The equation is parabolic because only the first derivative with respect to r occurs, whereas two derivatives with respect to z occur.

By further neglecting the coupling between azimuthal directions (that is, the derivatives with respect to the azimuthal angle θ), the two-dimensional parabolic wave Equation (7) is obtained. This is the basis for all the computer models of low-frequency acoustic propagation utilizing the parabolic approximation.

ELLIPTIC WAVE EQUATION:

$$\frac{1}{r} \frac{\partial}{\partial r} \left(r \frac{\partial p}{\partial r} \right) + \frac{\partial^2 p}{\partial z^2} + \frac{1}{r^2} \frac{\partial^2 p}{\partial \theta^2} + k_o^2 [n^2(r, z, \theta) + i\alpha(r, z, \theta)] p = 0 \quad (1)$$

$$k_o = \frac{\omega}{c_o} = \text{const}, \quad n = c_o / c(r, z, \theta) \quad (2)$$

Let $p(r, z, \theta, \omega) = \psi(r, z, \theta, \omega) H_o^{(1)}(k_o r)$ (3)

Approximations: 1. $k_o r \gg 1$ (far field) (4)

2. $|\frac{\partial \psi}{\partial r}| \ll k_o |\psi|$ (small angles) (5)

PARABOLIC WAVE EQUATION:

$$2ik_o \frac{\partial \psi}{\partial r} + \frac{\partial^2 \psi}{\partial z^2} + \frac{1}{r^2} \frac{\partial^2 \psi}{\partial \theta^2} + k_o^2 [n^2(r, z, \theta) - 1 + i\alpha(r, z, \theta)] \psi = 0 \quad (6)$$

Neglect coupling between azimuths:

$$i \frac{\partial \psi}{\partial r} + \frac{1}{2k_o} \frac{\partial^2 \psi}{\partial z^2} + \frac{k_o}{2} [n^2(r, z, \theta) - 1 + i\alpha(r, z, \theta)] \psi = 0 \quad (7)$$

Figure 1. PARABOLIC EQUATION METHOD

From a more fundamental point of view a more rigorous derivation can be obtained by noting that the basic approximation is analogous to factoring the elliptic equation into incoming and outgoing waves. Such a factorization is, in fact, possible, resulting in a pair of coupled parabolic wave equations, one for the outgoing wave and one for the backscattered wave. Note that such a formulation could, in principle, include a description of reverberation. All of the numerical work to date, however, has been based on the outgoing-wave parabolic equation.

Since the parabolic equation is not valid near the source, an asymptotic matching technique is required. Very near the source the exact acoustic field is known (especially, say, for an isotropic point source), and this interior solution must be matched to a solution of the parabolic equation in the far field.

One way to do this is indicated in Figure 2. Manipulation of Equations (8), (9), and (10) leads to an expression (Equation (11)) for the complex acoustic field at zero range which, when put into the parabolic wave equation as an initial condition, simulates in the far field a point source with unit pressure at a range of 1 yard. Finally, boundary conditions must be specified to solve the parabolic wave equation. To simulate the pressure release boundary condition at the surface, an image source, 180 degrees out of phase with the true source, is introduced (as shown in Figure 2). This forces the pressure to be identically zero at the surface.

The lower boundary condition is treated by extending the calculation grid beyond the floor of the ocean, as indicated in Figure 2. In this "mud" region well below the actual seafloor, an outgoing wave boundary condition is needed. Rather than directly

SOURCE MODELING — ASYMPTOTIC MATCHING

$$\text{Exact:} \quad |p|^2 = \frac{9}{r^2 + (z - z_o)^2} \approx \frac{9}{r^2} \left[1 - \frac{(z - z_o)^2}{r^2} \right] \quad (8)$$

$$\text{Parabolic approximation:} \quad |p|^2 = \frac{1}{r} |\psi|^2 \quad (9)$$

$$|\psi|^2 = \frac{9}{r} \left[1 - \frac{(z - z_o)^2}{r^2} \right] \quad (10)$$

$$\text{e.g.,} \quad \psi(z, 0) = A e^{-(z - z_o)^2 / \omega^2} \rightarrow A = \frac{3\sqrt{\lambda_o}}{\sqrt{\pi} \omega}, \quad \omega = \frac{\lambda_o}{\pi} \quad (11)$$

BOUNDARY CONDITIONS:

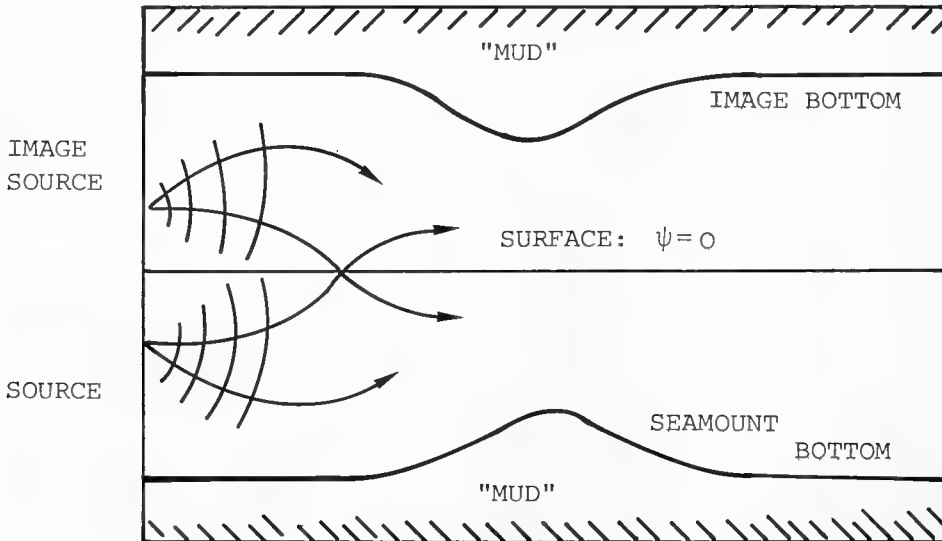


Figure 2. INITIAL AND BOUNDARY CONDITIONS

applying such a boundary condition, its equivalent is simulated by preventing waves that reach so far below the floor of the ocean from scattering back into the ocean. This is achieved by introducing a strong volume attenuation which absorbs all the acoustic waves that reach this subbottom layer, colloquially called mud. This is a numerical, artificial absorption introduced solely to remove reflected waves. There is, of course, a corresponding image mud in the upper ocean.

While substantial analyses have been performed on the validity of this approximation, it is still a rather open subject and there have not yet been developed necessary and sufficient conditions for its validity.

The best way, of course, is to compare it to field data, and this has been done in a number of cases by myself, and Spofford (1974) who also compared it with ray and normal-mode results. Such comparisons are not conclusive, however, nor are they a replacement for precise analytical estimates for the conditions under which the parabolic approximation is valid.

One such analytical approach is to begin with the geometrical acoustics approximation to the parabolic wave equation (Figure 3). The exact ray Equation (12) is shown for a two-dimensional stratified ocean, where z is the ray depth as a function of range r , and θ is the vertical angle of the ray (rather than the azimuthal angle, as earlier). In the parabolic approximation, the corresponding ray equation is given in Equation (13) and is the same except for the factor $1/(n \cos \theta)^2$. However, they both have as a first integral Snell's invariant as expressed in Equation (14).

RAY TRACING:

$$\text{Exact:} \quad \frac{d^2 z}{dr^2} = \frac{1}{(n \cos \theta)^2} \frac{1}{2} \frac{dn^2}{dz} \quad (12)$$

$$\text{Parabolic approximation:} \quad \frac{d^2 z}{dr^2} = \frac{1}{2} \frac{dn^2}{dz} \quad (13)$$

$$\text{Both give:} \quad n \cos \theta = \text{const} \quad (14)$$

Rays are same except for range scale.

NORMAL MODES EXPANSION:

$$\text{Exact:} \quad p = \sum_{\alpha} A_{\alpha} \phi_{\alpha}(z) e^{i \sqrt{k_o^2 + \mu_{\alpha}} r} \quad (15)$$

$$\text{Parabolic approximation:} \quad p = \sum_{\alpha} A_{\alpha} \phi_{\alpha}(z) e^{i \left(k_o + \frac{\mu_{\alpha}}{2k_o} \right) r} \quad (16)$$

Normal modes are the same.

$$\text{Phase error} \approx \frac{1}{8} \frac{\mu_{\alpha}^2}{k_o^3} r \approx 2\pi \quad \text{when} \quad r \approx 10^4 \text{ nm} \quad (17)$$

Figure 3. VALIDITY OF PARABOLIC APPROXIMATION
(2-D, Stratified Ocean)

Therefore, the rays which can be obtained from the parabolic wave equation are the same as the rays which can be obtained from the elliptic wave equation except for a shift in the range scale. This constant factor (or value of Snell's invariant) can be absorbed into the range for any one ray, but not for all rays. The approach used by AESD is to effectively make this change in range scale for those rays which tend to dominate the acoustic field. In this way, errors in the parabolic approximation can actually be reduced.

Because the parabolic equation is a wave equation, in the case of a stratified ocean the solution can also be expanded in terms of normal modes, as shown in (15) and (16) for the elliptic and parabolic solutions, respectively. The parabolic equation also has a continuous part to its spectrum, and the summation implicitly implies an integration over the continuous part of the spectrum as well.

Both the normal mode eigenvalues, μ_α , and eigenfunctions, ϕ_α , are the same for the elliptic and parabolic equations. However, the phase velocities (as reflected in the exponential factors in (15) and (16)) are different. By expanding the square root in (15) and retaining only the leading term in μ_α , the parabolic phase velocity is obtained. The error, therefore, for a single mode can be estimated by carrying the expansion to the quadratic term, as is shown in (17). At 100 Hertz for a typical mode in the sound channel, a phase error of 2π would be accumulated at a range of 10^4 nm. Hence, if no change is made in the range scale, as mentioned earlier, a range error of about 5 percent accumulates for a ray near 20 degrees.

In Figure 4, the parabolic wave equation is rewritten in terms of a differential operator, A, and a multiplication operator, B, leading to (20). Note that both n and α are variable quantities and A and B do not commute.

$$i \frac{\partial \psi}{\partial r} + \frac{1}{2k_o} \frac{\partial^2 \psi}{\partial z^2} + \frac{k_o}{2} \left[n^2(r, z, \theta) - 1 + i\alpha(r, z, \theta) \right] \psi = 0 \quad (18)$$

$$\text{Let } A = \frac{1}{2k_o} \frac{\partial^2}{\partial z^2} ; \quad B = \frac{k_o}{2} \left[n^2 - 1 + i\alpha \right] \quad (19)$$

$$\frac{\partial \psi}{\partial r} = iA\psi + iB\psi \quad (20)$$

$$\psi(z, r + \Delta r) = e^{iA\Delta r/2} e^{iB\Delta r} e^{iA\Delta r/2} \psi(z, r) \quad (21)$$

$$e^{iA\Delta r} \psi(z) = \mathcal{F}^{-1} \left\{ e^{-ik^2 \Delta r / 2k_o} \left[\mathcal{F} \psi(z) \right] \right\} \quad (22)$$

FEATURES:

1. Exponential accuracy in z
2. Second order accuracy in r
3. Exactly energy conserving (when $\alpha = 0$)
4. Unconditionally stable
5. Computationally efficient
6. Readily implemented.

Figure 4. SPLIT-STEP FOURIER ALGORITHM

The split-step Fourier algorithm is expressed in (21) as the solution at a new range, $r + \Delta r$, in terms of the solution at range r operated on by a product of three factors. A is a differential operator which, when carried in an exponent, is difficult to evaluate by direct methods. But in Fourier space the operator A is simply a multiplication and therefore this operator acting on a function of depth can be quickly and accurately evaluated by first Fourier-transforming the function of depth, then doing a multiplication by a precomputed and stored phase function, and finally inverting the Fourier transform (22).

One can prove by the Trotter product theorem of functional analysis that in the limit as Δr goes to zero, the iterated version of this does converge in norm (that is, in the space of discrete functions or functions defined on a discrete grid) to the solution of the parabolic-wave equation.

Some of the features of this algorithm are listed in Figure 4. The advantages of this method (listed in Figure 5) are that, without any extra effort or computation, it can treat range-dependent velocity profiles, range- and depth-dependent volume losses, and variable bathymetry (that is, the depth of the ocean can be an arbitrary function of range). It is easy to solve numerically by marching in range.

The disadvantages (also Figure 5) are that for very large angles with respect to horizontal, which sometimes occur with steep slopes, there are inaccuracies. (Recently, methods have been developed to reduce these inaccuracies.) Discontinuities require special treatment (essentially smoothing), but this can be done in a way that is consistent with the physics and mathematics of low-frequency

ADVANTAGES

1. RANGE-DEPENDENT VELOCITY PROFILES INCLUDED
2. RANGE- AND DEPTH-DEPENDENT LOSSES INCLUDED
3. VARIABLE BATHYMETRY INCLUDED
4. EASY TO SOLVE NUMERICALLY BY MARCHING IN RANGE

DISADVANTAGES

1. STEEP SLOPES (LARGE ANGLES) CAUSE INACCURACIES
2. DISCONTINUITIES OF VELOCITY, DENSITY, AND VOLUME LOSS NEED TO
BE SMOOTHED
3. AZIMUTHAL COUPLING NEGLECTED.

Figure 5. ADVANTAGES AND DISADVANTAGES OF THE
PARABOLIC-EQUATION METHOD

acoustic propagation. Also, the neglect of azimuthal coupling can be remedied at the cost of greater computer running times.

In summary, the technique treats a wave equation in an especially useful way by applying effective and very rapid computational methods to generate its solution. The basic program is easy to write because the algorithm is so simple and stable. For production runs on a daily basis, a highly optimized version of this program is needed, such as that developed at AESD by using machine language programming and sophisticated Fast Fourier Transform techniques. The AESD version has achieved enormous increases in speed over earlier versions.

APPLICATIONS

The following examples indicate the application of the parabolic-equation method to several problems in underwater acoustics. These are displayed in terms of iso-loss contours in range and depth from the effective "source" which may actually be the receiver. The top figure of each pair is the basic field contoured in 5-dB intervals. The lower figure represents a range-averaged field with only the 80- and 90-dB contours shown as light and heavy, respectively. The shaded regions are either less than 80-dB loss if inside the 80-dB contour, or greater than 90-dB loss when bordered by the 90-dB contour.

The first example corresponds to a simple pressure-gradient, or linear, profile in water 16,000 feet deep over a high-loss bottom. The effective "source" depth is 8,000 feet. Figure 6 illustrates the field contours for a frequency of 50 Hz. Point C is the location of a cusped caustic, the two smooth branches of which are migrating toward the surface and bottom with increasing range. In ray-tracing programs, the fields in these regions must be found by using uniform

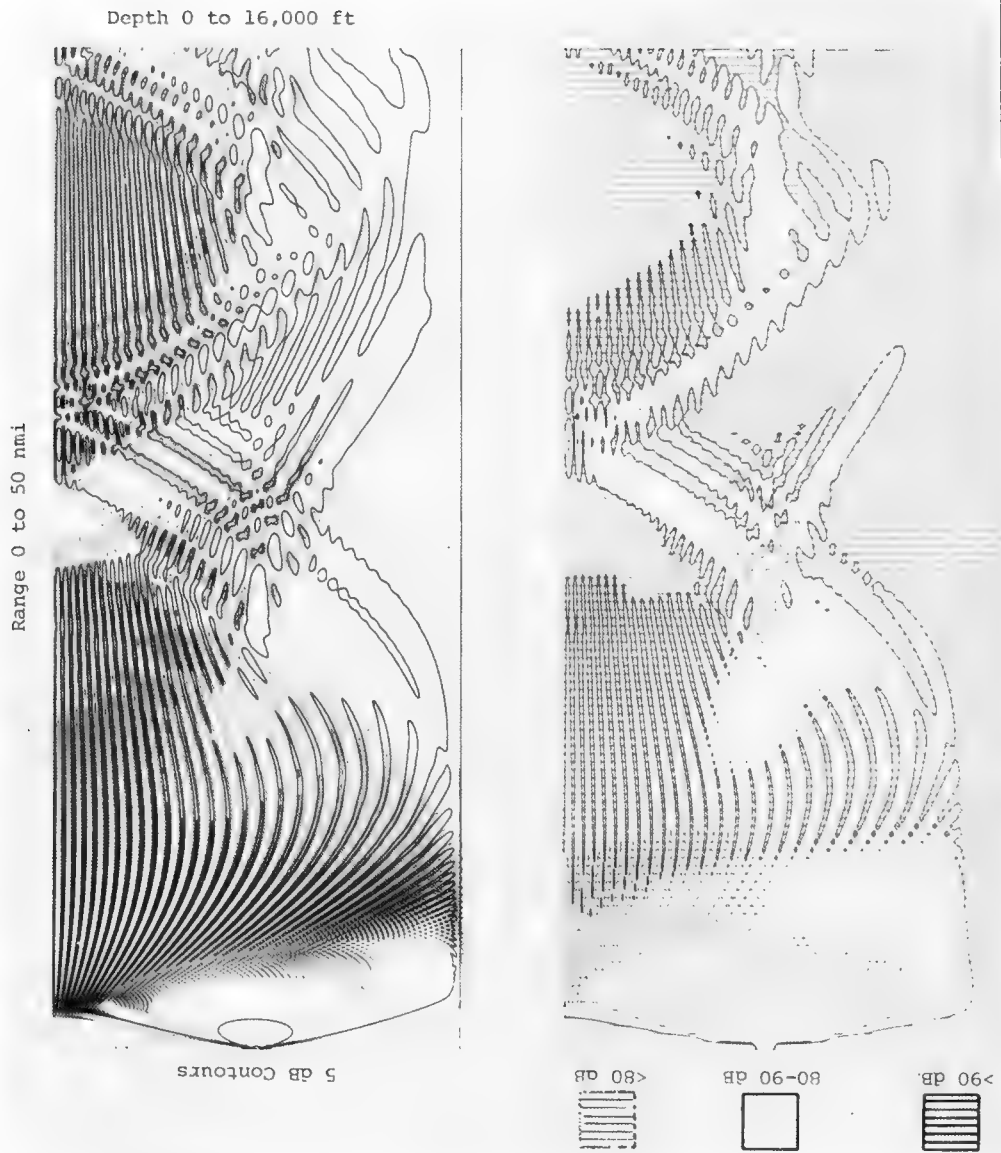


Figure 6. ISO-LOSS CONTOURS - PRESSURE-GRADIENT PROFILE, HIGH-LOSS BOTTOM
SOURCE AT 8000 FT, FREQUENCY OF 50 HZ

asymptotic expansions involving Pearcey functions for the cusp, and Airy functions for the smooth caustics. In the parabolic-equation method, such features are treated routinely.

Figures 7 and 8 correspond to the same geometry for frequencies of 100 and 200 Hertz, respectively. As the frequency increases, the diffraction effects are reduced and the caustics are more pronounced. At 200 Hertz, the second cusp, at twice the distance of the first, is clearly present. It must be re-emphasized that these contours are not rays. The ray-like patterns correspond to interference between up- and down-going rays near the surface, and between pairs of rays associated with smooth caustics.

The preceding three figures correspond to a bottom with high volume attenuation so that essentially no energy is returned when it enters the bottom. Figure 9 is for the same case as Figure 8 (200 Hertz) but with a low-loss bottom (simulated by a strong positive sound-speed gradient and no volume attenuation). Here the bottom-reflected paths are spectrally reflected and interfere with the RSR paths distorting the field contours even around the cusps.

The second example corresponds to the slightly more complicated environment of a bilinear profile. The ray trajectories for a source in the thermocline segment of the profile are shown in Figure 10, compliments of Richard Holford of Bell Labs. Note the formation of smooth and cusped caustics, RR caustics which effectively surface reflect, and the intersections of caustics. The correct ray treatments for these cases are extremely complex.

Figures 11 through 14 illustrate the field contours generated by the parabolic-equation method (again using a high-loss bottom) for frequencies of 50, 100, 200, and 400 Hertz. At the lower

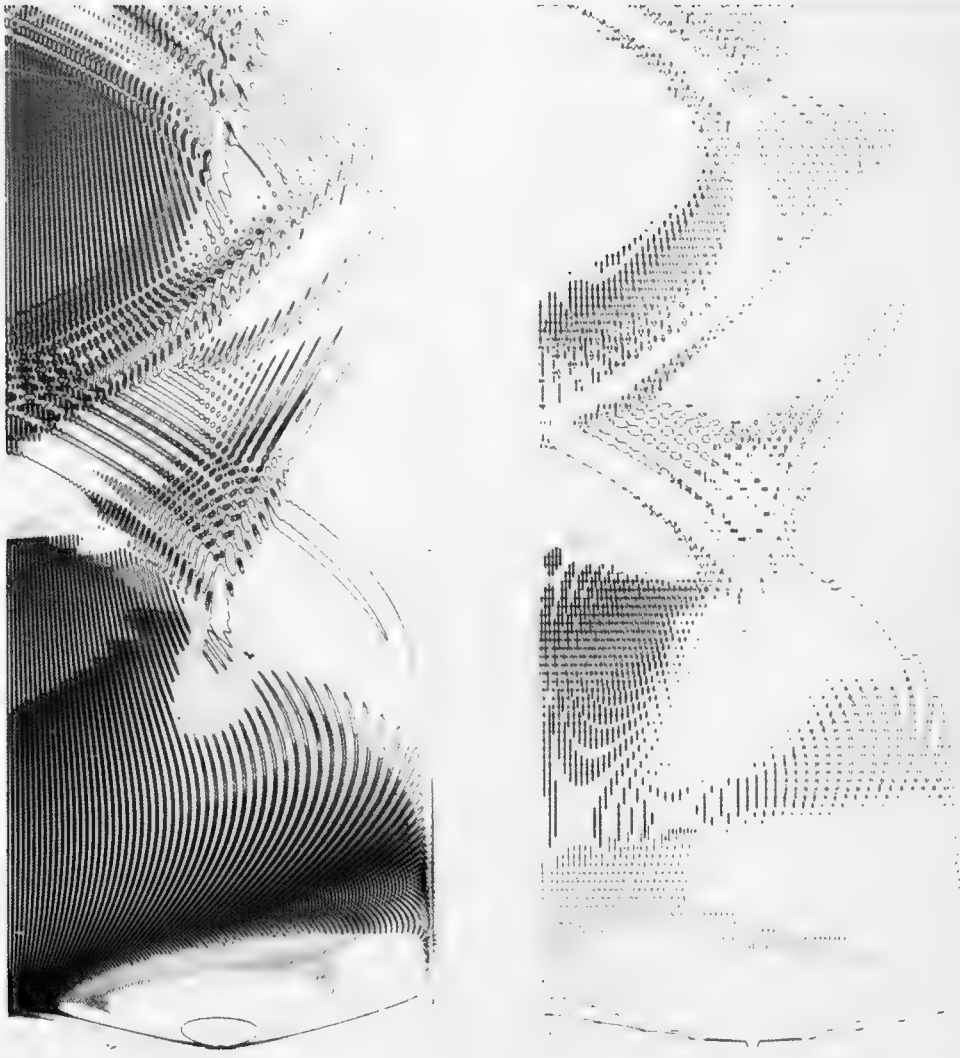


Figure 7. ISO-LOSS CONTOURS - PRESSURE-GRADIENT PROFILE, HIGH-LOSS BOTTOM
SOURCE AT 8000 FT, FREQUENCY OF 100 HZ

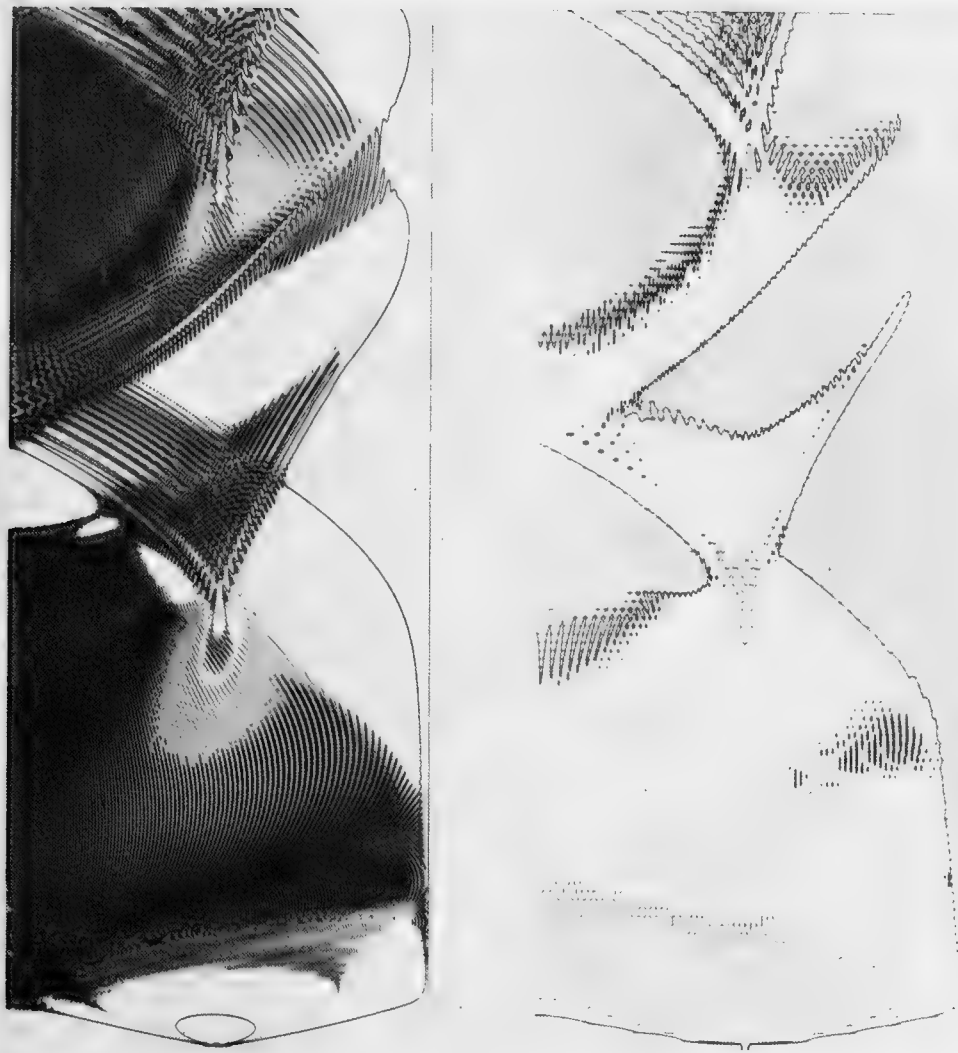


Figure 8. ISO-LOSS CONTOURS - PRESSURE-GRADIENT PROFILE, HIGH-LOSS BOTTOM SOURCE AT 8000 FT, FREQUENCY OF 200 HZ

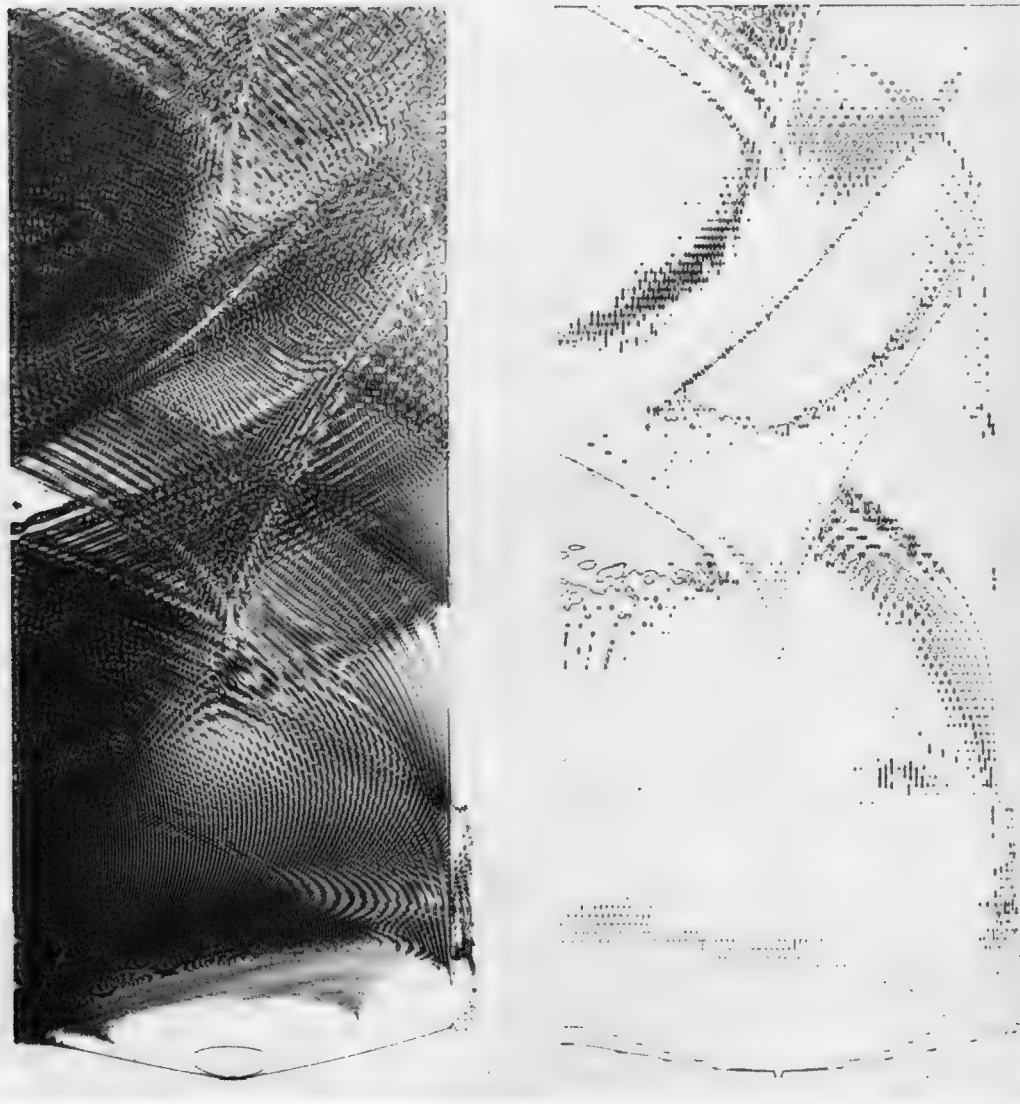


Figure 9. ISO-LOSS CONTOURS - PRESSURE-GRADIENT PROFILE, LOW-LOSS BOTTOM SOURCE AT 8000 FT, FREQUENCY OF 200 HZ

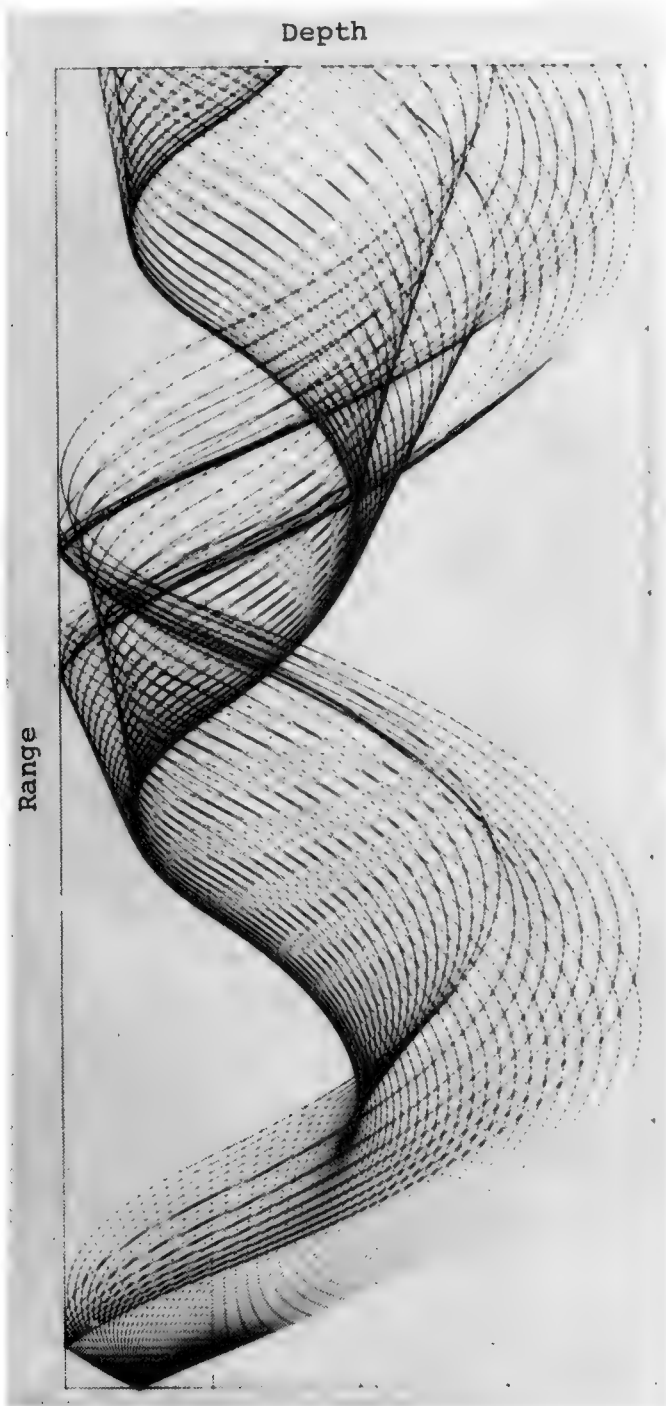


Figure 10. RR AND RSR RAYS FOR BILINEAR PROFILE

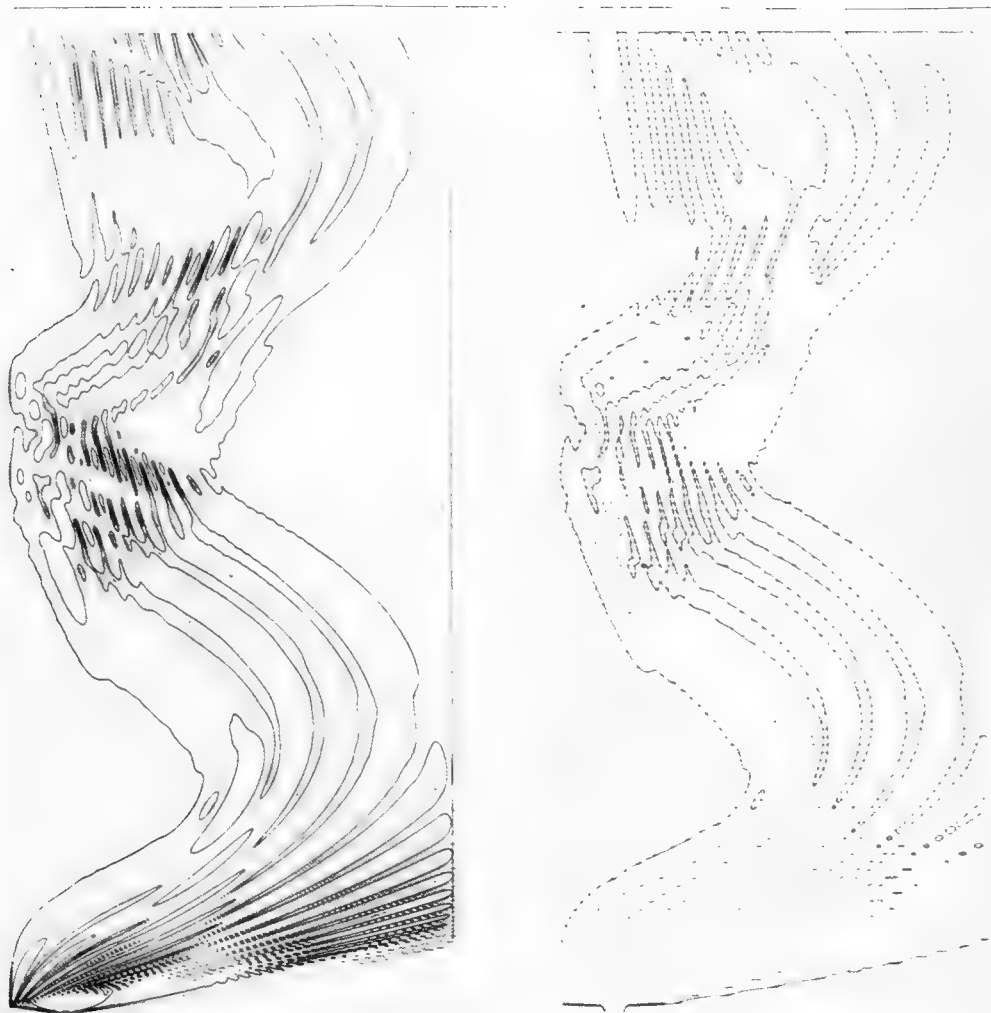


Figure 11. ISO-LOSS CONTOURS FOR BILINEAR PROFILE, HIGH-LOSS
BOTTOM, FREQUENCY OF 50 HZ

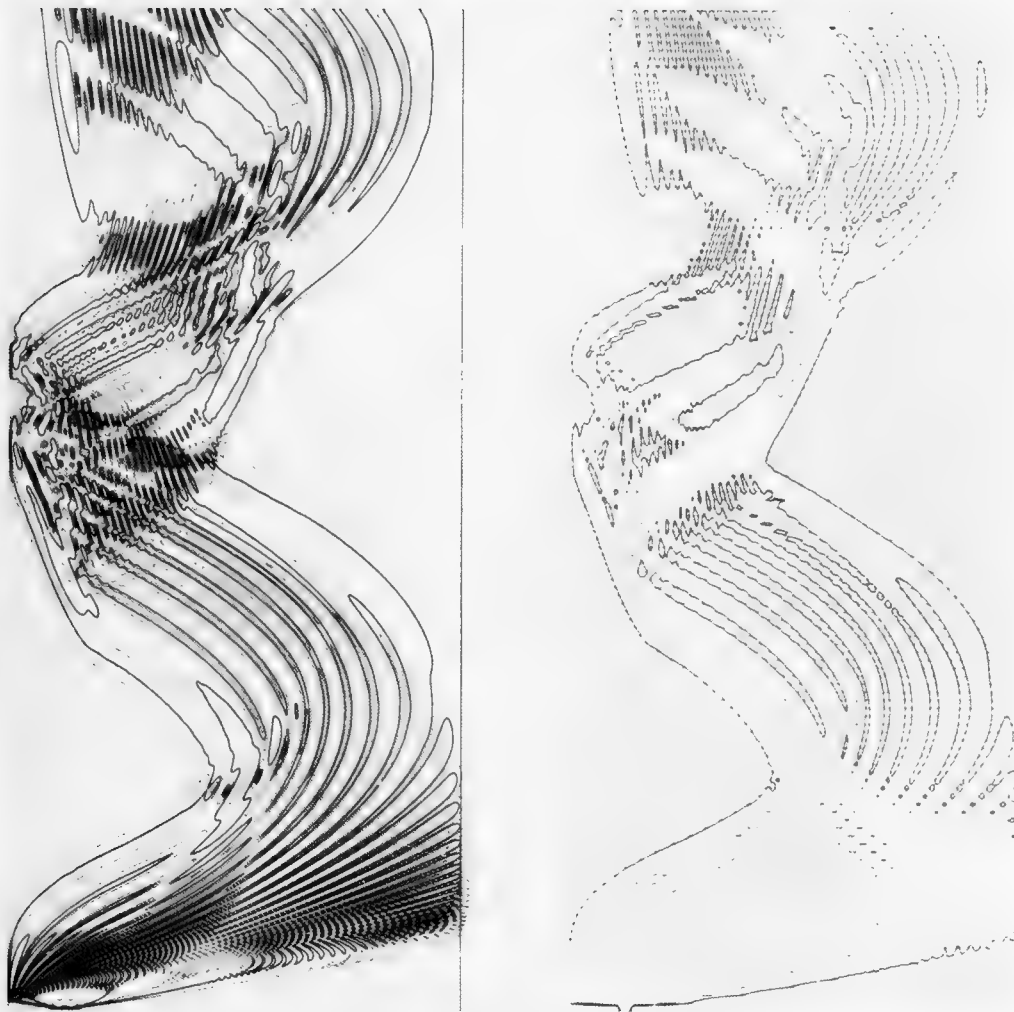


Figure 12. ISO-LOSS CONTOURS FOR BILINEAR PROFILE, HIGH-LOSS BOTTOM, FREQUENCY OF 100 HZ

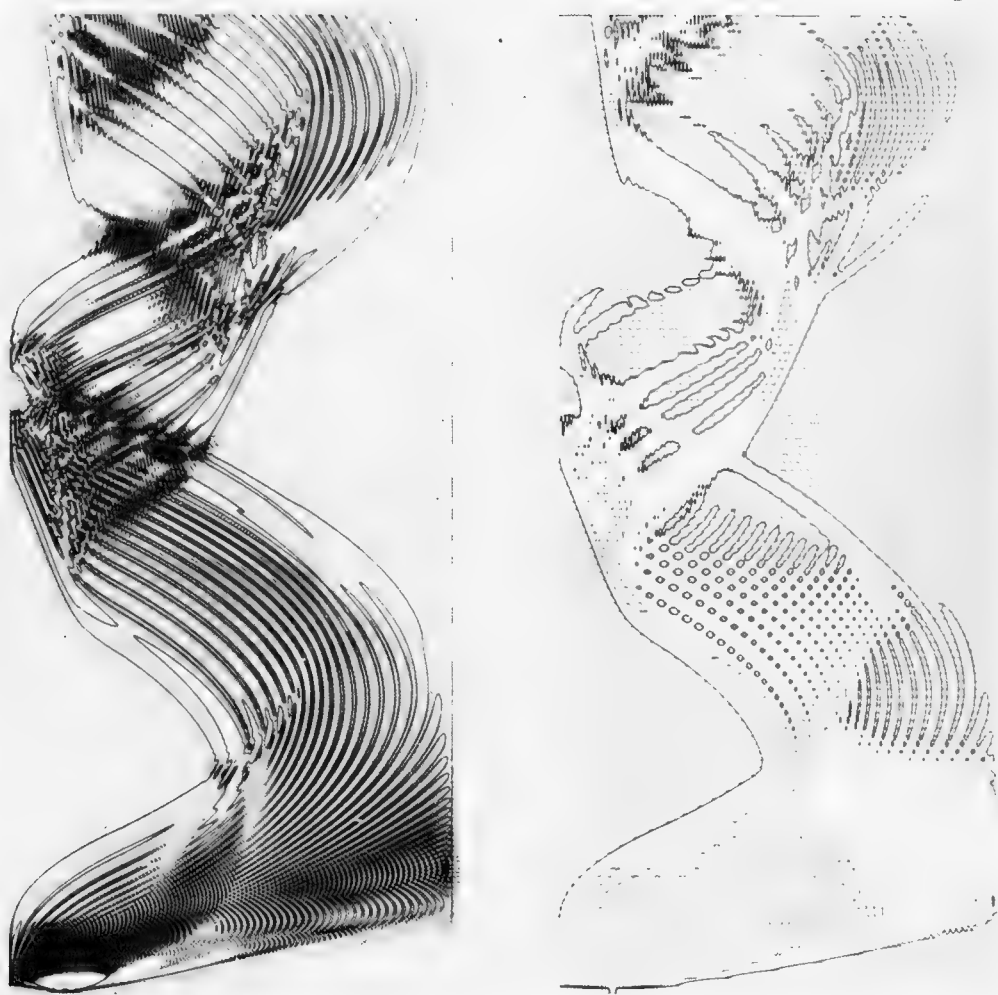


Figure 13. ISO-LOSS CONTOURS FOR BILINEAR PROFILE, HIGH-LOSS
BOTTOM, FREQUENCY OF 200 HZ

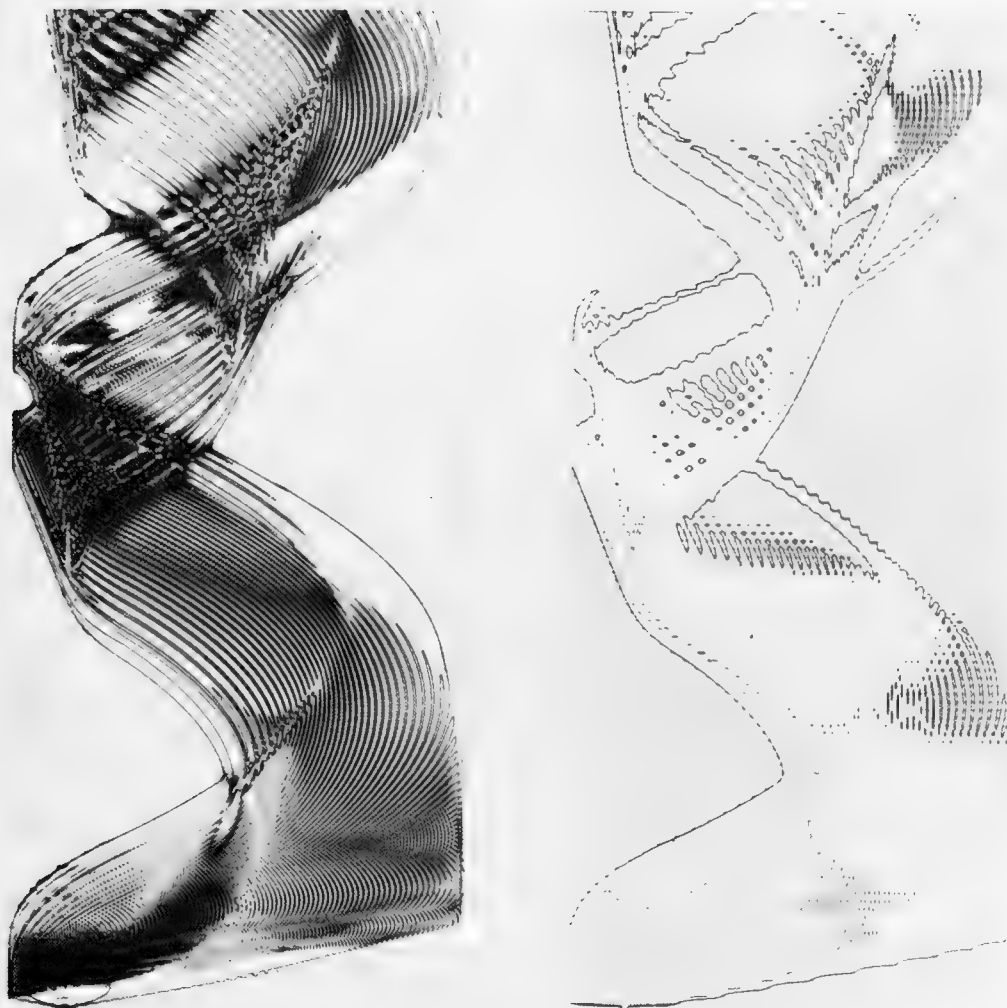


Figure 14. ISO-LOSS CONTOURS FOR BILINEAR PROFILE, HIGH-LOSS BOTTOM, FREQUENCY OF 400 HZ

frequencies, the cusped and smooth caustics near the surface are complicated by surface image interference of the diffraction field. Note the high degree of correspondence between the field contours at 200 Hertz and the illuminated regions according to the ray trajectories of Figure 10.

The third example is for the so-called canonical sound-speed profile of Walter Munk (1974). In this case (Figure 15), the source is on the axis and a high-loss bottom is placed at the reciprocal depth of the surface to eliminate RSR paths. The two focal regions on the axis reflect the basic asymmetry of the profile.

The fourth example illustrates effects associated with a range-dependent sound-speed profile. The entire field is shown in Figures 16 and 17 for the first and second 80-mile segments, respectively. The profile at the source (again on the axis) persists for the first 60 miles, at which point the axis is rapidly moved up, resulting in a concentration of energy near the surface. At a range of 120 miles, the profile rapidly changes back to the original profile, shifting the surface-concentrated energy deeper and leading to a continuous shadow-zone near the surface. Invoking acoustic reciprocity, for a shallow source moving away from an axis-depth receiver, the intermittent convergence-zone behavior of the signal would change to nearly continuous reception from 60 to 120 miles and then essentially no reception beyond. This behavior is a direct result of the strong horizontal gradients which an adiabatic normal-mode approach could not treat.

The following examples illustrate effects associated with range-variable bathymetry. Figure 18 displays the field contours for a high-reflectivity shoaling bottom where initially refracted energy

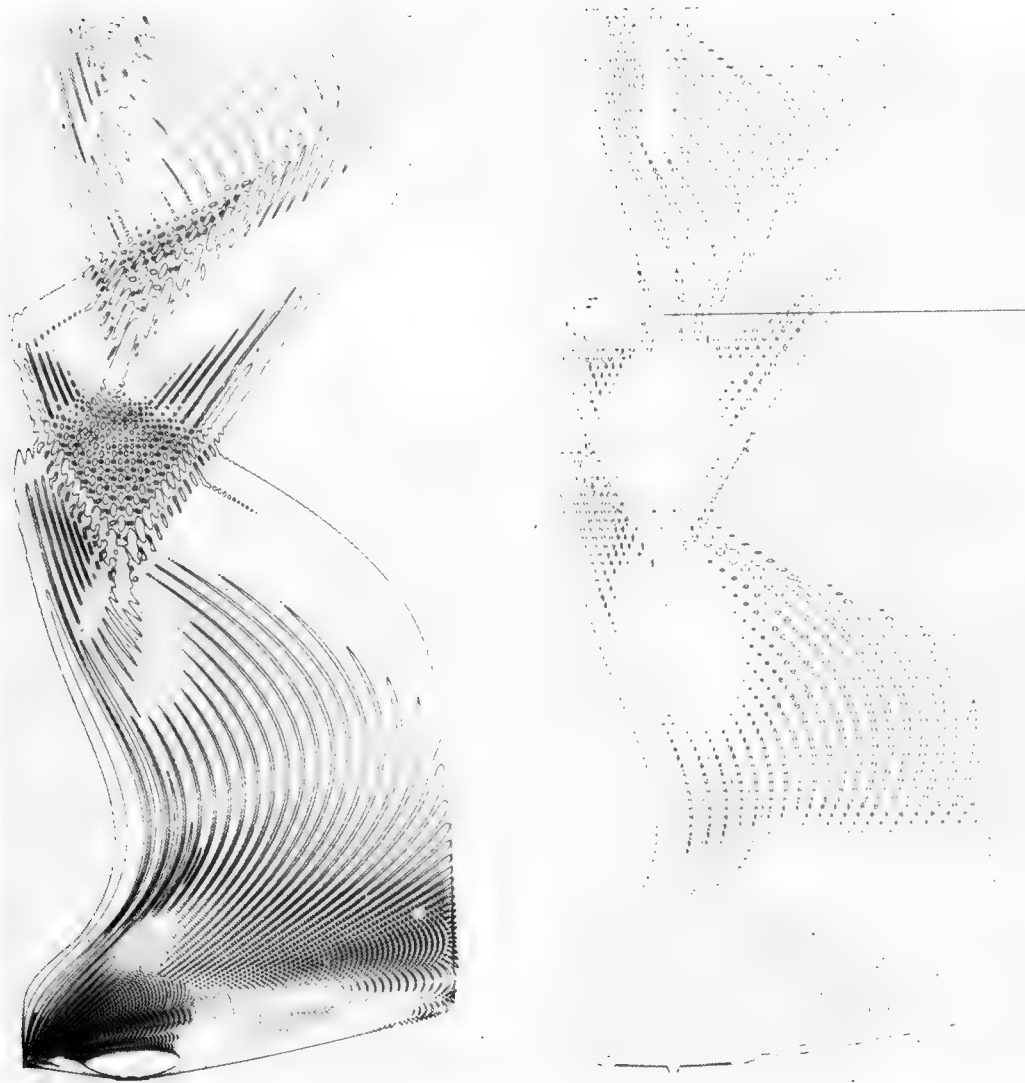


Figure 15. ISO-LOSS CONTOURS FOR MUNK'S CANONICAL PROFILE,
HIGH-LOSS BOTTOM AXIS-DEPTH SOURCE

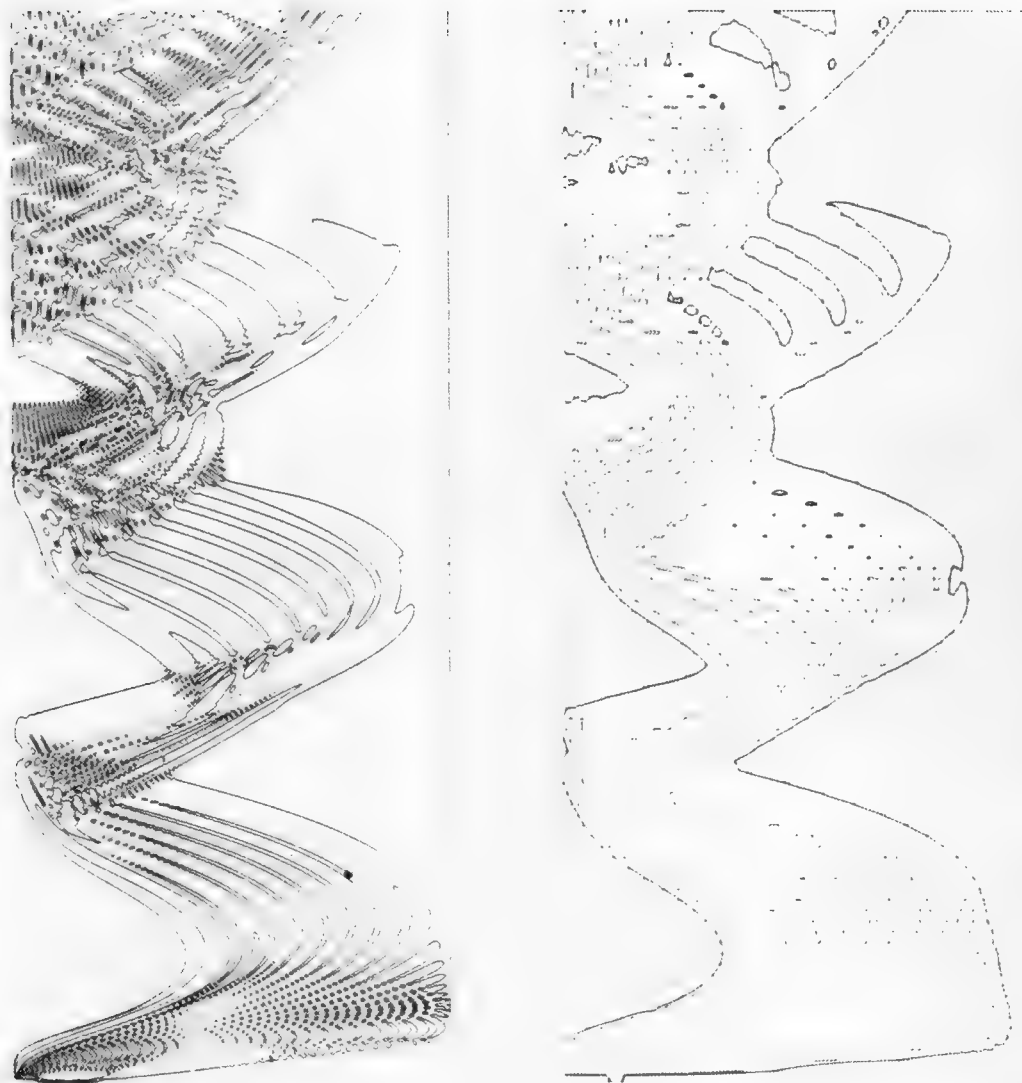


Figure 16. ISO-LOSS CONTOURS FOR RANGE-VARYING PROFILES, HIGH-LOSS BOTTOM, SHALLOW SOURCE, FIRST 80 MILES

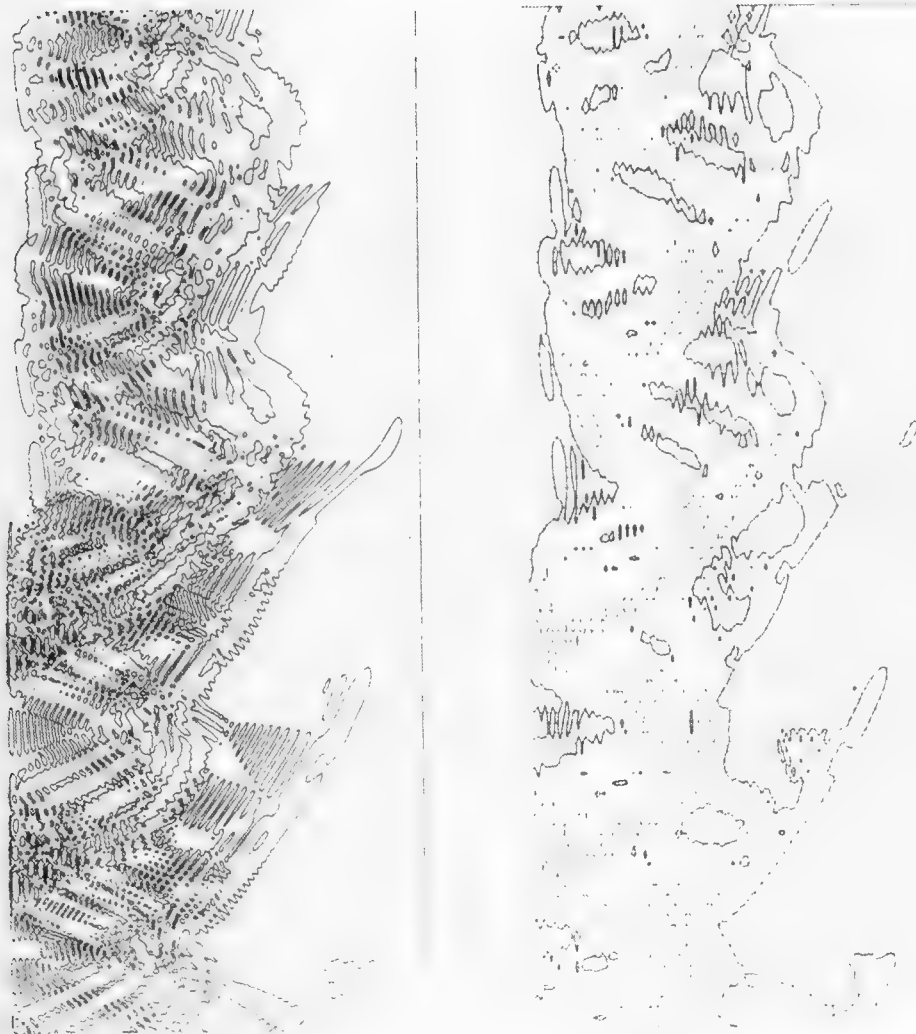


Figure 17. ISO-LOSS CONTOURS FOR RANGE-VARYING PROFILES, HIGH-LOSS BOTTOM, SHALLOW SOURCE, SECOND 80 MILES

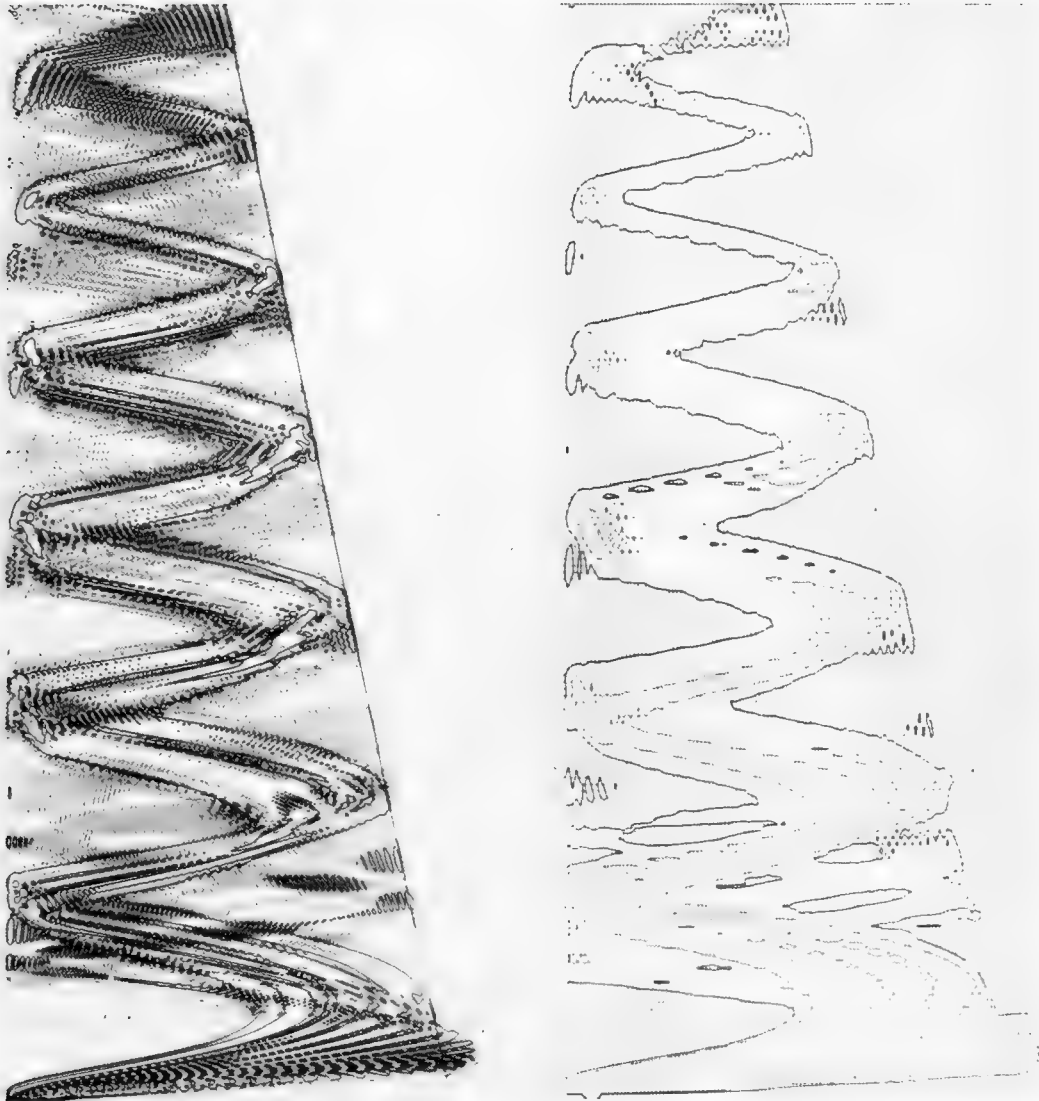


Figure 18. ISO-LOSS CONTOURS FOR LOW-LOSS SHOALING BOTTOM

is converted to SRBR and RBR leading to the so-called megaphone effect. Figures 19 and 20 illustrate the impact of a high-loss seamount on energy from an axial source and a near-surface source, respectively. In the first case, the source couples well to the near-axial modes which suffer little attenuation in passing the seamount. Hence, beyond the seamount, the high-angle modes are stripped away leaving the very distinct focal regions. For the shallow source which does not couple well with the axial modes, the seamount strips nearly all of the energy away. Figure 21 is for the shallow source where now the bottom is highly reflecting. Paths which before were annihilated by the seamount now steepen to SRBR going up the seamount and convert back to RSR and RR on the downslope.

RANDOM OCEANS

The final example of the use of the parabolic-equation method addresses the random ocean problem (Garrett and Munk, 1972; Munk, 1974). The main advantage of the parabolic-equation method is that it can take into account rapid range variations in the ocean environment. We now know that there are important random components in the acoustic sound speed due to internal-wave fluctuations and microfluctuations in the ocean temperature structure.

The following work was begun this summer with Stan Flatté and Walter Munk. This discussion is merely an introduction to the work which is covered in detail in subsequent papers (reproduced in these Proceedings).

The technique is summarized in Figure 22. By adding a time dependence to the sound speed (23), it can be expressed as a mean function of depth and range, and a fluctuating function of depth, range, and time. The refractive index (24) is then a sum of a deterministic part and a random part.

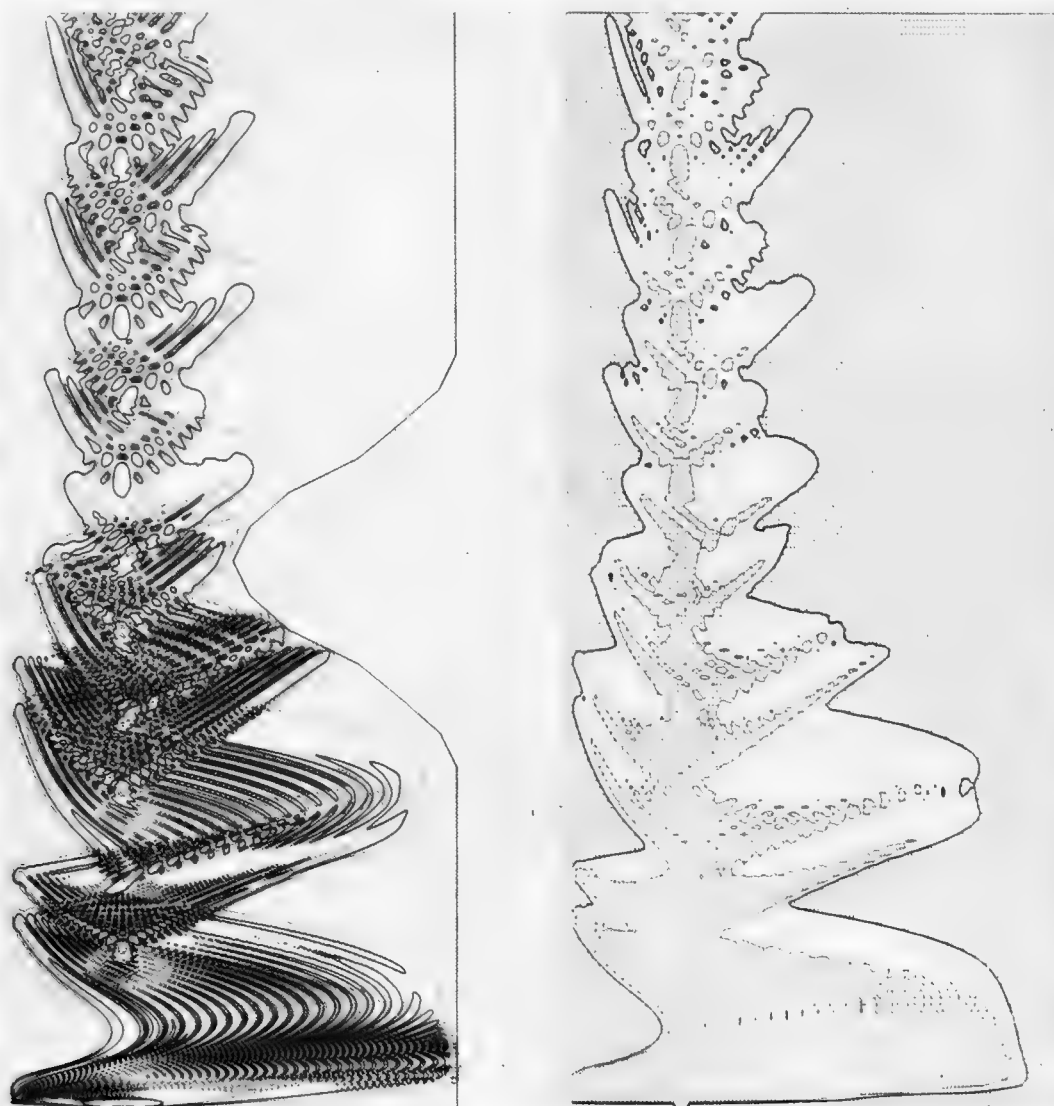


Figure 19. ISO-LOSS CONTOURS FOR HIGH-LOSS BOTTOM WITH SEAMOUNT AXIS-DEPTH SOURCE

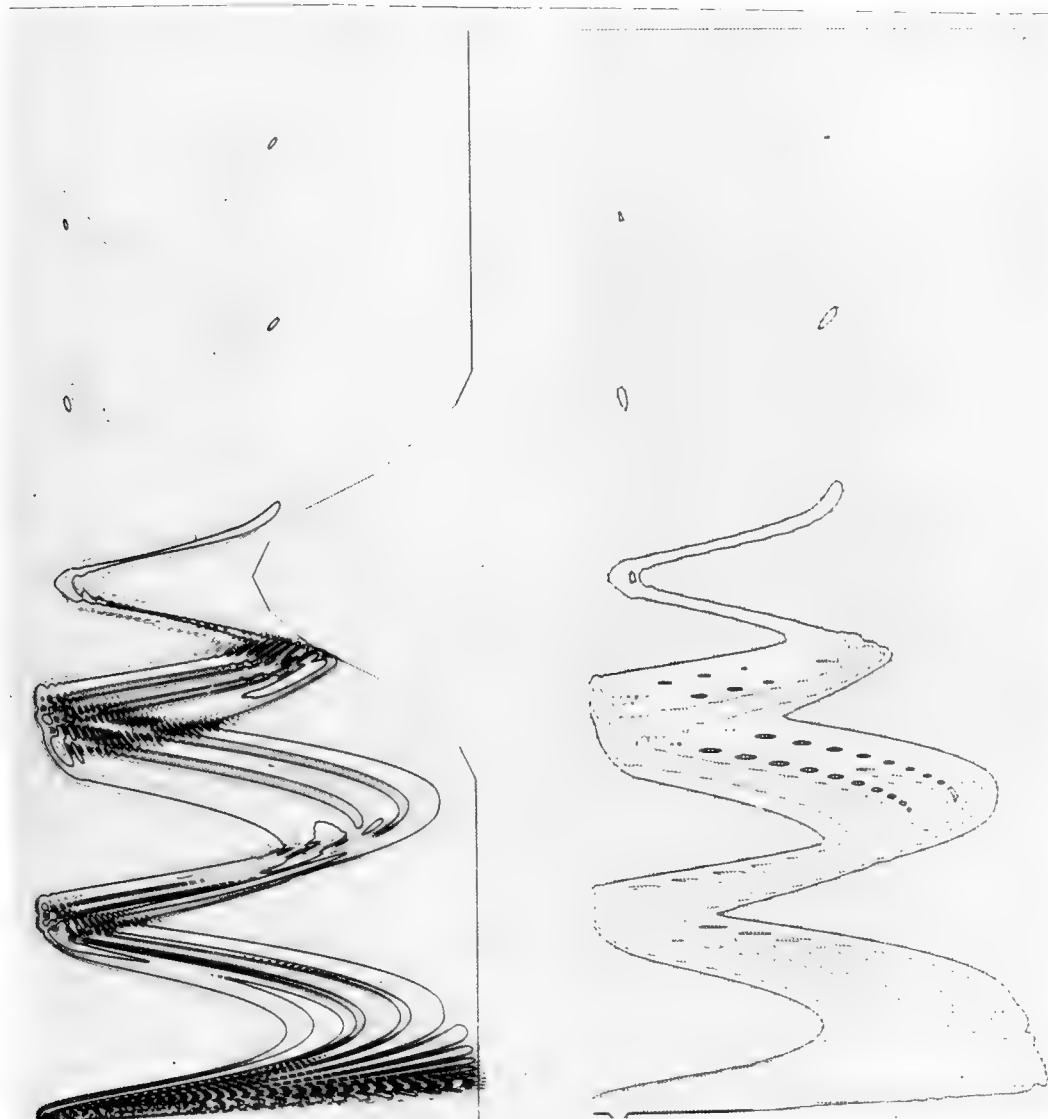


Figure 20. ISO-LOSS CONTOURS FOR HIGH-LOSS BOTTOM WITH SHALLOW SOURCE

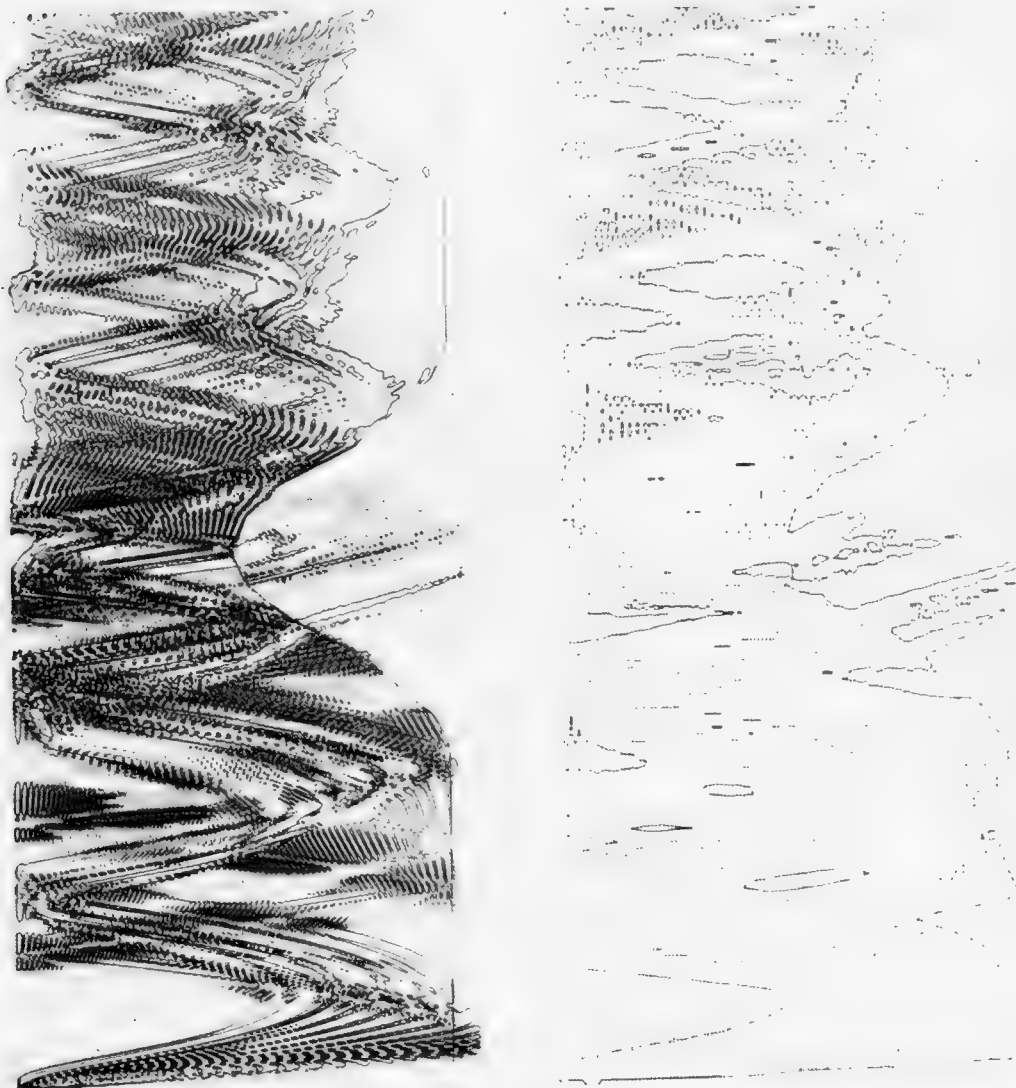


Figure 21. ISO-LOSS CONTOURS FOR LOW-LOSS BOTTOM WITH SHALLOW SOURCE

$$c(z,r,t) = \bar{c}(z,r) + \delta c(z,r,t), \quad (23)$$

where δc is a random function of z, r, t

$$n^2(z,r,t) = \frac{c_o^2}{c^2(z,r,t)} \approx \frac{c_o^2}{\bar{c}^2(z,r)} - 2 \frac{\delta c(z,r,t)}{c_o} \quad (24)$$

Use quasi-static approximation $\left(\omega_{\delta c} \ll \omega_o, \frac{c_o}{L_H} \right)$

$$i \frac{\partial \psi}{\partial r} + \frac{1}{2k_o} \frac{\partial^2 \psi}{\partial z^2} + \left[\frac{k_o}{2} \left(\frac{c_o^2}{\bar{c}^2} - 1 \right) - k_o \frac{\delta c(z,r,t)}{c_o} \right] \psi = 0 \quad (25)$$

The solution gives

$$p(r,z,t) = \psi(r,z,t) \frac{1}{\sqrt{r}} e^{i(k_o r - \omega_o t)}$$

$$\bullet \langle p(r_1, z_1, t_1) p^*(r_2, z_2, t_2) \rangle \quad (26)$$

Figure 22. RANDOM OCEAN PROCEDURE

Using the quasi-static approximation in which the frequencies of the fluctuations are small compared to both the carrier frequency and the transit time of the acoustic waves over a horizontal correlation length L_H , the parabolic wave equation for a random ocean with time-dependent fluctuations varying in both range and depth is expressed in (25).

The solution of this equation gives the pressure as a function of range and depth and time (26). It is a function of three variables, represented in the form of a complex envelope and a carrier wave; ψ is simply the complex-demodulated envelope which would be measured experimentally. Hence, ψ is a quantity that can be compared directly to experimental measurements of acoustic fluctuations in the ocean. Typical quantities of interest are correlations of the pressure at different ranges, depths, and times. This approach has been carried out numerically, and the results of that calculation are presented in subsequent workshop papers dealing with both theory and comparisons with experimental results.

Two additional theories are being developed in connection with this problem of wave propagation in random oceans. Using the analogy with the Schroedinger equation, following Pauli, a Pauli master equation can be derived using normal modes (Figure 23) (Agarwal, 1973). The envelope ψ is represented as a sum of normal modes (28) with random coefficients a_n . A density matrix (29) is defined as the correlation between normal-mode amplitudes, and coupling coefficients (30) between normal modes are used to represent the effects of the randomly fluctuating component of the sound speed.

Transition probabilities (31) are developed and finally a master equation (32) involving only the diagonal elements of the density

Normal modes:

$$\frac{1}{2k_o} \frac{\partial^2 \psi_n}{\partial z^2} + \frac{k_o}{2} \left(\frac{c_o^2}{\bar{c}^2(z)} - 1 \right) \psi_n = k_n \psi_n \quad (27)$$

$$\psi(z, r) = \sum_n a_n(r) \psi_n(z) e^{i k_n r} \quad (28)$$

Density matrix:

$$\rho_{nm}(r) = \langle a_n(r) a_m^*(r) \rangle \quad (29)$$

Coupling coefficients:

$$v_{nm}(r) = \frac{k_o}{c_o} \int dz \psi_n^*(z) \delta c(z, r) \psi_m(z) \quad (30)$$

Transition probability:

$$\gamma_{nm} = 2\pi \langle |\hat{\gamma}_{nm}(k_n - k_m)|^2 \rangle \quad (31)$$

Master equation:

$$\frac{\partial}{\partial r} \rho_{nn} = \sum_m \gamma_{nm} (\rho_{mm} - \rho_{nn}) \quad (32)$$

Figure 23. PAULI MASTER EQUATION PROCEDURE

matrix is obtained. These elements are simply the squared amplitudes of the normal modes.

Everything in Equation (32) is known and can be numerically obtained using computers. Comparisons are then possible between these normal-mode results and either numerical experiments (using the parabolic equation) or field data.

Another approach, outlined in Figure 24, is based on the wave-kinetic equation, basically applying transport theory to acoustic propagation of random oceans. The Wigner phase-space distribution function f defined in (33) is introduced where f is quadratic in the complex demodulated signal ψ and hence depends on depth z and range r as well as vertical angle θ . The ensemble average F (36) satisfies the integro-differential equation (37). This equation, which describes the evolution of the ensemble average Wigner distribution function (Tappert and Besieris, 1971; Besieris and Tappert, 1973), is essentially the covariance of the pressure.

Again, everything in this equation is known in terms of the fluctuations. It has the form of a classical radiation transport equation and numerical techniques may be used to solve it. The virtue of this approach is that it leads directly to the ensemble-average acoustic field (and hence mean intensities) not just at one point but at two points.

Figure 25 shows a simple example of this method, applying a diffusion approximation. The correlation function of pressure at two depths is obtained (41) as an exponential, and (42) gives the coherence length in depth as a function of range. This is a definite prediction of the theory that can be compared to either numerical experiments (for example, using the parabolic equation) or field data.

Wigner distribution:

$$f(z, \theta, r) = \frac{k_o}{2\pi} \int dz' e^{ik_o \theta z'} \psi^* \left(z + \frac{1}{2} z', r \right) \psi \left(z - \frac{1}{2} z', r \right) \quad (33)$$

where

$$\int f(z, \theta, r) d\theta = |\psi(z, r)|^2 \quad (34)$$

$$\int f(z, \theta, r) dz = |\hat{\psi}(\theta, r)|^2 \quad (35)$$

$$F(z, \theta, r) = \langle f(z, \theta, r) \rangle \quad (36)$$

$$\begin{aligned} \frac{\partial F}{\partial r} + \theta \frac{\partial F}{\partial z} + \frac{1}{2} \frac{\partial}{\partial z} \left(\frac{c_o^2}{c^2} - 1 \right) \frac{\partial F}{\partial \theta} \\ = \int d\theta' w(z, \theta, \theta') [F(z, \theta', r) - F(z, \theta, r)] \end{aligned} \quad (37)$$

where

$$\frac{dz}{dr} = \theta, \quad \frac{d\theta}{dr} = \frac{1}{2} \frac{\partial}{\partial z} \left(\frac{c_o^2}{c^2} - 1 \right) \quad (38)$$

and

$$w(z, \theta, \theta') = 2\pi k_o \hat{\Gamma} \left(z, \theta - \theta', \frac{1}{2} \theta^2 - \frac{1}{2} \theta'^2 \right) \quad (39)$$

Figure 24. WAVE KINETIC EQUATION

$$\frac{\partial F}{\partial r} + \theta \frac{\partial F}{\partial z} + \frac{1}{2} \frac{\partial}{\partial z} \left(\frac{c_o^2}{\bar{c}^2} - 1 \right) \frac{\partial F}{\partial \theta} = \frac{\partial}{\partial \theta} D(\theta, z) \frac{\partial F}{\partial \theta} \quad (40)$$

Take $\bar{c} = \text{const}$; $D = \text{const}$

$$\langle \psi^*(z + \frac{1}{2} z', r) \psi(z - \frac{1}{2} z', r) \rangle = e^{-\frac{1}{2} k_o^2 \langle \theta^2 \rangle z'^2} \quad (41)$$

$$z_{\text{coh}} \sim \frac{1}{k_o \langle \theta^2 \rangle^{1/2}} \sim \frac{L_v}{k_o (\delta c/c) \sqrt{L_H r}} \quad (42)$$

Figure 25. DIFFUSION APPROXIMATION

REFERENCES

- Agarwal, G. S., "Master Equation Methods in Quantum Optics," in *Progress in Optics*, Vol. XI:1-76, North-Holland, 1973.
- Barabanenkov, Yu. N., Yu. A. Kravtsov, S. N. Rytov, and V. J. Tatarskii, *Sov. Phys. Uspekhi*, 13:551 (1971).
- Benthien, G. W., D. F. Gordon, and L. E. McCleary, *J. Acous. Soc. Amer.*, 55:S45 (1974); also private communications with D. Gordon and others at NUC.
- Besieris, I. M., and F. D. Tappert, *J. Math. Phys.*, 14:1829 (1973).
- Flatté, S., and F. D. Tappert, JASON Report, Stanford Research Inst., 1974.
- Fock, V. A., *Electromagnetic Diffraction and Propagation Problems*, Pergamon Press, N. Y., 1965.
- Garrett, C., and W. Munk, *Geophys. Fl. Dyn.*, 2:225 (1972).
- Hardin, R. H., and F. D. Tappert, *SIAM Rev. (Chronicles)*, 15:423 (1973).
- Hasegawa, A., and F. D. Tappert, *Appl. Phys. Lett.*, 23:142 (1973); 23:171 (1974).
- Lecntovich, M., and V. Fock, *Zh. Eksp. Teor. Fiz.*, 16:557 (1946).
- Malyuzhinets, G. D., *Sov. Phys. Uspekhi*, 69:749 (1959).
- McDaniel, S. T., *J. Acous. Soc. Amer.*, 55:S45 (1974).
- Munk, W. H., *J. Acous. Soc. Amer.*, 55:220 (1974).
- _____, JASON Report, Stanford Research Inst., 1974.
- Munk, W., and S. Flatté, *Proceedings of this Meeting*.
- Spofford, C. W., *J. Acous. Soc. Amer.*, 55:S34 (1974); also private communications with R. Buchal and H. Brock at AESD.

Tappert, F. D., in *Lectures in Applied Mathematics*, Vol. 15, (ed.) A. C. Newell, Amer. Math. Soc., Providence, R. I., 215-216, 1974.

_____, *J. Acous. Soc. Amer.*, 55:S34 (1974).

Tappert, F. D., and I. M. Besieris, *Proc. Inter. Symp. on Electromagnetic Wave Theory*, Tbilisi, USSR, Sept. 1971.

Tappert, F. D., and R. H. Hardin, in AESD Tech. Note 73-05, (ed.) C. W. Spofford, ONR, Arlington, Va., Nov. 1973.

_____, _____, *Proc. Eighth Inter. Congress on Acoustics*, London 1974, p. 452.

Tappert, F. D., and C. N. Judice, *Phys. Rev. Lett.*, 29:1308 (1972).

DISCUSSION

Dr. J. B. Hersey (Office of Naval Research): First of all, I think our speaker is to be congratulated on an absolutely brilliant performance. I have been very excited to see some of the nagging problems of ocean acoustics, not necessarily finally solved but yielding some very, very intriguing and encouraging results. Congratulations, sir.

Dr. Tappert: Thank you.

Mr. E. D. Garabed (Naval Air Development Center): You mentioned that in this parabolic-equation method there was a limitation on angles that it can be used for. Can you give me some idea as to what that angular limitation is, in degrees?

Dr. Tappert: Roughly a 5 percent error at 20 degrees is introduced in the ray periods or modal phase velocities. The significance of this error really depends on what you want to measure, or what you want to get out of the calculation. Some things are computed more accurately than others.

For example, if you only want transmission loss, it doesn't really matter whether you have an error in the phase. But if you want to do beamforming with the complex signal, then you need accurate phase information as well.

There is no universal simple answer to your question. We have to make more computer runs, compare with more data, and do more analysis before we fully understand all the limits of the method. It is a flexible method. It is not just one simple formula that you do once and for all. There are ways to improve and extend and refine this parabolic-equation method.

Dr. H. Weinberg (New London Laboratory, Naval Underwater Systems Center): If I understand correctly, you use a virtual source to take into account the free surface. Would it be easy to take into account surface loss or its equivalent?

Dr. Tappert: One would think so, and I have struggled hard to find a way to do it, but with the algorithm that I described it seems to be difficult to relax the flat-surface boundary condition.

Dr. Weinberg: I don't see why it is more difficult for you to treat the free surface than some sort of boundary condition. Is that because of the algorithm you chose?

Dr. Tappert: It is because of the Fast Fourier Transforms. With other algorithms it would be easier to introduce surface losses and surface scattering. And I really do encourage others to look into other algorithms. There is nothing magic about this one. I am convinced that it is unusually efficient and effective and accurate, but again it would be worth knowing just how much better it is than other possible numerical algorithms.

Dr. S. W. Marshall (Naval Research Laboratory): I am getting back to times for computation again. Can you tell me whether you use software or hardware FFTs and what your computation time in long runs is?

Dr. Tappert: Yes. I use software FFTs, but coded in FORTRAN. At AESD they have a Compass-coded FFT. The difference is about 50 percent. You can in principle achieve gains of an order of magnitude by using hardware FFTs.

On a machine like the UNIVAC 1108 or IBM 370/165, without the fluctuations in the ocean, it takes roughly the same amount of machine time to compute the acoustic field as it takes the acoustic field to advance, which is roughly one mile per second, so if you are going 100 miles, it takes roughly 100 seconds.

Dr. R. M. Fitzgerald (Naval Research Laboratory): Regarding the approximation in small angle for the parabolic-equation method, I think you can show that the approximation is one in which the angles are restricted to a small cone but the direction of the cone is arbitrary.

Dr. Tappert: That is very true. Yes.

Dr. Fitzgerald: And in that way you can overcome the limitation now that you cannot treat steep rays. You do it by using separate cones and linearly superimposing the results.

Dr. Tappert: The problem I had in trying to work that out is how you superimpose. You certainly can take a cone of angles that is not oriented horizontally. For example, if you want to do the bottom bounce experiment, you take a cone going down and then it is

quite accurate within that cone. But I could never see a really good way to connect different cones without getting an interference pattern, a spurious interference pattern, where they connect. But if you have a way to do that, it would be quite an improvement.

Dr. Fitzgerald: I do.

Dr. Tappert: Good.

CALCULATION OF THE EFFECT OF INTERNAL
WAVES ON OCEANIC SOUND TRANSMISSION

Stanley M. Flatte

Frederick D. Tappert

Reprinted from the Journal of the Acoustical Society of America
Vol. 58, No. 6, December 1975

Calculation of the effect of internal waves on oceanic sound transmission

Stanley M. Flatté

University of California, Santa Cruz, California 95064

Frederick D. Tappert

Courant Institute of Mathematical Sciences, New York University, New York, New York 10012

(Received 22 August 1975)

The signal received by a hydrophone in the ocean many kilometers from a steady sound source fluctuates dramatically due to variations of the speed of sound in sea water. By inserting an empirical model of internal-wave-generated sound-speed variations into an acoustic-transmission computer code, we have shown that internal waves cause significant variations in sound transmission at 100 Hz, comparable in size and frequency to the variations observed in field experiments. We have also studied the usefulness of vertical hydrophone arrays.

Subject Classification: 30.25, 30.82; 28.60.

INTRODUCTION

Acoustic transmission in the ocean is profoundly affected by the dependence of the speed of sound on oceanic depth, range, and time. The speed of sound, in turn, is determined by oceanographic quantities: pressure, temperature, and to a lesser extent, salinity.

In a typical 4-km-deep ocean, the sound speed c has a minimum as a function of depth z at about 1 km, with a value close to 1500 m/sec. Values of c at the surface and bottom are a few percent higher than at the minimum. From an oceanographic point of view the minimum is due to the competition between the drop in temperature and the rise in pressure as one descends in the ocean. The minimum causes sound to be refractively contained in the volume of the ocean, resulting in a "sound channel," and making possible sound transmission over thousands of kilometers at frequencies below 1 kHz.¹ (Higher frequencies are absorbed.)

The sound-speed profile $c(z)$ varies with geographic position. For example, the sound channel minimum rises as one moves toward colder Northern waters. In addition, the depth of the ocean changes due to the topography of the bottom of the sea. Hence any acoustic transmission experiment over hundreds of kilometers or more will be subject to a range-dependent sound-speed profile. A great deal of work has gone into mapping the expected differences in transmission due to differences in geographical location.²

The strongest time variation of $c(z)$ occurs as a result of seasonal changes in temperature. These long-term time variations have also received considerable attention, although in principle the changes between winter and summer are no more difficult to deal with than a significant change in geographical position.

Any experimenter who has done a long-range acoustic transmission experiment can attest to the fact that considerable (5–30-dB) variations in signal are observed over periods ranging from a few minutes to several days, with several hours being typical.³ When surface interactions are absent or have been filtered out, and

for fixed source and receiver, these fluctuations must be caused by variations in the sound-speed field through which the sound passes, and the sound-speed variations must have an oceanographic origin. Yet until now almost no quantitative connection has been made between these "rapid" acoustic variations and any realistic oceanographic phenomenon. Over the years, however, there has been much speculation and order-of-magnitude correlation with internal-wave motions.⁴

The ocean contains a random field of internal waves, with periods ranging from $\frac{1}{3}$ to 24 h. The intensity of these waves has been estimated from measurements of temperature and current fluctuations in the ocean, and the associated effect on sound speed has been calculated.^{5,6} The root-mean-square sound-speed fluctuations due to internal waves is at a level of 10^{-4} , two orders of magnitude below the variation which causes the sound channel.⁵

In this paper we demonstrate that the internal wavefield in the ocean causes significant fluctuations in long-range acoustic signals, comparable in size and period to those observed in field experiments. Our method of calculation involves a computer code (developed by us) which propagates CW acoustic signals through a sound-speed field that depends on both depth and range. The code calculates the random part of the sound-speed field from an internal-wave spectrum, and simulates the time variation by stepping the internal wavefield in time, and propagating the acoustic signal at each time.⁷ We have used a frequency of 100 Hz.

In this paper we also demonstrate the usefulness of a vertical array of hydrophones in reducing intensity fluctuations in long-range acoustic transmission.

Other work relating acoustic fluctuations to internal waves has been in progress simultaneously with ours. DeFarrari considered only one internal wave, the internal tide, rather than a full spectrum.⁸ Porter *et al.* considered a full spectrum of internal waves, but used a thin-layer model for internal waves as they affect

acoustic signals.⁹ Their model cannot be complete as it fails for rays whose turning point occurs within the thin layer. We consider a full spectrum (excluding tides) and treat the acoustic–internal-wave interaction within the full volume of the ocean.

The remainder of the paper is organized as follows: Section I describes the sound-speed field derived from the internal-wave spectrum, and its computer realization. Section II describes the acoustic propagation method (which depends on the parabolic equation approximation) and its computer realization. Section III presents our quantitative results. Section IV is a summary and conclusion. The Appendix describes our method of vertical beamforming.

I. OCEAN SOUND-SPEED STRUCTURE

A. Deterministic profile

On the scale of the depth of the ocean (4 to 5 km) the sound speed as a function of depth z is determined by the gross behavior of the density, temperature, and salinity. We use the profile derived by Munk¹⁰ whose input is an exponentially decreasing density gradient. The resulting “canonical” profile is

$$c_{CP}(z) = c_1 \{1 + \epsilon [e^{-\eta} - (1 - \eta)]\},$$

where $\eta = 2(z - z_A)/B$. Note that $c_{CP}(z)$ has a minimum at z_A , that the width of the minimum is B , and the deviation of the sound speed from the minimum value c_1 is of the order ϵ .

Figure 1 shows $c_{CP}(z)$ for the typical (though not universal) values we have chosen for the parameters: $z_A = 1000$ m, $B = 1000$ m, $\epsilon = 0.57 \times 10^{-2}$, and $c_1 = 1500$ m/sec.

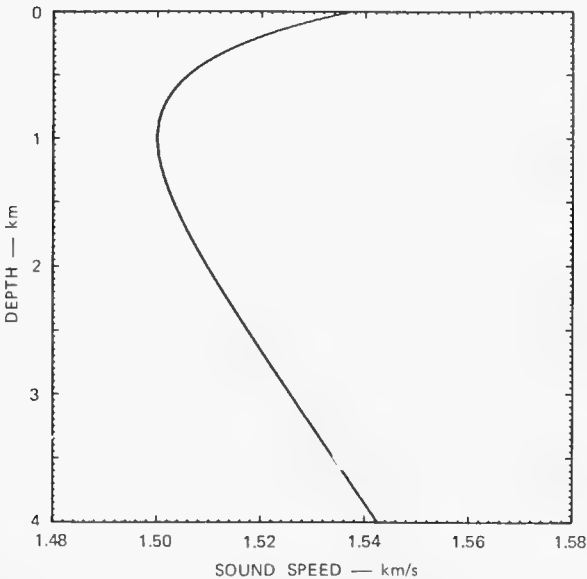


FIG. 1. Deterministic sound-speed profile as a function of ocean depth (Canonical Profile). The value of c at the minimum ($z_A = 1000$ m) is $c(z_A) = 1500$ m/sec.

One must point out that realistic ocean profiles in most cases have significantly different behavior from this general form. For example, within a few hundred meters of the surface a mixed layer usually results in a lowered sound-speed gradient. However, we ignore these details in our present treatment.

B. Internal waves

The density gradient in the ocean leads to the possibility of waves traversing the volume of the ocean just as the density discontinuity at the surface leads to the possibility of surface waves. The density gradient is usually presented in the form

$$N(z) \equiv \left(-\frac{g}{\rho_0} \frac{\partial \rho}{\partial z} \right)^{1/2},$$

where $N(z)$ is called the local stability (Brunt–Väisälä) frequency.

Following Garrett and Munk,⁵ we assume a stratified ocean with

$$N(z) = N_0 e^{-z/B},$$

where $N_0 = 3$ cycles/h.

Let $w(\vec{r}, t)$ be the vertical component of fluid velocity at position \vec{r} and time t . It can be shown¹¹ that w satisfies the equation

$$\frac{\partial^2}{\partial t^2} (\nabla^2 w) + N^2(z) \nabla_h^2 w = 0.$$

The eigenmodes of this equation can be found by taking

$$w = W(j, k, z) e^{i[k_1 x + k_2 y - \omega(j, k) t]},$$

where $k = (k_1^2 + k_2^2)^{1/2}$ is the horizontal wavenumber. Substituting and modifying our equation to account for the rotation of the earth, we find

$$\frac{\partial^2 W}{\partial z^2} + \left[\frac{N^2(z) - \omega^2}{\omega^2 - \omega_i^2} \right] k^2 W = 0,$$

where ω_i = inertial frequency = $(2 \text{ cycles/day}) \sin(\text{latitude})$. We will use $\omega_i = 1$ cycle/day. Boundary conditions are $W(z) = 0$ at surface and bottom (assumed flat).¹¹

A particular mode, characterized by mode number j and horizontal wave number k , will have a vertical velocity profile given by $W(j, k, z)$ and a definite frequency $\omega(j, k)$. Because every fluid element moves with the same frequency, the vertical displacement ξ of a fluid element from its equilibrium position for a single mode will also be proportional to $W(j, k, z)$. The sound-speed fluctuation δc is related to the displacement ξ by⁵

$$\delta c = c_1 \frac{\mu}{g} N^2(z) \xi \propto N^2(z) W(j, k, z).$$

Several examples of the sound-speed profiles due to particular modes are shown in Fig. 2.

The sound-speed fluctuations caused by a full internal wavefield may be represented as a linear superposition of eigenmodes, leading to

$$\delta c_{IW} = \text{Re} \left\{ \sum_{j, k_1, k_2} G(j, k_1, k_2) N^2(z) W(j, k, z) e^{i[k_1 x + k_2 y - \omega(j, k) t]} \right\},$$

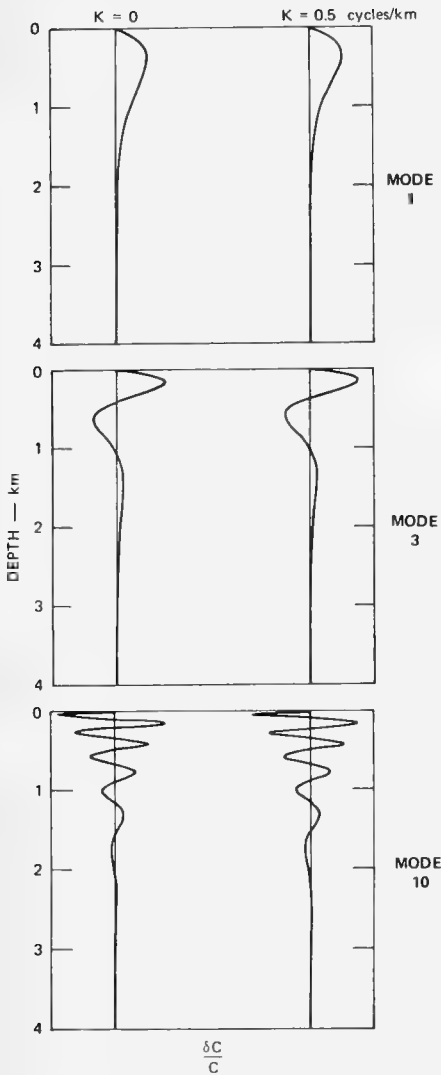


FIG. 2. Sound-speed profiles due to internal-wave modes. Realistic internal-wave spectra have significant intensities for horizontal wavenumber k less than about 0.5 cycles/km. Note that the major internal-wave contributions to sound-speed fluctuations occur at depths less than 1 km.

where the summation sign means integration over the continuous variables k_1 and k_2 . We normalize $W(j, k, z)$ so that

$$\int_0^{z_{\max}} N^4(z) W^2(j, k, z) dz = 1,$$

where z_{\max} is the depth of the ocean.

The numerical difficulty in projecting this three-dimensional field onto the two-dimensional vertical plane used in the acoustic propagation code has caused us to consider a simplified version of the internal wavefield where internal waves propagate only in (or opposite to) the direction that the sound waves propagate. In addition we combine real and imaginary parts to reduce fluctuations in the overall energy in the internal waves

as a function of time:

$$\delta c_{IW} = \frac{c_1}{\sqrt{2}} (\text{Re} \Delta + \text{Im} \Delta)$$

and

$$\Delta = \sum_{j,k} A(j, k) N^2(z) W(j, k, z) e^{i[kr - \omega(j, k)t]},$$

where r is the horizontal range.

The $A(j, k)$ are complex Gaussian random variables. From a synopsis of diverse oceanographic measurements, Garrett and Munk⁵ have proposed the following model:

$$\langle A(j, k) \rangle = 0$$

$$\langle A(j, k) A^*(j', k') \rangle = \delta_{jj'} \delta_{kk'} \times \beta^2 H(j) B(j, k),$$

where

$$H(j) = 6/(\pi j)^2,$$

$$B(j, k) = (2/\pi) k_j k^2 / (k^2 + k_j^2)^2,$$

$$k_j = (\pi/B) (\omega_i/N_0) j.$$

The spectrum is normalized so that

$$\sum_j \int_{-\infty}^{\infty} H(j) B(j, k) dk = 1 \text{ and } \int_{-\infty}^{\infty} B(j, k) dk = 1.$$

From the above equations it can be shown that

$$\int_0^{z_{\max}} \left\langle \left(\frac{\delta c_{IW}}{c_1} \right)^2 \right\rangle dz = \beta^2.$$

But Garrett and Munk⁵ have shown that

$$\left\langle \left(\frac{\delta c}{c_1} \right)^2 \right\rangle = \gamma^2 e^{-3z/B}.$$

Hence $\beta^2 = \gamma^2 B/3$ where γ is a measure of the fractional sound-speed fluctuations due to internal waves. From Ref. 4 we have $\gamma = 4.8 \times 10^{-4}$.

It is useful to point out a few properties of the dispersion relation and the spectrum. The frequency $\omega(j, k)$ varies between the inertial frequency (1 cycle/day) and N_0 (3 cycles/h). Frequency increases with increasing values of k and decreasing values of j .

For a fixed mode number j , the function $B(j, k)$ gives the relative contribution from each value of k . The peak of the k distribution is at k_j . The function $H(j)$ gives the overall contribution from each mode number j ; the gravest mode ($j=1$) has the largest contribution, with other modes decreasing as $1/j^2$. The relative intensities of the various modes are shown in Fig. 3.

Note that the magnitude of the sound speed fluctuation due to internal waves is $\delta c/c \sim 10^{-4}$, a factor of 100 below the magnitude of the deterministic structure. Also the spatial behavior of the sound-speed variations due to internal waves is of the order of a few hundred meters vertically and several kilometers horizontally. Figure 4 shows some typical sound-speed profiles due to internal waves.

C. Final expression for sound-speed structure

$$c(\vec{r}, t) = c_{CP}(z) + \delta c_{IW}$$

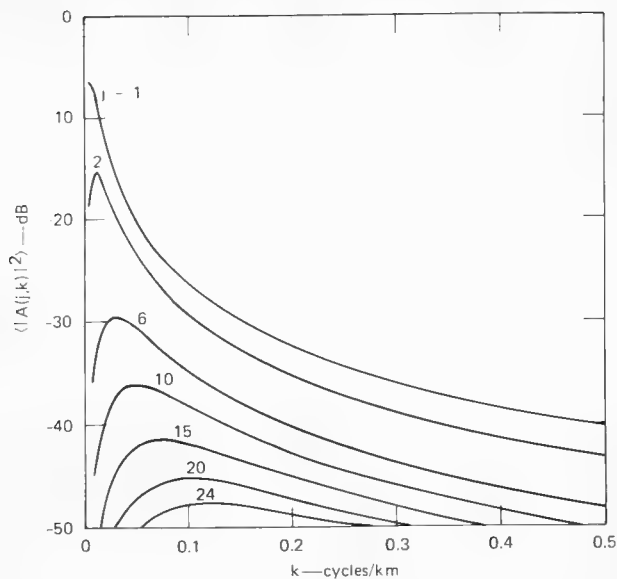


FIG. 3. Internal-wave spectrum as a function of mode number j and horizontal wavenumber k . Although large mode numbers contribute very little to the overall spectrum, they are crucial to understanding acoustic effects, since their vertical structure allows them to act as a scatterer of acoustic energy more readily than the relatively structureless low modes.

$$= c_1 \left(1 + \frac{\delta c}{c} \right),$$

where

$$\frac{\delta c}{c} \equiv \epsilon [e^{-\eta} - (1 - \eta)] + \frac{\delta c_{1W}}{c_1}.$$

D. Numerical realization of the internal-wave model

M. Milder's program (ZMODE)¹² was modified to numerically generate the eigenfunctions $W(j, k, z)$ and frequencies $\omega(j, k)$. Modes with $1 \leq j \leq 24$ were included. Values of k ranged from -0.5 to 0.5 cycle/km in 254 equal steps. The 6096 different $A(j, k)$ were generated according to a Rayleigh probability distribution in amplitude, and variance given by the spectrum described in Part B. The phase angle of each $A(j, k)$ is randomly generated in the region 0 to 2π . Using the above equations, our code can then generate the sound speed at any point in space and time.

II. PROPAGATION OF ACOUSTIC SIGNALS USING THE PARABOLIC EQUATION METHOD

A. Introduction

The parabolic equation method was originally developed by Leontovich and Fok in 1946 to study long-range propagation of radio waves in the troposphere.¹³ This method was introduced into the field of underwater acoustics by Tappert in 1972 and a computer program based on this method was developed by Tappert and Hardin to solve acoustic propagation problems of interest to the Navy.^{14, 15}

B. Approximations and ranges of validity

The wave equation for acoustic pressure $p(\vec{r}, t)$ is

$$\nabla^2 p - \frac{1}{c^2} \frac{\partial^2 p}{\partial t^2} = 0.$$

Our knowledge that c varies from a constant only by very small amounts, and that the variations are slow compared with the acoustic frequency allows us to use the following expression in cylindrical coordinates for the pressure (far from the source):

$$p(r, t) = \Psi_t(r, z, \varphi) \frac{e^{i(k_0 r - \omega t)}}{\sqrt{r}},$$

where the reduced wave function Ψ is labeled by the time t , because the $\delta c/c$ structure of the ocean is different for different times. Substituting in the full equa-

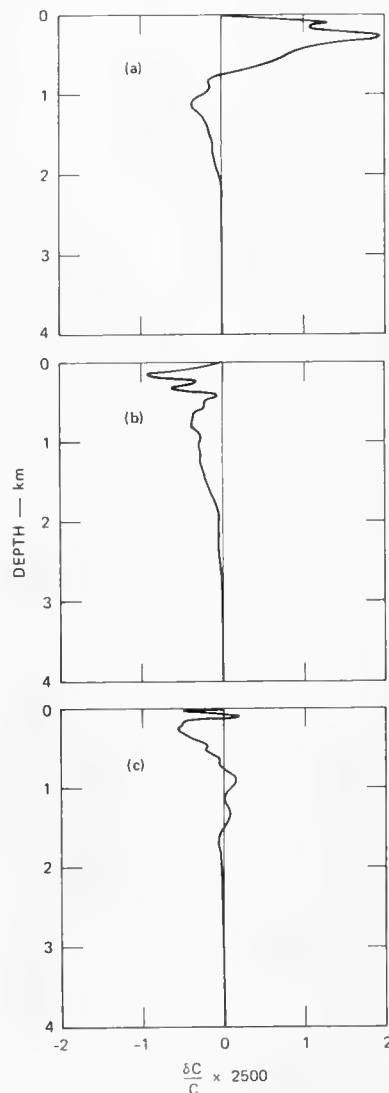


FIG. 4. Sound-speed profiles induced by a full spectrum of internal waves at a particular instant of time. Let r be the range from some arbitrary point, then (a) $r=0$, (b) $r=14$ km, and (c) $r=28$ km.

tion, neglecting time derivatives of Ψ and terms of order $1/(k_0 r)^2$, we find

$$\frac{\partial^2 \Psi}{\partial r^2} + \frac{1}{r^2} \frac{\partial^2 \Psi}{\partial \varphi^2} + \frac{\partial^2 \Psi}{\partial z^2} + 2ik_0 \frac{\partial \Psi}{\partial r} - 2k_0^2 \frac{\delta c}{c} \Psi = 0,$$

where $k_0 = \omega/c_1$, and we have assumed that $\delta c/c \ll 1$.

The key to the parabolic equation method involves the following additional physical approximations, based on the structure of $\delta c/c$:

$$\frac{\partial^2 \Psi}{\partial r^2} \ll 2ik_0 \frac{\partial \Psi}{\partial r},$$

if $k_0 L_v \gg 1$, where L_v is the vertical scale of sound-speed variations. This condition is equivalent to retaining only relatively forward scattering, which results in small changes in Ψ over an acoustic wavelength. It is valid if the objects off which the acoustic waves are scattering have sizes which are much larger than a wavelength; and

$$\frac{\partial^2 \Psi}{\partial r^2} \approx \frac{1}{r^2} \frac{\partial^2 \Psi}{\partial \varphi^2} \ll \frac{\partial^2 \Psi}{\partial z^2},$$

which is true because the canonical profile, which has 100 times the sound-speed fluctuation than the internal waves, affects the z coordinate only. More important, however, the internal-wave gradients in the vertical are an order of magnitude greater than the horizontal. The approximate wave equation is therefore

$$-\frac{1}{2k_0} \frac{\partial^2 \Psi}{\partial z^2} + k_0 \frac{\delta c}{c} \Psi = i \frac{\partial \Psi}{\partial r}. \quad (1)$$

As a result of our approximations, we have neglected all azimuthal correlations. Thus we cannot study azimuthal fluctuations. We can study fluctuations that can be observed in a single vertical plane, where azimuthal correlations have a small effect.

To summarize the approximations required for this parabolic equation to be valid we have the following quantities not yet defined: ω_{IW} = largest frequency involved in the internal wave spectrum, ≈ 3 cycles/h; L_H = minimum horizontal scale of sound-speed fluctuations, ≈ 1 km due to internal waves; L_V = minimum vertical scale of sound-speed fluctuations, ≈ 200 m due to internal waves. Validity of the parabolic equation requires: $\omega \gg \omega_{IW}$; $k_0 r \gg 1$; $L_H \gg L_V$; and $k_0 L_V \gg 1$. All conditions are well satisfied in our case, where $\omega = 100$ Hz.

C. Numerical realization

We solve Eq. 1 by the "split-step-Fourier" algorithm of Tappert and Hardin.¹⁶ Given $\Psi(r, z)$ we find the wave function at a new range from the following:

$$\Psi(r+dr, z) = \mathcal{F}^{-1} \{ e^{i\hat{A}dr} \mathcal{F} [e^{i\hat{B}dr} \Psi(r, z)] \},$$

where $B = -k_0 \delta c/c$ and $A = (1/2k_0) \partial^2 / \partial z^2$. Thus A and B are operators in z space (A being the Fourier transform of A) and \mathcal{F} is a fast Fourier transform operation.¹⁷ This algorithm is fast and very stable since the total acoustic energy $\int |\Psi|^2 dz$ is exactly conserved as a function of range when absorption is absent.

The FFT was used with 512 elements over a 4-km-

deep ocean, and the range step has been chosen as 0.5 km.

D. Acoustic source and boundary conditions

The acoustic field may be started with any function of depth $\Psi(0, z)$. A point source at $z = 1000$ m (the depth of the sound channel) with unit strength at one yard has been modeled by an asymptotic matching technique which prescribes the appropriate initial value.¹⁵

The ocean surface has been treated as a perfect pressure-release boundary so that $\Psi(r, 0) = 0$. This is accomplished through the use of a fast sine transform¹⁸ for the operation \mathcal{F} .

In order to model a completely absorbing ocean bottom, a gradual loss of amplitude is imposed on $\Psi(z)$ as z nears the ocean bottom. The functional form of the imposed loss at each step is the factor

$$L(z) = \exp \left[-\alpha dr \exp - \left(\frac{z - z_{\max}}{\beta} \right)^2 \right],$$

with $\alpha = 0.05/\text{m}$ and $\beta = 0.04 z_{\max}$.

This form effectively stops any acoustic energy from penetrating below about 500 m above the bottom. Even this attempt at acoustic impedance matching does cause some reflection off the bottom at an extremely low intensity level.

III. RESULTS

When an explosion is detonated deep in the ocean, a series of sharp reports are heard at ranges up to several thousand kilometers. The fact that each separate sound arrives without being dispersed in time implies that a geometrical-optics view of sound transmission in the ocean must have a great deal of merit. Ray tracing is a well-established technique for determining the character of oceanic sound transmission.

Figure 5 shows the ray paths where the sound speed

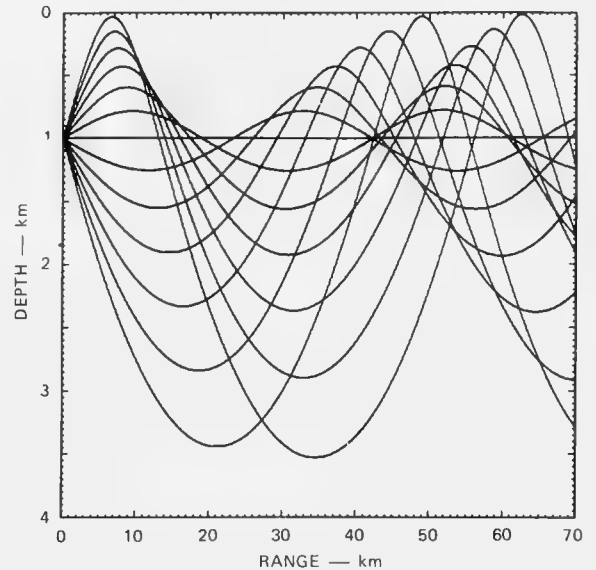


FIG. 5. Ray paths for the canonical sound-speed profile given in Fig. 1, with a source on the sound-channel axis.

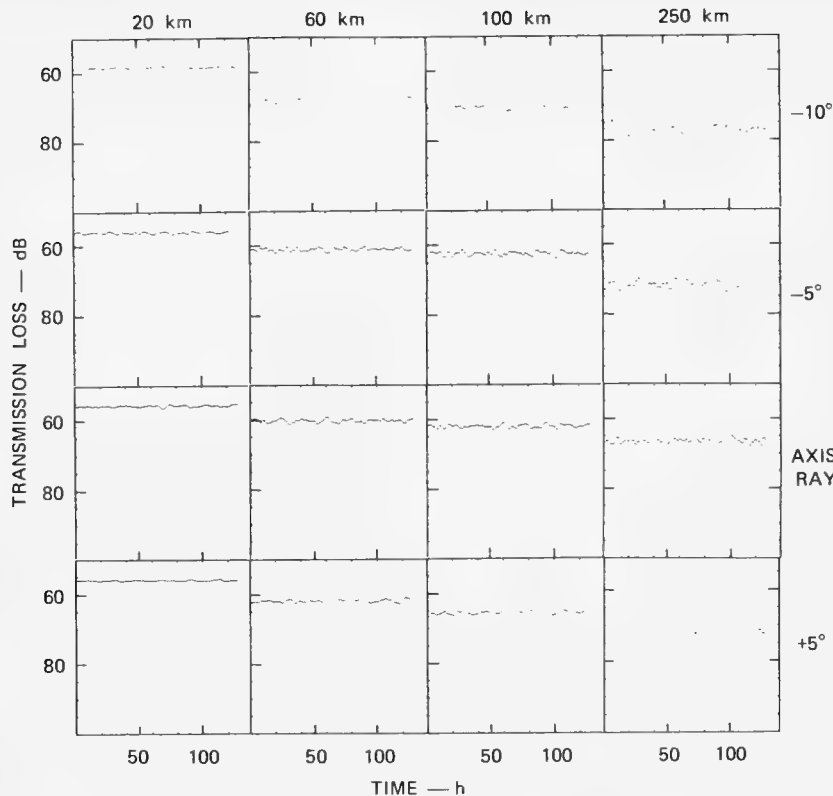


FIG. 6. Transmission-loss time series at several ranges and depths. Each section shows the intensity that would have been observed by a single hydrophone taking data once an hour for 128 h. Each column represents a particular range from the CW source. Each row represents a particular ray followed from the source. (Positive angles correspond to downward rays from the source.) That is, at each range, the depth is chosen as the depth that particular ray passes through at that range.

is given by the canonical profile¹⁰ and the source is on the sound axis ($z_A = 1000$ m). It is apparent that after a few tens of kilometers the sound arriving at various points has a complicated directional character due to multiple paths. For example, at 60 km on the axis sound should arrive from three well-separated directions. Note also that our absorbing bottom at 3.5-km depth prevents any surface or bottom reflected energy from propagating beyond about 20 km.

It is possible that some of our results for acoustic signals traveling through internal waves may be understood in terms of internal-wave effects on individual rays. It will be well to remember, however, that beyond the 20-km range a single hydrophone will in most cases receive more than one ray from the source. This multipath effect is crucial to understanding long-range fluctuations.

Figure 6 shows the computed transmission loss as a function of time at several ranges for 100-Hz acoustic signals traveling through the internal wavefield. The point source is at a depth of 1000 m. Each row shows results for a particular ray which has been followed from the source by integrating Snell's law (e.g., the hydrophone at 100-km range for the 6° ray is at the depth corresponding to the 6° ray at that range). The 1-h time steps clearly undersample the fluctuations, but the general character of the series is clear. We see that internal wave sound-speed fluctuations cause 5–30-dB fluctuations in received intensity, comparable in size to those observed in field experiments.³

We have used a vertical beamformer (see Appendix) to separate the different ray arrivals at various ranges and depths. Figure 7 shows a time history of one beamformer output. A single hydrophone would coherently add the many rays, each of which are seen in Fig. 7 to vary in direction and intensity. If the peak of the ray of interest is chosen at each time, then a time series for the intensity of that ray can be plotted. Figure 8 shows time series for the particular rays corresponding to the single hydrophone results in Fig. 6. It is evident that the fluctuations of a single ray are considerably muted compared with those of a single hydrophone which is subjected to a coherent addition of all rays.

Figure 9 shows the rms intensity variation as a function of range for four rays. $\{[(10 \log I)^2] - \langle 10 \log I \rangle^2\}^{1/2}$ is plotted. Both single hydrophone and ray-peak results are plotted. The reduction in fluctuation that results from selecting a ray peak is clear. In addition, the smoothness of the rms value as a function of range for the ray peak gives grounds for hope that a simple single-ray theory might be used to predict the range dependence of the fluctuations.

IV. SUMMARY AND CONCLUSIONS

We have developed a parabolic-equation acoustic propagation code which sends CW sound signals through a time-dependent random internal wavefield superimposed on a deterministic sound channel.⁷ The output is the complex pressure field as a function of

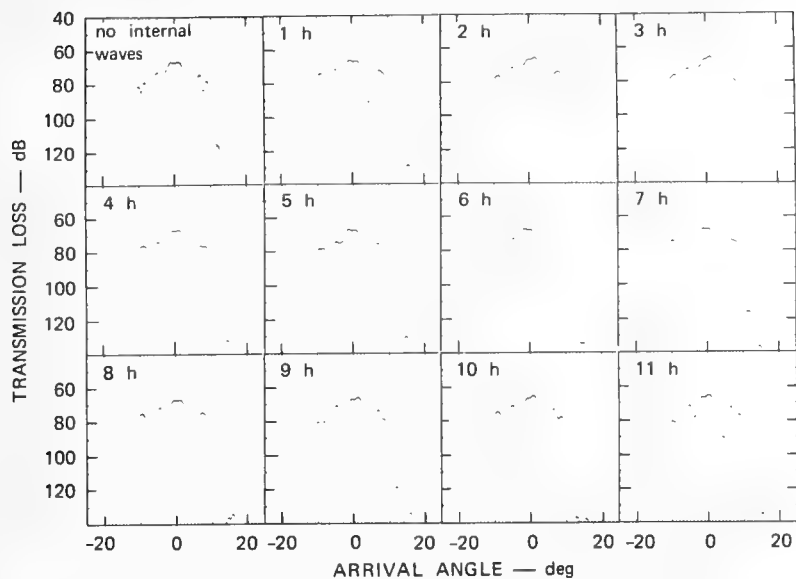


FIG. 7. Intensity as a function of vertical arrival angle determined by a 700-m vertical array of hydrophones (Gaussian $\sigma = 180$ m) centered on the sound-channel axis (depth 1 km) at a range of 250 km from the CW source.

range, depth, and time. Results at 100 Hz show that intensity fluctuations due to internal waves are significant and comparable in size (5–30 dB) to those observed in field experiments. Use of vertical beamformers as detectors has given insight into internal-wave effects on the sound energy, and will probably lead to a sensitive probe of the internal-wave spectrum. In addition, selection of vertical arrival angle by use

of a beamformer significantly reduces fluctuations over the single-hydrophone result.

We have presented only a small amount of data available from our computer simulation. In the future we expect to present results on phase fluctuations, frequency spectra of fluctuations, sensitivity to internal-wave parameters, and comparison with simpler calcu-

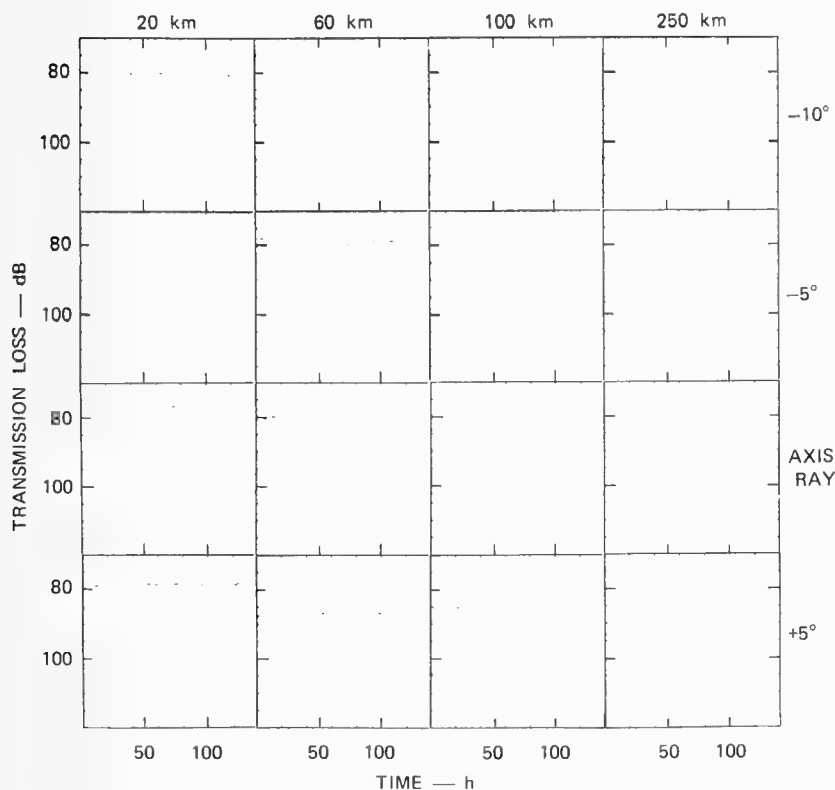


FIG. 8. Ray-peak transmission-loss time series at several ranges and depths. Each section shows the intensity that would have been observed by a 700-m vertical array (Gaussian $\sigma = 180$ m) looking at the ray peak. The sections correspond exactly to those shown in Fig. 6. The higher intensities in Fig. 8 are due to the summation over many hydrophones in the vertical array. Note the lower fluctuations in the single ray observations here compared to the single hydrophone (multiple ray) observations shown in Fig. 6.

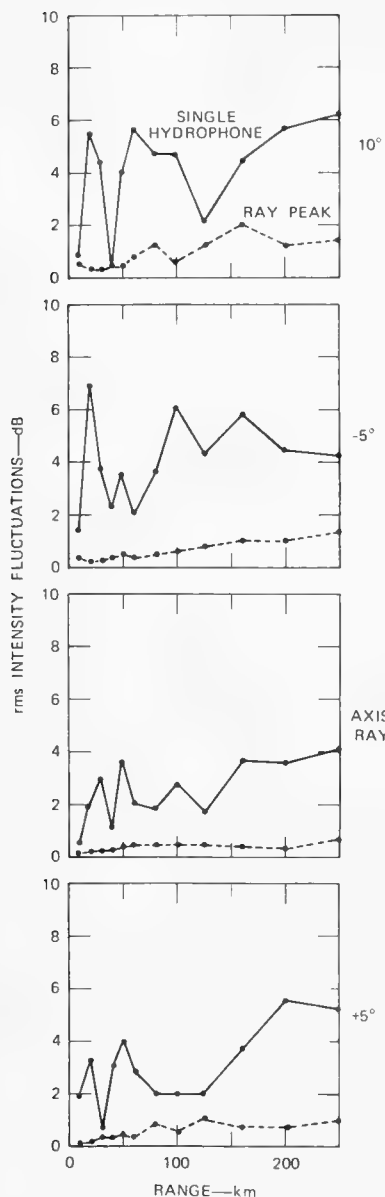


FIG. 9. Intensity fluctuations as a function of range for several rays. The solid line indicates the fluctuations from a single hydrophone placed at various ranges along the way. The rapid oscillations in the solid line are due to the rapidly changing multipath environment. It is interesting to note that the rms fluctuation from a large number of paths with random phases is expected to be 5.6 dB.¹⁹ The dashed line indicates the fluctuations observed in the ray peak determined from a 700-m vertical array (Gaussian $\sigma=180$ m). The result of selecting a single path is seen to be a reduction in fluctuations and a smoother dependence of these fluctuations on range.

lations of internal-wave effects on acoustic transmission.⁶

ACKNOWLEDGMENTS

This work is part of a larger study of the sources of acoustic fluctuations in the ocean begun by Walter Munk,

whose seminal influence and continual encouragement we gratefully acknowledge. Important conversations were had with Roger Dashen, Kenneth Watson, and Fredrik Zachariasen.

Our work was largely completed during the 1974 JASON Summer Study under the auspices of Stanford Research Institute. The support for our work has come from the Advanced Research Projects Agency, and part from the Office of Naval Research.

APPENDIX A: VERTICAL BEAMFORMING

The code we are using propagates sound waves from a point source along a vertical plane in an ocean with internal waves. In order to determine the directional character of the arriving signal at some position down-range from the source, we have formed a vertical array of receivers and combined the signals with phase delays to amplify the waves coming from particular directions.

Suppose $\Psi(z_i)$ are the wave amplitudes at a set of N points at a particular range spaced equally in depth z . The N points span the ocean depth z_{\max} , so that $z_{\max} = Nd$ where d is the spacing of the grid of receivers (d is 15.6 m in our case).

We define the amplitude arriving from a particular direction θ at a depth z as

$$\varphi(\theta) = \sum \Psi(z_i) \exp - \frac{1}{2} \left(\frac{z_i - z}{\sigma} \right)^2 \exp[-ik_0(z_i - z) \sin \theta],$$

where σ is a measure of the vertical aperture of the Gaussian array and k_0 is the acoustic wavenumber.

We have chosen $\sigma = 180$ m so that the angular resolution of the array is 0.5° at 100 Hz and the expected increase in intensity for a plane wave arrival, due to the large number of hydrophones being summed, is 14.6 dB. Also note that sidelobes of the receiving array are eliminated by the use of Gaussian shading—a practice that is easy to implement in our numerical experiments but inefficient in a field experiment.

¹M. Ewing and J. L. Worzel, "Long-range Sound Transmission," Geol. Soc. Am. Mem. 27, Part III (1948).

²See, e.g., P. R. Tatro and C. W. Spofford, "Engineering in the Ocean Environment," 1973 IEEE Int. Conf., 206-216; J. Northrop and J. G. Colborn, J. Geophys. Res. 79, 5633-5641 (1974).

³See, e.g., R. H. Nichols and H. J. Young, J. Acoust. Soc. Am. 43, 716 (1968); B. E. Parkins and G. R. Fox, IEEE Trans. AU-19, 158 (1971); J. G. Clark and M. Kronengold, J. Acoust. Soc. Am. 56, 1071-1083 (1974); G. E. Stanford, J. Acoust. Soc. Am. 55, 968-977 (1974).

⁴O. S. Lee, J. Acoust. Soc. Am. 33, 677 (1961); J. C. Beckerle, J. L. Wagar, and R. D. Worley, J. Acoust. Soc. Am. 44, 295 (1968); J. C. Beckerle, J. Acoust. Soc. Am. 45, 1050 (1969); E. J. Katz, J. Acoust. Soc. Am. 42, 83 (1967); V. A. Polyanskaya, Akus. Zh. 20, 95 (1974).

⁵C. Garrett and W. H. Munk, Geophys. Fluid Dyn. 2, 225-264 (1972); C. Garrett and W. H. Munk, J. Geophys. Res. 80, 291 (1974); W. H. Munk, private communication (1974).

⁶F. Zachariasen and W. H. Munk, unpublished.

⁷S. M. Flatté and F. D. Tappert, "A Computer Code to Calculate the Effect of Internal Waves on Acoustic Propagation in the Ocean," SRI publ. (in press). (Note that the internal-

- wave spectrum described in this article is an updated, different spectrum from the one in the SRI publication.)
- ⁸H. A. DeFarrari, J. Acoust. Soc. Am. **56**, 40-46 (1974).
 - ⁹R. P. Porter, R. C. Spindel, and R. J. Jaffee, J. Acoust. Soc. Am. **56**, 1426-1436 (1974).
 - ¹⁰W. H. Munk, J. Acoust. Soc. Am. **55**, 220-226 (1974).
 - ¹¹O. M. Phillips, *Dynamics of the Upper Ocean* (Cambridge U. P., Cambridge, England, 1966).
 - ¹²M. Milder, "Users Manual for the Computer Program ZMODE," RDA-TR-2701-001, R&D Associates, Santa Monica, CA (July 1973).
 - ¹³M. Leontovich and V. Fok, "Solution of the problem of propagation of electromagnetic waves along the earth's surface by the parabolic equation method," Zh. Eksp. Teor. Fiz. **16**, 557 (1946).
 - ¹⁴F. D. Tappert and R. H. Hardin, in "A Synopsis of the AESD Workshop on Acoustic Modeling by Non Ray Techniques, 22-25 May 1973, Washington, D. C.," AESD TN-73-05, ONR, Arlington, VA (Nov. 1973).
 - ¹⁵F. D. Tappert, "Parabolic equation method in underwater acoustics," J. Acoust. Soc. Am. **55**, S34 (A) (1974).
 - ¹⁶R. H. Hardin and F. D. Tappert, SIAM Rev. (Chronicles) **15**, 423 (1973); F. D. Tappert and R. H. Hardin, *Proceedings of the Eighth International Congress on Acoustics* (Goldcrest, London, 1974), Vol. II, p. 452.
 - ¹⁷We have ignored the fact that the internal waves are moving slightly while the acoustic signal is propagating (due to the finite speed of sound). This approximation is justified since the sound travels much more than a horizontal correlation distance during a time short compared to the internal-wave correlation time (Kenneth M. Watson, private communication, 1975).
 - ¹⁸We are indebted to H. Brock and C. W. Spofford of the Acoustic Environmental Support Detachment, ONR, for providing this subroutine.
 - ¹⁹I. Dyer, J. Acoust. Soc. Am. **48**, 337 (1970).

SOUND PROPAGATION THROUGH A FLUCTUATING
STRATIFIED OCEAN: THEORY AND OBSERVATION

W. H. Munk

F. Zachariasen

Reprinted from the Journal of the Acoustical Society of America
Vol. 59, No. 4, 818-838, April 1976

Sound propagation through a fluctuating stratified ocean: Theory and observation*

W. H. Munk

Institute of Geophysics and Planetary Physics, Scripps Institution of Oceanography, La Jolla, California 92037

F. Zachariasen

California Institute of Technology, Pasadena, California 91109

(Received 18 November 1975)

We have derived expressions for the mean-square phase and intensity fluctuations and their spectra for cw sound propagating through a channeled fluctuating ocean. The "supereikonal" approximation reduces to the geometric optics (eikonal) limit for short acoustic wavelengths: $\lambda \ll 2\pi L_H^2/R$ and $\lambda \ll L_V^2/(R \tan^2 \theta)$, where L_H and L_V are horizontal and vertical correlation lengths of the fluctuations, R is range, and $\tan \theta$ is the ray slope, replacing the traditional (and much more severe) Fresnel condition $\lambda \ll 2\pi L^2/R$ for a homogeneous isotropic ocean. The results can be expressed in closed form for an exponentially stratified ocean model and associated "canonical sound channel," with superimposed fluctuations from an internal wave model spectrum based on oceanographic observations. The parameters are the stratification scale B , the inertial and buoyancy frequencies ω_{in} and $n(z)$, the scale j_* of internal wave mode numbers, and the internal wave energy per unit area. The results are in reasonable agreement with numerical experiments based on the parabolic wave equation. For the "singlepath" 4-kHz transmission over Cobb Seamount the observed and computed rms fluctuations in phase are 1.6 and 2.5 cycles, respectively; in intensity these are 5.5 and 2.2 dB, respectively, with anomalous intensities measured at high frequencies ("sporadic" multipathing?). For the multipath 406-Hz MIMI transmission, we obtain 4×10^{-3} and $5 \times 10^{-3} \text{ sec}^{-1}$, respectively, for the experimentally determined and the computed rms phase rates.

Subject Classification: [43] 30.20, [43] 30.40; [43] 20.15.

LIST OF SYMBOLS

$C(\vec{x}), \delta C(\vec{x})$	sound velocity and fluctuations
$C(z); C_0, \bar{C}, \hat{C}$	mean velocity profile (z upwards); C at surface $z=0$ (ignoring mixed layer), at channel axis $\bar{z}=-\bar{h}$, at ray apex \hat{z}
$\text{rms } (\delta C/C)_0 = 4.9 \times 10^{-4}$	fractional surface fluctuation
$n(z); n_0, \bar{n}, \hat{n}$	buoyancy (Brunt-Väisälä) frequency
$\rho(\vec{x}, \vec{y}) = \left\langle \frac{\delta C(\vec{x})}{C} \frac{\delta C(\vec{y})}{C} \right\rangle$	covariance of fractional fluctuations
$V = 2q^2 \delta C/C$	perturbation "potential"
$\sigma, \vec{q}; \lambda = 2\pi/q$	frequency and wave number of sound signal; wavelength
$\omega, \vec{k}; k_H^2 = k_x^2 + k_y^2, k_v = k_z$	frequency and wave number of internal waves (H horizontal, V vertical)
$p(\vec{x}, t) \exp[i(qx - \sigma t)]$	sound pressure
X, ϵ, ϕ	log pressure, intensity, and phase
$G(\vec{x}), G(\vec{k})$	Green's function and Fourier transform
\perp, \parallel	perpendicular and parallel to ray path
$r(r_H, r_V)$	dimensions of ray tubes
$L(L_H, L_V)$	correlation lengths
$\eta = (z - \bar{z})/\frac{1}{2}B$	dimensionless distance above ray axis $\bar{z}(-1 \text{ km})$; $B(=1 \text{ km})$ is stratification scale
$\epsilon = 5.7 \times 10^{-3}$	perturbation coefficient [Eq. (84)]
$R^+, R^-, R^{+-} = R^+ + R^-; \bar{R}$	ranges of upper, lower and combined ray loops; axial ray loop
$S^+, S^-, S^{+-} = S^+ + S^-$	arc distances of upper, lower, and combined ray loops
$\delta = R^{+-} d^2 S^{+-} / d(R^{+-})^2$	ray parameter [Eq. (86)]
$\theta, \bar{\theta}$	ray inclination, axial ray inclination
\mathcal{R}	radius of curvature of ray

\sum_i, \sum_j, \sum_k
 j_*
 $\langle j^{-1} \rangle = 0.435$
 $F(\omega, j; z), G(\omega), H(j)$
 $E_o(\omega), E_i(\omega)$
 $\omega_{1n} = 7.3 \times 10^{-5} \text{ sec}^{-1}$
 $\omega_L^2 = \omega_{1n}^2 + n^2 \tan^2 \theta$
 $\bar{\omega} = \omega/2\pi, \bar{n} = n/2\pi, \text{ etc.}$
 $\bar{\omega}_{1n} = \frac{1}{24} \text{ cph}, \bar{n}_0 = 3 \text{ cph}, \bar{n} = 1.10 \text{ cph}$
 $\Delta = n \tan \theta / \omega_{1n}$
 $\alpha, \gamma, \beta = \alpha\gamma$
 $g(\beta, j_*)$
 $F_1, F_2; f_1, f_2$

summation over ray path i , internal wave mode j , ray loop k

Eq. (90), usually $j_* = 3$

Eq. (95) for $j_* = 3$

internal wave spectra

acoustic phase and intensity spectra

inertial frequency at 30° latitude

frequency limit

cyclical frequencies (usually in cycles per hour, cph)

Eq. (99)

Eq. (107)

Eq. (109)

Eqs. (96), (98), (102), (104)

INTRODUCTION

Sound scintillations in the sea may be regarded as the result of weak scattering. The fluctuations in sound velocity are small, typically $\delta C/C = 5 \times 10^{-4}$ in the upper layers, 3×10^{-6} at abyssal depths. But the range of propagation can be very long, and the cumulative effect pronounced. The fluctuations impose the ultimate limit to the acoustic resolution of objects, similar to the resolution limit of ground-based telescopes due to "atmospheric seeing."

Our purpose is to contribute toward a quantitative connection between two observational programs that have paid scant and reluctant attention to one another. Measurements and analysis of the fluctuating sound transmission have viewed the ocean as a transmission channel and described its properties by certain correlation functions that are not readily identified with known physical processes. Oceanographers have studied ocean variability with emphasis on the associated fluxes of momentum, energy, salt, etc. Starting from an idealized (but not absurd) model of ocean variability, our goal is to compute certain quantities of experimental interest, such as the mean square phase and intensity fluctuations of received sound pressure, and to compare these with measured values.

The procedure is to derive a formalism for which the geometric optics limit valid for short ranges is transparent, and the transition to larger ranges is easily visualized. Section I gives the solution for a homogeneous ocean, with the geometric optics limit subject to a Fresnel condition [Eqs. (35) and (39)]. But the real ocean is not homogeneous, nor is it isotropic. In Secs. II and III the solutions are generalized to apply to an inhomogeneous ocean [Eqs. (57) and (62)] and to the special case of a vertically channeled ocean [Eqs. (66) and (76)], respectively. The range of validity of geometric optics is now actually extended, and in addition we are able to obtain rather simple analytic expressions for quantities of experimental interest both within

and beyond the geometric optics regime.

We next introduce a specific gross sound velocity profile $C(z)$ with perturbation δC due to vertical straining of the gross structure from internal wave activity:

$$C(x, y, z, t) = C(z) + \delta C(x, y, z, t) + \dots$$

The effect of horizontal flow associated with internal waves is smaller than that of vertical straining. We also ignore intrusive and other forms of fine structure which, apart from their intrinsic temporal evolution, are carried around by currents and internal wave motion.

There are two immediate questions: are internal waves and internal tides (in contrast to turbulence, planetary waves, . . .) the principal source of fluctuations? Do we have an adequate statistical model of internal wave activity?

To the first question the answer is *yes* within a frequency interval between cycles per day and cycles per hour. Vertical displacements by internal waves are typically tens of meters and swamp other sources of fluctuations. The oceanographically more important planetary waves (related to the variability in ocean currents) are associated predominantly with horizontal displacements and are therefore of less consequence to the sound field; their frequency range is typically cycles per month to cycles per week. But in special frontal zones (e.g., near the Gulf Stream) the long-period changes in sound transmission are probably planetary wave related. Small-scale turbulence takes over below the Richardson length¹ $(\epsilon/n^3)^{1/2} = \text{order } (1 \text{ m})$. But for intermediary scales the buoyancy effects are predominant and the fluctuations are internal wave related. Reliance on laboratory concepts of homogeneous isotropic turbulence, though fashionable, seem to us to be entirely misplaced.

The answer to the second question is *no*. We shall apply the internal wave models by Garrett and Munk

(henceforth GM72 and GM75) with subsequent modifications.² The model is contrived, and not the result of the kind of the three-dimensional array measurements that are really needed. Information with respect to the high wave-number cutoff is particularly lacking. Still, there is sufficient evidence now to make the present exercise rewarding. And where evidence is lacking it points toward the inverse method of using acoustic observations to improve the description of internal waves.

We shall take an exponential stratification scale of 1 km. This same ocean model underlies both the inhomogeneity of the sound field [e.g., the "canonical sound channel $C(z)$ "] and the anisotropy of the δC fluctuations (the ratio of vertical to horizontal scale is typically 1:10). The solutions are now in simple form and require at most a single numerical integration; even this can be avoided in most applications by evaluating the integral near the ray apex.

Objections will be raised to the application of a model ocean. There are, of course, large geographic variations of the water column (acoustic experiments invariably fall into "anomalous" regions). Our position is that the geographic factor in sound transmission needs to be (and is in fact) taken seriously; but what is even more needed are explicit solutions that permit comparison with experiment and provide an insight into the role played by various ocean parameters, provided the underlying model, though idealized, has the fundamental properties of the world oceans.

I. HOMOGENEOUS OCEAN

The problem is to evaluate the pressure

$$\text{Re}[p(\vec{x}) \exp(-i\sigma t)] \quad (1)$$

at a point \vec{x} produced by a point source at the origin of frequency σ and wave number q (for convenience we take the source to have unit strength). We then write

$$p = \exp(iqx) (p_1 + ip_2) = |p| \exp(i\phi) = p_0 e^X, \quad (2)$$

$$X = X_1 + iX_2,$$

where $p_0(\vec{x}) = \exp(iq|\vec{x}|)/4\pi|\vec{x}| \equiv \exp(iqx)/4\pi x$ is the recorded pressure amplitude in the absence of any fluctuations, but allowing for geometric spreading. Hence $\phi = X_2$ is phase, and

$$I \equiv \log_e |p|^2 = \langle I \rangle + 2X_1, \quad \langle I \rangle = \log_e |p_0|^2 \quad (3)$$

is intensity (multiply by $10/\log_e 10$ to obtain dB; from now on we write \log for \log_e).

We assume the δC fluctuations, and hence within the approximation we shall use, the X fluctuations, to be Gaussian, so that $\langle X \rangle = 0$, $\langle e^X \rangle = \exp(\frac{1}{2}\langle X^2 \rangle)$. Some of the interesting observables are given by

$$\langle I^2 \rangle \equiv \langle (\log |p|^2)^2 \rangle = \langle I \rangle^2 + 4\langle X_1^2 \rangle, \quad (4)$$

$$\bar{I} \equiv \log \langle |p|^2 \rangle = \langle I \rangle + 2\langle X_1^2 \rangle, \quad (5)$$

$$\log \langle |p|^2 \rangle^2 = \langle I \rangle + \langle X_1^2 \rangle - \langle X_2^2 \rangle, \quad (6)$$

$$\langle \phi^2 \rangle = \langle X_2^2 \rangle, \quad \langle \phi I \rangle = 2\langle X_1 X_2 \rangle, \quad (7)$$

$$\left\langle \frac{p_1^2}{2} \right\rangle = \frac{1}{4} |p_0|^2 [\exp(2\langle X^2 \rangle) + \exp(2\langle X^{*2} \rangle)]$$

$$\pm 2 \exp(2\langle X_1^2 \rangle)], \quad (8)$$

where

$$\left\langle \frac{X^2}{2} \right\rangle = \frac{1}{2} \langle |X|^2 \rangle \pm \text{Re} \langle X^2 \rangle, \quad \langle X_1 X_2 \rangle = \frac{1}{2} \text{Im} \langle X^2 \rangle. \quad (9)$$

Let us begin our discussion by neglecting the effects of the sound channel. The problem of sound propagation in the presence of fluctuations superimposed on a homogeneous isotropic background is easier to set up and to visualize than the problem involving an inhomogeneous background, so it is conceptually advantageous to work out this case first. Later, when the inhomogeneous background representing the sound channel is introduced, the analysis can be carried out very much as in the homogeneous case, and the resulting formulae, while geometrically more complex, are entirely analogous to those obtained in the simpler example.

Our analysis will be based on the supereikonal approximation, and it will be convenient at this point to give a brief review of an earlier report of this method.³ The sound propagation from the source to the point \vec{x} is through an isotropic homogeneous ocean, in which the sound speed is C , on which is superimposed a fluctuation in sound speed $\delta C(\vec{x})$ which is, of course, very small compared to C . Mathematically, then, the pressure satisfies the wave equation

$$(\nabla^2 + q^2)p(\vec{x}) = V(\vec{x})p(\vec{x}), \quad (10)$$

where $q = \sigma/C$ for a source emitting sound of frequency σ , and where

$$V(\vec{x}) = 2q^2 \delta C(\vec{x})/C. \quad (11)$$

[For the inhomogeneous case we shall simply replace C by $C(\vec{x})$, and, accordingly, q by $\sigma/C(\vec{x})$.] The boundary condition associated with Eq. (10) is that as $\vec{x} \rightarrow 0$,

$$p(\vec{x}) \rightarrow 1/4\pi x. \quad (12)$$

Equation (10) may be cast into integral form through the use of the outgoing wave Green's function

$$(\nabla^2 + q^2)G(\vec{x} - \vec{y}) = \delta^3(\vec{x} - \vec{y}); \quad (13)$$

explicitly, we have

$$G(\vec{x}) = \exp(iqx)/4\pi x. \quad (14)$$

Then we may write, in place of Eq. (10),

$$p(\vec{x}) = G(\vec{x}) + \int d^3\vec{y} G(\vec{x} - \vec{y}) V(\vec{y}) p(\vec{y}). \quad (15)$$

Iteration of this integral equation generates the perturbation series for $p(\vec{x})$, which is more conveniently written in Fourier-transformed form as follows:

$$p(\vec{k}) = G(\vec{k}) + G(\vec{k}) \int \frac{d^3\vec{k}_1}{(2\pi)^3} V(\vec{k}_1) G(\vec{k} - \vec{k}_1) \\ + G(\vec{k}) \int \frac{d^3\vec{k}_1}{(2\pi)^3} \int \frac{d^3\vec{k}_2}{(2\pi)^3} V(\vec{k}_1) G(\vec{k} - \vec{k}_1) \\ \times V(\vec{k}_2) G(\vec{k} - \vec{k}_1 - \vec{k}_2) + \dots, \quad (16)$$

where

$$G(\vec{k}) = (k^2 - q^2 + i\epsilon)^{-1}, \quad (17)$$

and, of course, where

$$p(\vec{k}) = \int d^3\vec{x} \exp(-i\vec{k} \cdot \vec{x}) p(\vec{x}) . \quad (18)$$

The supereikonal approximation now consists of neglecting all momentum transfer correlations in the perturbation series. That is, we approximate $(k - k_1 - k_2 - \dots - k_n)^2 - q^2 + i\epsilon$ by $k^2 - 2k \cdot (k_1 + k_2 + \dots + k_n) + k_1^2 + k_2^2 + \dots + k_n^2 - q^2 + i\epsilon$, and neglect all terms of the form $\vec{k}_i \cdot \vec{k}_j$, when $i \neq j$. Note that the first approximation occurs in the second-order term in V . Once this simplification is made, the perturbation series can be summed exactly, and one obtains the result

$$p(\vec{x}) = \frac{(-i\pi)^{1/2}}{8\pi^2} \int_0^\infty \frac{d\beta}{\beta^{3/2}} \exp \left[i \left(\beta q^2 + \frac{x^2}{4\beta} + \beta I(\beta, \vec{x}) + i\epsilon \right) \right] , \quad (19)$$

where

$$I(\beta, \vec{x}) = \int \frac{d^3\vec{k}}{(2\pi)^3} V(\vec{k}) \int_0^1 ds \exp [i(s\vec{k} \cdot \vec{x} + \beta s(1-s)k^2)] . \quad (20)$$

This expression constitutes the supereikonal approximation to the pressure. The conditions under which it is valid are

$$q\lambda \gg 1, \quad qL \gg 1 ,$$

and

$$x \ll (1/q^2 L) (C/\delta C)^2 \quad (21)$$

(the last condition may in fact be too stringent). Here L is the correlation length of the sound speed fluctuations—i. e., the correlation function $\rho(\vec{x} - \vec{y}) \equiv \langle V(\vec{x})V(\vec{y}) \rangle / 4q^4$ vanishes when $|\vec{x} - \vec{y}| \gtrsim L$.

It is worth noting that if in Eq. (20) the $\beta s(1-s)k^2$ term is omitted from the exponent, we obtain

$$p(\vec{x}) = \frac{1}{4\pi x} \exp \left[ix \left(q^2 + \int_0^1 V(s\vec{x}) ds \right)^{1/2} \right] , \quad (22)$$

which is the conventional WKB, or eikonal, or geometrical optics, approximation to the pressure. The primary virtue of the supereikonal form, therefore, is that it contains as limiting cases *both* the conventional eikonal *and* the complete first-order perturbation-theory approximations.

While Eqs. (14) and (20) do constitute a closed-form solution for the pressure, the expressions are still a bit unwieldy, and further simplification is useful. To this end, let us evaluate the integral in Eq. (19) by stationary phase, keeping in mind that x and q are both large. The stationary phase point is β_0 , where

$$q^2 - \frac{x^2}{4\beta_0^2} + i(\beta_0 \vec{x}) + \beta_0 \frac{\partial}{\partial \beta} I(\beta, \vec{x}) \Big|_{\beta=\beta_0} - \frac{3}{2\beta_0} = 0 .$$

From Eq. (20), we may estimate that

$$\beta_0 \frac{\partial}{\partial \beta} I(\beta, \vec{x}) \Big|_{\beta=\beta_0} \sim \frac{q^2}{L^2} \cdot \frac{\delta C}{C} \cdot \beta_0 .$$

Hence, if

$$x < qL^2 C / \delta C , \quad (23)$$

the stationary phase point is accurately given by the solution of the simpler equation

$$q^2 - x^2 / 4\beta_0^2 = 0$$

and is located at $\beta_0 = x/2q$. Thus we find

$$p(\vec{x}) = \frac{\exp(iqx)}{4\pi x} \exp[(ix/2q) I(x/2q, \vec{x})] . \quad (24)$$

To approximately evaluate the integral I in this expression, we return to Eq. (19) and now expand in powers of the potential V in order to obtain the first-order contribution to the pressure:

$$p_1(\vec{x}) = \frac{(-i\pi)^{1/2}}{8\pi^2} \int_0^\infty \frac{d\beta}{\beta^{3/2}} \exp \left[i \left(\beta q^2 + \frac{x^2}{4\beta} + i\epsilon \right) \right] \times [i\beta \log I(\beta, \vec{x})] .$$

We may evaluate this integral by stationary phase as well; under the condition (23) the stationary phase point is again at $\beta_0 = x/2q$, and we obtain, in analogy to (24), the expression

$$p_1(\vec{x}) = \frac{\exp(iqx)}{4\pi x} \left[i \frac{x}{2q} \log I \left(\frac{x}{2q}, \vec{x} \right) \right] .$$

But we also know that

$$p_1(\vec{x}) = \int d^3\vec{x}' G(\vec{x} - \vec{x}') V(\vec{x}') G(\vec{x}') .$$

Thus we may eliminate $I(x/2q, \vec{x})$ from (24) to obtain

$$p(\vec{x}) = G(\vec{x}) \exp[X(\vec{x})] , \quad (25)$$

where

$$X(\vec{x}) = \frac{1}{G(\vec{x})} \int d^3\vec{x}' G(\vec{x} - \vec{x}') V(\vec{x}') G(\vec{x}') . \quad (26)$$

This is known as Rytov's approximation to the pressure. A direct derivation of it may be made by replacing the wave equation (10) by an equation for $\log[p(\vec{x})/G(\vec{x})]$ and solving this to first order in V .⁴ However the justification for the approximation is somewhat obscure in this direct derivation; in the approach via the supereikonal technique what is being left out is more clearly visualized.

In any event, depending on the validity of the criterion [Eq. (23)], one may use either the superikonal expression [Eq. (19)] or the Rytov expression [Eqs. (25) and (26)] to proceed further. We shall use Eqs. (25) and (26).

The Green's function G is given by Eq. (14); hence we may write for the quantity X the expression

$$X(\vec{x}) = \frac{1}{4\pi} \int d^3\vec{y} \frac{x}{y|\vec{x} - \vec{y}|} \exp[iq(y + |\vec{x} - \vec{y}| - x)] V(\vec{y}) . \quad (27)$$

Let us first comment on the geometrical optics limit of this expression. This limit results from an evaluation of $X(\vec{x})$ by the method of stationary phase. Provided that the Fresnel condition

$$x < qL^2$$

is met, the stationary phase path in Eq. (27) is the straight line joining 0 to \vec{x} , and the stationary phase value of $X(\vec{x})$ is just

$$X(x, 0, 0) = \frac{i}{2q} \int_0^x d\vec{x}' V(\vec{x}', 0, 0) , \quad (28)$$

which is immediately recognized as the correct geo-

metrical optics expression for the phase. The analogous expression for the amplitude in geometrical optics is obtained by keeping the second-order transverse derivatives in V as well.³

Returning to the general expression [Eq. (27)], let us first evaluate $\langle |X(\vec{x})|^2 \rangle$. For convenience, we shall choose \vec{x} to lie along the x axis, so that $\vec{x} = (x, 0, 0)$. We evidently have

$$\begin{aligned} \langle |X(\vec{x})|^2 \rangle = & \left(\frac{1}{4\pi} \right)^2 \int d^3\vec{y}_1 \int d^3\vec{y}_2 \frac{x^2}{y_1 |\vec{x} - \vec{y}_1| y_2 |\vec{x} - \vec{y}_2|} \\ & \times 4q^4 \rho(\vec{y}_1 - \vec{y}_2) \exp[iq(y_1 + |\vec{x} - \vec{y}_1| - x)] \\ & \times \exp[-iq(y_2 + |\vec{x} - \vec{y}_2| - x)], \end{aligned} \quad (29)$$

where we have introduced the correlation function

$$4q^4 \rho(\vec{y}_1 - \vec{y}_2) \equiv \langle V(\vec{y}_1) V(\vec{y}_2) \rangle. \quad (30)$$

We assume ρ to be independent of $\frac{1}{2}(\vec{y}_1 + \vec{y}_2)$ for the case of a homogeneous background.

It is convenient in Eq. (29) to shift to relative and center-of-mass coordinates. We define

$$\vec{y} = \vec{y}_1 - \vec{y}_2, \quad \vec{Y} = \frac{1}{2}(\vec{y}_1 + \vec{y}_2). \quad (31)$$

Then, if we assume that $\rho(\vec{y})$ cuts off for values of $y \gtrsim L$, where $L \ll x$, we may expand in y/Y . Thus Eq. (29) becomes

$$\langle |X(\vec{x})|^2 \rangle = \frac{q^4}{4\pi^2} \int d^3\vec{Y} \frac{x^2}{Y^2 |\vec{Y} - \vec{x}|^2} \int d^3\vec{y}$$

$$\langle X(\vec{x})^2 \rangle = \frac{q^4}{4\pi^2} \int d^3y_1 \int d^3y_2 \frac{x^2}{y_1 |\vec{x} - \vec{y}_1| y_2 |\vec{x} - \vec{y}_2|} \rho(\vec{y}_1 - \vec{y}_2) \exp[iq(y_1 + |\vec{x} - \vec{y}_1| - x)] \exp[iq(y_2 + |\vec{x} - \vec{y}_2| - x)]. \quad (36)$$

We again shift to the variables \vec{Y} and \vec{y} , and appeal to the vanishing of $\rho(\vec{y})$ for $y \gtrsim L$ to justify expanding in y/Y and $y/|\vec{x} - \vec{Y}|$. We obtain

$$\langle X(\vec{x})^2 \rangle = \frac{q^4}{4\pi^2} \int d^3Y \frac{x^2}{Y^2 |\vec{x} - \vec{Y}|^2} \exp[2iq(Y + |\vec{x} - \vec{Y}| - x)] \int d^3y \rho(y) \exp\left[\frac{iq}{4} \left(\frac{y^2 - (\vec{y} \cdot \hat{Y})^2}{Y} + \frac{y^2 - [\vec{y} \cdot (\hat{x} - \hat{Y})]^2}{|\vec{x} - \vec{Y}|} \right)\right]. \quad (37)$$

As before, we may evaluate the integral over d^3Y by stationary phase. This yields

$$\langle X(\vec{x})^2 \rangle = \frac{iq^3}{4\pi} \int_0^x ds \int dy_{||} \int d^2\vec{y}_{\perp} \rho(y_{||}, y_{\perp}) \frac{x}{s(x-s)} \exp\left[\frac{iq}{4} \left(\frac{1}{s} + \frac{1}{x-s} \right) y_{\perp}^2 \right], \quad (38)$$

where, again, “||” and “ \perp ” refer to directions parallel and perpendicular to \vec{x} .

At this point it is convenient to express $\rho(y_{||}, \vec{y}_{\perp})$ in terms of its Fourier transform, as given by Eq. (34). The integral over $dy_{||} d^2\vec{y}_{\perp}$ can then be carried out, and we finally obtain the relatively simple expression

$$\begin{aligned} \langle X(\vec{x})^2 \rangle = & -\frac{q^2}{4\pi^2} \int d^2\vec{k}_{\perp} \tilde{\rho}(0, \vec{k}_{\perp}) \int_0^x ds \\ & \times \exp[i(k_{\perp}^2/q)(s-x)s/x]. \end{aligned} \quad (39)$$

Equations (35) and (39) constitute our central results. They express the quantities of interest as integrals along unperturbed ray paths (in this case straight lines) of the Fourier transform of the correlation function $\tilde{\rho}(\vec{k})$ times rather simple geometrical factors. As we shall see later, entirely parallel expressions obtain in

$$\times \rho(\vec{y}) \exp(iq\vec{y} \cdot [\hat{Y} - (\hat{x} - \hat{Y})], \quad (32)$$

where \hat{Y} and $\hat{x} - \hat{Y}$ stand for unit vectors in the direction of \vec{Y} and $\vec{x} - \vec{Y}$, respectively, and we have written $|\vec{Y} \pm \frac{1}{2}\vec{y}| \approx Y$ and $|\vec{x} - \vec{Y} \pm \frac{1}{2}\vec{y}| \approx |\vec{x} - \vec{Y}|$ in the geometrical factors multiplying the exponentials. This approximation introduces a negligible error.

The integral over $d^3\vec{Y}$ may now be evaluated by stationary phase. The stationary phase path is the straight line joining 0 to \vec{x} , and the result is

$$\langle |X(\vec{x})|^2 \rangle = q^2 x \int dy_{||} \rho(y_{||}, 0), \quad (33)$$

where $y_{||}$ refers to the component \vec{y} in the direction parallel to \vec{x} .

Introducing the Fourier transform of the correlation function

$$\tilde{\rho}(\vec{k}) = \int d^3\vec{y} \exp(-i\vec{k} \cdot \vec{y}) \rho(\vec{y}), \quad (34)$$

permits us to rewrite Eq. (33) in the sometimes more convenient form

$$\langle |X(\vec{x})|^2 \rangle = \frac{q^2 x}{4\pi^2} \int d^2\vec{k}_{\perp} \tilde{\rho}(0, \vec{k}_{\perp}) \quad (35)$$

where “ \perp ” refers to the directions perpendicular to \vec{x} .

Next let us turn to $\langle X^2 \rangle$. We now have, instead of Eq. (29), the expression

the more difficult case of an inhomogeneous background medium.

The expression for $\langle |X(\vec{x})|^2 \rangle$, Eq. (35), is precisely the same result for this quantity obtained by using geometrical optics to compute $X(\vec{x})$ itself, and then calculating $\langle |X(\vec{x})|^2 \rangle$ from this. [This is easily seen by referring back to Eq. (28).] In contrast, Eq. (39) is *not* what one obtains for $\langle X(\vec{x})^2 \rangle$ from geometrical optics. Geometrical optics for this quantity is recovered if one expands the exponential in Eq. (39), a procedure that evidently is valid only if

$$\frac{k_{\perp}^2 (s-x)s}{q} \ll 1.$$

Since $k_{\perp} \sim 1/L$ and $s, x-s \sim x$, this condition can be more familiarly written

$$x \ll qL^2,$$

which we recognize as the Fresnel condition under which the geometrical optics approximation for $X(\vec{x})$ itself was valid in the first place.

Thus Eq. (39) constitutes an improvement over geometrical optics, while Eq. (35) coincides with geometrical optics. Conversely, geometrical optics for $\langle |X|^2 \rangle$ is valid out to a very large range, while geometrical optics for $\langle X^2 \rangle$ is valid only within the range $x < qL^2$.

It is of interest to study Eq. (39) in the limit of very long range. As $x \rightarrow \infty$, the integral over ds can be approximately evaluated, and we find³

$$\langle X^2(\vec{x}) \rangle \approx [iq^2 \rho(0)/2\pi] (\gamma + \log 4qx - \frac{1}{2}i\pi) \sim i \log x, \quad (40)$$

where $\gamma = 0.577\dots$ is Euler's constant, while for small x , satisfying the Fresnel condition, we have the geometric optics limit

$$\langle X^2(\vec{x}) \rangle \approx -\frac{q^2}{4\pi^2} \int d^2 k_L \tilde{\rho}(0, \vec{k}_L) \left(x - \frac{ik_L^2}{6q} x^2 + \dots \right). \quad (41)$$

Between these limits Eq. (39) provides a smooth transition. In contrast to Eq. (40) we have from Eq. (35) the result

$$\langle |X|^2 \rangle \sim x$$

for both large and small x .

II. INHOMOGENEOUS OCEAN

Now let us turn to the effects of the sound channel. That is, we must replace the nonfluctuating sound speed C in the homogeneous case by a (specified) function of position $C(\vec{x})$.

The wave equation for the pressure, which is our starting point, now becomes altered from Eq. (10) to the equation

$$[\nabla^2 + q^2(\vec{x})] p(\vec{x}) = V(\vec{x}) p(\vec{x}), \quad q(\vec{x}) = \sigma/C(\vec{x}), \quad (42)$$

still with the same boundary condition Eq. (12).

We must first study the nonfluctuating part of the problem, to evaluate the Green's function in the presence of the sound channel. This satisfies

$$[\nabla^2 + q^2(\vec{x})] G(\vec{x}, \vec{y}) = \delta^3(\vec{x} - \vec{y}). \quad (43)$$

Note that G is no longer a function only of $\vec{x} - \vec{y}$ as it was in the homogeneous case. We shall assume that geometrical optics provides a good approximation to the nonfluctuating sound channel problem. This means that we can represent $G(\vec{x}, \vec{y})$ as a sum of contributions from each ray joining \vec{x} and \vec{y} . To be specific, we may write

$$G(\vec{x}, \vec{y}) = \sum_{i=1}^{n(\vec{x}, \vec{y})} G_i(\vec{x}, \vec{y}), \quad (44)$$

where $n(\vec{x}, \vec{y})$ is the number of rays and G_i is the contribution of the i th ray. We have, in particular, for rays joining the origin and \vec{x} ,

$$G_i(\vec{x}, 0) = K_i(\vec{x}, 0) \exp\left(i \int_0^{\vec{x}} ds q[\vec{x}_i(s)]\right), \quad i = 1, \dots, n(\vec{x}), \quad (45)$$

where ds is an element of path length along the ray, $\vec{x}_i(s)$ is the i th ray joining 0 to \vec{x} , and K_i is a normalization factor.

Now when the fluctuations are turned on, the signals traveling on each of the rays joining the origin to the point of observation \vec{x} are subject to small-angle scatterings by the perturbing potential $V(\vec{x})$. The signals are thus deflected slightly from the undisturbed rays by each interaction with V . The repeated action of V thus produces, on each ray, a sort of random walk of the signal away from the original ray. When we average over an ensemble of perturbations V , the disturbed signals will fill up a tube surrounding the undisturbed ray. Provided that these tubes around each of the original rays do not overlap, the received pressure will be a sum of contributions from each ray tube. (Such tubes exist, of course, in the homogeneous case as well, but there they never overlap.)

We may estimate the radius of a ray tube as follows. The mean free path d between interactions of the signal traveling along a given ray with the perturbing potential V is of the order of $\delta C/kC$. Hence over a range x the number of scatterings is $n = x/d$. The average deflection angle due to each scattering is of order $1/kL_V$ vertically and $1/kL_H$ horizontally, where L_V and L_H are the vertical and horizontal correlation lengths of the sound speed fluctuations. Since the process is a random walk, the net displacement due to n collisions (when n is large) is proportional to \sqrt{n} , and hence the vertical and horizontal extents of the tube are, roughly,

$$r_V \sim \left(\frac{x}{q}\right)^{1/2} \frac{1}{qL_V} \left(\frac{C}{\delta C}\right)^{1/2}, \quad r_H \sim \left(\frac{x}{q}\right)^{1/2} \frac{1}{qL_H} \left(\frac{C}{\delta C}\right)^{1/2}.$$

Let us assume that the vertical extent of the tubes is small enough so that the tubes remain distinct. Then the pressure at \vec{x} is the sum of contributions from each tube

$$p(\vec{x}) = \sum_{i=1}^{n(\vec{x})} p_i(\vec{x}), \quad (46)$$

where $n(\vec{x})$ is the number of unperturbed rays joining the source to the point \vec{x} . We shall be interested in $p_i(\vec{x})$.

We note that $p_i(\vec{x})$ is the pressure that would be received at \vec{x} if the source were not isotropic, but rather emitted all its energy in the direction of the i th unperturbed ray. Thus $p_i(\vec{x})$ must satisfy the wave equation (42) but with an anisotropic boundary condition which itself depends on \vec{x} . To make this more precise, let us define $p_i(\vec{y}; \vec{x})$ to be the pressure at \vec{y} from a source at the origin which emits only within a small solid angle,⁵ around the direction of the i th perturbed ray joining the origin to \vec{x} . Thus $p_i(\vec{x}) = p_i(\vec{x}; \vec{x})$, and furthermore $p_i(\vec{y}; \vec{x})$ vanishes unless \vec{y} is inside the i th ray tube. Then

$$[\nabla_{\vec{y}}^2 + q^2(\vec{y})] p_i(\vec{y}; \vec{x}) = V(\vec{y}) p_i(\vec{y}; \vec{x}), \quad i = 1, \dots, n(\vec{x}). \quad (47)$$

In analogy with this definition of $p_i(\vec{y}; \vec{x})$, we may also define an "unperturbed" Green's function $G_i(\vec{y}; \vec{x}, 0)$, $i = 1, \dots, n(\vec{x})$, to satisfy

$$[\nabla_{\vec{y}}^2 + q^2(\vec{y})]G_i(\vec{y}; \vec{x}, 0) = 0 \text{ if } \vec{y} \neq 0, \quad (48)$$

$$G(\vec{x}, 0) = \sum_i G_i(\vec{x}; \vec{x}, 0),$$

again with the same boundary condition. This function, also, will vanish except when \vec{y} is near i th unperturbed ray.

We may now directly derive the analog of Eq. (25) by computing the quantity $\log p_i(\vec{y}; \vec{x})/G_i(\vec{y}; \vec{x}, 0)$ in perturbation theory, and using Eq. (43). We find, setting $\vec{y} = \vec{x}$, that

$$p_i(\vec{x}) = G_i(\vec{x}; \vec{x}, 0) \exp \left(\frac{1}{G_i(\vec{x}; \vec{x}, 0)} \int d^3 \vec{y} \times G(\vec{x}, y) V(y) G_i(y; \vec{x}, 0) \right). \quad (49)$$

Finally, we note that the presence of the function $G_i(\vec{y}; \vec{x}, 0)$ in Eq. (49) will restrict the integral over $d^3 \vec{y}$ to a region surrounding the i th ray from 0 to \vec{x} ; since inside this ray tube $G = G_i$, we can write

$$p_i(\vec{x}) = G_i(\vec{x}, 0) \exp \left(\frac{1}{G_i(\vec{x}, 0)} \int_{\text{ray tube}} d^3 \vec{y} \times G(\vec{x}, \vec{y}) V(\vec{y}) G(\vec{y}, 0) \right). \quad (50)$$

We have here replaced $G_i(\vec{x}; \vec{x}, 0)$ simply by $G_i(\vec{x}, 0)$. Equation (50) is evidently the generalization of the Rytov formula (25) to the situation of an inhomogeneous background and many rays. The expression clearly fails if the range is so large that the ray tubes overlap; otherwise the validity conditions are the same as those in the homogeneous background case.

We shall now use Eq. (50) to calculate the various averages of interest for the contribution of a single ray tube to the pressure in the presence of the sound channel. We shall, for simplicity, drop the index i , though we should keep in mind that when there are several unperturbed ray paths their contributions are to be added to obtain the total pressure. Our interest, then, will

be in the statistical fluctuations of the contributions of a single ray, or rather a single ray tube.

As in the homogeneous case, we define

$$X(\vec{x}) = \frac{1}{G(\vec{x}, 0)} \int d^3 \vec{y} G(\vec{x}, \vec{y}) V(\vec{y}) G(\vec{y}, 0), \quad (51)$$

and we wish to compute $\langle X^2 \rangle$ and $\langle |X|^2 \rangle$. We recall that assuming geometrical optics to be a valid approximation for the nonfluctuating background permits us to write the Green's function

$$K(\vec{x}, \vec{y}) \exp[iqS(\vec{x}, \vec{y})], \quad (52)$$

where

$$qS(\vec{x}, \vec{y}) = \int_{\vec{x}}^{\vec{y}} ds q[\vec{x}(s)], \quad (53)$$

and where the normalization factor is

$$K(\vec{x}, \vec{y}) = \frac{1}{4\pi} \left(\det \frac{\partial}{\partial x_{1j}} \frac{\partial}{\partial y_{1j}} S(\vec{x}, \vec{y}) \right)_{\vec{x}_1 = \vec{y}_1 = 0}^{1/2}. \quad (54)$$

Here \perp refers to directions perpendicular to the ray. [An excellent approximation to this, for our purposes, is to write simply $K(\vec{x}, \vec{y}) = (4\pi|\vec{x} - \vec{y}|)^{-1}$, as in the homogeneous ocean case; we need to be careful about deviations from homogeneity only in the phase.] In Eq. (53) the line integral is along the ray of interest joining the points \vec{x} and \vec{y} .

To repeat our earlier calculations requires us to introduce the correlation function $\rho(\vec{y}_1, \vec{y}_2)$. In the homogeneous case, this quantity depended only on the separation $\vec{y} = \vec{y}_1 - \vec{y}_2$. Now, however, because of the background inhomogeneities, it will also depend on $\vec{Y} = \frac{1}{2}(\vec{y}_1 + \vec{y}_2)$ (actually it will depend only on the mean depth $\frac{1}{2}(z_1 + z_2)$ because the inhomogeneities depend only on depth). Thus we must now define the correlation function by

$$4q^4 \rho(\vec{y}, \vec{Y}) \equiv \langle V(\vec{y}_1) V(\vec{y}_2) \rangle.$$

As before, let us look first at $\langle |X|^2 \rangle$. We have

$$\langle |X(\vec{x})|^2 \rangle = 4q^4 \int d^3 \vec{Y} \left(\frac{K(\vec{x}, \vec{Y}) K(\vec{Y}, 0)}{K(\vec{x}, 0)} \right)^2 \int d^3 \vec{y} \rho(\vec{y}, \vec{Y}) \exp \{ i q [S(\vec{x}, \vec{Y} + \frac{1}{2} \vec{y}) - S(\vec{x}, \vec{Y} - \frac{1}{2} \vec{y}) + S(\vec{Y} + \frac{1}{2} \vec{y}, 0) - S(\vec{Y} - \frac{1}{2} \vec{y}, 0)] \}, \quad (55)$$

and we must keep in mind that we are to integrate only over the ray tube surrounding the unperturbed ray of interest. In the homogeneous background case we expanded the exponent in powers of \vec{y} , because $\rho(\vec{y})$ vanished for large $|\vec{y}|$. We may do the same here. Thus

$$\langle |X(\vec{x})|^2 \rangle = 4q^4 \int d^3 \vec{Y} \frac{K(\vec{x}, \vec{Y}) K(\vec{Y}, 0)}{K(\vec{x}, 0)} \int d^3 \vec{y} \rho(\vec{y}, \vec{Y}) \times \exp \{ i q [\vec{y} \cdot \vec{\nabla}_Y [S(\vec{x}, \vec{Y}) + S(\vec{Y}, 0)]] \}. \quad (56)$$

The integral on $d^3 \vec{Y}$ is again to be evaluated by stationary phase. The stationary phase path is evidently the unperturbed ray joining the origin to the observation point \vec{x} . Hence we may write

$$\langle |X(\vec{x})|^2 \rangle = \frac{q^2}{4\pi^2} \int_0^{\vec{x}} ds \int d^2 \vec{k}_\perp(s) \bar{\rho}(\vec{k}_\perp(s), \vec{Y}(s)), \quad (57)$$

in complete parallel to the homogeneous case. Here the line integral on ds is along the unperturbed ray, $\vec{k}_\perp(s)$ refers to the component of \vec{k} perpendicular to the ray at s , $\vec{Y}(s)$ is a point on the ray at s , and

$$\bar{\rho}(\vec{k}_\perp, \vec{Y}) \equiv \int d^3 \vec{y} \exp(-i \vec{k}_\perp \cdot \vec{y}) \rho(\vec{y}, \vec{Y}). \quad (58)$$

Next we turn to $\langle X^2 \rangle$:

$$\langle X(\vec{x})^2 \rangle = 4q^4 \int d^3 \vec{Y} \frac{K(\vec{x}, \vec{Y}) K(\vec{Y}, 0)}{K(\vec{x}, 0)} \int d^3 \vec{y} \rho(\vec{y}, \vec{Y}) \times \exp \{ i q [S(\vec{x}, \vec{Y} + \frac{1}{2} \vec{y}) + S(\vec{x}, \vec{Y} - \frac{1}{2} \vec{y})]$$

$$+ S(\vec{Y} + \frac{1}{2}y, 0) + S(\vec{Y} - \frac{1}{2}y, 0) - 2S(\vec{x}, 0)] \}. \quad (59)$$

Now when we expand the exponent in powers of \vec{y} the linear terms vanish, so that we have

$$\begin{aligned} \langle X(\vec{x})^2 \rangle &= 4q^4 \int d^3\vec{Y} \frac{K(\vec{x}, \vec{Y})K(\vec{Y}, 0)}{K(\vec{x}, 0)} \\ &\times \exp\{2iq[S(\vec{x}, \vec{Y}) + S(\vec{Y}, 0) - S(\vec{x}, 0)]\} \\ &\times \int d^3\vec{y} \rho(\vec{y}, \vec{Y}) \exp[\frac{1}{4}iqy_i y_j A_{ij}(\vec{Y})], \end{aligned} \quad (60)$$

where we define

$$A_{ij}(\vec{Y}) = \frac{\partial}{\partial Y_i} \frac{\partial}{\partial Y_j} [S(\vec{x}, \vec{Y}) + S(\vec{Y}, 0)]. \quad (61)$$

Evaluation of the integral on $d^3\vec{Y}$ by stationary phase again selects as the stationary phase path the unperturbed ray joining 0 to \vec{x} . The integral on $d^3\vec{y}$ can then be done by introducing the Fourier transform $\tilde{\rho}(\vec{k}, \vec{Y})$ as in Eq. (58). Finally we obtain

$$\begin{aligned} \langle X(\vec{x})^2 \rangle &= -\frac{q^2}{4\pi^2} \int_0^x ds \int d^2\vec{k}_\perp(s) \tilde{\rho}(\vec{k}_\perp(s) \vec{Y}(s)) \\ &\times \exp[(i/q)k_{\perp i}(s)k_{\perp j}(s)A^{-1}(\vec{Y}(s))_{ij}]. \end{aligned} \quad (62)$$

The notation is as in Eq. (57), and the result is again in complete analogy to the homogeneous case.

Most of the comments we made in Sec. I concerning the results in the homogeneous background apply here as well. The expression for $\langle |X|^2 \rangle$ is again just that obtained in the geometrical optics approximation, but that for $\langle X^2 \rangle$ is not. Geometrical optics for $\langle X^2 \rangle$ is valid provided that

$$(1/q)k_{\perp i}(s)k_{\perp j}(s)A^{-1}(\vec{Y}(s))_{ij} \ll 1. \quad (63)$$

This is the analog of the Fresnel condition.

III. CHANNЕLED OCEAN

Let us next apply our general results, Eqs. (57) and (62), to the specific case of a channeled ocean with its associated cylindrical symmetry. We shall choose the z axis as the vertical with z positive upward. We shall choose the unperturbed ray of interest to lie in the x, z plane, and we shall confine ourselves to situations in which the source and receiver lie at the same depth. Thus the source is at the point $(x, y, z) = (0, 0, 0)$ and the receiver is at the point $(R, 0, 0)$ where R is the range. The unperturbed ray path joining these two points will be denoted $z(x)$; thus $z(0) = 0$, $z(R) = 0$ and

$$\theta(x) = \tan^{-1} \left(\frac{dz(x)}{dx} \right)$$

is the angle the ray makes with the horizontal at the point x . The element of path length along the ray is then given by

$$ds = [1 + \tan^2 \theta(x)]^{1/2} dx.$$

The expressions (57) and (60) for $\langle |X|^2 \rangle$ and $\langle X^2 \rangle$ both involve integrals of the Fourier components of the correlation function over a plane perpendicular to the ray path at each point along the ray. With our geometry, the wave number $\vec{k}(s)$ perpendicular to the ray has

x, y , and z components

$$\vec{k}(s) = (-k_x \tan \theta, k_y, k_z),$$

and the element of surface area perpendicular to the ray is

$$d^2\vec{k}_\perp(s) = dk_y dk_z / \cos \theta.$$

Thus Eq. (57) becomes

$$\begin{aligned} \langle |X|^2 \rangle &= \frac{q^2}{4\pi^2} \int_0^R dx \sec^2 \theta \int_{-\infty}^{\infty} dk_y \int_{-\infty}^{\infty} dk_z \\ &\times \tilde{\rho}([-k_x \tan \theta(x), k_y, k_z], z(x)). \end{aligned} \quad (64)$$

Now it turns out to be more convenient to express the correlation function $\tilde{\rho}$ in terms of the variables ω and j , the frequency and mode number of the internal waves, rather than the wave numbers k_y and k_z . The transformation to these new coordinates is accomplished as follows: horizontal and vertical components of wave number

$$k_H = (k_x^2 \tan^2 \theta + k_y^2)^{1/2}, \quad k_V = k_z$$

have the approximate dispersion relations [Eq. (92)]

$$k_H = j\pi B^{-1}(\omega^2 - \omega_{in}^2)^{1/2}/n_0, \quad k_V = j\pi B^{-1}n/n_0.$$

Then we note the definition

$$\begin{aligned} \int \frac{d^3\vec{k}}{(2\pi)^3} \tilde{\rho}(\vec{k}, z) &= \frac{1}{4\pi^2} \int k_H dk_H \int dk_z \tilde{\rho}(k_H, k_z, z) \\ &= \sum_j \int_{\omega_L}^n d\omega F(\omega, j; z), \end{aligned} \quad (65)$$

where $F(\omega, j)$ is the spectrum of $\delta C/C$, and

$$\omega_L^2 = \omega_{in}^2 + n^2 \tan^2 \theta.$$

The internal wave vector \vec{k} has an inclination k_V/k_H ; group velocity is at right angles, with inclination k_H/k_V , and its component in the plane of sound propagation is $k_x/k_V < k_H/k_V$. At $\omega = \omega_L$, $k_H/k_V = (\omega_L^2 - \omega_{in}^2)^{1/2}/n = \tan \theta$; lesser frequencies have $k_x/k_V < \tan \theta$, and are excluded from consideration in the stationary phase approximation.

Thus Eq. (64) may be replaced by

$$\begin{aligned} \langle |X|^2 \rangle &= 2\pi^{-1} q^2 n_0 B \int_0^R dx \sec^2 \theta \sum_j j^{-1} \int_{\omega_L}^n d\omega \\ &\times (\omega^2 - \omega_L^2)^{-1/2} F(\omega, j; z). \end{aligned} \quad (66)$$

In this expression z , n , and θ are of course functions of x , to be evaluated at each point along the unperturbed ray as x varies from source to receiver.

A similar transformation may be carried out for $\langle X^2 \rangle$, the other quantity of interest. The only complication here is that it is necessary to evaluate the matrix A_{ij} , introduced in Eq. (61), at each point along the ray. The symmetry associated with a channeled ocean makes this relatively easy to do, as follows. First, in the horizontal plane the unperturbed sound speed is constant. Hence the optical path between any two points $(x_1 y_1 z_1)$ and $(x_2 y_2 z_2)$ can be written

$$\begin{aligned} S(x_2 y_2 z_2; x_1 y_1 z_1) &\approx x_2 - x_1 + (y_2 - y_1)^2 / 2(x_2 - x_1) \\ &+ S'_1(x_2 z_2, x_1 z_1), \end{aligned} \quad (67)$$

provided that $x_2 - x_1 \gg y_2 - y_1$, $z_2 - z_1$. Therefore the matrix A_{ij} has the form

$$A_{ij} = \begin{pmatrix} A'_{xx} & 0 & A'_{xz} \\ 0 & R/x(R-x) & 0 \\ A'_{zx} & 0 & A'_{zz} \end{pmatrix}, \quad (68)$$

at an intermediate point x along the ray joining source to receiver, where the 2×2 matrix A'_{ij} now is defined in the vertical xz plane only.

The matrix A'_{ij} has the form

$$A'_{ij} = A'_{xx} \begin{pmatrix} \tan^2 \theta & -\tan \theta \\ -\tan \theta & 1 \end{pmatrix};$$

it has one zero eigenvalue, associated with an eigenvector parallel to the ray, and one nonzero eigenvalue A'_x with eigenvector $k_i = (-k_x \tan \theta, k_z)$ perpendicular to the ray. The quantity $k_{1i} k_{1j} (A'^{-1})_{ij}$ is just k_1^2 / A'_x . Since $A'_x = (1 + \tan^2 \theta) A'_{xx}$, we have $k_1^2 / A'_x = k_x^2 / A'_{xx} = k_z^2 / A'_{zz}$. Thus computing any matrix element of A'_{ij} is sufficient to allow us to obtain the quantity we need. At this point we shall drop the primes.

There are a few regimes where A_{xx}^{-1} may be obtained without specific assumptions regarding the form of the sound channel.

First, for very deep rays, the sound channel varies nearly linearly with depth, and the rays are nearly arcs of circles. For this case, to first order in the radius of curvature, the quantity A_{xx} has the same value as in a homogeneous ocean:

$$A_{xx}^{-1} = x(R-x)/R.$$

Second, for near axis rays, the sound channel is nearly a parabolic function of depth, so that the rays are nearly sinusoidal. Then we find

$$A_{xx}^{-1} = (1/K) \sin Kx \sin K(R-x) / \sin KR,$$

where $2\pi/K$ is the wavelength of the sinusoidal ray. Thus $\pi/K \approx \bar{R}$, the range of an axis loop. Note that this approximation to A_{xx}^{-1} becomes infinite when the receiver is located at axis crossings of the ray. These points are caustics for sinusoidal rays. Caustics are, in general, points at which A_{xx}^{-1} diverges, that is, where $A_{xx} = 0$. When this occurs, the matrix A_{ij} takes the simple form

$$A_{ij} = \begin{pmatrix} 0 & 0 & 0 \\ 0 & R/x(R-x) & 0 \\ 0 & 0 & 0 \end{pmatrix},$$

so that the passage from Eq. (60) to Eq. (62) becomes altered, because the second-order term in the trans-

verse derivative of the optical path no longer dominates. To calculate $\langle X^2 \rangle$ correctly in this region, we would have to keep third-order derivatives of $S(\vec{x}, \vec{y}) + S(\vec{y}, 0)$ [cf. Eqs. (59)–(61)]. As we shall see in Sec. VIII, the effect of caustics on our theoretical predictions is to introduce false narrow spikes in $\langle X^2 \rangle$ at the caustic positions. Presumably, there is in fact some unusual structure at these points due to the different behavior of the integral in Eq. (59), but our theory, to the level to which we have carried it, cannot correctly describe this structure.

A third regime in which we can obtain A_{xx}^{-1} without knowledge of the details of the sound channel is that of very long ranges, in which the rays contain a large number of loops. In this case, the optical path length S_1 in the vertical plane from the origin to a point (x, z) , plus the optical path length S_2 from (x, z) to the receiver at $(R, 0)$, can be written

$$S = S_1((x, z), (0, 0)) + S_2((R, 0), (x, z)) \\ = n_1 S_1^+(R_1^+) + \Delta S_1(x, z) + n_2 S_2^+(R_2^+) + \Delta S_2(x, z), \quad (69)$$

where $n_{1,2}$ are the number of double loops in the first (second) path, $S_{1,2}^+$ is the optical path length of one double loop, $R_{1,2}^+$ is the range of one double loop, and $\Delta S_{1,2}(x, z)$ is the remaining path length from the end of the last double loop to the point (x, z) . Evidently

$$x = n_1 R_1^+ + \Delta x_1, \quad R - x = n_2 R_2^+ + \Delta x_2,$$

with $\Delta x_{1,2} \ll x$, $R - x$ and $\Delta S_{1,2} \ll S_{1,2}^+$. Thus we may approximately write

$$S = n_1 S_1^+(x/n_1) + n_2 S_2^+(R - x/n_2). \quad (70)$$

Therefore

$$A_{xx} = \frac{\partial^2 S}{\partial x^2} \Big|_{\text{unperturbed ray}} = \left(\frac{1}{n_1} + \frac{1}{n_2} \right) \frac{d^2 S^+(R^+)}{d(R^+)^2}. \quad (71)$$

Since $n_1 + n_2 = R/R^+$, and since $n_1 = x/R^+$; $n_2 = (R - x)/R^+$, we have

$$A_{xx} = [R/x(R-x)] \delta, \quad \delta = R^+ d^2 S^+ / d(R^+)^2, \quad (72)$$

and therefore

$$A_{xx}^{-1} = (\tan^2 \theta / \delta) x(R-x) / R.$$

Other than in these cases, A_{xx}^{-1} depends on the sound channel, and we shall defer further discussion of it to Sec. IV.

Let us now return to Eq. (62). Once we have obtained A_{xx}^{-1} , we can write the exponent in the integrand of Eq. (62) as

$$\frac{1}{q} k_{1i}(s) k_{1j}(s) A^{-1}(\vec{y}(s))_{ij} = \frac{1}{q} \left(k_y^2 \frac{x(R-x)}{R} + \frac{k_z^2}{A_{xx}} \right). \quad (73)$$

Hence, using the dispersion relations for horizontal and vertical components of wave numbers, we find

$$\langle X^2 \rangle = 2q^2 \pi^{-1} n_0 B \int_0^R dx \sec^2 \theta \sum_j j^{-1} \int_{\omega_L}^{\omega} d\omega (\omega^2 - \omega_L^2)^{-1/2} F(\omega, j; z) \exp \left[\frac{i}{q} \left(\frac{j\pi}{B} \right)^2 \left(\frac{x(R-x)}{R} \frac{\omega^2 - \omega_L^2}{n_0^2} + \frac{n^2}{n_0^2} \frac{1}{A_{xx}} \right) \right]. \quad (74)$$

Geometrical optics is valid when the exponent in this equation is much less than one; this is the analogue of the Fresnel condition in the channelled ocean.

Except when the receiver is in the vicinity of a caustic, it is in general the case that the k_y^2 term in the exponent, which is associated with horizontal spreading,

is much smaller than the term with A_{ss}^{-1} . This is because, as we shall see below, the spectrum $F(\omega, j; z)$ tends to weigh small values of ω much more heavily. Thus for most purposes we can ignore this term, and replace Eq. (74) by the much simpler expression

$$\langle X^2 \rangle = -2q^2 \pi^{-1} n_0 B \int_0^R dx \sec^2 \theta \sum_j \frac{1}{j} \exp(i\beta_j^2 z) \times \int_{\omega_L}^n d\omega \frac{F(\omega, j; z)}{(\omega^2 - \omega_L^2)^{1/2}}, \quad (75)$$

where

$$\beta = (\pi/B)^2 (n/n_0)^2 1/qA_{\text{ss}}. \quad (76)$$

Using the special expressions for A_{ss} derived above applicable to specific regimes; we can write, for single loop downward rays,

$$\beta = \beta_{\text{SL}} \equiv \left(\frac{\pi}{B}\right)^2 \left(\frac{n}{n_0}\right)^2 \frac{x(R-x)}{qR};$$

for near axis rays

$$\beta = \beta_{\text{NA}} \equiv \left(\frac{\pi}{B}\right)^2 \left(\frac{n}{n_0}\right)^2 \frac{1}{qK} \frac{\sin Kx \sin K(R-x)}{\sin KR};$$

and for the long-range many-loop situation,

$$\beta = \beta_{\text{ML}} \equiv \left(\frac{\pi}{B}\right)^2 \left(\frac{n}{n_0}\right)^2 \frac{x(R-x)}{qR} \cdot \frac{\tan^2 \theta}{\delta}.$$

Equations (66) and (75) are as far as we can go toward computing the quantities of interest without committing ourselves to a particular spectrum F , and a particular sound channel and associated ray paths. It therefore now becomes necessary to turn to a discussion of these, and Secs. IV–VI will be devoted thereto.

IV. CANONICAL SOUND CHANNEL

Let $T(z)$, $S(z)$, $P(z)$ designate the undisturbed distributions of temperature, salinity, and pressure. The velocity of sound is a known empirical function of these variables, $C(z) = C(T, S, P)$, having typically a minimum value $C = \bar{C}$ at some depth $\bar{z} = -\bar{h}$ and increasing by a few percent towards top and bottom. The (fractional) velocity gradient can be written

$$C^{-1} \partial_z C = \alpha \cdot \partial_z T + \beta \cdot \partial_z S + \gamma \cdot \partial_z P, \quad (77)$$

with

$$(\alpha, \beta, \gamma) = C^{-1} \cdot (\partial_T, \partial_S, \partial_P) C.$$

The temperature gradient is the sum of potential and adiabatic gradients, $\partial_z T = \partial_z T_P + \partial_z T_A$, so that

$$C^{-1} \partial_z C_A = \alpha \cdot \partial_z T_A + \gamma \cdot \partial_z P = (-0.03 - 1.11) \times 10^{-2} \text{ km}^{-1} = -1.14 \times 10^{-2} \text{ km}^{-1} \equiv -\gamma_A \quad (78)$$

is the fractional velocity gradient in an adiabatic isohaline ocean. In analogy, we define a potential velocity gradient such that

$$\partial_z C = \partial_z P + \partial_z C_A = \partial_z C_P - C \gamma_A,$$

and write the potential gradient in terms of the buoyancy frequency $n(z)$:

$$C^{-1} \partial_z C = (\mu/g) n^2(z) - \gamma_A, \quad (79)$$

$$n^2(z) = -g \rho^{-1} \partial_z \rho_P = g(a \partial_z T_P - b \partial_z S) = g a \partial_z T_P (1 - Tu), \quad (80)$$

where the "Turner number"

$$Tu = \frac{b \partial_z S}{a \partial_z T_P}$$

gives the relative contributions of salt and (potential) temperature to the potential density stratification. In Eq. (79)

$$\mu = (\alpha/a) s(Tu), \quad \alpha/a = 24.5,$$

$$s(Tu) = (1 + cTu)/(1 - Tu), \quad c = a\beta/\alpha b = 0.049,$$

using the numerical values

$$\alpha = 3.19 \times 10^{-3} (^\circ\text{C})^{-1}, \quad a \approx 0.13 \times 10^{-3} (^\circ\text{C})^{-1},$$

$$\beta = 0.96 \times 10^{-3} (\text{‰})^{-1}, \quad b = 0.80 \times 10^{-3} (\text{‰})^{-1},$$

$$\gamma = 1.11 \times 10^{-2} \text{ km}^{-1}.$$

The a value is typical of conditions in the sound channel (it may vary by as much as 50% between surface and bottom). In shallow water the n^2 term dominates, and the velocity increases upwards; in deep water $n^2 \rightarrow 0$ and the velocity increases downwards at the rate γ_A . At the axis of the sound channel $\partial_z C = 0$, hence

$$n(\bar{z} = -\bar{h}) \equiv \bar{n} = (g\gamma_A/\mu)^{1/2}. \quad (81)$$

An exponential stratification model

$$n = n_0 e^{z/B}, \quad B = 1 \text{ km},$$

$$n_0 = 5.2 \times 10^{-3} \text{ sec}^{-1} \quad (\bar{n}_0 = 3 \text{ cph}), \quad (82)$$

gives a reasonable fit to the oceans beneath the thermocline⁶ (we ignore the surface mixed layer and interpret n_0 as a surface extrapolated value). The sound axis is at a depth

$$-\bar{z} = \bar{h} = B \log(n_0/\bar{n}) = 0.89 \text{ km} + \frac{1}{2} B \log s, \quad (83)$$

compared to typically observed values 0.7–1.5 km. Geographic variations in the sound axis are associated with the temperature dependence of \bar{n} through the α parameter, and with the salinity dependence of $s(Tu)$. We take $\bar{h} = 1 \text{ km}$. In terms of a dimensionless distance η above the sound axis, the velocity profile can be simply written

$$C = \bar{C} [1 + \epsilon(e^\eta - \eta - 1)], \quad \epsilon = \frac{1}{2} B \gamma_A = 5.7 \times 10^{-3}, \quad (84)$$

$$\eta = (z - \bar{z})/\frac{1}{2} B.$$

The coefficient ϵ is readily interpreted as the fractional adiabatic velocity increase over a scale depth. Equation (84) is a reasonable description of an oceanic sound channel (Fig. 1), given in terms of physical constants of seawater and the stratification parameters n_0 , B , Tu .

We require certain geometric properties of the sound channel. Let $z(x)$ denote a ray with inclination $dz/dx = \tan \theta$ and curvature $d^2z/dx^2 = \sec^2 \theta \cdot d\theta/dx$. From Snell's law $\cos \theta = C/\bar{C}$, where \bar{C} is the velocity at the ray apex. Hence

$$\mathcal{R}^{-1} \equiv \frac{d^2z}{dx^2} = \sec^2 \theta \cdot \frac{d\theta}{dz} \tan \theta = \frac{2\epsilon}{\bar{C}} \sec \theta (1 - e^\eta) \approx \gamma_A (1 - e^\eta). \quad (85)$$

The range of a double loop⁶ is

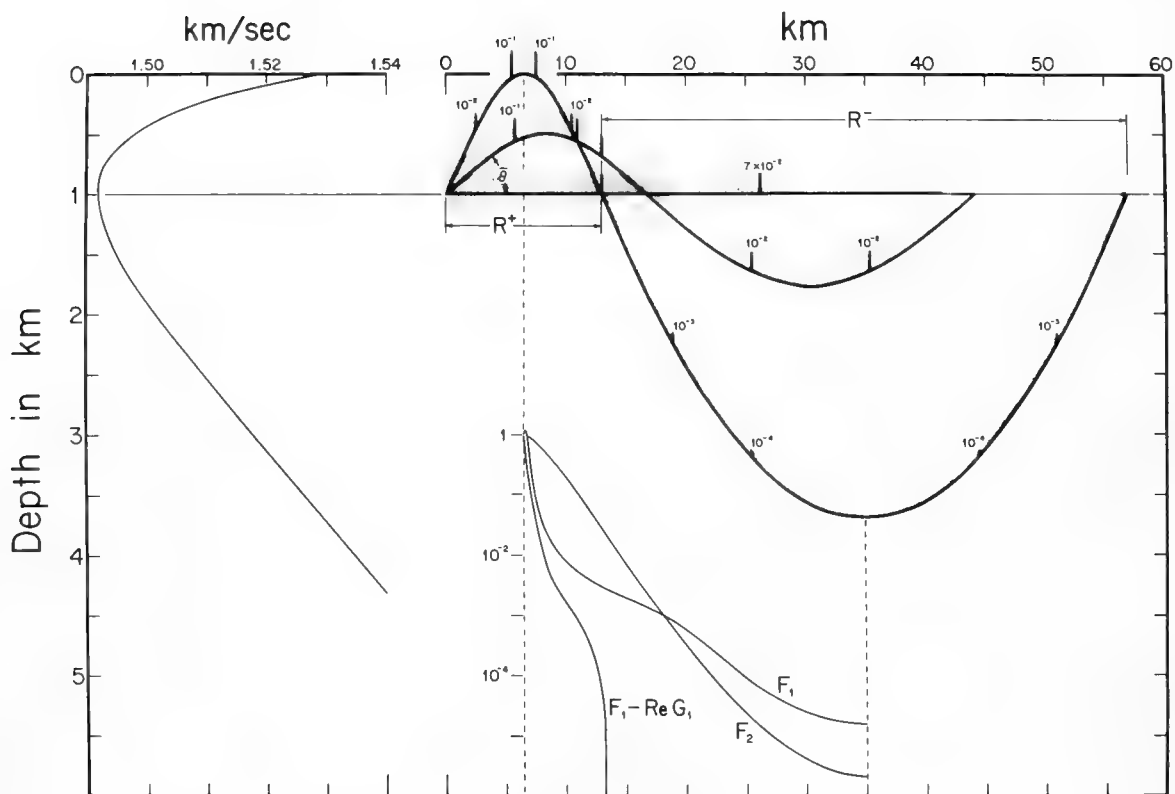


FIG. 1. Canonical sound channel (left) and the corresponding rays for $\bar{\theta} = 12.7^\circ$ (surface limited), 5.2° , and 0° (axial ray). The contribution to F_1 from various parts along the three ray paths is indicated by the vertical extent of the shaded band (plotted logarithmically). F_1 is plotted separately at the bottom of the figure for the surface limited ray, together with F_2 and $F_1 - \text{Re}G_1$, thus indicating the relative apex contributions toward mean-square phase, rate of phase, and intensity. ($F_1 - \text{Re}G_1$ applies only to a source at $x=0$ of a receiver at R^* .)

$$R^{*-} \equiv R^* + R^- = \pi B \epsilon^{-1/2} \left(1 + \frac{1}{12} \hat{\phi}^2 + \dots \right),$$

where $\phi^2 = (C - \bar{C})/(\epsilon \bar{C})$, and the "optical" path length equals

$$S^{*-} = R^{*-} - \frac{1}{12} \pi B \epsilon^{-1/2} \hat{\phi}^2 \left(1 + \frac{1}{2} \epsilon \hat{\phi}^2 + \dots \right).$$

We will require

$$\delta \equiv R^{*-} \frac{d^2 S^{*-}}{d(R^{*-})^2} = -12\epsilon(1 + \dots). \quad (86)$$

Finally, we can (laboriously) compute A_{**}^{-1} for a complete loop. We find

$$A_{**}^{-1} = -\frac{3B}{4} \frac{1}{\sqrt{2\epsilon}} \frac{\phi^2}{\hat{\phi}^3} \left[\left(1 + \frac{\hat{\phi}^2}{6} - \frac{\sqrt{2}}{3} \frac{\hat{\phi}^2}{\phi} \right)^2 - \frac{2}{9} \frac{\hat{\phi}^2(\hat{\phi}^2 - \phi^2)}{\phi^3} \left(1 - \frac{\hat{\phi}}{2\sqrt{2}} \sin^{-1} \frac{\phi}{\hat{\phi}} \right)^2 \right].$$

It will also be of interest to have the value of this quantity at the apex of a ray. This is

$$\hat{A}_{**}^{-1} = -\frac{3B}{4} \frac{1}{\sqrt{2\epsilon}} \frac{1}{\hat{\phi}} \left(1 + \frac{\hat{\phi}^2}{6} - \frac{\sqrt{2}}{3} \hat{\phi} \right)^2.$$

For upward rays, $A_{**}^{-1} \approx x$ near $x=0$ and $A_{**}^{-1} \approx R^* - x$ near $x=R^*$ (Fig. 2), and A_{**}^{-1} has zeros at the caustics of rays propagating to the right from $x=0$ and to the left from

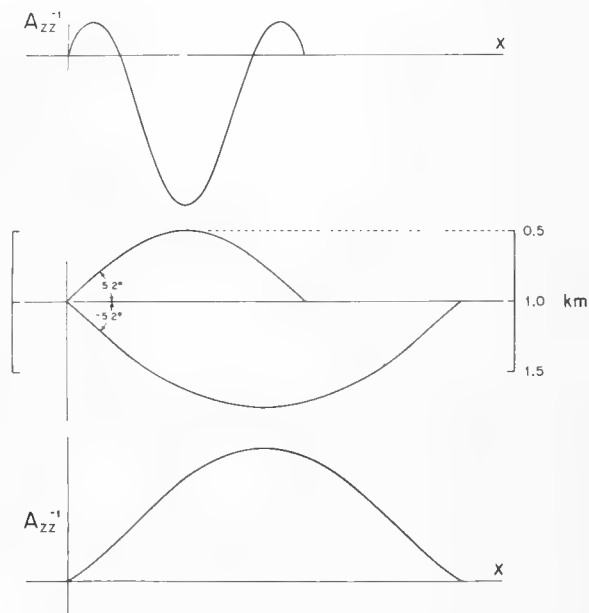


FIG. 2. A_{**}^{-1} for a 5.2° upward loop (top) and downward loop (bottom), with the $\pm 5.2^\circ$ ray itself shown in the center, all plotted as functions of horizontal distance x .

$x=R^*$. For downward rays, A_{xx}^{-1} is reasonably well approximated simply by $x(\bar{R}-x)/\bar{R}$.

V. FLUCTUATIONS IN SOUND VELOCITY

In the presence of an internal wave field with vertical displacements ξ , a particle momentarily at z comes from a rest height $z-\xi$. The resulting velocity fluctuation at a fixed depth z is

$$\delta C/C \approx \delta C/C = \alpha \delta T + \beta \delta S + \gamma \delta P,$$

where

$$\delta T = \xi \cdot \partial_z T_p, \quad \delta S = \xi \cdot \partial_z S, \quad \delta P = \rho g \xi \cdot \Delta \rho / \rho$$

are the internal wave-produced fluctuations in T , S , P . The wave-induced pressure fluctuations at a fixed depth are reduced by a factor $\Delta \rho / \rho (\approx 10^{-3})$ over the pressure fluctuation $\rho g \xi$ experienced by a fixed water particle. Henceforth the effect on δC of the internal wave associated pressure fluctuations will be neglected, and so

$$\delta C = \xi (\partial_z C - \partial_z C_A) = \xi \partial_z C_p; \quad (87)$$

e.g., the internal waves convect the potential velocity gradient as defined in Eq. (79):

$$\delta C/C = n^2(z) \mu \xi / g. \quad (88)$$

The rms vertical displacement is given by (GM72)

$$\text{rms}(\xi) = \text{rms}(\xi_0)(n/n_0)^{-1/2}, \quad \text{rms}(\xi_0) = 7.3 \text{ m},$$

relative to its near-surface value, and so increases with depth as $n^{-1/2}$; accordingly

$$\text{rms}(\delta C/C) = \text{rms}(\delta C/C)_0 (n/n_0)^{3/2}, \quad (89)$$

with

$$\text{rms}(\delta C/C)_0 = \mu n_0^2 \text{rms}(\xi_0) / g,$$

decreases exponentially with depth with a scale $\frac{2}{3}B = 0.67 \text{ km}$. For orientation, set $s=1$ and $\mu=24.5$; typical values are given in Table I. In very deep water $\delta C/C$ is of order 10^{-5} , and accordingly the rms fluctuations in sound velocity are a few cm/sec. The rms horizontal velocity components associated with internal waves are (GM72)

$$\text{rms}(u) = \text{rms}(u_0)(n/n_0), \quad u_0 = 4.7 \text{ cm/sec},$$

leading to the values in the last column. The last two columns give relative perturbations in sound propagation associated with vertical displacement and horizontal particle velocity, respectively. The latter effect is much smaller (except in very deep water), and will be ignored subsequently. On the other hand, the u effects dominate at and below inertial frequencies, so that planetary waves with their quasihorizontal particle motions affect sound transmission by Mach refraction.

TABLE I. Typical values with $s=1$ and $\mu=24.5$.

	z (km)	\bar{n} (cph)	n (rad/sec)	rms ξ (m)	rms $\delta C/C$	rms u/C
thermocline	$z_0 = 0$	3.00	5.2×10^{-3}	7.3	4.9×10^{-4}	3.1×10^{-5}
sound axis	$\bar{z} = -1.0$	1.10	1.9×10^{-3}	12.0	1.1×10^{-4}	1.1×10^{-5}
bottom	$z = -4.5$	0.094	1.7×10^{-4}	41.2	2.8×10^{-6}	1.0×10^{-6}

VI. INTERNAL WAVE MODEL

Fluctuations in the vertical structure of temperature and salinity were discovered by Petterson, Helland-Hansen, and Nansen soon after the turn of the century. Since that time there has been a vast literature on the subject (over 500 references were compiled by Roberts⁷) consisting mostly of reports on temperature and current fluctuations at moored instruments, and of a few horizontal temperature profiles from tows behind ships. In the past three years, the technology of continuous vertical profiling of currents with freely dropped instruments has been developed, providing additional information. A three-dimensional trimooring (IWEX) was installed in 1973 off the American east coast, and we may expect some very useful additional results.

On the basis of this myriad of observations, Garrett and Munk have contrived successive models² (GM72, GM75) of internal wave spectra. They placed particular emphasis on multiple recordings, separated vertically on the same mooring or horizontally on neighboring moorings, which had shown that fluctuations of frequencies as low as 1 cph were uncorrelated for vertical separations exceeding a few hundred meters, and for horizontal separations exceeding a few kilometers. These coherences were interpreted as a measure of reciprocal bandwidth: for separations larger than the reciprocal bandwidth, different wave numbers interfere destructively, and coherence is lost. The following conclusions were reached: (i) Observations can be reconciled with the dispersion law and wave functions of linear internal wave theory. (ii) Towed records are insensitive to the ship's course, and moored records are similar for the two velocity components, thus indicating some degree of horizontal isotropy; the evidence is certainly incompatible with internal waves propagating along narrow horizontal beams. (iii) Coherences are incompatible with a model consisting of just the gravest one or two vertical modes (except at tidal frequencies). The GM72 model had equal contributions from modes 1 to 20, and none beyond mode 20. But this is too broad; recent measurements by Cairns⁸ are consistent with a mode weighting according to $(j^2 + j_*^2)^{-1}$ with $j_* \approx 3$. (iv) The myriad of observations, taken over the years at many depths off the American west and east coasts, Hawaii, near Bermuda and Gibraltar, in the Bay of Biscay, and the Mediterranean, agree to within an order of magnitude. This suggests some universality in the internal wave spectrum, perhaps due to saturation effects such as those limiting surface waves of high frequency.

We use the GM75 spectrum, somewhat modified for the Cairns observations:

$$\langle \xi^2(z) \rangle = \int_{\omega_{1n}}^{n(z)} d\omega \sum_{j=1}^{\infty} F_c(\omega, j; z),$$

$$F_c(\omega, j; z) = \langle \xi^2(z) \rangle G(\omega) H(j),$$

$$G(\omega) = \frac{4}{\pi} \frac{\omega_{1n}(\omega^2 - \omega_{1n}^2)^{1/2}}{\omega^3}, \quad \int_{\omega_{1n}}^{n(z)} G(\omega) d\omega \approx 1,$$

$$H(j) = (j^2 + j_*^2)^{-1} \left/ \sum_1^\infty (j^2 + j_*^2)^{-1} \right., \quad (90)$$

$$\sum_{j=1}^\infty H(j) = 1,$$

between the inertial frequency $\omega_{in} = 2 \sin(\text{latitude})$ cpd and the buoyancy frequency $n(z) \gg \omega_{in}$, and zero otherwise, where

$$\sum_1^\infty (j^2 + j_*^2)^{-1} \approx \frac{1}{2} j_*^{-2} (\pi j_* - 1) \quad \text{for } j_* \geq 1.$$

Similarly for the spectrum of $\delta C/C$

$$F_{\delta C/C}(\omega, j; z) = \langle (\delta C/C)^2 \rangle G(\omega) H(j) \\ = \langle (\delta C/C)_0^2 \rangle (n/n_0)^3 G(\omega) H(j). \quad (91)$$

For ω not too close to $n(z)$, the dispersion relations

$$\iiint F(\vec{k}) \cos k_x x d\vec{k} = \int_{\omega_{in}}^{n(z)} d\omega \int_0^\infty dk_H F(k_H, \omega) \cdot (2\pi)^{-1} \int_{-\pi}^\pi d\alpha \cos(k_H \cos \alpha X) = \int_{\omega_{in}}^{n(z)} d\omega \int_0^\infty dk_H F(k_H, \omega) J_0(k_H x) \\ \approx \int_{\omega_{in}}^{n(z)} d\omega G(\omega) \sum_j H(j) J_0(k_H x) \approx 1 - 8\pi^{-1} j_* (\omega_{in}/n_0) [\log(n/\omega_{in}) - \frac{1}{2}] |x|/B,$$

$$\sum H(j) \cos k_y z \approx 1 - (\pi j_* - 1) (n/n_0) |z|/B,$$

which suggest the coherence scales

$$L_H = \frac{\pi(n_0/\omega_{in})B}{8j_* [\log(n/\omega_{in}) - \frac{1}{2}]}, \quad L_V = \frac{Bn_0/n}{\pi j_* - 1}. \quad (94)$$

Setting $\omega_{in} = 7.3 \times 10^{-5} \text{ sec}^{-1}$ (30° latitude), $n_0 = 5.3 \times 10^{-3} \text{ sec}^{-1}$, $B = 1 \text{ km}$, gives the values in Table II. (The near-bottom value of L_V is meaningless.) The assumption of spherical symmetry (so popular to scattering theorists) is useless to oceanographic application.

VII. FLUCTUATIONS IN MODEL OCEAN

Armed with the specific ocean model described in Secs. IV–VI, we can now proceed with the evaluations of the general expressions (66) and (75) for the quantities $\langle |X|^2 \rangle$ and $\langle X^2 \rangle$. Let us first look at $\langle |X|^2 \rangle$.

Substitution of the spectrum (91) into (66) yields

$$\langle |X|^2 \rangle = \langle (\delta C/C)_0^2 \rangle \langle j^{-1} \rangle q^2 B \bar{R} F_1(R), \quad (95)$$

$$F_1(R) = \frac{8}{\pi^2} \frac{\omega_{in}}{n_0} \frac{1}{\bar{R}} \int_0^R dx \sec^2 \theta n^3 \int_{\omega_L}^n \frac{d\omega}{\omega^5} \left(\frac{\omega^2 - \omega_{in}^2}{\omega^2 - \omega_L^2} \right)^{1/2}$$

TABLE II. Typical values for $\omega_{in} = 7.3 \times 10^{-5} \text{ sec}^{-1}$ (30° latitude), $n_0 = 5.2 \times 10^{-3} \text{ sec}^{-1}$, and $B = 1 \text{ km}$. The near-bottom value of L_V is meaningless.

	z (km)	n (rad/sec)	L_H (km)	L_V (km)
thermocline	-0.1	5.2×10^{-3}	2.5	0.12
sound axis	-1.3	1.9×10^{-3}	3.4	0.32
bottom	-4.5	1.7×10^{-4}	27.0	(3.63)

are

$$k_H = j\pi B^{-1} n_0^{-1} (\omega^2 - \omega_{in}^2)^{1/2}, \quad k_V(z) = j\pi B^{-1} n(z)/n_0 \quad (92)$$

for the horizontal and vertical components of wave number. The spectrum in k_H, j space is accordingly

$$F_{\delta C/C}(k_H, j) = F_{\delta C/C}(\omega, j) \frac{d\omega}{dk_H} \\ = \left\langle \left(\frac{\delta C}{C} \right)^2 \right\rangle \frac{4(\omega_{in}/n_0) B^{-1} k_H^2 j H(j)}{[k_H^2 + (j\pi B^{-1} \omega_{in}/n_0)^2]^2} \quad (93)$$

for $0 \leq k_H \leq k_V = j\pi B^{-1} n(z)/n_0$. Equations (90)–(93) are essentially WKB approximations, and they fail near the boundaries and the turning depths (GM72).

Coherence scales can be estimated from the Fourier transforms:

$$= \frac{4}{\pi^2} \frac{1}{\omega_{in} n_0^2} \frac{1}{\bar{R}} \int_0^R dx \sec^2 \theta n^3 f_1(\Delta), \quad (96)$$

and

$$f_1(\Delta) = \frac{1}{\Delta^2 + 1} + \frac{\Delta^2}{2(\Delta^2 + 1)^{3/2}} \log \frac{(\Delta^2 + 1)^{1/2} + 1}{(\Delta^2 + 1)^{1/2} - 1}, \quad (97)$$

with

$$\Delta = (n/\omega_{in}) \tan \theta. \quad (98)$$

$F_1(R)$ as here defined is a dimensionless number of order one when R is of the order of \bar{R} , the range of a loop ($\bar{R} = \frac{1}{2} B \pi \epsilon^{-1/2} = 20.8 \text{ km}$). It is for this reason that the factor \bar{R} has been explicitly separated out in Eq. (95).

The quantity $\langle j^{-1} \rangle$ represents the average of j^{-1} weighted by the internal wave spectrum $H(j)$. We have

$$\langle j^{-1} \rangle = \left(\sum_j j^{-1} (j^2 + j_*^2)^{-1} \right) / \left(\sum_j (j^2 + j_*^2)^{-1} \right) \\ = 0.730, 0.647, 0.519, 0.435, 0.379, 0.340 \quad (99)$$

for $j_* = 0, 1, \dots, 5$. An approximate expression is $\log(4j_*^2 + 1)/(\pi j_* - 1)$.

For axial rays, $\theta = \Delta = 0$, $f_1(0) = 1$, and $n = \bar{n}$ is a constant. Hence $F_1(R)$ becomes simply proportional to R ; we have

$$F_1(R) = \frac{4}{\pi^2} \frac{\bar{n}^3}{\omega_{in} n_0^2} \frac{R}{\bar{R}} = 1.436 \frac{R}{\bar{R}} \equiv \bar{F}_1(R). \quad (100)$$

For upward rays turning near the surface, the major contribution to the integral defining $F_1(R)$ comes from the ray apex (Fig. 1); here the equation of the ray is, approximately,

$$z(x) \approx \hat{z} - (1/2R)(x - \hat{x})^2,$$

and

\hat{z} in km

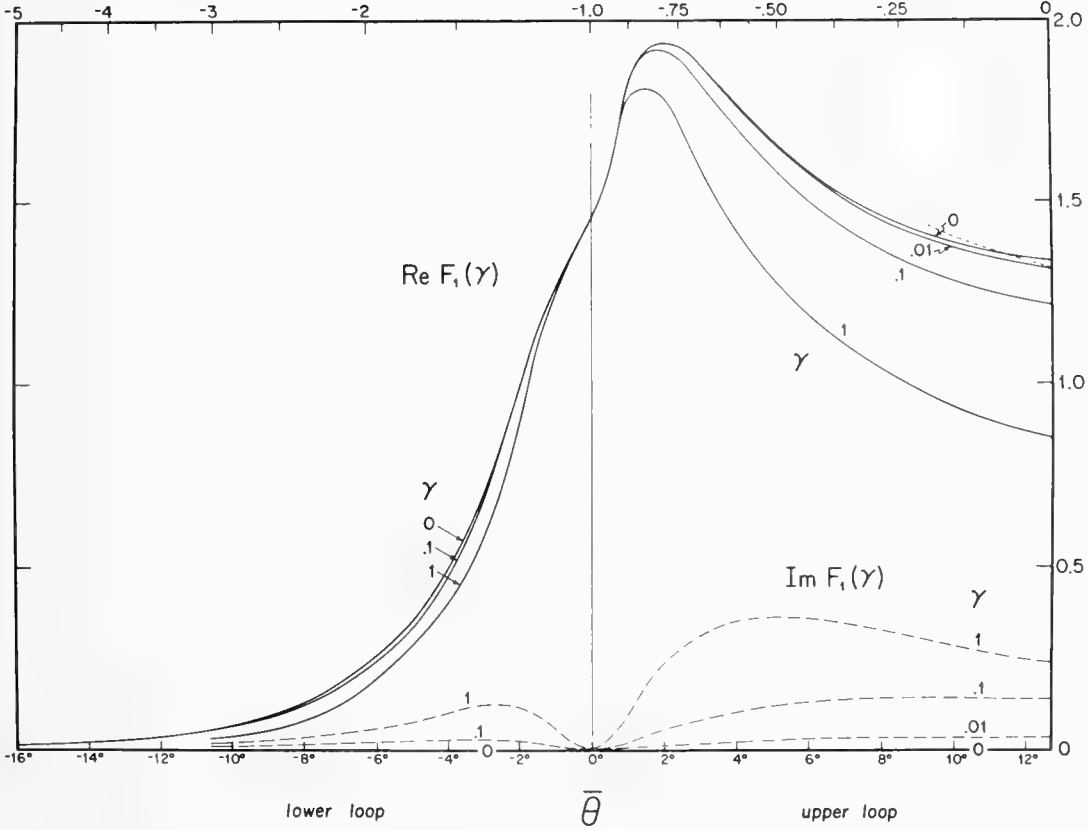


FIG. 3. Plots of $F_1(\gamma)$ from a numerical integration of Eq. (113). $\text{Re } F_1(\gamma)$ is proportional to the loop contributions towards $\langle X^2 \rangle$. $\text{Re } F_1(0) = F_1^*$ corresponds to Eq. (96) for a single upward ($\bar{\theta}$ positive) or downward ($\bar{\theta}$ negative) loop. The short-dashed curve gives the apex approximation [Eq. (101)] to F_1^* .

$$\Delta = n(x - \hat{x}) / \omega_{1n} R,$$

where (\hat{x}, \hat{z}) is the position of the apex and R is the ray curvature at the apex. The function $f_1(\Delta)$ cuts off rapidly with increasing Δ , and therefore we can write, approximately,

$$F_1(R) \approx \hat{F}_1(R) = \frac{4}{\pi^2} \frac{\hat{n}^3}{\omega_{1n} n_0^2} \frac{1}{R} \int_{-\infty}^{\infty} f_1(\Delta) dx = \frac{2R\hat{n}^2}{Rn_0^2} \quad (101)$$

times the number of upward loops.

For a single complete upward (downward) loop with range $R^+(R^-)$ we denote $F_1(R^+)$ simply by F_1^+ . Then for a complete double loop, with range R^{+-} , we have

$$F_1^{+-} \equiv F_1(R^{+-}) = F_1^+ + F_1^-.$$

If the double loop has an apex near the surface, then $F_1^+ \approx \hat{F}_1$ and $F_1^- \approx 0$; thus

$$F_1^{+-} \approx \hat{F}_1.$$

The results of a numerical evaluation of F_1^+ and F_1^- as a function of ray angle $\bar{\theta}$ are shown in Fig. 3, as is the apex approximation \hat{F}_1 , which is seen to be an excellent approximation for $\bar{\theta} \gtrsim 5^\circ$. The largest value of F_1^+ occurs at a ray angle $\bar{\theta}$ near 2° , and a corresponding

apex depth of 750 m; deeper rays are reduced by the smaller value of n^3 , rays of shallower apex are reduced by a smaller radius of curvature R .

We shall also need the variance of $\dot{X} = dX/dt$; this is found by inserting ω^2 in Eq. (66) under the integral sign. The result is

$$\langle |\dot{X}| \rangle = \omega_{1n} n_0 \langle (\delta C/C)_0^2 \rangle \langle j^{-1} \rangle q^2 B \bar{R} F_2, \quad (102)$$

where

$$\bar{R} F_2 = 8\pi^2 n_0^{-3} \int_0^R dx \sec^2 \theta n^3 \log \left(\frac{n}{\omega_{1n}} \right) f_2(\Delta) \quad (103)$$

and

$$f_2(\Delta) = \left(\log \frac{n}{\omega_{1n}} - \frac{1}{2} \log \frac{\Delta^2}{4} - \frac{1}{2(1+\Delta^2)^{1/2}} \log \frac{(1+\Delta^2)^{1/2} + 1}{(1+\Delta^2)^{1/2} - 1} \right) / \log \frac{n}{\omega_{1n}}. \quad (104)$$

For the axial ray (where $f_2 = 1$) and near surface rays we have, respectively,

$$\bar{F}_2 = 8\pi^2 (\hat{n}/n_0)^3 (R/\bar{R}) \log \bar{n}/\omega_{1n} = 0.132 R/\bar{R}, \quad (105)$$

$$\hat{F}_2 = 8\pi^2 (\frac{2}{3}\pi)^{1/2} (B|\mathcal{R}|)^{1/2} (\bar{R})^{-1} (\hat{n}/n_0)^3 \log(\hat{n}/\omega_{1n}). \quad (106)$$

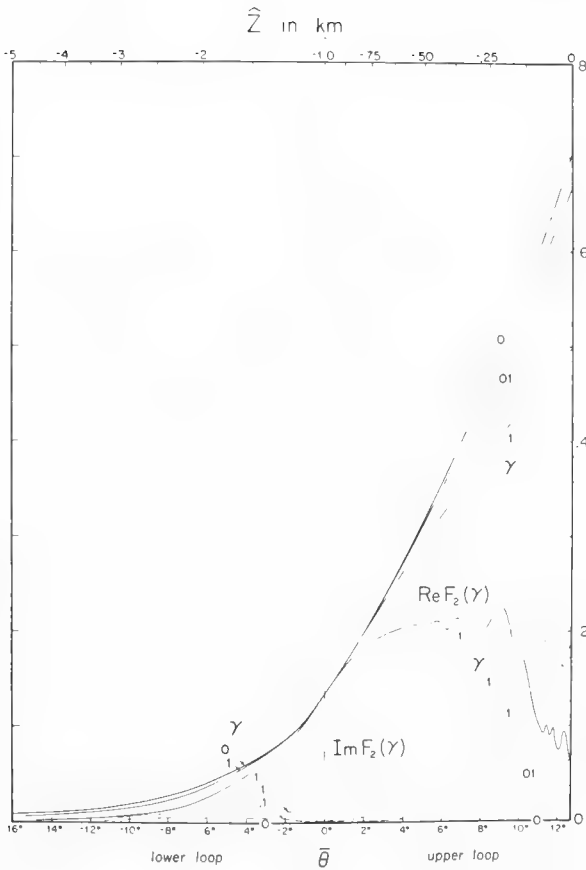


FIG. 4. Plots of $F_2(\gamma)$, proportional to the loop contributions towards $\langle \dot{X}^2 \rangle$. See Fig. 3.

F_2 is less peaked at the apex than F_1 and decreases monotonically with apex depth (Fig. 4).

Let us next turn to the quantity $\langle X^2 \rangle$. From Eqs. (75) and (91) we find

$$\langle X^2 \rangle = - \langle (\delta C/C)_0^2 \rangle \langle j^{-1} \rangle q^2 B \bar{R} G_1(R), \quad (107)$$

where

$$G_1(R) = \frac{4}{\pi^2} \frac{1}{\omega_{1a} n_0^2} \frac{1}{R} \int_0^R dx \sec^2 \theta n^3 f_1(\Delta) g(\beta, j_*) . \quad (108)$$

Here we have defined

$$g(\beta, j_*) = \left\langle \frac{1}{j} \right\rangle^{-1} \sum_{j=1}^{\infty} \frac{1}{j} \frac{1}{j^2 + j_*^2} \exp(i\beta j^2), \quad (109)$$

and we recall from Eq. (76) that

$$\beta = (\pi/B)^2 (n/n_0)^2 1/qA_{**} .$$

Note that as $\beta \rightarrow 0$, $g(\beta, j_*) \rightarrow 1$ and thus $G_1 \rightarrow F_1$ and hence $\langle X^2 \rangle \rightarrow - \langle |X|^2 \rangle$.

An approximate analytic expression for $g(\beta, j_*)$ is

$$g(\beta, j_*) = \frac{[\exp(-i\beta j_*^2) Ei(i\beta(j_*^2 + \frac{1}{4})) - Ei(\frac{1}{4}\beta)]}{\log(4j_*^2 + 1)} .$$

Thus for small β , we have

$$g(\beta, j_*) = - \frac{\pi j_*^2}{2 \langle j^{-1} \rangle (\pi j_*^2 - 1)} |\beta| + \dots, \quad (110)$$

and hence for small β ,

$$G_1(R) = F_1(R) - \frac{2}{\pi} \frac{1}{\langle j^{-1} \rangle} \frac{j_*^2}{\pi j_*^2 - 1} \frac{1}{\omega_{1a} n_0^2} \frac{1}{R} \int_0^R dx \times \sec^2 \theta n^3 f_1(\Delta) |\beta| + \dots$$

For very long ranges where many loops are involved, we may simplify the integral in Eq. (108) as follows. First replace β by the many loop long range value β_{ML} :

$$\beta_{ML} = (\pi/B)^2 (n/n_0)^2 [x(R-x)/qR] \tan^2 \theta / \delta \equiv \alpha_{ML} \gamma(x), \quad (111)$$

where

$$\gamma(x) \equiv x(R-x)/B^2 R q . \quad (112)$$

Next note that γ varies rather little over one loop. Then the integral from 0 to R may be broken up into a sum of integrals over each of the loops. In any given loop, say the k th one, γ has very nearly the value $\gamma(x_k) \equiv \gamma_k$, where x_k is the position of the midpoint of the loop. Thus we may write, in place of Eq. (108),

$$G_1 = \sum_{k=1}^{K^*} F_1^*(\gamma_k) + \sum_{k=1}^{K^*} F_1^-(\gamma_k),$$

where K^* is the number of $\frac{\omega_{1a} n_0^2}{\omega_{1a} n_0^2}$ loops, and where

$$F_1^*(\gamma_k) = \frac{4}{\pi^2} \frac{1}{\omega_{1a} n_0^2} \frac{1}{R} \int_{x_k - R^*/2}^{x_k + R^*/2} dx \times \sec^2 \theta n^3 f_1(\Delta) g(\beta_k, j_*), \quad (113)$$

with

$$\beta_k = \pi^2 (n/n_0)^2 (\tan^2 \theta / \delta) \gamma_k .$$

Here $x_k \pm R^*/2$ are the positions of the two ends of the loop. We note that as $\gamma_k \rightarrow 0$, $F_1^*(\gamma_k) \rightarrow F_1^*$ as defined earlier.

The variation of $F_1^*(\gamma)$ with γ is shown in Fig. 3. Large deviations from F_1^* begin to become apparent when γ is of order one. The maximum γ that occurs over a range R is $R/4B^2q$; thus G_1 is not very different from F_1 until ranges of order $4B^2q$.

All of the foregoing results and definitions may be summarized in the following relation:

$$\begin{bmatrix} - \langle X^2 \rangle \\ + \langle |X|^2 \rangle \\ - \langle \dot{X}^2 \rangle \\ + \langle |\dot{X}|^2 \rangle \end{bmatrix} = \left\langle \left(\frac{\delta C}{C} \right)_0^2 \right\rangle \langle j^{-1} \rangle q^2 B \bar{R} \begin{bmatrix} G_1 \\ F_1 \\ \omega_{1a} n_0 G_2 \\ \omega_{1a} n_0 F_2 \end{bmatrix} . \quad (114)$$

The quantities of actual interest to us are not quite $\langle X^2 \rangle$ and $\langle |X|^2 \rangle$, but rather the mean-square phase and intensity fluctuations. These, we recall from Eqs. (4), (6), and (9), are related to $\langle X^2 \rangle$ and $\langle |X|^2 \rangle$ through

$$\langle \phi^2 \rangle = \frac{1}{2} (\langle |X|^2 \rangle - \text{Re} \langle X^2 \rangle) \quad (115)$$

and

$$\langle \iota^2 \rangle - \langle \iota \rangle^2 = 2 (\langle |X|^2 \rangle + \text{Re} \langle X^2 \rangle) . \quad (116)$$

Thus we find

$$\begin{pmatrix} \langle \phi^2 \rangle \\ \langle \iota^2 \rangle - \langle \iota \rangle^2 \end{pmatrix} = \left\langle \left(\frac{\delta C}{C} \right)_0^2 \right\rangle \langle j^{-1} \rangle q^2 B \bar{R} \begin{pmatrix} \frac{1}{2} \\ 2 \end{pmatrix} (F_1 \pm \text{Re} G_1) . \quad (117)$$

For small β , $\text{Re}G_1 - F_1$, so that

$$\langle \phi^2 \rangle - \langle \delta C / C_0 \rangle \langle j^{-1} \rangle q^2 B \bar{R} F_1 ; \quad (118)$$

this is simply the conventional geometrical optics expression for phase fluctuations. Intensity fluctuations, however, depend on the *difference* between F_1 and $\text{Re}G_1$,

$$F_1 - \text{Re}G_1 = \frac{4}{\pi^2} \frac{1}{\omega_{1n} n_0^2} \frac{1}{R} \int_0^R dx \sec^2 \theta n^3 f_1(\Delta) (1 - g(\beta, j_*)) \quad (119)$$

and thus vanish in the small β limit. Indeed, for small β , using Eq. (110), we find

$$\begin{aligned} \langle \epsilon^2 \rangle - \langle \epsilon \rangle^2 &= 4\pi \left\langle \left(\frac{\delta C}{C} \right)_0^2 \right\rangle \frac{j_*^2}{\pi j_* - 1} \frac{q}{B \omega_{1n} n_0^4} \int_0^R dx \\ &\times \sec^2 \theta n^5 f_1(\Delta) \left| \frac{1}{A_{xx}} \right|, \end{aligned} \quad (120)$$

and this does *not* coincide with any geometrical optics expression.

It is also of interest to compute the spectra of phase and intensity fluctuations. For this purpose, we return to Eqs. (66) and (75), and to Eq. (91), but we do not now carry out the integral over $d\omega$. For a given value of ω , we integrate over a ray path, keeping in mind that there is a complicated set of forbidden ray sections, depending on the value of ω relative to ω_L , \hat{n}^- , and \hat{n}^+ (Fig. 5). For very low frequencies the ray is too steep to permit "stationary-phase interaction" with internal waves. For the high frequencies ω may exceed $n(z)$ along some portions of the ray, and internal wave solutions do not exist. The phase and intensity spectra are given by

$$\begin{aligned} \left[\frac{E_\phi(\omega)}{E_i(\omega)} \right] &= \frac{8}{\pi^2} \left\langle \left(\frac{\delta C}{C} \right)_0^2 \right\rangle \left\langle \frac{1}{j} \right\rangle q^2 B \frac{\omega_{1n}}{n_0^2 \omega^3} \int_0^R dx \sec^2 \theta n^3 \\ &\times \left(\frac{\omega^2 - \omega_{1n}^2}{\omega^2 - \omega_L^2} \right)^{1/2} H(n - \omega) H(\omega - \omega_L) \\ &\times \left[\frac{\frac{1}{2}(1 + \text{Reg}(\beta, j_*))}{2(1 - \text{Reg}(\beta, j_*))} \right]. \end{aligned} \quad (121)$$

For the important range $\omega_L \ll \omega < \hat{n}^-$ the entire integration path is permitted and the spectra vary as ω^{-3} .

VIII. COMPARISON WITH NUMERICAL EXPERIMENTS

As a first application, and test, of the results we have obtained we shall make a comparison with a set of "numerical experiments."⁹ These consist of numerical solutions of the parabolic wave equation in the same sound channel we have discussed here, and with a sequence of internal wave realizations from a two-dimensional projection of the spectrum described in Sec. VI.¹⁰ The "numerical experiments" use an acoustic frequency of 100 Hz, and propagate sound up to ranges of 100 km; the remaining parameters are the "standard ones" listed in Secs. IV–VI. In all cases the acoustic transmitter is located on the sound axis, at a depth of 1000 m. The receiver consists of a vertical array of hydrophones, 700 m long, centered on the ray in question, which allows an angular resolution of $1\frac{1}{2}^\circ$.

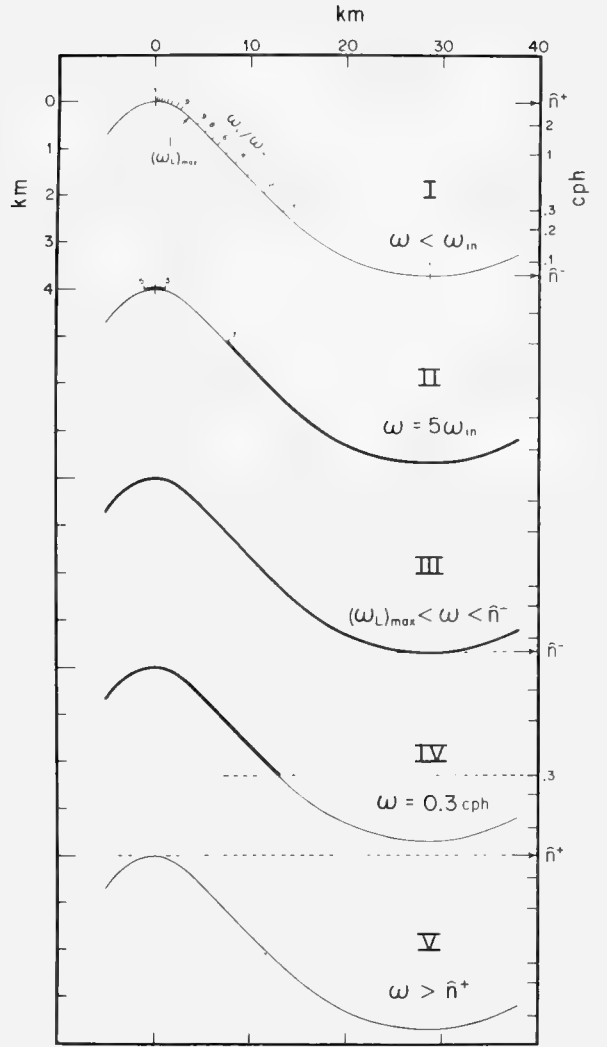


FIG. 5. Internal wave contributions toward frequency spectra of acoustic phase and intensity come from "permitted" sections of the ray path (heavy lines). There are no internal wave contributions to frequencies less than the inertial frequency (I) and larger than the apex buoyancy frequency (V) because no such internal waves exist. The entire ray contributes toward the central band III between $(\omega_L)_{\max}$ (typically $10 \omega_{1n}$) and the buoyancy frequency at the lower turning point (for deep rays III does not exist). For lower frequencies, the upper sections of the ray are too steep to permit "stationary-phase interaction" (II), and high frequencies exceed the buoyancy frequency of the deep ray section (IV).

A. Phase fluctuations

Solid lines in Fig. 6 show the results of the "numerical experiment" for 128 realizations (to which one may assign a statistical error of perhaps $\pm 20^\circ$). The dotted lines are the predictions of the theory outlined in Sec. VII, and specifically of Eq. (118). Evidently the agreement is satisfactory. Overall magnitudes differ between theory and experiment by about (20–30)% (except for the -1° ray) and the general shapes coincide as well. For the steep rays ($\pm 9^\circ$ and to a lesser extent $\pm 5^\circ$) the

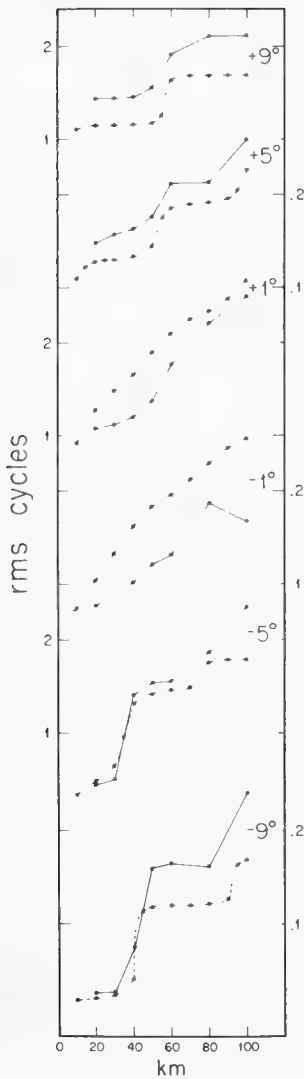


FIG. 6. Comparison of calculated (dotted lines) and "experimental" (solid lines) rms phase fluctuations at 100 Hz as function of range for six rays with inclinations on the axis ranging between $\pm 9^\circ$. Lines connect calculated values, with no attempt at interpolation.

rms phase is nearly a step function of range, reflecting the fact that the major contribution to the integral in Eq. (96) comes when the rays cross an apex, and that there is little contribution while the ray is deep. The near axis rays ($\pm 1^\circ$), on the other hand, vary much more smoothly with range (nearly like $R^{1/2}$).

B. Intensity fluctuations

Table III shows the rms intensity fluctuations for the same six rays, at various ranges. Since the numerical experiment makes use of a vertical beam former rather than a single hydrophone to select different rays, the theoretical calculations described in Sec. VII must be somewhat modified. There intensity fluctuations were calculated for a fixed receiver position; here we must calculate fluctuations for a fixed receiver angle but having a variable vertical position. This amounts to replacing the quantity A_{**}^{-1} in Eq. (120) by a different geo-

metrical factor B_{**}^{-1} , defined to be the second derivative with respect to z of the optical path length from the transmitter to a receiver located at a fixed range and seeing a fixed vertical angle, rather than one located at a fixed range and height. This quantity has been evaluated numerically, and then Eq. (120) has been used, in order to obtain the theoretical values shown in the table.

The quantity B_{**}^{-1} can be evaluated analytically for linear and quadratic sound channels (with circular and sinusoidal rays) which approximate the real sound channel for deep and near-axial rays, respectively. We find

$$B_{**}^{-1} = x, \quad B_{**}^{-1} = \frac{1}{K} \frac{\sin Kx \cos K(R-x)}{\cos KR} \quad (122)$$

for deep and near-axial rays, respectively, where $2\pi/K$ is the wavelength of the sinusoidal rays, so that π/K is the range of one loop. We remind the reader that

$$A_{**}^{-1} = \frac{x(R-x)}{R}, \quad A_{**}^{-1} = \frac{1}{K} \frac{\sin Kx \sin K(R-x)}{\sin KR}$$

are the corresponding quantities for a fixed-point receiver. Thus, for near-axial rays, B_{**}^{-1} becomes infinite when the receiver is located at the turning point of the rays. It is here that all rays are parallel; this is the analogue of a caustic for a beam former receiver. As we have already remarked in Sec. III, when the receiver is placed near a caustic, our approximate expressions [Eq. (75)] fail; to correct it would require keeping the effect of horizontal spreading in Eq. (74). We are therefore able to compare our calculated values with the "experimental" ones only if we avoid placing the receiver near a (beam former type of) caustic. For near-axis rays, where we can use Eq. (122), these caustics occur at ranges $R \approx (n + \frac{1}{2})\pi/K$; since $\pi/K \approx \bar{R} = 20$ km for near-axis rays, there are caustics of ranges of 10, 30, 50, ... km. For off-axis rays, the positions of caustics must be determined numerically. The entries in Table III are made by avoiding these.

The agreement between theory and "experiment" is

TABLE III. RMS intensity fluctuations in dB. The upper (lower) number in each entry is the theoretical ("experimental") value.

Ray angle	Range (km)						
	20	30	40	50	60	80	100
+ 9°	1.00 (0.73)	...	1.21 (0.82)	1.34 (1.20)
+ 5°	1.10 (0.44)	...	1.12 (0.50)	1.39 (0.62)	1.31 (0.64)
+ 1°	0.79 (0.34)	...	1.03 (0.41)	...	1.31 (0.60)	1.57 (0.74)	1.80 (0.95)
- 1°	0.66 (0.30)	...	1.07 (0.43)	...	1.39 (0.61)	1.70 (0.56)	2.20 (0.46)
- 5°	...	0.38 (0.41)	...	0.94 (0.61)	...	1.19 (1.02)	1.29 (0.84)
- 9°	0.09 (0.06)	0.18 (0.07)	0.29 (0.31)	0.78 (0.63)	...

TABLE IV. The measured rms values of travel time and intensity.

Frequency (nominal)	4 kHz	8 kHz
Travel time	0.384	0.374 msec
Intensity	5.2	5.7 dB

satisfactory for the off-axis rays but for near-axis rays the theory seems to overestimate the size of the fluctuations; in particular, the $\pm 1^\circ$ rays are predicted to have fluctuations that are larger by a factor of two to three than the “experiment” shows. This discrepancy is possibly related to the fact that we use the linear approximation to the dispersion [Eq. (92)], or that the WKB approximation underlying the theory does not allow the reduction in vertical displacement near the boundaries, or to the two-dimensional character of the “experiment,” or, finally, to the failure of the expansion in power of acoustic wavelength over the vertical correlation length of the fluctuations at this wavelength.

IX. SINGLEPATH EXPERIMENT ON COBB SEAMOUNT

Ewart¹¹ has measured amplitude and phase (transit time) fluctuations between a fixed transmitter and receiver on Cobb Seamount ($46^\circ 46'$ N, $130^\circ 47'$ W). The sound axis is shallow, 400 m, as is characteristic of high latitude. Setting $\bar{z} = -0.4$ km in Eq. (84), we construct a ray path through source and receiver (both at 1000 m depth) separated by 17.2 km, with a lower turning point at a depth of 1350 m, in agreement with ray tracing based on locally measured sound profiles (Fig. 4, Ewart). Further, the measured $n(z)$ is very close to our experimental model [Eq. (82)]. Ewart obtained 144.5 h of records (with minor gaps) based on 8-cycle pulses at 4166 Hz and 16-cycle pulses at 8333 Hz transmitted alternately every 15.7 sec. The measured rms variations are given in Table IV.

Ewart remarks on the strong tidal contribution to the travel time spectra, and on the important effect on intensity by sporadic multipaths associated with sound velocity fine structure. We note that the results are similar at the two frequencies (as expected); the rms phase at 4 kHz is 3.84×10^{-4} sec \times 4166 Hz = 1.60 cycles.

The maximum value of β is 10^{-5} (7 km from turning point), so geometric optics applies, and according to Eq. (118)

$$\langle \phi^2 \rangle = \langle (\delta C/C)_0^2 \rangle \langle j^{-1} \rangle q^2 B \bar{R} F_1(0) = 251.7 \text{ rad}^2$$

for rms $(\delta C/C)_0 = 4.9 \times 10^{-4}$, $\langle j^{-1} \rangle = 0.435$, $q = 1.745 \times 10^4 \text{ rad km}^{-1}$ (for 4166 Hz), $B = 1$ km, $R = 20.8$ km, $n_0 = 5.2 \times 10^{-3} \text{ sec}^{-1}$, $\omega_{1a} = 1.06 \times 10^{-4} \text{ sec}^{-1}$ (46.75° latitude), and $F_1(0) = 0.38$ (from a numerical integration). Thus rms $\phi = 2.53$ cycles, compared to 1.60 measured.

Similarly the intensities are found from Eq. (120), using $A_{**}^{-1} = x(R-x)/R$ which is appropriate for a single lower loop. The result is $\langle \epsilon^2 \rangle - \langle \epsilon \rangle^2 = 0.245$, or

$$(10/\log 10) (0.245)^{1/2} = 2.15 \text{ dB},$$

TABLE V. Variation with model parameter j_* .

	observed	$j_* = 3$	$j_* = 4$	$j_* = 5$
rms ϕ in cycles	1.6	2.5	2.2	2.0
rms ϵ in dB	5.5	2.2	2.8	3.4

as compared to the observed rms value of 5.5 dB. (A more accurate form for A_{**}^{-1} will increase the calculated value slightly.) Observations and computation of both phase and intensity are roughly within a factor of 2 and can be brought into better accord by increasing the model parameter j_* (Table V).

A more sensitive test consists of comparing computed¹² and observed spectra (Fig. 7). The computed phase spectrum is high, as expected from the rms values, but in the principal band between inertial and buoyancy frequencies the computed ω^{-3} slope is reasonably consistent with the observed spectral slope. The observed phase spectrum continues smoothly beyond the computed n cutoff. Computed intensities completely fail to account for the observed high frequencies. Dashen (private communication) has demonstrated that the high-frequency phases and intensities are due to interference between “sporadic multipaths.” (Ewart has remarked on the occasional arrival of multiple pulses.) A discussion goes beyond the scope of this paper.¹³

X. MULTIPATH EXPERIMENT MIMI

The most persistent measurements of ocean propagation are the 406-Hz transmission of MIMI¹⁴ between Eleuthera (Bahamas) and Bermuda. The measured $\phi(t)$ and $\epsilon(t)$ are completely dominated by the effects of multipath interference, and are not simply related to the $\phi_i(t)$ and $\epsilon_i(t)$ along any singlepath i with which our paper is concerned. However, it is possible to use the measured multipath spectra to *infer* rms ϕ_i for a typical singlepath.¹⁵ Results are given in Table VI.

For a “back-of-the-envelope” comparison (after two years) with our results we use the axial approximation (105) in Eq. (102):

$$\begin{aligned} \langle \dot{\phi}_i^2 \rangle &= \langle (\delta C/C)_0^2 \rangle \langle j^{-1} \rangle q^2 B \bar{R} \omega_{1a} n_0 \bar{F}_2 \\ &= 8\pi^{-2} \langle (\delta C/C)_{ax}^2 \rangle \langle j^{-1} \rangle q^2 B R \omega_{1a} n_0 \log \bar{n} / \omega_{1a}. \end{aligned} \quad (123)$$

Using $q = 1701 \text{ rad km}^{-1}$ for 406 Hz, rms $(\delta C/C)_0 = 4.9 \times 10^{-4}$, $\langle j^{-1} \rangle = 0.435$, $B = 1$ km, $\omega_{1a} = 7.3 \times 10^{-5} \text{ sec}^{-1}$, $n_0 = 5.2 \times 10^{-3} \text{ sec}^{-1}$, $\bar{n} = 1.9 \times 10^{-3} \text{ sec}^{-1}$ and Eq. (89), this simple expression leads to excellent agreement with the measurements (Table VI). For the surface limited ray we use the apex approximation (106) with $\bar{n} = n_0$ and a radius of curvature $R = 13.7$ km [Eq. (85)] to obtain

$$\begin{aligned} \langle \dot{\phi}_i^2 \rangle &= 8\pi^{-2} (\frac{2}{3}\pi)^{1/2} \langle (\delta C/C)_0^2 \rangle \langle j^{-1} \rangle q^2 B^{3/2} R^{1/2} \\ &\quad \times \omega_{1a} n_0 \log(n_0/\omega_{1a}) \end{aligned}$$

per double loop, leading to somewhat larger values.

Table VII summarizes a more precise calculation, allowing for the proper “ray mix.” From Eqs. (102) and (103)

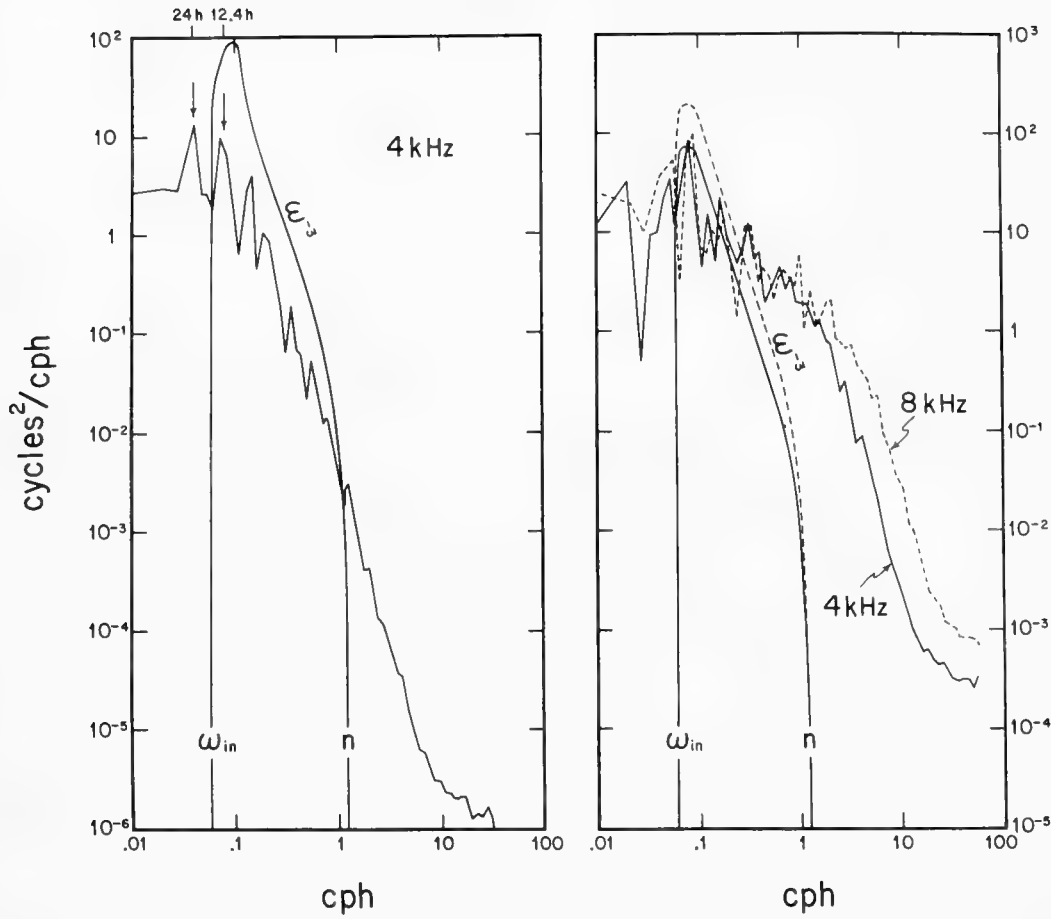


FIG. 7. Computed (smooth curves) and observed spectra of phase (left) and intensity (right) at Cobb Seamount. Only the 4-kHz results are shown for phase; at 8 kHz computed and observed values both are higher by 6 dB.

$$\langle \dot{\phi}_i^2 \rangle = \left\langle \left(\frac{\delta C}{C} \right)_0^2 \right\rangle \langle j^{-1} \rangle q^2 B \bar{R} \omega_{1a} n_0 \sum_i \frac{\Delta \bar{\theta}_i}{\Sigma \Delta \bar{\theta}_i} \times \sum_{\#}^{\kappa^*} \frac{1}{2} [F_2^+(0) + F_2^+(\gamma_k)] .$$

The summation i extends over 34 rays in the order of decreasing inclination $\bar{\theta}_i$ of the axial source. For even numbers of loops, values of $\pm \bar{\theta}_i$ pair with precisely the same statistics, but for odd numbers of loops there is an extra upper loop for positive $\bar{\theta}$ and an extra downward loop for negative $\bar{\theta}$. Each ray is weighted according to the difference $\Delta \bar{\theta}_i$ between adjoining rays, and this emphasizes the near axial rays.

The number of loops varies from 60 ($K^+ = 30$, $K^- = 30$) for the near-axial rays ($\bar{\theta} = \pm 1^\circ$) to 44 ($K^+ = 22$) for the surface-limited rays. The largest γ_k is at the central loop, $x = \frac{1}{2}R$, $\gamma = R/4B^2q = 0.184$ and even then the difference between $F_2(\gamma)$ and $F_2(0)$ is slight. We may then use the geometric optics formula

$$\langle \dot{\phi}_i^2 \rangle = \left\langle \left(\frac{\delta C}{C} \right)_0^2 \right\rangle \langle j^{-1} \rangle q^2 B \bar{R} \omega_{1a} n_0 \sum_i \frac{\Delta \bar{\theta}_i}{\Sigma \Delta \bar{\theta}_i}$$

$$\times [K^+ F_2^+(0) + K^- F_2^-(0)] .$$

The summand (last column of Table VII) is fairly uniformly distributed among all contributing rays.

The agreement between computed and measured values of $\langle \dot{\phi}_i^2 \rangle$ is rather too good.

TABLE VI. Measured and computed MIMI parameters.

	Midstation	Bermuda
Range	550 km (nominal)	1250 km
Number of paths	14	34
Number of double loops		
Surface limited ray (SLR)	10	22
Near axial ray	13	30
rms $\dot{\phi}_i$ inferred from MIMI	$2.8 \times 10^{-3} \text{ sec}^{-1}$	$4.0 \times 10^{-3} \text{ sec}^{-1}$
rms $\dot{\phi}_i$ computed		
Axial ray	$2.9 \times 10^{-3} \text{ sec}^{-1}$	$4.4 \times 10^{-3} \text{ sec}^{-1}$
Apex approximation, SLR	$4.6 \times 10^{-3} \text{ sec}^{-1}$	$6.8 \times 10^{-3} \text{ sec}^{-1}$
Weighted average	$3.5 \times 10^{-3} \text{ sec}^{-1}$	$5.2 \times 10^{-3} \text{ sec}^{-1}$

TABLE VII. Calculations of $\langle \phi_1^2 \rangle$ for Bermuda. $\bar{\theta}_i$ are the inclinations at the axial source of all possible rays to an axial receiver at 1250-km range, consisting of K^+ upper loops of range R^+ and R^- lower loops of range R^- (see Fig. 1). $F_2^+(0)$ are the dimensionless contributions per ray loop to $\langle \phi_1^2 \rangle$ as read from Fig. 4, leading to the dimensionless weighted sum $(\Delta\theta/\Sigma\Delta\theta)(K^+F_2^+ - K^-F_2^-)$.

$\bar{\theta}_i$	K^+	R^+	K^-	R^-	$\Delta\theta$	F_2^+	F_2^-	Sumand
12.7	22	12.8	22	44.0	0.60	0.703	0.011	0.362
12.3	23	12.9	22	43.3	0.60	0.680	0.012	0.367
11.5	23	13.2	23	41.2	0.60	0.630	0.014	0.342
11.2	24	13.4	23	40.4	0.55	0.614	0.015	0.319
10.3	24	13.7	24	38.4	0.55	0.560	0.018	0.293
10.0	25	13.9	24	37.6	0.55	0.545	0.019	0.298
9.2	25	14.2	25	35.8	0.55	0.500	0.021	0.276
9.0	26	14.4	25	35.0	0.55	0.490	0.022	0.281
8.1	26	14.8	26	33.3	0.60	0.448	0.028	0.286
7.8	27	15.1	26	32.4	0.60	0.435	0.029	0.288
6.9	27	15.5	27	30.8	0.60	0.395	0.035	0.268
6.5	28	15.9	27	29.8	0.65	0.375	0.038	0.288
5.7	28	16.4	28	28.2	0.70	0.343	0.045	0.292
5.1	29	16.7	28	27.4	0.85	0.315	0.050	0.344
4.0	29	17.5	29	25.6	1.05	0.274	0.062	0.394
3.0	30	18.2	29	24.3	1.50	0.235	0.073	0.529
1.0	30	19.8	30	21.9	2.00	0.165	0.107	0.628
-1.0	30	19.8	30	21.9	1.80	0.165	0.107	0.628
-2.6	29	18.5	30	23.8	1.50	0.219	0.078	0.501
-4.0	29	17.5	29	25.6	1.10	0.274	0.062	0.394
-4.8	28	16.8	29	26.9	0.85	0.300	0.054	0.326
-5.7	28	16.4	28	28.2	0.70	0.343	0.045	0.292
-6.2	27	16.0	28	29.2	0.65	0.365	0.040	0.274
-6.9	27	15.5	27	30.8	0.60	0.395	0.035	0.268
-7.4	26	15.3	27	31.6	0.60	0.418	0.031	0.270
-8.1	26	14.8	26	33.3	0.55	0.448	0.028	0.286
-8.5	25	14.7	26	33.9	0.55	0.469	0.025	0.262
-9.2	25	14.2	25	35.8	0.55	0.500	0.021	0.276
-9.6	24	14.0	25	36.6	0.55	0.512	0.020	0.271
-10.3	24	13.7	24	38.4	0.55	0.560	0.018	0.293
-10.6	23	13.6	24	39.0	0.55	0.585	0.016	0.293
-11.5	23	13.2	23	41.2	0.60	0.630	0.014	0.342
-11.8	22	13.1	23	41.8	0.60	0.652	0.013	0.338
-12.7	22	12.8	22	44.0	0.60	0.703	0.011	0.362

XI. CONCLUDING REMARKS

We end up, after lengthy derivations, with quite simple and transparent formulae for the acoustical fluctuations. The formulae make explicit the dependence of the various oceanographic and acoustic parameters. The need is to apply these results to a variety of experimental situations.

For Project MIMI the measured acoustical fluctuations are dominated by the statistics of multipath interference. The observations yield but one parameter which is sensitive to the ocean model: $\langle \phi_1^2 \rangle$. Values at midstation and Bermuda are close to those computed for an internal wave model based entirely on oceanographical observations. (There are no free factors in this comparison.) The agreement could be made even closer by a reasonable adjustment of internal wave parameters. We conclude that internal waves play an important and probably dominant role in producing the acoustical fluctuations.

The MIMI transmissions are characterized by many *deterministic* multipaths as determined by the gross profile $C(z)$; the statistical results are not affected by the additional *sporadic* multipaths resulting from a fine-structure δC . In contrast, the Cobb Seamount experiment has a single deterministic path, but because of the

high acoustic frequency, sporadic multipaths play an important role in producing high-frequency fluctuations of intensity and phase. Dashen (private communication) has shown that an extension of the present analysis, based on the same ocean model, can account quantitatively for the high frequencies in terms of sporadic multipathing, but this goes beyond the scope of our paper. The mean-square quantities, in contrast, are dominated by low frequencies and can be estimated from singlepath theory. We find measured and computed rms fluctuations to be within a factor of 2.

ACKNOWLEDGMENTS

This work has been strongly dependent on the closely related efforts of R. Dashen and S. Flatté. The theoretical framework was set in an earlier report written by C. Callan and F. Zachariasen. We wish to express our gratitude to Callan, Dashen, and Flatté.

*This work was performed during the 1974 and 1975 JASON Summer Studies under the auspices of Stanford Research Institute, supported by the Advanced Research Projects Agency. ¹Using $\epsilon = 10^{-4} \text{ cm}^2 \text{ sec}^{-3}$ for the dissipation per unit mass, and $n = 10^{-3} \text{ sec}^{-1}$ for the buoyancy frequency.

²C. J. R. Garrett and W. H. Munk, "Space-Time Scales of Internal Waves," *Geophys. Fl. Dynam.* **2**, 225-264 (1972); C. J. R. Garrett and W. H. Munk, "Space-Time Scales of Internal Waves: A Progress Report," *J. Geophys. Res.* **80**, 291-297 (1975); J. L. Cairns and G. O. Williams, "Internal Wave Measurements from a Midwater Float II," *J. Geophys. Res.* (1976) (in press). The model initials suggest some planned obsolescence and have allowed the authors to bring out new models from time to time.

³C. G. Callan and F. Zachariasen, Stanford Research Institute Technical Report No. JSR-73-10, April 1974 (unpublished).

⁴See L. Chernov, *Wave Propagation in a Random Medium* (McGraw-Hill, New York, 1960); and V. I. Tatarski, *The Effects of the Turbulent Atmosphere on Wave Propagation* (unpublished).

⁵We do not have to be very precise about how we define this angle.

⁶W. Munk, "Sound Channel in an Exponentially Stratified Ocean, With application to SOFAR," *J. Acoust. Soc. Am.* **55**, 220-226 (1974), Fig. 1 (based on Pingree and Morrison). (In that paper, z is positive downward.) See also Fig. 1 in GM72, Ref. 2.

⁷J. Roberts, University of Alaska IMS Report No. R73-4 (1973) (unpublished).

⁸J. Cairns and G. Williams, "Internal Wave Measurements from a Midwater Float II," *J. Geophys. Res.* (in press) (1976).

⁹S. M. Flatté and F. D. Tappert, "Calculation of the Effect of Internal Waves on Oceanic Sound Transmission," *J. Acoust. Soc. Am.* **58**, 1151-1159 (1975).

¹⁰The numerical experiment uses the exact wave functions for the exponential model ocean, weighted according to Eq. (90), whereas our analytical model is based on the corresponding WKB approximation.

¹¹T. E. Ewart (unpublished).

¹²The computed phase spectrum [Eq. (119)] is in units of $\text{rad}^2/\text{rad/s}$; multiply by $(2\pi)^{-2}/(3600/2\pi)$ to get $\text{cycles}^2/\text{cph}$. For the intensity spectrum [Eq. (120)] multiply by $(10/\log 10)^2/(3600/2\pi)$ to get dB^2/cph .

¹³Roger Dashen has pointed out that the shallow sound axis ($\bar{z} = -0.4 \text{ km}$ as compared to the canonical $\bar{z} = -1 \text{ km}$) can be expected to produce smaller $\delta C/C$ fluctuations, given a canonical internal wave field. The reduction is proportional

to the potential velocity gradient $\partial_z C_p$ [Eq. (87)], and hence to $\bar{n}^{-2} \sim e^{-2z/B}$ [Eqs. (79), (81)]. The reduction in rms $\delta C/C$ is by a factor 3.3. This would more nearly align observed and computed phase spectra, but at the expense of an even larger discrepancy in the intensities.

¹⁴ For *Miami-Michigan* project, starting with J. C. Steinberg and T. G. Birdsall, "Underwater Sound Propagation in the Straits of Florida," J. Acoust. Soc. Am. **39**, 301–315 (1966).

For a recent paper see J. G. Clark and M. Kronengold, "Long-period Fluctuations of CW Signals in Deep and Shallow Water," J. Acoust. Soc. Am. **56**, 1071–1083 (1974).

¹⁵ F. Dyson, W. Munk, and B. Zetler, "An Interpretation in Terms of Internal Waves and Tides of Multipath Scintillations Eleuthera to Bermuda," J. Acoust. Soc. Am. (1976) (in press).

INTERPRETATION OF MULTIPATH SCINTILLATIONS ELEUTHERA
TO BERMUDA IN TERMS OF INTERNAL WAVES AND TIDES

Freeman Dyson

Walter Munk and Bernard Zetler

Reprinted from the Journal of the Acoustical Society of America
Vol. 59, No. 5, May 1976.

Interpretation of multipath scintillations Eleuthera to Bermuda in terms of internal waves and tides*

Freeman Dyson

The Institute for Advanced Study, School of Natural Sciences, Princeton, New Jersey 08540

Walter Munk and Bernard Zetler

Institute of Geophysics and Planetary Physics, Scripps Institution of Oceanography, La Jolla, California 92093

(Received 10 December 1975)

Rate-of-phase and intensity spectra due to time-varying *multipath* interference depend essentially on a single parameter ν^2 which can be interpreted as the mean-square rate-of-phase for any typical *single* path. MIMI 406-Hz phase and intensities are consistent with $\nu^{-1} = 270$ and 357 sec for Eleuthera to Bermuda and Eleuthera to midstation transmissions, respectively, compared to 192 and 286 sec from a ray-geometric calculation using an internal wave model based on oceanographic observations. Internal tides play a significant but not dominant role.

Subject Classification: [43]30.20,[43]30.35.

INTRODUCTION

The purpose of this paper is to compare some statistical properties of random vector fields with measured cw transmissions of MIMI¹ between Eleuthera (Bahamas) and Bermuda. (Among the previous analyses we refer particularly to the work of Clark; Dyer; DeFerrari; and Jacobsen.²) The observational material, generously made available to us by John G. Clark, consists of intensity $I(t)$ (decibels, arbitrary reference) and phase $\Phi(t)$ (in cycles), as presented by the top two curves of Fig. 1, a selected portion is shown point by point in Fig. 2. The observed acoustic pressure fluctuations (frequency $\sigma = 406$ Hz) relative to some (reference) scale p_0 can be written

$$p(t)/p_0 = x(t) \cos \sigma t + y(t) \sin \sigma t,$$

where x, y are slowly varying (compared to σ) amplitudes.³ The original measurements consist of the 5-min averages⁴ of amplitudes

$$X(t) = \frac{1}{\delta t} \int_0^{\delta t} x(t) dt = R(t) \cos \phi(t), \quad (1)$$

$$Y(t) = R(t) \sin \phi(t),$$

which are related to the plotted time series (as furnished to us) according to

$$I = 20 \log R, \quad (2)$$

$$\Phi = \phi / 2\pi.$$

We have then reconverted to

$$X = 10^{I/20} \cos 2\pi \Phi, \quad (3)$$

$$Y = 10^{I/20} \sin 2\pi \Phi.$$

For statistical theory, it is convenient to refer to

$$\epsilon = \ln R^2 = \frac{\ln 10}{10} I. \quad (4)$$

A suitable intensity reference is

$$\epsilon_0 = \ln \langle R^2 \rangle \text{ or } I_0 = 10 \log \langle R^2 \rangle.$$

I. MEASURED VARIANCE IN MULTIPATH PHASE AND INTENSITY

Only fractional cycles are measured, and there is an ambiguity concerning the integer number of cycles. Normally this can be resolved by the continuity of the time series. Phase *difference* over the sampling interval $\delta t = 5^m$ has an rms value of $\delta \Phi = 0.24$ cycles, at Bermuda, and the (Gaussian) probability for $|\delta \Phi|$ to exceed $\frac{1}{2}$ cycle is 4% (8% were observed). A restriction to $|\delta \Phi| \leq \frac{1}{2}$ cycle (which can be attained by adding and subtracting integer cycles) is not realistic. We have edited the observations to remove phase "kinks," replacing the reported value Φ by $\Phi \pm 1, \Phi \pm 2, \dots$ cycles when required to make the *adjusted* phase difference $\delta \Phi_n = \Phi_{n+1} - \Phi_n$ subject to the restriction

$$|\delta \Phi_n - \frac{1}{2}(\delta \Phi_{n+1} + \delta \Phi_{n-1})| \leq \frac{1}{2} \text{ cycles.}$$

This is essentially placing an upper limit on second differences in phase; 5% of the Bermuda observations and 1.5% for the midstation were adjusted accordingly. Figure 3 shows a sample of $\delta \Phi$ before and after adjustment, and Fig. 4 the reconstituted $\Phi = \sum \delta \Phi$. Midstation phases are not severely altered by phase adjustments. At Bermuda the low (week-to-week) frequencies bear no resemblance to the midstation trend and are considerably altered by the phase adjustment; however, the high-passed records (tidal frequencies and higher) are not significantly altered. We conclude that sampling was adequate for midstation phases and high-frequency Bermuda phases, but that sampling was not adequate to obtain low-frequency trends at Bermuda. Adjusted mean-square phases and phase differences are given in Table I.

Multipath intensities are characterized by occasional deep fades (Figs. 1 and 2). They are *censored* for a subsequent analysis of fade statistics, by replacing the recorded values of I by $I_0 - F$ whenever $I < I_0 - F$, but otherwise leave I unchanged; censored X and Y are subsequently computed according to Eq. (3). Accordingly the three columns in Table I refer to the removal of fades exceeding $F = \infty, 20, 10$ dB (the first column then

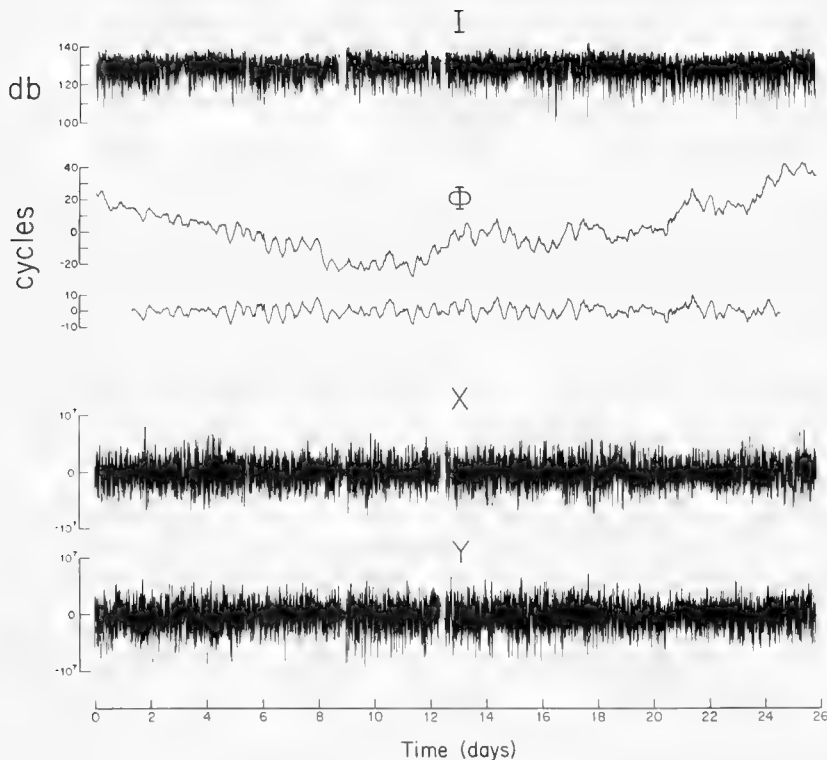


FIG. 1. Plots of measured intensity I , phase Φ , and high-passed phase, and of the components X and Y (in arbitrary pressure units) of acoustic pressure at Bermuda, 22 Sept. –17 Oct. 1973.

refers to the uncensored record). A typical signal-to-noise ratio is 27 dB [Ted Birdsall (personal communication)], and a removal of deeper fades (say $F=30$ dB) would be associated with noise statistics rather than

multipath statistics.

The crucial importance of sampling needs to be stressed. From a numerical experiment (Sec. VII) we

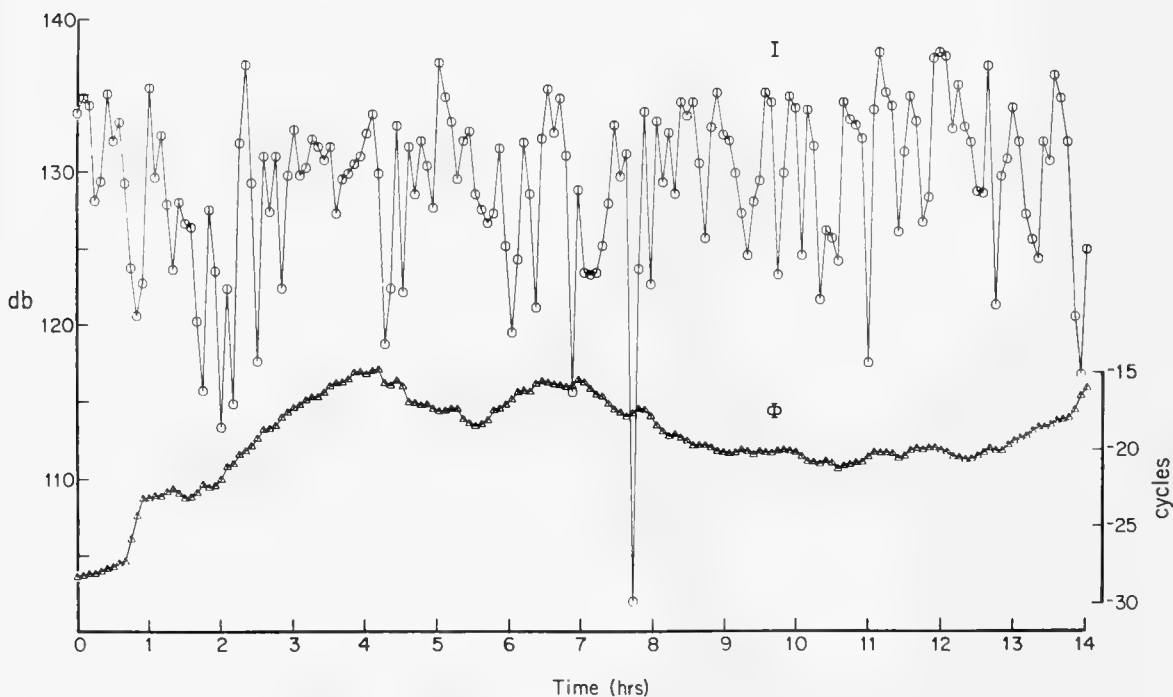


FIG. 2. A 14-h sample of intensity I and phase Φ drawn on an enlarged scale.

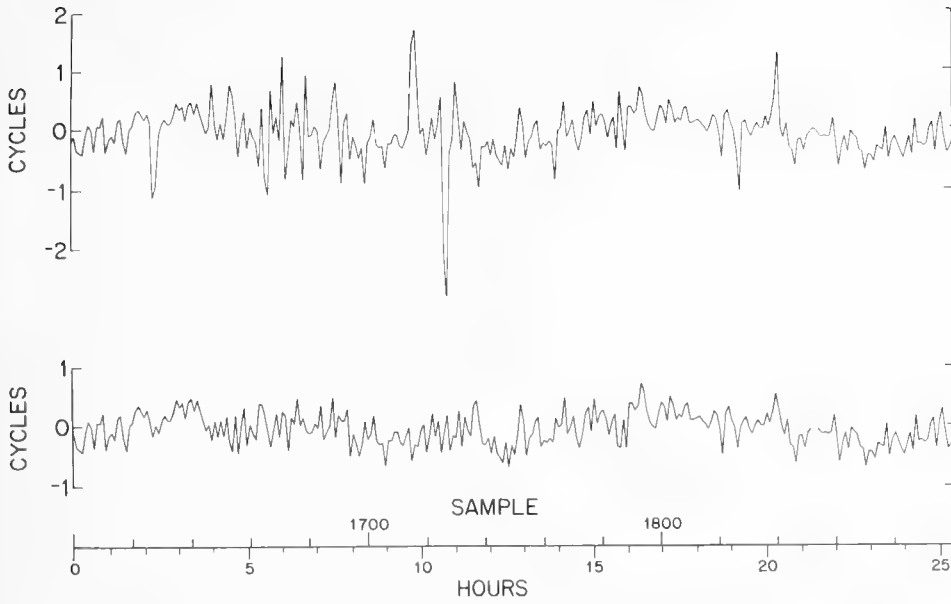


FIG. 3. Bermuda phase differences $\delta\phi$ before (top) and after adjustment (bottom).

learn that sampling at $\frac{1}{2}$ -min intervals would have avoided all ambiguities. As it is, the 5-min averaging suppresses the high frequencies, and the phase ambiguities dominate the low frequencies.

II. THE STATISTICAL MODEL

We shall compare the observed data with a crude statistical model of a multipath acoustic signal. In the model, the components of the signal are

$$X = \sum_{i=1}^n X_i, \quad (5)$$

$$Y = \sum_{i=1}^n Y_i,$$

resulting from the superposition of n single-path components

$$X_i = R_i \cos \phi_i, \quad (6)$$

$$Y_i = R_i \sin \phi_i.$$

The amplitudes R_i and phases ϕ_i of the single-path components are independent random variables. We use the notation $\langle \rangle$ to indicate a statistical average over all single path signals simultaneously, while $\langle \rangle_i$ denotes an average over the R_i and ϕ_i in one single path. We make three further assumptions concerning the single-path signals:

(1) Fluctuations in phase are more important than fluctuations in amplitude, or in symbols (with dot accent designating d/dt)

$$\langle \dot{R}_i^2 \rangle_i \ll \langle R_i^2 \rangle_i \langle \dot{\phi}_i^2 \rangle_i. \quad (7)$$

(2) The time scale $(\dot{\phi}_i)^{-1}$ for a phase ϕ_i to change by 1 rad is on the average short compared with the time scale $(\phi_i/\dot{\phi}_i)$ for the phase variation to change direction, or in symbols

$$\langle \ddot{\phi}_i^2 \rangle_i \ll \langle \dot{\phi}_i^4 \rangle_i. \quad (8)$$

(3) Each phase velocity $\dot{\phi}_i$ is a Gaussian random variable, so that

$$\langle \dot{\phi}_i^4 \rangle_i = 3(\langle \dot{\phi}_i^2 \rangle_i)^2. \quad (9)$$

In Appendix A it is verified that property (2) holds for the single-path phases predicted by the ocean model which we describe in Sec. IV. Properties (1) and (3) also hold in the same model. We suppose that the fre-

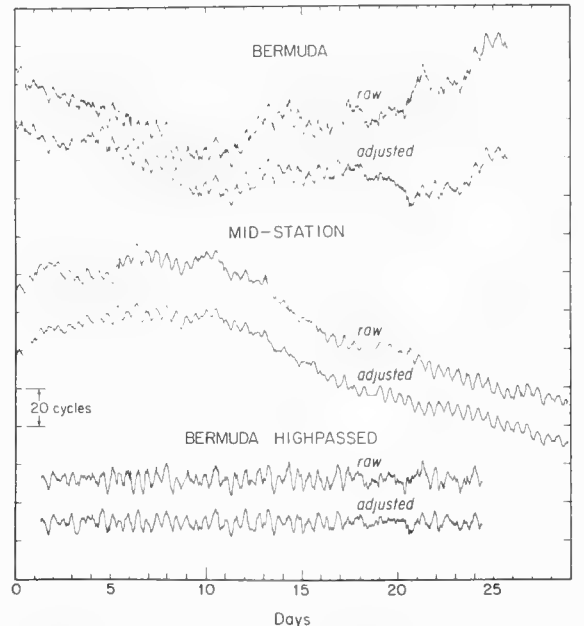


FIG. 4. Bermuda and midstation phases before and after adjustment.

TABLE I. Adjusted phase and intensity statistics at 406 Hz for data interval $\delta t = 5.0394$ min. The columns marked ∞ , 20, 10 correspond to the suppression of fades exceeding ∞ (no change), 20, 10 dB, respectively. X , Y , $R = (X^2 + Y^2)^{1/2}$ in arbitrary pressure units; to correct to absolute level (dB/ μ B), subtract 169.0 dB for midstation and 173.0 dB for Bermuda.

	Midstation			Bermuda		
Range from Eleuthera (km)	550 (nominal)			1250		
Record length	8255 terms = 29.0 days			7366 terms = 25.8 days		
$\langle \dot{\phi}^2 \rangle$, $\langle (\delta \dot{\phi})^2 \rangle$ (cycles ²)	548, 0.029			110, 0.060		
F (dB)	∞	20	10	∞	20	10
Number of terms replaced	0	114	1076	0	79	746
$\langle X^2 \rangle$ ($\times 10^{-13}$)	8.73	8.73	8.79	0.668	0.667	0.671
$\langle Y^2 \rangle$ ($\times 10^{-13}$)	8.70	8.70	8.76	0.655	0.655	0.659
$\langle (\delta X)^2 \rangle$ ($\times 10^{-13}$)	6.08	6.08	6.14	0.797	0.797	0.806
$\langle (\delta Y)^2 \rangle$ ($\times 10^{-13}$)	5.92	5.92	5.98	0.790	0.791	0.799
$\langle R^2 \rangle$ ($\times 10^{-13}$)	17.43	17.43	17.55	1.323	1.322	1.330
I_0 (dB)	142.41	131.22
$\langle I \rangle$ (dB)	139.22	139.27	139.82	128.61	128.65	129.06
$\langle I^2 \rangle - \langle I \rangle^2$ (dB ²)	38.79	35.87	23.37	31.84	30.18	22.52
$\langle (\delta I)^2 \rangle$ (dB ²)	24.10	21.77	13.09	48.17	45.31	30.34
$\langle \delta I \cdot \delta \dot{\phi} \rangle$ (dB cycles)	0.55	0.52	0.38	1.15	1.13	0.92

quency ν defined by

$$\nu^2 = \langle \dot{\phi}_i^2 \rangle_i \quad (10)$$

is the same for every single-path signal. The root-mean-square multipath signal amplitude μ is defined by

$$\mu^2 = \sum_i \langle R_i^2 \rangle_i. \quad (11)$$

It turns out that all important statistical properties of the multipath signals are determined by the parameter ν .

III. CARTESIAN STATISTICS

The statistical model of Sec. II predicts a covariance function for the multipath signal X which is a sum of contributions from the single-path components, namely,

$$\langle X(t)X(t+\tau) \rangle = \sum_i \langle R_i^2 \rangle_i \langle \cos \phi_i(t) \cos \phi_i(t+\tau) \rangle_i. \quad (12)$$

Now we assume that for each single-path the root-mean-square phase fluctuations are of the order of one cycle or larger, that is to say

$$\langle [\phi_i(t)]^2 \rangle_i > (2\pi)^2. \quad (13)$$

This is not really an additional assumption but is already implied by (8). [The ocean model (Sec. IV) gives rms $\phi_i = 8\pi$ for Bermuda.] We are also assuming that the single-path phase differences $[\phi_i(t) - \phi_i(t+\tau)]$ are Gaussian random variables, with a variance

$$\langle [\phi_i(t) - \phi_i(t+\tau)]^2 \rangle_i \cong \nu^2 \tau^2, \quad (14)$$

according to Eq. (10). Putting together Eqs. (12), (11), and (14), we find

$$\langle X(t)X(t+\tau) \rangle = \frac{1}{2} \mu^2 \exp(-\frac{1}{2} \nu^2 \tau^2). \quad (15)$$

The Fourier transform of this quantity is the spectrum of $X(t)$, namely,

$$F_X(\omega) = (2\pi)^{-1/2} \langle \mu^2 / \nu \rangle \exp(-\frac{1}{2} \omega^2 / \nu^2); \quad (16)$$

and similarly for $F_Y(\omega)$. The advantage of the Cartesian spectra over the more traditional polar coordinate representation involving intensity and phase (to be discussed later) is that the Cartesian multipath and singlepath spectra are simply related. It is disappointing that the inequality (13) applies, so that the Cartesian statistics (single path or multipath) provide only such limited information about the ocean medium, namely, the two parameters μ and ν . (This limitation would not apply at short ranges or low frequencies.)

Figure 5 shows the Cartesian spectra with plots of Eq. (16) drawn for indicated values of ν^{-1} . An alternative method for estimating the value of ν is to use the formula

$$\nu^2 = \frac{\langle X^2 \rangle + \langle Y^2 \rangle}{\langle X^2 \rangle + \langle Y^2 \rangle}. \quad (17)$$

The values so inferred are summarized in the first two lines of Table II.

IV. INTERNAL WAVES

These values can be compared with those derived from a theory of sound propagation through a fluctuating stratified ocean. Starting with a spectrum of internal waves⁵ empirically derived from various oceanographic measurements, Munk and Zachariasen⁶ obtain

$$\langle \dot{\phi}_i^2 \rangle_i = 8\pi^{-2} \langle (\delta C/C)^2_{\mathbf{a}1s} \rangle q^2 B R \omega_{1s} n_0 \ln(n_{\mathbf{a}1s}/\omega_{1s}) \langle j^{-1} \rangle, \quad (18)$$

for a ray along the sound axis. Here n_0 , $n_{\mathbf{a}1s}$ are values of the buoyancy frequency at the surface and sound axis, and $\delta C/C$ is the sound velocity perturbation due to internal waves, q is acoustic wavenumber, B the scale depth of stratification ($dn/dz = -z/B$), R is range, ω_{1s} is inertial frequency, and j is the internal wave

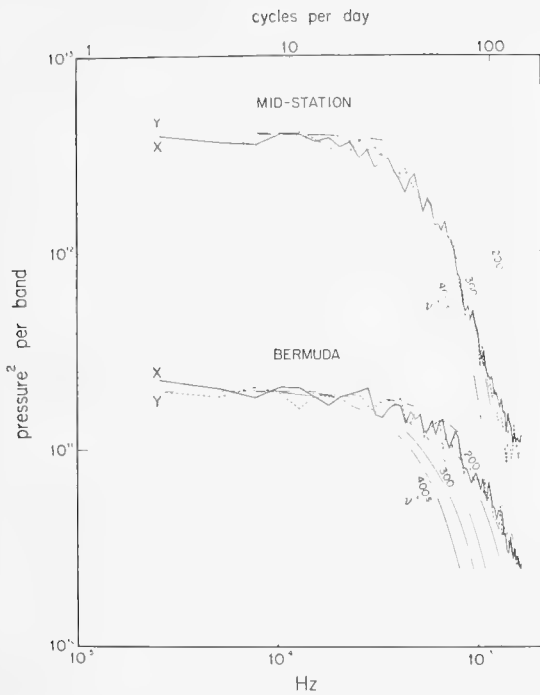


FIG. 5. Spectra of the Cartesian pressure components X , Y (in arbitrary units) per bandwidth 2.58×10^{-5} Hz. The computed curves are drawn for indicated values of ν^{-1} in seconds.

mode number. An internal-wave-weighted average of j^{-1} equals $\langle j^{-1} \rangle = 0.44$, 0.34 for a mode scale number $j_*=3, 5$, respectively. The values so computed are in very close agreement to those inferred from the acoustic observations (Table II). A detailed calculation allowing for the proper ray mix leads to somewhat larger values.

The important feature is that there are no free parameters in this comparison between observed and computed values. We conclude that internal waves consistent with oceanographic observations can account for the measured acoustic fluctuations. Considering the idealization of the ocean model the agreement is rather too close. In particular, the assumed exponential stratification and resulting canonical sound channel fail to allow for the important intrusion of Mediterranean water. For further detail we refer to the original paper.

V. PHASE AND INTENSITY STATISTICS

The observed data (for example, Figs. 1 and 2) are customarily plotted in terms of intensity and phase. We are therefore interested in calculating the statistical behavior of ϵ and ϕ predicted by our model, these quantities being related to the Cartesian amplitudes by Eqs. (6)–(8). The statistical behavior of ϵ and ϕ is dominated by the effects of “fade outs,” which are brief periods during which both X and Y are small and ϕ is rapidly changing. It is convenient to define a fade-out precisely as a time interval in which

$$R < \epsilon \mu, \quad (19)$$

where ϵ is an arbitrarily chosen threshold fraction, and μ is the root-mean-square value of R according to Eq. (11). (The multipath intensity drop $F = 20 \log_{10} \epsilon^{-1}$ dB, so $\epsilon = 0.1$ corresponds to a 20-dB fade-out.) If the number n of single-path signals is large enough, we expect to find the statistical behavior of the multipath fade-outs to be independent of the details of the single-path components. We conjecture that “large enough” means only that (1) $n \geq 3$, and (2) no one single-path component dominates the others. The conditions appear to be amply fulfilled⁶: $n = 14, 34$ for midstation and Bermuda, respectively, and the relative contributions among these paths varies by less than a factor of two.

We assume that n is “large enough” so that the multipath components X and Y and their rates-of-change \dot{X} and \dot{Y} are independent Gaussian random variables. We then have two numerical predictions for the behavior of ϵ and ϕ . The statistical variance of ϵ is

$$\langle \epsilon^2 \rangle - \langle \epsilon \rangle^2 = \pi^2/6, \quad (20)$$

and so rms $I = \pi^{1/2} 10/\ln 10 = 5.57$ dB as compared to the measured values 6.2 and 5.6 dB for midstation and Bermuda, respectively. The correlation between the rates of change of ϵ and ϕ is

$$C = \frac{\langle \dot{\epsilon} \dot{\phi} \rangle}{(\langle \dot{\epsilon}^2 \rangle \langle \dot{\phi}^2 \rangle)^{1/2}} = \frac{2}{\pi} = 0.63, \quad (21)$$

as compared to 0.66 and 0.68 for midstation and Bermuda. The relations (20) and (21) are independent of the details of the fade-outs, but to obtain further information about the behavior of ϵ and ϕ we must examine the fade-outs more closely. The model predicts the following statistical properties of fade-outs.

- (1) The fraction of time occupied by fade-outs is

$$p(\epsilon) = \epsilon^2. \quad (22)$$

- (2) The average duration of a fade-out is

$$\tau = \frac{1}{2} \pi^{3/2} \epsilon \nu^{-1}. \quad (23)$$

- (3) The average interval between fade-outs is

$$T = [\tau/p(\epsilon)] = \frac{1}{2} \pi^{3/2} (\epsilon \nu)^{-1}. \quad (24)$$

To form an easily visualizable picture of the fade-out process, we suppose that the signal components (X, Y) drift past zero at uniform speed during the fade-out interval. For this uniform-drift picture to be approximately valid, we require that the change in the speed

TABLE II. Comparison between measured and computed values of ν = rms $\dot{\phi}$.

	ν (sec ⁻¹)	
	Midstation	Bermuda
Acoustic measurements (MIMI)		
Fig. 5	2.8×10^{-3}	4.0×10^{-3}
Eq. (17)	2.8×10^{-3}	3.7×10^{-3}
Theory based on internal wave model ⁵		
Eq. (18) for $j_*=3$	2.9×10^{-3}	4.4×10^{-3}
Ray mix for $j_*=3$	3.5×10^{-3}	5.2×10^{-3}

TABLE III. Computed fade-out statistics.

	Midstation, $\nu^{-1} = 5.9$ min			Bermuda, $\nu^{-1} = 4.2$ min		
	$F = \infty$,	20,	10 dB	$F = \infty$,	20,	10 dB
Fractional time (Eq. 22)	0	10^{-2}	10^{-1}	0	10^{-2}	10^{-1}
Duration (Eq. 23)	0	1.6	5.3 min	0	1.1	3.7 min
Interval (Eq. 24)	∞	165	53 min	∞	111	37 min

\dot{X} during the interval be less than \dot{X} itself. In terms of statistical averages, we require

$$\tau^2 \langle \ddot{X}^2 \rangle < \langle \dot{X}^2 \rangle. \quad (25)$$

Now our assumptions (7), (8), (9) imply

$$\langle \dot{X}^2 \rangle = \frac{3}{2} \mu^2 \nu^4, \quad \langle \ddot{X}^2 \rangle = \frac{1}{2} \mu^2 \nu^2, \quad (26)$$

and therefore the condition (25) becomes

$$\frac{3}{4} \pi^3 \epsilon^2 < 1. \quad (27)$$

The condition is barely satisfied with $\epsilon = 0.1$, and so we assume in the following discussion that $\epsilon \leq 0.1$ ($F \geq 20$ dB).

The computed fade-out statistics (Table III) for 10-dB fades do not satisfy this condition. Further, the 5-min averages in the observations will suppress most of the 20 dB and a good fraction of the 10-dB fade-outs. Thus, there is little left for a quantitative comparison. The computed durations are consistent with the observation that for midstation 92% (61%) and for Bermuda 100% (90%) of the 20- (10-) dB fade-outs consist of single terms, that is, the duration is less than 5 min. We expect to miss most of the 20-dB fade-outs, and many of the 10-dB fade-outs, particularly at Bermuda. In fact, 97 (567) were observed at midstation compared to 275 (860) computed, and 34 (375) at Bermuda compared to 371 (1125) computed. All one can say is that the results do not contradict the computations, but for adequate studies one will need to sample at least once per minute.

VI. RANDOM WALK AND SPECTRA

We picture the movement of the multipath signal (X, Y) as a two-dimensional zig-zag random walk, shown schematically in Fig. 6. The track is composed of discrete straight segments of mean duration t_c (to be estimated). We assume that the motion in each segment is uniform and that the tracks in different segments are uncorrelated. Then the behavior of the multipath phase ϕ is defined if we assign a probability distribution $Q(\theta)d\theta$ for finding a phase change $\Delta\phi$ in the range $[\theta, \theta + d\theta]$ in a given segment of track. Values of $\Delta\phi$ close to $\pm\pi$ are associated with fade-outs.

The zig-zag walk model is not intended as a quantitative representation of reality but only as a guide to the analysis of observations. In particular, it does not make sense to try to compute the distribution function $Q(\theta)$ exactly. We have two pieces of information about $Q(\theta)$.

(1) The probability of a fade-out in any one segment of the track is

$$4\epsilon\pi^{1/2} Q(\pi) = (t_c/T), \quad (28)$$

where T is the interval between fade-outs given by Eq. (24). We thus obtain the estimate

$$Q(\pi) = (2\pi^2)^{-1} \nu t_c. \quad (29)$$

(2) The average phase change per segment is related to the mean value of $|\dot{\phi}|$ which we obtain from Eqs. (11) and (26):

$$\langle \Delta\phi \rangle = \int |\dot{\phi}| Q(\theta) d\theta = \langle |\dot{\phi}| \rangle t_c = \nu t_c. \quad (30)$$

We assume for $Q(\theta)$ the simple form

$$Q(\theta) = (2\pi)^{-1} (1 + b \cos \theta), \quad (31)$$

and use the two conditions (29) and (30) to determine the two parameters t_c and b . The result is

$$b = \pi^2(2\pi^2 - 4)^{-1} = 0.63, \quad (32)$$

$$\nu t_c = \pi(1 - b) = 1.17.$$

The mean-square phase change per segment is

$$\langle (\Delta\phi)^2 \rangle = \int \theta^2 Q(\theta) d\theta = \frac{1}{3} \pi^2 - 2b = 2.04. \quad (33)$$

This means that the root-mean-square phase change per segment of track is 1.43 rad or 82°. Over a time t long compared with t_c the mean-square phase wander is

$$\begin{aligned} \langle [\phi(t) - \phi(0)]^2 \rangle &= a \nu t, \\ a &= \frac{\langle (\Delta\phi)^2 \rangle}{\nu t_c} = \frac{2\pi(\pi^2 - 5)}{3\pi^2 - 12} = 1.74. \end{aligned} \quad (34)$$

The model is of course very crude; from a numerical experiment (Sec. VII) we find

$$\langle [\phi(t) - \phi(0)]^2 \rangle = 2.78 \nu t.$$

Over a month's duration the expected random phase walk

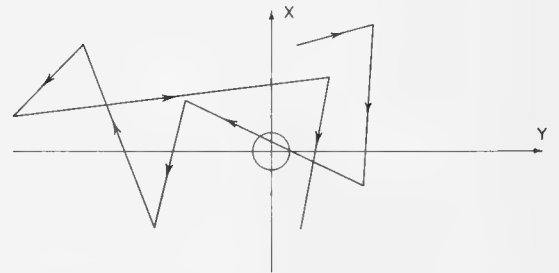


FIG. 6. Random-walk model of multipath signal in the (X, Y) plane. A fade-out occurs when the track crosses the small circle of radius $\epsilon\mu$.

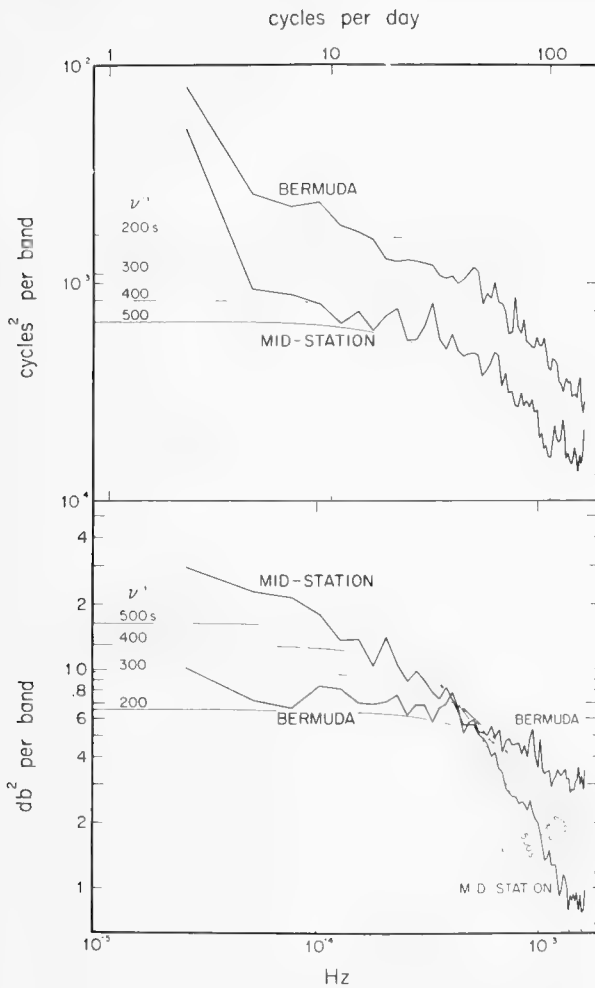


FIG. 7. Spectra of phase difference and intensity (bandwidth 0.915 cpd). The computed curves are drawn for indicated values of ν^{-1} in seconds. The area under the intensity spectra (e.g., the mean-square fluctuations) is independent of ν .

is by $(2.78 \nu t)^{1/2}/2\pi = 20-30$ cycles (for comparison, see Fig. 4).

We next obtain from the random walk model predicted spectra for the quantities ϵ and ϕ . The spectrum of the Cartesian components X , Y was already given by (13) in Sec. III.

The high-frequency spectra of ϵ and ϕ are dominated by the fade-outs. Each fade-out is approximated by a segment of track in which the Cartesian components (X, Y) move linearly, so that

$$\epsilon(t) = \ln[V^2(t - t_m)^2 + R^2], \quad (35)$$

$$\phi(t) = \arctan[V(t - t_m)/R] + \text{const}, \quad (36)$$

where V , R and t_m are random variables. Taking Fourier transforms of Eqs. (35) and (36) and averaging over the variables V , R , t_m , we find the spectra

$$F_\phi(\omega) = \frac{1}{4} F_\epsilon(\omega) = \frac{1}{2} \nu^2 \omega^{-3} \quad (37)$$

valid at high frequencies when $\omega \gg \nu$. In performing these averages we used the probability distribution of

fade-outs given by Eqs. (22) and (24).

The spectrum at low frequencies will be dominated by the phase-wandering described by Eq. (34). The Fourier transform of Eq. (34) gives

$$F_\phi(\omega) = (a\nu/\pi) \omega^{-2}, \quad (38)$$

for $\omega \ll \nu$. In the case of ϵ , we expect $F_\epsilon(\omega)$ to be finite at low frequencies since $\epsilon(t)$ does not wander but remains bounded as $t \rightarrow \infty$. We know the total variance of ϵ from Eq. (20), so that

$$\int_0^\infty F_\epsilon(\omega) d\omega = (\pi^2/6). \quad (39)$$

Spectra consistent with Eqs. (37)–(39) are

$$F_\phi(\omega) = \frac{1}{2} \nu^2 \omega^{-2} [\omega^2 + c^2 \nu^2]^{-1/2}, \quad (40)$$

$$F_\epsilon(\omega) = 2\nu^2 [\omega^2 + 12\pi^2 \nu^2]^{-3/2},$$

where $c = \frac{1}{2} \pi a^{-1} = 0.90$. Both spectra show the expected transition from low- to high-frequency behavior at $\omega \approx \nu$.

We cannot expect this crude model to give exact quantitative information about the spectra. Accordingly we modify Eqs. (38) and (37) to the form

$$F_\phi(\omega) = \alpha \times a \nu \pi^{-1} \omega^{-2}, \quad (41)$$

$$F_\epsilon(\omega) = \frac{1}{4} F_\phi(\omega) = \beta \times \frac{1}{2} \nu^2 \omega^{-3},$$

for low and high frequencies, respectively. A numerical experiment (Sec. VII) can be fitted to

$$\alpha = 1.6, \quad \beta = 2.0,$$

which gives

$$F_\phi(\omega) = \nu^2 \omega^{-2} (\omega^2 + 1.27 \nu^2)^{-1/2}, \quad (42)$$

$$F_\epsilon(\omega) = 4\nu^2 (\omega^2 + 2.43 \nu^2)^{-3/2}.$$

Figure 7 shows the comparison between the computed spectra (42) and the observed spectra.⁷ The overall agreement is not good. The high phase values at the lowest frequency band (over and above random walk) could be the result of coherent modulation by large-scale ocean features; some of it might be due to tides (Sec. VIII). The predicted ω^{-1} and ω^{-3} rollofs for rate-of-phase and intensity spectra are borne out at midstation. The high-frequency Bermuda intensities are aliased from undersampling.

Computed mean-square variations are

$$\langle \dot{\phi}^2 \rangle = \int_0^{\omega'} F_\phi(\omega) d\omega = \frac{1}{2} \nu^2 \sinh^{-1}(2\omega'/\nu),$$

$$\langle \dot{\epsilon}^2 \rangle = \int_0^{\omega'} F_\epsilon(\omega) d\omega = 2\nu^2 [\sinh^{-1} \alpha - \alpha(1 + \alpha^2)^{-1/2}], \quad (43)$$

$$\alpha = (\pi/2\sqrt{3}) \omega'/\nu,$$

and these become logarithmically infinite as $\omega' \rightarrow \infty$. The upper limit is set by the integration time δt , and crudely $\omega' = 2\pi/\delta t$. Results are given in Table IV.

TABLE IV. Root-mean-square phases and intensities ($\omega' = 0.0208 \text{ sec}^{-1}$).

	Mid station, $\nu^{-1} = 357 \text{ sec}$		Bermuda, $\nu^{-1} = 250 \text{ sec}$	
	rms $\delta\phi$	rms δI	rms $\delta\phi$	rms δI
Computed (Eq. 43)	0.19 cycles	7.0 dB	0.26 cycles	8.9 dB
Observed (Table I)	0.17	4.9	0.25	6.9

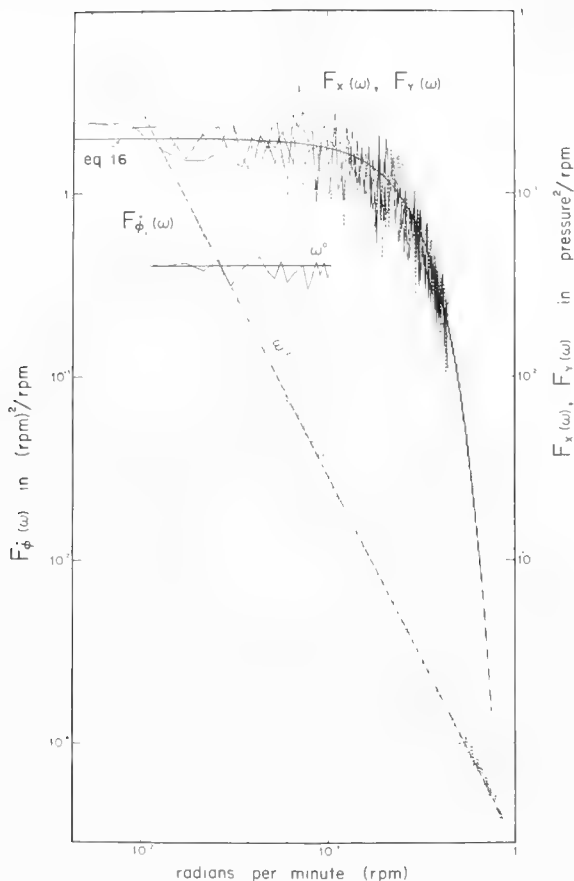


FIG. 8. Computer simulation of multipath statistics. The curves labeled $F_{\dot{\phi}_i}(\omega)$ give the average spectra of the random single-path input functions $\dot{\phi}_i(t)$; solid: a bandlimited (2–24 cpd) uniform spectrum, and dashed: a ω^{-2} spectrum above 2 cpd. For both cases $\langle \dot{\phi}_i^2 \rangle = 1/(5 \text{ min})^2$. The resulting spectra of the multipath Cartesian components $X(t)$ and $Y(t)$ (solid for ω^0 , dashed for ω^{-2}) are in good accord with the predicted Gaussian behavior [Eq. (16)]. At high frequencies the computed spectra are too wiggly to be plotted; they fall within the limits of the shaded band.

VII. NUMERICAL EXPERIMENT

Figures 8 and 9 show the results of numerical experiments. The singlepath series $\delta\phi_i(t)$ were generated from random numbers for two cases: (1) a bandlimited (2–24 cpd) white spectrum and (2) an ω^{-2} spectrum for $\omega > 2$ cpd (computed by accumulating random $\delta^2\phi_i$). The singlepath phase series are formed by $\phi_i(t) = \sum_{i=0}^9 \delta\phi_i(t)$, and the multipath according to

$$X(t) = \sum_{i=1}^{10} R_i \cos\phi_i = R \cos\phi, \quad (1)$$

and similarly for $Y(t)$, with R_i arbitrarily set to 0.1. Spectra were computed for X , Y , ϕ , $\dot{\phi}$. This computation was repeated ten times (using, of course, different random noise series), and an average of the spectra so obtained has been plotted. The results are essentially the same for the ω^0 and ω^{-2} spectra of $\dot{\phi}_i$ (which bracket the theoretical ω^{-1} spectrum⁵), as expected.

For both cases we have taken $\nu^2 = \langle \dot{\phi}_i^2 \rangle = 1/(5 \text{ min})^2$,

representative of MIMI. The input series consist of 2880 terms each, interpreted as a one-day record at $\frac{1}{2}$ -min intervals. This sampling rate δt was chosen by trial and error to avoid ambiguities in multipath phase during occasional fade-outs. It would thus appear that $\nu\delta t = \frac{1}{10}$ would give adequate sampling for a field experiment.

Figure 8 shows the average of the 100 input spectra, and the associated Cartesian spectra according to Eq. (16); these provide a check on the numerical experiment. The spectra $F_i(\omega)$ and $F_{\dot{\phi}_i}(\omega) = \omega^2 F_{\phi_i}(\omega)$ in Fig. 9 have been fitted by Eqs. (42).

VIII. TIDES

The tidal contribution to the acoustic fluctuations has been emphasized in the literature,⁸ perhaps because of a superficial resemblance of the phase fluctuation $\phi(t)$ to tidal records (Fig. 4). Our conclusion is that tides play a significant but not dominant role. We shall discuss three hypotheses: a coherent modulation of the acoustic transmission by surface tides; a coherent modulation by internal tides at the terminals; an incoherent modulation by internal tides along the entire transmission path. Unfortunately, the evidence does not lead to a clear-cut decision.

For orientation we have put together an order-of-magnitude summary (Table V) of amplitudes of tides and internal waves (a rash extrapolation of recent com-

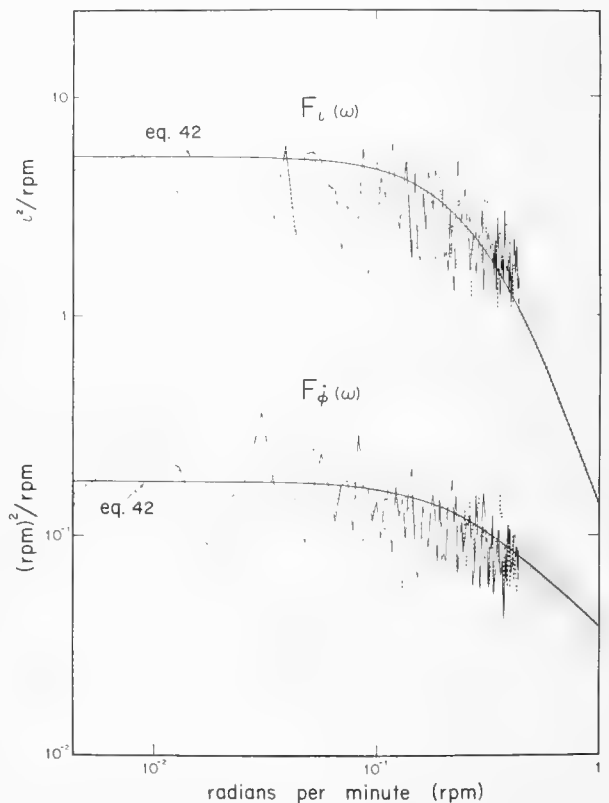


FIG. 9. Spectra of multipath intensity and rate of phase from the numerical experiment, corresponding to $F_{\dot{\phi}_i}(\omega) \sim \omega^0$ (solid) and ω^{-2} (dashed), respectively.

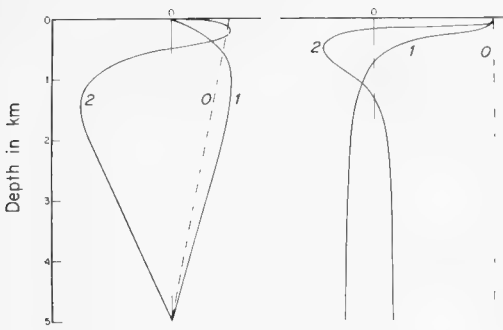


FIG. 10. Profiles of vertical displacement ζ (left) and horizontal velocity u (right) for surface (mode 0) and internal (1, 2) tides. Scale is arbitrary.

pilations⁹). For the internal continuum estimates are based on a recent version of the GM75 model.⁵ All phases are considered random, and so the totals are summations in squared amplitudes. Actual values depend on the local temperature and salinity profiles, and vary considerably from place to place. Mode numbers refer to the number of zero crossings of the horizontal current $u(z)$ (Fig. 10). Here we distinguish between surface tides (mode 0) with a uniform current from top to bottom, and internal waves and tides (modes 1, 2, ...). Surface tides have wave lengths of 3000 km, internal tides 100, 60 km for modes 1, 2. Surface tides are known to be sharply peaked at M_2 frequency; internal tides are intermittent and broadened.

The sound velocity is perturbed by both vertical displacement and horizontal currents:

$$\delta C/C \approx (10, 1, 0.01) \times 10^{-5}$$

for $\zeta = 1$ m, at depths of 0.1, 1, 4 km ,

$$\delta C/C \approx 0.7 \times 10^{-5}, \quad \text{for } u = 1 \text{ cm/sec, at all depths .}$$

For surface tides it would appear that for a typical ray path the u effect dominates, but for internal waves and tides the ζ effect clearly dominates except at abyssal depths. Further, most of the u energy (but only a fraction of the ζ -energy) is at inertial frequencies, yet we will show that there is no discernible inertial peak in the acoustical spectra.

To study tidal and inertial effects we need to analyze the acoustic records at high resolution. Accordingly the records were divided into the initial and final one-half months (somewhat overlapping for Bermuda), and the spectra computed for each harmonic. In this way the spectra are computed at precisely the frequencies of major tidal constituents. The two spectra are combined for obtaining the average power in each band. The statistical reliability is manifestly poor; there are only two degrees of freedom in the fortnightly analysis, and somewhat less than four degrees in the combined analysis. Phase spectra (Table V) show a significant semidiurnal tidal peak, Cartesian spectra (Table VII) do not. (ζ spectra likewise have no tidal peak.) We estimate 2.5 square cycles (subtracting background) in the semidiurnal Φ peak at Bermuda, as compared to a total variance of 35 square cycles (excluding subinertial drift). For the important $\delta\Phi$ spectrum, tides account for 4×10^{-3} square cycles out of a total of 60×10^{-3} square cycles.

The simplest interpretation is that *the current associated with surface tides (wavelength 3000 km) coherently modulates phase along all paths*. The travel time R/C is modified by a fraction u/C , and

$$\Delta\Phi = 2\pi\sigma(R/C)(u/C) = 2.3 \text{ cycles ,}$$

for $2\pi\sigma = 406$ Hz, $R = 1250$ km, $u = 1$ cm/sec, $C = 1.5$ km/sec. As a model of coherent phase modulation, set

TABLE V. Representative magnitudes in the Northwest Atlantic for the vertical displacement ζ and horizontal velocity u of tides and internal waves at thermocline, sound channel and abyssal depths ($h = 0.1, 1, 4$ km). See text.

Designation (mode)	surface (0)		internal (1)		internal (2)		internal \sum_I^∞	
$h(\text{km})$	$\zeta(\text{m})$	$u(\text{cm/sec})$	$\zeta(\text{m})$	$u(\text{cm/sec})$	$\zeta(\text{m})$	$u(\text{cm/sec})$	$\zeta(\text{m})$	$u(\text{cm/sec})$
<i>Diurnal tides</i>								
0.1	0.1	0.2						
1	0.08	0.2	20%–30% of semidiurnals					
4	0.02	0.2						
<i>Semidiurnal</i>								
0.1	0.5	1	1.4	0.9	1.2	0.8	3	2
1	0.4	1	2.3	0.3	2	0.2	5	.6
4	0.1	1	4.6	0.2	4	0.2	10	.5
<i>Inertial cusp ($\omega_1 < \omega < 2\omega_1$)</i>								
0.1			1.8	2.8	1.6	2.4	4	6
1	small		3.2	1.8	2.8	1.6	7	4
4			15	0.5	13	0.4	33	1
<i>Total continuum (including cusp)</i>								
0.1			3.2	3.2	2.8	2.8	7	7
1	no estimate		5.5	1.8	4.8	1.6	12	4
4			23	0.5	20	0.4	50	1

TABLE VI. Spectra of phase difference $\delta\Phi$ and phase Φ in cycles² per band (band width is 0.072 cpd=2/month). The spectra of phase difference are given separately for the first and second fortnight.

Bermuda					Midstation			
cpd	1st.	$\delta\Phi$ 2nd	Comb.	Φ Comb.	1st	$\delta\Phi$ 2nd	Comb.	Φ Comb.
Subinertials								
0.07	0.05×10^{-3}	0.10×10^{-3}	0.07×10^{-3}	54.38	0.07×10^{-3}	0.01×10^{-3}	0.04×10^{-3}	46.65
0.14	0.08	0.05	0.07	7.40	0.04	0.00	0.02	14.81
0.21	0.07	0.00	0.04	1.86	0.04	0.01	0.02	6.83
0.29	0.03	0.04	0.03	3.94	0.01	0.01	0.01	4.29
0.36	0.06	0.12	0.09	2.21	0.08	0.00	0.04	2.54
0.43	0.02	0.08	0.05	1.49	0.07	0.01	0.04	2.48
0.50	0.09	0.01	0.05	0.99	0.01	0.01	0.01	0.78
0.57	0.01	0.04	0.02	0.69	0.01	0.02	0.02	0.91
0.64	0.06	0.02	0.04	0.27	.00	0.02	0.01	0.36
0.72	0.11	0.04	0.08	0.77	.01	0.01	0.01	0.45
0.79	0.06	0.00	0.03	0.32	.02	0.03	0.02	0.35
			0.57×10^{-3}	74.32			0.24×10^{-3}	80.45
Diurnals								
Inertials	0.86	0.02×10^{-3}	0.11×10^{-3}	0.29	0.01×10^{-3}	0.00×10^{-3}	0.01×10^{-3}	0.30
	0.93(O_1)	0.07	0.03	0.15	0.05	0.00	0.03	0.30
	1.00(K_1)	0.04	0.23	0.14	0.02	0.03	0.03	0.16
	1.07	0.12	0.04	0.08	0.12	0.01	0.05	0.23
	1.14	0.10	0.08	0.09	0.09	.03	0.06	0.26
	1.21	0.06	0.16	0.11	0.36	.03	0.03	0.35
	1.29	0.20	0.02	0.11	0.29	0.10	0.08	0.21
	1.36	0.17	0.10	0.14	0.13	.02	0.01	0.12
			0.78×10^{-3}	1.86			0.30×10^{-3}	1.93
Semidiurnals								
1.60	0.27×10^{-3}	0.13×10^{-3}	0.20×10^{-3}	0.28	0.03×10^{-3}	0.10×10^{-3}	0.06×10^{-3}	0.06
1.66	0.05	0.31	0.18	0.24	0.14	0.22	0.18	0.04
1.73	0.81	0.40	0.61	0.34	0.04	0.05	0.04	0.20
1.80	0.23	0.21	0.22	0.25	0.01	0.29	0.15	0.14
1.86	3.44	1.83	2.63	1.84	0.13	0.89	0.51	0.16
1.93(M_2)	0.87	1.91	1.39	0.86	3.08	1.62	2.35	1.64
2.00(S_2)	1.88	0.17	1.02	0.53	0.64	2.12	1.38	0.79
2.06	0.71	0.42	0.57	0.32	0.01	0.24	0.13	0.24
2.13	0.19	0.30	0.24	0.17	0.01	0.06	0.03	0.03
2.19	0.44	0.13	0.29	0.08	0.01	0.06	0.04	0.10
			7.35×10^{-3}	4.91			4.87×10^{-3}	3.40
Total Variance, ¹⁰ all frequencies								
Fortnight	60×10^{-3}	60×10^{-3}	60×10^{-3}	90	31×10^{-3}	27×10^{-3}	29×10^{-3}	98
Total			60×10^{-3}	110			29×10^{-3}	548

$$Re^{j\Phi} = \sum_i R_i e^{j(\Phi_i + \Delta\Phi)} = e^{j\Delta\Phi} \sum_i R_i e^{j\Phi_i}, \quad j = \sqrt{-1}, \quad (44)$$

and so the multipath phase is rotated by the single-path phase shift $\Delta\Phi$. The measured 2.5 square cycles in the semidiurnal tidal peak of multipath phase corresponds to an amplitude of $\sqrt{2 \times 2.5} = 2.2$ cycles, in close agreement with the computed 2.3 cycles for a typical tidal current. But for the Cartesian multipath, the tidal energy peak is reduced by the number of paths ($n = 34$ for Bermuda) and should no longer be discernible. So the hypothesis is in very satisfactory agreement with observations.

But it turns out that the MIMI propagation path runs through the MODE expedition area,¹¹ the only place

where a grid of deep-sea tidal pressure measurements have ever been taken (Fig. 11). Currents can be computed from the pressure gradients. M_2 tidal currents have amplitude close to 1 cm/sec, but the MIMI path is almost at right angles to the major axis of the tidal ellipse, and the MIMI component is small and poorly determined (Table VIII). (A computer model of tides¹² has the minor axis in opposite phase.) We expect the tidal phase (Greenwich epoch °G) of maximum current towards Bermuda to coincide with minimum acoustic phase; i.e., $180^\circ + ^\circ G$ for $\Phi(t)$ should be about 180° to agree with MODE measurements. In fact, phases vary from fortnight to fortnight; there is no resemblance between midstation and Bermuda.

The variability from fortnight to fortnight of a

TABLE VII. Power per band (bandwidth is 0.072 cpd=2/month of $F_X(\omega)+F_Y(\omega)$ for the first and second fortnight, and for the combined record.

		Bermuda			Midstation			
		cpd	1st	2nd	Comb.	1st	2nd	Comb.
Subinertials								
0.07		0.34×10 ¹¹	0.24×10 ¹¹	0.29×10 ¹¹	0.51×10 ¹²	0.14×10 ¹²	0.32×10 ¹²	
0.14		0.12	0.22	0.17	0.12	0.60	0.36	
0.21		0.22	0.07	0.15	0.65	0.43	0.54	
0.29		0.12	0.08	0.10	0.10	0.24	0.17	
0.36		0.02	0.17	0.08	0.43	0.07	0.24	
0.43		0.23	0.19	0.21	0.06	0.37	0.22	
0.50		0.12	0.04	0.08	0.46	0.10	0.28	
0.57		0.08	0.18	0.13	0.37	0.30	0.33	
0.64		0.17	0.16	0.16	0.16	0.29	0.22	
0.72		0.15	0.04	0.09	0.08	0.17	0.13	
0.79		0.13	0.53	0.33	0.36	0.44	0.40	
		1.70	1.91	1.80	3.28	3.17	3.23	
Diurnals								
Inertials	0.86	0.27×10 ¹¹	.24×10 ¹¹	0.25×10 ¹¹	0.24×10 ¹²	0.15×10 ¹²	0.20×10 ¹²	
	0.93(<i>O</i> ₁)	0.06	.16	0.11	0.57	0.10	0.34	
	1.00(<i>K</i> ₁)	0.08	.21	0.15	0.15	0.72	0.44	
	1.07	0.29	.12	0.20	0.82	0.47	0.64	
	1.14	0.04	.03	0.04	0.24	0.20	0.22	
	1.21	0.17	.07	0.12	0.36	0.64	0.50	
	1.29	0.10	.11	0.10	0.26	0.10	0.18	
	1.36	0.36	.08	0.22	0.13	0.25	0.19	
		1.37	1.02	1.19	2.78	2.63	2.71	
Semidiurnals								
1.60		0.32×10 ¹¹	0.14×10 ¹¹	0.23×10 ¹¹	0.22×10 ¹²	0.06×10 ¹²	0.14×10 ¹²	
1.66		0.13	0.12	0.13	0.07	0.19	0.13	
1.73		0.21	0.16	0.18	0.24	0.09	0.16	
1.80		0.04	0.08	0.06	0.27	0.05	0.16	
1.86		0.23	0.10	0.17	0.42	0.09	0.25	
1.93 (<i>M</i> ₂)		0.01	0.22	0.11	0.43	0.04	0.23	
2.00 (<i>S</i> ₂)		0.07	0.14	0.10	0.39	0.19	0.29	
2.06		0.19	0.01	0.10	0.89	0.30	0.59	
2.13		0.19	0.04	0.11	0.13	0.05	0.09	
2.19		0.18	0.13	0.16	0.39	0.11	0.25	
		1.57	1.14	1.35	3.45	1.16	2.31	
Total variance, all frequencies								
Fortnightly				132×10 ¹¹	174×10 ¹²			

broadened semidiurnal phase-peak is in line with the known character of *internal* tides. (At Bermuda the spectral peak occurs at one harmonic below *M*₂ frequency.) Internal tides have wavelengths short compared to the acoustic paths, and one would expect them to produce an incoherent phase modulation. An exception might be the terminal effects. Internal tides are generated by conversion from surface to internal modes in regions of prominent bottom topography, which is just where the hydrophones are located. In such regions the internal tides may dominate, whereas in the open sea internal tides typically have 10% of the internal wave energy. Take a large vertical tidal displacement $\xi = 10$ m, corresponding to $\delta C/C = 10^{-4}$ at 1-km depth; then in a near zone of radius $R = \lambda/2\pi$, with $\lambda = 100$ km for the wavelength of the lowest internal tide mode, we have

$$\Delta\Phi = 2\pi\sigma(R/C)(\delta C/C) = 2.6 \text{ cycles.}$$

This suggests that the location of the acoustic source and receiver in the generating area of internal tides may be a significant factor.

TABLE VIII. *M*₂ component of tidal current and acoustic phase.

Tidal current, azimuth 55°		Amplitude	°G
MODE measurements		0.3 cm/sec	180
Parke-Hendershott model		0.5	20
Acoustic phase $\Phi(t)$		Amplitude	180° + °G
Midstation	1st fortnight	1.8 cycles	78
	2nd fortnight	1.1	260
Bermuda	1st fortnight	0.3	105
	2nd fortnight	1.3	179

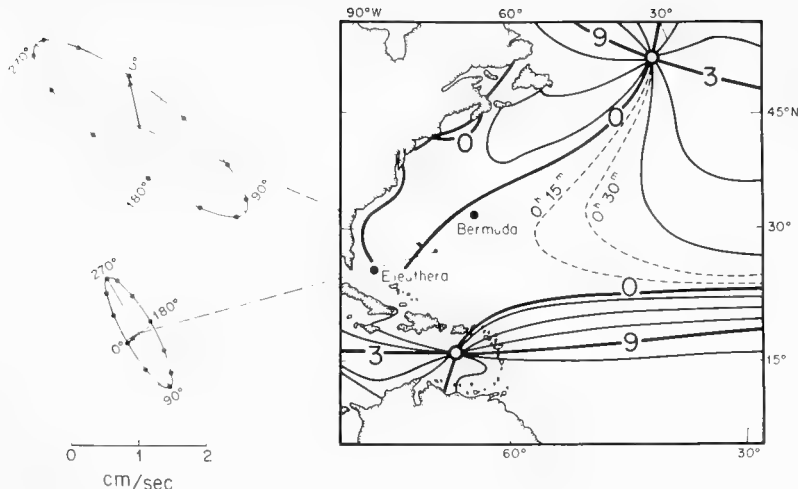


FIG. 11. M_2 tidal currents in MODE area between Eleuthera and Bermuda. The arrow toward $0^\circ G$ refers to the current vector (scale below) when the Moon passes over the Greenwich meridian; $30^\circ G$, $60^\circ G$, ..., refers to other Greenwich epochs. The upper ellipse refers to a computer model by Parke and Hendershott, the lower ellipse is based on deep-sea tide measurements.

Finally, there is the possibility of *incoherent* phase modulation by internal tides along the entire path. This is then analogous to the incoherent modulation by internal waves in general. Internal tides have typically one-third the amplitude of the internal waves (Table V), and so contribute 10% to $\langle \phi_i^2 \rangle$. If this were the only contribution, then because of the periodic input at tidal frequencies ω_T , the multipath spectra would be concentrated at ω_T , $2\omega_T$, $3\omega_T$, ..., and the local energy density would be high. In the presence of internal waves there is interaction with all frequencies, but some remnant of the tidal line spectrum can be expected to remain. The problem needs further consideration.

ACKNOWLEDGMENTS

John Clark and his associates have furnished the acoustic records on which this analysis is based. Flicki Dormer and Betty Ma have carried out the data reduction. Discussions with Ted Birdsall have been most helpful.

APPENDIX A.

Equation (10) can be written

$$\langle \phi_i^2 \rangle = \nu^2 = \nu_0^2 \int_{\omega_{1n}}^n \omega^{-1} d\omega = \nu_0^2 \ln s, \quad (A1)$$

where $s = n/\omega_{1n} \gg 1$. Hence

$$\langle \phi_i^2 \rangle = \nu_0^2 \int_{\omega_{1n}}^n \omega d\omega \approx \frac{1}{2} n^2 \nu_0^2$$

and

$$\frac{\langle \phi_i^2 \rangle}{3 \langle \phi_i^2 \rangle^2} = \frac{n^2}{6 \nu_0^2 \ln s} = 0.03 e^{-2x/b}$$

for $n = n_0 e^{-x/b}$, $n_0 = 5.2 \times 10^{-3} \text{ sec}^{-1}$, $\nu^2 = 3.2 \times 10^{-5} \text{ sec}^{-2}$.

APPENDIX B.

In some oceanic models we may have a relation

$$\langle \phi_i^4 \rangle = f \langle \phi_i^2 \rangle^2, \quad (B1)$$

with a coefficient f replacing the 3 which appears in Eq. (9). In this case the following changes need to be made in the results of Secs. II and III:

$$\langle \ddot{X}^2 \rangle = \frac{1}{2} f \mu^2 \nu^4, \quad (B2)$$

$$\frac{1}{4} f \pi^3 \epsilon^2 < 1, \quad (B3)$$

$$t_c = f^{-1/2} \nu^{-1}, \quad (B4)$$

$$Q(\pi) = (2\pi^2)^{-1} f^{-1/2}, \quad (B5)$$

$$\langle \Delta \phi \rangle = f^{-1/2}, \quad (B6)$$

$$\langle (\Delta \phi)^2 \rangle = (\pi/3) f^{-1/2} + (\pi^2/8) f^{-1/2} (\pi f^{1/2} - 1)^{-1}, \quad (B7)$$

$$\alpha = (\pi/3) + (\pi^2/8) (\pi f^{1/2} - 1)^{-1}. \quad (B8)$$

For example, if $f=9$, $\alpha=1.19$ and $c=\pi/2\alpha=1.32$ in Eq. (40').

APPENDIX C.

The mean-square vertical displacement is given by

$$\langle \xi^2 \rangle = \frac{1}{2} B^2 E \frac{n_0}{n} \int_{\omega_{1n}}^{\infty} \frac{\omega_{1n} (\omega^2 - \omega_{1n}^2)^{1/2}}{\omega^3} d\omega \sum_{j=1}^{\infty} \frac{(j^2 + j_*^2)^{-1}}{J},$$

where

$$J = \sum_{j=1}^{\infty} (j^2 + j_*^2)^{-1} \approx 0.468.$$

The relative contribution

$$\int_{\omega_{1n}}^{\omega} \dots d\omega$$

equals

$$\begin{aligned} \frac{2}{3} - (\sqrt{3}/2\pi) &= 0.39, \quad \text{from } \omega_{1n} \text{ to } 2\omega_{1n} \\ &= 1, \quad \text{from } \omega_{1n} \text{ to } \infty, \end{aligned}$$

whereas the j contributions are

$$0.214, 0.164, 1, \quad \text{for } j=1, j=2, \sum_{j=1}^{\infty}.$$

Similarly,

$$\langle \mu^2 \rangle = \frac{3}{2} B^2 E n n_0 \int_{\omega_{1n}}^{\infty} \frac{4}{3\pi} \frac{\omega_{1n}(\omega^2 + \omega_{1n}^2)}{\omega^3(\omega^2 - \omega_{1n}^2)^{1/2}} d\omega \sum_{j=1}^{\infty} \frac{(j^2 + j_n^2)^{-1}}{J},$$

$$\frac{2}{3} + \frac{1}{2\pi\sqrt{3}} = 0.76, \quad \text{from } \omega_{1n} \text{ to } 2\omega_{1n}$$

$$= 1, \quad \text{from } \omega_{1n} \text{ to } \infty,$$

with the j contributions as before.

*The work on random vector statistics was started during the 1974 JASON Summer Study under the auspices of Stanford Research Institute, supported by the Advanced Research Projects Agency. Subsequent analysis has been supported by the Office of Naval Research.

¹For *Miami-Michigan* project, starting with J. C. Steinberg and T. G. Birdsall, "Underwater Sound Propagation in the Straits of Florida," J. Acoust. Soc. Am. **39**, 301-315 (1966). For a recent paper see J. G. Clark and M. Kronengold, "Long-period fluctuations of CW signals in deep and shallow water," J. Acoust. Soc. Am. **56**, 1071-1083 (1974).

²J. G. Clark, "Ray Propagation in an Underwater Acoustic Channel with Time Varying Stratification," Tech. Rep. ML 70107 (University of Miami, Rosenstiel School of Marine and Atmospheric Science, 1970); I. Dyer, "Statistics of Sound Propagation in the Ocean," J. Acoust. Soc. Am. **48**, 337-345 (1970); J. G. Clark, N. L. Weinberg, and M. J. Jacobson, "Refracted, Bottom-Reflected Ray Propagation in a Channel with Time-Dependent Linear Stratification," J. Acoust. Soc. Am. **53**, 802-818 (1973). H. A. DeFerrari, "Effects of horizontally varying internal wavefields on multipath interference for propagation through the deep sound channel," J. Acoust. Soc. Am. **56**, 40-46 (1974). H. DeFerrari and R. Leung, "Spectrum of phase fluctuations caused by multipath interference," J. Acoust. Soc. Am. **58**, 604-607 (1975).

³Surface scattered arrivals differ in frequency from σ by roughly ± 0.1 Hz (the frequency of ocean waves) and are removed by narrow-band filtering. Bottom-scattered arrivals are greatly attenuated.

⁴In fact the phases were computed 32 times for each 5 min period and then averaged [T. Birdsall (private communication)]; this may account for the reasonable behavior of phase spectra (as compared to intensity spectra) at the high frequency limit. It is the reason for the phase jumps between 5 min readings (Sec. I).

⁵C. J. R. Garrett and W. H. Munk, "Space-Time Scales of

Internal Waves: A Progress Report," J. Geophys. Res. **80**, 291-297 (1975). J. L. Cairns and G. O. Williams, "Internal Wave Observations from a Midwater Float: Part II," J. Geophys. Res. (in press) (1976).

⁶W. H. Munk and F. Zachariasen, "Sound Propagation Through a Fluctuating Stratified Ocean: Theory and Observation," J. Acoust. Soc. Am. (in press) (1976).

⁷Units are a bother, but the usual way out of plotting logarithmically and labeling decibels won't do. $F_{\phi}^*(\omega)$ has the dimension of frequency, and the spectrum is a plot of frequency versus frequency, derived as follows: In Eq. (41) and (43), both $\dot{\phi}$ and ω are in radians per second, and $F_{\phi}^*(\omega)$ gives the contribution, per unit band (rps), to $\langle \dot{\phi}^2 \rangle$ in (rps)²; hence $F_{\phi}^*(\omega)$ has the dimensions (rps)²/rps = rps. The measured time series is $\delta\phi$: the phase difference (in cycles) during an interval δt . The contributions to $\langle (\delta\phi)^2 \rangle$ are distributed among 64 frequency bands between 0 and $(2\delta t)^{-1}$, each of width $(128 \delta t)^{-1}$ cps = $2\pi(128 \delta t)^{-1}$ rps. The plotted spectrum is then

$$F_{\phi\phi}(\omega) = \frac{1}{4\pi^2} (\delta t)^2 2\pi(128 \delta t)^{-1} F_{\phi}^*(\omega)$$

$$= \frac{\nu \delta t}{256\pi} \left(1.27 + \frac{\omega^2}{\nu^2}\right)^{-1/2},$$

with ν in sec⁻¹, $\delta t = 300$ sec, and $\omega(\text{Hz}) = (2\pi/86400) \dot{\omega}(\text{cpd})$. The plotted intensity spectrum is

$$F_I(\tilde{\omega}) = \left(\frac{10}{\ln 10}\right)^2 \frac{2\pi}{128\delta t} F_I(\omega).$$

⁸N. L. Weinberg, J. Clark, and R. P. Flanagan, "Internal tidal influence on deep-ocean acoustic-ray propagation," J. Acoust. Soc. Am. **56**, 447-458 (1974).

⁹L. Magaard and W. D. McKee, "Semi-diurnal Tidal Currents at 'Site D,'" Deep-Sea Res. **20**, 997-1009 (1973). C. Wunsch, "Internal Tides in the Ocean," Rev. Geophys. Space Phys. **13**, 167-182 (1975). C. N. K. Mooers and D. A. Brooks, "Tidal and Longer Period Fluctuations of Internal and External Fields in the Florida Current, Summer 1970," Deep-Sea Res. (in press) (1976). M. G. Briscoe, "Preliminary Results from the Tri-moored Internal Wave Experiment (IWEX)," J. Geophys. Res. **80**, 3872-3884 (1975).

¹⁰For midstation, the total $\langle \phi^2 \rangle$ greatly exceeds both fortnightly $\langle \phi^2 \rangle$, see Fig. 4.

¹¹B. Zetler, W. Munk, H. Mofjeld, W. Brown, and F. Dormer, "MODE tides," J. Phys. Oceanogr. **5**, 430-441 (1975).

¹²M. Parke and M. Hendershott (personal communication).

ACOUSTIC PROPERTIES OF THE SEA FLOOR

John Ewing

Lamont-Doherty Geological Observatory
Columbia University
Palisades, New York

Studies of the reflection and refraction of sound by the ocean bottom and sub-bottom have provided the basis for characterizing geographical regions (provinces) in terms of sound velocity versus depth functions. Velocity gradients vary appreciably from province to province in response to variations in sediment type and in mode and rate of deposition. When the gradient is expressed as $V = V_0 + KT$ (where T is one-way travel time) the value of K generally lies between 0.5 and 1 sec^{-1} . These values represent average gradients in 1 km or more of sedimentary section.

Recent analysis of two data sets from the Hatteras abyssal plain has provided an opportunity to examine local variations in the velocity versus depth function and to investigate energy distribution among the various reflected and refracted paths. The region can be characterized reasonably well by two linear velocity versus depth functions: $V = 1.5 + 2T$ for the upper 400-500 meters and $V = 1.9 + T$ for the lower part of the sedimentary section. Standard deviations of sound velocity in the two data sets are between 50 and 100 meters per second.

For frequencies in the range of 60 Hz and lower, the signal amplitudes associated with rays penetrating to a reflector 500 meters deep in the sediments are, in a substantial range of grazing angles, 6 to 10 decibels higher than amplitudes associated with rays reflecting from the sea floor and shallow interfaces. Comparably high signal amplitudes are received at discreet ranges from still deeper levels, down to the top of the igneous basement. Some variations in signal level can be related to multipath interference and geometrical focusing effects, as well as to change in coefficient of reflectivity associated with incident angle.

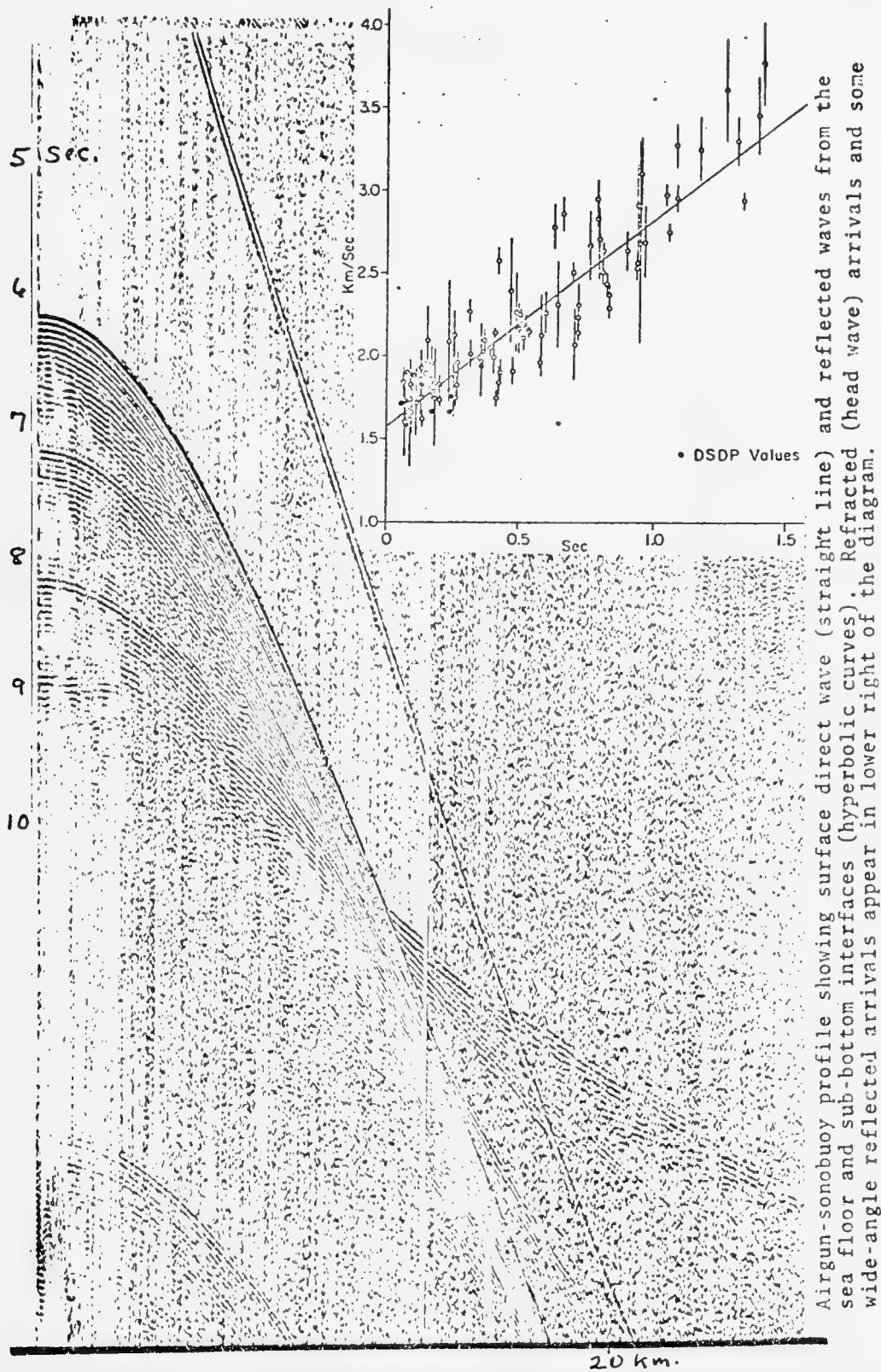
The following is a brief summary of work we have been doing in the marine seismology group at Lamont on ocean bottom acoustics. We

have been looking at bottom effects through the use of expendable sonobuoys and air gun sound sources and have recorded a large number of variable-angle reflection profiles. Since our ships travel around the earth widely, this has given us a chance to look at the bottom of the ocean in many places and to compare the behavior in one place with that in another.

Although not completely satisfied with the quality of each of our measurements, I do think that our total data bank is starting to give meaningful information about what is going on, particularly at low frequencies, when sound encounters the bottom.

Figure 1 is an example of an airgun-sonobuoy reflection profile, the ordinate representing reflection time and the abscissa representing distance. At these low frequencies (about 20 to 60 Hz), several reflectors appear quite clearly as a distinct reflection hyperbolic curve. The sea floor reflection intercepts the ordinate at about 6.2 seconds and prominent reflections from within the sedimentary section have intercepts of about 7.2 and 8.2 seconds. The intercept at about 9 seconds corresponds to igneous basement. It is quite clear at ranges between about 12 and 16 km (corresponding to grazing angles on the bottom of 30 degrees or so) that a lot of these reflection curves are starting to run together. When they do, we get some interference patterns showing up and the signal levels observed in that part of the profile vary extremely widely over (I would guess) something like 20 dB.

Even before we get to these moderately small grazing angles, at frequencies in the vicinity of 20 Hz, we are already getting a lot of energy from the sub-bottom interfaces. By the time the grazing angle reaches 45 degrees, in many places we get at least as much low-frequency energy from reflectors at depths of 500 meters or more as



Airgun-sonobuoy profile showing surface direct wave (straight line) and reflected waves from the sea floor and sub-bottom interfaces (hyperbolic curves). Refracted (head wave) arrivals and some wide-angle reflected arrivals appear in lower right of the diagram.

Figure 1. AIRGUN - SONOBUOY PROFILE

we get from the sea bottom. That says at least two things to me: That many sub-bottom interfaces have rather high reflectivity and, probably to nobody's surprise, that the attenuation in these moderately soft sediments is certainly not very high for frequencies in the 20 Hz range.

We see this low attenuation demonstrated in a slightly different way as we travel along almost any ocean basin where the igneous rock surface of the earth's crust is covered by a variable thickness of sediment. As you cross such a bottom and make a low-frequency echo sounding record, you can see little difference in the intensity of the reflections from the basement surface whether it is covered by a few tens of meters or a few hundreds of meters of sediment.

We have recently made several airgun-sonobuoy measurements in the Hatteras abyssal plain in connection with some joint work with NUSC. I was particularly interested in the Hatteras abyssal plain because I remember from some of the early work in bottom loss measurements made at 3.5 kHz that the Hatteras abyssal plain was considered to be about as good a reflecting bottom as we knew. We knew from piston coring and some of the Glomar Challenger work that this abyssal plain had quite a lot of sand and silt in it, so it ought to be a good reflecting bottom. We also knew there was another reflector about 500 meters below bottom, one that we observed very broadly over the North Atlantic Ocean, and we knew that it corresponded to some closely spaced layers of chert (flint) in otherwise soft sediment. I was quite interested to see how the reflectivity of the sea floor in this nice, smooth abyssal plain would compare with the reflector about 500 meters below the sea floor that I knew had some fairly hard rock associated with it.

Sure enough, in all of the profiles there, by the time we were out to grazing angles of 30 degrees, we consistently had signal levels coming from this subsurface reflector anywhere from 6 to 10 dB higher than signal levels from the sea bottom. In some places, usually at grazing angles of 30 to 45 degrees, it was common for the largest signal received in any part of the signal train to be coming from even deeper than the 500-meter level, sometimes coming from the top of the igneous rock itself, 1,000 meters or more below bottom.

One thing more. Notice in Figure 1 that at these farther ranges some signals are arriving appreciably ahead of the reflected signals. These are head waves coming from some of the deeper, high-velocity layers. Although they are interesting and important to us in geophysics, they do not carry much energy. They may appear to be rather energetic in the figure, but that is because this particular buoy is an SSQ41 buoy with AGC.

To summarize this part of my talk — there are large areas of the sea floor where, at frequencies below 100 Hz, appreciably more energy is returned to the surface by reflection from interfaces well below the bottom (hundreds of meters) than is returned from the sea floor itself.

We also get velocity information from the airgun-sonobuoy profiles. The technique that we have been using is rather standard, developed for geophysicists by Dix many years ago. It is known as the $X^2 - T^2$ method and is a purely geometrical treatment of the problem that depends on the fact that the shot point and receiving point separate during the experiment.

These measurements are easy to make. From them we can calculate interval velocities for each layer that is bounded by distinct

interfaces. If in one province we get enough such measurements, we can construct a plot of interval velocity versus depth in the sedimentary column.

We usually plot the depth function in one-way travel time, in seconds. The inset in Figure 1 shows a velocity/depth plot for the western North Atlantic rise. Here, as in most other places, we find that we can fit these data with a function that is linear in time although not quite linear in depth. If we express $V = V_0 + kT$, where T is one-way travel time vertically through the sedimentary section, k in this equation is in units of km/sec^2 . Most physicists, I think, tend to think of sound-speed gradients in depth rather than time, which are typically expressed in terms of kilometers per second per kilometer or just in seconds⁻¹. In most of the velocity range that we are dealing with in soft marine sediments, these two types of gradients turn out to be only about a factor of two apart. In other words, a gradient of about one per second corresponds to a k of approximately two kilometers per second per second.

In a lot of our measurements of this type from around the world, we characterize different areas in terms of this value, k , which, in fact, is characterizing the sea bottom in terms of velocity gradient in the sediment. Before I summarize these measurements, refer again to the inset in Figure 1. I pointed out that there is quite a lot of scatter in these data. The reason we can get this many data points is that the geology changes even in a rather local region. At one place we may see a reflector at some depth below the sea bottom; in other places we may be measuring it at half that depth or twice that depth. So if we make enough measurements, we get a fairly good distribution of layer thicknesses, and, therefore, we get several values of T . For each value of T , which is a measure of depth in the section, we calculate interval velocity so we can get a good distribution of velocities versus depth.

In the areas that we characterize by certain values of k , we notice that typically the standard deviation in velocity determination is about 100 meters per second. I have not been satisfied with that value; I thought we could probably do better. One of the reasons we wanted to do the set of measurements in the Hatteras abyssal plain was it gave us a chance to go to a localized area and do several of these experiments to see how much the scatter in determining velocity resulted from real geological change and how much, perhaps, resulted from some shortcoming in our method.

It turned out that in the closely grouped measurements in the Hatteras abyssal plain the velocity scatter did not appreciably change over what we had derived from 30 or 40 measurements over the whole Hatteras abyssal plain and part of the lower continental rise. This result caused us to consider whether our treatment of these data was paying enough attention to the details of the structure in the water column.

We had initially treated the water column in the $X^2 - T^2$ calculations as though it were a constant velocity layer, figuring that we were working mainly with rather steep ray paths for which the constant velocity assumption should produce only a small error. In our first attempt to improve this model, we divided the water layer into several layers, but this did not seem to reduce the scatter in the velocity versus depth determinations. A better water model shifted the average somewhat, not surprisingly, but it didn't really take the scatter out of these data.

A scheme proposed by George Bryan and representing an effort to escape the water layer model is demonstrated in Figure 2. It is a very simple two-layer model, water and sediment with a reflector at the bottom of each layer. The reflection curves and ray paths are shown.

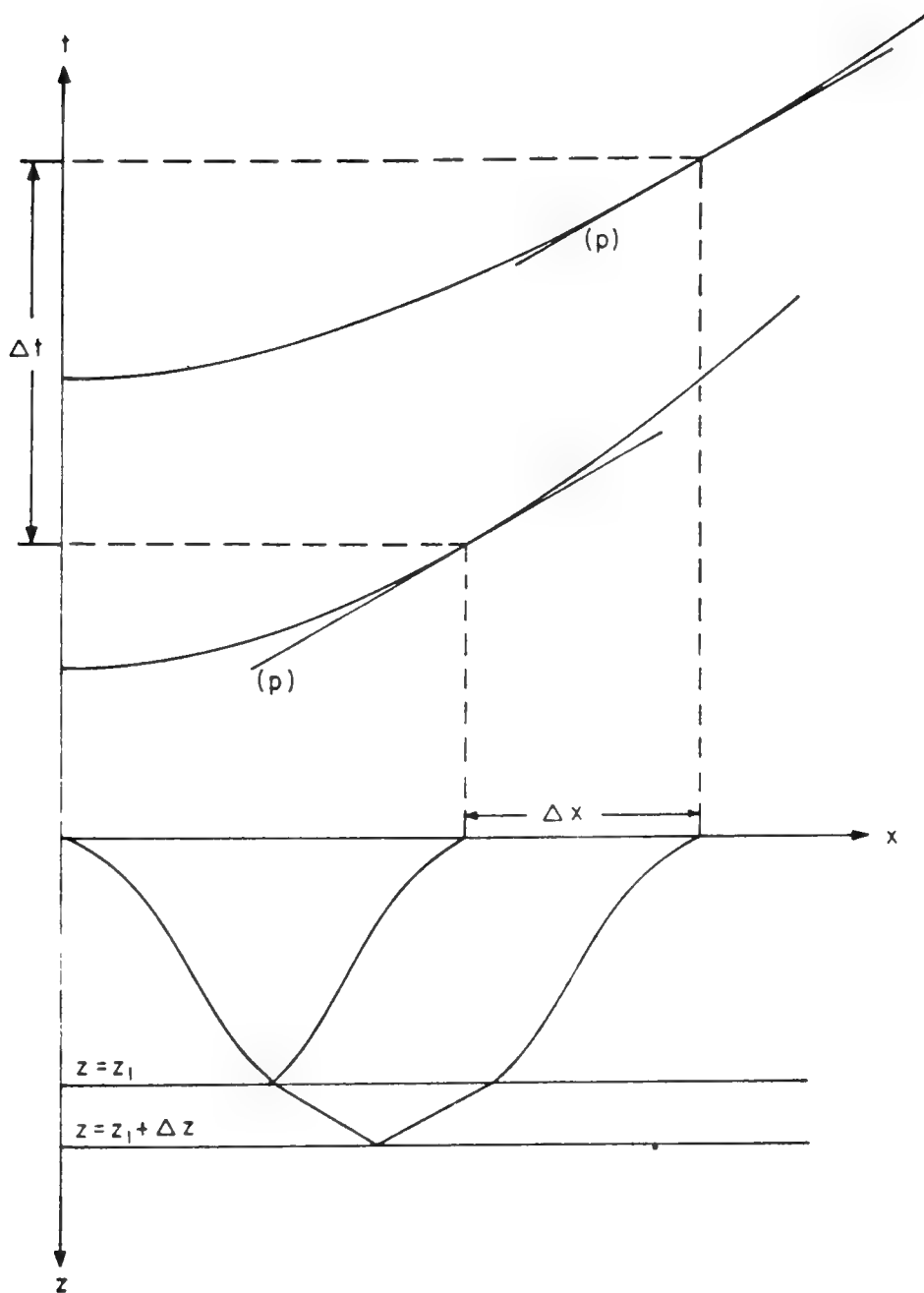


Figure 2. DIAGRAM (FROM BRYAN, 1974) SHOWING RELATIONSHIP OF BOTTOM-REFLECTED AND SUB-BOTTOM-REFLECTED RAYS WITH DERIVATIVES OF TIME VERSUS DISTANCE CURVES

As you can see from the model, it is possible to take pairs of rays in which the rays from the bottom reflection and from the sub-bottom reflection are parallel to each other in the water column. If we differentiate these reflection curves, the derivative tells us the slope of the curve, of course, and, physically, the inclination of the ray at the sea surface at that point. In effect, if we go along these reflection curves and find pairs of derivatives that are the same, we are finding pairs of rays (of which one is a bottom reflection and one is a sub-bottom reflection) that have traveled parallel, and presumably equal, time paths through the water. Thus, each pair of common derivatives gives us a ΔX and a ΔT associated with the path through the sediment layer, as shown in the diagram. We then carry out this procedure over a wide range of ΔX s and ΔT s, plot an $X^2 - T^2$ profile and get a value of interval velocity for the sediment layer.

We treated a substantial amount of our data in this way and we still have a lot of scatter — more than I like. This treatment should take account of the water structure, but, of course, it only takes account of a fixed water structure. No matter how you analyze these data, the water layer is a part of the model and if it changes significantly during the course of the experiment, you still have a problem.

We plan to put our entire experiment on the bottom of the ocean as one way to answer the question for certain whether our scatter in velocities versus depth results from the water column or from geology. I'd be very surprised and disappointed if there were no geological effect. But I have yet to be convinced that all of the variations are geological ones.

Figure 3 shows the distribution of our sonobuoy wide-angle reflection measurements on a world basis. The boxes indicate areas where we seem to have enough measurements in a geologically definable province to characterize it. Figure 4 shows a value of k (gradient) for each of these same areas.

Do not pay any attention to the central equatorial Pacific area. It indicates a very high value of gradient with a k value of 3.9. Although the value is correct, it represents a special case of some very thin, low-velocity sediments on top and some very high-velocity limestone at the bottom. It more properly ought to be treated as a two-layer case. The other numbers are the best values we can produce at present. Remember that the numbers represent k in the linear expression $V = V_0 + kT$.

Our methods of measuring from the surface are just not good enough to determine with precision the uppermost sediment velocity (< 100 meters thickness), but some characteristics of these data give us very good reason to believe that in the uppermost 100 meters or so is a considerably steeper gradient than the value listed for the entire section.

I want to discuss now the distribution of sediments. This is important because if negative bottom loss is a reality, it is because velocity gradients (and good sub-bottom reflectors) form, in effect, an acoustic lens at certain ranges. The more sediment we have, the more possibilities we have for acoustic lenses of various characteristics, to say nothing of the smoothing effects of substantial thicknesses of sediments. So it is of some interest to us, I think, to know the distribution of sediments around the world.

Figure 5 gives the distribution for the Atlantic. Although you cannot see the thickness contours, you can see the hatched region in

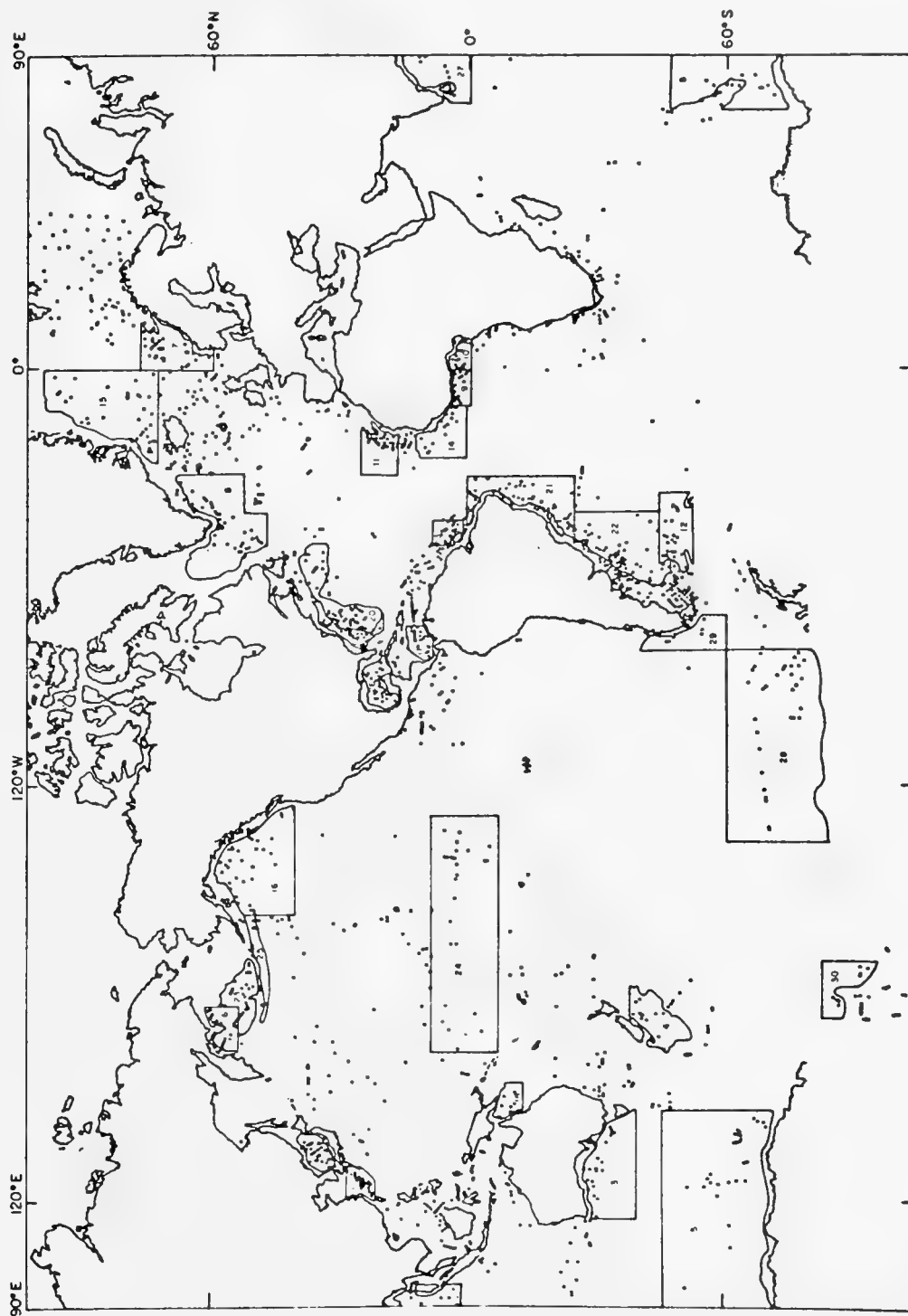
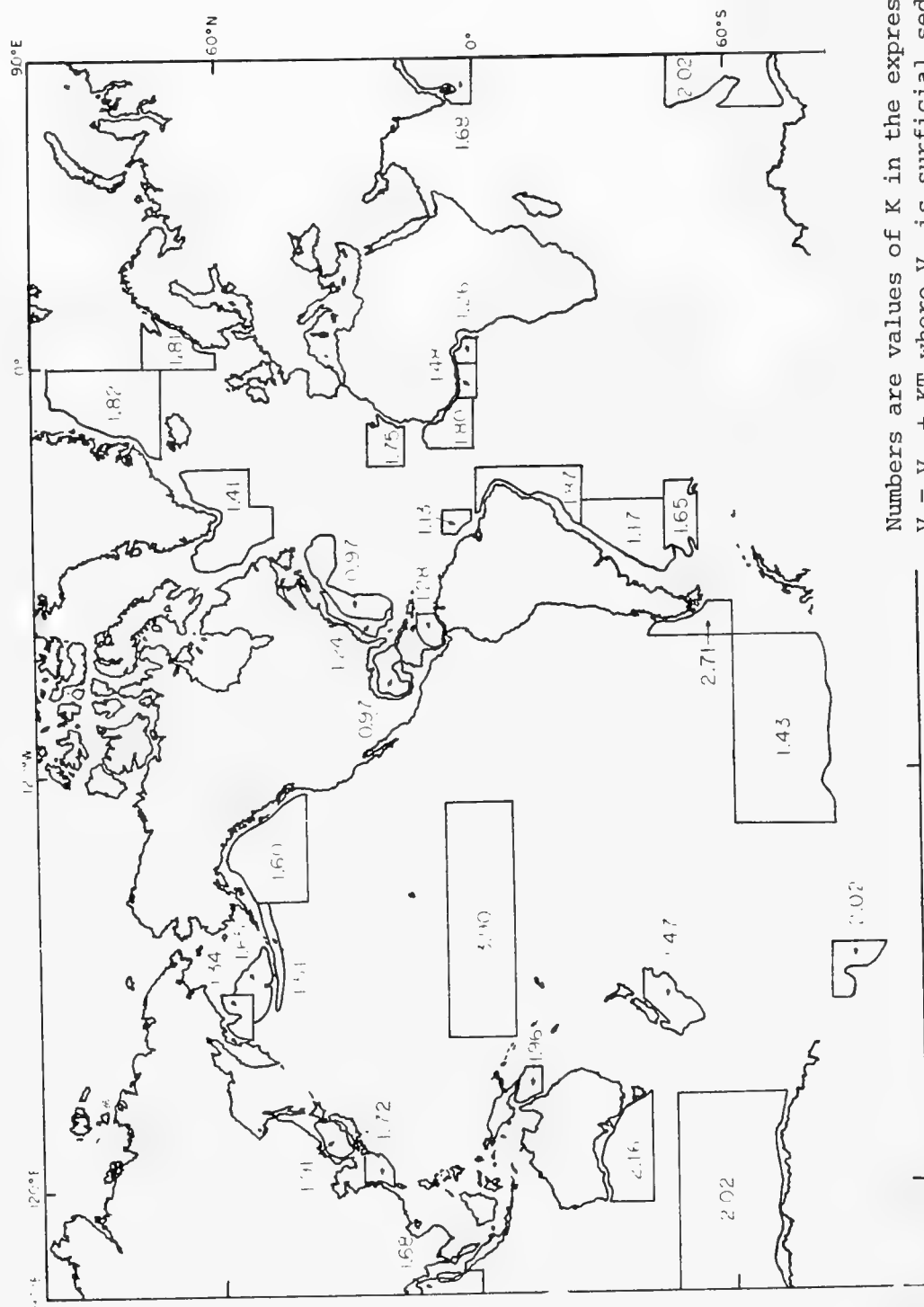


Figure 3. DISTRIBUTION OF AIRGUN-SONOBUOY STATIONS WITH OUTLINED AREAS EXHIBITING SIMILAR SEDIMENT SOUND VELOCITY VERSUS DEPTH FUNCTIONS (Numbers in boxes indicate number of measurements.)



Numbers are values of K in the expression $V = V_0 + KT$ where V_0 is surficial sediment velocity and T is one-way travel time.

Figure 4. MEASURED VALUES OF SEDIMENT SOUND VELOCITY GRADIENT

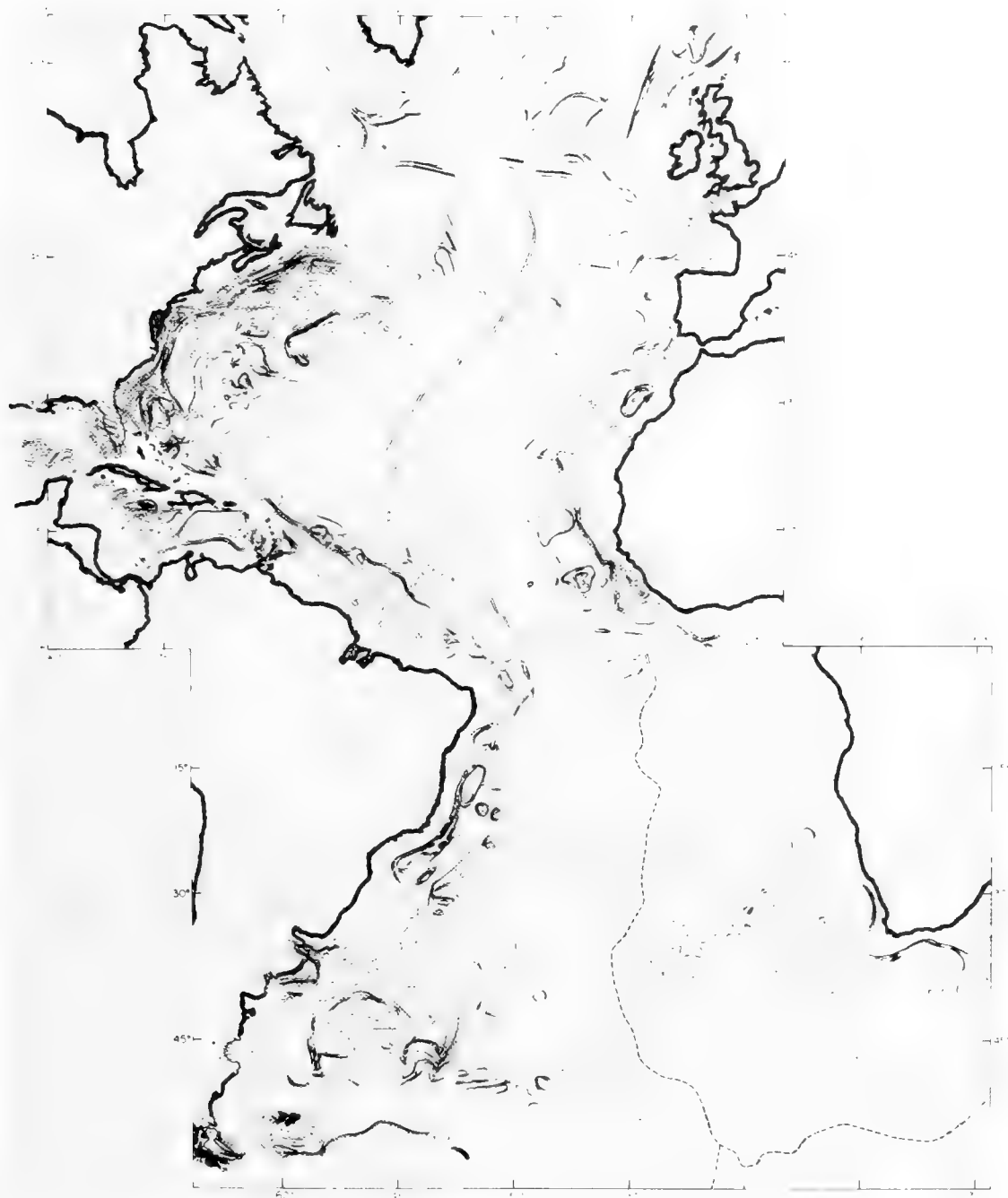


Figure 5. SEDIMENT DISTRIBUTION IN THE ATLANTIC OCEAN

the middle of the ocean where there are less than 100 meters of sediment. The stippled area on either side has more than a kilometer of sediment. Close to the continental margins on either side are as much as 5 or 6 kilometers of sediment.

Figure 6 is a similar display for the North Pacific Ocean. In this area, and in several other localized areas, we now have more detailed charts but this shows the general distribution. As in the Atlantic, we find little sediment, less than 100 meters, in broad areas. Sediments in the northeastern part are much thicker because of a great addition of turbidite sediments (detrital sediments). There is a nice thick belt of sediments along the equator caused by upwelling of deep water and high biogenic productivity. In the western Pacific, we find a distinct case of a two-layer situation with a thin layer of soft sediment overlying a much thicker layer of very hard sediment, the hard sediment being a cherty limestone.

Figure 7 shows the results of one of the JOIDES holes in the western Pacific where we paid particularly close attention to several factors. The reflection profile is traced on the right and next to it are shown interval velocities. The lithologic section that was cored is in the middle. This is a hole about 1,200 meters deep. The heavy trace on the left is a plot of the age of the sediment down the hole in millions of years. The dashed trace is the drilling record in terms of drilling time in minutes per meter.

We got nice correlations in the drilling record with the reflectors at about 600 meters and 800 meters. Most of the upper 600 meters of the section is just ooze, a microfossil ooze. At 600 meters, an exceedingly sharp interface occurs where chert (flint) layers have developed. This interface represents the rather abrupt transition between soft sediment, that you can make a mud ball out of, and these very hard chert layers that you can make arrowheads out of.



Figure 6. SEDIMENT DISTRIBUTION IN THE NORTH PACIFIC OCEAN

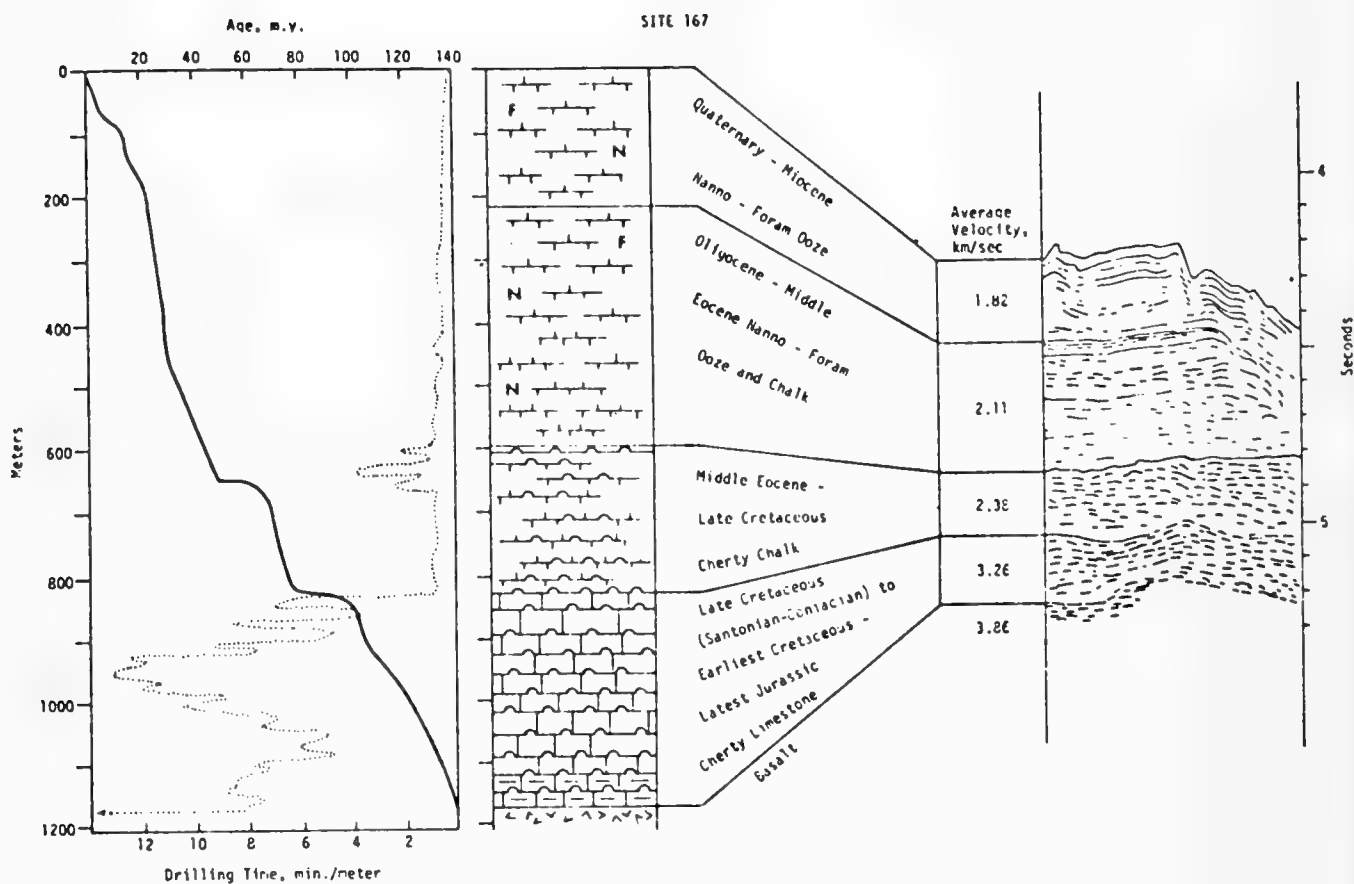


Figure 7. COMPARISON OF SEDIMENT AGE, DRILLING RATE, STRATIGRAPHIC SECTION, SEISMIC PROFILER RECORD AND COMPUTED INTERVAL VELOCITIES FOR DSDP SITE 167

Below the 600-meter interface is reasonably firm sediment down to about 800 meters where calcium carbonate chalk turns to limestone, really hard limestone. This transition also produces a very good reflection and a very sharp drilling break. At 1,200 meters we hit basalt under the limestone.

We now have several such holes from the JOIDES program that are well enough cored and geophysically examined so that we are starting to know what causes a lot of our reflectors. I think you can understand that it is not only interesting to us in a geological sense to identify the reflectors, but that the identification also permits us to use geological reasoning to interpolate between data points and gradually to build up a more complete geoacoustic model.

Figure 8, a section based on seismic data and drilling in the Atlantic, is the southern part of the Hatteras abyssal plain. We have identified some friendly Atlantic reflectors here. We have an interface in the sediments, fairly shallow in some places, deeper in others, labeled "A" which we now know is a series of chert beds, nearly the same age as those in the Pacific. A thick layer of clay is underneath, then again nice hard limestones (β) near the base of the section, and then the basalt (B).

REFERENCES

Dix, C. H., *Geophysics*, 20:68-86 (1955)

Bryan, G. M., "Sonobuoy Measurements in Thin Layers," in Physics of Sound in Marine Sediments, L. Hampton, ed., Plenum Press (1974)

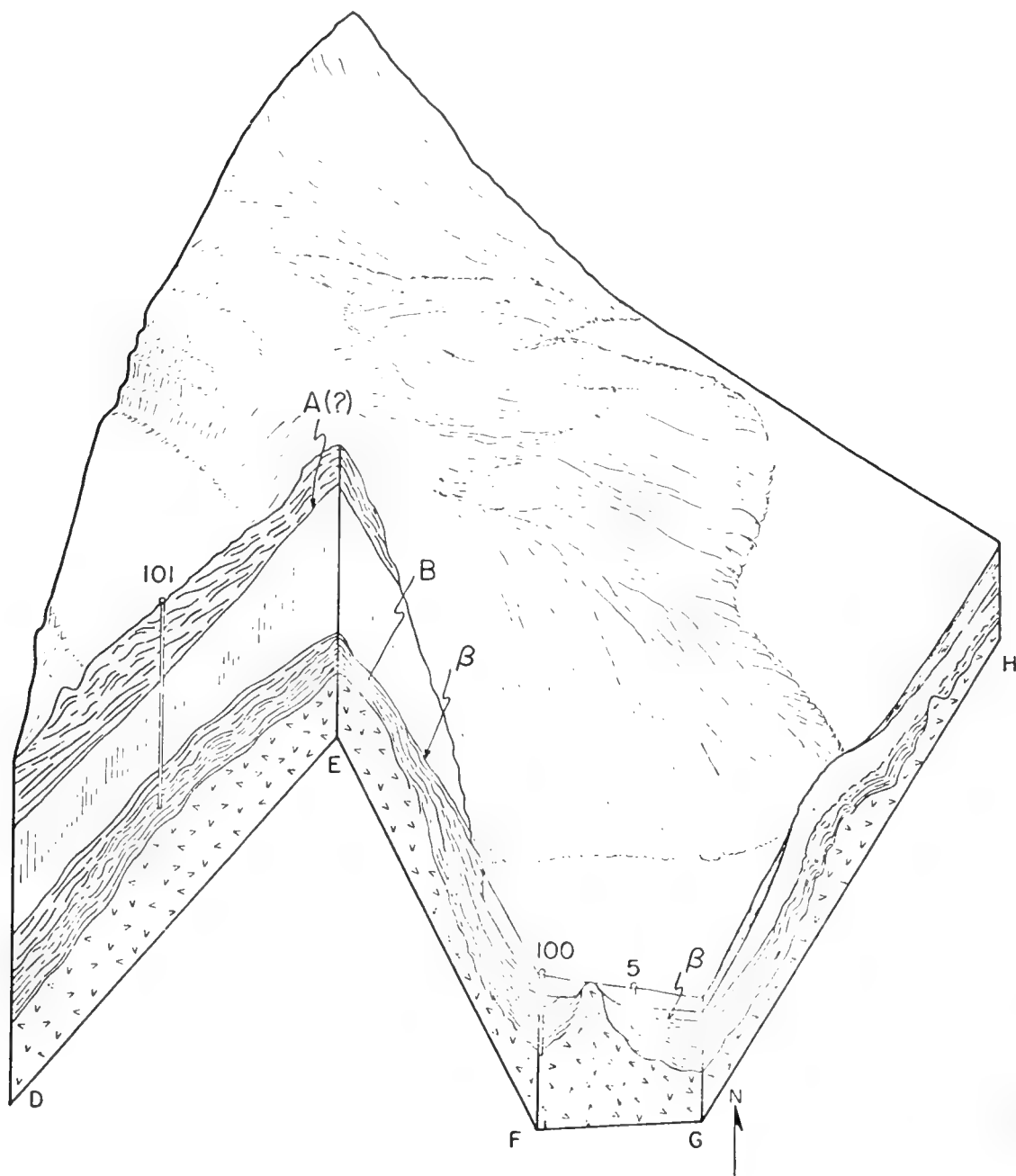


Figure 8. BLOCK DIAGRAM SHOWING PRINCIPAL REFLECTORS AND
SEDIMENT LITHOSTRATIGRAPHIC UNITS IN THE WESTERN
PART OF THE NORTH ATLANTIC

DISCUSSION

DR. W. H. MUNK (Institute of Geophysics and Planetary Physics, University of California at San Diego): Is the scatter on Figure 1 oceanographic or geological? Also, are there any measurements on land in sediments that could give a clue as to whether the order of scattering there is consistent or not with geologic inhomogeneities?

MR. EWING: We have some data that really made me suspect most strongly that it was the water column that was causing this. For example, in the Hatteras abyssal plain which our seismic data indicates to be a nicely layered section of sediment, the individual reflectors can be followed for hundreds of miles. The bottom seems to be just a beautiful cake of sediment. The data scatter represents a standard deviation of a hundred meters per second.

We can move up onto the continental shelf where from a geological point of view I would expect a bigger variation in geology, and there we get maybe half of that standard deviation. I think that is because we removed a lot of the water problem by going to shallow water.

DR. H. WEINBERG (New London Laboratory, Naval Underwater Systems Center): It seems to me that you are using ray theory at low frequencies and shallow grazing angles, and we have seen that this is one case when ray theory can really get you into a lot of trouble. Have you every tried to incorporate a better theory than regular ray theory; what would happen if you treated the propagation loss directly?

MR. EWING: We are concentrating primarily at the moment on developing the best model we can for velocity gradient. Working at appropriate incidence angles keeps you away from ray theory problems.

DR. WEINBERG: I found that the grazing angle can be 10 degrees. For example, if you go to the extreme case, the ray that grazes the ocean bottom has an infinite propagation loss, and that would tell you that you had a negative infinity bottom loss.

DR. M. SCHULKIN (Naval Oceanographic Office): If you consider the bottom in terms of velocity gradient and absorption, that is, consider it was an extension of the water medium, you do get convergence zone type propagation from very steep velocity gradients. It is possible to get an effect of negative bottom loss in the first bottom bounce region. Of course, beyond that it goes off as 3 dB per distance doubled as far as the loss goes. So that you only get this apparent gain in that first zone. But the rays penetrate the bottom and you just carry the ray tracing procedure through with the correction for the convergence effects.

DR. WEINBERG: That is a possible explanation, but there is another one. If you just take the velocity gradient in deep water and you have a positive velocity gradient going down, instead of using plane waves use Airy function solutions and you may do away with the negative bottom loss.

MR. W. H. GEDDES (Naval Oceanographic Office): There are a number of alternative explanations. I wouldn't want to hold out for the ray trace solution without saying that the negative loss is a flag indicating that the model (used in this way) is going to produce some strange answers. What I really want to hold out for is an appreciable amount of energy being refracted through the bottom and that it may not be a reflection arrival at all. I don't hold for the negative losses is what I'm saying.

DR. J. S. HANNA (Office of Naval Research, AESD): I didn't want to say too much right at this point about these problems with negative reflectivity because I had some comments I was expecting to give this evening in my discussion which are germane to some of the shortcomings or deficiencies in the transmission loss model used to reduce these data.

There are several effects one needs to worry about — the kinds that were mentioned here earlier as well as the implications of third-octave band processing with regard to whether you are adding these arrivals coherently or incoherently.

The particular model that was used here assumed that the four arrivals added without regard to phase. This is not strictly speaking true at low frequencies with third-octave processing.

DR. S. M. FLATTE (University of California, College at Santa Cruz): I wanted to ask Ewing a question. When you are comparing two paths where you try to cancel out the effect of the water column, there are of necessity still two paths which go through different parts of the water column. What is the typical difference in travel time that would have been assumed equal that would cause your scatter in points on the velocity determination?

DR. EWING: Which are the other two paths, Stan, that you are talking about?

DR. FLATTE: The direct path goes through a different part of the water than the one which has traversed the bottom layer.

MR. EWING: It goes through a different part of the water, yes, and our only assumption was that if there is no horizontal variation, then we should have eliminated most of the problems with the water column. The fact that we did not eliminate most of the problems led

us to suspect that we do have to worry quite a lot more about the horizontal changes.

DR. FLATTE: Right. And my question is a quantitative one. What horizontal difference does there have to be in order for you to get the scatter you observed?

MR. EWING: I'm not sure I can answer you without a little thinking.

DR. FLATTE: If it's a hundred meters — If it's a fifteenth of a second — I'm not really sure that it is though because you have to determine velocity and depth of layer at the same time. But if it is a fifteenth of a second — what model could you make of the water column that would do that? Because internal waves can't do it I'm sure, at the expected level of 10^{-4} for $\delta c/c$.

MR. EWING: It does not take a very big change. You see, the derivative of the reflection curves gives us the angle of the ray at the sea surface. If this ray has encountered very much of a perturbation anywhere near the surface it works on an awful long lever to change the angle of incidence on the bottom, and the angle of incidence on the bottom in our kind of analysis is very critical. A rather small angle change near the surface makes a big change in ΔX versus ΔT in the bottom layer.

DR. FLATTE: Might it be milliseconds' difference in travel time that could be the effect?

MR. EWING: It's more the effect of changing the direction of the ray, of course, than it is of anything else.

DR. FLATTE: Yes, but your experimental data are just travel time.

MR. EWING: Yes.

DR. FLATTE: And so the question is whether it is difference in travel time you might have observed.

MR. EWING: I would need to do a little arithmetic before I could answer you for sure. I don't know what the scale is.

MR. R. L. MARTIN (New London Laboratory, Naval Underwater Systems Center): Santanello and Bernstein at NUSC have also done several measurements of bottom loss, and they have observed this negative bottom loss below 10 degrees grazing. They approach the analysis quite differently. They took the broadband signal and isolated the direct and the first bottom-reflected pulse, and then ran the filtering after that; rather than taking the propagation model over the entire path, they just took the differences in the propagation over the path increment differences of the direct and bottom-reflected arrivals.

I would guess that this illuminates two questions that arise in processing these data and coming up with negative bottom loss. One is sensitivity of it to the particular propagation model used, and the other is the coherent effect through narrowband filters. So negative bottom loss has been observed using different analysis methods.

DR. A. O. SYKES (Office of Naval Research): Does sedimentary ooze act more like a fluid or like a solid?

MR. EWING: More like a fluid.

DR. HANNA: Referring to the comment that was just made here by Bob Martin, if you are taking the difference in transmission loss along those two paths it still presumes that your model for transmission loss in the water is sufficiently good to get both of those right. If the path interacts with either boundary, there are still the influences of caustic shadows on the field and things of that

sort which seem to be present every time you get to the geometry corresponding to low grazing angles.

So there are still possible complications I think that need to be properly considered even if you tried to improve the experimental range.

DR. J. L. WORZEL (Marine Science Institute Geophysics Laboratory): I think John Ewing's answer to Al Sykes' question needs a little modification. The oozes on the bottom act like a liquid when they have high porosity, but as they get buried deeper the porosity is reduced and then they no longer act like that.

DR. SCHULKIN: One of the questions is: What is the sound speed and absorption as a function of porosity? Also, how does porosity vary with depth beneath the surface of the bottom? When do shear waves start in?

MR. EWING: Well, we know very low velocity shear waves can be developed in very short sediments. We have observed them.

DR. HANNA: I have a question related back to the problem of the scatter of the data you referred to. Just to make sure that I didn't misinterpret some of the things that you said before, I would like to go back and refresh myself.

I thought I understood you to say that if G is of the order 1 per second then K is of the order of 2?

MR. EWING: More or less, yes.

DR. HANNA: Then the question I have refers to the accuracy of the resolution in time that you can achieve for the one-way travel time.

If I understood you properly, I believe the records showed a pass band from 20 to 40 Hertz or something of that sort. It would seem to me that, just very crudely speaking, the time resolution implied by that pass band might be of the order of tens of milliseconds. I wonder what possible influence that resolution might have on the scatter of the data that you plotted here. Using your value of 2 for K, this resolution would translate into something like 50 or 100 meters per second scatter.

MR. EWING: I guess the answer comes in two parts. How accurately can we time an arrival? The question I guess then is what does that arrival really mean particularly if you are in a region where you are having an interference of two low frequency signals? I completely agree that this is a possible source of our problem.

The kind of data we are normally using, a reflection arrival for instance, we usually just pick on the basis of like phase but not precisely like phase. I mean whether it's positive or negative. In very low frequency situations, of course, that gives potentially a rise of big timing errors. I'm aware of that.

We are trying to stay with arrivals that are separated enough in time. I guess another part of my sidestepping your direct question is the answer I gave to Walter Munk. We do the same thing when we work with the sediments on the continental shelf. We treat that data in exactly the same way. Yet we get a much smaller distribution, much tighter distribution.

In other words, if we go to a rather localized area and shoot a dozen sonobuoys in this fashion and plot them up this way with different filter settings, we can pick different levels in the sediment usually because some level will be reflective for one frequency, another level will be more reflective for another frequency.

So we divide up the sediment column and calculate one of the regression curves. By doing this we get a lot of statistical leverage in a shallow area. We always wind up with a much tighter regression plot than we do in the deep water.

There is maybe one exception to that, and that is the Bering Sea. There we have 50 or 60 measurements distributed sort of all over the whole basin and they group in quite tightly around regression curves. Whether it's because the Bering Sea is a little more stable oceanographically, I don't know. We're still struggling.

MR. C. W. SPOFFORD (Office of Naval Research): On these phase differences, John, is the bottom flat enough that you can consider those two rays to be identical in the water column? That is, one ray doesn't spend another 10 meters or so in the bottom in depth which could give you some huge differences here I would think? Is the bottom flat enough to ignore this effect?

MR. EWING: I think in the Hatteras abyssal plain it is. Those abyssal plains are the flattest things known in nature as far as I know. We cannot measure the slope with an echo sounding system that measures to plus or minus a fathom.

DR. HERSEY: The grades are typically one in five thousand in the central portion of abyssal plain.

THE EFFECT OF ROUGH INTERFACES ON SIGNALS THAT PENETRATE THE BOTTOM

C. W. Horton, Sr.

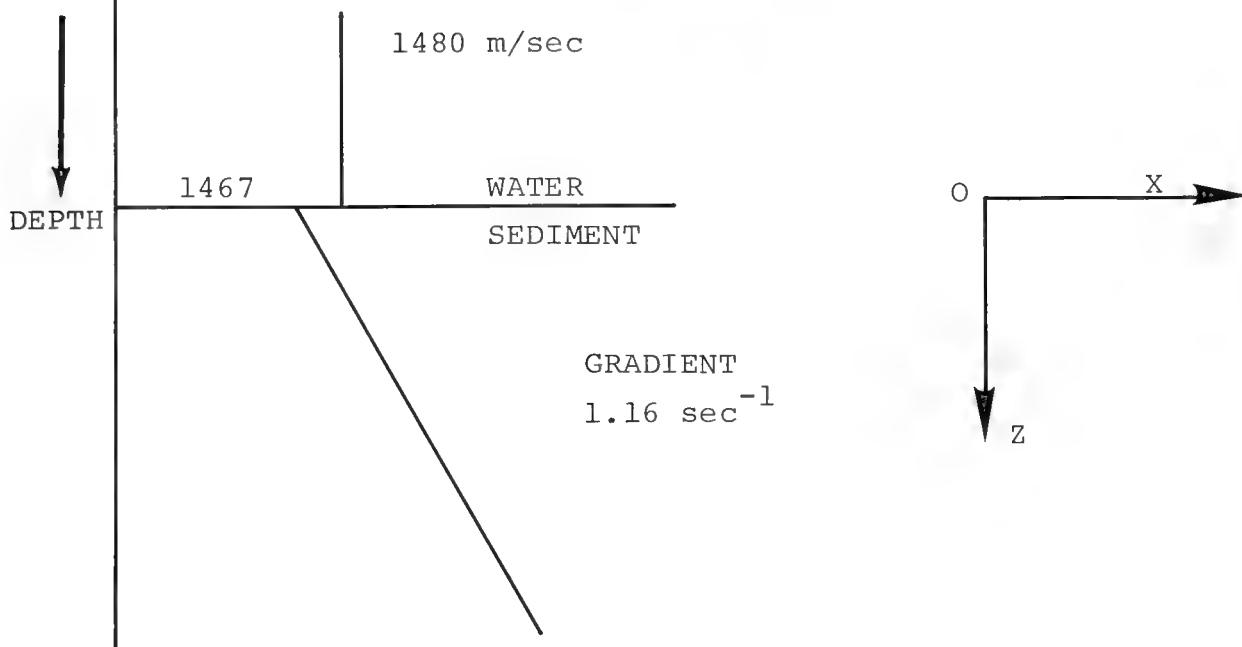
Applied Research Laboratories
The University of Texas at Austin

R. J. Urick (1973) stressed the importance of sound transmission through the ocean floor in the computation of reflection loss at the ocean bottom. Strong sub-bottom reflecting layers are not necessary since the wave is refracted upwards when there is a strong velocity gradient, as in sedimentary layers with the properties described by E. Hamilton (1974) for the abyssal plain in the northern Pacific Ocean. The Green's function for a point source in a liquid with a linear velocity gradient was derived by C. L. Pekeris (1946) and D. H. Wood (1969). This function is used in the Helmholtz integral for the inhomogeneous medium to calculate the properties of the sound beam that enters the bottom, is refracted in a circular arc, and returns to the water column. The effects of roughness at the interface are introduced using the analytical techniques pioneered by Eckart (1953). The amplitude of the coherent wave and the statistics of phase and amplitude fluctuations will be discussed. Of particular interest are turbidite layers since the acoustic velocity is less than that of water and the normal reflection coefficient may be very small.

This paper addresses the effects of bottom roughness on sound which refracts in the ocean bottom. The analysis involved a number of simplifying approximations which can be refined in later work.

Figure 1 displays the environmental parameters of concern to the problem of rays that enter the bottom and are refracted back into the water column. For numerical examples, values obtained by Hamilton (1974) in the Japan Sea abyssal plain will be used. The linearization of the square of the refractive index (Equation 1) permits the solution to be expressed in terms of Airy functions, and

HORTON: THE EFFECT OF ROUGH INTERFACES ON SIGNALS
THAT PENETRATE THE BOTTOM
VELOCITY



[JAPAN SEA ABYSSAL PLAIN
HAMILTON (1974)]

$$n^2(z) = \left[\frac{V(0)}{V(z)} \right]^2 = 1 - az \quad (1)$$

$$V(z) \cong V(0) + \frac{1}{2} az^2 \quad (2)$$

$$1/a \sim 750\text{m}$$

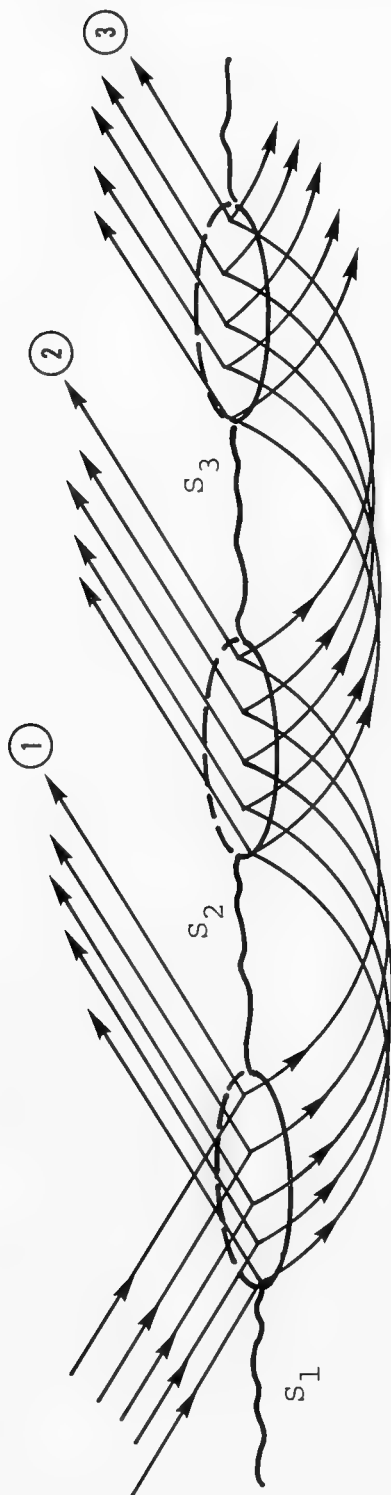
Figure 1. ENVIRONMENTAL PARAMETERS

the parameter "a" can be related to the gradient in the sediment via the approximation (Equation 2). Given a narrow beam impinging on the bottom, the refracted path in the bottom will be as shown in Figure 2 with subsequent multiple reflections. A phase shift of $\pi/2$ occurs at each turning point in the sediment.

Two papers treat this problem. One is by Morris (1970) in which reflection bottom-loss curves are computed for the linear gradient using the refracting layer plus an additional semi-infinite layer below the sediment. In the second, Brekhovskikh (1960) treats the case of a continuous velocity value across the interface (that is, without the step discontinuity shown in Figure 1). Both papers treat plane waves and obtain a complex reflection coefficient. Brekhovskikh (Equation 3) assumes no losses in the bottom and, hence, the reflection coefficient has unity magnitude. Morris (1970) adds attenuation in the bottom, and the refracting waves have less than unity magnitude.

A major point of this paper is that if the problem is actually for narrow beams, the result should be similar to a Rayleigh-type plane-wave reflection coefficient, expandable in an infinite series corresponding to the multiple bounces. This is analogous to the treatment of a transmission line where the transmission loss through it is calculated using a continuous wave but it can be expressed as an infinite series of multiple reflections from the two ends of the transmission line. When the result in Equation 3 is expanded properly, it should become a reflection coefficient for the surface with separate amplitudes for the successive waves corresponding to the refracted and reflected paths in the bottom.

Brekhovskikh analyzes the case where there are no losses in the bottom and the velocity is continuous from the water into the bottom.



PHASE SHIFT
 $\pi/2$

FOR PLANE WAVES, AND $n(0) = 1$,

$$V = \frac{\left(J_{-2/3}^{-J_{2/3}} \right) + i \left(J_{1/3}^{+J_{-1/3}} \right)}{\left(J_{-2/3}^{-J_{2/3}} \right) - i \left(J_{1/3}^{+J_{-1/3}} \right)} \quad (3)$$

EXPAND AS INFINITE SERIES OF MULTIPLE BOUNCES.

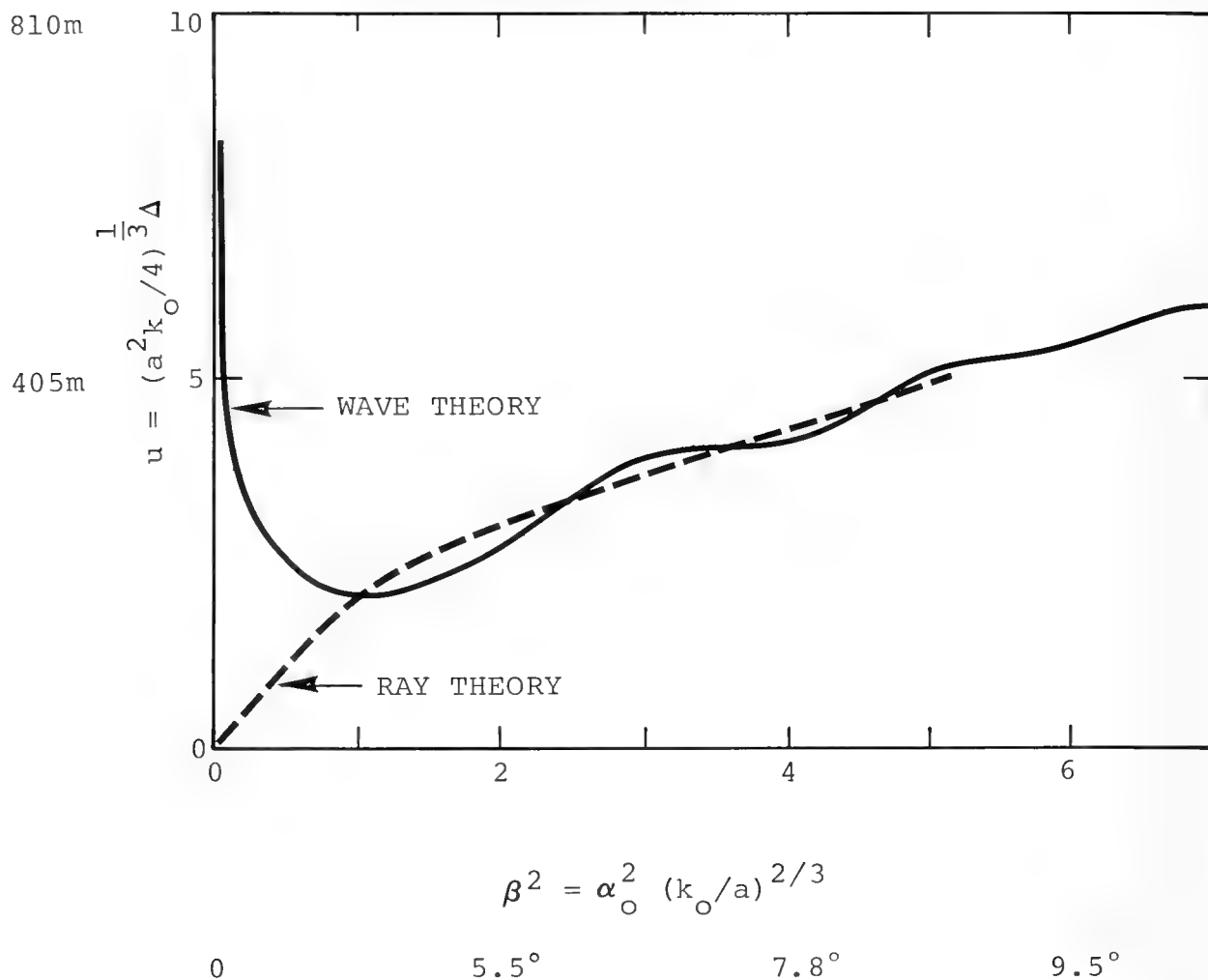
Figure 2. SCHEMATIC OF MULTIPLE REFLECTION AND BOTTOM REFRACTION

He obtains the curve shown in Figure 3 for the dimensionless displacement, u , of the wave that is refracted in the bottom as a function of the dimensionless grazing angle, β . Δ is the actual displacement, and α_0 the grazing angle. For the model from Hamilton's paper, numerical values are shown for the grazing angle in degrees and the horizontal displacement in meters on the beam between entry and reemergence.

Brekhovskikh shows that the wave theory and the ray theory give good agreement beyond $\beta = 1$. The subsequent discussion will be restricted to grazing angles for which ray theory can be employed in the bottom with some safety.

When there is attenuation in the bottom (Figure 4), there will be losses on the refracted path and presumably the subsequent reflections will be of minor importance. In Morris's paper, the plane wave reflection coefficient is used and the interference between the returned paths after successive bounces is extremely sensitive to the grazing angle. Hence, the resulting bottom-loss curves have a strong ripple associated with the interference. If the interference is removed by separating Paths 1 and 2, either in space or in time, (or if there is an intromission condition with a very small reflection coefficient for Path 1), then Path 2 should dominate the field.

The theory in which the velocity is strictly a linear function of depth (rather than n^2 linear as above) has been developed extensively in a paper by Pekeris (1946) who solved the Green's function for a point source in a linear gradient medium, and in a later paper by D. H. Wood (1969). The Green's function is given by Equation (4) in Figure 5 for a source at the origin of the coordinate system where z is the depth and r is the distance from the source.



$k_O = 2\pi/\text{WAVE LENGTH IN WATER}$

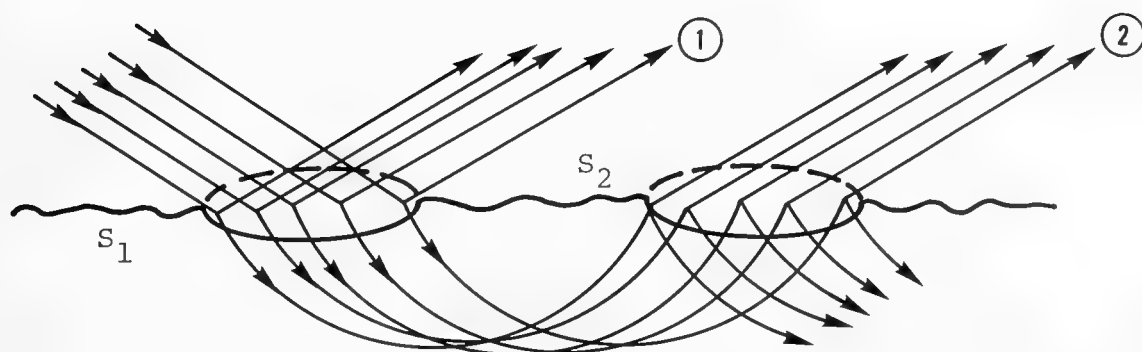
$\alpha_O = \text{GRAZING ANGLE}$

$\Delta = \text{DISPLACEMENT OF BEAM}$

$1/a \sim 750\text{m}$

$f = 1 \text{ kHz}$

Figure 3. BREKHOVSKIKH's COMPARISON FOR
WAVE THEORY AND RAY THEORY



PATHS ① AND ② MAY BE SEPARATED IN TIME

OR IF

$$\frac{\rho\text{-SEDIMENT}}{\rho\text{-WATER}} > \frac{\text{VEL. WATER}}{\text{VEL. SEDIMENT}} > 1,$$

BOTTOM LOSS ON REFLECTION IS LARGE AND

PATH ② DOMINATES

Figure 4. CONDITIONS FOR THE REFRACTED PATH TO DOMINATE

$$G(x, y, z) = z \sqrt{\frac{1}{2} \frac{c_o}{\gamma} \left(z + \frac{1}{2} \frac{c_o}{\gamma} \right)} \frac{e^{\frac{i\phi}{nR}}}{nR} \quad (4)$$

$$\phi = \sqrt{\frac{\omega^2}{\gamma^2} - 1} \tanh^{-1} \frac{r}{R} \quad (5)$$

$$c(z) = c_o + 2\gamma z$$

$$r^2 = x^2 + y^2 + z^2$$

$$R^2 = x^2 + y^2 + \left(z + \frac{c_o}{\gamma} \right)^2$$

SOURCE AT (0,0,0)

γ = SOUND SPEED GRADIENT

SOURCES: PEKERIS, JASA 18, 295 (1946)

D.H. WOOD, JASA 46, 1333 (1969)

Figure 5. GREEN'S FUNCTION FOR A POINT SOURCE
IN A LINEAR GRADIENT MEDIUM

This particular form of the Green's function is not genuinely symmetric in source and receiver as a Green's function should be. The source is singled out by being placed at the origin leading to the asymmetry in z which is the location of the field point. In some subsequent expansions, the order of the z term will be switched because of this asymmetry and this can be easily justified by appealing to physical intuition. As is well known, in the linear velocity medium rays are circles whose centers lie on the plane where the velocity goes to zero. R , as seen in Figure 6, is the distance from the "image" source a distance z above this plane to the observation point.

The view being taken of the bottom is shown in the middle portion of Figure 6, where the ray enters in the first region, is refracted downward, and emerges at the exit region through a different patch of the ocean floor. It may also have reflected one or more times in the middle region. A set of local coordinate systems is introduced in the lower portion of Figure 6, where it is assumed that the ocean may have a mean displacement in the entry region referred to the mean value of the sea floor in the reflection region, and the exit region may have yet another mean displacement. Hence, there will be phase differences involved in the travel paths in the bottom associated with these mean displacements. The phases can be given additional statistical fluctuations associated with roughness in the local areas where the sound enters the bottom, reflects, and emerges. The distance L between the coordinate origins at the entry and exit regions is the horizontal distance of the refracted beam in the bottom.

At this point, it is convenient to make a number of assumptions. First, the regions should be well separated, that is, they should have small linear dimensions compared to L . When L is large compared to

HORTON: THE EFFECT OF ROUGH INTERFACES ON SIGNALS
THAT PENETRATE THE BOTTOM

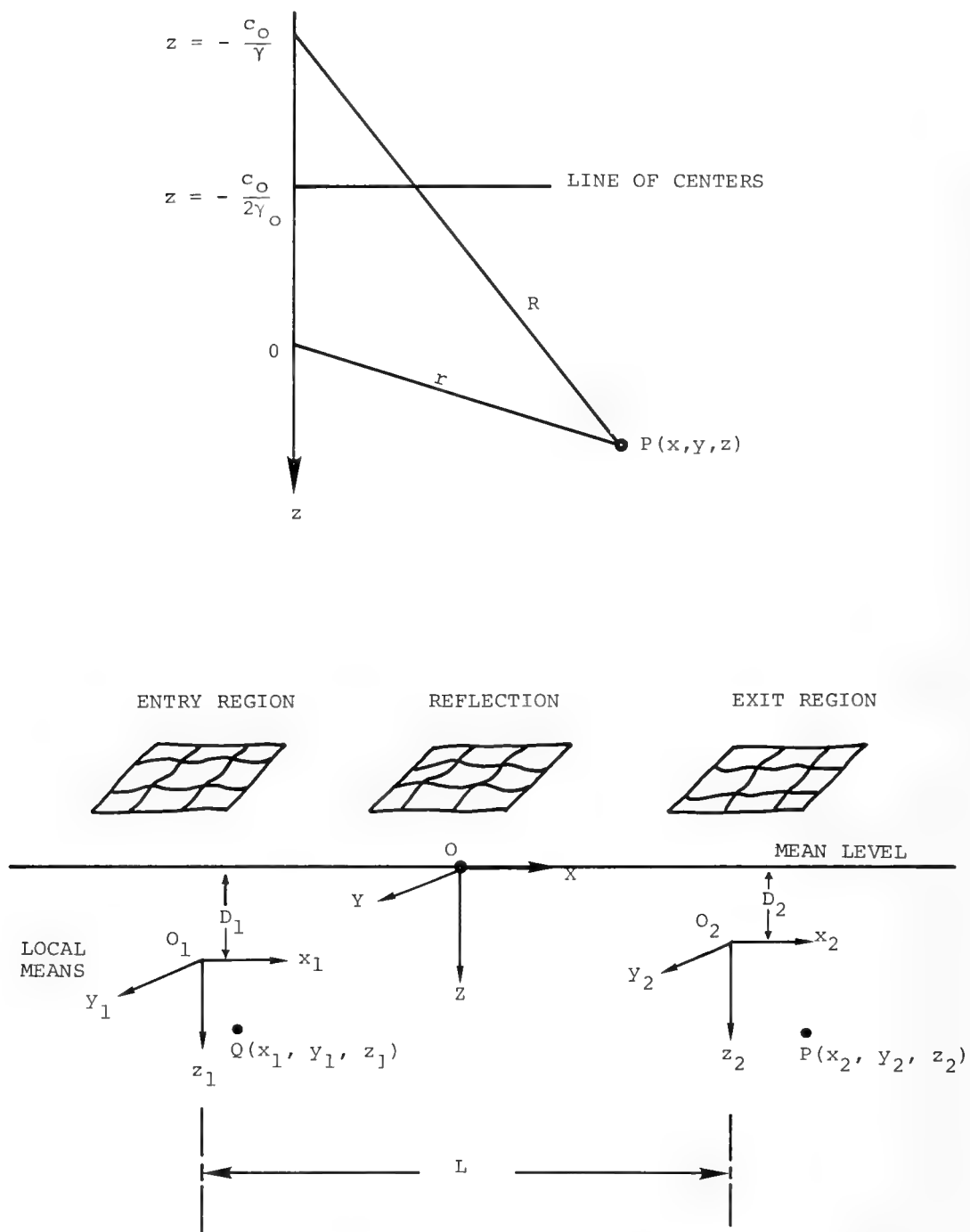


Figure 6. GEOMETRY FOR APPLICATION OF GREEN'S FUNCTION

the size of the entry area, it will be shown that the Green's function can be expanded about the origin, O_2 , and will be locally a plane wave emerging at the surface.

The approximations used are listed in Figure 7. The increments δx , δy , δz , relate to the differences between the variable points in the two little areas, and the z coordinate then contains the difference in the local mean depths, δD . Expanding all quantities to linear terms in δx , δy , δz , and δD , the Green's function reduces to Equation (6) in Figure 8, where the phase consists of two terms. ϕ_0 is the phase length between O_1 and O_2 , and ϕ_1 contains local departures from ϕ_0 associated with entry and exit points (x_1, z_1) and (x_2, z_2) , respectively. ϕ_1 is quite accurately approximated by a local plane wave (Equation 9) of emergent angle θ_e .

Note that ϕ_1 is not symmetric in (x_1, z_1) and (x_2, z_2) . This is the point alluded to earlier. If the field point (x_2, z_2) is taken as a new source, then the behavior near the origin has the wrong sign. To remedy this, the first term is always the field point and the second term is always the source coordinate.

This result is summarized in Figure 9. A source ray enters the bottom at point Q at some angle θ_e , emerging at point P at the same angle. The variable phase delays associated with roughness at points Q and P can then be added to the geometric phase delay via ϕ_1 .

The Helmholtz formula (Equation 11) in Figure 10 is used to calculate the field at the point P integrated over the area of insonification. For the Green's function, the linear approximation is used which simplifies the normal gradient in the integral leading to Equation 12.

$$r^2 = (L + \delta x)^2 + (\delta y)^2 + (\delta D + \delta z)^2$$

$$R^2 = (L + \delta x)^2 + (\delta y)^2 + \left(\frac{c_o}{\gamma} + \delta D + \delta z\right)^2$$

DEFINE $R_o^2 = L^2 + \left(\frac{c_o}{\gamma}\right)^2$

BASIC APPROXIMATIONS

$$L \gg \delta x, \delta y, \delta z, \delta D$$

$$2\sqrt{\frac{c}{2\gamma} \left(z_2 + \frac{c}{2\gamma}\right)} \cong \frac{c_o}{\gamma}$$

$$\sqrt{\frac{\omega^2}{\gamma^2} - 1} \cong \frac{\omega}{\gamma} \quad \begin{array}{l} \gamma \sim 1 \text{ sec}^{-1} \\ \omega > 600 \text{ sec}^{-1} \end{array}$$

AND EXPANDING: $\tanh^{-1} \frac{r}{R}$ TO LINEAR TERMS

IN $\delta x, \dots,$

Figure 7. APPROXIMATIONS

$$G = \frac{c_o}{\gamma R_o L} e^{i\phi_o + i\phi_1} \quad (6)$$

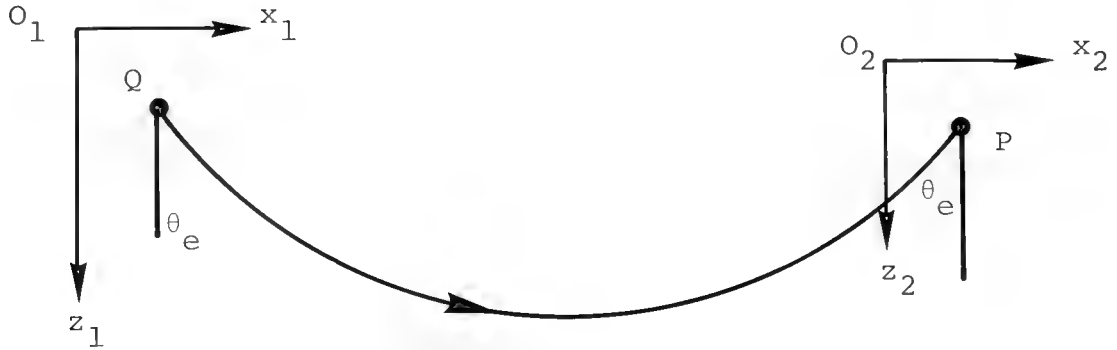
$$\phi_o = k_o \frac{c_o L}{\gamma R_o} \left[1 + \frac{1}{3} \left(\frac{L}{R_o} \right)^2 - \frac{c_o L}{\gamma R_o^2} \left\{ 1 + \left(\frac{L}{R_o} \right)^2 \right\} \frac{\delta D}{L} \right] \quad (7)$$

$$\begin{aligned} \phi_1 = k_o \frac{c_o}{\gamma R_o} \left\{ 1 - \left(\frac{L}{R_o} \right)^4 \right\} (x_2 - x_1) \\ - k_o \frac{L}{R_o} \left(\frac{c_o}{\gamma R_o} \right)^2 \left\{ 1 + \left(\frac{L}{R_o} \right)^2 \right\} (z_2 - z_1) \end{aligned} \quad (8)$$

FOR THE PHYSICAL PARAMETERS IN THE PROBLEM, THE
LATTER CAN BE APPROXIMATED VERY CLOSELY BY

$$\phi_1 = k_o \left[\sin \theta_e (x_2 - x_1) - \cos \theta_e (z_2 - z_1) \right] \quad (9)$$

Figure 8. GREEN'S FUNCTION WITH APPROXIMATIONS



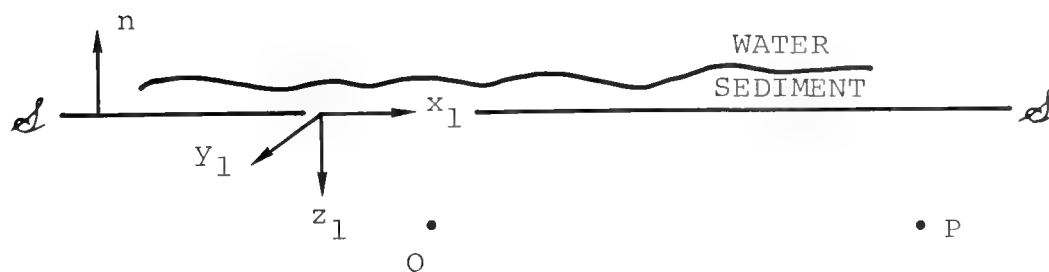
$$e^{i\phi_1} = e^{ik_o \left[\sin \theta_e (x_2 - x_1) - \cos \theta_e (z_2 - z_1) \right]} \quad (10)$$

BEHAVES PROPERLY AT P

BUT IF WE THINK OF P AS A SOURCE AND Q AS THE DETECTOR,
 z_2 and z_1 , MUST BE INTERCHANGED. THIS IS IMPORTANT IN
THE HELMHOLTZ FORMULATION.

Figure 9. CONVENTION REGARDING SOURCE AND FIELD POINTS
TO REMEDY ASYMMETRY IN GREEN'S FUNCTION

HORTON: THE EFFECT OF ROUGH INTERFACES ON SIGNALS
THAT PENETRATE THE BOTTOM



THE HELMHOLTZ INTEGRAL FOR POINTS P AND Q BELOW \mathcal{S} IS

$$\phi(P) = \frac{1}{4\pi} \int \left\{ G \frac{\partial \phi}{\partial n} - \phi \frac{\partial G}{\partial n} \right\} d\mathcal{S} \quad (11)$$

NOW $\frac{\partial}{\partial n} = - \frac{\partial}{\partial z_1}$ and

$$+ \frac{\partial G}{\partial n} = - \frac{\partial G}{\partial z_1} = + i k_o \cos \theta_e G,$$

SO

$$\phi(P) = \frac{-1}{4\pi} \int \left\{ + \frac{\partial \phi}{\partial z_1} + i k_o \cos \theta_e \phi \right\} G d\mathcal{S} \quad (12)$$

IF ϕ IS LOCALLY A PLANE WAVE WITH ANGLE OF
INCIDENCE, θ_w , IT WILL BE REFRACTED INTO THE BOTTOM
WITH REFRACTION ANGLE θ_B .

Figure 10. HELMHOLTZ AND GREEN'S FUNCTIONS

The variable displacement of the surface in Figure 11, at the point of entry, produces a variable phase delay δ (Equation 13). To the simplest approximation it is actually a difference of the slant path in the water associated with the entry angle and the slant path in the sediment associated with the refracted angle. This makes the effect much smaller than in scattering, say, from a free surface or from a reflecting bottom. That is, only the difference in the acoustic delays in the two media accumulates, so that a large surface displacement actually produces a relatively small change in the phase. Hence, Equation (13) is the variable phase to be inserted across the area of integration, being the random displacement of the surface. Again assuming that the normal gradient of the field in the bottom is the vertical gradient, there are two final approximations: first, that the angle θ_e in the Green's function is the same as the refracted angle θ_B of the wave entering the bottom; and second, that the wavenumber k_B for the refracted wave and k_o for the Green's function are the same. With this approximation the field $\phi(P)$ is expressed in Equation (14) as the integral over the insonified region of the refracted wave incident on the bottom times the Green's function integrated over the insonified area.

Hence, the wave impinging on the bottom is refracted in the bottom yielding ϕ . There is a phase variation with x across the area of insonification, but the Green's function to the linear approximation used here has exactly the same phase variation because of the agreement of phase at the boundary. That is, the x variation of phase in the one function is exactly canceled by the variation in the Green's function, leaving only the variable phase delay associated with roughness.

A VERTICAL DISPLACEMENT $\zeta(x_1, y_1)$ WILL PRODUCE
A PHASE DELAY, δ

$$\delta = \left\{ \frac{2\pi}{\lambda_W} \frac{1}{\cos \theta_W} - \frac{2\pi}{\lambda_B} \frac{1}{\cos \theta_B} \right\} \zeta \quad (13)$$

WHERE W: WATER B: BOTTOM

FURTHER, IN THE MEDIUM AT THE ANGLE θ_B ,

$$+ \frac{\partial \phi}{\partial z_1} = + i k_B \cos \theta_B \phi$$

WITHIN THE ACCURACY OF THE LINEAR APPROXIMATION,

$$\theta_e = \theta_B, \quad k_O = k_B$$

SO

$$\phi(P) = \frac{-i k_B 2 \cos \theta_B}{4\pi} \int \phi G d\mathcal{A} \quad (14)$$

Figure 11. VARIABLE PHASE DELAY AND ITS EFFECT ON ϕ

The integral is performed in Figure 12 where m designates the phase delay per unit displacement. By introducing plane-wave approximations, the field ϕ at the point P just under the emergent area is given by the integral shown in Equation (15) over the area of insonification.

The last factor in Equation (15) represents the local plane wave about the field point P , emerging at the exit region.

The integral is a stochastic integral and, if the insonified area is large compared to the correlation distance of the displacement, ζ , the exponential can be expanded in a convergent series (Equation 16). $\langle \zeta \rangle$ is the average value of the displacement and since the local origin is on the mean surface, $\langle \zeta \rangle = 0$.

Hence, there is no phase shift associated with entry into the bottom. $\langle \zeta^2 \rangle$ is the mean square displacement and results in a loss of amplitude. For abyssal plains $(\langle \zeta^2 \rangle)^{1/2}$ is of the order of 3 to 10 centimeters and there is very small loss of amplitude associated with entry into the bottom. Hence, there is a coherent wave arriving at the exit region with very little loss.

The same type of analysis can be repeated almost word for word for the emergent ray, resulting in a second slight loss of amplitude associated with the mean square displacement at exit region. Typically, the entry and exit regions are far enough apart (several hundred meters) that there is no statistical correlation between $\langle \zeta^2 \rangle$ at point Q .

In summary, it appears that moderate roughness at the bottom-water interface will produce essentially no loss of amplitude on entering or leaving the bottom, and the strength of the refracted

HORTON: THE EFFECT OF ROUGH INTERFACES ON SIGNALS
THAT PENETRATE THE BOTTOM

LET

T = TRANSMISSION COEFFICIENT

a = AREA OF INSONIFICATION

$$m = 2\pi \left\{ \frac{1}{\lambda_w \cos \theta_w} - \frac{1}{\lambda_B \cos \theta_B} \right\}$$

THE FIELD AT P IS THE PLANE WAVE

$$\phi(P) = \frac{C}{L} \iint_a e^{im\zeta(x_1, y_1)} dx_1 dy_1 \cdot e^{ik_B [x_2 \sin \theta_B - z_2 \cos \theta_B]} \quad (15)$$

WHERE

$$C = -i \left(\frac{c_o}{\gamma R_o} \right) \frac{k_B \cos \theta_B}{2\pi} T e^{i\phi_o}$$

NOW

$$\iint_a e^{im\zeta} dx_1 dy_1 = a \left\{ 1 - im\langle \zeta \rangle - \frac{1}{2} m^2 \langle \zeta^2 \rangle + \dots \right\} \quad (16)$$

$$\langle \zeta \rangle = 0$$

NO PHASE SHIFT

$$\langle \zeta^2 \rangle^{1/2} \sim 0.03 \approx 0.1 \text{ m, ABYSSAL PLAINS}$$

Figure 12. RESULTING FORMS

path will depend on the reflection coefficient at the interface and the attenuation the path receives in the sediment.

REFERENCES

- Brekhovskikh, L. M., *Waves in Layered Media*, pp. 117-122, 189-193, Academic Press, 1960.
- Eckart, C., *J. Acoust. Soc. Am.* 25, 566, 1953.
- Hamilton, E. L., "Geoacoustic Models of the Sea Floor," in *Physics of Sound in Marine Sediments*, Ed. Loyd Hampton, Plenum Press, 1974.
- Morris, H., *J. Acoustic Soc. Am.* 48, 1198, 1970.
- Pekeris, C. L., *J. Acoust. Soc. Am.* 18, 295, 1946.
- Urlick, R. J., "Underwater Sound Transmission Through the Ocean Floor," in *Physics of Sound in Marine Sediments*, Ed. Loyd Hampton, Plenum Press, 1974.
- Wood, D. H., *J. Acoust. Soc. Am.* 46, 1333, 1969.

HORTON: THE EFFECT OF ROUGH INTERFACES ON SIGNALS
THAT PENETRATE THE BOTTOM

DISCUSSION

DR. IRA DYER (Department of Ocean Engineering, Massachusetts Institute of Technology): I understand your conclusion to be that moderate roughness does not substantially affect the computations of refracted paths in the bottom sediments.

DR. C. W. HORTON, SR.: Yes.

DR. DYER: Does this include the effect of scattering of this energy outside the angles at which you might expect to receive these bottom refracted paths?

DR. HORTON: I should have mentioned in my discussion and didn't that this refraction path is essentially unique. That is to say, for one configuration of source and receiver in the water there will be only one path through the bottom that gives you the travel time that you will see. This is borne out by the experimental data.

The loss of amplitude I referred to represents, I believe, all the data that is scattered in directions other than the refracted path. So they are essentially refracted out of this acoustic bundle and don't arrive at the emerging point.

DR. DYER: And nonetheless small?

DR. HORTON: Nonetheless small for the moderate amplitudes.

BOTTOM PROPERTIES FOR LONG-RANGE PROPAGATION PREDICTION

Aubrey L. Anderson

Applied Research Laboratories
The University of Texas at Austin
Austin, Texas

Loss of acoustical energy propagating to long ranges in the ocean is predicted with computerized mathematical models (propagation models), many of which treat the ocean bottom as either a reflecting interface or as part of the propagation path (a penetrable boundary). In many models, the bottom is included as an interface which is characterized by a plane-wave amplitude reflection coefficient. The reflection coefficient (or bottom loss) is obtained either from bottom-loss measurements or from calculations using mathematical models of the bottom as an acoustical reflector (bottom-loss models). Bottom-loss models require, as input, detailed information on the physical properties and layering of the bottom material. This presentation relates the topics of bottom-loss measurements and models, bottom physical properties and topography to long-range propagation. Sensitivity of propagation loss to bottom parameters is discussed.

INTRODUCTION

The ocean bottom is one of the boundaries with which a propagating underwater sound wave may interact. In some cases our present techniques for including bottom interaction in propagation models do not allow accurate prediction of propagation when bottom interaction is significant. Perhaps this is because our input information is incomplete, or perhaps our method of including the bottom influence should be refined.

Several topics are of interest in the bottom interaction problem. These include:

- Models of bottom interaction presently used in propagation models
- Models that allow the inclusion of bottom effects: bottom-loss models and geoacoustic models.
- The order of magnitude of observed and predicted bottom loss values
- Measurement techniques and presently available data for acoustical and other physical properties of the bottom
- The sensitivity of bottom loss to variations of the input sediment parameters
- The sensitivity of propagation predictions to variations in the bottom information.

Unresolved issues concerning bottom properties for long-range propagation include the following questions:

- What is the sensitivity of predicted long-range, low-frequency propagation loss to variations in the sediment, either bottom loss or physical parameters?
- What is the sensitivity of bottom loss to sediment parameter variation?
- To what depth and in what detail do we need sediment information to predict bottom loss?
- What information do we now have and what techniques need further measurement?

Two general techniques treat mathematical propagation problems. These are, of course, ray theory and wave theory. Each technique may treat the bottom as a reflecting surface or as part of the propagation path.

For example, in the ray-theory models we identify eigenrays by searching through ray families until we find two that bracket a

receiving point and then converge on an eigenray. Once the eigenrays are identified, one way of treating the influence of the boundaries and in particular the bottom is through an interface reflection coefficient, a Rayleigh plane-wave reflection coefficient.

Either method of treating the bottom requires more detailed information about the physical properties of the bottom sediments. These physical properties include acoustical properties such as speed of propagation and attenuation and are combined in what Hamilton (1974) calls a geoacoustic model.

In some cases when the boundary is treated as a reflecting interface, we can go through an intermediate model, feeding the geoacoustic model information into a mathematical model for computing bottom loss. An alternative is to structure the measurements of bottom loss into an empirical model.

BOTTOM-LOSS MODELS

Figure 1 illustrates some of the bottom-loss models. Standard empirical bottom-loss models consist of tables of bottom loss versus grazing angle. Probably the earliest of these came from the AMOS program, another set was developed at Fleet Numerical Weather Central based on the MGS data, and some have been based on the FASOR data. NAVOCEANO also has a set. Other measurement programs have produced what can be considered as empirical bottom-loss models at various frequencies.

Mathematical models progress through a series of increasing complexity using plane interfaces, plane layers, plane waves. Models with liquid layers can progress to layered models that support shear waves. More complex models may have gradients of the acoustical

A. MEASUREMENTS (EMPIRICAL MODELS)

1. "STANDARD" TABLES AMOS
 MGS
 FASOR

2. SPECIALIZED

B. MATHEMATICAL MODELS

1. PLANE INTERFACE
2. ROUGH INTERFACE
3. PENETRABLE ROUGH INTERFACE
4. SEDIMENT PARAMETERS → GEOACOUSTIC MODEL

Figure 1. BOTTOM-LOSS MODELS

parameters with depth. Effects of rough interfaces have been studied by Horton (1976). All of these require some type of geoacoustic model.

GEOACOUSTIC MODEL

A geoacoustic model may be described as a quantitative description of the pertinent sediment and water parameters, particularly the former. This description includes at least the following:

- Layering that exists and depths of these layers
- Compressional-wave speed and attenuation
- Shear-wave speed and attenuation
- Density
- Gradients, if they exist, of speed and density
- Bottom topography.

BOTTOM-LOSS VALUES

Figure 2, an example of an empirical model, shows the low-frequency bottom loss versus grazing angle model. There are several notable features of these curves. For the lower three curves, the bottom loss goes to zero between 10 and 20 degrees. This feature indicates a critical angle effect which implies no attenuation in the sediments. But when you put attenuation in, you don't see this zero bottom loss except at zero grazing angle. For the two higher bottom loss curves, we see that the loss does not go to zero even at zero grazing angle and this implies considerable influence of topography in these two classes of the empirical model.

Figure 3 is a mean bottom-loss curve (Urick, 1974). Observe some differences from numbers in Figure 2.

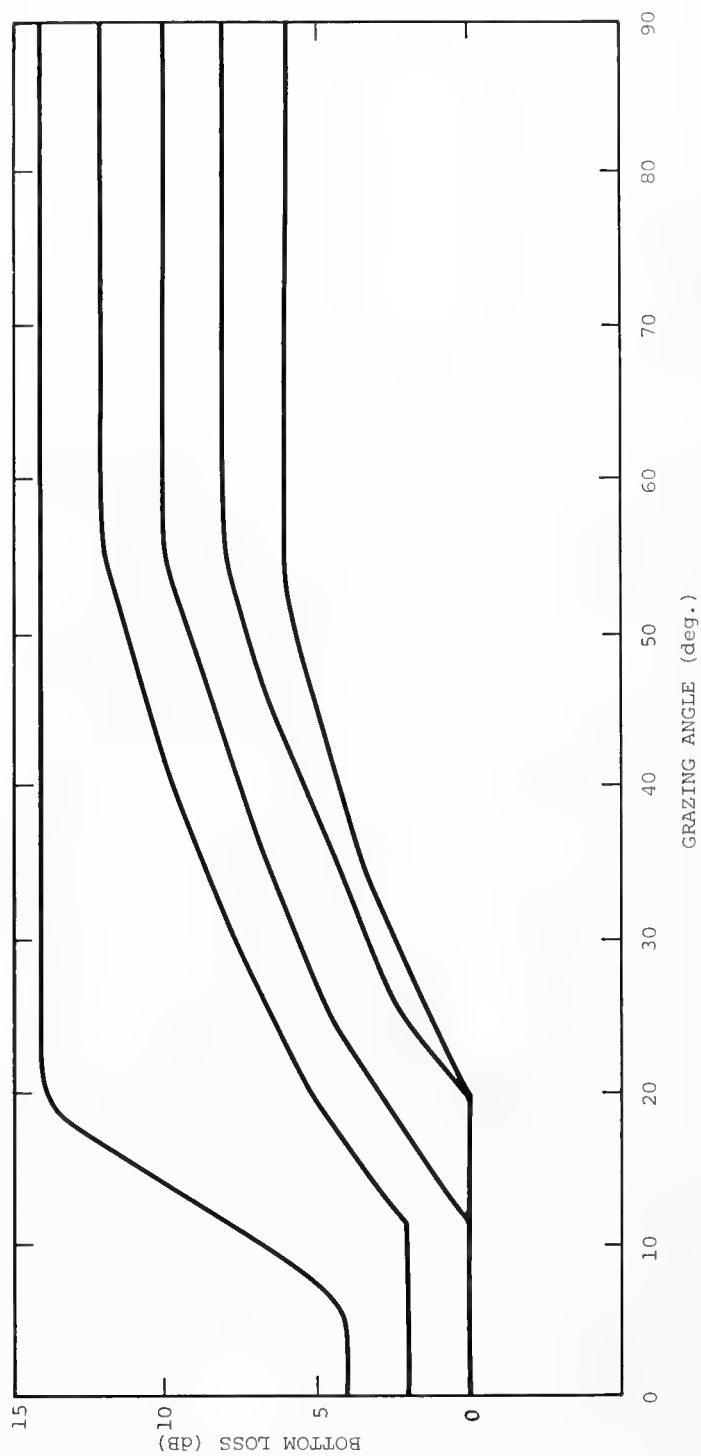
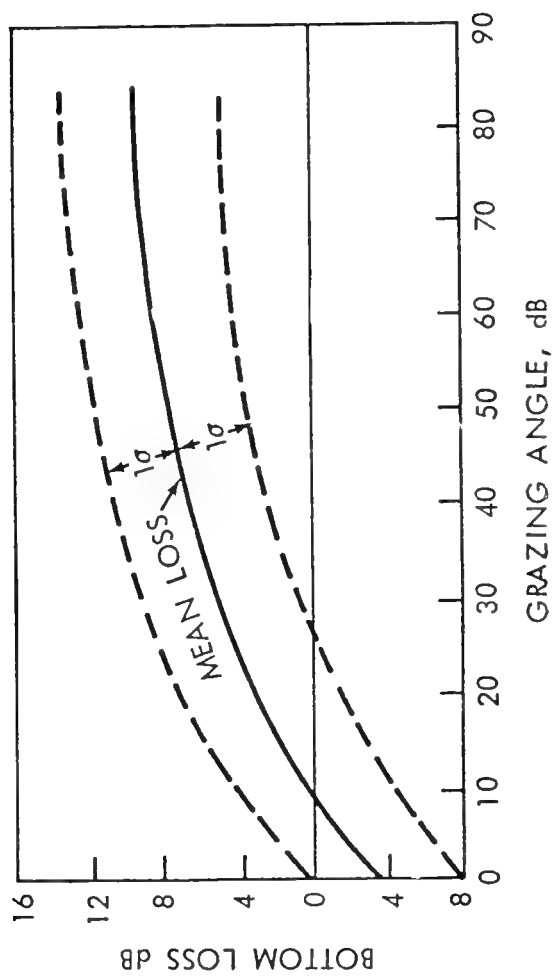


Figure 2. BOTTOM-LOSS CURVES Set 1



Source: Urlick, 1974.

Figure 3. MEAN BOTTOM-LOSS CURVE

Figure 4 presents a comparison (Bucker, 1974) with data and a computation with a linear-gradient model of Morris. The data are for one-third octave at 50 Hz and the theory (solid line) is for continuous wave.

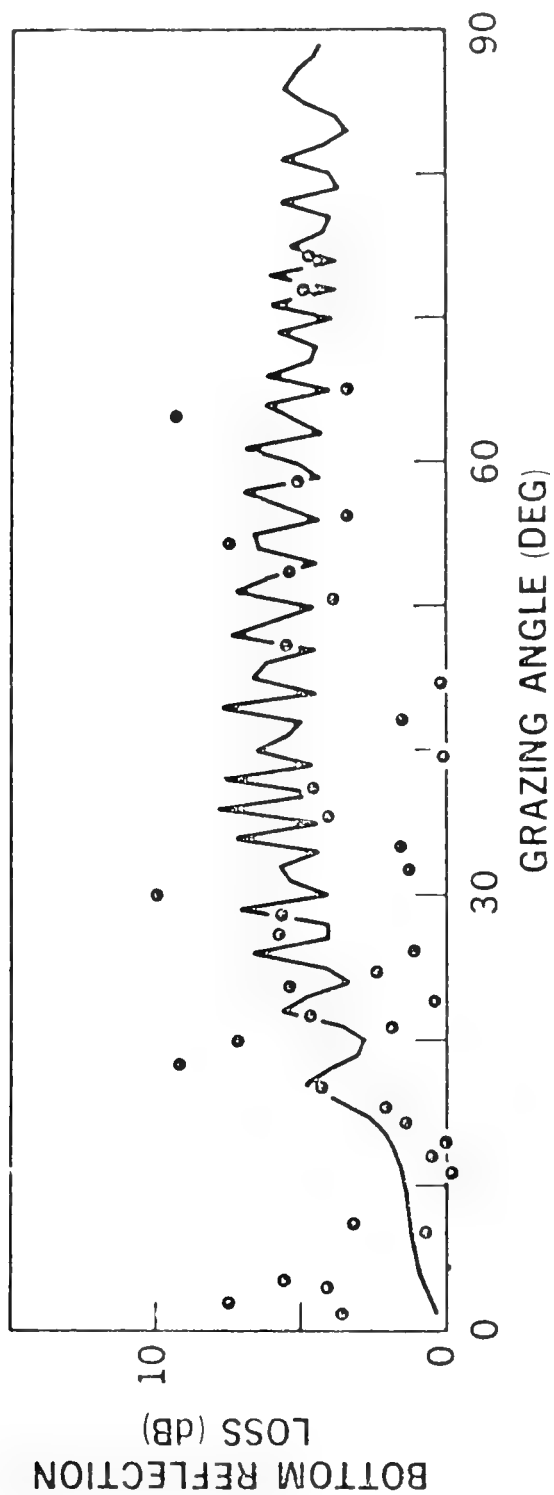
BOTTOM PHYSICAL PARAMETERS

There are essentially three depth intervals into which sediment can be broken for measurement techniques: surficial sediments, corer-depth sediments, and deeper sediments.

In the surficial sediments, acoustical properties have been measured fairly extensively, especially the compressional-wave speed at higher frequencies. The surficial sediment includes about the first meter. These have been probed by everything from divers to the diving saucer, with various types of probes, and with self-operating units. Considerable information is available in the literature about some of the parameters. Physical properties have also been studied extensively using grab samples and cores.

Corer-depth sediments extend from the one-meter depth to perhaps 30 or 40 meters for the very long cores. Acoustical information is available to this depth from high-resolution sub-bottom profiling in some regions. Core sediment samples are measured in the laboratory and these values are then extrapolated to *in situ* values. Compressional wave speed and attenuation are studied, especially again at high frequencies.

Recently, a different technique was instituted for corer-depth sediments by ARL/Austin. It is a device called a profilometer which projects a pulse across the diameter of the corer as the core is being taken and measures compressional-wave speed and attenuation in the sediment at a carrier frequency of 200 kHz.



Source: Bucker, 1974

Figure 4. BOTTOM-LOSS VS GRAZING ANGLE

Measurement information on the deeper sediments comes from sub-bottom profiling of one kind or another; e.g., reflection and refraction profiling. Most of the information concerns the speed of propagation of compressional waves which is converted into information about depths to sub-bottom reflectors.

Physical information comes from drilled samples. Considerable information is being compiled by the Deep Sea Drilling Project. An interesting idea might be velocity-logging these holes.

Most available data on the bottom physical and acoustical parameter values are for high frequencies and compressional-wave speed.

In surface sediments, Hamilton (1974) has added to our knowledge of *in situ* values of surficial sediment speed and of techniques for extrapolating laboratory measurements to *in situ* values.

Figure 5 represents something like 3,000 measurements of speed of propagation of compressional waves, and they are plotted as a ratio of speed of propagation in the sediment to that in the water. They show the well known, somewhat well defined relationship between speed of compressional-wave propagation in sediments and porosity. These are high-frequency values.

The values go from something like 0.95 or about 5 percent lower than the value in bottom water to almost 30 percent higher than the value in bottom water. Sound-speed values outside this range of variation are anomalous for unconsolidated sediments. Such values are usually associated with gas in the sediment in some form. In shallow water sediments, gas will exist as a phase, a gaseous phase, and it will decrease the value of speed of propagation. In deeper water, it is more likely to exist as a gas hydrate or clathrate, and it will

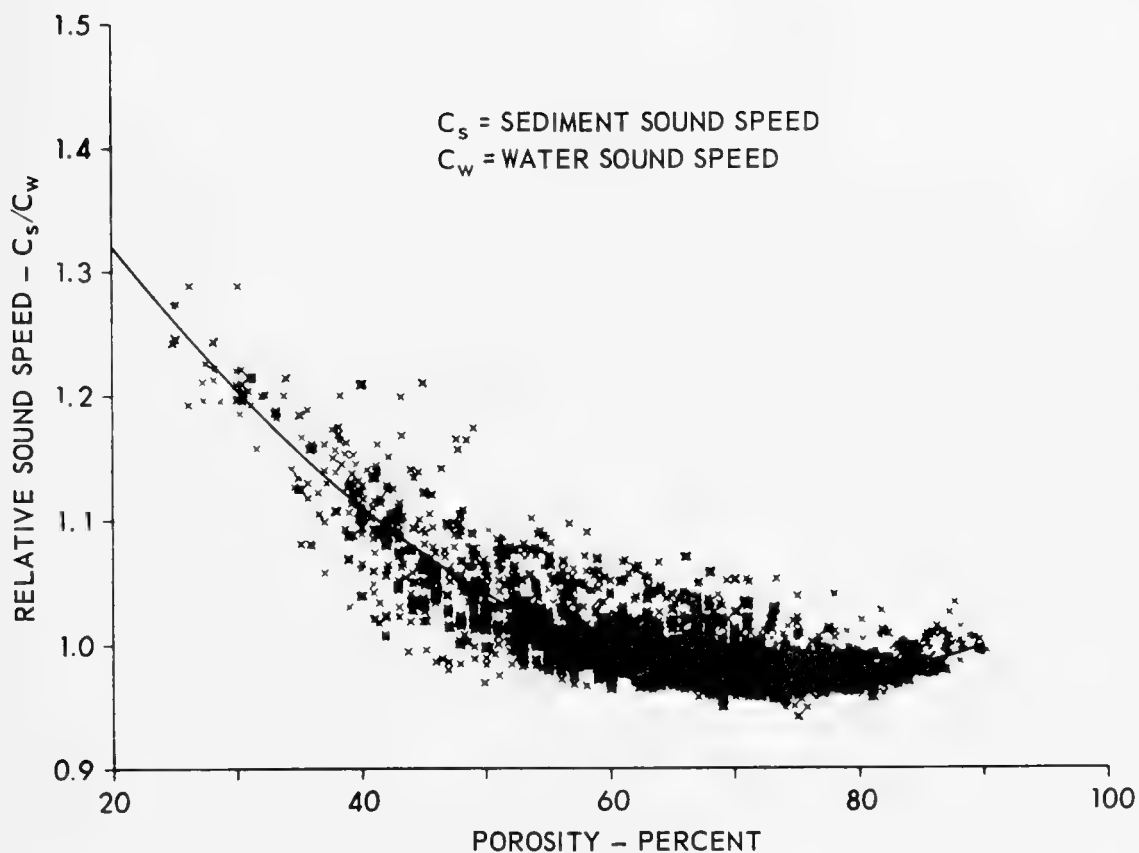


Figure 5. RELATIVE SOUND SPEED (RATIO OF SPEED IN SEDIMENT TO SPEED IN WATER) VS SEDIMENT POROSITY (AFTER AKAL, 1972)

greatly increase the speed of propagation. In the latter case, the sediment essentially looks like it is partially lithified.

Figure 6 shows the interval velocity for a region and Hamilton's estimate of the best fit line to the instantaneous velocity data. In this example, the instantaneous velocity, which is the one that would go into a propagation model, is nonlinear over an extended depth interval. However, the interval velocity, which is the average velocity over the measured depth interval, remains somewhat linear.

Compressional-wave attenuation is another important parameter. Figure 7 is a compilation from a large number of sources of data for acoustical attenuation in dB per meter versus frequency. These results are for measurements which were made in clays and silts. It is a presentation which is similar to what Hamilton uses.

Several things can be seen. One is the order of magnitude of the attenuation. Another is the absence of any data for anything below 1 kHz.

Another observation is that over short frequency intervals in any given sediment the attenuation may not vary linearly with frequency. But if we take the overall behavior as we go down the graph, attenuation varies linearly with frequency. If this is true, and certainly these data seem to indicate that it is, then it suggests a way to get a number for the attenuation at low frequencies. We must decide what value we are going to accept for attenuation at some high frequency and extrapolate linearly downward to a lower frequency of interest. We hope to improve upon this extrapolation in the future.

If we accept that attenuation is described as a linear function of frequency — that is, the attenuation coefficient is equal to

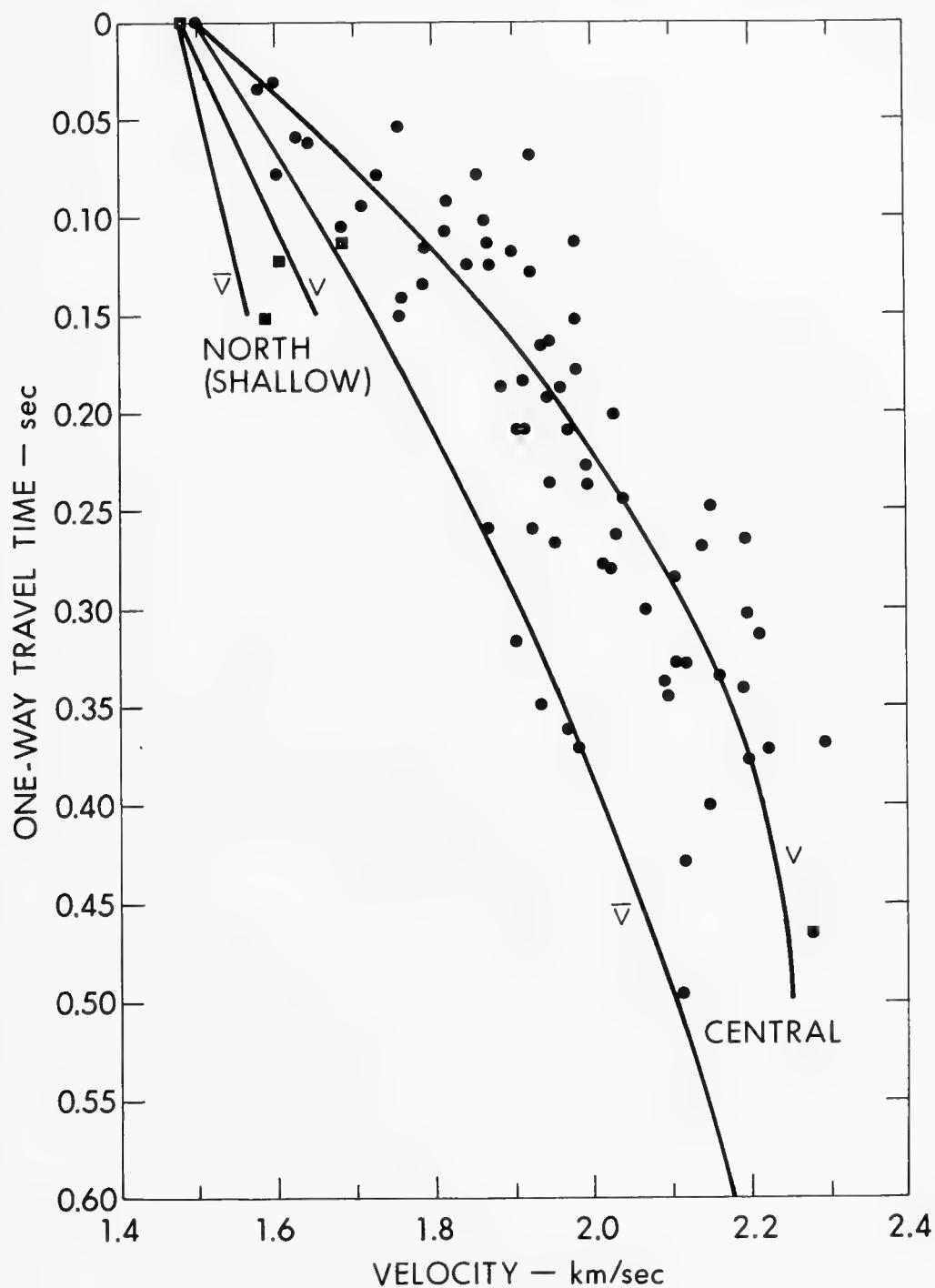


Figure 6. TRAVEL TIME VS VELOCITY

(Source: Hamilton, 1974)

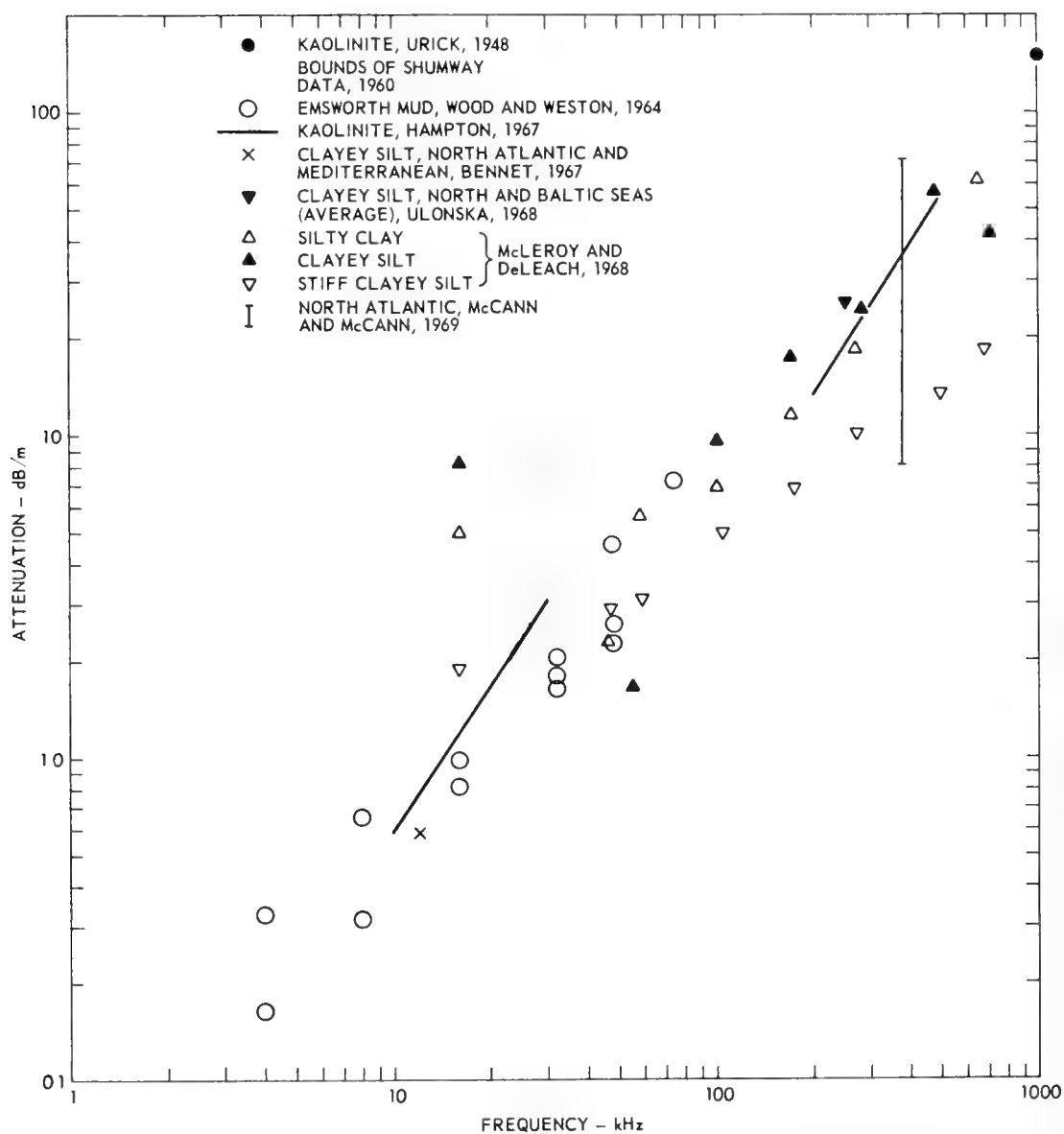


Figure 7. ACOUSTICAL ATTENUATION VS FREQUENCY IN CLAYS AND SILTS (LESS THAN 1% SAND)

some K' times frequency to the first power — and we examine data that Hamilton (1974) has presented on attenuation for Pacific sediments and data that Smith has presented for attenuation in Atlantic sediments, then we find that we can plot the values of the coefficient K' versus the mean grain size of the sediment, Figure 8. The resulting relationship will help us select the K' to be extrapolated as a linear function of frequency.

Other bottom parameters in the geoacoustic model include bulk wet density, which is usually measured with samples, and shear-wave speed which has been measured only in a very limited manner. Bucker (1974) appears to be one of the few who has actually made these measurements. He measured Stonely waves and interpreted them in terms of velocity of propagation of shear waves.

The answer to the question raised earlier about whether these sediments behave as liquids or as solids depends on what you mean by the question. If the question is "Do shear waves propagate?" the answer depends on whether there is a finite value of dynamic shear modulus. Values of dynamic shear modulus have been measured in most ocean sediments somewhere on the order of 10^8 to 10^9 dynes per square centimeter. Propagation speeds of the shear waves are something on the order of a tenth of the value of propagation speeds for the longitudinal waves.

In near-shore sediments, very high porosity sediments, harbors and lagoons, we find even lower values of shear modulus. The lowest values of dynamic shear modulus are exhibited by freshly mixed, pure laboratory clays like Kaolinite, for which values of less than 10 meters per second are predicted for shear-wave speeds from measured values of dynamic shear modulus.

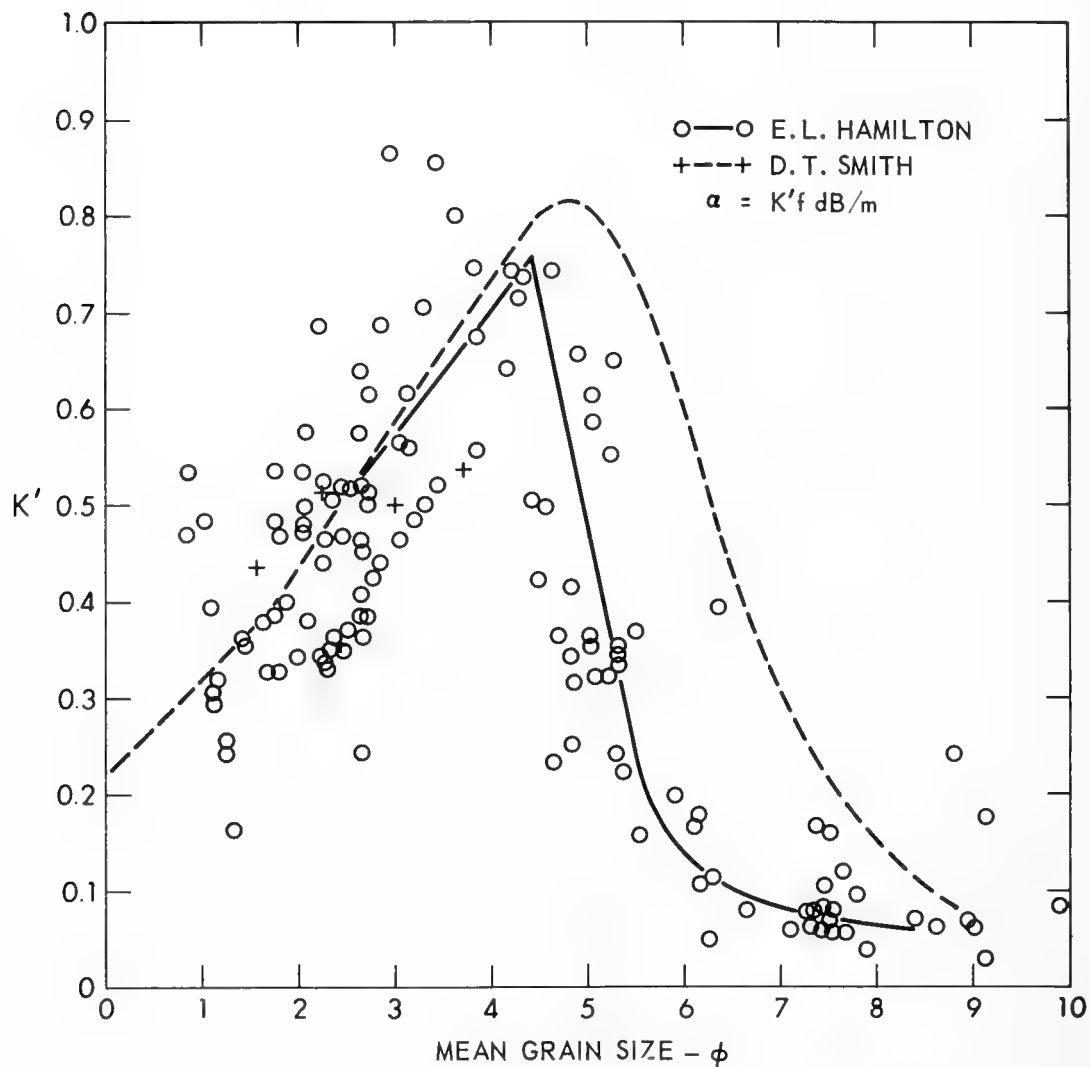


Figure 8. MEAN GRAIN SIZE VS ATTENUATION CONSTANT K'

Shear wave attenuation measurements are few. Some measurements of the complex dynamic shear modulus allow prediction of a shear wave attenuation.

What does all this have to do with bottom loss and with propagation loss at low frequencies? What is the sensitivity of this thing we call bottom loss (which is an input to ray-theory models) to variations in sediment parameters?

The simplest reflection models, using a liquid layer without any attenuation, a single layer overlain by water, can fit some of the things that we see in Figure 9. Judicious selection of the sound-speed ratio can make the critical angles fit, and juggling the density ratio can cause the bottom-loss values at normal incidence to fit. Unfortunately, when this is done, the grazing-angle segment just above the critical angle does not fit these data. This seems to indicate that the single bottom layer is far too simple a model. Disagreement is not as bad as one might expect. The important thing is that this shows realistic values of speed of propagation and of density for bottom sediments. One problem, however, is that some of the bottom loss obviously is going to be contributed by topographic effects which are not included here.

Figure 10 shows the results for a water layer overlying a two-layer bottom. This three-layer model, with a clay overlying sand in the bottom, is shown merely to indicate the type of variation that is shown at 100 Hz for a value of attenuation obtained by the extrapolation process mentioned earlier. The sound speeds are 1,501 meters per second in the water, 1,531 meters per second in the clay, and 1,657 in the silty sand, with realistic values for density and with a 100-meter thickness for the clay layer.

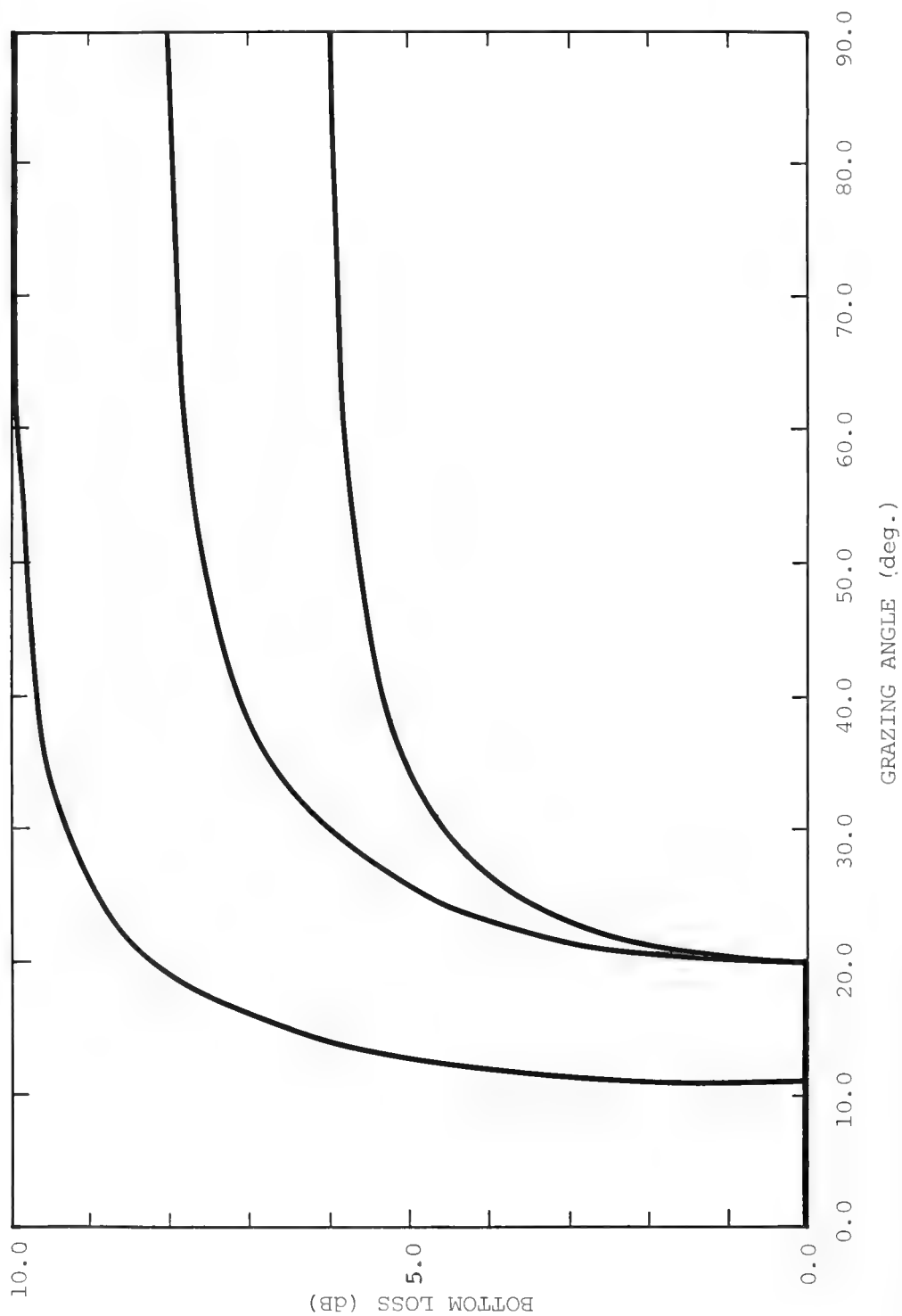


Figure 9. BOTTOM-LOSS VERSUS GRAZING ANGLE
SINGLE LIQUID LAYER BOTTOM

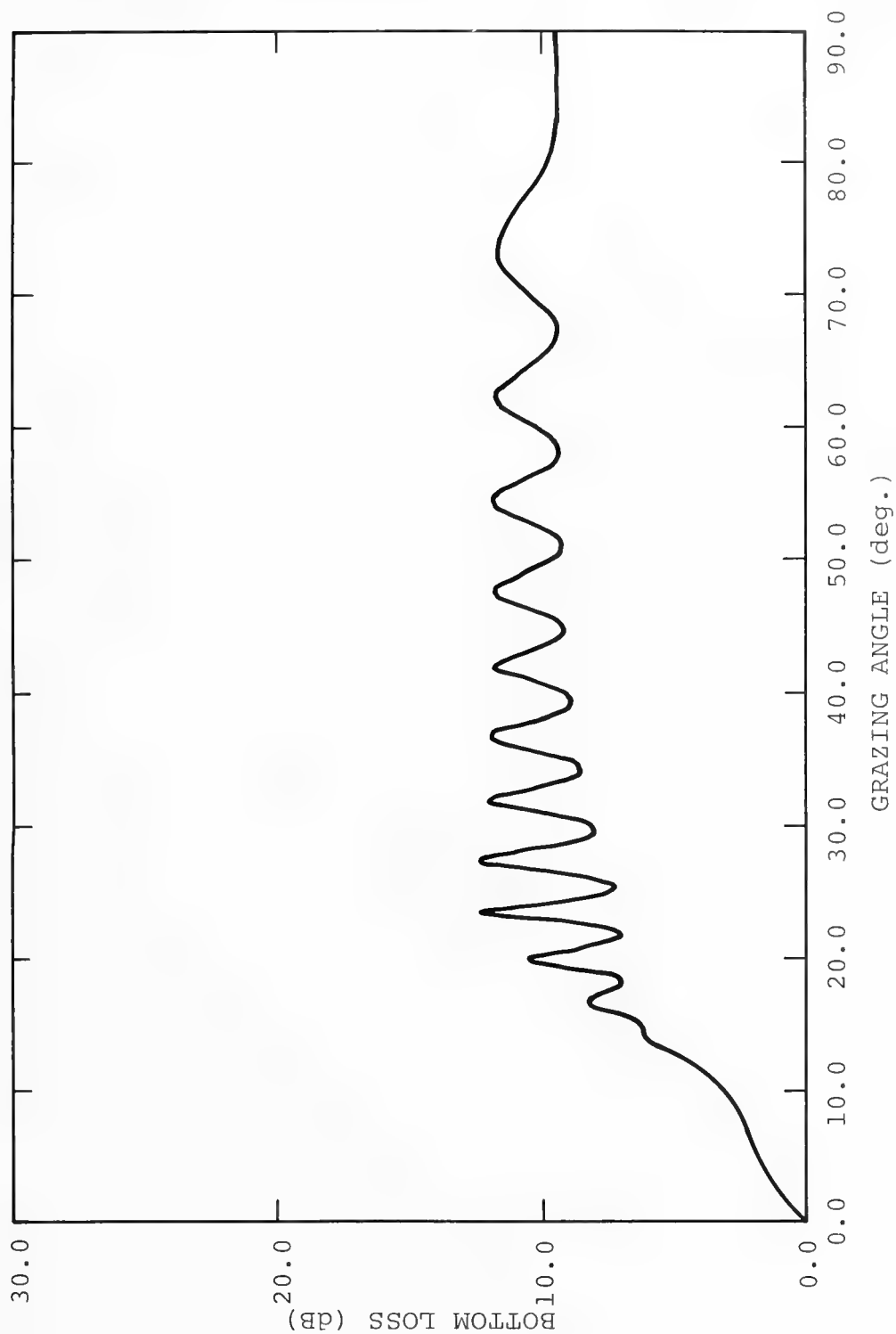


Figure 10. BOTTOM-LOSS VS GRAZING ANGLE
THREE LAYER MODEL
(CLAY LAYER THICKNESS=100m)

We see the indicated interference structure in the variation of bottom loss with grazing angle. Why do this? If we extend the depth of the layer, we will see to what depth we must go before we begin to lose the effect of the clay/sand interface.

Figure 11 shows the results when the intermediate layer is 200 meters thick. The interference structure is reduced, but still present. Figure 12 shows results for a layer thickness of 500 meters. Figure 13 is for 1,000 meters. The interference structure is gone. Thus, for a layer of this thickness and the assumed attenuation, the Rayleigh reflection-coefficient model indicates that the lower interface with a sand layer does not influence the bottom loss.

Doing this for the same type of clay overlying basalt, where we have a considerable impedance contrast between the clay and the basalt, the following results are calculated.

In Figure 14, the highly variable curve is for 70 meters of clay overlying basalt. The smooth curve is for a 1,000-meter thick clay layer over basalt.

These results indicate that if the reflection model used here were valid for bottom regions described by the parameters assumed here for the clay layer, and if we knew the information about the sediment column to 1,000 meters depth, we wouldn't have to know anything about it from there on down.

Also, we have seen instances where there is considerable energy return from 2 to 3 kilometers. The result described above is critically dependent on the value of attenuation that is used for the layer. Also, the model used for the calculations does not include gradients in the layers. This work is being extended to include gradients in the bottom.

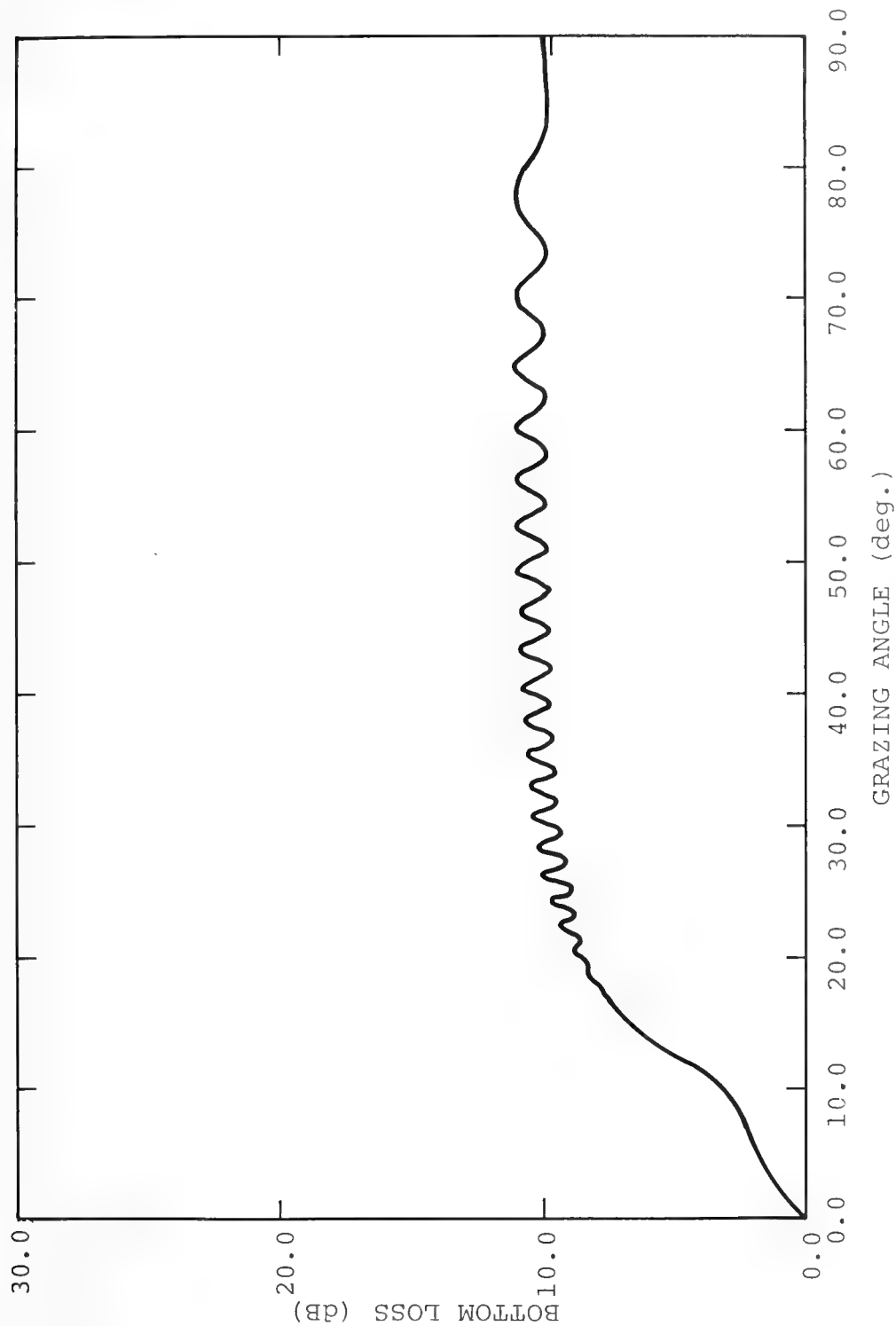


Figure 11. BOTTOM-LOSS VS GRAZING ANGLE
THREE LAYER MODEL
(CLAY LAYER THICKNESS=200m)

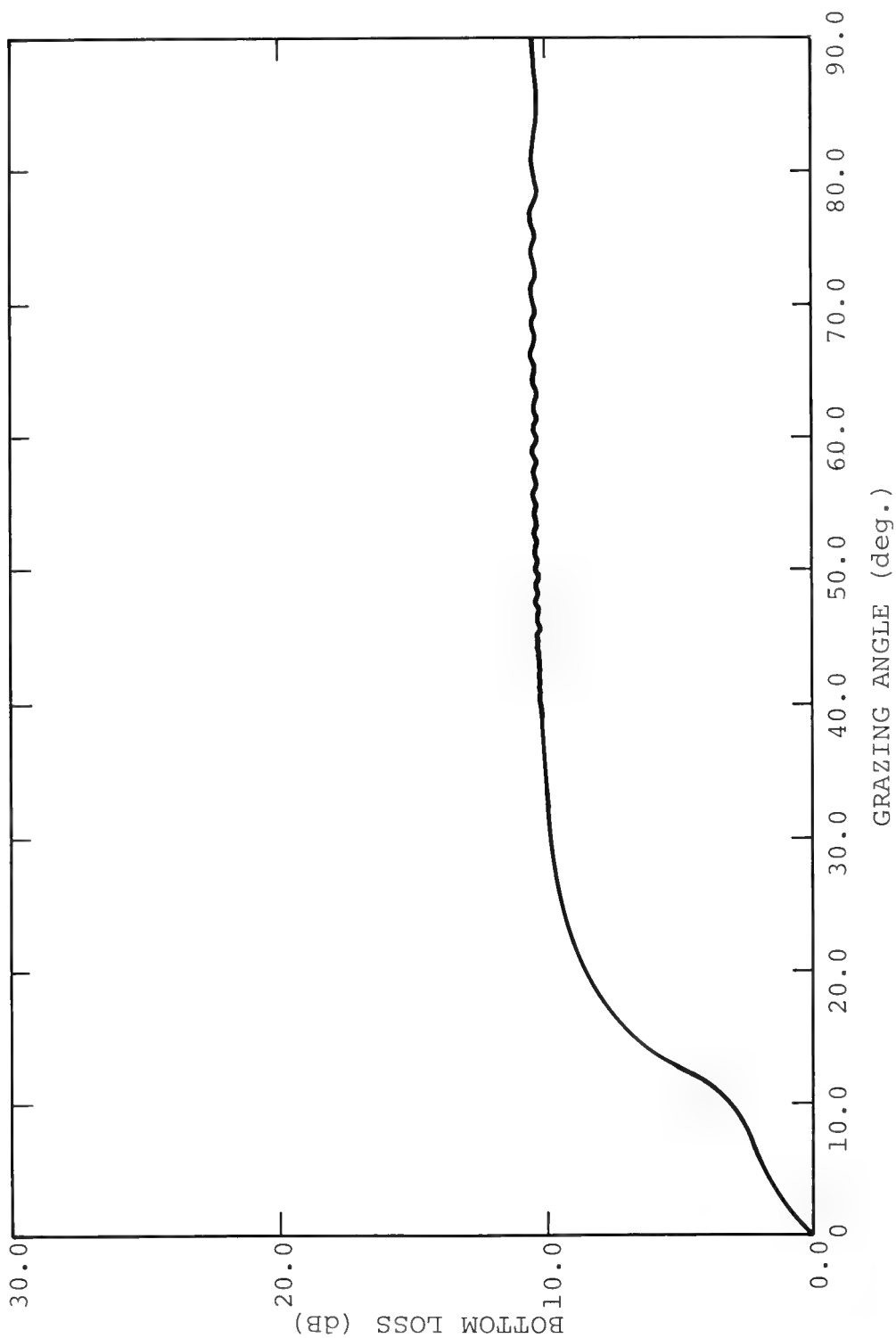


Figure 12. BOTTOM-LOSS VS GRAZING ANGLE
THREE LAYER MODEL
(CLAY LAYER THICKNESS=500m)

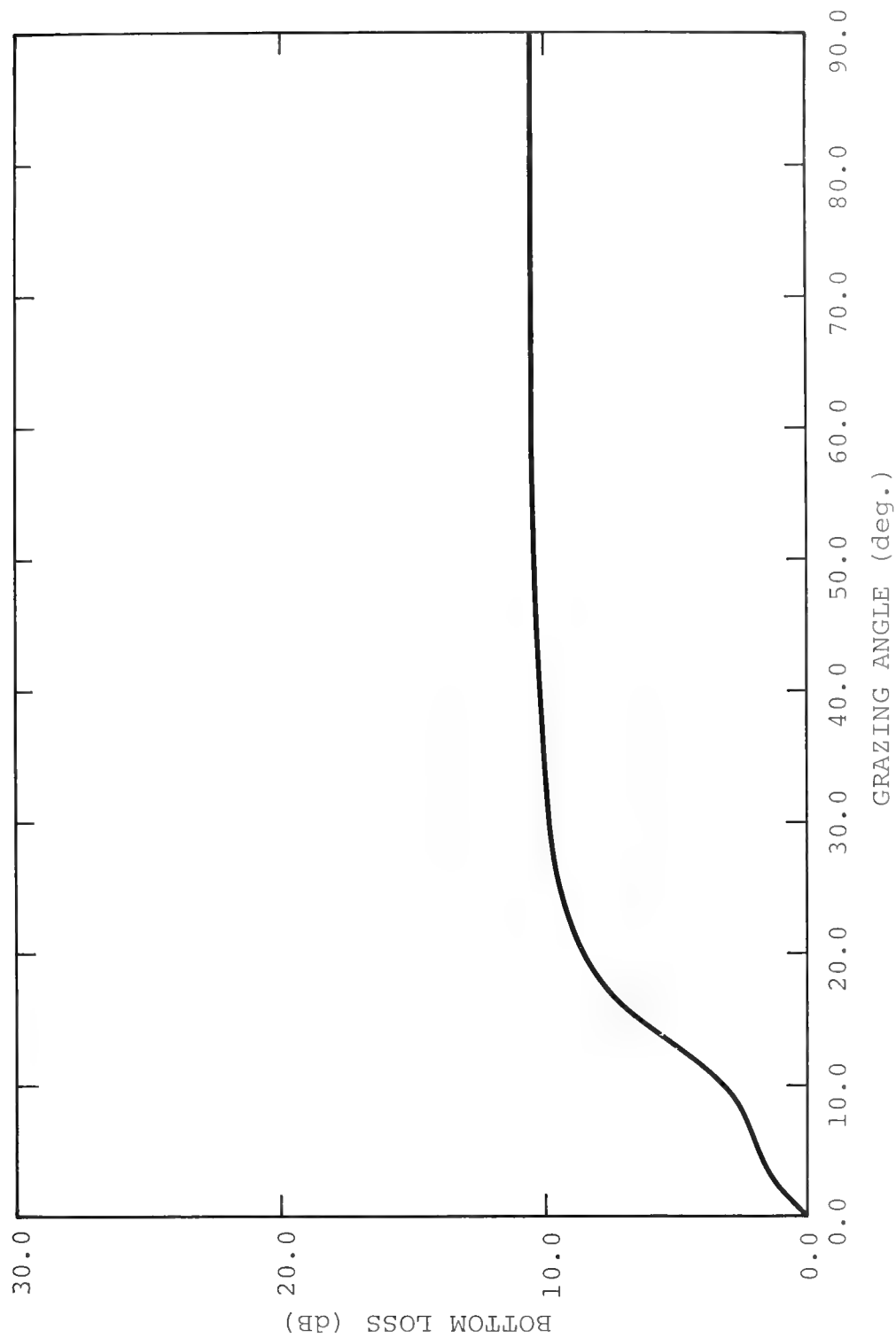


Figure 13. BOTTOM-LOSS VS GRAZING ANGLE
THREE LAYER MODEL
(CLAY LAYER DEPTH=1000m.)

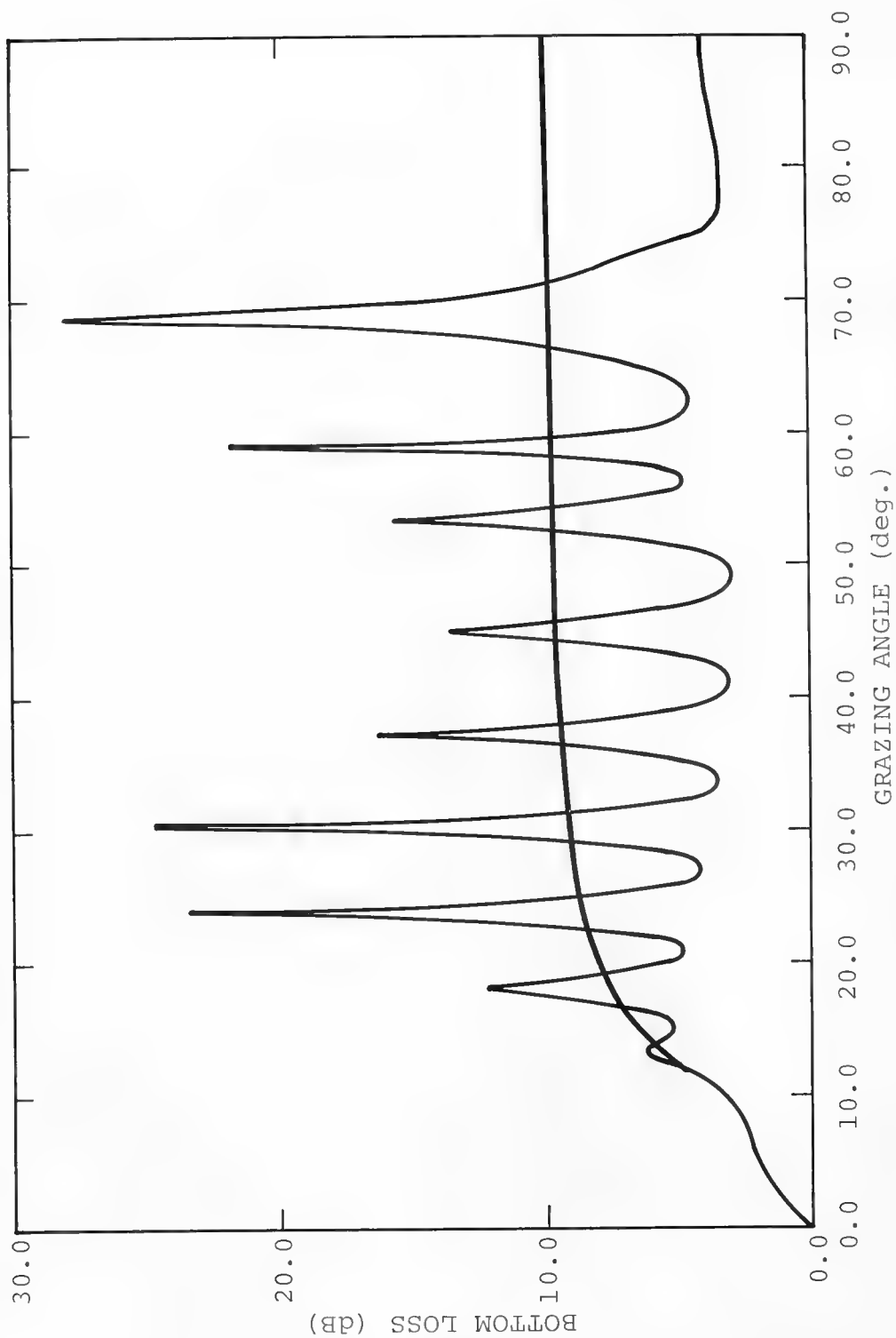


Figure 14. BOTTOM-LOSS VS GRAZING ANGLE:
CLAY OVERLAYING BASALT

REFERENCES

- Bucker, H. P., "Sound Propagation Calculations Using Bottom Reflection Functions," in *Physics of Sound in Marine Sediments*, L. Hampton (ed.), Plenum Press, 1974.
- Hamilton, E. L., "Geoacoustic Models of the Sea Floor," in *Physics of Sound in Marine Sediments*, L. Hampton (ed.), Plenum Press, 1974.
- Horton, C. W., These Proceedings.
- Urick, R. J., "Underwater Sound Transmission Through the Ocean Floor," in *Physics of Sound in Marine Sediments*, L. Hampton (ed.), Plenum Press, 1974.

DISCUSSION

Mr. Charles Spofford (Office of Naval Research): What value do you get by extrapolating Figure 7 to 100 Hz?

Dr. A. L. Anderson: About 0.026 dB per meter, something like that.

Mr. Spofford: We have seen data in certain areas where there is a very thick unconsolidated sediment. Assuming a 20-degree ray and a refracting gradient of one in the bottom, the ray spends about 1,000 meters in the bottom per bounce.

We have seen data where essentially that ray appears to have bounced up to about 10 or 20 times even out to 200, 250, and 300 miles without suffering appreciable loss. Figure 7 would lead to about 20 dB in 200 miles. I would say if it has lost anything it might be about 2 dB. It is that little.

Dr. A. L. Anderson: I think there are two significant points. One is, as I pointed out, this calculation was made for a model without gradients, so we need to remember that, although it is not particularly germane to your point, Also, I think that you may very well have a good, if not the only, way of actually measuring attenuation at a given frequency in the sediments.

Dr. D. C. Stickler (Applied Research Laboratory, Pennsylvania State University): I would like to point out that in your models of plane-wave reflection coefficients, your layer media, that some of those same effects can be observed even without the layering.

If you consider the full effect of a point source in the isovelocity halfspace and higher speed bottom, you can observe some of these oscillations away from the grazing angle and the breakaway from the 0 dB loss above the line.

Dr. A. L. Anderson: Precisely, which says you must consider something other than a plane-wave reflection coefficient.

Dr. D. C. Stickler: Yes. If you do the full-wave solution for a point source in isovelocity halfspace over a higher speed isovelocity halfspace and examine just the reflected field, then these oscillations above grazing are present and the breakaway from the zero reflection coefficient is also observed and is not related to layering at all and is also frequency-dependent.

Dr. W. H. Munk (Institute of Geophysics and Planetary Physics, University of California at San Diego): Question based on ignorance. Are there good statistical models of the sea bottom? And, I mean it in the sense of existing statistical models of the sea surface that I am familiar with which have indicated that scattering from an angle of incidence steeper than the root mean square slope behaves

entirely differently than scattering at angles of incidence much less than the root mean square slope. One region is specular and in another case it is backscattering. Are there similar kinds of considerations for sea-floor scattering?

Dr. M. Schulkin (Naval Oceanographic Office): Not quite, but there is a spectrum of the sea floor bottom that has been proposed — K^{-3} .

Dr. Munk: Is that taken seriously?

Dr. Schulkin: Well, until there is something to replace it, it is semi-serious.

Dr. Munk: It goes down to what short wave length? Two hundred meters?

Dr. Schulkin: Yes.

Dr. Donald Ross (Tetra Tech, Inc.): May I make a comment on some model work? We are closely associated with the work that is going on at Naval Undersea Center in which a computer model for propagation, FACT model and FACT extended, is being compared with hundreds of experimental measurements in the low-frequency regions and we are finding that the models do well in the region in which you have refracted rays and that they are extremely sensitive to bottom loss in the region in which the bottom is involved, that the bottom loss is apparently averaging of the order of 1 dB, and that a quarter of a dB difference in the loss per bottom bounce makes a significant difference in the results that you get when you are comparing the experiment and the propagation model.

In all of your graphs it is very hard to see a quarter of a dB and in order to make significant calculations, we need bottom loss to a quarter dB.

I think that this may mean that the way to get it is to make measurements of propagation and deduce backwards what the bottom loss must have been rather than to try to calculate it or make direct measurements of bottom loss.

FORWARD SCATTERED LOW-FREQUENCY SOUND FROM THE SEA SURFACE

W. I. Roderick

Naval Underwater Systems Center
New London Laboratory
New London, Connecticut

Low-frequency propagation over long ranges can have propagation paths that interact with the time-varying sea surface. Theoretical predictions and experimental observations of specularly reflected CW acoustic signals indicate that the long gravity waves on the sea surface modulate the amplitude and phase of the incident signal. The Doppler spectrum of the modulated signal consists of a discrete frequency component centered at the carrier and a continuous spectrum that is positioned symmetrically about the carrier. The continuous spectrum consists of energy that has been scattered close to the specular direction and that, when summed with the specularly reflected signal produces amplitude and phase modulation. A review is given of important contributions to our understanding of the forward scattered Doppler spectrum and its functional relationship to geometrical, acoustical, and sea surface parameters.

This paper is an informal review of one particular aspect of forward scattered sound from the sea surface and that is the Doppler spectrum that would be received in the specular direction. The Doppler spectrum is the spectrum resulting from amplitude and phase modulation of an acoustic signal reflected and scattered from a time varying surface.

About 1965, Wysor Marsh looked at two separate aspects of scattering, one of which was the Doppler spectrum (Marsh and Kuo, 1965). It is interesting to look at that report written 9 years ago and at a time when there had been no prior direct measurement of the Doppler spectrum in the specular direction. Wysor observed in

some low-frequency, long-range propagation data, published by Ken Mackenzie (1962), that the envelope of the signals had periods on the order of ocean swell waves and the spectrum looked narrowband. Based on a resonance scattering theory he developed in the early 60s, he derived the Doppler spectrum which was good to first order effects and included multiple-bounce surface interactions. Remarkable intuitive reasoning at that time put the theoretical prediction of the Doppler spectrum ahead of the experimental evidence.

What criterion do we use to distinguish between a rough and smooth surface? Lord Rayleigh took a simple approach (Beckmann and Spizzichino, 1963), pictured in Figure 1. He simply considered the phase difference between rays reflected from an uneven surface. For the wave shown, the crest to trough height is h , the grazing of the acoustic rays is ϕ , and the acoustic wave length is λ — Walter Munk might say here that this does not look like a sea surface wave, but he must consider that the wave was measured on the east coast of the United States.

Very simply, Rayleigh reasoned that if the phase difference is near zero, then the surface isn't very rough, that is, the path-length difference is small. As the phase difference approaches π there will be cancellation of energy in that direction and hence the energy must have been scattered elsewhere — this would constitute a rough surface. A criterion to separate smooth and rough surfaces is to choose a point midway between zero and π , say $\pi/2$. As you can see, the wave length, grazing angle, and wave height must be specified to define the roughness. These three parameters crop up again with the same relationship in more elaborate scattering models. As an example of the above, consider long-range propagation with a 5-degree grazing angle at the surface and an rms wave height of 2 feet — this

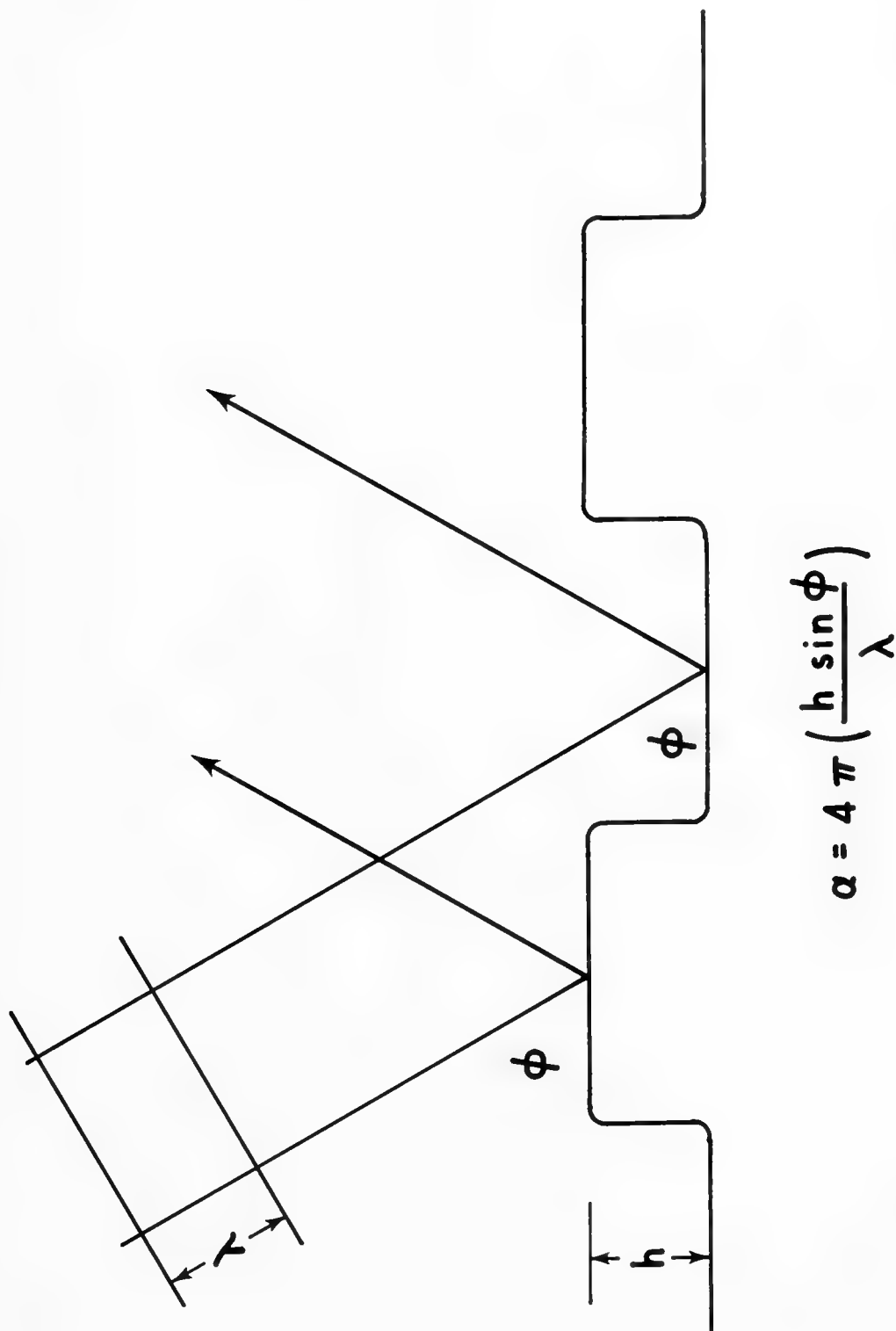


Figure 1. SCATTERING FROM AN IDEALIZED UNEVEN SURFACE

condition would require an acoustic frequency of less than 1,000 Hz to constitute a low-roughness surface.

About 1966, Allen Ellinthorpe published an article (Ellinthorpe, 1966) on sea-surface induced frequency smear. It should be noted that Doppler spectrum, frequency smear, and frequency spread all have the same meaning. Ellinthorpe was interested in determining the integration time for a communication system and performed a surface scattering experiment in Bermuda. To compare the experimental results, he derived the Doppler spectrum of the forward scattered sound based on a phase modulation technique. Assumptions were made that the surface scattered signal was only phase modulated, the surface wave height h was a Gaussian random variable, and the power spectral density of the surface waves was given by a Bretschneider spectrum. With these assumptions, he uses an equation derived by Middleton to determine the power spectral density of a signal that is phase modulated by a random variable that has a known power spectral density. The phase modulation index is given by a .

Ellinthorpe compares the theoretical results that were derived, based on the Middleton equation, to experimental data measured off the coast of Bermuda. In Figure 2, I have selected a comparison made at two frequencies. You can see that the agreement is close in the spectral peaks, but the spectral width of the predicted is narrower than the measured. In general, this is true of all his predictions. The predictions do not give an absolute value of the energy in the carrier and sidebands, and the predictions were obtained by varying the parameters to obtain a best fit. No oceanographic data were available. There is something of interest that will come up later — the sidebands of the measured spectrum are asymmetrical as shown for the carrier frequency of 856 Hz.

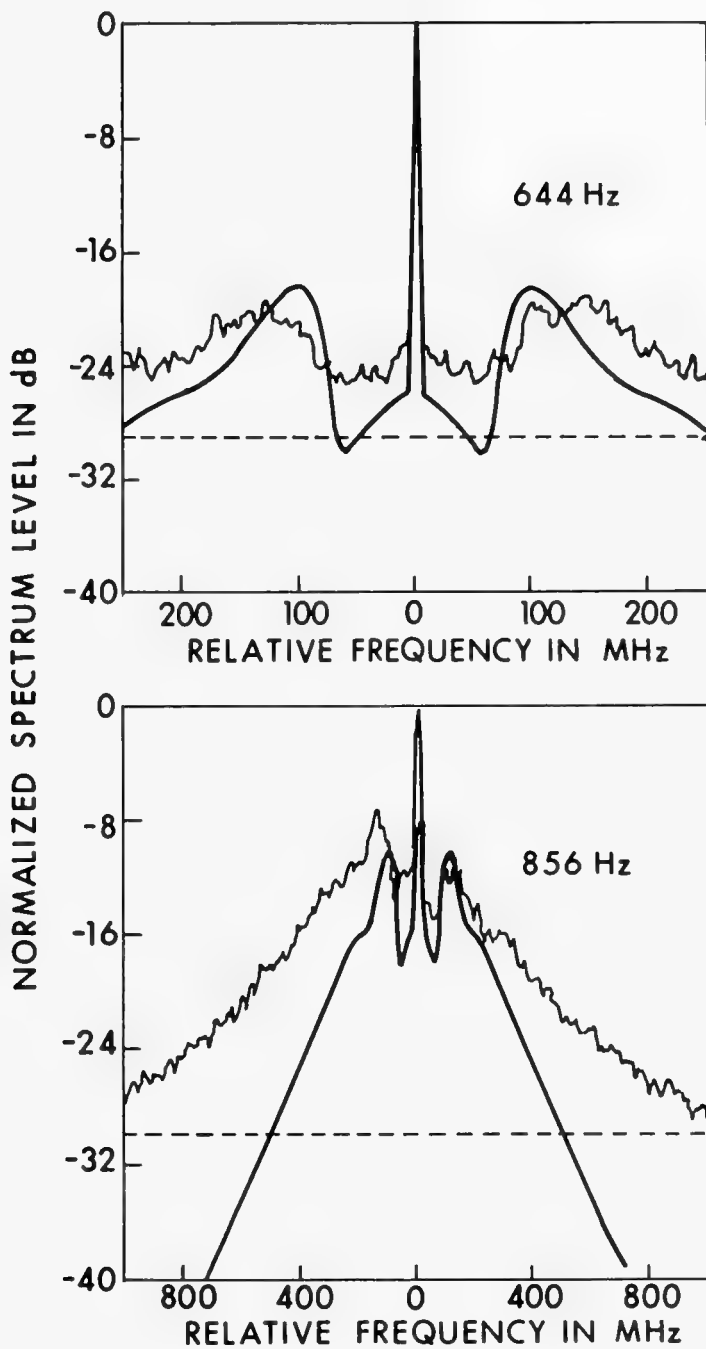


Figure 2. DOPPLER SPECTRUM AT TWO FREQUENCIES
(from Ellinor, 1966)

In 1967 B. E. Parkins of BTL published an article (Parkins, 1967) on the Doppler spectrum of scattered sound from a slightly rough and a very rough sea surface. He used what is termed a physical optics approach in his derivation, which is based on the Helmholtz Integral. The approach is based on some fundamental concepts introduced by Carl Eckart in 1953 on scattering from the sea surface (Eckart, 1953). Eckart's approach is one of the most elegant treatments you will find on surface scattering and before discussing Parkins derivation, we will review some of these concepts.

The evaluation of the Helmholtz Integral

$$4\pi P_1(A) = \iint \left\{ \frac{\partial P_1}{\partial v} \left[\frac{\exp(ikr_1)}{r_1} \right] - P_1 \frac{\partial}{\partial v} \left[\frac{\exp(ikr_1)}{r_1} \right] \right\} dS \quad (1)$$

requires knowledge of two boundary conditions — the value of the re-radiated pressure P_1 on the surface and the value of the derivative of the reradiated pressure $\partial P_1 / \partial v$ on the surface with respect to the surface normal. By assuming that the sea surface is pressure release, the reradiated pressure is set equal to the incident pressure with a 180-degree phase shift.

$$P_0 + P_1 = 0 \text{ on } S \quad (2)$$

To find the value of the derivative of the reradiated pressure with respect to the normal to the surface, Eckart assumes that the slope of the surface irregularities is small and finds the derivative with respect to the normal to the plane surface on which the gentle undulations are superimposed.

$$\frac{\partial P_0}{\partial v} = - \frac{\partial P_1}{\partial v} \text{ on } S \quad (3)$$

There are certain inherent assumptions with these boundary conditions and further approximations were generally made to obtain tractable solutions. One is the Kirchhoff method — that the acoustic field at any point on the surface can be approximated by the field that would be on a plane tangent to that point on the surface. Another is the Fraunhofer phase approximation — in the expansion of the phase of an exponential only the linear terms in the spatial coordinate system are retained. Claude Horton has shown the necessity in certain geometrical situations where also quadratic terms should be retained to yield the familiar Fresnel approximation (Melton and Horton, 1970). Inherent in Eckart's approximation for the normal derivative of the reradiated pressure is the implication of a surface with zero slope. It is also inherently assumed that there is no shadowing such that each facet on the sea surface is completely insonified. Brekhovskikh (1952) has given some restrictions on angle of incidence, surface curvature, and acoustic wavelength for complete insonifications of the surface irregularities. Research, both theoretical and experimental, at the Applied Research Laboratory, University of Texas, into the validity of the above approximations and assumptions has been extremely useful to other investigators in surface scattering.

We can take the same approach used by Eckart and solve the resulting equation for a traveling sinusoidal surface given by

$$\zeta(x,y,t) = h \cos [\omega_s t - kx \cos \alpha - ky \sin \alpha] \quad (4)$$

With the proviso that the surface slopes are small and other geometric approximations are met, the solution can be compared to experimental results. Roderick (1968, 1969) conducted small-scale tank experiments in which acoustic waves were scattered from a traveling sinusoidal surface created by an electrical-mechanical wave generator. Wave heights and surface wave lengths were accurately measured over the

insonified area, and conditions could be generated that modeled low-frequency sound propagation interacting with the gravity waves of the sea surface. Predictions were made for the normalized pressure reflected and scattered from a traveling sinusoidal surface of angular frequency ω_s , wave height h , and wave number k . The wave is propagating in a direction that makes an angle α with a vertical plan containing the angle of incidence and reflection.

An interesting result is observed for the scattered sound: the spectrum of the reradiation contains upper and lower sidebands positioned symmetrically about the transmitted frequency ω and displaced from ω by multiples of the surface frequency. The amplitudes of the frequency components are given by Bessel functions of the first kind and of order n . The argument of the Bessel functions are dependent on the angles of incidence and scatter, wave height, and acoustic wave number. These relationships are summarized in the following equation:

$$\rho = \sum_{n=-\infty}^{+\infty} F_n(\theta_1, \theta_2, \theta_3) J_n(c_n kh) \cdot \exp \left\{ \left[-i (\omega - n\omega_s) t - \frac{n\pi}{2} + \phi_n \right] \right\} \quad (5)$$

When the surface wave length is much larger than the acoustic wave length, most of the acoustic energy is scattered close to the specular direction, and it is not possible to resolve the specularly scattered signal (see Figure 3). The acoustic energy is scattered in space in selected directions determined by the familiar diffraction-grating equation of order n . (This same equation appeared in Flatté's talk (these Proceedings) during the discussion of the interaction of internal waves and acoustic fields.) The carrier frequency is

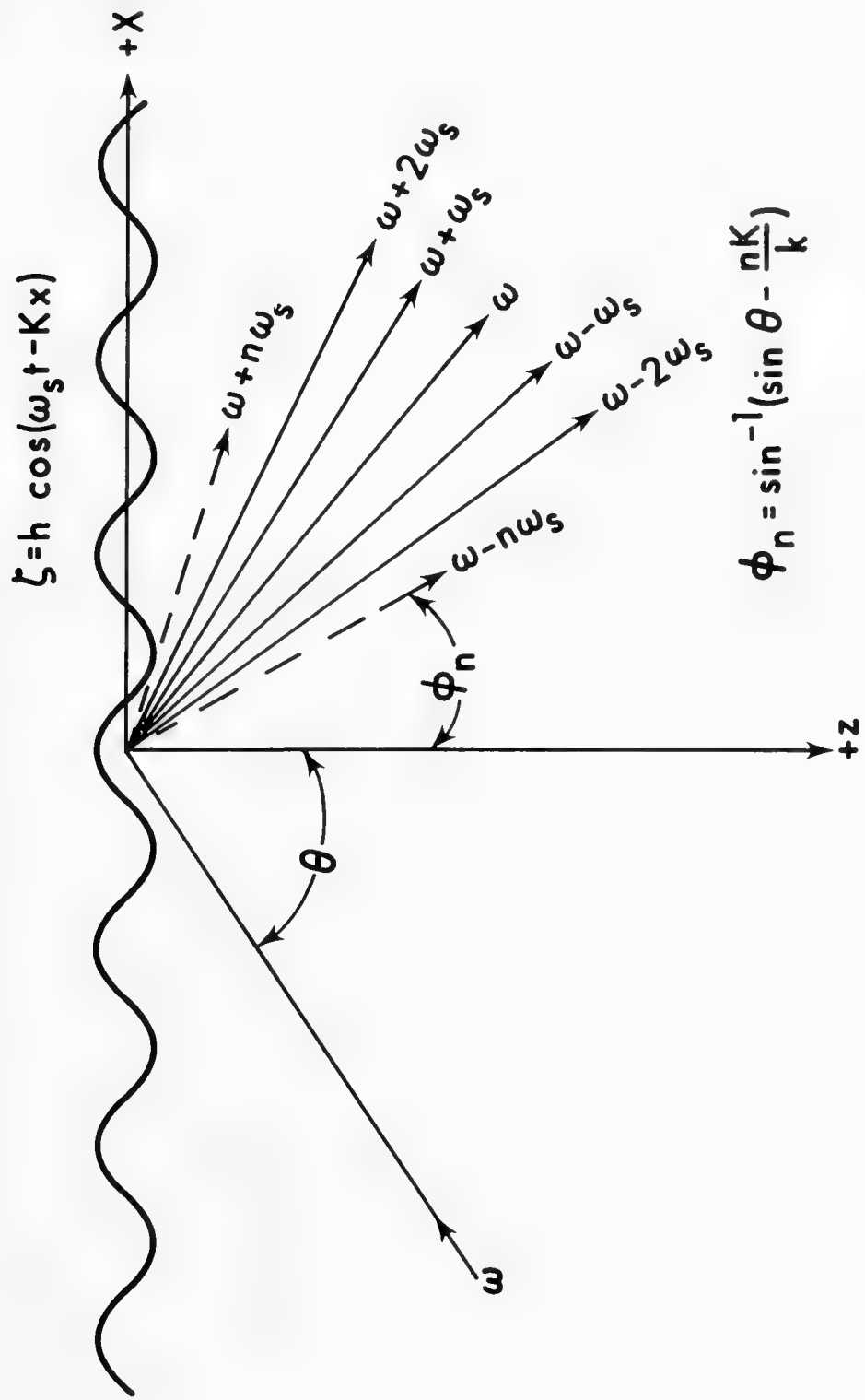


Figure 3. RAY SCATTERING DIAGRAM

reflected specularly and for small acoustic-to-surface wavelength ratios the energy is scattered in space symmetrically about the specular direction. For the direction of surface wave propagation shown, you would receive a down-Doppler in the backscatter direction. On the other side of the specular direction you would receive an up-Doppler. Reversing the direction of surface wave propagation, you would also reverse the directions of the Doppler shifts, e.g., an up-Doppler would be received in the backscatter direction.

The scattering directions of the n^{th} order sidebands are given by the angles θ_2 and θ_3 ;

$$\theta_2 \approx \theta_1 - \frac{n}{\cos \theta_1} \frac{\lambda_a}{\lambda_s} \cos \alpha \quad (6)$$

$$\theta_3 \approx -n \frac{\lambda_a}{\lambda_s} \sin \alpha \quad (7)$$

where θ_2 is the angle measured from the normal to the surface and is an angle of elevation, and θ_3 is an azimuthal angle measured from the vertical plane containing the angle of incidence and reflection. The directions in which the energy is scattered are functions of the ratio of the acoustic-to-surface wavelength, the angle of incidence, and the direction of surface wave propagation.

The effect on the azimuthal scattering angle θ_3 by the direction of surface wave propagation and the acoustic-to-surface wavelength ratio is shown in Figure 4. For small ratios the scattering is close to the specular direction, and it is not possible to resolve only the specular component at the transmitted frequency. The Doppler frequencies are scattered on each side of the specular direction.

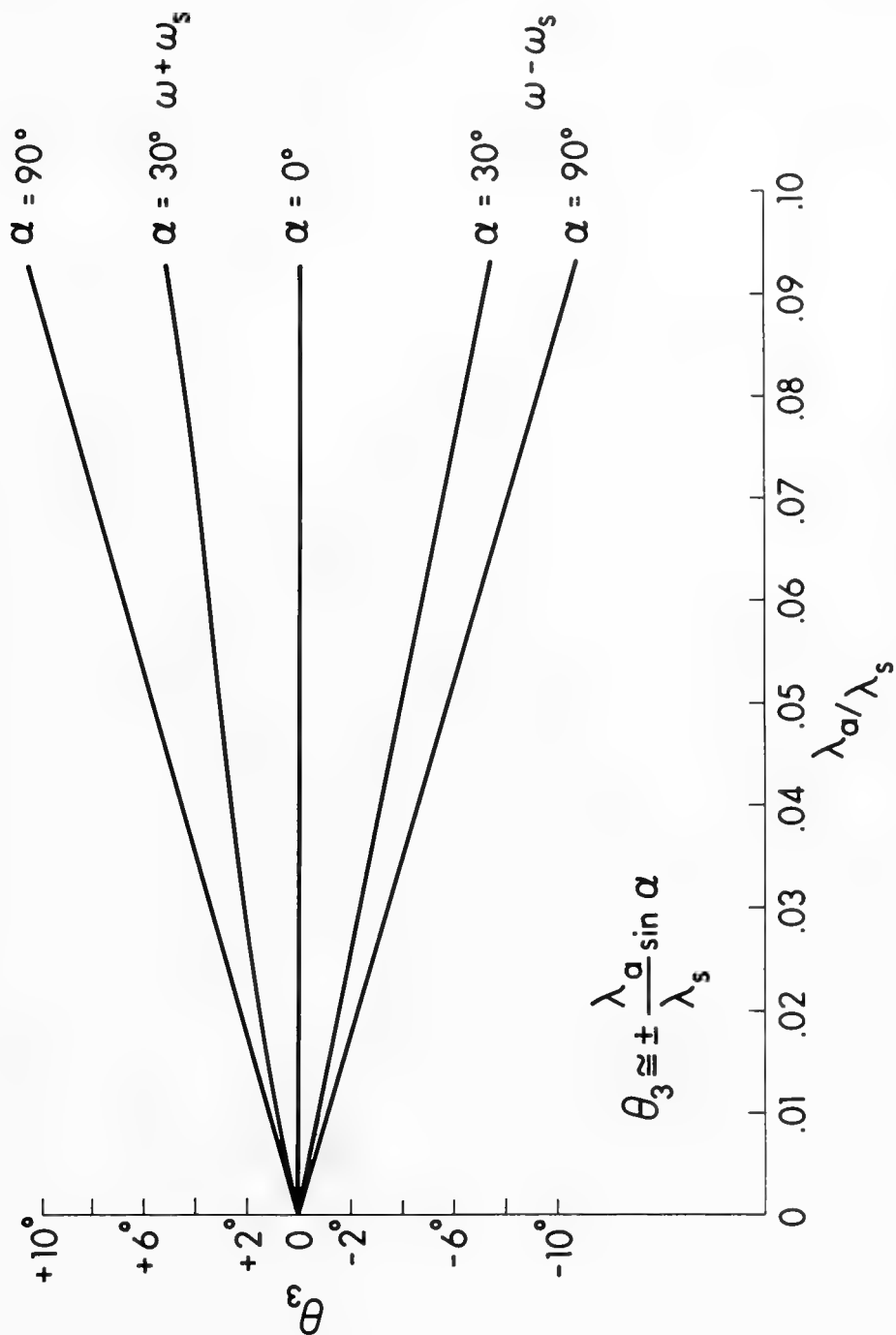


Figure 4. AZIMUTHAL SCATTERING ANGLE VERSUS ACOUSTIC-TO-SURFACE WAVELENGTH RATIO

As mentioned previously, low-amplitude sinusoidal waves were created on the water surface of an anechoic tank. A micrometer was supported above the surface and lowered to measure the wave height. The surface wavelength was measured from two wave-height sensors and the results compared well to the dispersion equation for gravity waves. With knowledge of acoustic parameters and geometry, predictions can be made for the scattered field. The spectrum on the upper left of Figure 5 is the amplitude frequency spectrum of an acoustic signal reflected from a calm surface. The other three spectra are the returns, measured in the specular direction, from a surface of 4.5 Hz with waves propagating in directions equivalent to up-wind, down-wind, and cross-wind. The wave heights for the three cases were the same. Note that in each spectrum the sideband frequencies are symmetrical about the carrier and displaced from the carrier by the surface frequency, 4.5 Hz. The sideband frequencies for the 4.5-Hz surface waves were scattered within 3 degrees of the specular direction and the energies in the sideband frequencies are identical regardless of the direction of surface wave propagation.

Looking only in the specular direction, it is not possible to observe the effects of the spatial scattering of the sidebands (see Figure 6). Placing a hydrophone 10 degrees off specular and toward the backscatter direction, the Doppler shift was measured at a surface frequency of 6.0 Hz. The surface waves were propagating in a direction equivalent to up-wind and, as expected, an up-Doppler was obtained. There are no lower sideband frequencies and the spectrum consists of the first- and second-order sidebands. Reversing the direction of the surface waves, we obtain a down-Doppler, as shown in the bottom spectrum. The received signal consists of just the lower sidebands. The wave heights for these two cases were not the same.

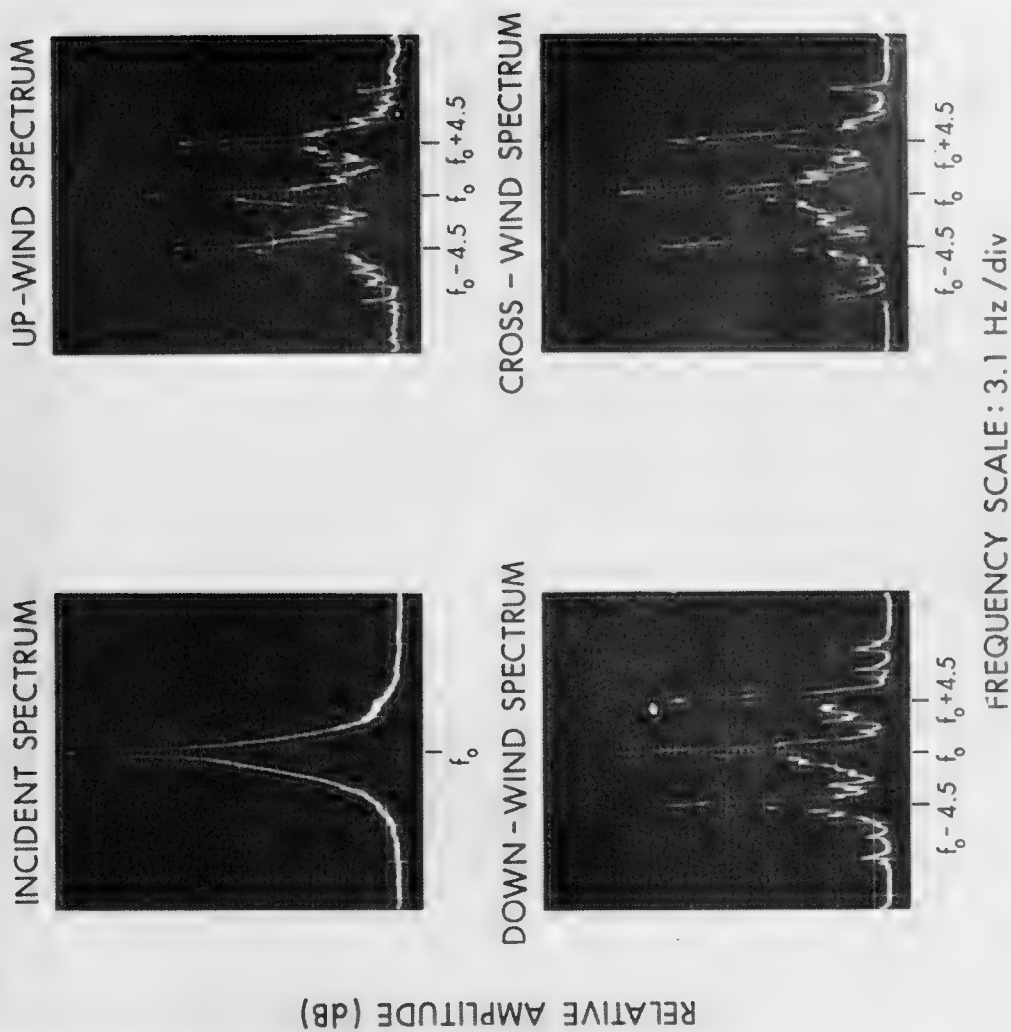


Figure 5. REFLECTED SPECTRA VERSUS SURFACE-WAVE DIRECTIONALITY

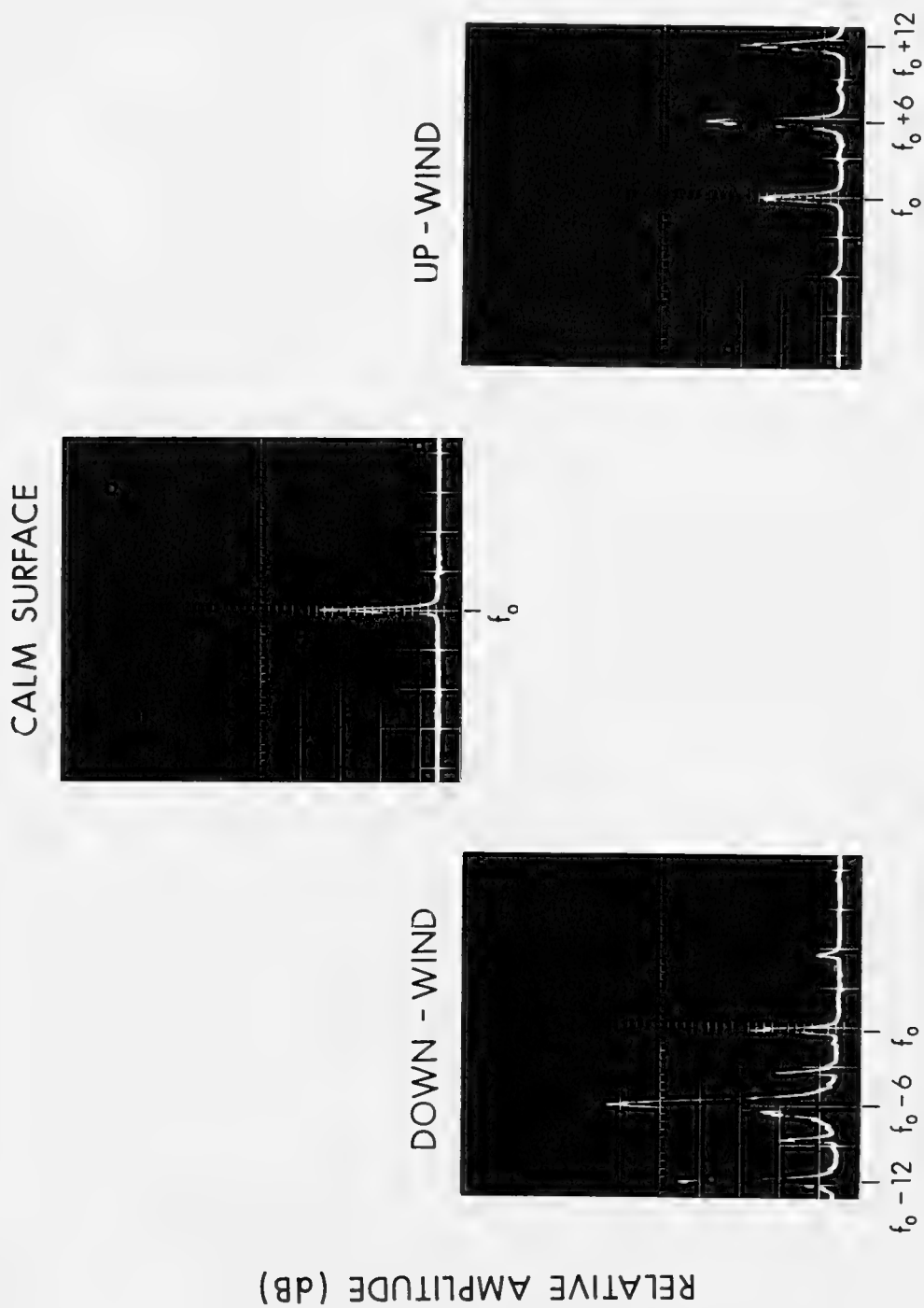


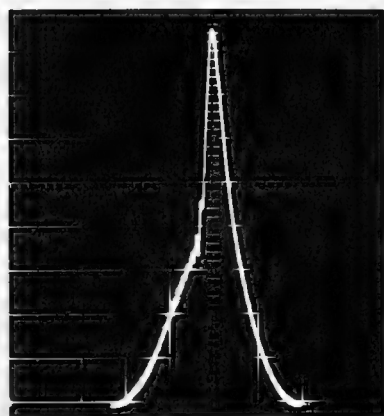
Figure 6. SPECTRA FOR OFF-SPECULAR RECEPTION

As mentioned previously, Parkins predicted the Doppler spectrum of an acoustic signal reradiated from the ocean surface using physical-optics techniques. He uses basically the same formulation of the Helmholtz Integral as Eckart, but also includes a slope correction term originally formulated by Brekhovskikh and Isakovich (1952). The Doppler spectrum is obtained through the Fourier transform of the reradiated autocovariance function. For low frequencies, the Doppler spectrum consists of a specularly reflected component at the frequency of the incident radiation and two scattered components that are Doppler shifted symmetrically about the incident frequency. The magnitude of the deviation of the sideband frequencies is the same and depends on the angles of incidence and observation relative to the wind direction and also on the incident frequency.

In 1970, Ben Cron and I did some experimental measurements (Roderick and Cron, 1970) of the Doppler spectrum. An acoustic path that included a surface reflection at a grazing angle of 7 degrees was used between the DOSS array and the TVA. The DOSS array consists of two magnetostrictive scrolls which generate 750 and 1,500 Hertz in the water. The TVA consists of 40 hydrophones positioned in a vertical array and was used to beamform to receive the surface reflected signals and minimize undesirable multipaths. The spectrum in the upper left of Figure 7 represents the spectrum of the signal incident on the surface. Before we go any further, the analysis was done on a real-time spectrum analyzer in a frequency range of zero to five Hertz. The acoustic signals were bandshifted to a center frequency of 2.5 Hertz. On the upper right of Figure 7 is a spectrum of the wave height measured at Argus Island using a resistive wave staff. The wave height was measured at the same time as the acoustic reflections from the surface and at a location which was 30 miles west of the ionified area. The spectrum in the lower left is from the

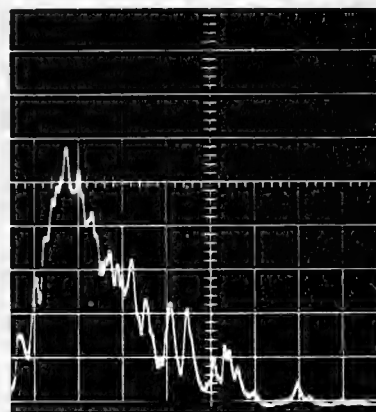
WIND SPEED: 25 KNOTS

INCIDENT SPECTRUM



2.5 Hz

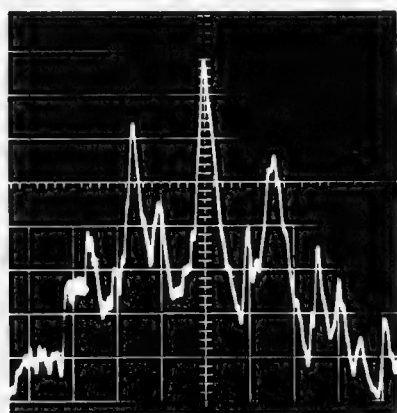
OCEAN SPECTRUM



0.5 Hz

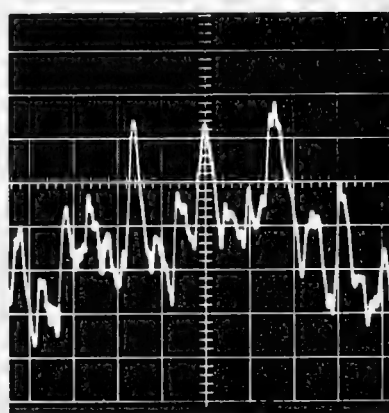
REFLECTED SPECTRA

750 Hz



2.5 Hz

1500 Hz



2.5 Hz

RELATIVE AMPLITUDE (db)

FREQ. SCALE: 0.1 Hz / DIV

Figure 7. RELATED SPECTRA

750 Hertz transmitted signal. Note that the sidebands are displaced equally from the carrier. The spectrum obtained at the transmitted frequency of 1,500 Hertz shows significantly more energy in the sideband frequencies. (All vertical scales are 5 dB per division.)

The spectra shown in Figure 8 are for two consecutive pulses reflected from the surface and separated in time by 3 minutes. Note again that the sideband frequencies are displaced symmetrically about the carrier and peaked at the frequency of maximum energy on the surface.

For a wind speed of 35 knots, the reflected spectra (Figure 9) have their first-order sidebands peaking at approximately 0.07 Hertz. It can be seen that the carrier frequency is suppressed for the 1,500-Hertz case; thus, almost all the received energy is contained in the scattered frequency components. The ocean spectra recorded for this wind speed of 35 knots are also peaked at 0.07 Hertz.

In a recent JASA article, Vertner Brown and George Frisk (1974) reported on Doppler spectrum measurements conducted in the open ocean in the frequency range of 100 to 500 Hertz. The statistics of the sea surface were measured simultaneously with acoustic data by a surface-sensing buoy. The acoustic spectra are compared with the surface-wave spectra at each of the transmitted frequencies in Figure 10. For small surface roughness, the acoustic spectra contain the discrete carrier frequency component with sidebands symmetrically positioned about the carrier. For moderate roughness, marked asymmetry in the acoustic spectra and strong spectral components that are not prominent in the surface spectra are found.

Harry DeFerrari and Nghiem-Phu (1974) published the scattering functions of various acoustic arrivals over a propagation path of

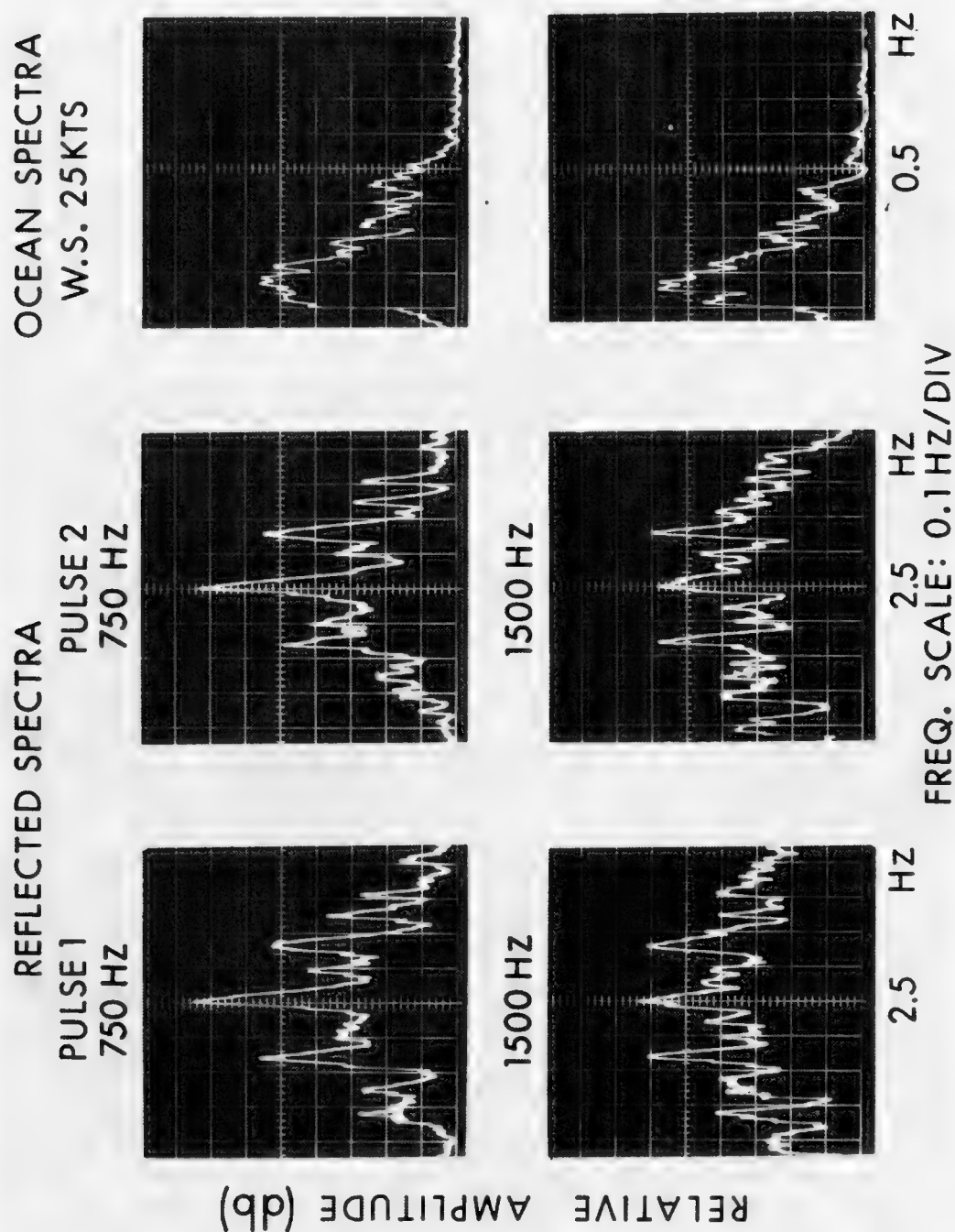


Figure 8. SPECTRA FOR TWO PULSES 3 MINUTES APART

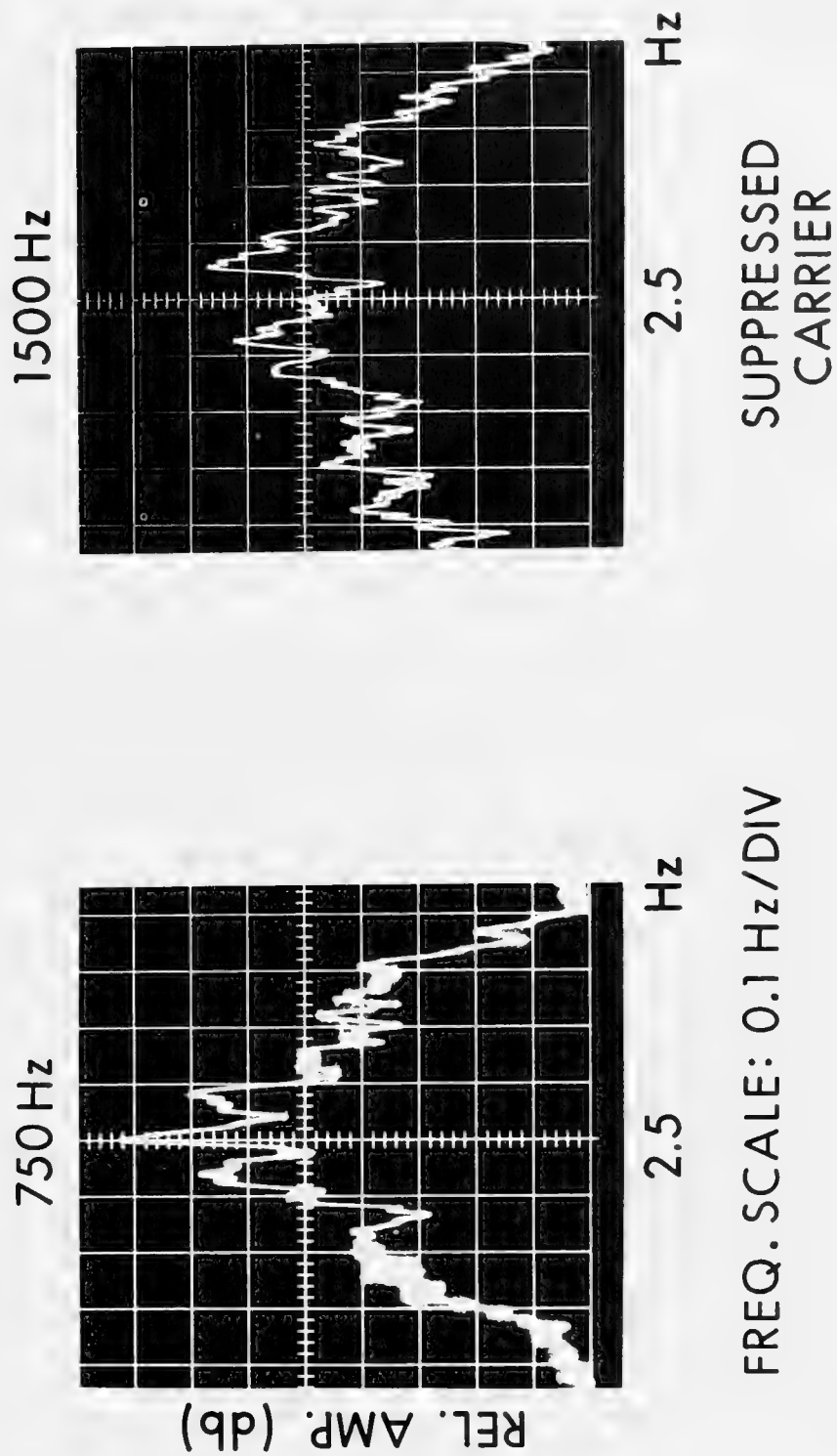


Figure 9. REFLECTED SPECTRA FOR WIND SPEED OF 35 KNOTS

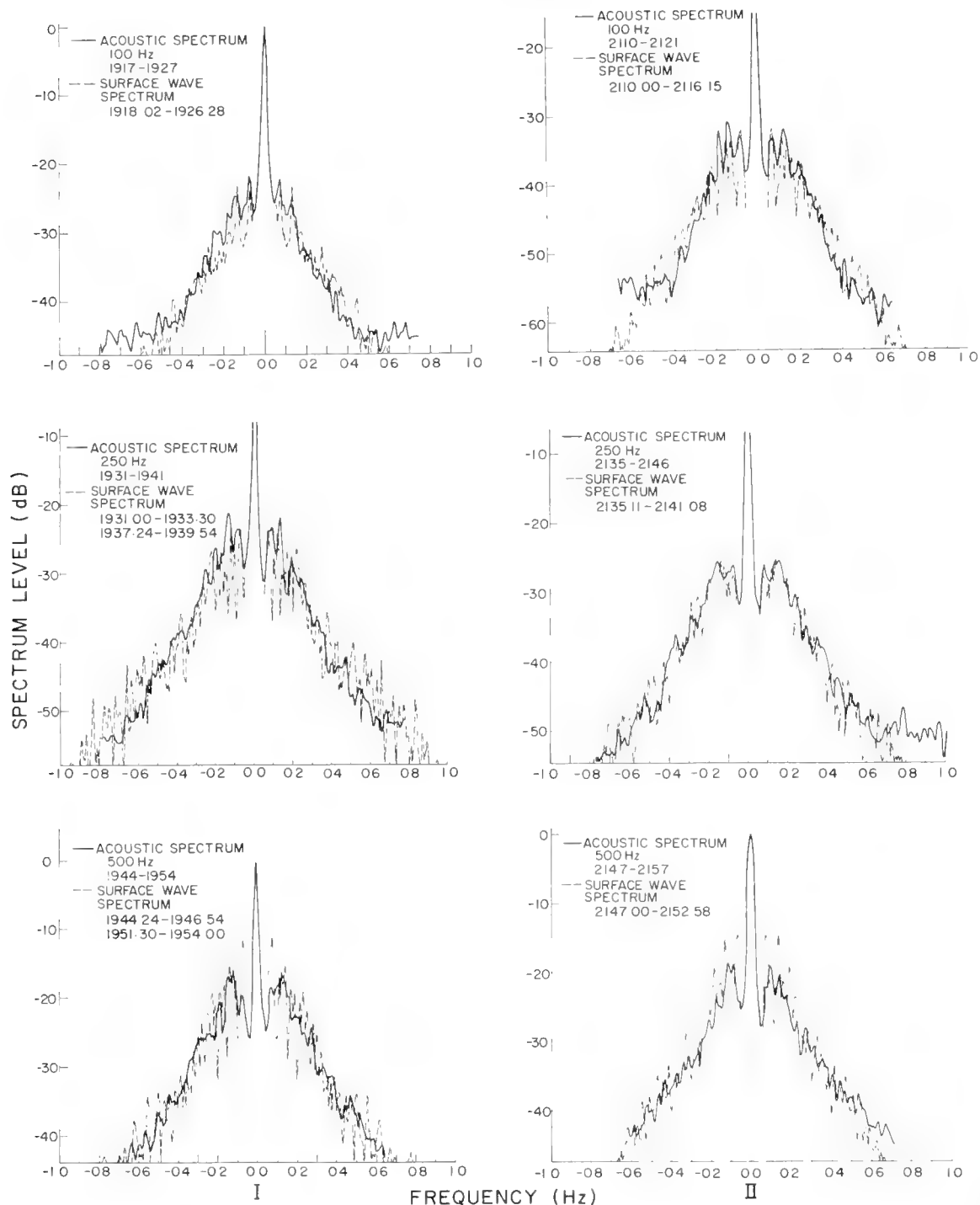


Figure 10. DOPPLER SPECTRUM MEASUREMENTS
AT 100, 250, AND 500 Hz
(from Brown and Frisk, 1974)

7 nautical miles. The scattering function, as shown in Figure 11, is a three-dimensional description of the transmission in terms of the intensity, frequency, and delayed time of arrival. For surface-reflected-bottom-reflected arrivals, the Doppler spectrum has sideband frequencies at surface-wave frequencies. The scattering function was measured during typical summer conditions with onshore winds of 10 to 15 knots. Asymmetrical sidebands were observed in some of the scattering functions.

Asymmetrical sidebands can result when scattering occurs from a multi-frequency surface (see Figure 12). Consider the case of a two-frequency surface: the magnitude of each frequency component is proportional to the product of two Bessel functions and the sideband frequencies represent all possible combinations of the carrier and multiples of each surface frequency. If the surface frequencies are commensurable, then each sideband frequency is made up of a vector summation of the individual terms. In general, this will result in asymmetrical sidebands. The spectrum shown for surface frequencies of 4 and 6 Hertz has asymmetrical sidebands at a difference frequency of 2 Hertz from the carrier.

The AFAR range has also been used (O'Brien, et al., 1974) to measure the Doppler spectrum at different transmitted center frequencies. At 600 Hertz (see Figure 13), the received energy is coherent and predominately in the carrier frequency. As the frequency increases, the Doppler spectrum consists of more and more incoherent scattered acoustic energy. The sea state was 0.45 meters rms.

In terms of the Doppler spectrum, we want to know what has been done; where we are; and what needs to be done. I have tried to illustrate the state of these affairs. We have made enough

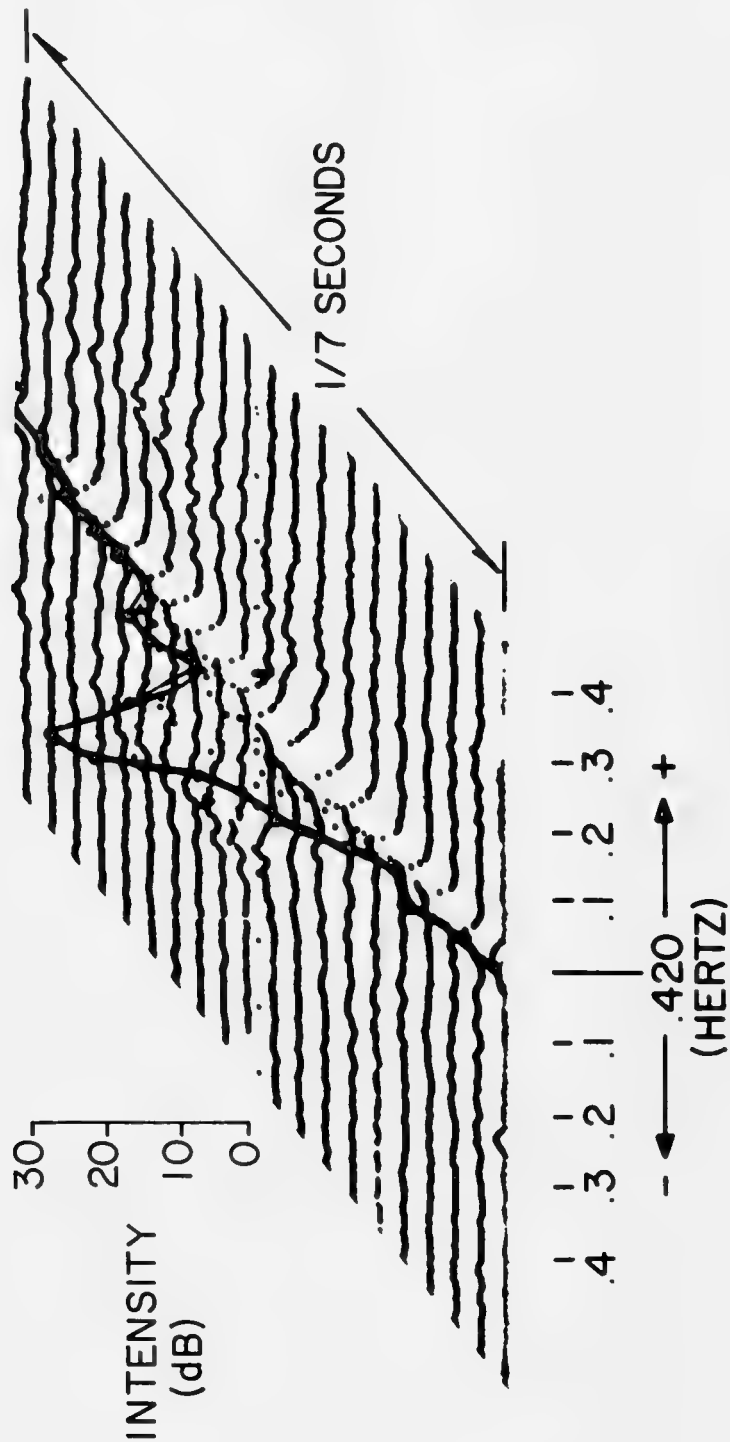


Figure 11. SCATTERING FUNCTION
(from DeFarrari and Nghiem-Phu, 1974)

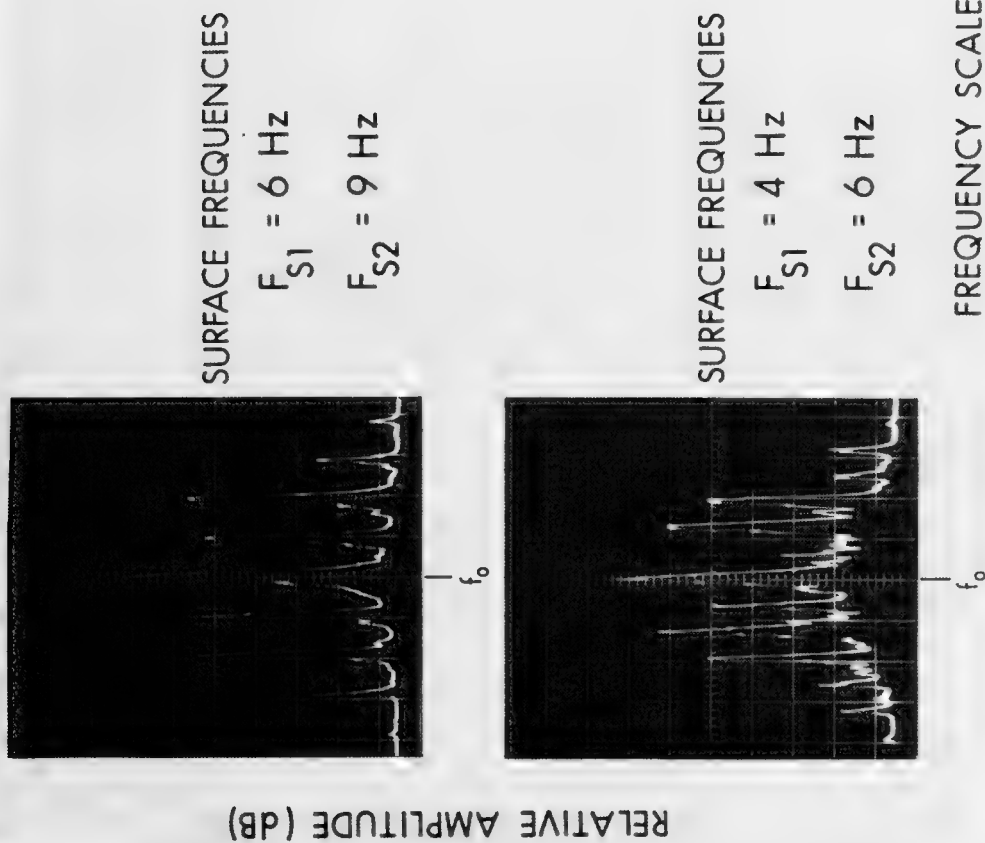


Figure 12. REFLECTED SPECTRA FOR TWO-FREQUENCY SURFACE

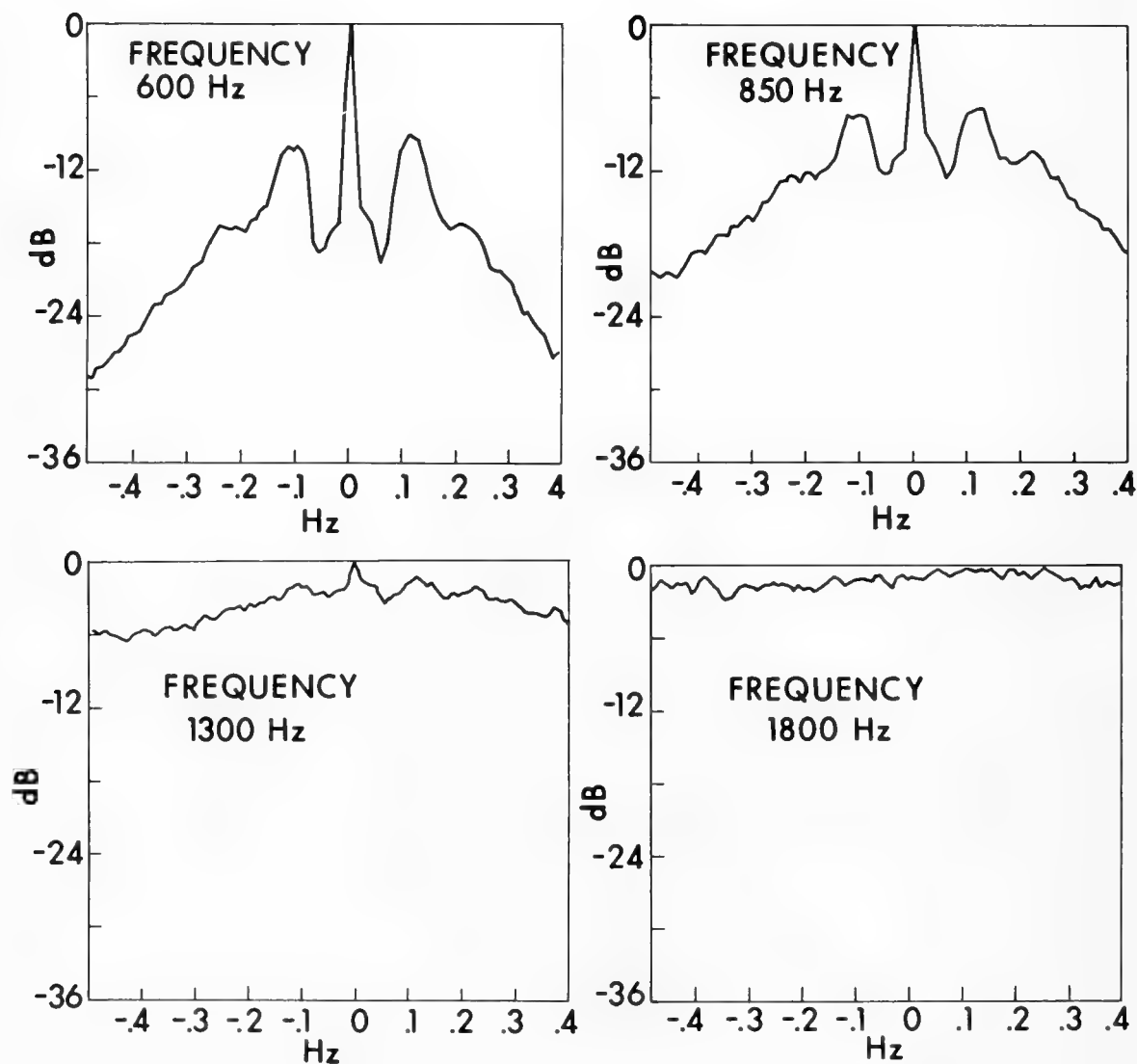


Figure 13. DOPPLER SPECTRA AT SELECTED FREQUENCIES
(from O'Brien, Pearson and Freese, 1974)

measurements of the relative energy in the Doppler spectrum with supporting oceanographic data. You could fill a bookcase with the various theoretical models that are available in predicting scattered sound from the sea surface. However, I cannot determine whether the present models are adequate enough to produce the absolute value of the coherent as well as incoherent energy of the Doppler spectrum. To my knowledge, there has not been any deep ocean measurement of the absolute value of the Doppler spectrum. Lastly, there are measured asymmetrical sidebands obtained by various experimentalists — theoretical predictions should be made to compare to these results.

In the remaining time, I would like to give a brief overview of an experimental program in measuring bistatic reverberation from the sea surface presently being conducted in the Block Island-Fishers Island Range. A parametric source (Figure 14) is being used to generate a narrow beam of acoustic energy incident on the sea surface. The source characteristics of wide bandwidth, narrow beam width, and no sidelobes result from the array of virtual sources created by the nonlinear interaction of the acoustic waves in the water medium. The reverberation from the surface is received on the vertical array of transducers and the information is cabled to shore. As you may be aware, the reverberation Doppler spectrum is a function of the sea-surface directional wave spectrum. To obtain an estimate of this spectrum, an array of five upward-looking transducers is used to measure the wave height as a function of time. The near-field characteristics of the transducers are used to isonify a small spot on the surface. The transducers are positioned to obtain equispaced cross-power spectral-density functions.

A typical beampattern of the parametric source measured at a difference frequency of 7 kHz is shown in Figure 15. Note the absence

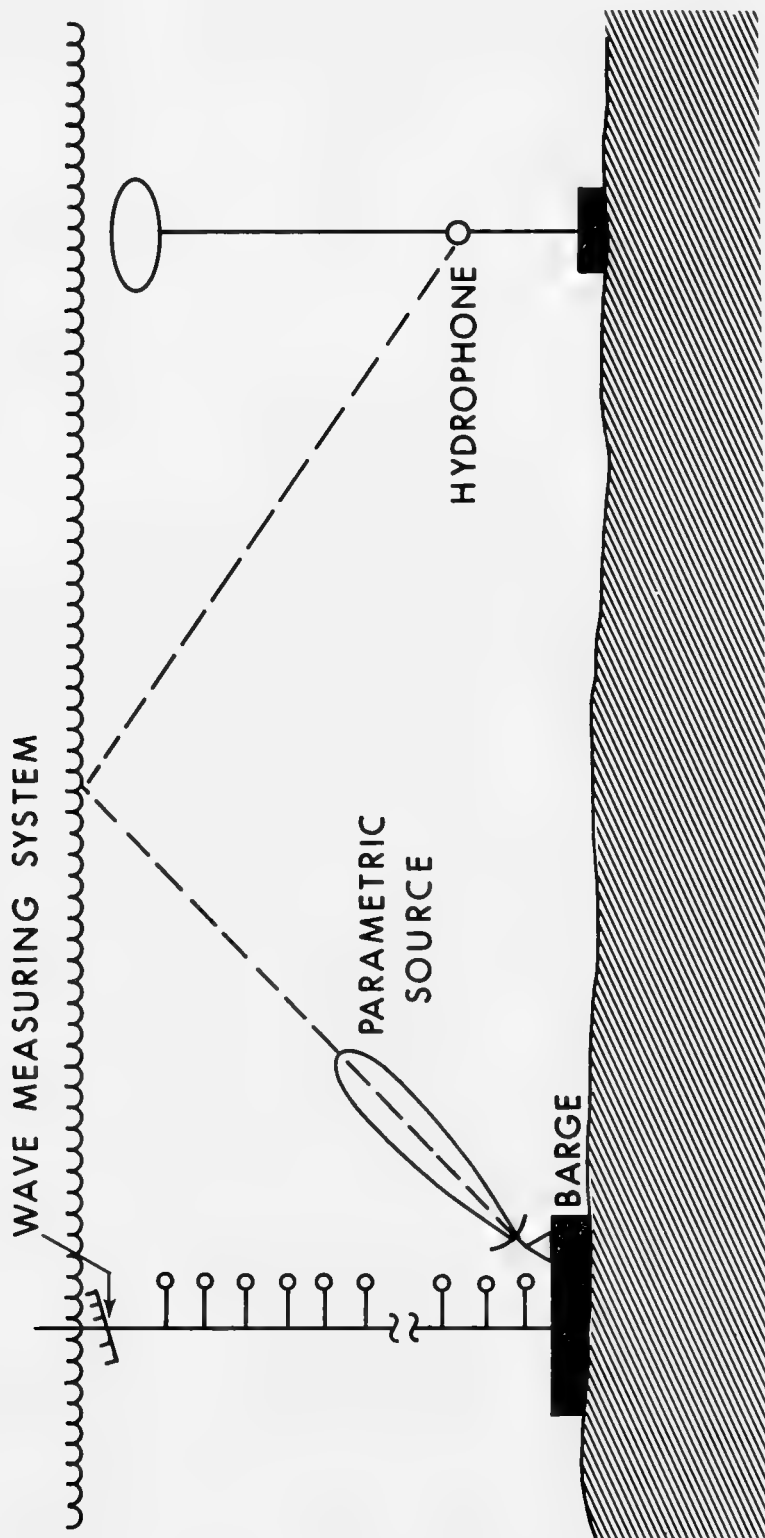


Figure 14. BISTATIC MEASURING SYSTEM

DIFFERENCE FREQ: 7 kHz
SOURCE LEVEL: 174 dB// $\mu\text{Pa} \cdot \text{m}$
DRIVE LEVEL: 800 V_{p-p}
PRIMARY CENTER FREQ: 260 kHz

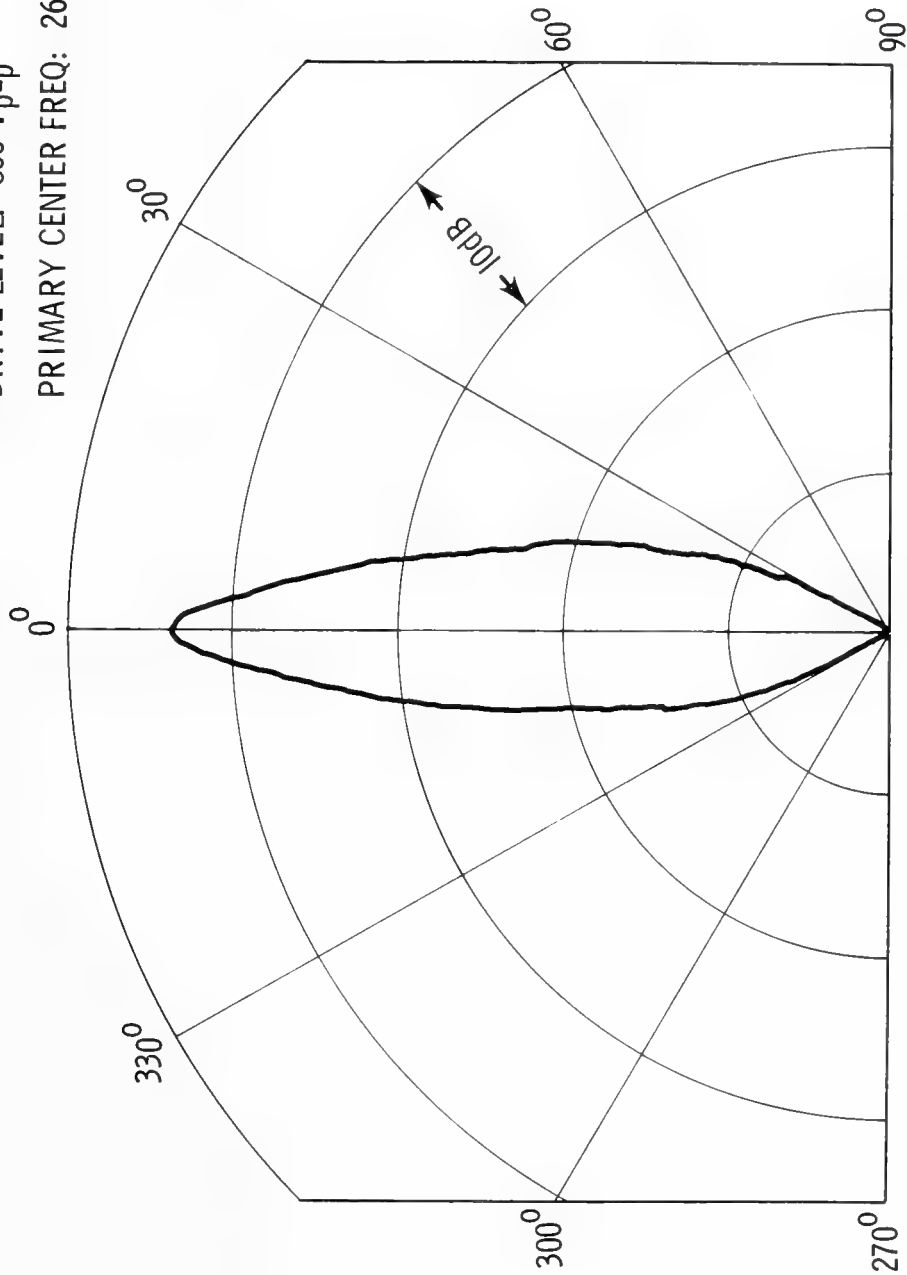


Figure 15. DIFFERENCE-FREQUENCY BEAM PATTERN

of sidelobes, and the narrow beamwidth of the major lobe. A 10-inch diameter piston transducer operating at a reasonable frequency of approximately 250 kHz was used as a source.

Figure 16 displays recordings of wave height versus time measured at five discrete points on the sea surface. The sensors are positioned in a line array and, if you look closely, you can see the phase relationship as the surface waves propagate across the array.

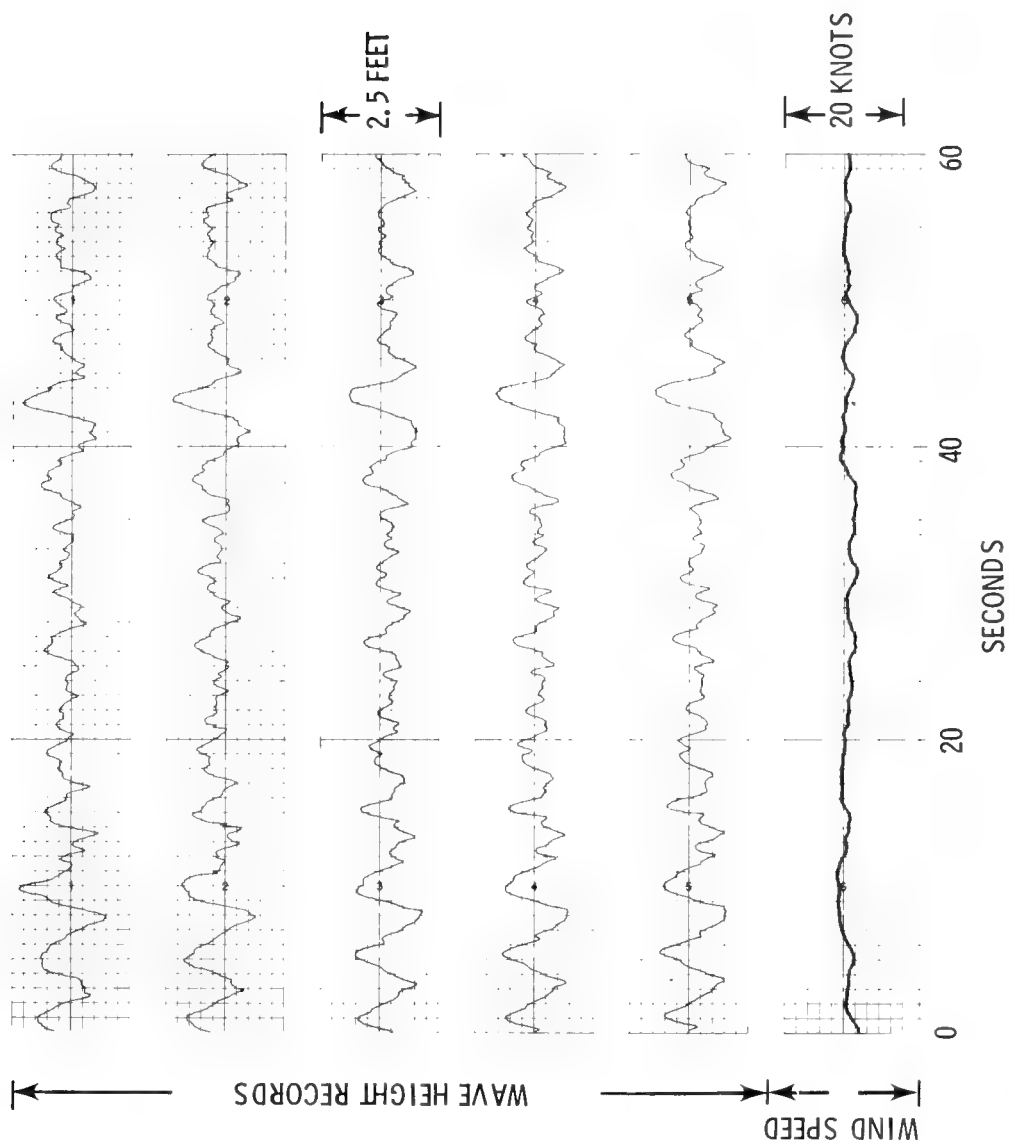


Figure 16. WAVE-HEIGHT AND WIND-SPEED RECORDS

REFERENCES

- Beckmann, P., and A. Spizzichino, *The Scattering of Electromagnetic Waves from Rough Surfaces*, The Macmillan Co., New York, 1963.
- Brekhovskikh, L. M., and M. A. Isakovich, "Diffraction of Waves from a Rough Surface," translated from the Russian by R. N. Goss, Naval Electronics Laboratory, Rpt. No. 14888, 1952.
- Brown, M. V., and G. V. Frisk, "Frequency smearing of sound forward-scattered from the ocean surface," *J. Acoust. Soc. Am.* 55:744-749, 1974.
- DeFerrari, H. A., and Lan Nghiem-Phu, "Scattering function measurements for a 7-nm propagation range in the Florida Straits," *J. Acoust. Soc. Am.* 56:47-52, 1974.
- Eckart, C., "The scattering of sound from the sea surface," *J. Acoust. Soc. Am.* 25:556-570, 1953.
- Ellinthorpe, A. W., "Frequency smearing on undersea acoustic paths with fixed end points," *J. of Underwater Acoust.*, 16, 427-435, 1966.
- Mackenzie, K. V., "Long-range shallow-water bottom reverberation," *J. Acoust. Soc. Am.* 34:62-66, 1962.
- Marsh, H. W., and E. Y. T. Kuo, "Further results on sound scattering by the sea surface," AVCO Marine Electronics Office, 1965.
- Melton, D. R., and C. W. Horton, Sr., "Importance of the Fresnel correction scattering from a rough surface: I. Phase and Amplitude Fluctuations," *J. Acoust. Soc. Am.* 47:290, 1970.
- O'Brien, G. J., J. H. Pearson, and H. A. Freese, "Surface-induced frequency smears on forward scatter paths," Naval Underwater Systems Center, TE-68-74, 1974.
- Parkins, B. E., "Scattering from the time-varying surface of the ocean," *J. Acoust. Soc. Am.* 42:1262-1267, 1967.
- Roderick, W. I., "Acoustic spectra of specular and near specular scattering from a three-dimensional traveling sinusoidal surface," paper presented to the 78th Meeting of the Acoustical Society of America, 1968.

RODERICK: FORWARD SCATTERED LOW-FREQUENCY SOUND FROM THE SEA SURFACE

Roderick, W. I., "Frequency spectra of forward-scattered underwater sound from a traveling sinusoidal surface," Navy Underwater Sound Lab., Rpt. No. 988, 1969.

Roderick, W. I., and B. F. Cron, "Frequency spectra of forward scattered sound from the ocean surface," *J. Acoust. Soc. Am.* 48:759-766, 1970.

DISCUSSION

Dr. P. W. Smith (Bolt, Beranek, and Newman, Inc.): The example or the explanation you gave of the asymmetrical sidebands suggested to me that they were a peculiarity of the signal reflection that would not result if you averaged over many reflections.

Mr. Roderick: The spectrum I showed was a single time record with only 2 degrees of freedom. In other spectra that have been ensemble-averaged (including Brown's, DeFerrari's, and some results as seen on the BIFI range), one sideband can be down perhaps 5 or 6 dB. You have a good statistical confidence in the spectrum due to the large number of degrees of freedom.

Dr. Ira Dyer (Department of Ocean Engineering, Massachusetts Institute of Technology): Bill, what hope would you hold out in using an acoustic system for getting the wave spectra, wave number spectra as well, of the ocean surface or any other rough scatterer?

Mr. Roderick: I think this can be done — with some qualifications. Bob Williams did his Ph.D. thesis on measuring the gravity wave spectrum based on acoustic results.

Unfortunately, he had a horrendous problem. His acoustic path involved many surface reflections and he had very poor control over geometry. I think he only got fair results, mostly because of the experimental setup. I think it can be done.

Dr. Walter W. Munk (Institute of Geophysics and Planetary Physics, University of California at San Diego): The corresponding electromagnetic scattering problem which is very similar has recently been attempted — a real comparison between the backscattered energy with the backscattering geometry, and that computed from wave measurements. Even an absolute comparison was attempted, and it came out 2 or 3 dB off on the absolute comparison, but quite well on the relative.

COHERENCE

Theodore G. Birdsall

Cooley Electronics Laboratory
University of Michigan

My theme is that much of the randomness in underwater acoustics is not "inherent" randomness, but rather is the manifestation of complicated deterministic phenomena.

INTRODUCTION

What is "coherence" and, more important, what good is "coherence?" Definitions can be "sticky." The pun is intentional. Coherent means to consist of parts that stick together, that are logically consistent.

In various disciplines coherence has taken on special meanings, often related to techniques of quantifying (measuring) the degree of coherence. Quantification is necessary, but it can carry hidden assumptions that can confuse and even impede progress. For example, a correlation coefficient and its decay in time or space is most appropriate for first order Markov processes. The more sophisticated "coherence function" is most useful for wide-sense stationary Gaussian random processes.

This paper is concerned with underwater acoustic propagation, with "coherence" meaning the consistency of reception across time, frequency, and space. The viewpoint is that of a signal processor, concerned with extracting information from acoustic receptions. This means information about propagation, or extracting operational information about targets or false targets.

Signal coherence is most important in weak signal situations; that is, when the signal power is small compared to the noise power or the signal's own reverberation power. The sub-discipline known as

"signal detection theory" is a study of precisely how uncertainty about signal waveform and uncertainty about the noise characteristics, together with interfering power, affect signal-processing design. Perhaps more important, it studies how uncertainty and noise combine to limit ultimate performance in signal detection and information extraction. The theoretical results are complicated, but there are some guiding general principles.

One such general principle is that the effective signal-to-noise ratio after processing will fall off sharply at low signal-to-noise inputs. Just where this 'suppression effect' cuts in depends on the degree of uncertainty about the signal and noise characteristics. When the input is well above the 'knee' most reasonable processors work about equally well, and signal uncertainty is not very important. The other side of the coin is that processors can be designed to dig information out of weak receptions only if there is substantial knowledge of signal characteristics and this knowledge is used. Said again, if detailed signal knowledge is available and is used, it may mean tens-of-dBs of processing gain.

BRIEF HISTORICAL REVIEW

Twenty years ago many U.S. propagation people doubted that there was sufficient stability in signals propagated over long distances to support detailed signal knowledge. There were notable exceptions. Project Artemis of Hudson Labs was a courageous step forward in investigating propagation stability as seen at a very large receiving array. One must qualify all experimental results as being specific to the areas and frequencies studied. For Artemis that means for the Atlantic area south of Bermuda and in the neighborhood of 400 Hz. Artemis established the predominance of RSR (refracted, surface-reflected) paths for long-range propagation, and the importance of the bottom topography and local internal waves in the neighborhood of a slope mounted array.

The measures of space coherence were primarily (1) pulse time of arrival, and (2) the linear correlation coefficient estimated from clipped processing. That correlation would drop sharply to one-half, and then fall off slowly as the spacing increased. Tracking and prediction of non-plane wave fronts was limited by the speed and size of the available computers.

In the same time frame the NEL studies with pseudo-noise transmissions, controlled transmissions that covered over one-third of an octave, showed substantial waveform repeatability.

Almost all experiments over long ranges involve at least one moving platform. Great care has been taken to reduce the fluctuation of the platform, through using submarines and drifting ships. This care is influenced by the experimenter's opinion of the stability of the medium. There is little to be gained by reducing the platform instability effects far below the effects that will be caused by the medium. As instrumentation improves we often repeat the old experiments and get different results. In a drifting-ship to bottomed-receiver experiment in 1963, using CW (a 420 Hz tone), across the Straits of Florida, a frequency stability of 4 millihertz was observed. That stability was comparable to the frequency source stability and to the ship station keeping. Subsequent fixed-site experiments with improved sources confirmed this stability in the Straits of Florida and over the old Artemis range in the Atlantic.

This millihertz frequency stability is a nice example of the complexity of 'coherence'. It does not mean that the received signal looks like a pure tone. The signal shows substantial amplitude fluctuations and some phase fluctuations, which are now recognized as the effect of forward scattered surface reverberation. Mother Nature thoughtfully arranged for this reverb to lie in frequency sidebands some 50 to 500

millihertz to either side of the carrier frequency. That reverberation is part of the 'incoherent' part of the reception; its lack of structure makes it much less useful than the stable signal line. Measure its power and then filter it out; once removed the remainder is the signal that possesses the millihertz stability. That is lesson number one: partially coherent signals may sometimes be separated into coherent and incoherent parts. The separation increases our understanding of propagation. The coherent part is operationally much more effective at low signal-to-noise for detection and identification, and worthy of further study.

Studies of the isolated stable line showed that life is really not simple. In a multipath situation - and that is the usual situation for many of us - it is common for the amplitude of the line to vary substantially, while the phase of the line (or its instantaneous frequency) has such slow variations that it reflects tidal and internal-wave behavior. If one models 'paths' as slowly and independently varying, the model disagrees. However, if one models 'paths' as slowly and dependently varying, reacting to the same global temperature variations, then the model begins to fit. That brings in lesson number two: the propagation may be coherent, that is, complicated but logically consistent and dependent of the same variations, and yet yield some measurements that appear to be incoherent. It is up to the scientist and the sonar designer to seek, recognize, and capitalize on whatever 'coherence' nature provides.

NON-MARKOV COHERENCE

There is a natural tendency to believe that 'coherence' should behave in a Markov fashion in all dimensions. We seek coherence distances, coherence time constants, coherence bandwidths. We ask 'how far apart do receptions have to be before coherence drops to one-over-e?' as if that just has to be an intelligent question.

Does the consistency of propagation break down as signal frequencies are separated? It is common to experience different fades at signals just a few Hertz apart. I would like to cite just one study to indicate that the behavior in frequency is more coherent, and more complicated, than a Markov process. Single-path loss measurements were made at 61 frequencies spaced 5/6 Hz apart, covering the regime from 395 Hz to 445 Hz over a period of 7 hours. The transmission was over 43 miles across the Straits of Florida. The loss contours as a function of frequency and time show a lot of pattern; I hope enough to encourage studies that go after the whole surface, and enough to discourage attempts at determining a correlation bandwidth. The frequency deviation plot for the same data shows major peaks of the order of one millihertz wide. Low-magnitude broadband ripples and changes slide across frequencies in time; however, the entire band has a reasonable unity. Of course it is only about one-sixth of an octave, but that is all many sonars (active) cover. Incidentally, these data were taken with nine-foot seas overhead.

Correlation time-constants for multipath propagation are another popular concept. In some locations it may be a valid description of multipath behavior. Again, I would like to cite one study to indicate that multipath propagation may be more coherent than suspected, but that much careful work will have to be done to discover the coherent parts and to use them. The data spans one day, and used a continuous transmission designed to yield the same time resolution as a 20 millisecond pulse repeated every 1.2 seconds (but with 18 dB more processing potential). The data taken in November 1971 show a dominant 30-millisecond arrival alternately merging and contrasting with a following weaker arrival. This routine structure shows a dramatic change both in the duration of the arrival and in the phase pattern.

The arrival frequency shifted 0.5 millihertz and 12 hours later changed again by 0.8 millihertz. Even the weak trailing arrivals show repeatable phase often lasting for hours. There is strong evidence of consistence and pattern, but it is complicated, and one time-constant does not describe this type of data.

HALF-TIME SUMMARY

Coherence is a complicated subject, but worth pursuing because of the potential gain in apt signal processing at low signal-to-noise ratios. Coherent propagation may lead to complex receptions which must be sorted out, and some physical measurements will appear to be much more coherent than others. The lack of regularity in one class of measurement does not imply incoherent propagation, and simple measurements of correlation may be deceptively uninformative.

In the second half of this paper a model of propagation from a submerged moving source will be presented to show how a complicated and apparently incoherent signal may be received even though the propagation itself is totally coherent, totally deterministic. The model agrees well with measurements in many respects, but I beg your indulgence for leaving that to another paper. The purpose of this presentation is to emphasize my theme: *Much of the randomness in underwater acoustics is not inherent randomness, but is rather a manifestation of complicated deterministic phenomena.*

AN EXAMPLE MODEL

Picture a deep ocean with a single classical sound speed profile that applies everywhere, and a fixed source at 150 meters depth and 600 km from a deep receiver. The numbers are purely for example sake. This source emits a steady pure tone, let us say at 250 Hz.

All this is said to formulate a multipath situation. Paths will appear in pairs, with one path of each pair leaving the source at some depression angle, and the other path of the pair leaving the source at an elevation angle of almost equal magnitude. The difference in the absolute value of the angles is quite small, of the order of .1 degree. At the assumed long range there will be several such pairs, and the reception will be the vector sum over all paths with their travel times and losses; it will be a 250 Hz signal.

Now let the source open range at 6 knots. Grossly speaking this will cause a 0.5-Hz Doppler shift. Speaking more carefully, there will be a $0.5 \cdot \cos(\text{angle})$ shift. Consider one pair of paths. If their angles differ by 0.1 degree, their Doppler shifts will differ by 0.152 millihertz. That's not much, but therein lies the key number in this model. Since the difference is so small no current receiver will separate them, and their sum will appear as a single frequency, with an apparent fade rate of 109 minutes. (Of course I am thinking about much shorter observation times than 109 minutes.) The conclusion is that the 'insignificant' differential Doppler will have almost no effect on the measured frequency, but has a substantial effect on the measured amplitude.

There will be a number of ray-path pairs. For simplicity assume that a hypothetical analyzer can isolate two pairs in one narrow filter with relative frequencies and amplitudes as listed below:

rel. freq.	-.0100	-.0092	0	.0005
rel. amp. (dB)	P-1	P-3	P	P-2

The amplitude, linear with pressure, will show rapid fluctuations with a period of 100 seconds separating deep fades about every 13 minutes. A phase tracker shows the instantaneous frequency of the reception fluctuating wildly at the 100-second rate, but using the

phase tracker's average slope yields frequency estimates which have a 'capture' behavior, locking onto the frequency of the momentarily largest line pair.

This example was based on only 2 path pairs, and the 2.7 km range change was ignored in the calculations to emphasize the simple beat. Add a few more path pairs, take into account the opening range and the attendant path and angle changes, and you will obtain a complicated fade pattern, and a frequency estimate that hops around. Is that bad? No, that's good! It's a basic part of propagation, and it occurs in every test and every operational situation with a moving source at long range and not on the surface. The fluctuations were coherent. There was no randomness in the example.

That concludes coherence lesson number three: not everything that varies is a random variable, nor do fluctuating receptions imply incoherent propagation.

APOLOGY

My brief history omitted reference to almost everyone, and I owe an apology both to the researchers and to this audience if they were expecting a scholarly review.

FLUCTUATIONS: AN OVERVIEW

Ira Dyer

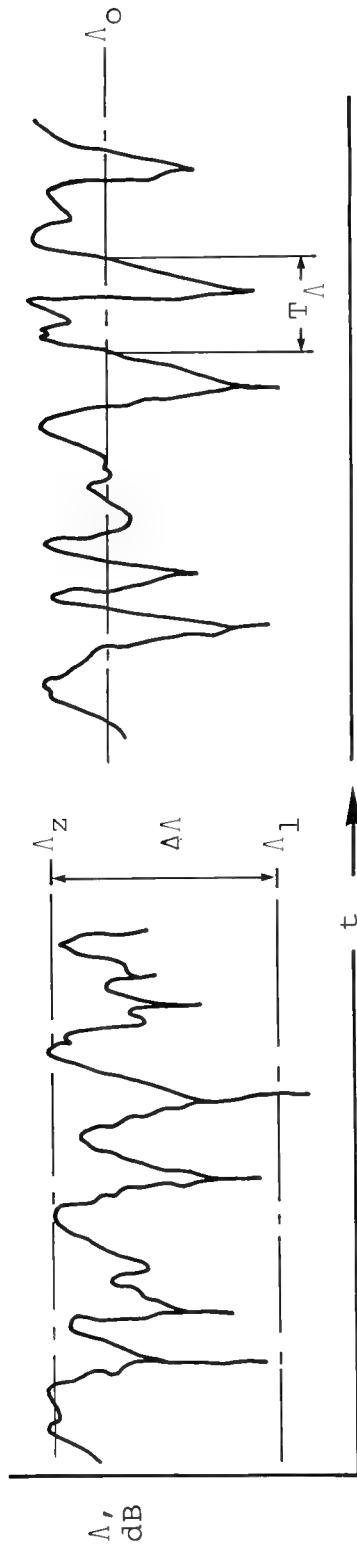
Department of Ocean Engineering
Massachusetts Institute of Technology
Cambridge, Massachusetts

The study of fluctuations is hampered by a diversity of definitions and language. I propose that theories and experiments be distinguished as to 1) Averaging Algorithms, 2) Source/Receiver Motion, and 3) Ocean Dynamics. Confusions in the interpretation or comparison of recent results can be reduced thereby. Several results are discussed within this framework.

More particularly, a format for studying short-time-averaged amplitude (envelope) fluctuations is proposed. Envelope statistics for phase random processes are well known for sample sets with fixed mean; these statistics change significantly for sample sets with varying mean, as is often the case for sets extending over time durations and spatial extents involved in detection by typical sonars. The format includes metrics such as the fluctuation (fading) period, the fluctuation (interference) scale, and more generally their corresponding spectra. Some recent results are discussed in these terms.

There is no clear, accepted way to distinguish between various categories of fluctuations. This paper addresses, therefore, the question of time series that may be observed in the ocean; it applies equally to spatial series that may also be observed in the ocean in the study of coherence. Figure 1 defines certain terms of importance to time series; a comparable set of definitions exists for the spatial series.

Two quantities are typically of interest: the amplitude, which may be the decibel level, A (or the intensity, I , or the RMS value, $|p|$), and the phase, θ , which could just as well be the tilt angle or the bearing angle.



$P(\Lambda)$ OR $P(I)$ OR $P(|p|)$; $P(\Theta)$

$$\Delta \Lambda(Q) \quad Q = \int_{-\infty}^{\Lambda_1} P(\Lambda) d\Lambda = \int_{\Lambda_z}^{\infty} P(\Lambda) d\Lambda \quad (Q \approx 0.025)$$

$$T_{\Lambda}^{-1} = 1/2 \int_{-\infty}^{\infty} |s| P(\Lambda_0, s) ds$$

$$s = d\Lambda/dt \quad \left(T_{\Lambda}(\Lambda_0) = T_{\Lambda}(\mu_{\Lambda}) \right)$$

$$\rho(\tau) = \frac{\langle \Lambda(t) \Lambda(t+\tau) \rangle}{\langle \Lambda^2 \rangle} \quad \left(\rho(\tau_{\Lambda}) = \frac{1}{e} \right)$$

Figure 1. PARAMETERS IN TIME SERIES

The time series, $\Lambda(t)$, has a probability density, $P(\Lambda)$, and a spread, $\Delta\Lambda(Q)$ called the fading range. This can be defined in terms of the cumulative probability distribution, and in the subsequent results it will correspond to the fading range where 2.5 percent of the lowest levels and 2.5 percent of the highest levels are discarded.

Similarly, a period, T_Λ , can be defined as the time between crossings of a level Λ_0 going in the same direction. The period is, in fact, a function of that level.

The crossing period T is therefore related to the crossing rate T_Λ^{-1} which is given by the integral of the absolute magnitude of the slope of the curve times the joint probability density of that particular level which it crosses and the slope itself. In the subsequent results, the periods will correspond to the crossing level that is the mean of the time series. In case of phase, for example, that mean will often be zero.

A third measure, the autocorrelation, ρ , is defined in the usual way, and the time, τ , will correspond to the $1/e$ point on that autocorrelation function.

Figure 2 summarizes some of the knowledge acquired by those working on the Eleuthera-Bermuda experiment. There are several fading types. The very fast fading type extends from an averaging time of perhaps ten times the period of the sound wave itself up to approximately 15 seconds. A fading in this domain of averaging time and record time — that is, the length of time we look at a record — is usually incorporated within scattering theories and scattering experiments.

Fading Type		Amplitude			Phase		
T_A	T_R	$\Delta\lambda$	T_λ	τ_λ	$\Delta\theta$	T_θ	τ_θ
Very slow 40 dy	1 yr	5 dB	4 mon				
Slow 2 dy	40 dy	15 dB	30 dy		70 cy	30 dy	
Intermediate 2 hr	2 dy	5 dB	12 hr		10 cy	12 hr	
Fast 15 sec	2 hr	20 dB	25 min	5 min	5 cy	80 min	25 min
Very fast 10/f	15 sec			(Scattering fluctuations)			

Figure 2. TEMPORAL CHARACTERISTICS
 (Eleuthera/Bermuda, $f = 400$ Hz, $R = 700$ nm, $v = 0$)
 DeFERRARI; STANFORD; WEINBERG, CLARK, FLANAGAN

At the other extreme are very slow fades which have been described as seasonal fluctuations. Perhaps the record time for these is as long as 1 year and averaging times of 1 month or more might be used.

Between these obvious extremes are other kinds of fading, perhaps three or more, worth distinguishing between because they appear to be associated with separate mechanisms. For example, fast fading fluctuations tend to have a fading range of 20 dB in amplitude, a period of about 25 minutes, and a decorrelation time of about 5 minutes. The phase, on the other hand, typically ranges over 5 cycles with a 60- to 80-minute period, and perhaps a 25-minute decorrelation time.

The intermediate fades yield rather different numbers. It should be emphasized that this particular set of experiments is for one frequency with fixed source and receiver locations. Hence, the only motion that does occur is, in fact, the motion of the ocean. For the intermediate fades, there is a definite period of 12.4 hours, with a somewhat reduced fading range on amplitude and an increased fading range on phase.

Figure 3 illustrates a possible mechanism for the fast-fading case which leads to the general result that the fading period on amplitude is related to the fading period on phase by the simple ratio π/θ_{rms} .

The argument proceeds from a modal interference picture which treats the mean square pressure as a sum of sinusoids. Whenever the phase difference between pairs of modes approaches twice the average phase, an amplitude beat is generated. Hence, that amplitude beat is given whenever the average phase is of the order of π . Typical

MODAL INTERFERENCE

$$\langle p^2 \rangle \sim \sum_i (\sum \cos \theta_i)^2 + (\sum \sin \theta_i)^2 \quad (\text{equal energy paths})$$

name and add modes m and n such that

$$\frac{\theta_m + \theta_n}{2} = \theta_{av}$$

$$\frac{\theta_p + \theta_q}{2} = \theta_{av}$$

p and q

$$\begin{aligned} & \cdot \\ & \cdot \\ & \cdot \end{aligned} \quad \left(\frac{\Delta_{ij}}{2} \right) \sim \cos^2 \frac{\Delta_{mn}}{2} + \cos^2 \frac{\Delta_{pq}}{2} + \dots$$

$$\langle p^2 \rangle \sim \sum_{ij \text{ pairs}} A_{ij} \cos^2 \left(\frac{\Delta_{ij}}{2} \right) \sim \cos^2 \frac{\Delta_{mn}}{2} + \cos^2 \frac{\Delta_{pq}}{2} + \dots$$

A_{ij} slow function θ_{av}

$$\Delta_{mn} = \theta_m - \theta_n$$

$$\text{largest } \Delta_{ij} \approx 2 \theta_{av}$$

$$\text{amplitude beat: } \theta_{av} \approx \pi$$

$$T_\Lambda \approx T_\theta \frac{\pi}{\theta_{rms}} \approx T_\theta \frac{\sqrt{2}}{\theta \Delta \theta_{cycles}}$$

$$\text{also } \tau_\Lambda \approx \tau_\theta \frac{\sqrt{2}}{\Delta \theta_{cycles}}$$

Figure 3. POSSIBLE MECHANISM FOR FAST-FADING

amplitude periods are then on the order of 1.5 divided by the number of fade cycles. Referring back to Figure 2, for fast fading, $T_{\theta}/\Delta\theta = 16$ minutes, which is approximately two-thirds of the observed T_{Λ} of 25 minutes. The agreement for the decorrelation times is not as good but still in the right ballpark. This argument does not seem to work for the other fading types which suggests that for this particular frequency range and these particular choices of averaging times and record lengths the underlying mechanisms may be different. The intermediate fading rates may, in fact, be related closely to the modal interference that is caused by internal-wave motion, and the slow rates may be caused by planetary waves that have a different kind of behavior with respect to the fading process.

The results of Figure 2 should not imply that a simple reduction of experiments to a single number table is, in fact, possible. Figure 4 displays results obtained by Stanford (1974), where two amplitude time series are spatially separated by only 40 meters vertically and 80 meters horizontally. The periods of fade, T_{Λ} , differ by a factor of 2, although the amplitude fade range is about the same.

Figure 5 illustrates results obtained by Spindel et al. (1974), and the experiment differs in two respects from that reported previously: the range is somewhat different; and, perhaps more significantly, there is a drift velocity of about a third of a knot, rather than a zero range rate. (Nonetheless, as will be shown subsequently, this drift rate may be not too significant.) More importantly, these results show a tremendous depth dependence to the fading. The fading range on phase is of the order of 26 cycles with a period of 140 minutes for the deep receiver. For the shallow receiver above the main sound channel, the fading range is 10 cycles with a fading period of 64 minutes.

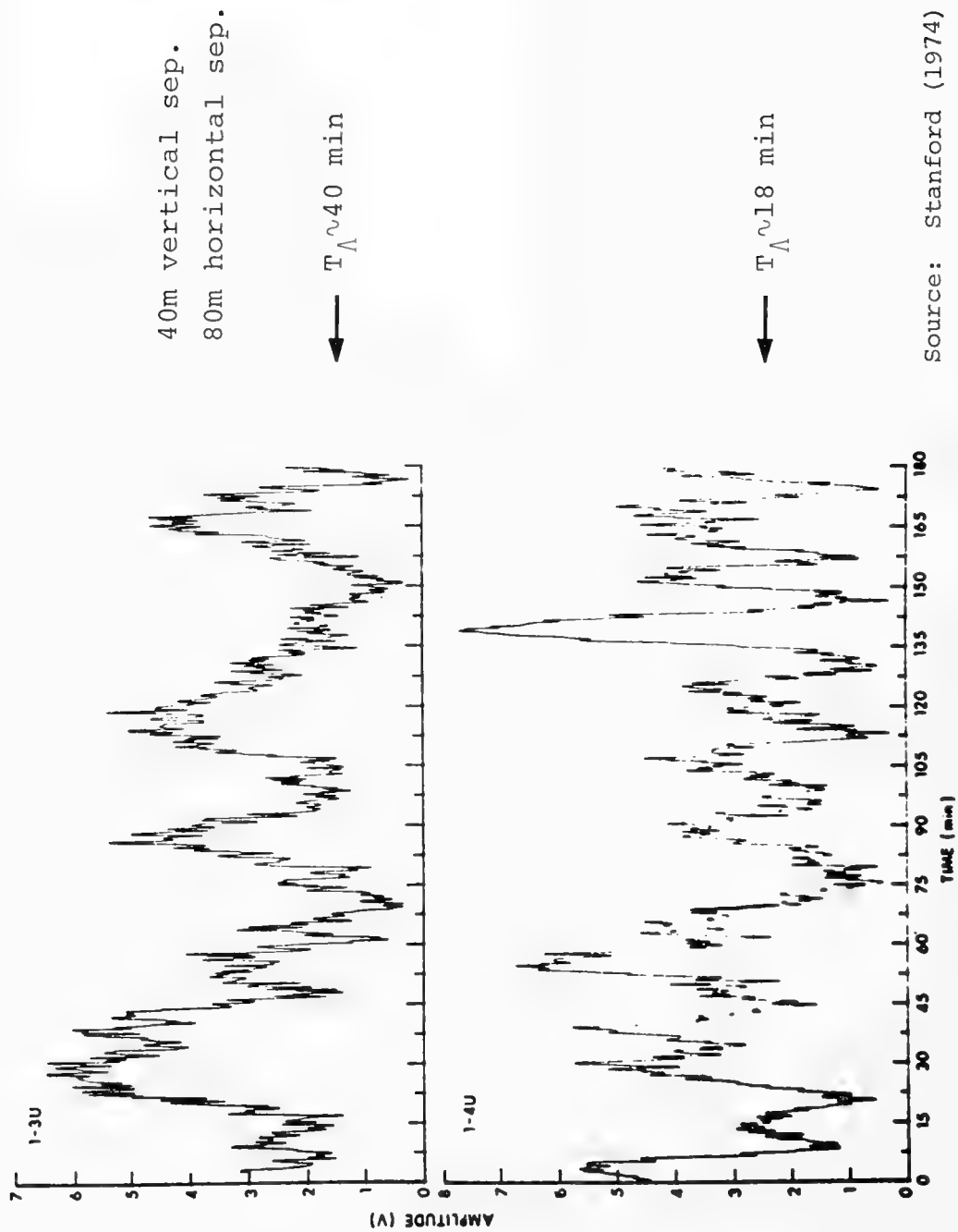
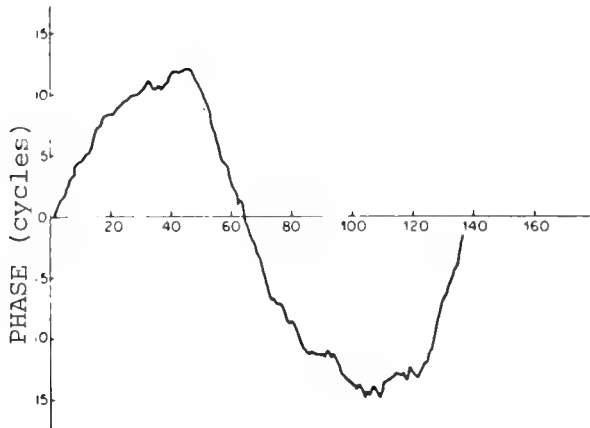


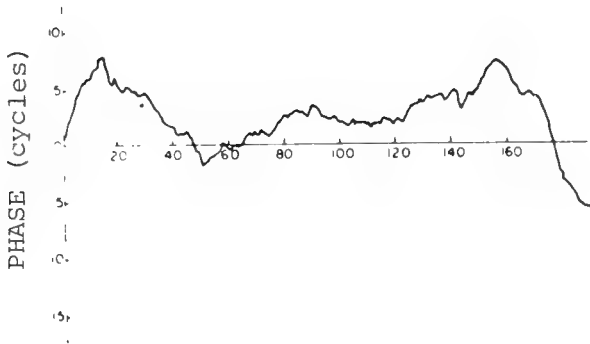
Figure 4. SPATIAL DEPENDENCE OF TEMPORAL VALUES

$$R = 110 \text{ nm}$$

$$v_r \sim 1/3 \text{ kt}$$



1500m depth
 $\Lambda_\theta \sim 26 \text{ cyc}$ $T_\theta \sim 140 \text{ min}$



305m depth
 $\Lambda_\theta \sim 10 \text{ cyc}$ $T_\theta \sim 64 \text{ min}$

Source: Spindel, Porter and Jaffe

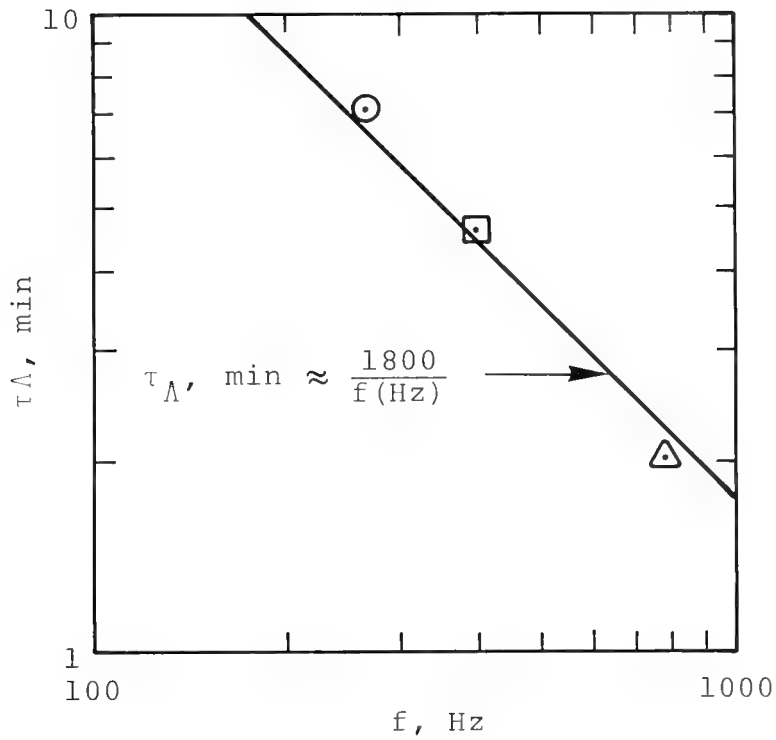
Figure 5. SPATIAL DEPENDENCE OF TEMPORAL VALUES

These results indicate that it is impossible to state on a single-number basis what the fading parameters are. Nonetheless, it is possible to discuss trends in these data and to try to understand why changes such as these occur.

Figure 6 shows results taken under more or less comparable conditions, where the decorrelation time for amplitude, τ_A , is plotted versus the carrier frequency. There were three experiments: one by Nichols and Young (1968) at about 270 Hertz, DeFerrari's (1974) (which was included in Figure 2) at about 400 Hertz, and Webb and Tucker (1970) at about 800 Hertz. The decorrelation time seems to be reasonably described by something that is intuitively appealing — namely, that the frequency times time is a constant approximated by 1800 (when the frequency is in Hertz and the decorrelation time is in minutes). This suggests, for example, that at 100 Hertz the decorrelation time may be as long as 18 minutes.

The previous results have been attributed to effects of ocean dynamics. Figure 7 addresses the question: What about making measurements with moving platforms? For moving platforms, the notion of a spatial scan is introduced. There are spatial fluctuations in the acoustic field if the ocean is considered completely stationary or "frozen." These fluctuations are described in terms of a correlation coefficient relating changes in range and changes in depth. A rangewise scale, ℓ_r , and a depthwise scale, ℓ_z , are then defined in terms of the $1/e$ points in the correlation coefficient.

Preston Smith proposed a theory which may have a direct bearing on these measures. In the second case of an isogradient duct, the radial or the rangewise scale was found to be proportional to the wavelength divided by the square of an angle, θ_ℓ . This angle is, in fact, the angle that encloses all the refracted rays that are



○ Nichols and Young

□ DeFerrari

△ Webb and Tucker

Figure 6. DECORRELATION TIME AND CARRIER FREQUENCY
FAST FADING (Ocean Dynamics)

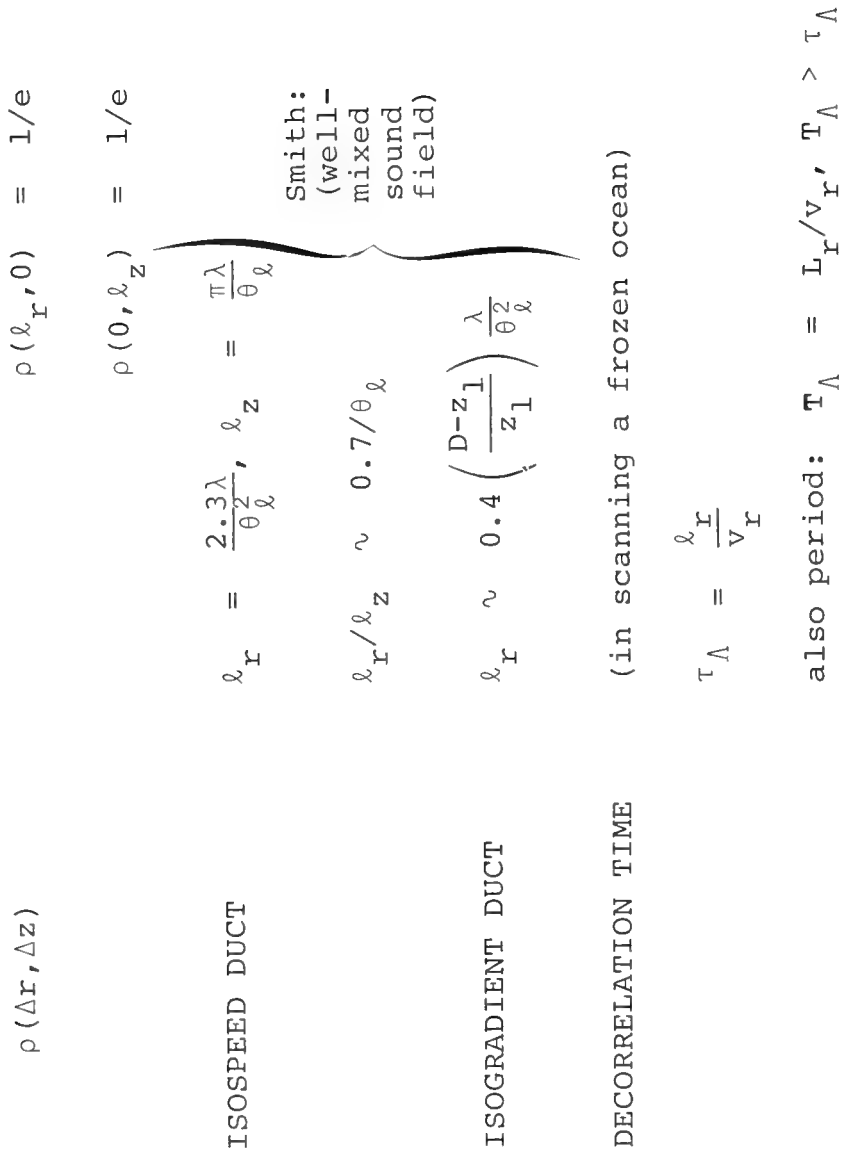


Figure 7. SPATIAL VARIATIONS OF SOUND FIELD STRUCTURE (Frozen Ocean Fluctuations)

trapped in the duct. The constant of proportionality involves parameters such as the depth of the receiver, z_1 , and the depth of the duct, D .

Using this scale, or whatever scale is appropriate to the problem of interest, the decorrelation time is determined by the scale length and the range rate. When making measurements with a moving platform, the impact of this time on the measurements must be addressed.

Notice that the decorrelation time for platform motion and ocean dynamics is proportional to the wavelength, as shown in Figure 6. Hence, there should be a particular value of range rate which makes the two decorrelation times equal. This speed depends on the path geometry but for this case appears to be on the order of 3 to 5 knots. That is, if the ocean is scanned at speeds substantially in excess of 3 to 5 knots, the fluctuation time scale will be governed by the structure that exists in the ocean as if the ocean were standing still and didn't have, say, internal waves. On the other hand, if the ocean were scanned at speeds significantly less than a few knots (for example, the one-third of a knot in drift used by Spindel et al. (1974), the time scales may well be those associated with internal waves or other ocean dynamics.

Some evidence for this is indicated by the NRL experiments where range rates were 7 knots and horizontal scale lengths of 65 kilometers were measured corresponding to the convergence zone spacings. A closer examination of their spectral decomposition in wave number (really interference scales) shows at 14 Hertz about a 9 kilometers interference length which is roughly consistent with the results in Figure 7.

The transmission-loss data shown in Figure 8 were supplied by Earl Hays and are a good example of the effects of platform motion.

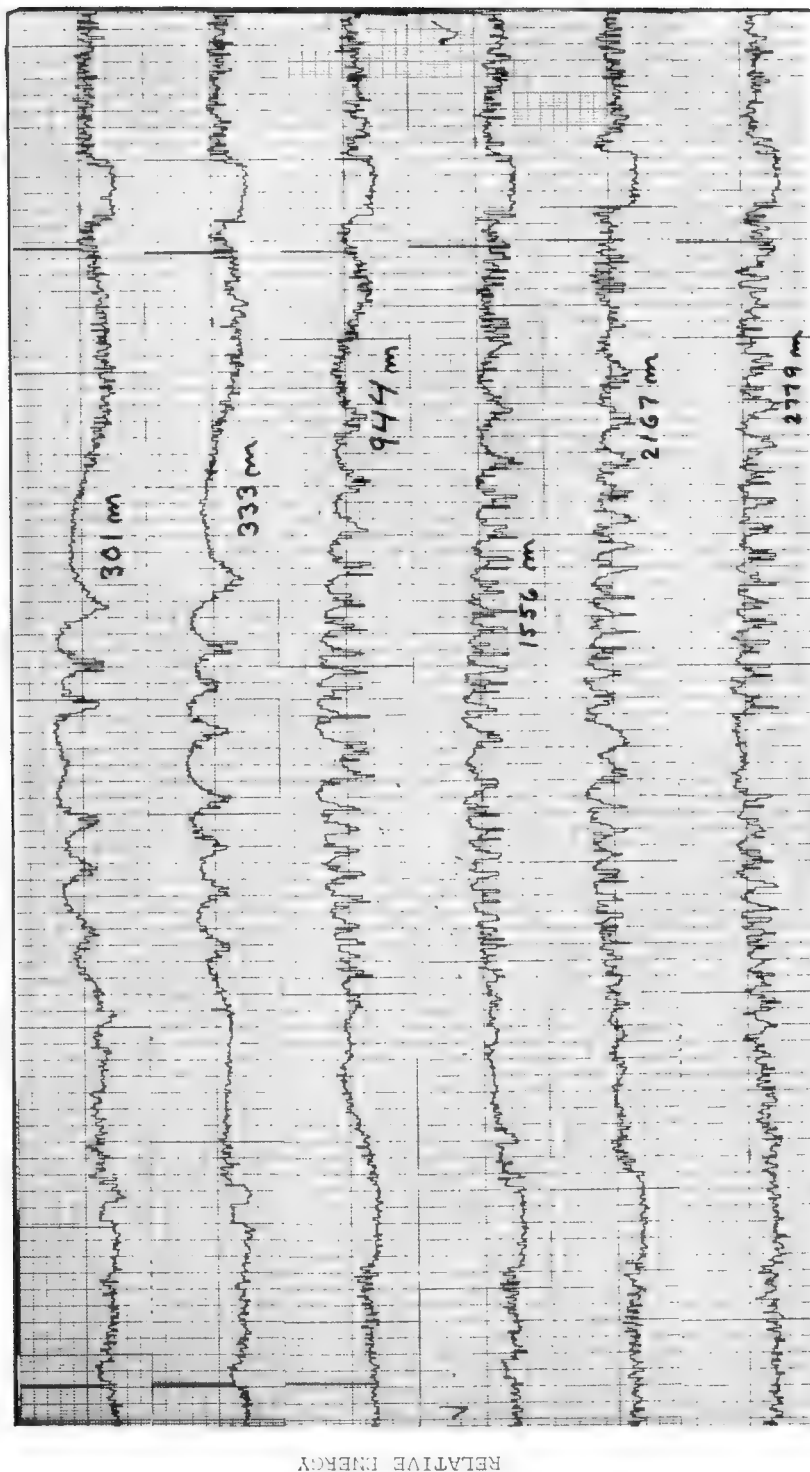


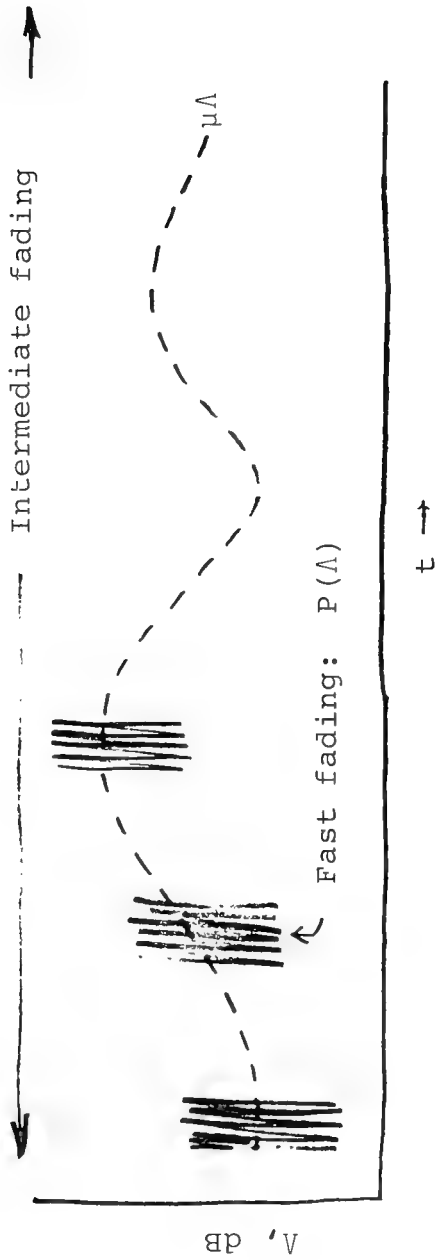
Figure 8. TRANSMISSION LOSS DATA SHOWING EFFECTS OF PLATFORM MOTION

The experimental geometry consisted of a fixed string of receivers at the depths indicated and a source closing from a range of 7 miles to a closest-point-of-approach of 2 miles and continuing on out to about 7 miles. The source frequency is 130 Hertz and the source speed is 6 knots.

Notice that for the shallow (300-meter) receivers, periodicity is about 10 minutes, whereas for the deeper receivers, between 2,000 and 3,000 meters, the periodicity is of the order of one or two minutes. These time scales are consistent with the spatial scales that exist in the ocean, as sampled by the various source-receiver geometries. The temporal scales associated with internal-wave motion in this geometry would lead to periods of 40 to 50 minutes for this frequency. This is a good example of an experiment which yields time scales that result from the structure of the acoustic field in the ocean and not from the ocean dynamics.

The conclusions these various results suggest are that the ocean can move and hence give some structure to received-signal fluctuations and, also, the platforms can move resulting in additional fluctuation structure. Both of these possibilities must be considered. In fact, in many practical circumstances there are sources moving near 6 knots and a technique is needed to combine situations where fluctuations due to platform motion and ocean dynamics are comparable. No theory adequately takes both into account. In fact, no theories adequately treat either of the two separate mechanisms.

Figure 9 addresses a few more facets of the fluctuation problem. In a data record which addresses fast fading but is also long enough to include, for example, intermediate fading, variations appear in the mean, μ_{Λ} , of the individual fast-fade processes.



Fast Fading (Modal Interference):

$$P(\Lambda) = \frac{1}{a\mu_x} \exp \left[\frac{\Lambda}{a} - \frac{e^{\Lambda/a}}{\mu_x} \right] \rightarrow \begin{cases} I: & \text{exponential} \\ |p|: & \text{Rayleigh} \end{cases}$$

$$a = 10 \log e = 4.34$$

$$\mu_\Lambda = 10 \log \mu_x - a\gamma = 10 \log \mu_x - 2.5 \text{ dB}$$

$$\sigma_\Lambda = a\sqrt{\pi^2/6} = 5.6 \text{ dB}$$

$$\Delta\Lambda (0.025) = 21 \text{ dB}$$

Figure 9. AMPLITUDE STATISTICS

In many cases the probability density for amplitude, $P(\Lambda)$, for fast fading results from a phase random process and for the intensity is exponential, while for the rms pressure it is Rayleigh. These are equivalent statements and for the logarithmic distributions, the mean is depressed by 2.5 decibels and the standard deviation is 5.6 decibels. This result assumes enough paths (10 or more) to justify an asymptotic limit.

For this distribution, the fading range (throwing away 5 percent of the extremes) is about 21 dB, which is consistent with short observation periods (under 2 hours) for the frequency of 400 Hertz.

The next step (Figure 10) is to describe the amplitude statistics for a longer period of time than that which just corresponds to each of the fast-fading segments.

If the probability densities of the individual processes are known, the final probability density is found by averaging $P(\Lambda)$ over the variation of the mean itself, $P(\mu_\Lambda)$. For example, for fast fading alone, the probability density of the mean is a delta function, yielding back the phase random process. For predominantly slow fading, variations in the mean may be reasonably given by a Gaussian process which generates a sufficiently large spread in the mean that the probability density of the logarithmic amplitudes approach a Gaussian distribution. There is evidence that, in fact, this occurs when data are included from experiments over time periods of 30 to 40 days.

In the intermediate fading-rate case, the results are not so easily described. Figure 11 shows results obtained by John Clark (1974) and his colleagues last year, where the signal histograms (essentially the probability densities) are plotted as a function of time. Each

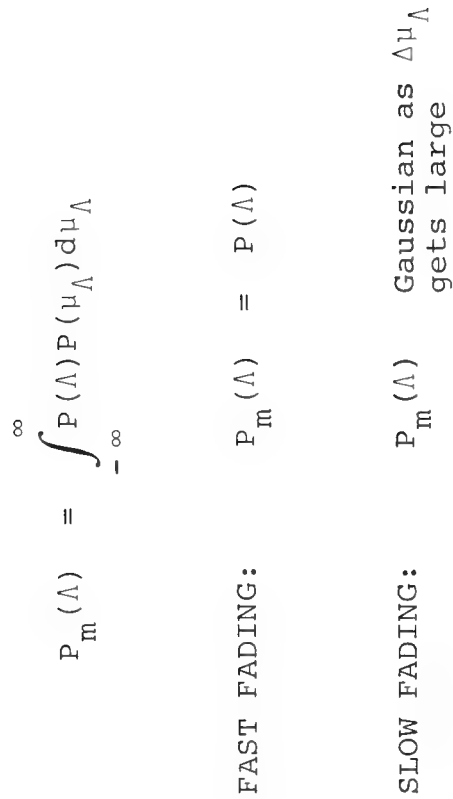


Figure 10. STATISTICS FOR VARYING MEAN

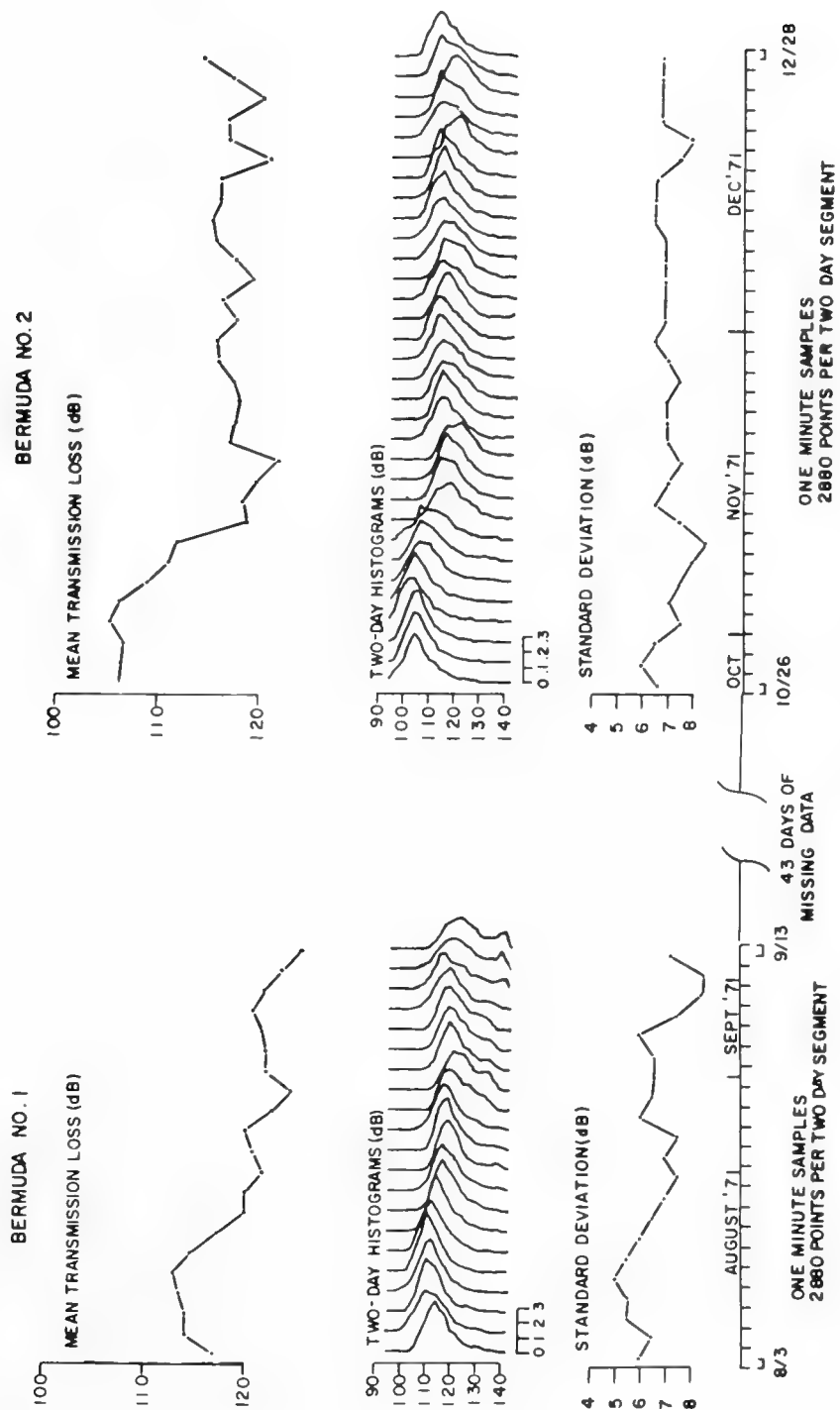


Figure 11. INTERMEDIATE FADING RATE STATISTICS

probability density represents data taken over 2 days. The individual densities are somewhat skewed as expected, but the individual densities change with time. While the probability density of either entire group has not been generated, the supposition is that it may approach in and of itself a Gaussian distribution. Note that the means of the distributions change with time as do the standard deviations.

The final figure (Figure 12) shows one possible way to treat this. The solid curve corresponds to a single population consisting of phase-random multipaths. It is skewed with the 2.5-dB depression in the mean. (That is, the most probable value is 2.5 dB higher than the mean value.) If seven such processes are added, uniformly spaced with a spread in means of 6 dB, the resulting distribution is easily integrated (since it consists of a sum of delta functions) and leads to the dashed curve in Figure 12. Two things have happened: First, the standard deviation has increased beyond 5.6 dB (the dotted curve is broader than the solid curve); and, second, there is less skew and peakedness in the distribution. In general, as the spread becomes larger, the dashed curve becomes more and more Gaussian in nature.

SUMMARY

In conclusion, there are many measures of fading. It is going to be important to recognize various regimes of time for time series and space for space series. It is equally important to indicate which fluctuations are averaged out and which are included through the length of the record.

The understanding of the sub-processes is quite far along; however, it is difficult if not impossible to include everything that is observed. A more likely approach is to formulate very clear statements about the particular process being investigated at a particular time, recognizing the diverse underlying mechanisms.

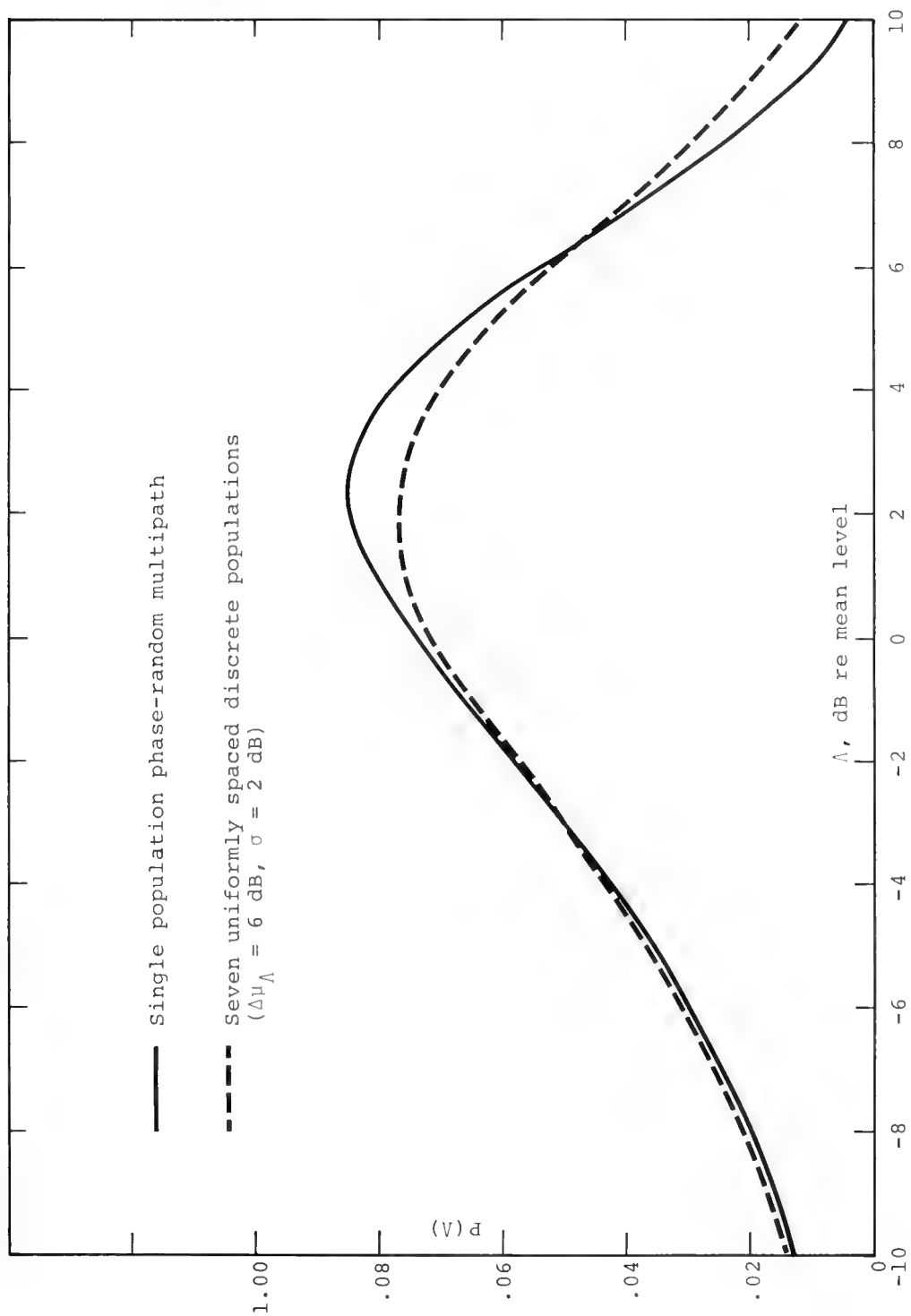


Figure 12. EXAMPLE FOR INTERMEDIATE FADING

REFERENCES

- Clark, J. G., and M. Kronengold, "Long-period fluctuations of CW signals in deep and shallow water," *J. Acoust. Soc. Am.* 56: 1071-1083, 1974.
- DeFerrari, H. A., "Effects of horizontally varying internal wave-fields on multipath interference for propagation through the deep sound channel," *J. Acoust. Soc. Am.* 56:40-46, 1974.
- Nichols, R. H., and H. J. Young, "Fluctuations in low-frequency acoustic propagation in the ocean," *J. Acoust. Soc. Am.*, 43: 716-722, 1968.
- Spindel, R. C., R. J. Porter, and R. J. Jaffe, "Long range sound fluctuations with drifting hydrophones," *J. Acoust. Soc. Am.* 56: 440-446, 1974.
- Stanford, G. E., "Low frequency fluctuations of a CW signal in the ocean," *J. Acoust. Soc. Am.* 55:968-977, 1974.
- Webb, D. C., and M. J. Tucker, "Transmission Characteristics of the SOFAR Channel," *J. Acoust. Soc. Am.* 48:767-769, 1970.
- Weinberg, N. L., J. G. Clark, and R. P. Flanagan, "Internal tidal influence on deep-ocean acoustic ray propagation," *J. Acoust. Soc. Am.* 56:447-458, 1974.

SOUND PROPAGATION IN A RANDOM MEDIUM

Robert H. Mellen

New London Laboratory
Naval Underwater Systems Center
New London, Connecticut

For more than a decade we have been trying to identify and measure the various factors within the water column that contribute to the low-frequency attenuation in sound channels. Experiments have been carried out in a number of bodies of water, including fresh-water lakes, to study effects of temperature, salinity, and other environmental factors. The results show an anomalous attenuation in seawater below 1 kHz in excess of the magnesium-sulfate relaxation contribution. A new relaxation mechanism involving boron has been identified by Fisher and Yaeger. A second anomaly is frequency-independent over considerable ranges and is thought to arise from scattering by random variations in refractive index. Comparison of the scatter loss estimated from random variations in sound-speed profiles shows order-of-magnitude agreement with a wide range of experimental results. Effects of the random component of sound speed on spatial and temporal coherence within the channel are discussed.

INTRODUCTION

For more than a decade we have been trying to identify the sources and behavior of the various components within the water column that contribute to the attenuation of low-frequency sound in the sea. In 1967 we began a series of experiments designed to study the differences in various bodies of water, both fresh and saline, of different temperatures and other environmental factors. The map in Figure 1 shows the regions that were studied and I would like to discuss the results of these experiments (Browning and Thorp, 1972).

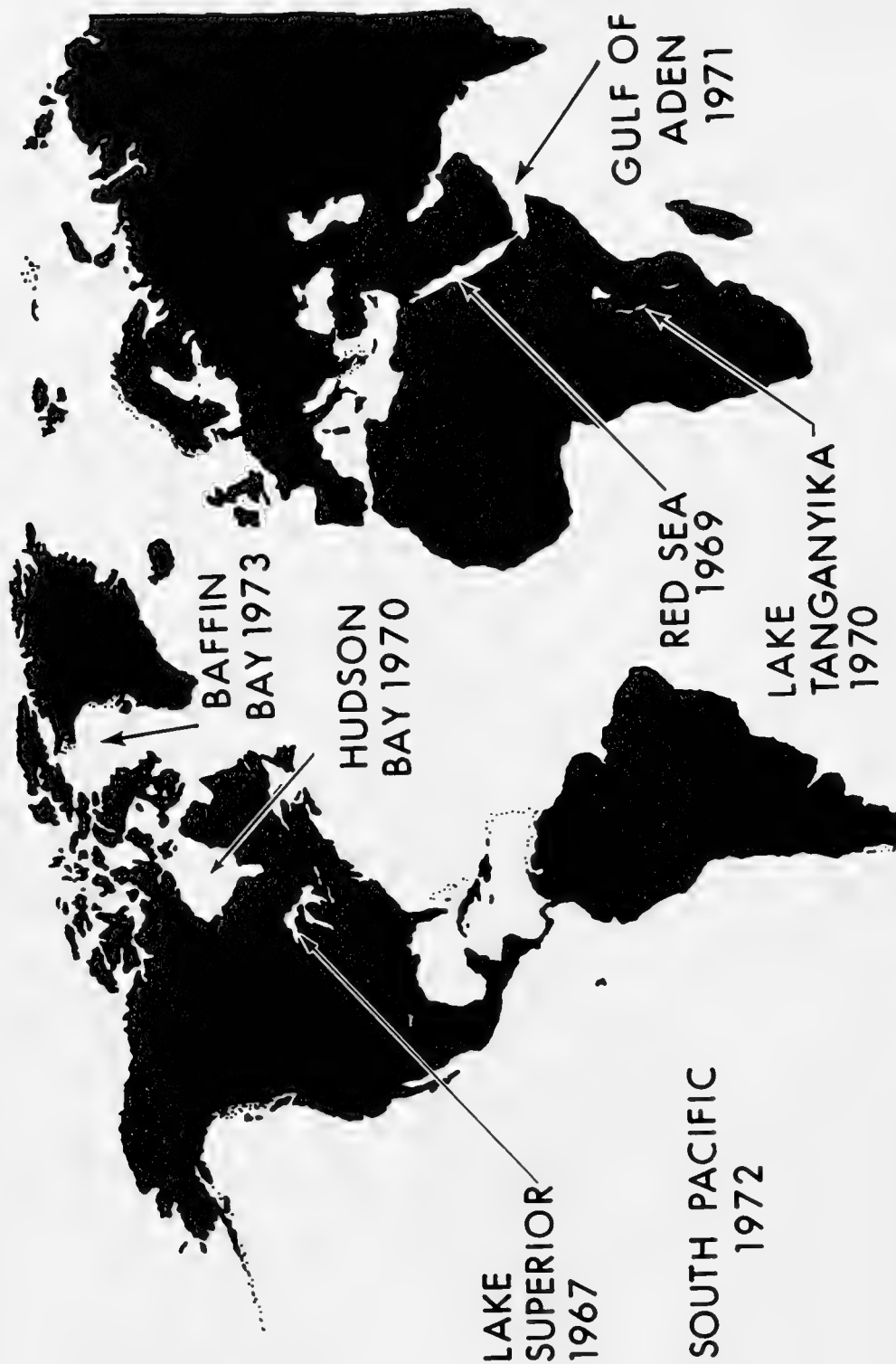


Figure 1. NUSC ATTENUATION EXPERIMENTS, 1967 to 1973

Our technique was designed for simplicity of data analysis and is represented pictorially in Figure 2. To eliminate boundary effects, we made the experiments during the period when the surface temperatures were sufficiently high to form a sound channel. SUS charges were detonated on the channel axis as the transmitting ship opened range. The signals were received by a hydrophone located on the channel axis and recorded for later analysis.

Analysis was accomplished by using 1/3-octave filters and measuring the total received energy arriving through refractive paths. This is no problem since arrivals reflected at the boundaries can usually be separated in time. If not, they can be ignored since they are more severely attenuated at least at the frequencies of interest. The results are plotted in decibels (corrected for cylindrical spreading vs range) for each of the filter frequencies. An example is shown in Figure 3. Then by linear regression analysis, we obtain the attenuation coefficient. The validity of the cylindrical-spreading approximation and the neglect of bottom loss above a critical frequency were checked by DiNapoli (1971) in his Fast Field Program and will be discussed later by Browning (in these Proceedings).

ATTENUATION EXPERIMENTS

The saltwater results shown in Figure 4 together with earlier work supported the conclusion of Thorp (1965) that the coefficients below 1 kHz were anomalously high. The dashed line is the Marsh-Schulkin curve that includes the MgSO_4 relaxation absorption. The excess absorption below 1 kHz is greater than predicted by roughly a factor of 10. Thorp fitted the anomaly to a relaxation formula with a relaxation frequency of 1 kHz.

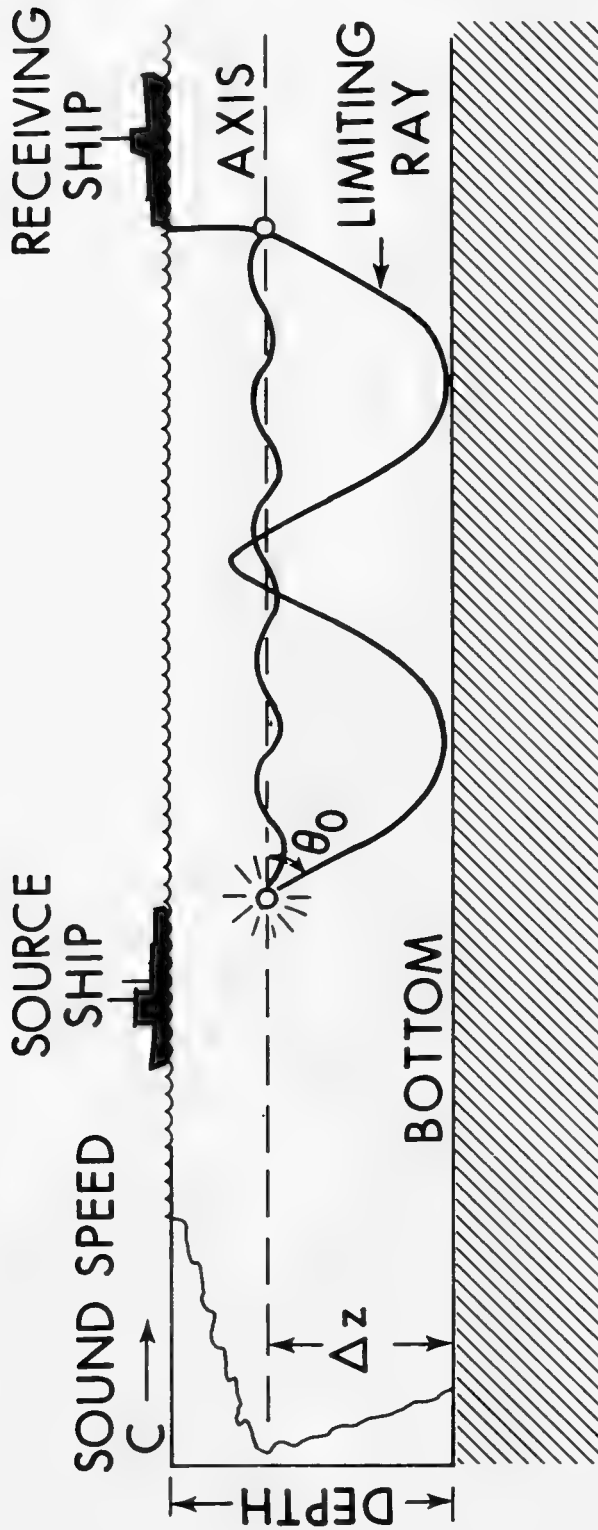


Figure 2. SOUND-CHANNEL ATTENUATION EXPERIMENT

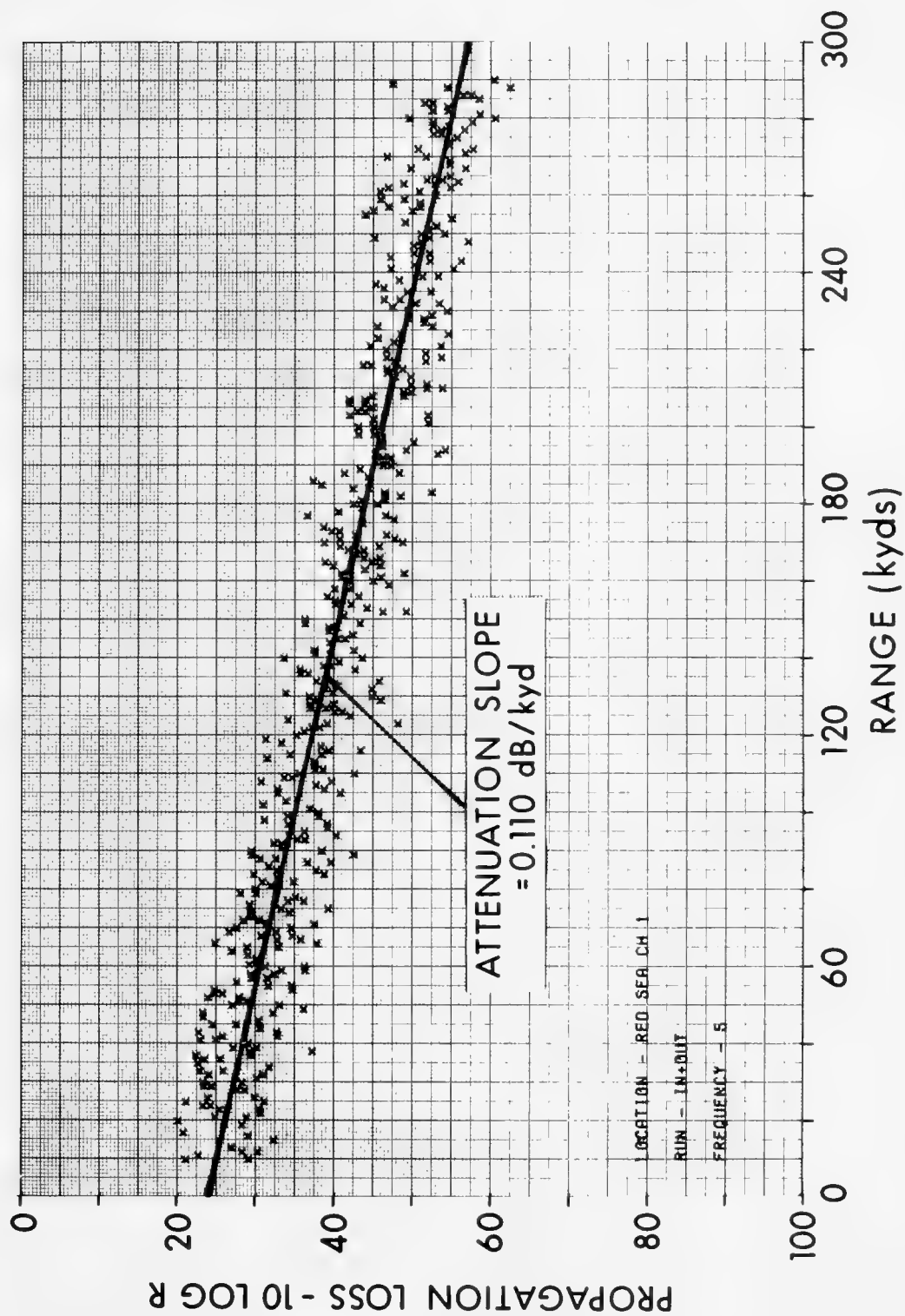


Figure 3. REGRESSION ANALYSIS OF ATTENUATION DATA AT 1410 HZ

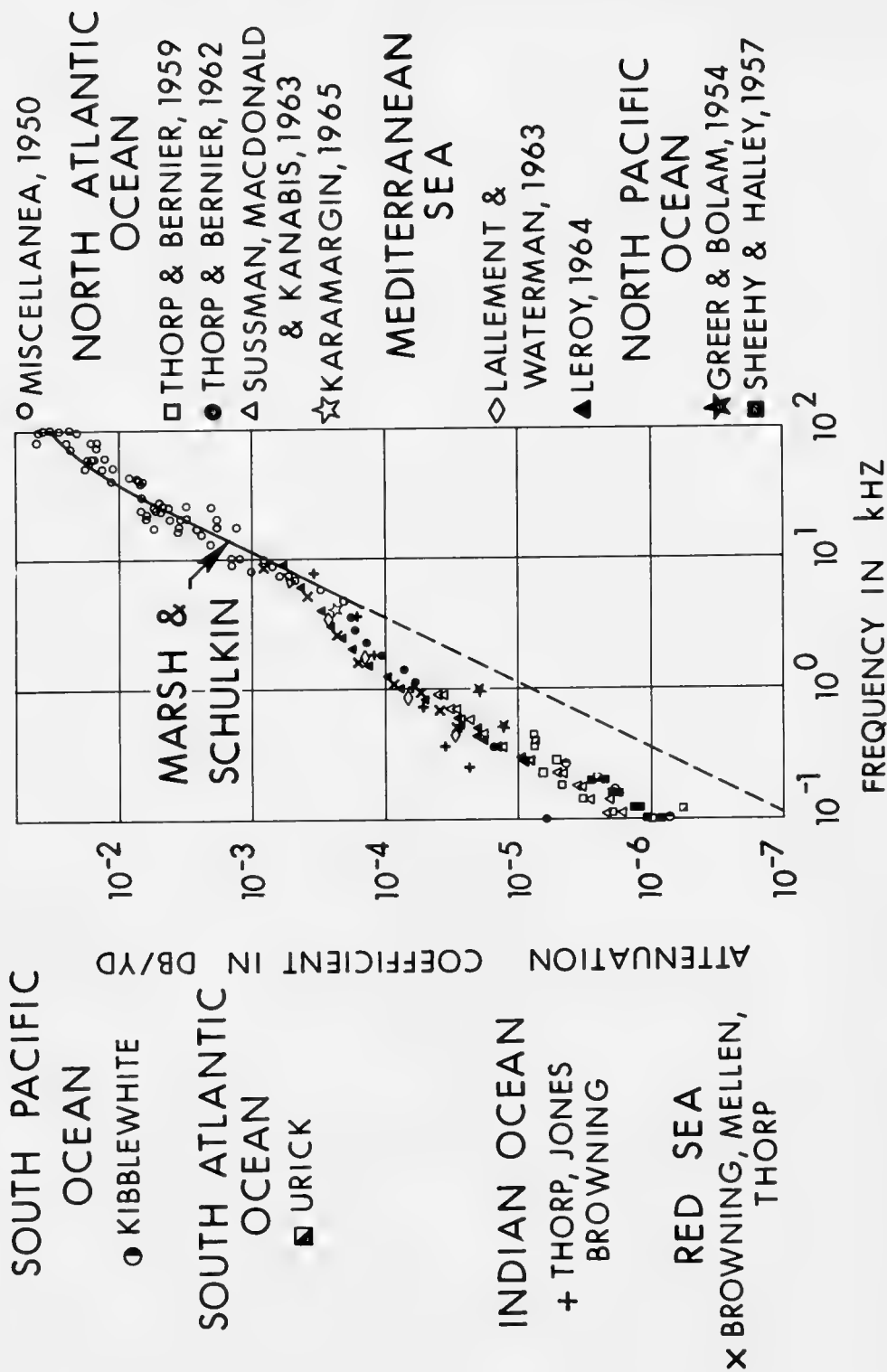


Figure 4. SUMMARY OF ATTENUATION-COEFFICIENT MEASUREMENTS

The resulting attenuation shown in Figure 5 is a three-component model consisting of:

- The fresh water viscous component
- The MgSO_4 relaxation component
- The anomaly which has recently been identified as a second relaxation involving the boron content in seawater (Yaeger et al., 1973).

Thus, we may now say that all three components are absorptive and do not involve scattering or other anomalies.

Several of the experiments do not follow the three-component absorption model very well at all and Hudson Bay (Browning, 1971) is one of those cases (see Figure 6). Since we have no reason to suspect either the experiment or the absorption model, it is plausible that the excess arises from some other mechanism. If we subtract the theoretical from the experimental, we find that the excess attenuation coefficient is a constant 0.04 dB/kyd over the frequency range. This might suggest another relaxation below 100 Hz; however, this hypothesis must be rejected for other reasons. A more likely cause is forward scatter from inhomogeneities within the water columns.

As a first attempt to test this forward scattering hypothesis, we have investigated the turbulent cell model of Chernov (1962). In Figure 7 we see a plane wave progressing through a perturbed medium where the refractive-index inhomogeneities are random, roughly spherical, and have a scale size a_0 . The wavefront becomes corrugated and the ray angles become randomly distributed. Energy is conserved.

In a sound channel, energy is normally trapped for all angles less than some critical angle, θ_0 , and leaks out for larger angles (see Figure 8). Because of the diffusion by the inhomogeneities,

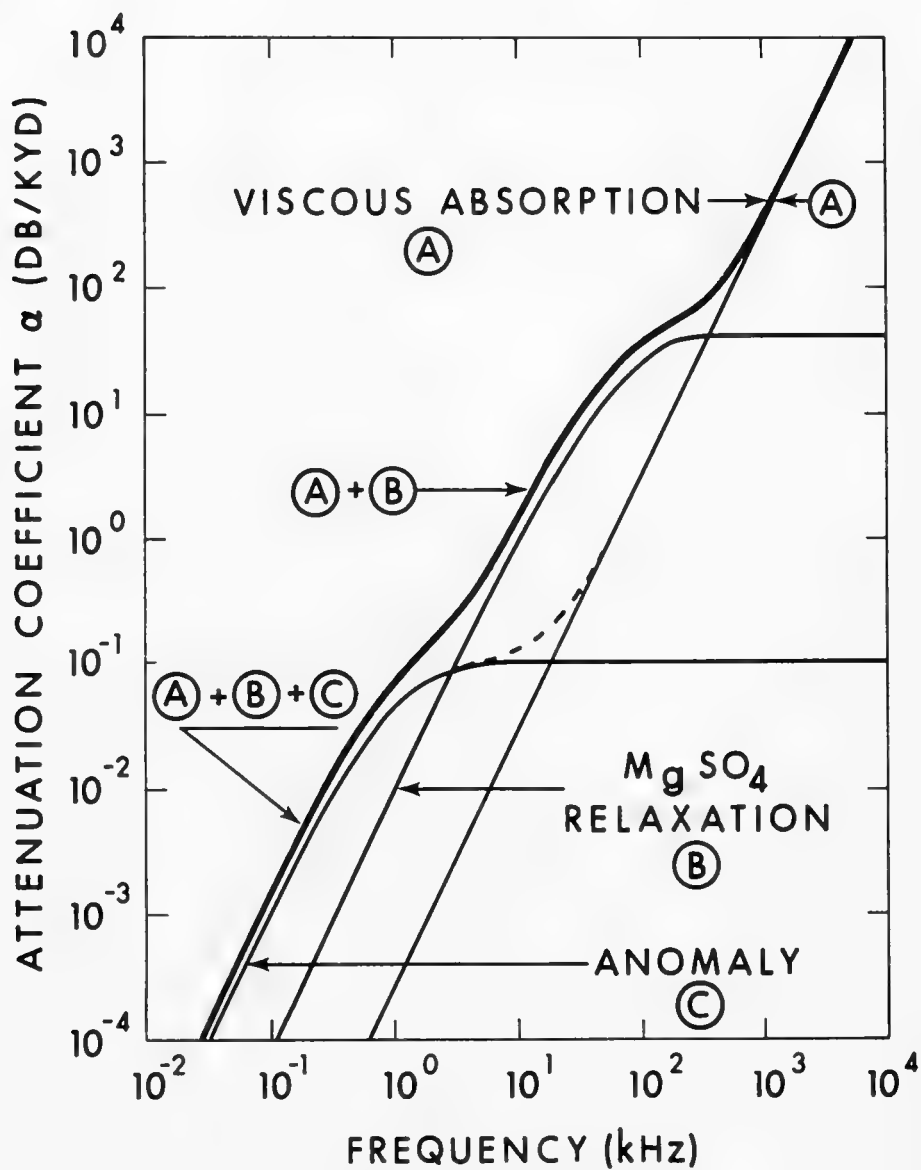


Figure 5. ATTENUATION OF SOUND IN SEAWATER

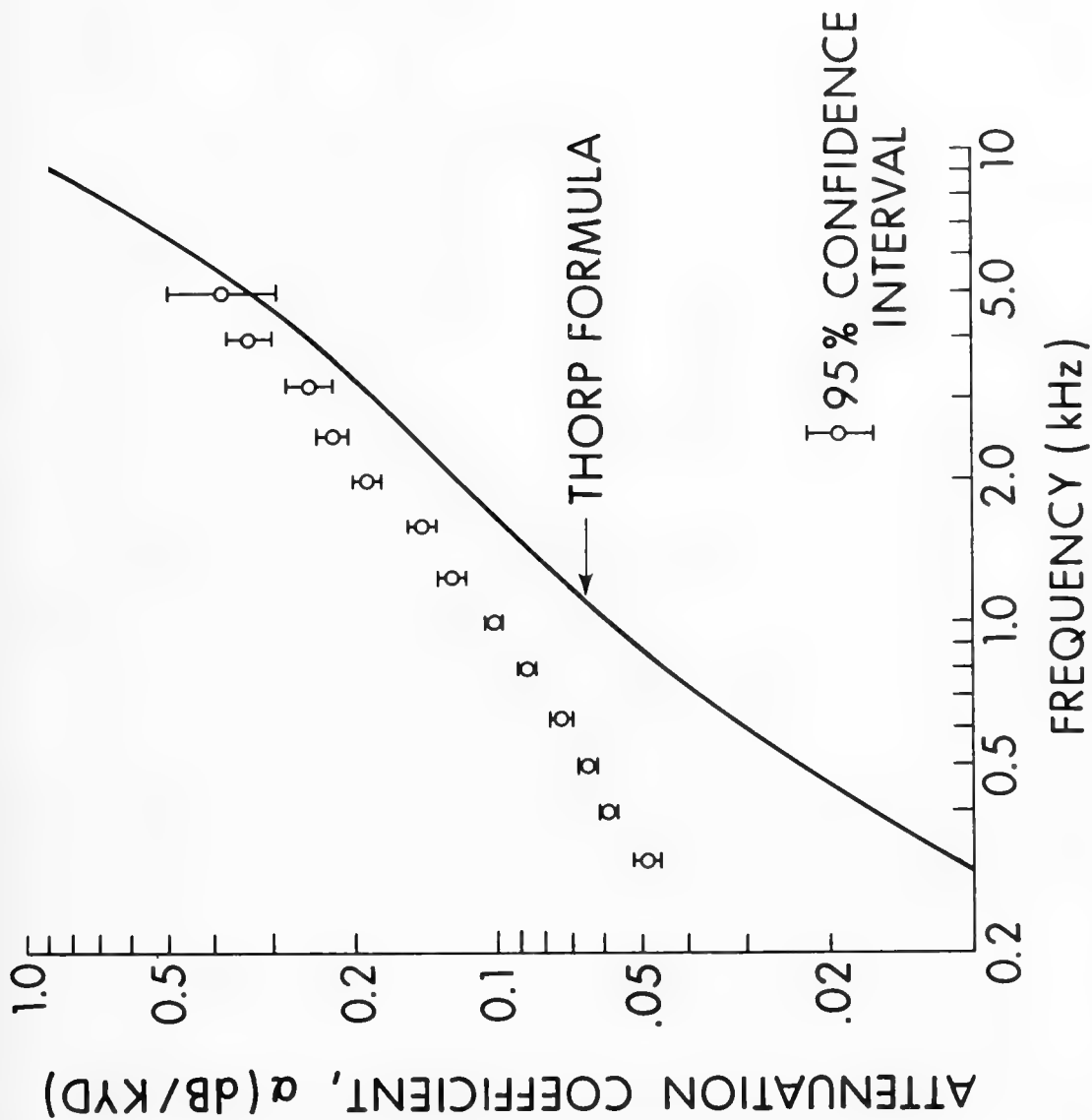


Figure 6. HUDSON BAY-1970 EXPERIMENTAL ATTENUATION RESULTS

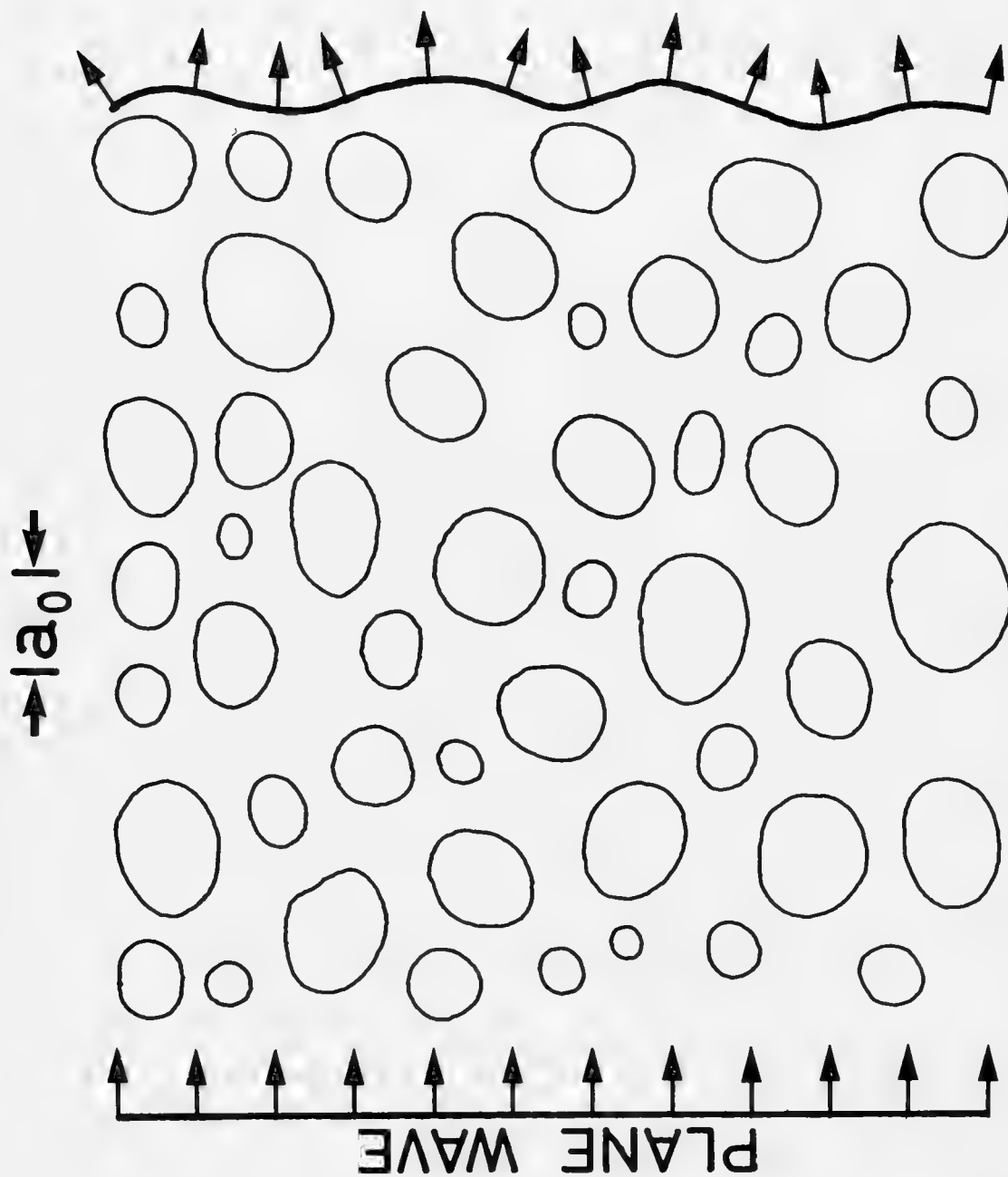


Figure 7. PLANE WAVE PASSING THROUGH A MEDIUM WITH RANDOM INHOMOGENEITIES

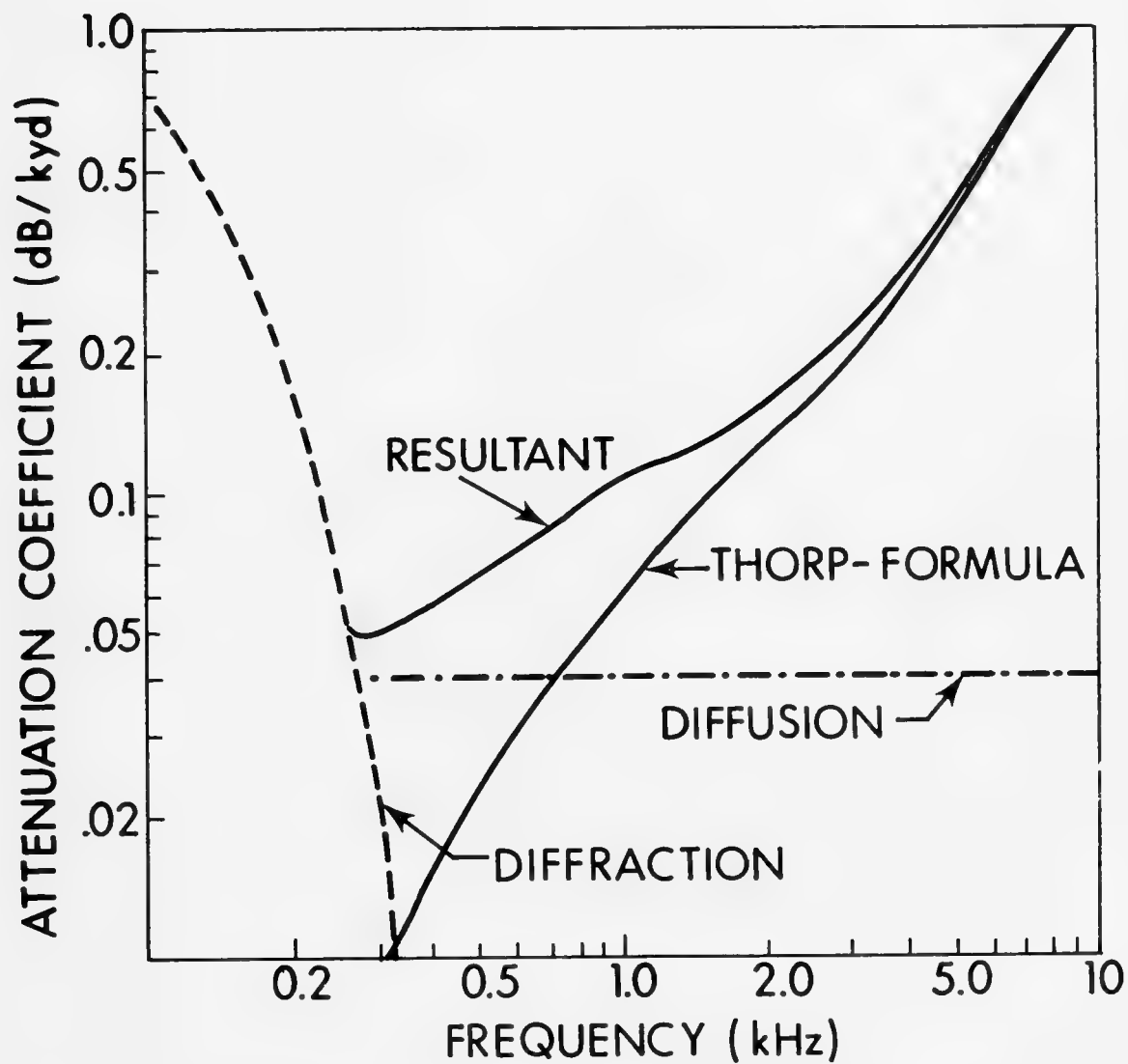


Figure 8. SOUND-CHANNEL ATTENUATION (THEORETICAL)

the angular distribution of normally trapped rays increases so that energy is continuously lost from the channel. The sound channel attenuation model includes absorption, diffusion loss (Mellen et al., 1974), and diffraction loss. Here the diffraction component is for the first normal mode only and assumes an infinitely lossy bottom.

These data can be fitted empirically, as shown in Figure 9, by adding an extra loss independent of frequency. For the Hudson Bay experiment, the excess is 0.04 dB/kyd while for the Gulf of Aden (Browning et al., 1973) value, it is 0.02 dB/kyd. The MgSO_4 component was corrected for temperature, -1.5°C for Hudson Bay and $+15^\circ\text{C}$ for the Gulf of Aden. The most significant difference between the two experiments is that the Thorp coefficient for the Gulf of Aden is only 0.6 that for Hudson Bay, which suggests differences in boron chemistry of the two bodies of water.

Once the possibility of a constant diffusion loss independent of frequency was accepted, the results of Lake Superior (Browning et al., 1968), shown in Figure 10, became clear. At first we had guessed that the Thorp relaxation was common to both salt- and fresh water, with only the MgSO_4 component missing in Lake Superior. It was later found that the necessary boron content did not exist in Superior which gave strong support to the scattering hypothesis.

We have used the term "independent of frequency" to describe diffusion which is, of course, a large ka_0 approximation. For $ka_0 \ll 1$, we expect the loss to fall off. There may be a hint of reduced scatter at 630 Hz which would make the scale size $a_0 = 0.5$ m.

Further support to the scattering hypothesis was given by the experiments in the South Pacific (Bannister, 1976) which show an excess absorption of 0.002 dB/kyd (see Figure 11). Like the North

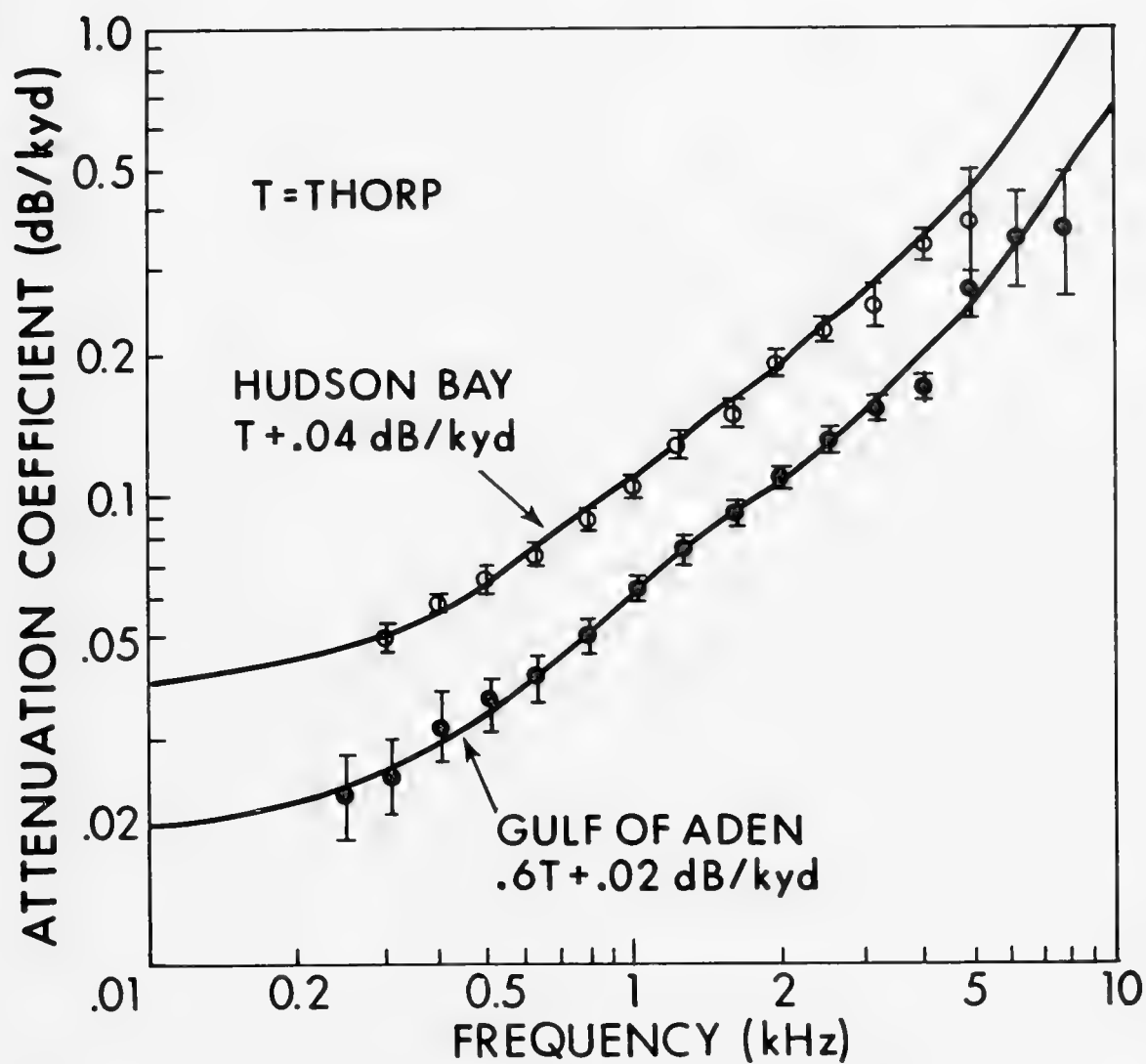


Figure 9. SOUND-CHANNEL ATTENUATION (EXPERIMENTAL)

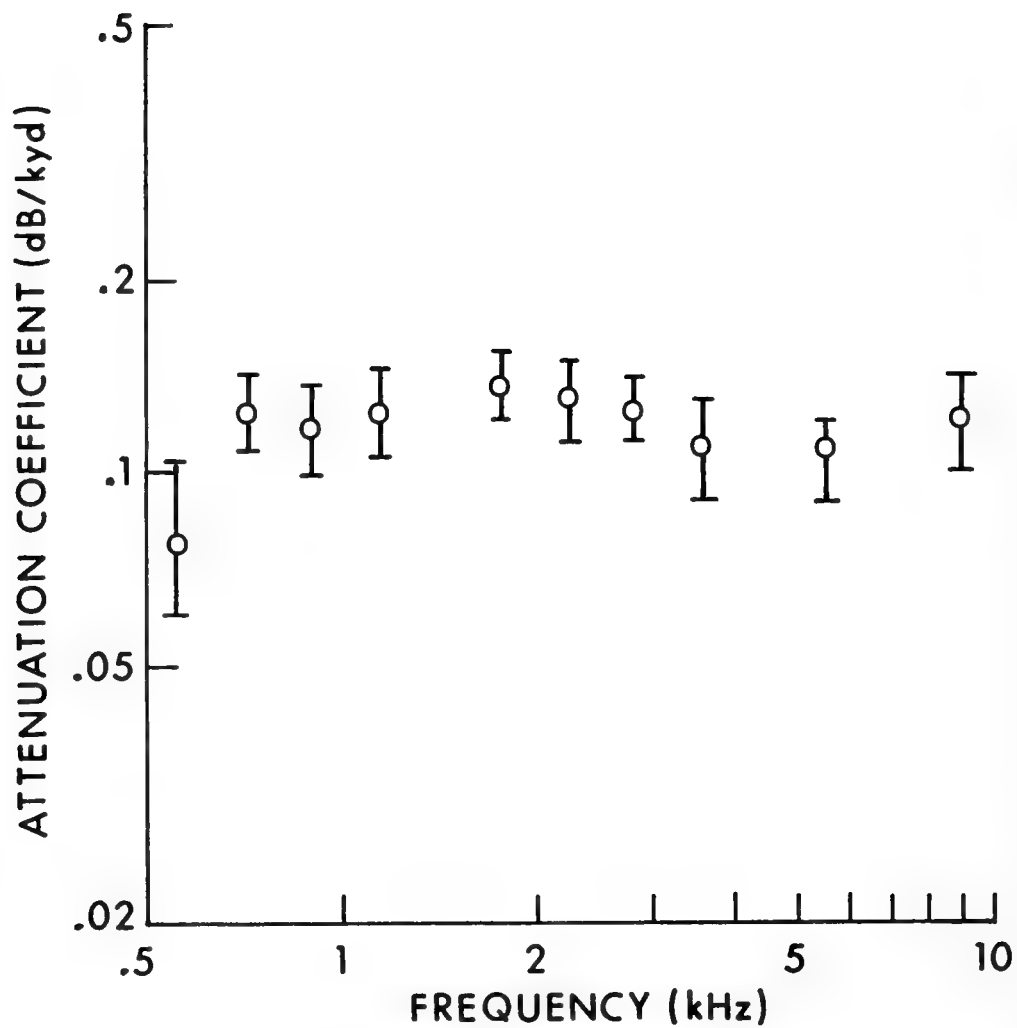


Figure 10. ATTENUATION COEFFICIENT IN LAKE SUPERIOR

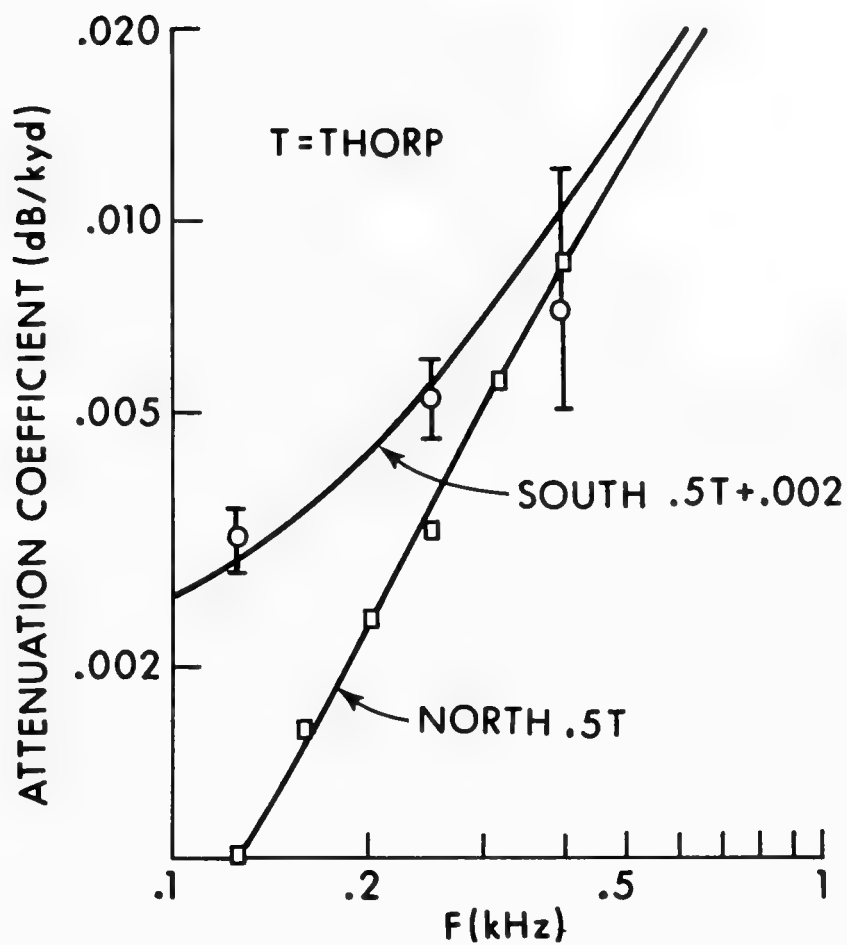


Figure 11. ATTENUATION COEFFICIENT
IN THE SOUTH PACIFIC

Central Atlantic, the North Central Pacific waters show no measurable scatter. The Thorp coefficient is estimated to be 0.5 in both cases.

Another experiment, shown in Figure 12, was done much earlier in the Gulf of Maine* and shows excess absorption similar to that for Hudson Bay. In fact, the two are almost identical except for the lower frequency points which are lacking in Hudson Bay. The diffraction curve was based on infinitely lossy bottom as before and, while the attenuation increases with decreasing frequency, the rate is slower than predicted, probably because of finite bottom loss. Any fall-off of diffusion loss at lower frequencies is obscured by diffraction, however.

The latest experiment was done in Baffin Bay (Browning et al., 1974) in 1974. The results in Figure 13 also show a constant loss of 0.02 dB/kyd above 200 Hz with a rapid fall-off below that frequency. Since Baffin Bay is much deeper than Hudson Bay or the Gulf of Maine, the low frequency values are not obscured by diffraction. The f^4 dependence below 200 Hz suggests Rayleigh scatter from globs of scale size $a_o = 3$ m with $\mu^2 = 2 \times 10^{-7}$.

From ray diffusion theory we have devised a simple formula, shown in Figure 14, for the sound-channel diffusion attenuation involving μ^2 , the variance of index of refraction, a_o , the scale size, and Δz , the depth from the channel axis to the bottom. Using the values $\mu^2 = 10^{-7}$ and $a_o = 15$ m obtained from analysis of the SVP in Hudson Bay and the Mediterranean, we see that the values predicted for shallow channels ($\Delta z = 100$ m) and the deep channels ($\Delta z = 2,000$ m) are in reasonably good agreement with experimental values. If a_o is

* Unpublished BBN data.

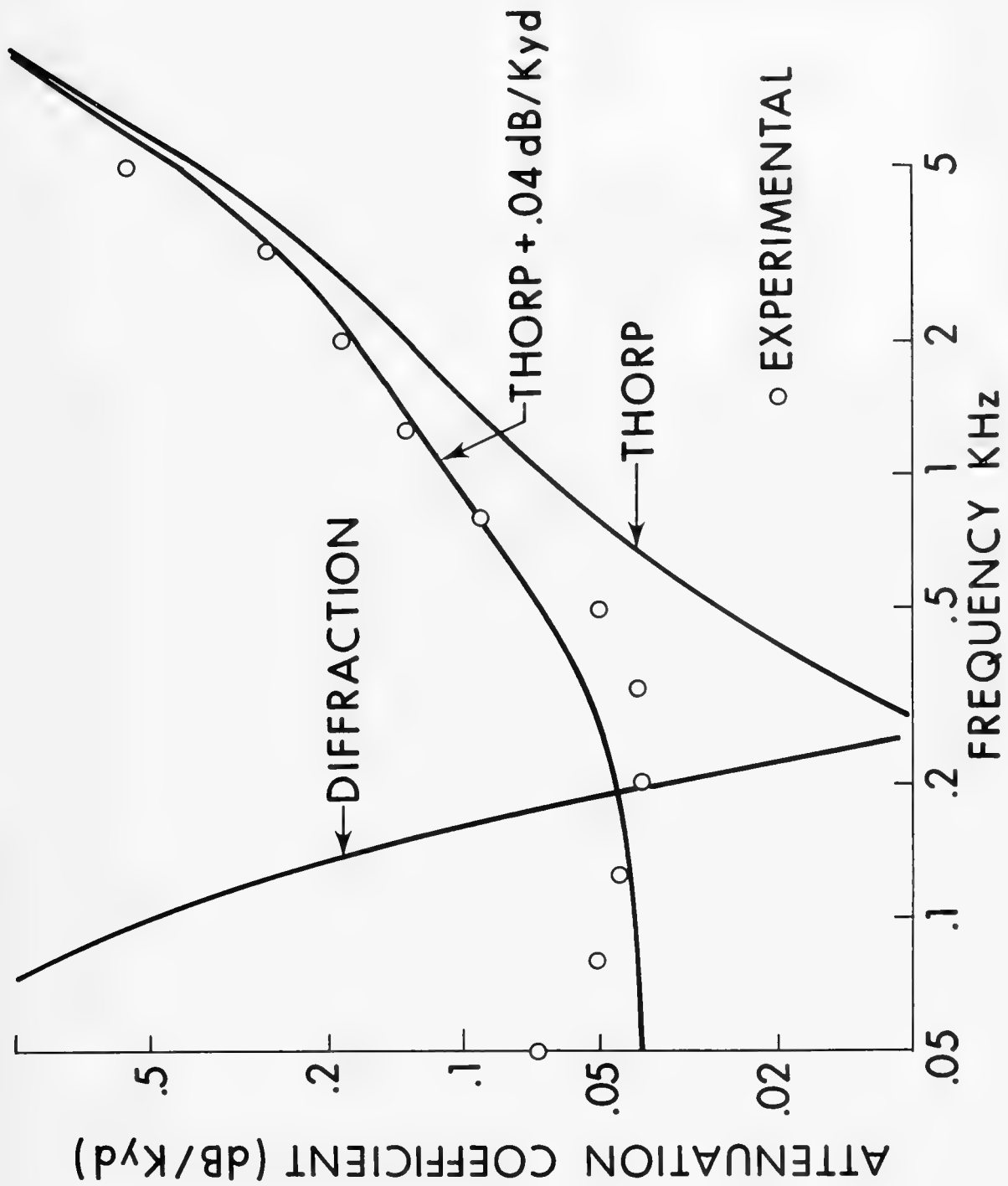


Figure 12. ATTENUATION COEFFICIENT IN THE GULF OF MAINE

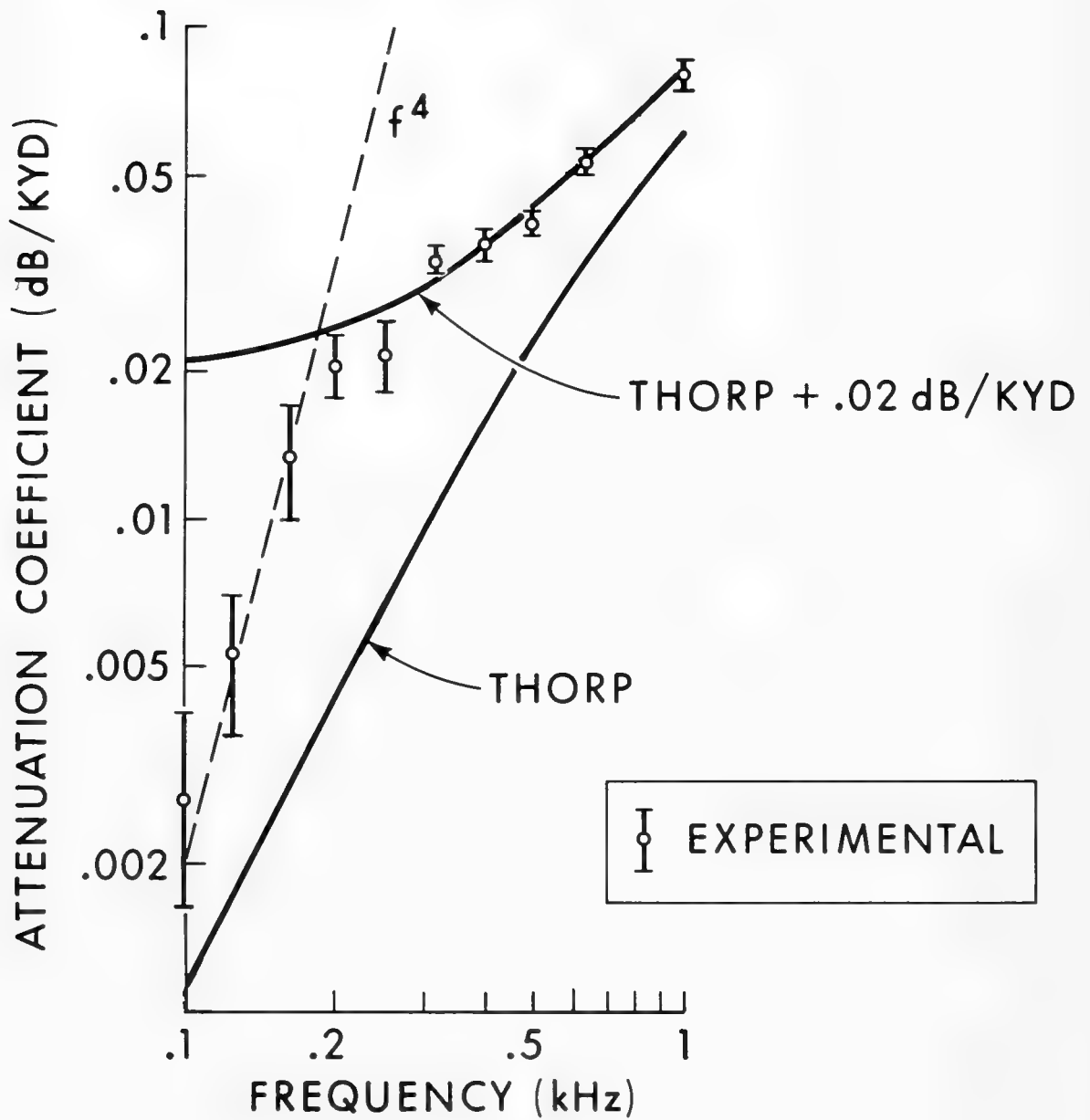


Figure 13. ATTENUATION COEFFICIENT IN BAFFIN BAY

DIFFUSION ATTENUATION

$$\alpha = 8 \times 10^8 \frac{\mu^2}{a_o \Delta z} \text{ dB/KM}$$

$$\mu^2 = \overline{(\Delta c / \bar{c})^2} \approx 10^{-7}$$

$$a_o \approx 15 \text{ M}$$

CHANNEL DEPTH Δz	ATTENUATION
100 M	.05 dB/KM
2000 M	.003 dB/KM

Figure 14. ATTENUATION INDUCED BY DIFFUSION

changed to 3 m, as predicted from Rayleigh scatter in Baffin Bay, the result is 0.03 dB/km and agrees very well. It thus appears that while most of the variability of scattering loss depends on the strength of the channel, the smaller scale size is responsible for the large value for Baffin Bay.

Although the values of scattering loss may or may not be important to a sonar problem since it can be very small, the information about what is happening to signal coherence within the channel certainly should be valuable. For example, we can see in Figure 15 the effect of scatter on 400 Hz signal fluctuation for two hydrophones separated by 100 m. In this experiment done by Stanford (1974) in Bermuda, the time fluctuations are quite incoherent and seem to have two scales, the longer one probably related to internal waves and a shorter scale that may be related to turbulence.

The spectrum of the time fluctuations (Figure 16) definitely shows a break above 10 cycles/hour which varies with the seasonal thermocline. The latter scale size compares to that associated with scatter loss if the ocean currents are one- or two-tenths of a knot.

The effect of scatter on spatial coherence is also important. Kennedy (1969) at Bermuda varied the vertical separation of two hydrophones and measured the CW signal correlation between them. The correlation distance appears to be close to our estimated value based on $a_0 = 15$ m (Figure 17).

SUMMARY

Our results are summarized in Figure 18; we have observed both the Thorp (boron) relaxation and also what we believe to be forward scatter loss in a number of sound channels throughout the world. The coefficient of the Thorp term is unity in the North Atlantic water

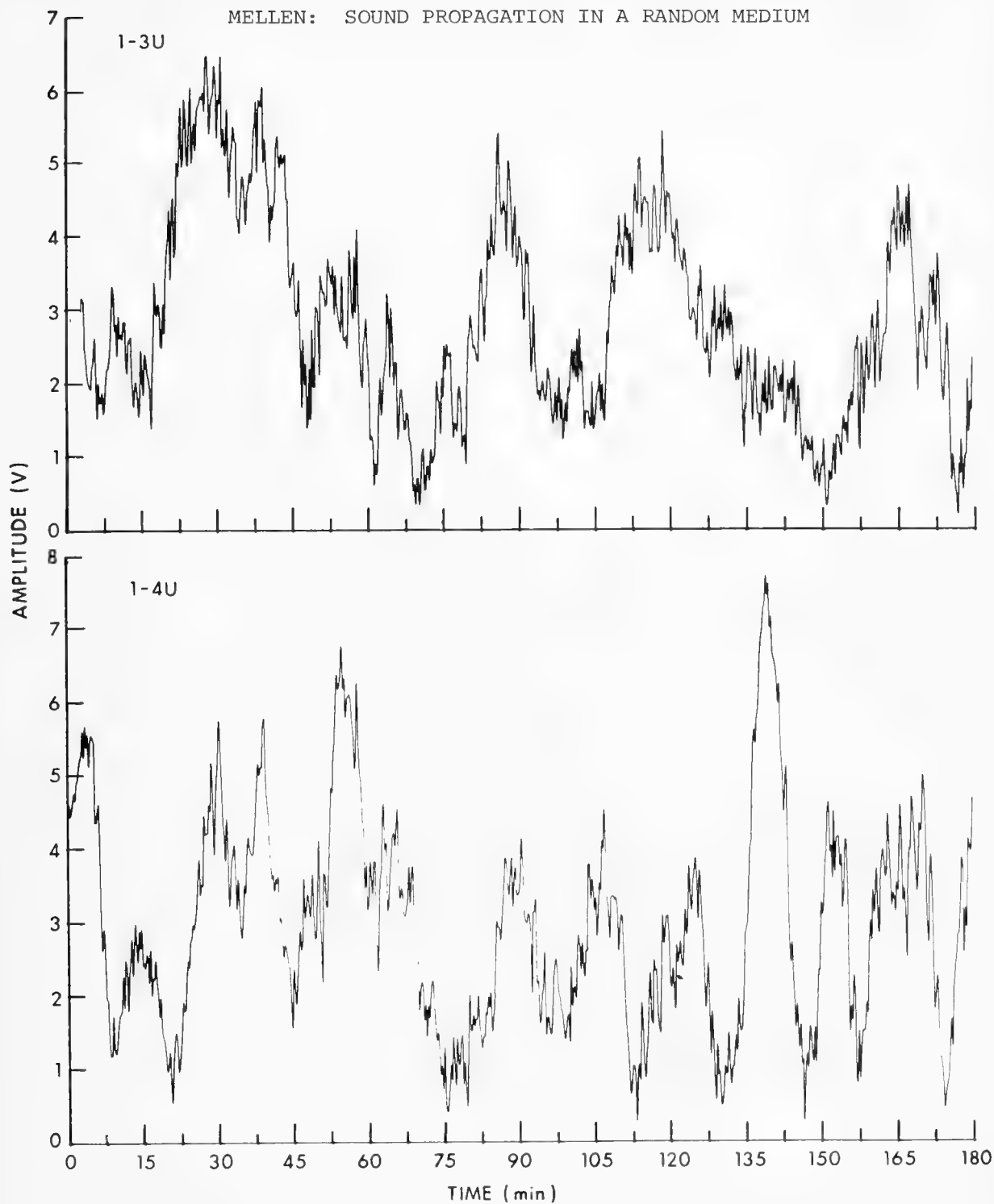


Figure 15. SIGNAL FLUCTUATION AT 400 Hz
FOR TWO HYDROPHONES SEPARATED
BY 100 METERS

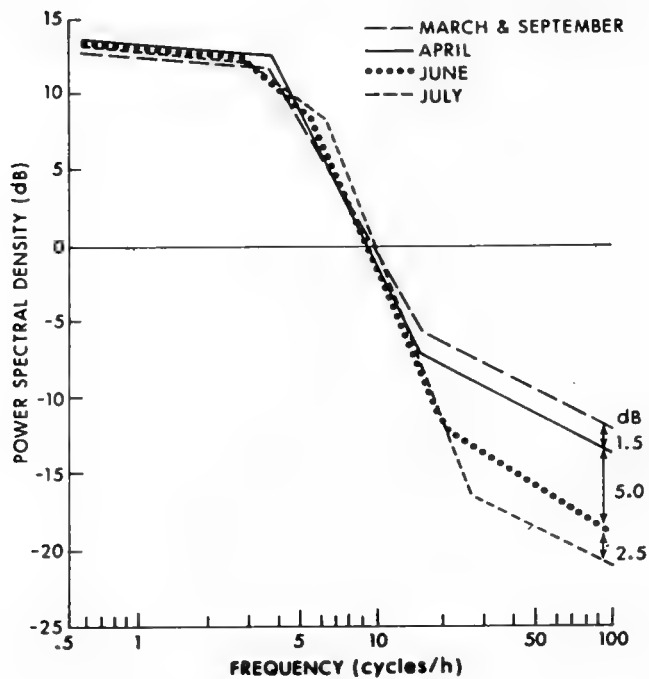


Figure 16. SPECTRUM OF TIME FLUCTUATIONS

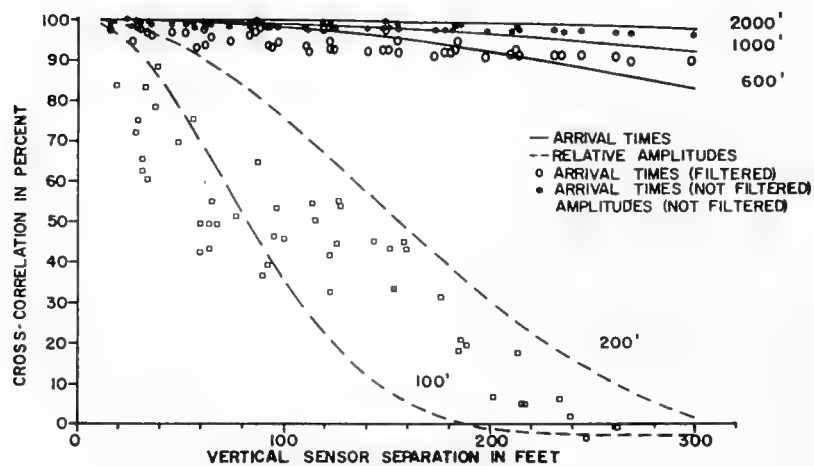


Figure 17. SPATIAL COHERENCE AT BERMUDA



Figure 18. SUMMARY OF ATTENUATION EXPERIMENTS

but only 0.6 in the Gulf of Aden and 0.5 in the Pacific, suggesting possible differences in the boron chemistry of these waters. The regions where large amounts of scattering occur suggest turbulence induced by current shear. In the North Central Pacific and North Central Atlantic and Red Sea, there is no measurable scatter at all. (The point of division between moderate and severe scatter is taken as $\mu^2/a_0 = 10^{-8}/\text{m}$ rather than the magnitude of scatter loss since the latter depends strongly on the channel strength.)

REFERENCES

- Bannister, R. W., "Discontinuities observed in low-frequency long-range propagation," in these Proceedings, 1976.
- Browning, D. G., "Project CANUS: Sound propagation and reverberation Measurements in Hudson Bay," NUSC Tech. Report 4221, 1 Dec. 1971.
- _____, "Environmental factors affecting low-frequency propagation," in these Proceedings, 1976.
- Browning, D. G., R. H. Mellen, J. M. Ross and H. M. Merklinger, "Low-frequency sound attenuation in Baffin Bay," 88th ASA Meeting, St. Louis, MO., 5-8 Nov. 1974.
- Browning, D. G., E. N. Jones and W. H. Thorp, "Low-frequency attenuation in the Gulf of Aden," NUSC Tech. Report 4501, 5 Mar. 1973.
- Browning, D. G., and W. H. Thorp, "Attenuation of low-frequency sound in the ocean — NUSC Research Program 1967-1972," NUSC Tech. Report 4581, 4 Jan. 1972.
- Browning, D. G., W. H. Thorp, F. C. Friedel and R. F. LaPlante, "Project Hiawatha long-range shallow-water sound propagation in Lake Superior," USL Tech. Memo. No. 221-173-68, 20 June 1968.
- Chernov, L. A., "Wave Propagation in a Random Medium," New York: McGraw-Hill, Chapter II, 1962.
- DiNapoli, F. R., "Fast field program for multilayered media," NUSC Tech. Report 4103, 26 Aug. 1971.

- Kennedy, R. M., "Phase and amplitude fluctuations in propagating through a layered ocean," *J. Acoust. Soc. Am.*, 46:737-745, 1969.
- Mellen, R. H., D. G. Browning and J. M. Ross, "Attenuation in randomly inhomogeneous sound channels," *J. Acoust. Soc. Am.*, 56:80-82, 1974.
- Stanford, G. E., "Low-frequency fluctuations of a CW signal in the ocean," *J. Acoust. Soc. Am.*, 55:968-977, 1974.
- Thorp, W. H., "Deep-ocean sound attenuation in the sub- and low-kilocycle-per-second region," *J. Acoust. Soc. Am.*, 38:648-654, 1965.
- Yaeger, E., F. H. Fisher, J. Miceli and R. Bressel, "Origin of the low-frequency sound absorption in sea water," *J. Acoust. Soc. Am.*, 53:1705-1707, 1973.

DISCUSSION

Dr. D. C. Stickler (APL, Pennsylvania State University):

Referring to Figure 17, what was the difference between the correlation that fell off rapidly and those that didn't?

Dr. Mellen: Two hydrophones at Bermuda were separated in the vertical. The correlation between the two of them was measured as a function of the separation distance. The dashed curves are from Chernoff estimating at 100-feet and 200-feet correlation distance.

Dr. P. W. Smith (Bolt, Beranek, & Newman, Inc.): You picked out my favorite example of something I completely fail to understand. They have here a single path going up which may be significant on a ray picture vertexing 124 feet, I think it was, below the surface, then going down to the bottom, coming in at very shallow grazing angle. And what I completely fail to understand is how they can get such high correlation in the arrivals -- in the phase or arrival times -- over their separation between the transducer pairs and this very short correlation interval in the amplitudes. Does anyone have any guesses?

Dr. Mellen: I can't answer that question. I only used this to illustrate the correlation distances to compare with the 15 meters that we measure in the Mediterranean and the Hudson Bay.

Dr. Smith: I don't think that the behavior of the time and amplitude would be consistent with the theory with which it is being compared.

Dr. Walter H. Munk (Institute of Geophysics and Planetary Physics, Univ. of Calif., San Diego): There is something else I completely don't understand, and other non-acousticians who have looked at your results are equally confused. Figure 16 has power spectral densities in dB, and I don't understand those units. Spectral density is units

of something per unit frequency band.

Dr. Ira Dyer (Massachusetts Institute of Technology):
That's mislabeled actually.

Dr. R. R. Goodman (Naval Research Laboratory): On your last picture (Figure 18) where you showed the areas of anomalously high absorption, with the exception of the Gulf of Aden, they are all shallow water results, aren't they?

Dr. Mellen: Baffin Bay is also deep water.

Dr. Goodman: How deep is it?

Dr. Mellen: About 2,000 meters.

Dr. Goodman: One thing I would like to point out with respect to the Hudson Bay results and perhaps Lake Superior as well as any shallow water. You are putting a tremendous amount of faith in the shallow-water propagation loss that you are taking out of these data. If you are talking about shallow-water propagation over a hundred miles you are talking about an accuracy out to a hundred miles of 5 decibels in the model, and that's better than any model I know today for shallow water.

Dr. Mellen: Again, all we do is linear regression to the data. We don't worry about absolute values or how it got there. We start at very long distances. For instance, in Baffin Bay we measure only from 100 kilometers to 400 kilometers in that region. And the propagation is extremely well behaved, and you really believe the results.

Dr. Goodman: You're subtracting off a transmission loss term. You have to be.

Dr. Mellen: Subtracting out cylindrical spreading.

Dr. Goodman: Right. Do you have faith in cylindrical spread-

ing to that accuracy?

Dr. Mellen: Absolutely.

Dr. Goodman: That's curious, because I don't.

Mr. P. H. Lindop (Admiralty Research Laboratory): We have some unpublished results for sound channels in the Western Mediterranean, Eastern North Atlantic, and the Southern Norwegian Sea. Looking at these rough results we don't see anything anomalous. We take out cylindrical spreading and we don't see anything of the order that you have seen.

Dr. Mellen: In the Mediterranean?

Mr. Lindop: In the Western Mediterranean and the Eastern North Atlantic.

Dr. Mellen: I'm not quite sure where these results came from. These were taken from Bill Thorp's notes, and were part of the JOAST experiment. Two areas, one in the Tyrrhenian Sea and the other east of Malta, were both measured. Now, if this was east of Malta, there is a very strong ocean front which could be responsible for the relatively large amounts of scatter that were observed.

Mr. Charles W. Spofford (Office of Naval Research): In the Hudson Bay and Baffin Bay, were you using 1/3-octave filtering?

Dr. Mellen: Yes. All the experiments are 1/3-octave filters. We haven't progressed to the sophistication of FFT.

Mr. Spofford: Have you taken your mode model or FFP and run it to simulate the 1/3-octave filter to convince yourself that the spreading is cylindrical when viewed through the 1/3-octave filters?

Dr. Mellen: Dave Browning is going to talk about that tomorrow.

Dr. F. D. Tappert (Courant Institute of Mathematical Sciences, New York University): Your shallow-water results have been criticized,

and I'd like to take issue with the deep-water results. It's very difficult over long ranges to accurately compute the transmission loss, and it's known not to be simple cylindric spreading in general.

Dr. Mellen: You're talking about the PARKA results now?

Dr. Tappert: PARKA and the South Pacific results. And you showed some results for the Atlantic, deep water.

Dr. Mellen: Right. That was Thorp's original data set for the North Atlantic. The North Central Atlantic didn't show any scattering. In Thorp's original compilation, there is no scattering at all except maybe a very, very tiny bit at the extremely low frequencies.

But on the ATOE experiment there was strong evidence of scattering. We can do two experiments. In one experiment we see lots of scattering, and in the other experiment we don't. And it's real.

Dr. Tappert: I'm sure the effect is real. But whether we can measure it quantitatively and make agreements with theory is another issue.

Dr. Mellen: Well, let's say using this technique we found the boron relaxation -- which nobody believed at that time. So now we are finding something else besides the boron relaxation. We're talking about finding scatter.

Dr. Smith: I have a comment which stems from our treatment of some of the Gulf of Maine shallow water data. I thought I'd try some curve-matching to the data. The water was roughly 200 meters deep. We had transmission loss data in third-octave bands at ranges from something like 2 kilometers to 150. I thought I'd match the curve for 1 kHz with the equation

$$TL = C + N \log R + \alpha R$$

for values of N equal to 10, 15, and 20, choosing C and α in each case

to get a best match. Obviously, I was going to select either 10, 15 or 20 depending on the standard deviation of the data points from the trend curve. However, the standard deviation for those three values of N ranged only from 1.1 to 1.4 dB. I decided that was not a very sensitive test. There was a more sensitive test: The match for $N=20$ had a negative value of α !

If one is going to use $10 \log R + \alpha R$ as a transmission loss law, you'd better be sure that all significant components of the energy are being attenuated at the same rate, because that is a fundamental assumption behind the law. A good example where it fails is the classical shallow-water, isospeed theory where the modal attenuated coefficient is quadratic in the mode number; this leads to transmission loss varying as $15 \log R + \alpha R$. This example illustrates the fact that the slope of transmission loss curve with range is strongly affected by differential attenuation of the different components.

In our massaging of the data in the Gulf of Maine at 1 kHz we found that this kind of differentially attenuated energy was at least as important as the ducted energy out to ranges of something like 40 kyd. That was the transition range where they were about equally important.

Now, the trouble is, if you start out at 40 kyd in order to be sure that most of the energy is ducted and not differentially attenuated, you've got only a factor of four on range before you start running into noise or land as the case might be. You can't make a very sensitive test of scope with the available data given the normal scatter of points from any trend curve. Based on my personal experience I would be very skeptical about assuming $10 \log R$ in cases such as that.

Dr. Mellen: We have an initial spherical spreading region while the sound channel is being set up. After that we have a mode

stripping region through which we progress into a region of one mode propagation.

For example, in Baffin Bay, the smallest range was 100 kilometers, the largest one was 400. The sound channel filled up in mode strip much before that. So we had no problems there from say 50 kilometers on to 400.

Dr. M. Schulkin (Naval Oceanographic Office): I don't consider it using the same attenuation behavior if you have to take a half of Thorp or six-tenths of Thorp or 0.75 of Thorp. You're not really tying things down.

Dr. Mellen: No, of course not, but these are things now that can be examined. If it turns out that the Thorp coefficient is constant in the Pacific and the Gulf of Aden and so forth, the same as it is in the North Atlantic, then we are going to have a check that there is something wrong with our experiments.

Right now I say that for some reason or other there is less boron absorption in the Pacific than there is in the Atlantic. I don't know why.

Dr. Schulkin: It's a hypothesis.

Dr. Mellen: Yes.

Dr. Schulkin: But let me check one more point. The parabolic equation requires $5 \log R$. Is this true? The intensity varies as $1 \text{ over } R$?

Dr. Tappert: No, there is cyclindrical spreading built in but on top of that you have all other attenuation mechanisms that may exist.

Dr. Weinberg: In all of these experiments the source and the receiver were very carefully placed in a well defined channel and

were already beyond the region where the bottom is important. What other mechanism is there if there isn't cylindrical spreading?

Dr. Smith: Well, I agree with you if you accept conventional wisdom that the bottom strips everything off and there are no contributions left and if then you accept that the ocean is homogeneous you're going to get cylindrical spreading. There are situations where I know some of those assumptions are not right.

Dr. Weinberg: Right, but we are not talking about those situations. We are talking about very carefully planned experiments where we are sure to put things right on the axis or as close as possible.

Dr. Smith: Gulf of Maine may not be one of those you want to point at then.

Dr. Tappert: One problem. The very theory that explains this scattering attenuation predicts that the fluctuations will also fill in modes as they are stripped off. As some are stripped off, others are filled in by the random fluctuations. So you are not left with just the single mode. Therefore, the attenuation without the scattering will not be purely cylindrical.

Dr. Goodman: We are talking about a very tiny effect on a large propagation, and what we really have to do is determine the confidence limits we have on what is left over. I think the only way this will ever become convincing to anyone is to have a very careful analysis of all of the elements that contribute to the total loss and some sort of error analysis on how well you can trust your models.

Most of us don't have that kind of faith in our models. I think it's up to you to put down some numbers so that the confidence limits are valid for taking a guess. We would certainly like to see something like boron. It's an interesting problem. But the question really

is: have we seen evidence that is statistically significant after we have subtracted off all of these things?

Dr. Mellen: You still don't believe the boron?

Dr. Goodman: I haven't seen any error analysis.

Dr. Smith: I want to suggest in that same vein that it is very difficult to establish confidence. We need all the measurements we can get, not just total integrated transmission loss. An experiment should be planned to make other measurements of transmission, whether it be signal envelope, coherence, directionality, or whatever. By using that information as well as the transmission loss and testing the results against a model for the physics of the situation, one's confidence would be increased.

Mr. R. L. Martin (New London Laboratory, Naval Underwater Systems Center): I believe that the original work that Bill Thorp did at least prior to 1968 did not use total energy at all. He looked at the peak envelope of the classic SOFAR arrival, and he was just concerned with the amplitude of that envelope and how that changed with range.

He did not use the total energy, but he did make a comparison of the two methods in the PARKA exercise and they came out with the same results.

I just bring up that point to indicate he initially dealt only with those rays that were very close to the axis.

Dr. Smith: Some of his work I thought he time-gated and then got the energy in what he thought was ducted.

Mr. Martin: Not his initial work though.

Dr. Mellen: All the later stuff was total energy in the window.

Mr. Martin: When he did that work in the PARKA exercise he did find he didn't get any difference.

Mr. Smith: Of course, those are two experiments which are particularly well designed in nice deep water, good channels and good measurement positions. Also, we want to remember the recent work that was interpreted as showing negative bottom reflection losses. We have got to bring all our information about the physics together, it seems to me, and make a consistent whole of it.

Mr. Pedersen: There is a problem with using peaks of convergence zones to do this because if you include the diffraction correction, the loss drops off as $R^{5/3}$.

Mr. Martin: But it isn't a convergence zone. It's the SOFAR shape. While there is a lot of rays in there that are adding coherently and somewhat incoherently, you're doing regression analysis to get rid of the incoherent.

Mr. Pedersen: If you look at one caustic in the convergence zone and you identify it in the first one and second one, and so on, that level drops off as $R^{5/3}$.

Dr. Hersey: I think I'll make one attempt to bring the wrath of everybody down on my head because this particular controversy has been bubbling in our community for some time and it has seemed to me that as we have talked about it and as new results have become available from various parts of the world, some very imaginative choices have been made of experimental locations, and there is an excellent body of data available from just the group at New London that has done so much of this work, and there are other data samples like the PARKA set that they participated in, all of which are sufficiently well documented to see what the attenuation coefficient is as a function of the data analysis model.

We now have the parabolic equation model. We have some rather sophisticated ray models.

It sounds to me offhand as though it might be feasible to make that kind of a study and see whether the attenuation coefficient results are highly dependent on the model used to reduce the data. Because the data are bound to be good data.

Dr. Mellen: We rely mostly on the agreement with the FFP, although I don't know whether we have used CONGRATS 5 or anything like that yet.

Dr. Hersey: That, you see, you have right in your own group. But here's a case where we have an excellent data bank. The fact that the work was concentrated in one place is perhaps a strong argument for consistency in the way the work was done. And if we as a community would manage to make use of our several model designs to see how sensitive the reduction of the data is to models, we would at least have a basis for answering some of the worries that were expressed here this afternoon.

When that has been done we would all have a basis for making an estimate of what we ought to do next. Is it a critical experiment? Or a critical series of experiments? Or are we beginning to approach understanding?

Dr. S. M. Flatte (University of California, College of Santa Cruz): I wanted to mention that last summer our group made some parabolic equation runs which attempted to indicate what the scattering in the sound channel would be from internal wave models. I would emphasize that you have to have a model of everything that is happening in the ocean to decide what the scattering is.

However, it would be at this point rather easy for us to propagate any number of modes through internal waves and find out what the scattering due to that would be.

Dr. Mellen: From your data, presented last night, I made an estimate it would be not measurable.

Dr. Flatte: You mean because of the range?

Dr. Mellen: No, because of the large scale size of the internal waves. In other words, I think we're dealing with a smaller scale size which increases the scattering loss.

Dr. Flatte: If you really have to go down 15 meters, then you're right. Internal waves will not explain it.

Dr. Mellen: It isn't that far off though, because even though your scale size for the horizontal is much larger, your vertical scale size is smaller because of the ellipticity in the internal wave inhomogeneity.

Dr. Flatte: The vertical scale size is what I'm talking about. The vertical scale size in the internal waves is like 200 meters.

Dr. Mellen: The scattering will depend upon the diffusion constant which goes as μ^2/a_0 (see Figure 14) in the geometrical acoustics limit. But if these inhomogeneities are not spherical as we said, then they are multiplied by the ratio of the horizontal major axis to the vertical minor axis. You get that much more diffusion if the things are lenticular.

Dr. Flatte: Then we're going to multiply your 15 meters by a factor of approximately 10 to account for the ellipticity, which makes it very close to internal waves.

Dr. Mellen: Right. Yes.

PHASE FLUCTUATIONS, COHERENCE AND INTERNAL WAVES

R. C. Spindel

Woods Hole Oceanographic Institute
Woods Hole, Massachusetts

Observations of low-frequency, long-range acoustic transmissions have revealed a correspondence between acoustic phase variations and internal oceanic effects such as tidal cycles, transport phenomena, geostrophic flow and internal gravity waves. For periods less than the local inertial period and greater than the local buoyancy (Brunt-Vaisala) period, internal waves appear to be the predominant cause of acoustic phase fluctuations (in the absence of severe multipath). Measurements of 220 Hz and 406 Hz transmissions at ranges from 200 to 1200 km using free-drifting receivers of varying depth have substantiated this conjecture. The empirical acoustic phase spectrum is proportional to a theoretical phase spectrum constructed by using a simple ray theory in conjunction with a hypothesized internal wave spectrum (Garrett and Munk). Furthermore, a predicted dependence of fluctuation energy on depth is observed in these data.

These measurements have been used to determine a mixed space-time coherence function as a function of range which establishes the oceanic limit of array resolution. The simple ray-internal wave theory predicts coherence parameters that compare favorably with data. Data collected to date have suggested several important areas for future consideration.

INTRODUCTION

Recent observations of low-frequency, long-range acoustic transmissions have revealed a correspondence between acoustic phase variations and internal oceanic effects such as tidal cycles, transport phenomena, geostrophic flow and internal Rossby and gravity waves (Steinberg, et al., 1973; Weinberg, et al., 1974; DeFarrari, 1974; Baer and Jacobson, 1974; Franchi and Jacobson, 1973; Spindel, et al., 1974; Porter, et al., 1976; and Stanford, 1974). From a physical

oceanographic standpoint the causal relationships between ocean parameter variability and acoustic phase variability suggest techniques for measuring oceanographic phenomena. From an operational viewpoint, the performance of detecting and tracking systems is strongly dependent on the phase stability of the ocean transmission path. In both cases the connection between ocean parameters and acoustic phase must be understood.

Fixed system studies (in which source and receiver are rigidly attached to the ocean floor) conducted in the 200 to 800 Hz region of the spectrum have shown that for periods less than the local inertial period and greater than the local buoyancy period, internal gravity waves appear to be the predominant cause of acoustic phase fluctuations. These periods range from about 5 minutes to 1 day at a latitude of 30° . Time scales of this order are of utmost interest in array tracking and detection applications.

PHASE FLUCTUATIONS

Phase fluctuation data collected at Woods Hole exhibit most of the features found in data obtained by the Institute for Acoustic Research in Miami, the New London Laboratory of the Naval Underwater System Center, the Bell Telephone Laboratories, and others. The experiments conducted at Woods Hole, however, have significant differences, and this is reflected in some of the observations we have made. Woods Hole data are not obtained with a fixed system. The acoustic source is moored at varying depth, and receivers are either free-drifting, towed, or moored. Receivers are suspended in mid-ocean at depths varying from 300 to 1500 meters. Receiving hydrophones sweep out synthetic spatial and temporal apertures several kilometers in length and several hours in duration.

The technique used to form these apertures and to compensate them for motion of the receiving hydrophone has been reported in a previous paper (Porter, Spindel and Jaffee, 1973). In brief, receiving hydrophones are suspended within range of a bottom moored navigation net consisting of three acoustic sources emitting continuous tones in the 12 to 13 kHz region. Receiver motion is manifest as Doppler shifts in these tones. Doppler shifts are translated into equivalent motion. With the current version of the system, receiver motion is tracked to within $1/4$ wavelength at 12 kHz, about 3 centimeters. Long-range acoustic transmissions at 220 and 406 Hz are simultaneously received by the moving hydrophone. Doppler shifts due to receiver motion are resolved into equivalent phase shift at 220 and 406 Hz. This shift is subtracted from total accumulated phase leaving a residual phase variation in the long-range transmission resulting solely from variations in the intervening water mass.

Figure 1 shows the deployment of a typical navigation net and the generation of five distinct apertures labelled 130, 131, 132, 133, 135 from 3 to 8 km in length. The time span of each aperture is indicated by time in minutes along each drift path.

Figure 2 is a schematic illustration of received low-frequency transmission. The carrier at 220 or 406 Hz is received at frequency f_r , displaced from f_o by the Doppler shift due to receiver drift. Spread about f_r results from variation in drift rate, and from variations in the transmission medium. When scattering from the sea surface is significant, it appears as sideband energy about the carrier with peaks at multiples of the peak frequency of the surface wave spectrum. The Doppler correction scheme removes variations f_d . The signal is then heterodyned down to dc, and variations resulting from surface scatter are removed by filtering around the carrier.

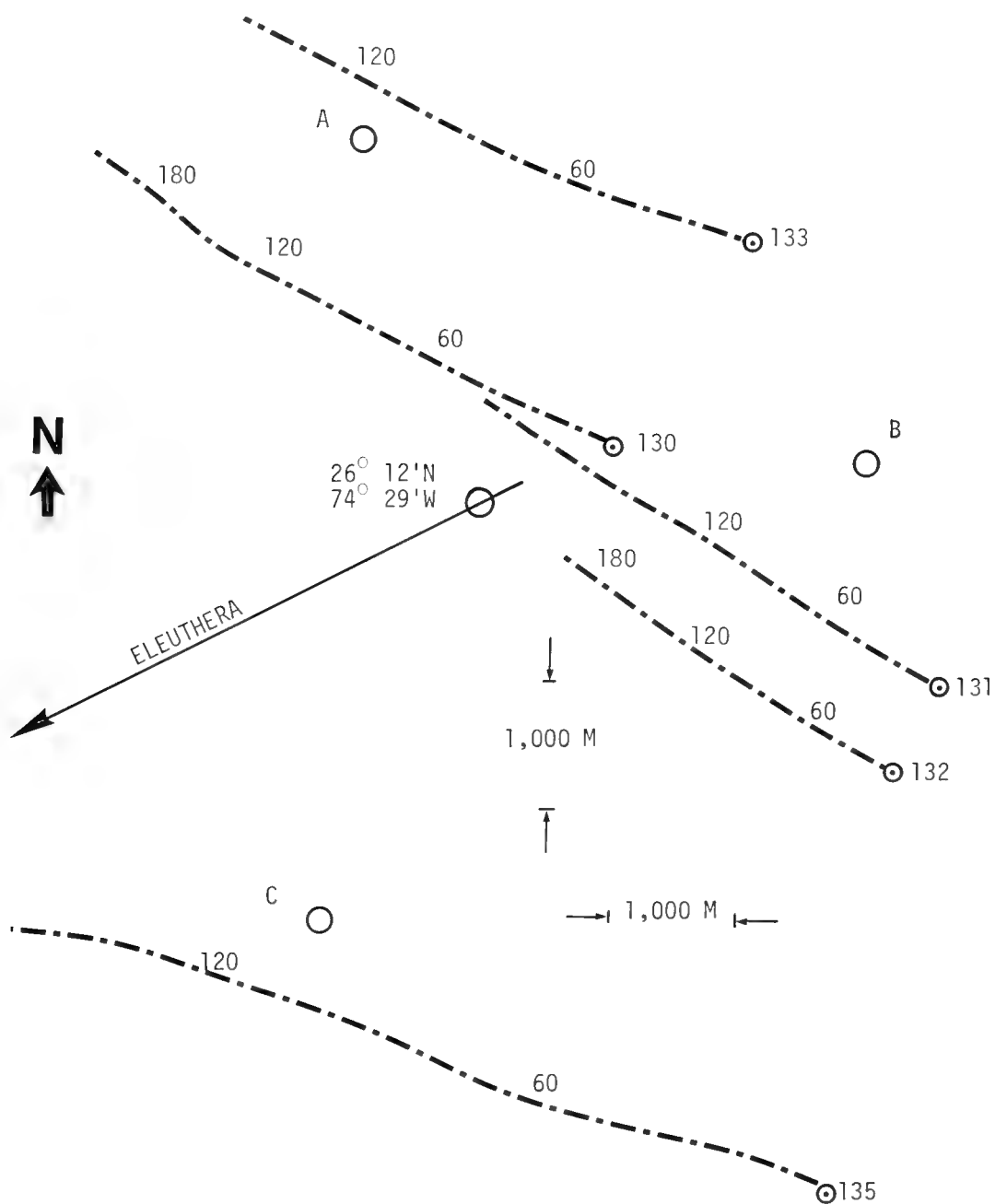


Figure 1. TYPICAL NAVIGATION NET DEPLOYMENT (CIRCLES) AND SYNTHETIC APERTURE GENERATION

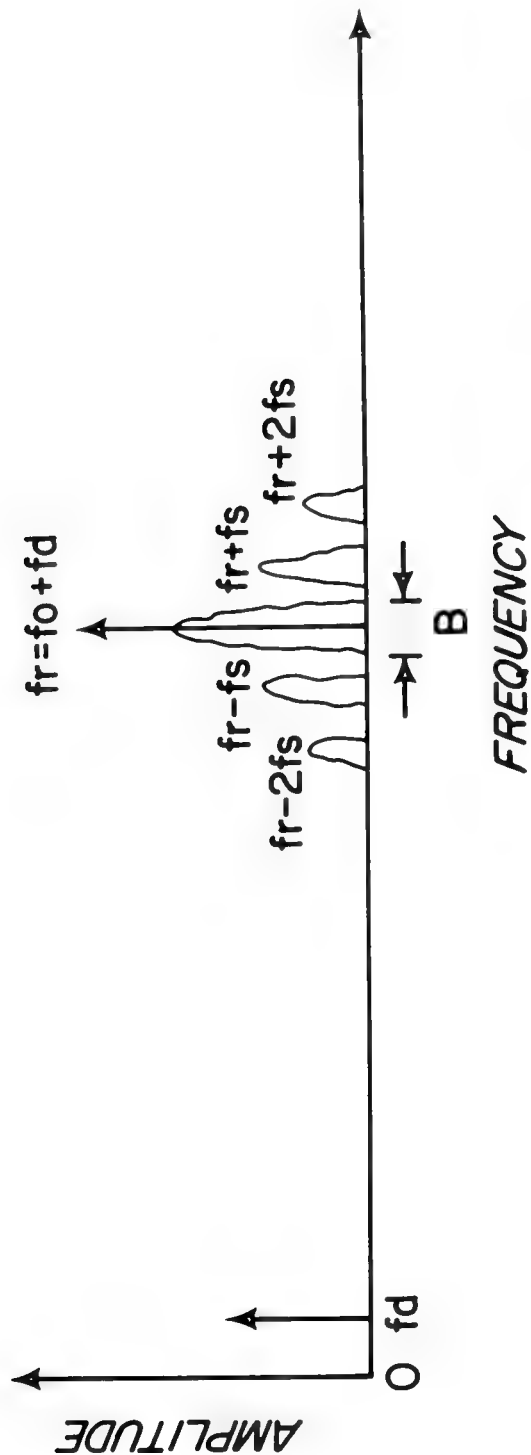


Figure 2. SCHEMATIC ILLUSTRATION OF FREQUENCY SPECTRUM OF RECEIVED SIGNAL

The result of this processing is a signal at dc, the fluctuations of which are due to fluctuations in the ocean transmission path.

Figure 3 illustrates the ray path geometry between the point of signal transmission and a receiver located about 210 km away. Typical samples of received acoustic phase are shown in Figure 4 for a receiver at a depth of 300 meters. Over an approximate 3-hour interval spanning an aperture of 3.5 km, peak-to-peak phase fluctuations are about 7 cycles. Two more examples of raw phase fluctuations are shown in Figures 5 and 6. Here we have compared fluctuations at two frequencies approximately an octave apart. Both frequencies were recorded and processed simultaneously. Careful examination of these figures indicates that observed phase fluctuations are approximately twice as great in the 406 Hz data. This suggests that the scale of inhomogeneities encountered by the acoustic transmission is large compared to a wavelength. Thus, the transmissions are affected independently, and notions of simple frequency scaling appear to hold.

One implication is that large-scale phenomena, internal waves for example, are primarily responsible for fluctuations in this frequency range.

INTERNAL WAVES AND PHASE FLUCTUATIONS

Some rather simple theoretical ideas contribute strongly to our assumption that internal waves are the predominant factor in generating phase fluctuations at these acoustic frequencies and ranges. The frequency of internal wave oscillation is bounded at the lower end by the local inertial frequency and at the upper end by the local buoyancy frequency, $n(z)$, a function of depth. Figure 7 illustrates the relationship between sound velocity variations and internal wave parameters. Sound velocity fluctuations are proportional to the

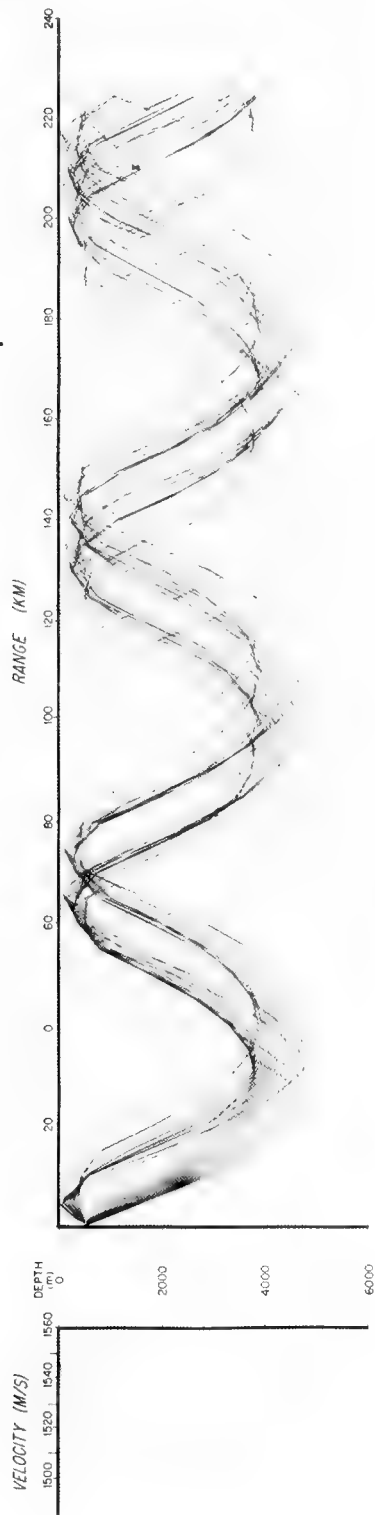


Figure 3. RAY TRACE FOR TRANSMISSION PATH

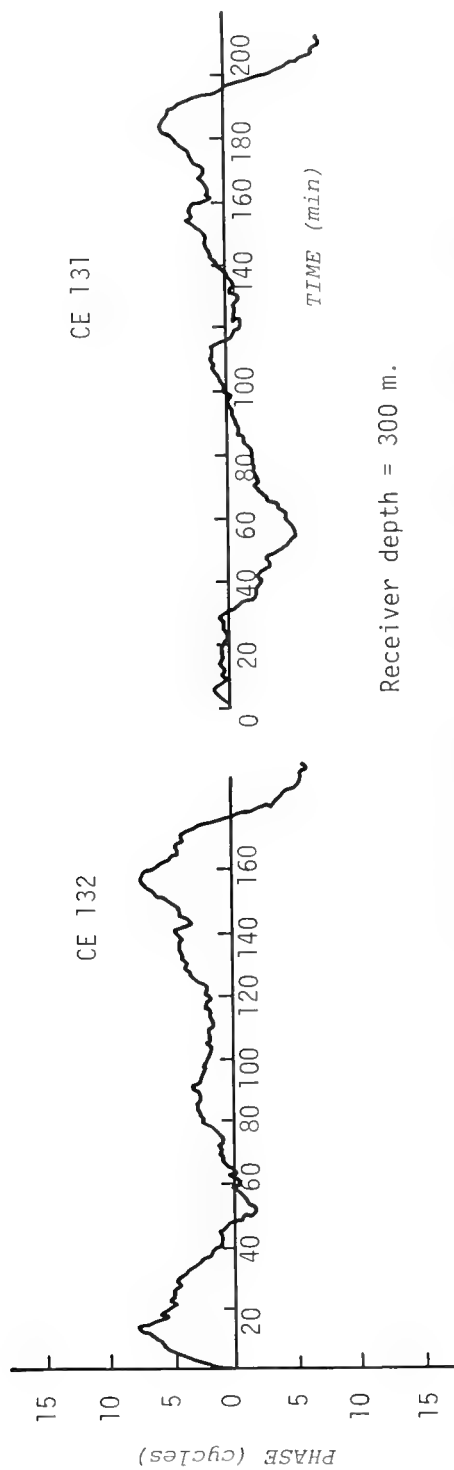


Figure 4. PHASE FLUCTUATIONS AT 406 HZ AND 210 km

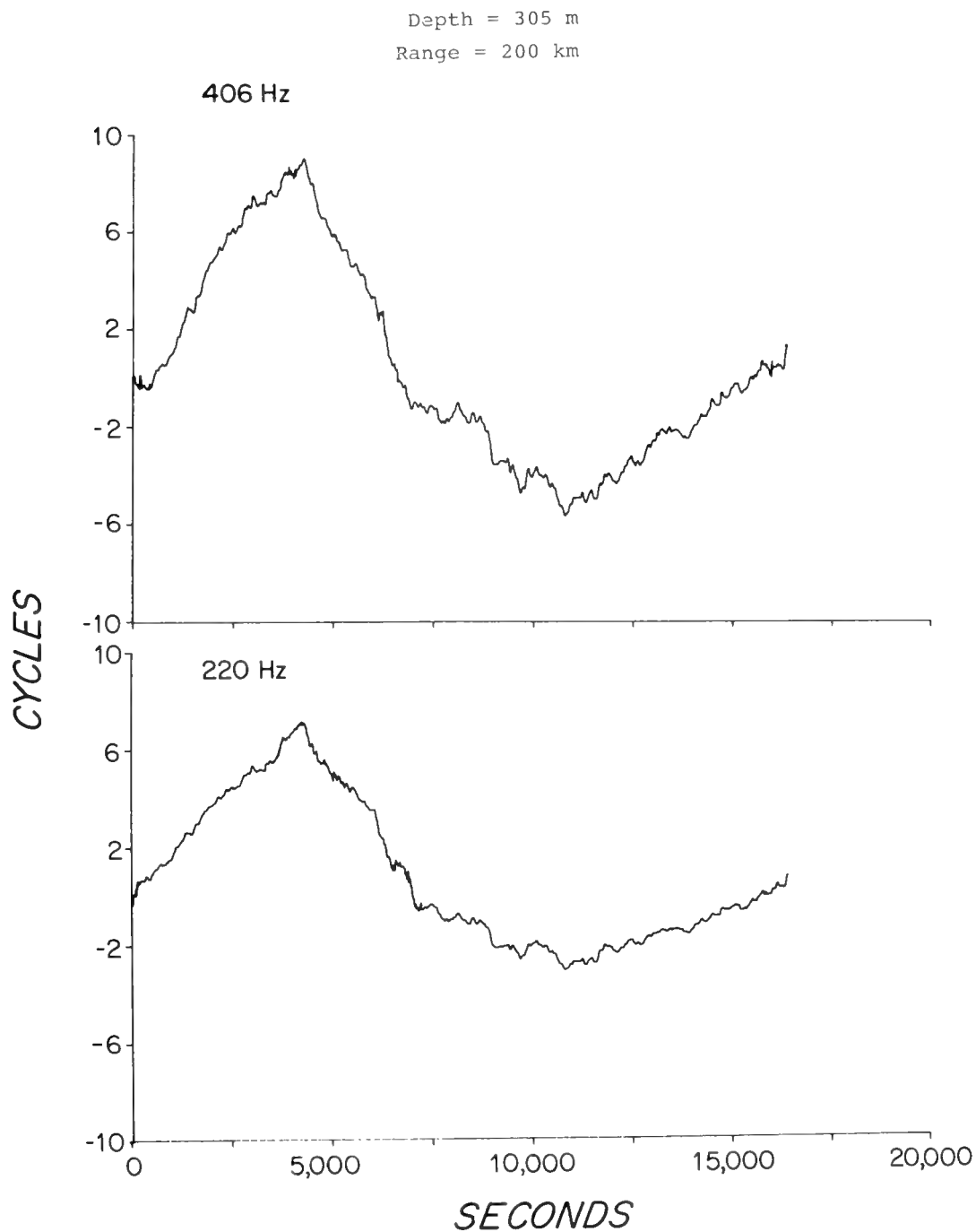


Figure 5. PHASE FLUCTUATIONS COMPARED FOR 220 AND 406 Hz

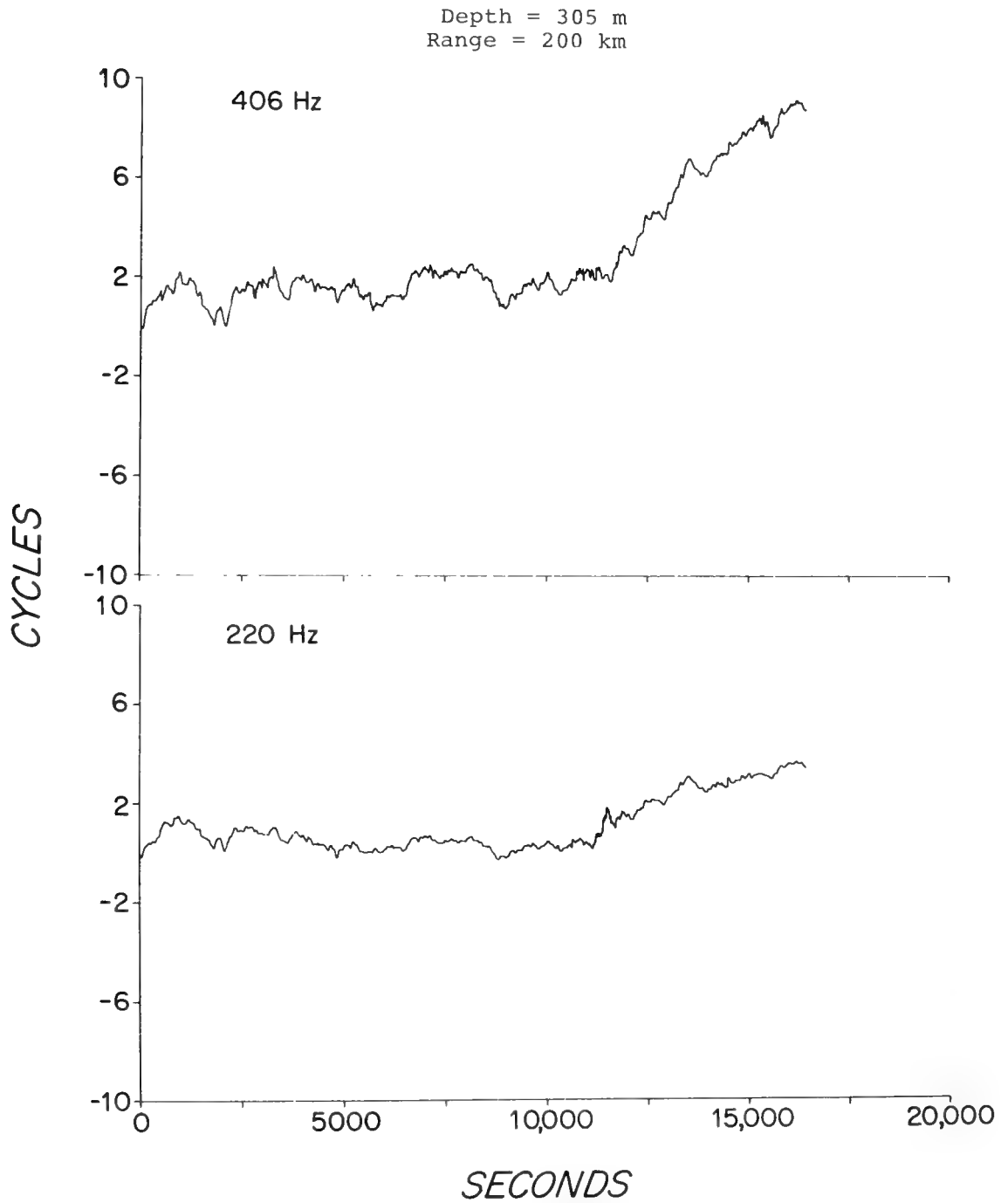


Figure 6. PHASE FLUCTUATIONS COMPARED FOR 220 AND 406 Hz

INTERNAL WAVE OSCILLATIONS ARE
BOUNDED BY BUOYANCY FREQUENCY $n(z)$,

$$n^2(z) \propto T_z$$

$$\frac{\Delta C}{C_0} = \delta \epsilon T_z \propto \delta n^2(z)$$

$$\delta \propto n^{-\frac{1}{2}}(z)$$

so

$$\frac{\Delta C}{C_0} \propto n^{\frac{3}{2}}(z)$$

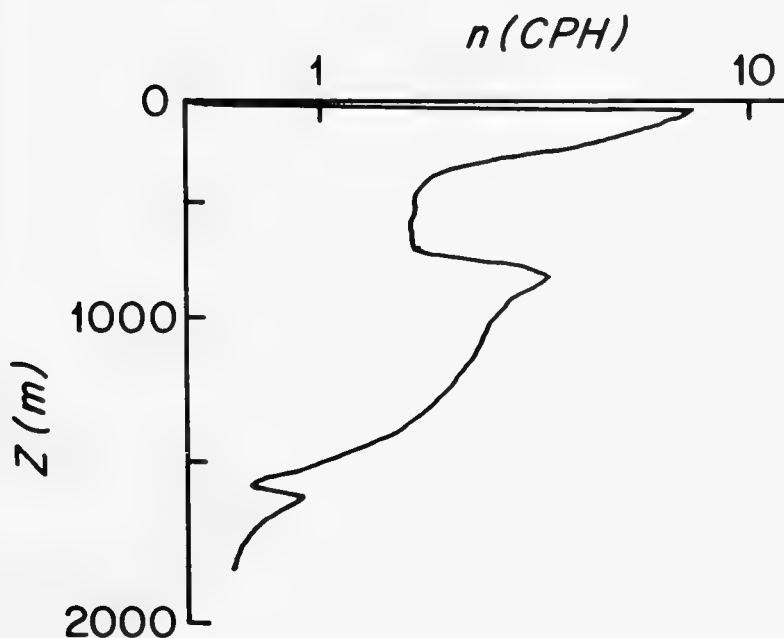


Figure 7. SOUND SPEED FLUCTUATIONS RELATED
TO LOCAL BUOYANCY FREQUENCY

amplitude of the internal wave δ and the temperature gradient T_z , which in turn is proportional to the buoyancy frequency. Thus, maximum variations in sound speed due to internal wave action occur at the depth where $n(z)$ is greatest. This is usually near the main thermocline as illustrated by the sample buoyancy frequency profile shown.

On the basis of this analysis, the internal wave field is modeled as affecting a traveling acoustic wave only in a thin layer at thermocline depth as shown in Figure 8. A ray passing through the layer will experience a phase advancement or retardation depending upon whether the immediate sound velocity of the layer is greater or less than the average sound velocity. Figures 9 and 10 outline the theoretical analysis necessary to complete the internal wave-acoustic wave interaction model. The internal wave field is modeled as a random superposition of waves concentrated in a layer of thickness η . The field is characterized by a frequency-wavenumber spectrum proportional to the internal wave model proposed by Garrett and Munk (1972).

The phase change $\Delta\theta$ of an acoustic signal due to a single passage through the internal wave layer is proportional to acoustic frequency, the angle with which the ray enters the layer ϕ_g , and the internal wave spectrum. The spectrum of the resulting acoustic phase variations $F_\theta(\omega_g)$ is proportional to the number of times the ray has passed through the layer, M , and the square of the acoustic frequency. It is also a function of the inertial frequency ω_i and cuts off at the local buoyancy frequency n_0 .

Figure 11 shows a plot of this theoretical spectrum as a heavy solid line together with measured phase spectra for receivers at two different depths. The light solid line represents data at 1500 m, the dashed line at 305 m. Transmission range was about 200 km. These

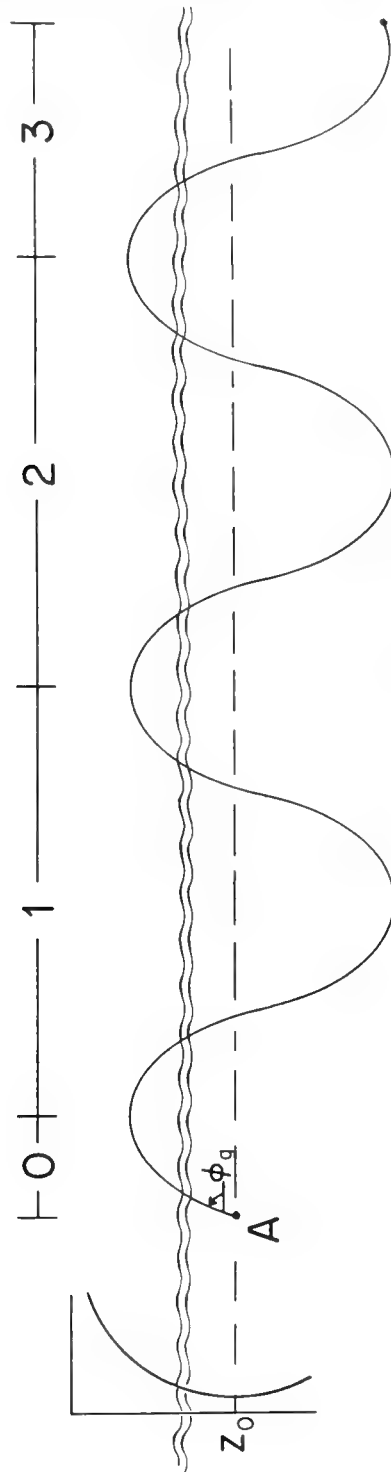


Figure 8. INTERNAL WAVE LAYER MODEL

SOUND VELOCITY AS A FUNCTION OF
INTERNAL WAVE DISPLACEMENT:

$$\frac{\Delta C}{C_0} = \delta \epsilon T_z$$

$$\delta = F(\alpha, \omega_g, z) e^{j2\pi(\alpha r - \omega_g t)}$$

ACOUSTIC THICKNESS:

$$\eta = \int \frac{\Delta C}{C_0} dz \doteq N_a(\alpha, \omega_g) e^{j2\pi(\alpha r - \omega_g t)}$$

$$N_a(\alpha, \omega_g) \propto E^{\frac{1}{2}}(\alpha, \omega_g) \quad [\text{GARRETT \& MUNK}]$$

Figure 9. LAYER MODEL PARAMETERS

PHASE CHANGE DUE TO SINGLE PASSAGE THROUGH LAYER

$$\Delta \theta = \frac{N_a}{\lambda \sin \phi_g} e^{j 2 \pi (a r - \omega_g t)}$$

PHASE SPECTRUM :

$$F_{\theta}(\omega_g) = \frac{4 K_a M \omega_i}{\omega_g^3 \lambda^2 \sin^2 \phi_g} \sqrt{\omega_g^2 - \omega_i^2}$$

$$\omega_i < \omega_g < n_0$$

$$\omega_g > n_0$$

Figure 10. MODEL RESULTS--PHASE CHANGE DUE TO INTERNAL WAVES, PHASE SPECTRUM

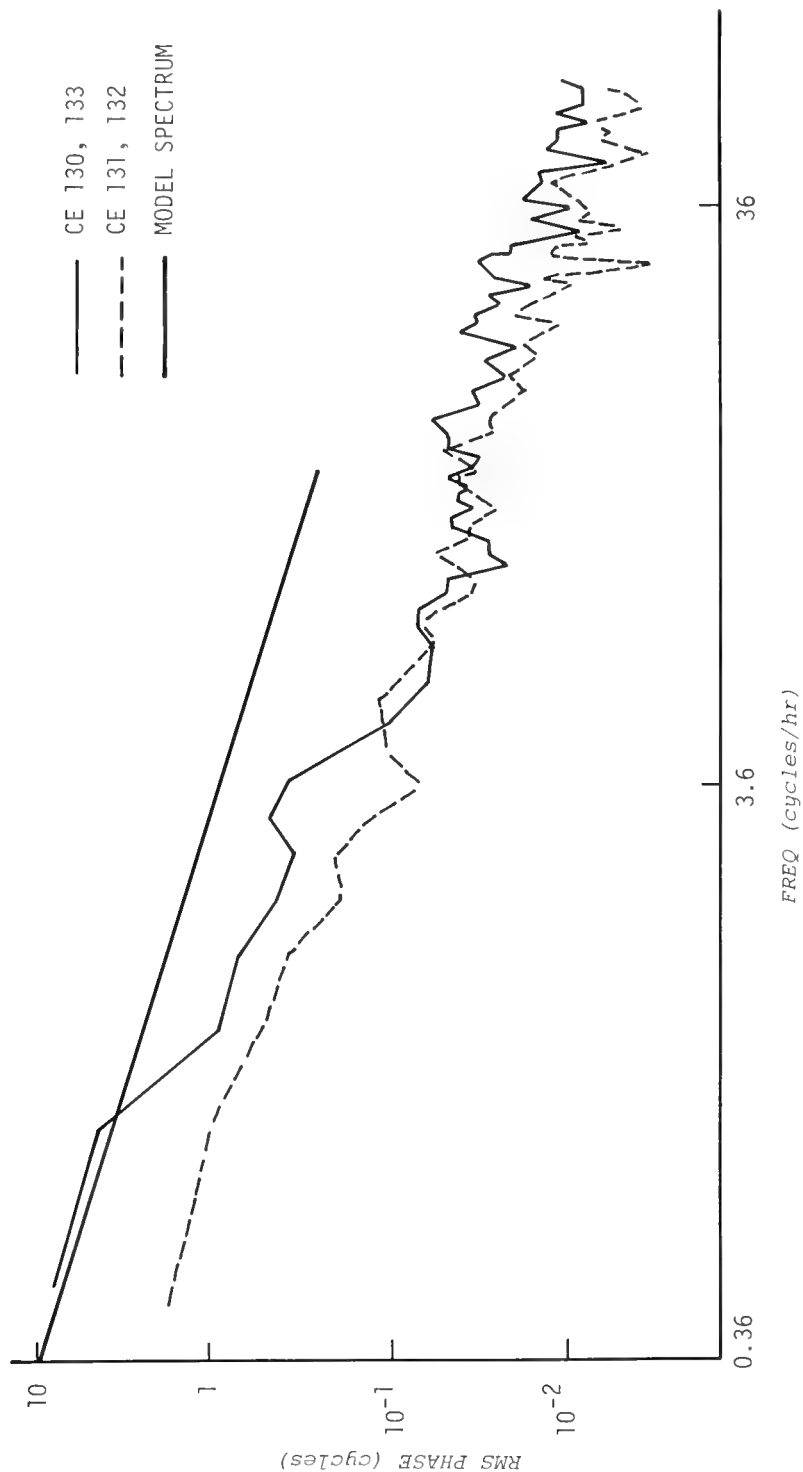


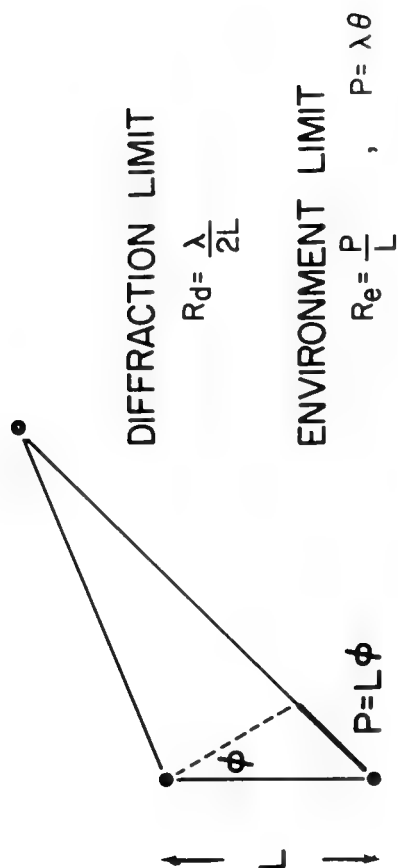
Figure 11. MODEL PHASE SPECTRUM AND DATA COMPARED

data fall off with a slope of approximately of -2 as predicted by the model, and in this respect these data lend credence to the model. Data taken at greater depth show more rms phase fluctuation which supports the notion of an equivalent internal wave layer. Rays to the deeper phone have spent a greater fraction of their travel time in or about the layer. There is no cut-off at the bouyancy frequency, contrary to the model prediction. This result has appeared in the work of others, Stanford (1974) for example. At present we attribute this lack of abrupt fall-off to the contaminating effects of microstructure which may begin to dominate at higher frequencies. We shall return to this point below.

It seems safe at this juncture in our current understanding of phase fluctuations to assert that internal waves are the dominant cause of fluctuations at these acoustic frequencies and that such fluctuations range in period from several minutes to a day. It is important to appreciate that the term "internal waves" can cover a host of phenomena, including tidal waves, Rossby waves, more classic internal waves, and wavelike behavior of microstructure.

COHERENCE

Oceanic induced phase fluctuations establish limits on array performance. Upper bounds on coherent array processing gains are only approached when the signal received across the array is phase coherent from array element to element. The pointing accuracy or resolving power of an array is critically dependent on the phase coherence of the acoustic transmission path. Figure 12 illustrates these ideas. A simple two-element array of length L receiving energy from a distant acoustic source (point source) is said to be working at the utmost limit of its resolving power when the random phase difference along the two paths is less than $1/2$ cycle. This phase difference is



ENVIRONMENTAL LIMITED ARRAY

$$R_e > R_d$$

$$P > \frac{\lambda}{2}$$

THEORY

$$\overline{\Delta \theta^2(\omega_g)} = \frac{M}{\lambda^2 \sin^2 \phi_g} \int_0^\infty N_a^2(\alpha, \omega_g) d\alpha$$

$$\overline{P^2} = 2\lambda^2 \Delta^2 \theta$$

$$\overline{P^2(\omega)} \propto \frac{ME}{\sin^2 \phi_g} \propto M$$

Figure 12. FACTORS AFFECTING ARRAY RESOLUTION

equivalent to a path length variation of $\lambda/2$ meters. The beamwidth of the array at this limit is $\lambda/2L$ radians. Fluctuations in phase resulting from the ocean environment must therefore be less than $1/2$ cycle or $\lambda/2$ meters for the array to achieve its diffraction limit. If the phase fluctuations are greater than $1/2$ cycle, the resolving power of the array is said to be environmentally limited.

The acoustic-internal wave theory outlined above predicts an rms path length change that is proportional to f and to the number of times the ray crosses the internal wave layer, i.e., distance. It predicts that rms phase fluctuations will reach a limit at some separation of sensors, and that the magnitude of fluctuation at this separation is proportional to distance. It is interesting to note that the performance of an environmentally limited array continues to increase linearly with array length since $R_e = P/L$, and P becomes constant.

Figure 13 shows phase fluctuation data at 406 Hz and two ranges, 200 and 1200 km, as a function of array length. Both curves rise to a plateau, about 13 meters of equivalent rms path length change at 200 km and 40 meters at 1200 km. Theory predicts values of about 15 and 45 meters, respectively. The environmental limit at 200 km would thus be avoided for all $\lambda/2 > 13$ m, or $f < 50$ Hz. At 1200 km, $f < 20$ Hz ensures diffraction rather than environmental limited performance. These curves were computed from data gathered during synthetic aperture formation and therefore represent a limit imposed by temporal as well as spatial variations. In that sense, they can serve as an upper bound on coherent array performance. It is expected that actual performance of a fixed spatial array will be somewhat better.

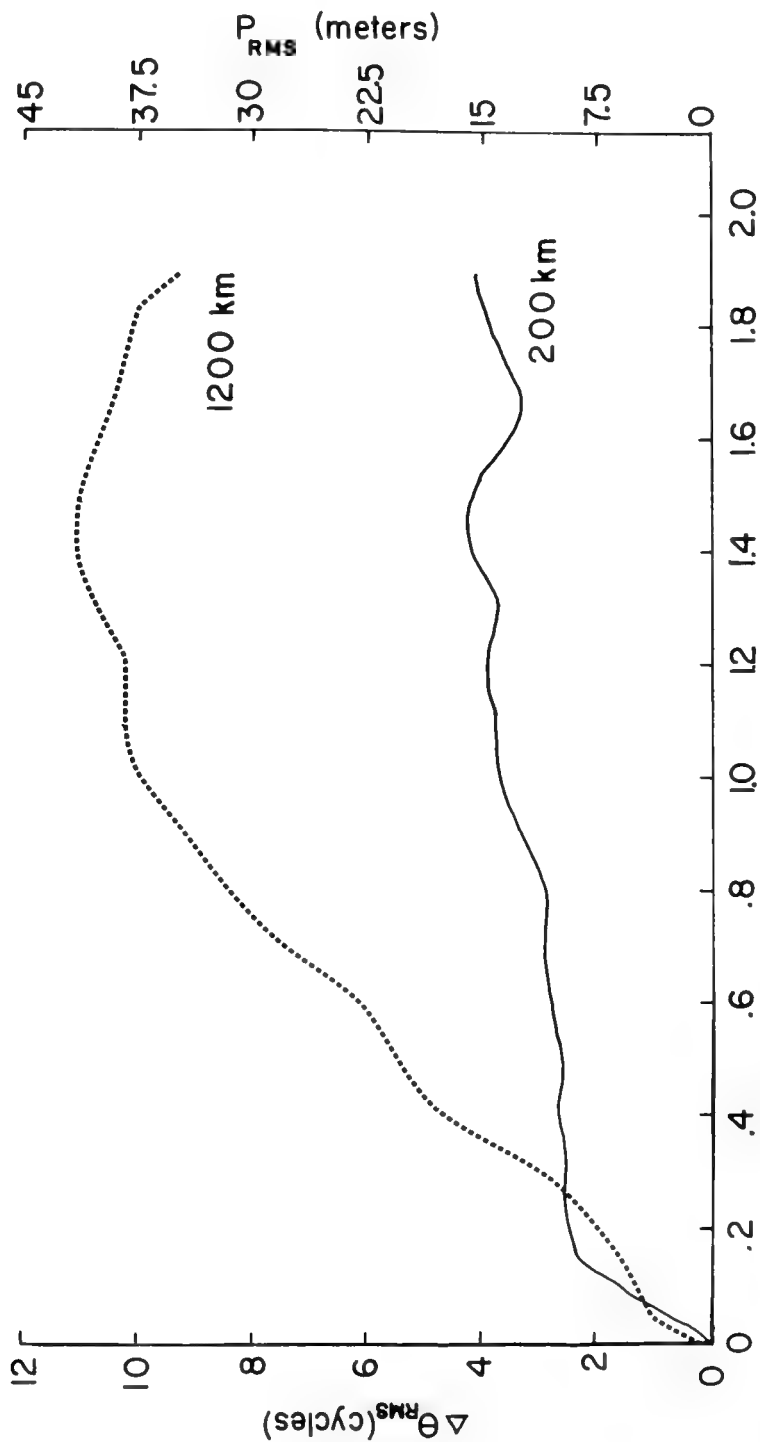


Figure 13. RMS PHASE FLUCTUATION AND EQUIVALENT PATH LENGTH CHANGE VERSUS ARRAY LENGTH

CONCLUSIONS, PROBLEMS, AND RECOMMENDATIONS

This paper has presented some illustrative data and theoretical notions that summarize much of our current appreciation for the phase fluctuation problem in long-range acoustic transmissions. We have restricted our presentation to Woods Hole data because we feel that they illustrate the major effects of internal waves on phase stability, and its consequences regarding array performance. Some large data sets obtained by other researchers support our notions, while others give us pause. Longer time series illustrate effects not seen in our data, such as tidal cycles and variations resulting from seasonal changes. These are important, too, and critically so if acoustics is to be used as a tool for studying large-scale oceanographic phenomena.

An example of the type of behavior we do not fully understand is shown in Figures 14A and 14B.* It shows the amplitude and phase spectra of a 367 Hz tone transmitted between Eleuthera and Bermuda. The phase spectrum falls off as f^2 with no apparent cut-off at the local buoyancy frequency. The amplitude spectrum, however, falls rapidly at the buoyancy frequency. Our feeling has been that environmental effects would be most visible in the acoustic phase, and that multipath effects would so distort the amplitude fluctuations as to make environmental-acoustic amplitude comparisons difficult indeed. Apparently this is not the case for data such as these have been obtained by the Institute for Acoustical Research and others. A similar spectrum of amplitude fluctuations calculated at Woods Hole using transmissions from free-drifting SOFAR floats at 270 Hz and a range of 600 miles is shown in Figure 15.** Again the buoyancy

* Reproduced from a paper by G. Stanford (1974).

** Figure 15 courtesy of L. Baxter III.

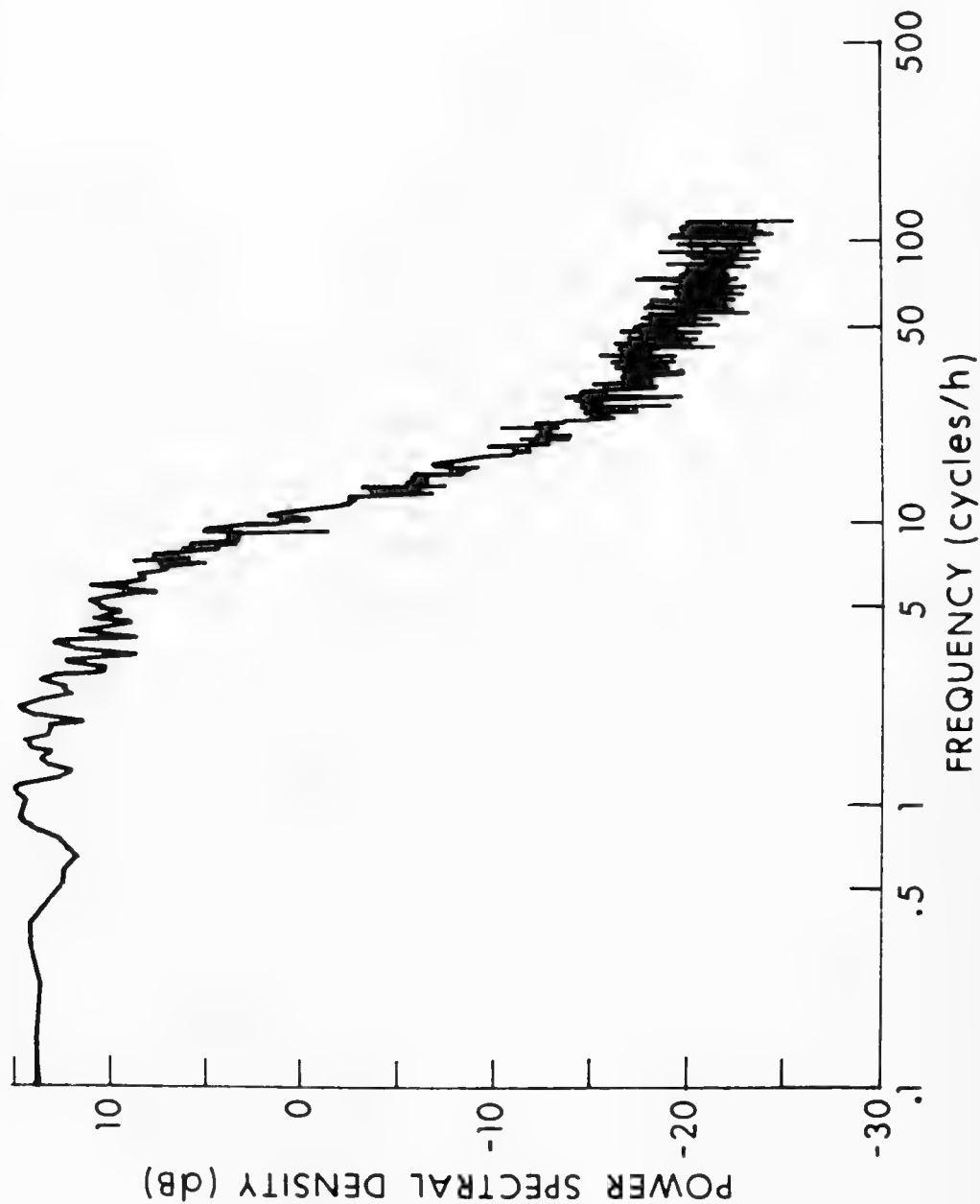


Figure 14-A. SPECTRA OF AMPLITUDE FLUCTUATIONS AT 367 Hz at 700 MILES

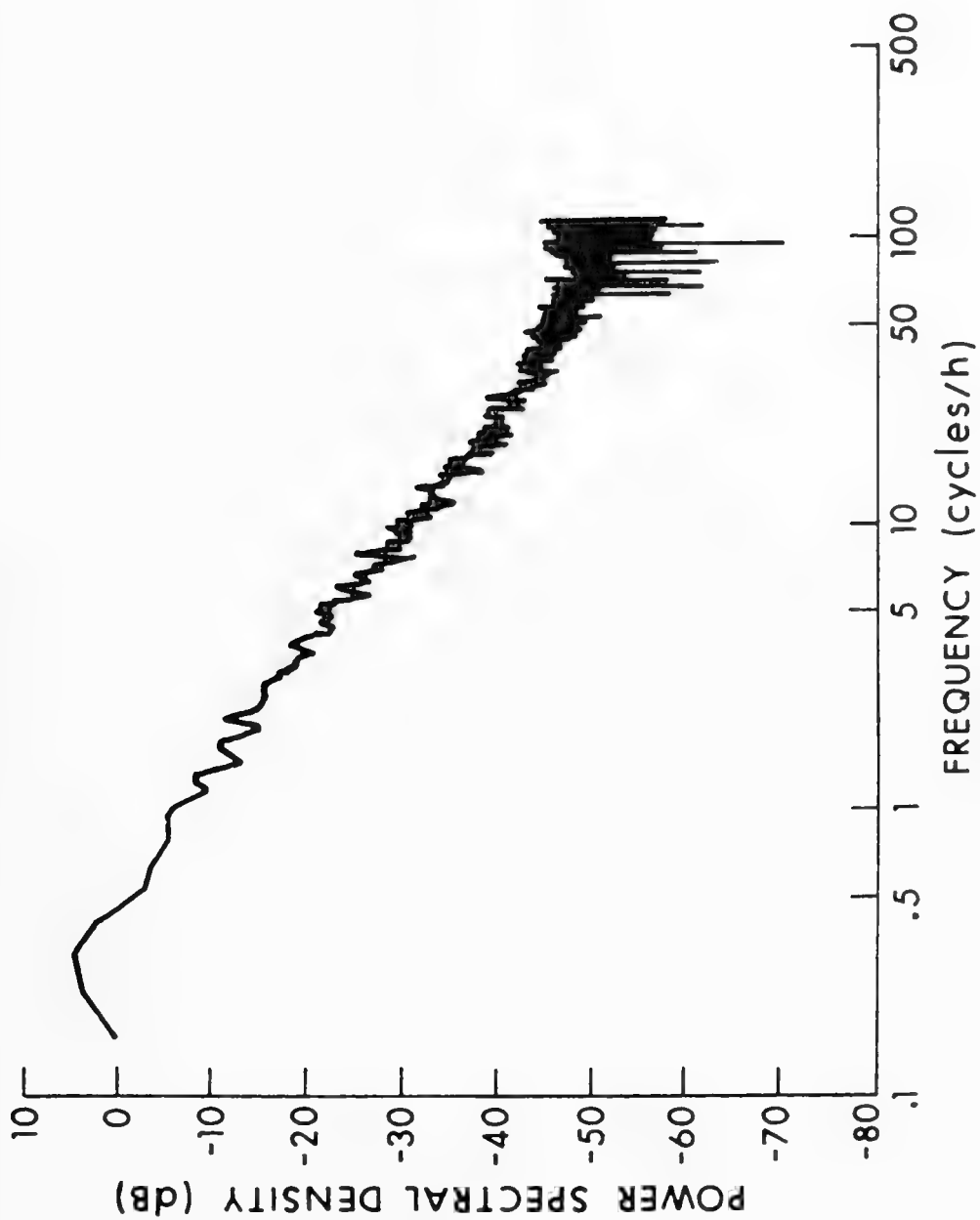


Figure 14-B. SPECTRA OF PHASE FLUCTUATIONS AT 367 Hz AT 700 MILES

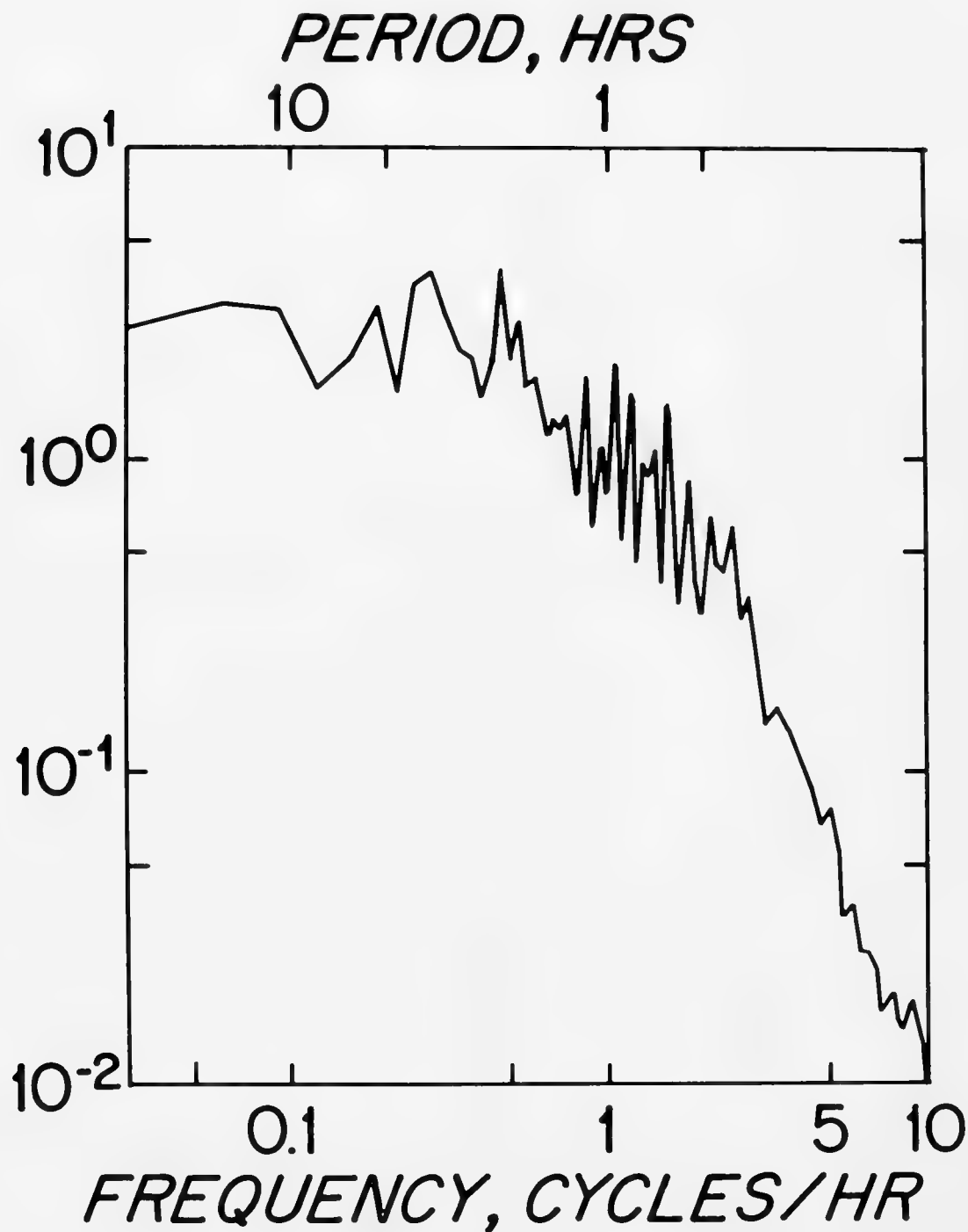


Figure 15. SPECTRUM OF AMPLITUDE FLUCTUATIONS
FROM SOFAR FLOAT

frequency cut-off is quite clear and dramatic. This is only one illustration of our present lack of understanding and consequent inability to predict and forecast.

A firm connection between oceanographic effects and acoustic effects must be established to allow the most effective exploitation of ocean transmission paths. Well controlled experiments are necessary to sort out the host of contributing factors such as microstructure, internal waves, cyclonic and anti-cyclonic eddies. Experiments must be conducted in a variety of locations to learn whether results at one point can be extrapolated to another. Similarly, experiments must be conducted at a variety of frequencies and ranges to establish the scaling laws so necessary for accurate prediction. Perhaps most important of all, however, is the need to coordinate acoustic experiments with strong physical oceanographic programs, so we can significantly increase our understanding of acoustic variability.

REFERENCES

- Baer, R. N., and M. J. Jacobson, "Analysis of the Effect of a Rossby Wave on Sound Velocity in the Ocean," *J. Acoust. Soc. Am.* 55, 1178-1189, 1974.
- DeFerrari, H. A., "Effects of Horizontally Varying Internal Wave Fields on Multipath Interference for Propagation Through the Deep Sound Channel," *J. Acoust. Soc. Am.* 56, 40-46, 1974.
- Franchi, E. R., and M. J. Jacobson, "An Environmental-Acoustics Model for Sound Propagation in a Geostrophic Flow," *J. Acoust. Soc. Am.* 53, 835-847, 1973.
- Garrett, C., and W. Munk, "Space Time Scales of Internal Waves," *Geophys. Fluid Dynam.* 2, 225-264, 1972.
- Porter, R. P., R. C. Spindel, and R. J. Jaffee, "CW Beacon System for Hydrophone Motion Determination," *J. Acoust. Soc. Am.* 53, 1691-1699, 1973.

Porter, R. P., R. C. Spindel, and R. J. Jaffee, "Acoustic-Internal Wave Interaction at Long Ranges in the Ocean," *J. Acoust. Soc. Am.* (in press).

Spindel, R. C., R. J. Porter, and R. J. Jaffee, "Long Range Sound Fluctuations with Drifting Hydrophones," *J. Acoust. Soc. Am.* 56, 440-446, 1974.

Stanford, G., "Low Frequency Fluctuations of a CW Signal in the Ocean," *J. Acoust. Soc. Am.* 55, 968-977, 1974.

Steinberg, J. C., et al., "Transmission Fluctuations," Institute for Acoustical Research, Miami Division, Palisades Geophysical Institute, Final Report IAR 73001, June 1, 1973.

Weinberg, N. L., J. G. Clark, and R. P. Flanagan, "Internal Tidal Influence on Deep-Ocean Acoustic-Ray Propagation," *J. Acoust. Soc. Am.* 56. 447-458, 1974.

DISCUSSION

Dr. S. M. Flatte (University of California College at Santa Cruz):
I think there is a difficulty in the way you treated the effect of internal waves on the phase fluctuations. Before I describe the difficulty, let me say that I believe that treating it properly will not change your qualitative result, with which I agree wholeheartedly — that is, that internal waves cause the type of fluctuations we are observing. But I think it will change the quantitative comparisons.

If you take a source and a receiver which are connected by a path such as shown in Figure 8, then the question is: What is the region of this path where the internal waves make the biggest effect?

You suggested that there was a fixed depth. The fluctuation formula which you gave (in Figure 10) for $F_0(w_g)$ varied as $1/\sin^2 \phi_g$ where ϕ_g is the angle the ray makes with respect to the internal wave

layer. You immediately see that there is a problem when ϕ_g is 0. That is, $F_\theta(w_g)$ blows up.

Dr. R. C. Spindel: We are quite aware of that.

Dr. Flatte: Right. I am sure you are. The result of this, of course, is if this layer happens to occur at the horizontal turning point of the ray, then this does not apply any more because the ray is actually curved. The point is, though, that the path does spend a great deal more time in the layer near its turning point than in any other layer that it is traversing.

Dr. Spindel: Yes.

Dr. Flatte: From our studies, at least in the type of profile we were working with, which was quite different from considering a particular layer, a factor-of-10 more time is spent in the region near the upper turning point than in any other region.

So I would be surprised if your profile was such that the effect at the turning point, which has a factor-of-10 enhancement due to the flatness of the ray, was unimportant compared to the region of your fixed depth.

Dr. Spindel: Yes. We're quite aware of the limitations of the ray theory, and that is basically —

Dr. Flatte: This is not a limitation of the ray theory. That is, I think you could apply the ray theory with this except that the result would be you would get most of your contribution from the region where the ray is flat.

Dr. Spindel: Yes, if that is the region where the internal waves have their largest effect. I think they do in that portion of the water column.

Dr. Flatte: That is right.

Dr. Spindel: That is true. We are aware of that. We are also aware of the sensitivity of the model to selection of that angle, ϕ_g . Even if you were to assume that that layer were not in a particularly difficult area (where the rays turn, for example) but were lower, the model is quite sensitive. Angles are quite shallow at which rays enter and leave the layer.

We are not really propounding the theory as one which explains all the interactions between internal waves and acoustics. But what we wanted to point out was that the environmental effects of internal waves are mirrored in the acoustic phase. And I think we can do that although we cannot predict absolute levels, which is basically what that factor is.

Dr. Flatte: I agree with you completely and that, in fact, the results do show the internal waves compare quite favorably with these data. I would like to make one more comment that has to do with the one I made last night about the difficulty with computer codes.

Roger Dashen and Walter Munk did an integral over the ray path and found that in fact for our case the main contribution came from the turning point.

The theoretical prediction which was given to me to compare with what came out of the computer code was that if you plot the rms phase fluctuation, as a function of range, you expect rather small fluctuations before the turning point. And as soon as you reach the area of the turning point, there should be a rather sharp jump. When I looked at the computer code, I did see a reasonably small fluctuation up until the turning point, although the quantitative agreement has

yet to be established. At the turning point I also observed a sharp rise, but I can't tell how much because it was above a cycle. And at that point we are stuck, whereas your data are fine enough that you can follow the phase through several cycles and find out what is happening.

Dr. R. P. Porter (Woods Hole Oceanographic Institute): I want to reinforce your comment. We attribute the depth dependence we see in our phase fluctuations precisely to that turning point argument, coupled with the fact that the layer of nearly constant sound velocity occurs right near the region where the internal wave activity appears to be the greatest.

We feel it is a qualitative conclusion that we really can't test accurately because of the breakdown of the ray theory in that region. But we have come to that same conclusion.

Dr. Flatte: Why do you think the ray theory has broken down? Why not just integrate the true path through that region? You know the length.

Dr. Porter: Because it is a caustic. I do not think it is valid —

Dr. H. A. DeFerrari (Rosenstiel School of Marine and Atmospheric Science, University of Miami): We do not know where the ray turns. There is an ambiguity. As the grazing angle becomes small, any slight perturbation to the sound-speed profile causes a turn. So if you want to integrate through there, you may not be on the same ray that strikes your receiver.

Dr. Porter: Put it another way. In that ray you have diffraction effects.

Dr. Flatte: The integral converges. There are certain regions where you have to worry about it breaking up and causing a completely new ray. But you can also form criteria for that not happening. We have done some work in that respect, too.

Dr. DeFerrari: This is a problem that was in the Acoustical Society several years back. Whether or not one added in a phase shift of $\pi/4$ at that point or not. This is part of that integral you are talking about. I don't know whether it was ever really settled or not.

Dr. P. W. Smith (Bolt, Beranek, and Newman, Inc.): Yes, it was not. (Laughter)

Dr. Flatte: I have another question concerning the quantitative comparison that you made of the phase fluctuations. How did you treat the combination of several rays? There were several rays going from source to receiver. Right?

Dr. Spindel: Four rays.

Dr. Flatte: How do you treat the combination in order to get a total phase prediction for the model?

Dr. Spindel: The total field at the receiver is simply a summation of the effects of those four rays. We have computed the phase at the receiving point for each of the four rays, we sum that, and separate that resulting equation into an amplitude and a phase factor and that is the phase.

Dr. Flatte: So the internal wave model predicts the phase fluctuation of each ray and to compare with data you perform a summation of those rays?

Dr. Spindel: Yes.

Dr. Flatte: But in a random way?

Dr. Spindel: The randomness comes in because of the randomness of that layer. That layer is a superposition really of many internal waves.

Dr. Flatte: But the internal wave predicts the average fluctuation in one ray or another. It does not predict how the combination will occur unless you assume you know the amplitude of fluctuations and their distribution and then form some kind of a statistical combination.

Dr. J. G. Clark (Institute for Acoustical Research): You did not describe internal wave field statistics?

Dr. Spindel: Yes, and the resulting received signal is really just a superposition, that is, a linear combination of all the rays.

Dr. Flatte: You assumed equal amplitude?

Dr. Spindel: Yes.

Mr. C. W. Spofford (AESD, Office of Naval Research): I have here three figures that are the results of a numerical experiment which I think bears on these phase statistics. It was stimulated by a question I asked Bob Porter about a year or so ago at an Acoustical Society meeting when I first heard of the technique of the drifting floats, because I was concerned that he was taking out the phase assuming that it was essentially linear in range. And I think we have seen ample evidence today it is not.

I actually made a numerical calculation using the parabolic-equation program extracting the phase as a function of range at

selected depths. We went out one convergence zone, using a frequency of only 50 Hz because such computations are too expensive at 400 Hz. A Bermuda-type profile was used over a high-loss bottom with a source on the axis. Figure D-1 shows the transmission loss and phase variations as a function of range. The phase has been de-meant over the 50-mile interval and the residual variations are plotted in cycles. Note that in this case of axis-to-axis propagation, the phase varies from linear only by about one quarter of a cycle. But here is the propagation loss going along. I don't know if I am willing to multiply it by 8 to scale it up to 400 Hz or not.

One of the phase flip questions occurred to me when examining the results near 22 nautical miles. There was a particularly deep null in transmission loss, and the phase changes by nearly 180 degrees; actually, it is about 135 degrees.

We ran this case again with very fine resolution in range and the phase was totally continuous through there. There were no discontinuities. I concede that if you are measuring the phase near such a point, and the signal level has dipped down into noise there is no way to track the phase. But there is no reason, no physical reason, for the phase to be discontinuous.

Figure D-2 corresponds to the same source but to receiver depth of 300 feet. Here the phase and loss curves overlap. Note that the phase-variation scale has been compressed to handle the 14-cycle variation over the entire range.

As you come up into the convergence zone, some fairly dramatic things are happening in terms of phase.

Figure D-3 is for a 1000-foot receiver depth where the up-and-down-going convergence zones overlap more. Here the phase scale is changed again.

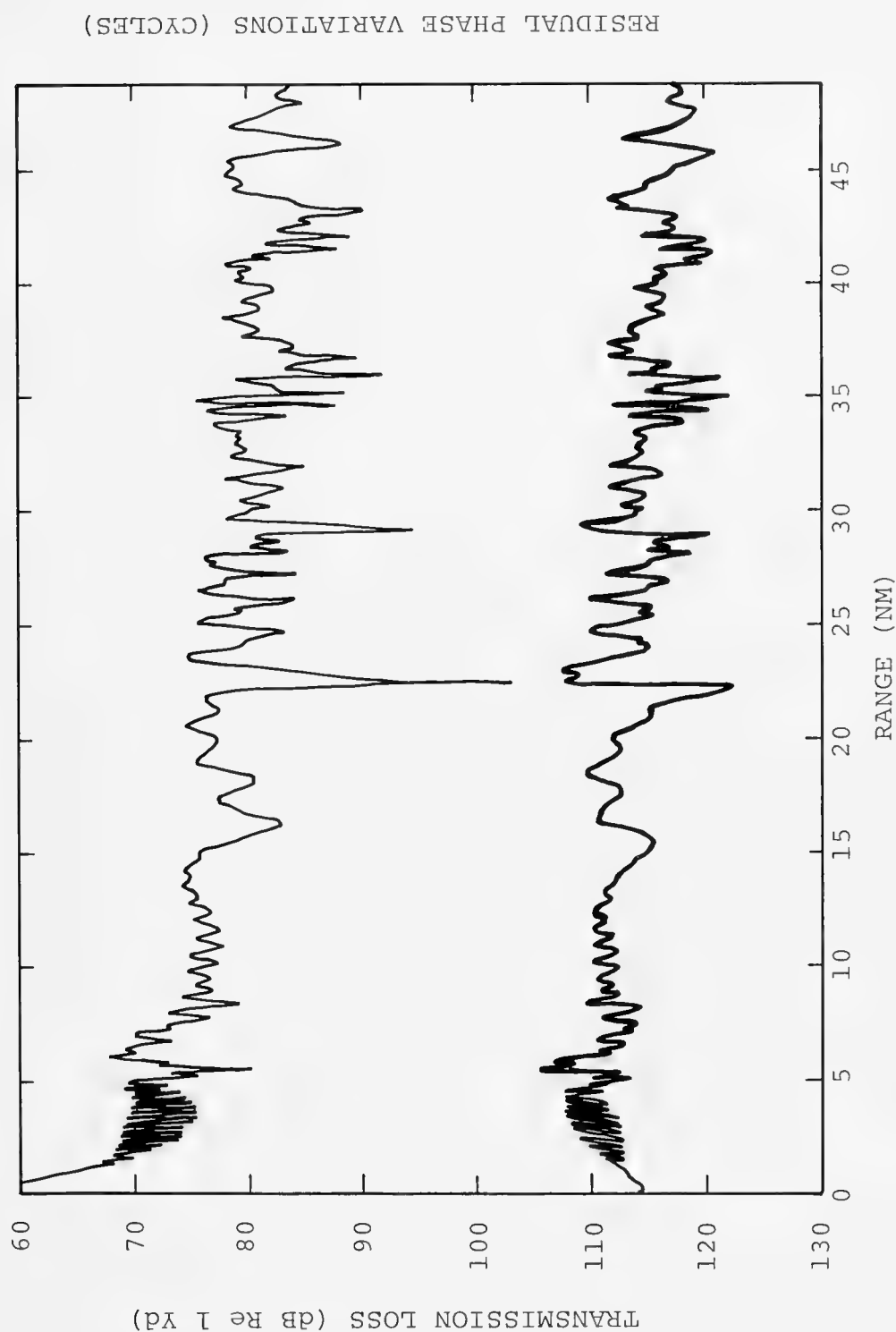


Figure D-1. TRANSMISSION LOSS AND PHASE VERSUS RANGE FOR BERMUDA-LIKE PROFILE. FREQUENCY = 50 Hz, AXIS DEPTH SOURCE, RECEIVER AT AXIS.

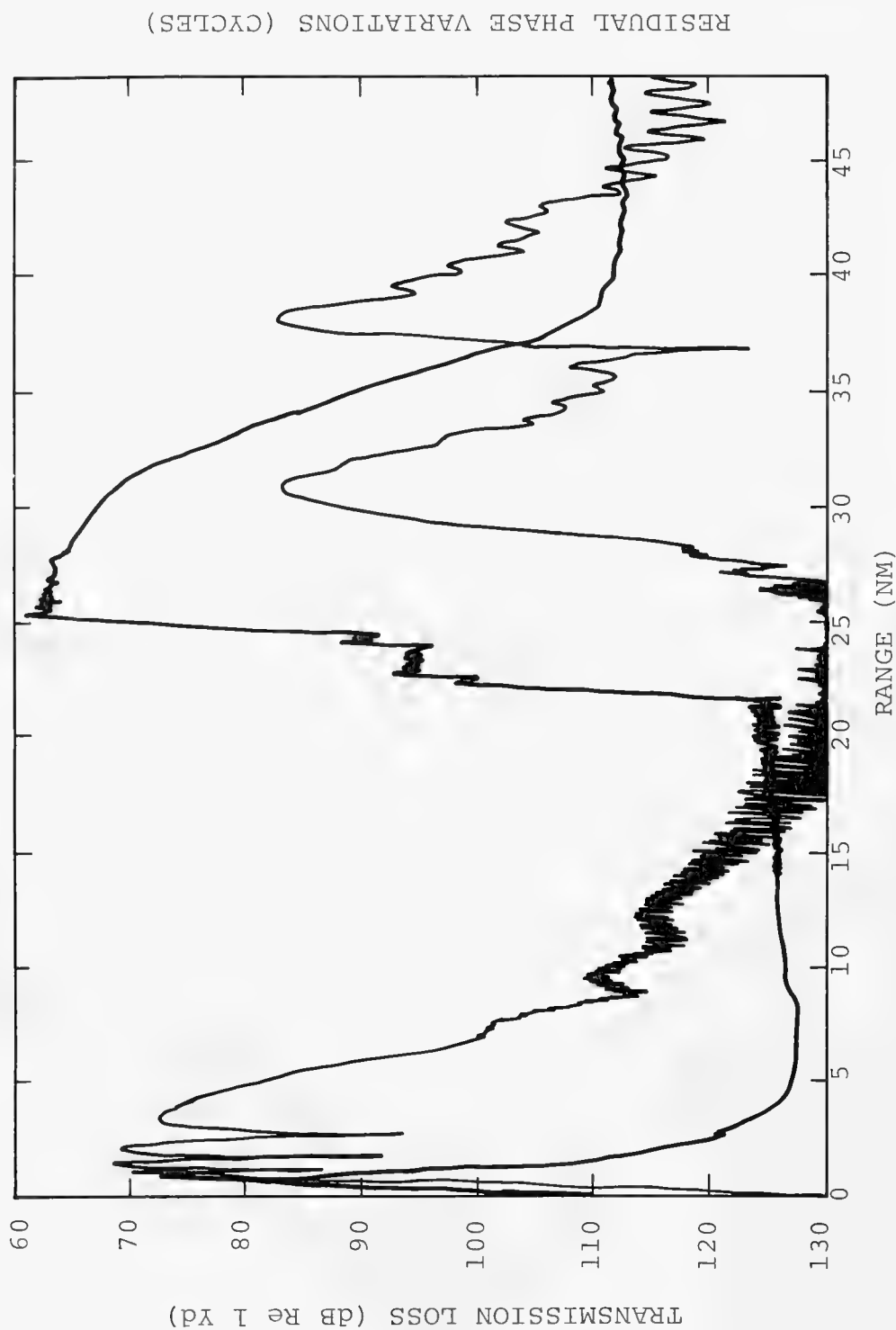


Figure D-2. TRANSMISSION LOSS AND PHASE VERSUS RANGE FOR BERMUDA-LIKE PROFILE.
FREQUENCY = 50 Hz, AXIS DEPTH SOURCE, RECEIVER AT 300 FT.

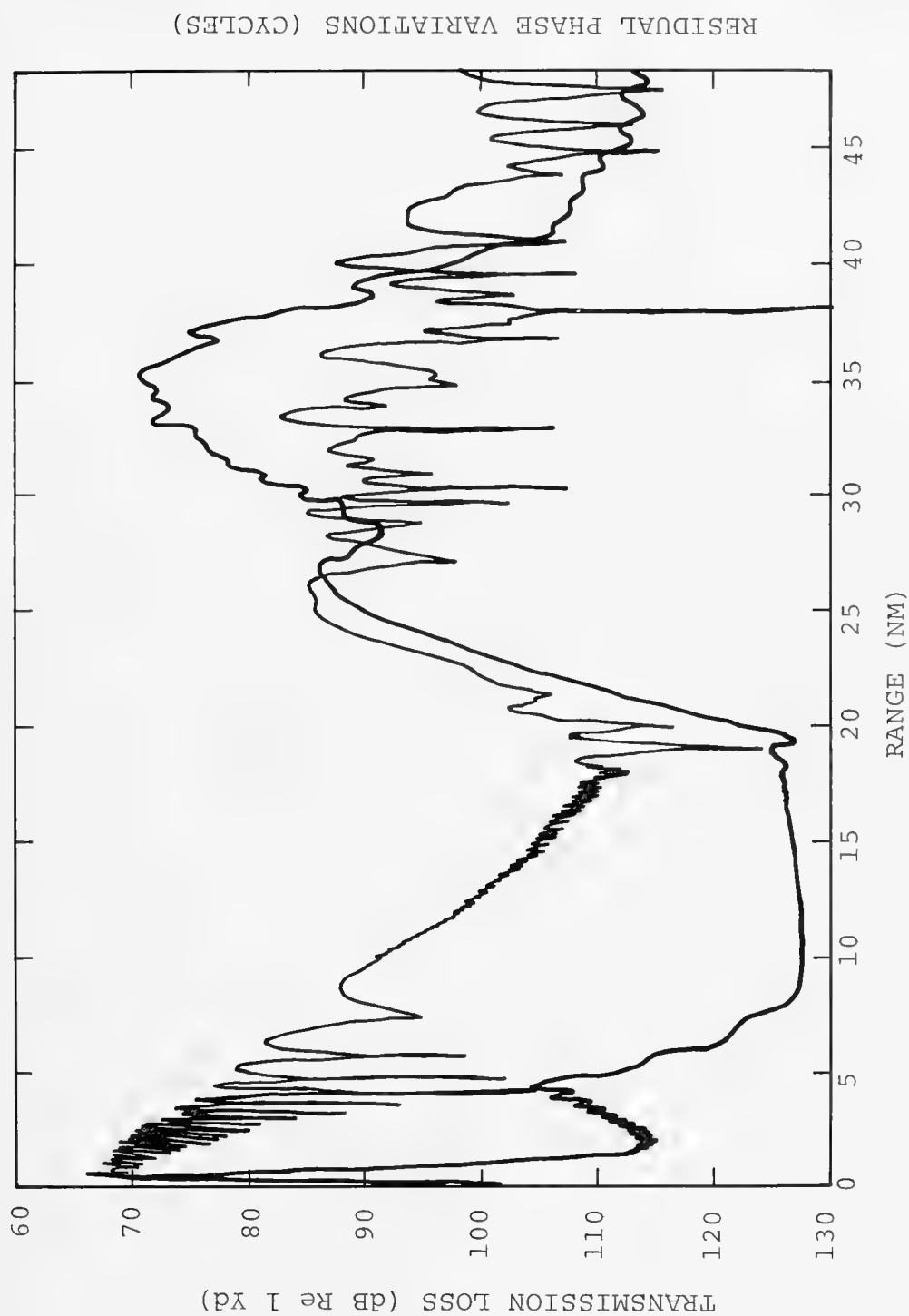


Figure D-3. TRANSMISSION LOSS AND PHASE VERSUS RANGE FOR BERMUDA-LIKE PROFILE.
FREQUENCY = 50 Hz, AXIS DEPTH SOURCE, RECEIVER AT 1000 FT.

The point I wanted to raise is that phase, even in a frozen deterministic ocean, is not linear in range. And I am concerned with techniques which remove a linear phase trend and assume that the residual fluctuations are due to internal waves or other random-ocean effects.

In summary, there is a natural non-linearity in phase in the ocean.

Mr. M. A. Pedersen (Naval Undersea Center): You took out a constant velocity, didn't you?

Mr. Spofford: I accumulated a phase for the entire range.

Mr. Pedersen: Yes, but you removed it by taking out a constant phase velocity?

Mr. Spofford: Yes. Essentially.

Mr. Pedersen: And as you move into different parts of the convergence zones you have different phase velocities because you have different vertical angles.

Mr. Spofford: Absolutely.

Mr. Pedersen: So it will progress this way.

Mr. Spofford: I was expecting to get phase variations. The question I was not sure of was how quickly they might change with range.

Now, his measurement only went over a fraction of a mile, I think, in range. So I do not think it is driving the problem in terms of the kinds of things he measured. I think it will introduce a variation or non-linearity in phase on the order of about one cycle at 400 Hz.

Dr. Clark: Over what?

Mr. Spofford: Over the fraction of a mile. There is a ripple on the order of a cycle in phase.

Dr. Clark: You took a linear phase trail out of this?

Mr. Spofford: I went back and looked at half-mile regions, removing the linear trend, and still ended up with residual fluctuations of about a cycle in phase extrapolated to 400 Hz.

Dr. Clark: You made a comment on that last slide that you did not see any reason for a phase flip in the deep fade. Is that right?

Mr. Spofford: No, I did not say that. I said the phase flip is continuous in the model at least. Such physics does not have discontinuous phase. The problem is, it is always at these nulls in transmission where you are probably looking at noise.

Dr. Clark: Right.

Dr. M. Schulkin (Naval Oceanographic Office): One remark on the last slide that Dr. DeFerrari showed. Were those Doppler shifts measured?

Dr. DeFerrari: No.

Dr. Schulkin: Was it just coincidence that you chose 8 seconds?

Dr. DeFerrari: I started at 8 and then on down.

Dr. Schulkin: They are as close to sinusoidal effects as you are going to get in the ocean. You are apt to pick up an 8-second swell by measurement, and I just wondered if you did.

Dr. DeFerrari: No, the first one was measured and it probably was 8 seconds. They are typically 8 to 10 seconds.

Dr. Schulkin: It was measured?

Dr. DeFerrari: Yes. The first set of a few. Yes. That is what it looks like. The swell comes in very strong. The wind-driven waves are much less compared to the real spectrum. I have done that with surface data at the same time and compared the spectra and it looks just about like the wave spectra, that the wind waves fall out much more rapidly than the actual spectrum.

I have also done it as a function of frequency and a number of other things.

Dr. R. M. Fitzgerald (Naval Research Laboratory): I wanted to make a quick comment on the physical nature of discontinuous phase jumps. What we have is a physical field, a pressure field. When you decompose that field into phase and amplitude, that is unphysical, if you like.

However, when the amplitude vanishes, the phase is not determined. So when the amplitude truly vanishes, the phase can change discontinuously in the physical pressure field.

Dr. T. G. Birdsall (Cooley Electronics Laboratory): Some people have had a lot of experience trying to read data through those points, because it is the nastiest point in the world. The nicest thing is to run three frequencies through it, you know, an epsilon apart on either side —

Mr. Spofford: I would argue in a deterministic physical model like this that the amplitude probably cannot vanish.

Dr. Flatte: The chances of it vanishing are zero.

Dr. Birdsall: But it happens, though. That's the trouble with probability zero. It always keeps happening.

Dr. S. W. Marshall (Naval Research Laboratory): This question is to Bob Spindel. Bob, you made a statement that beyond the limit that the environment places on the array you can expect to get gain from that array. Please clarify that.

Dr. Spindel: You can continue to get increased resolution by increasing the size of your array. This is simply a consequence of the fact that as you separate sensors, the phase fluctuations between the two sensors appear to saturate at a particular level. They do not increase beyond that level.

So your angular resolution is determined by that phase fluctuation divided by the length of the array. So that you can do better and better by making your array longer and longer. It does not mean that you should do that. You might be buying very little. As a matter of fact, you do buy very little every time you double a long array in terms of the expense of doing it.

Dr. W. H. Munk (University of California at San Diego): May I make two comments? One, to those of us who are pushing internal waves as a cause of acoustic fluctuations, it certainly is disconcerting, to say the least, that acoustic spectra seem to pay no attention to the high frequency cutoff of internal waves. Spectra merrily go by without change in slope. I don't like it.

But I do want to point out something kind of interesting. The same happened to be the case for measurements of the up and down motion of the internal waves. All of such measurements before

January 1974 did not show any effect of the Vaisala frequency, and all measurements since January 1974 have shown sharp cutoffs. Very curious discontinuity.

There at least we do know the answer other than people finding what is fashionable at the moment. Those before were moored measurements, and the whole field was convected past the fixed transducers, so that to some extent you got a mixture of the spatial as well as the temporal variation. And there is no cutoff in the spatial variation at high wave number.

So you might think of that as a Doppler shift or a Doppler smear cutoff. If the tides convect your whole field by variable speed, it is certainly going to blur and maybe even eliminate the cutoff.

When people went to other kinds of instrumentations, like capsules that yo-yoed but stayed with the water column, then all of a sudden the cutoff did, thank heaven, appear. It was a 20 dB cutoff and was very pretty.

And I am hoping against hope somehow that in some future experiments in acoustics suddenly a sharp Vaisala cutoff will appear. I do not know how.

Dr. Clark: Where would you expect that, Walter?

Dr. Munk: At the local Vaisala — I don't know. That is a good point. There is, of course, great smearing if you have rays which have gone through the whole water column. I hadn't thought of that. And that really in a way changes the situation from the internal wave experiment I mentioned.

Dr. Clark: In that data that I gave you, you will find a knee at about one cycle per hour.

Dr. Munk: That is a very good point, John. For those acoustic measurements which sample a large depth of water column you would, in fact, have a good excuse for not seeing a sharp cutoff.

Dr. Clark: It is not sharp but there is a definite knee there so you can see that.

Dr. Munk: The other point is more serious. I have an impression that these phase and intensity fluctuations are very model-dependent that no matter what kind of a model you put into the ocean, as long as it is not complete nonsense, you are going to find excellent agreement with observations.

I have seen this now at least in four or five different models. Jacobsen puts in planetary waves, and by cooking them up a little they show a record that he says looks like precisely the record that you obtained.

Other people like us have put in internal wave observations and they look lovely. So does your group.

And, finally, you, to make it even worse, show that under certain conditions you don't need any disturbance at all. You just need interference.

I think there is a lesson to be learned there one should face — that when it comes to multipath, the statistics you get are probably highly dependent on path interference and very unsensitive to the ocean model itself which is good if you are an acoustician, because you might get some good results without having to study the ocean.

It is bad for us oceanographers because we are probably not going to be able to use that kind of statistics ever to learn anything sensible about the ocean.

Dr. Clark: Can I make a comment, Walter? On that first model study I did in the Straits of Florida, I tried to predict some statistical characteristics of the amplitude rather than the phase. This is a more significant comparison, I believe. As we know, amplitude is a non-linear function of the environment. So, if you can predict the frequency content of that thing, then you have done something.

Let's hope if we go ahead and do the complete job, that everything will smear out.

Dr. Birdsall: I hope the ability of all the models to predict it means that we do have to get more quantitative and perhaps richer experiments where we measure more than just one kind of thing so that we can start to split across the various types of models.

FIXED-SYSTEM MEASUREMENTS OF TIME-VARYING MULTIPATH AND DOPPLER SPREADING

H. A. DeFerrari

Rosenstiel School of Marine and Atmospheric Science

Signals transmitted through ocean channels will be spread in time because of multipath and spread in frequency because of scatter from the ocean wave surface. Fixed-system measurements in the Florida Straits and between Eleuthera and Bermuda make possible the observation of time-varying multipath interference and Doppler spectra. Results are summarized for several short experiments using CW (420 Hz) and pulse CW transmissions.

Fully coherent ray models are used to interpret experimental results. These models predict the transmission loss and travel time along all paths with sufficient accuracy to allow the coherent addition of arrivals at the receiver. Time-varying CW multipath interference is simulated by introducing perturbations to the sound-speed field and generating time series of phase and transmission-loss fluctuations for comparisons with experimental results. Model computations show that horizontally invariant internal waves produce sound-speed perturbations that cannot cause both the phase and transmission loss fluctuations which are consistent with experiment. When horizontal fluctuations are introduced to the sound-speed perturbations, statistics of CW transmission fluctuations match experimental results.

Pulsed CW transmission can also be simulated by coherent addition of received pulses. Broadband characteristics of received signals exhibit selective fading. The frequency of the fade is sensitive to small perturbations of sound speed while the fade bandwidth depends on average characteristics of the propagation channel and is relatively insensitive to the typically observed fluctuations of sound speed.

Doppler spectra and scattering functions are presented and discussed. Combined propagation and scattering models show that unsymmetric surface-scatter sidebands can result from bottom interactions.

This paper consists of the presentation and discussion of some results from fixed-system measurements. Basically three types of phenomena are described:

- Time-varying multipath for CW signals
- Time-varying multipath for broadband signals
- Doppler spreading

Before presenting these data I would like to discuss a model used for their interpretation. The basic model is a bilinear profile with quasi-static fluctuations. A surface scattering model is included on each path, and the paths are added coherently.

Figure 1 shows typical range-averaged profile between Eleuthera and Bermuda and a bilinear fit to it. We don't have any experimental data of the sound speed fluctuations there, so for perturbations of this profile we use a calculation made by Dr. Moore at the University of Miami of the first-mode internal wave for an internal tide of wavelength 150 kilometers. Figure 2 shows the resulting perturbed profiles, and Figure 3 shows the bilinear approximations to them. The perturbations can then be described in terms of two parameters: the depth D of the axis and the bilinear angle α . This model can be made range-dependent, as shown in Figure 4. The sound-speed profile becomes a function of range by segmenting it and allowing the profile to change with range and also with time. Figure 5 shows the bilinear fit to some actual sound-speed measurements made about mid-range in the Florida Straits. One profile was obtained every two hours for four days. If you look at the sequence closely, you can see the effects of a tide. The gradients change and the knee rises and falls by the tidal periodicity.

The bottom sketch in Figure 6 is the surface scatter model we will use. There is a specular reflection, unshifted in frequency, from the surface waves, and Doppler-shifted sidebands separated in frequency from the carrier by multiples of the surface-wave frequency. We have

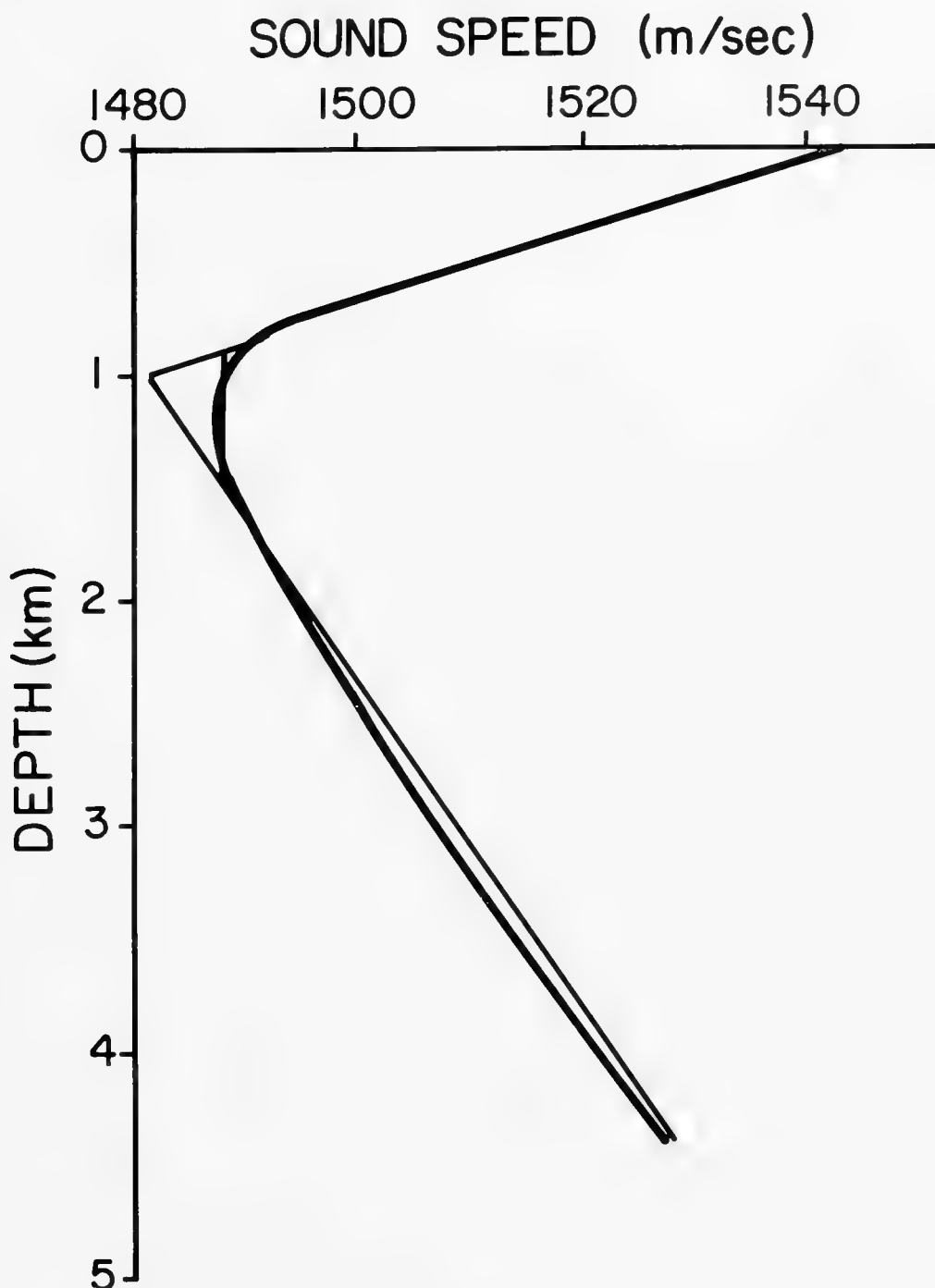


Figure 1. TYPICAL RANGE-AVERAGED PROFILE AND BILINEAR FIT

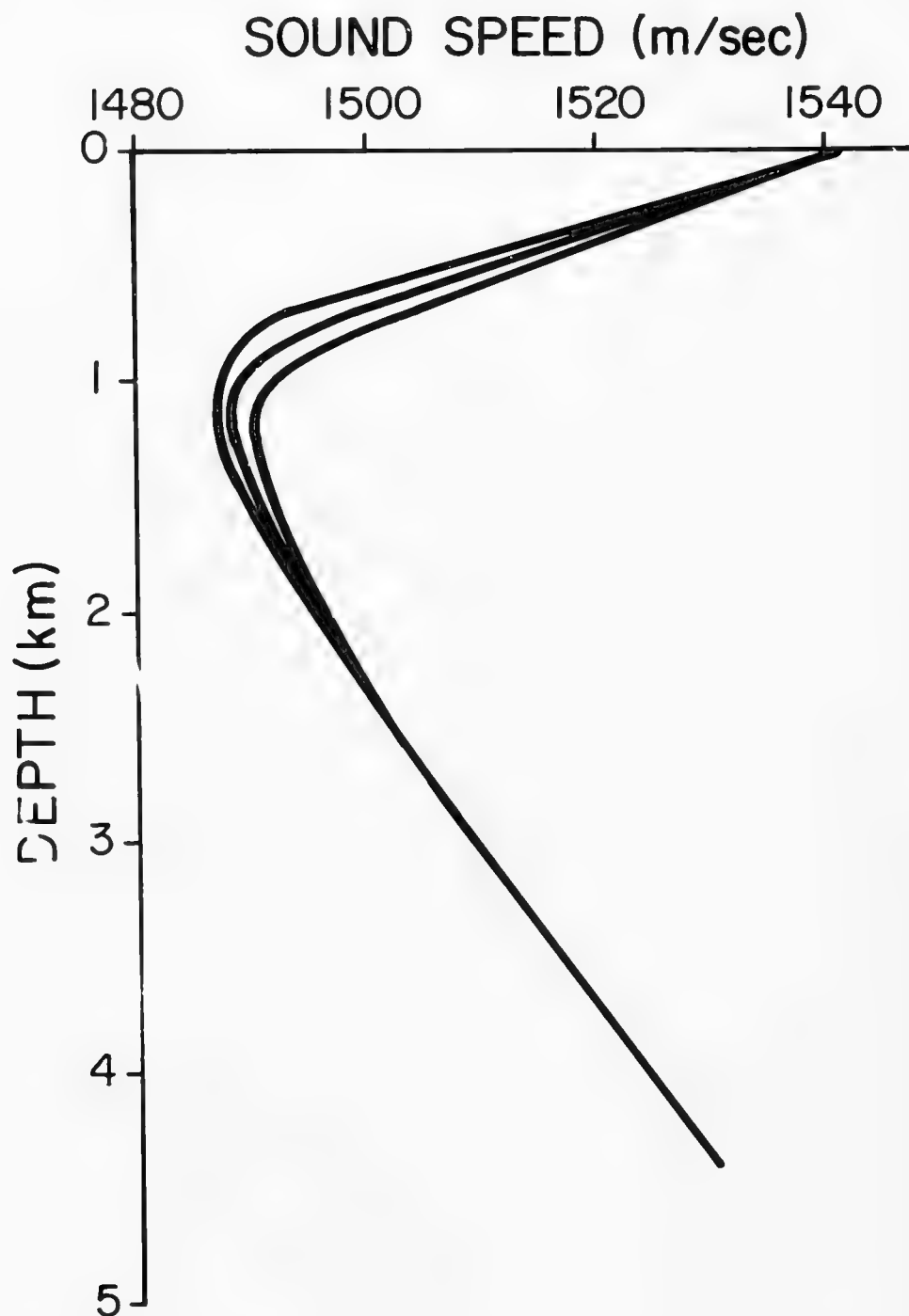


Figure 2. PERTURBED PROFILES FOR FIRST MODE INTERNAL WAVE

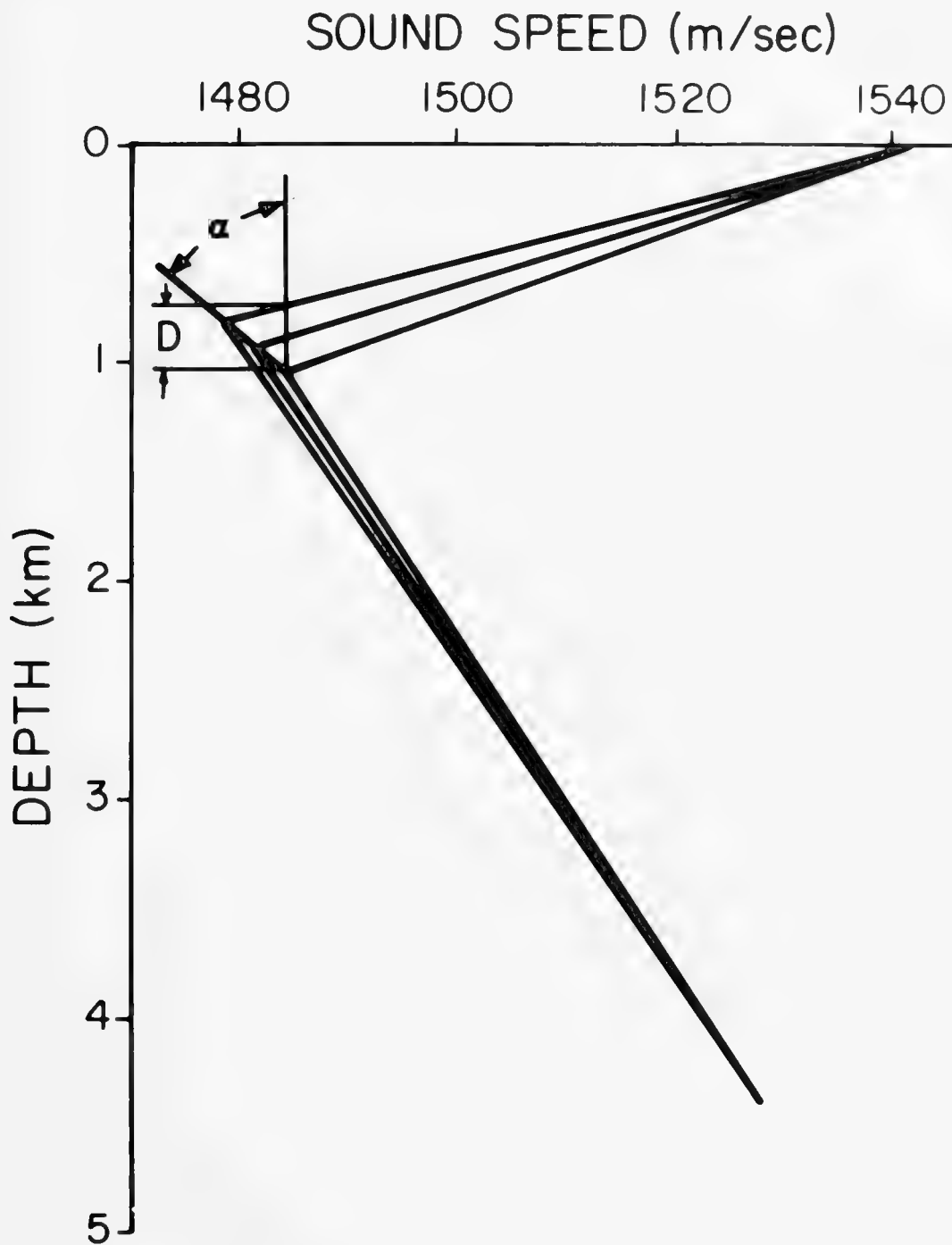


Figure 3. BILINEAR FITS TO PERTURBED PROFILES

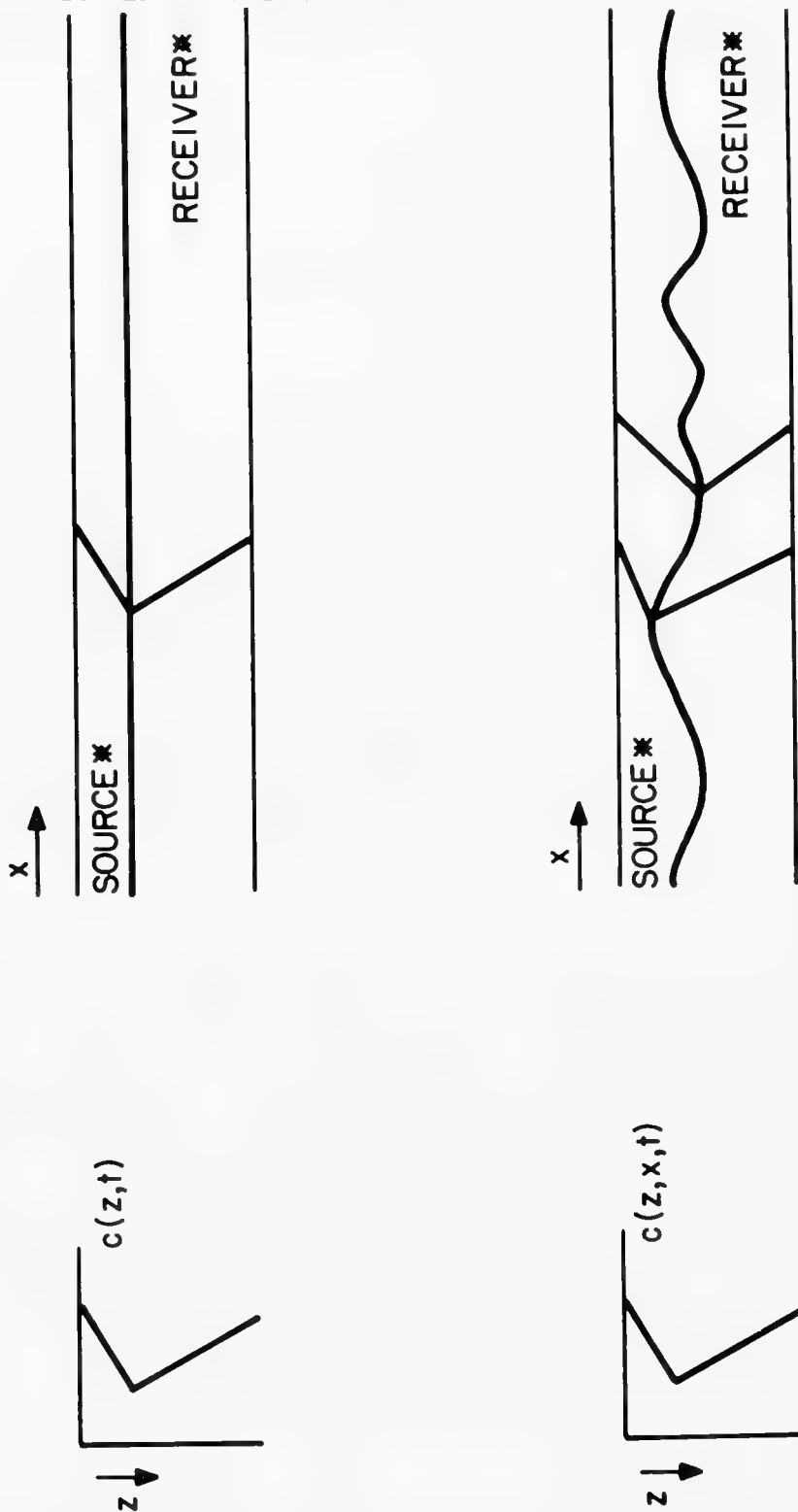


Figure 4. RANGE DEPENDENT PROFILE CONSTRUCTED FROM PERTURBED PROFILES

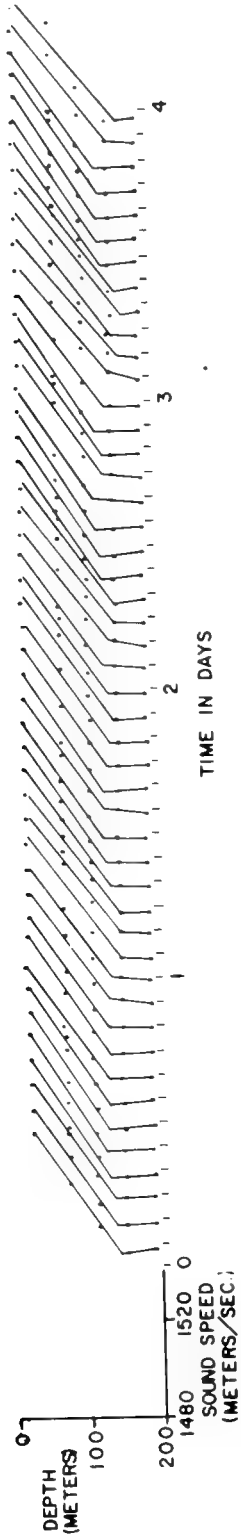
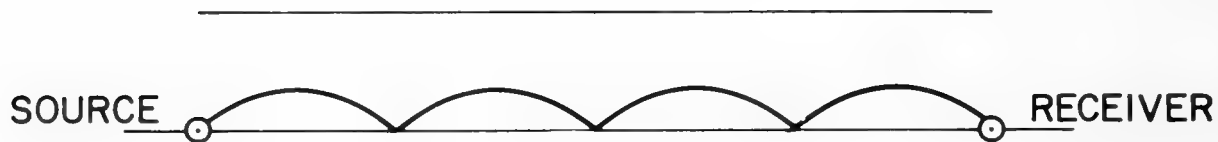
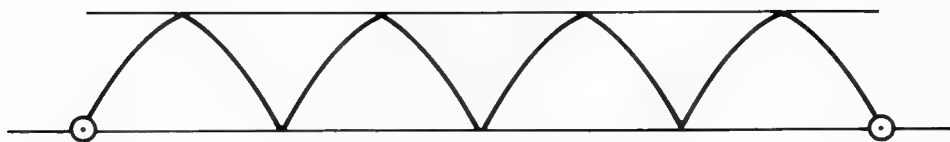


Figure 5. BILINEAR FITS TO SOUND-SPEED PROFILE MEASUREMENTS

TYPES OF RAY PATHS



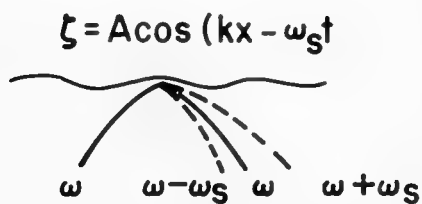
RBR



SRBR



SCATTERED SRBR



"ECKART" SCATTER MODEL

Figure 6. RAY PATHS AND SURFACE SCATTER MODEL

algorithms that can track rays incident on the surface all along the propagation path and find those scattered rays which hit the receiver. Thus, multiple scattering along the path can be accounted for.

The types of ray paths that can be expected in the Florida Straits are shown in the other diagrams on Figure 6. The downward refracting profile leads to rays which are refracted bottom-reflected (RBR) and surface-reflected bottom-reflected (SRBR). The SRBR rays can be surface scattered (as in the illustration) after any number of specular bounces. This happens to be a ray which reflects specularly twice, then upscatters and reflects specularly as its new angle before reaching the receiver. The model does all the bookkeeping for these paths.

We will now discuss the data. Figure 7 shows CW propagation loss for the 700-mile range between Eleuthera and Bermuda over a 48-hour period; typical multipath deep fades (30 dB or so) are shown with their associated phase shifts. If the fades are very deep the phase shift appear to be 180 degrees. Most of the phase fluctuations are quasi-periodic, varying with the tidal component.

It's interesting to compare these sorts of fluctuations with what we see at other ranges. Figure 8 compares propagation-loss and phase data for the 700 nautical mile range to Bermuda, the 300-mile range to Eleuthera and the 7-mile range in the Florida Straits. They all have the characteristic dropouts in signal level due to multipath influence. The principal difference between them is that for the longer ranges the fades are more rapid than for the shorter ranges. However, the fades tend to have the same magnitude, typically 15 to 30 dB for deep-fading events. The phase has similar characteristics, with smooth variations (showing a strong tidal periodicity in the Eleuthera data) plus a number of rapid shifts of 180 degrees associated with deep fades.

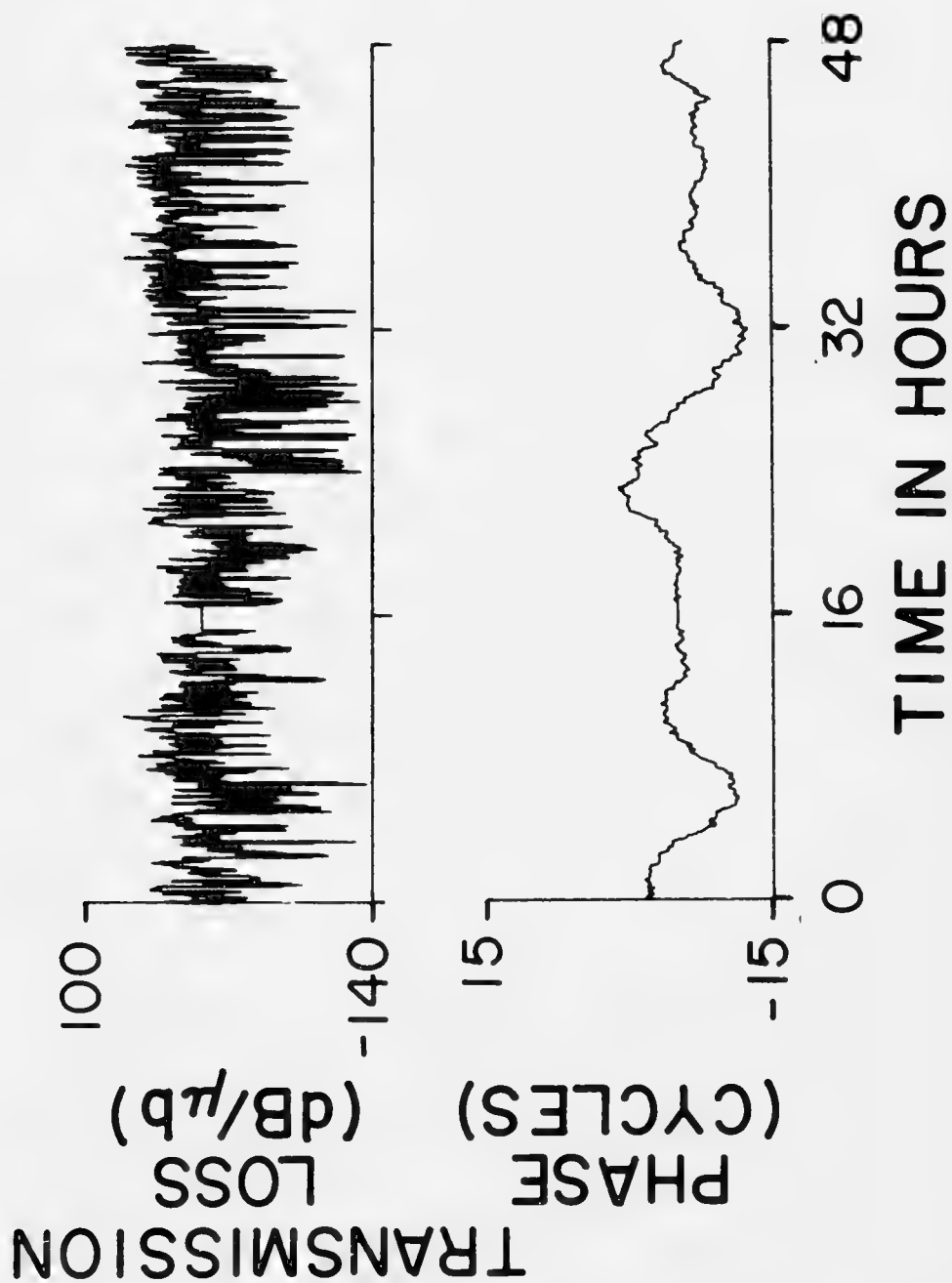


Figure 7. C.W. TRANSMISSION BETWEEN ELEUTHERA AND BERMUDA (407Hz)

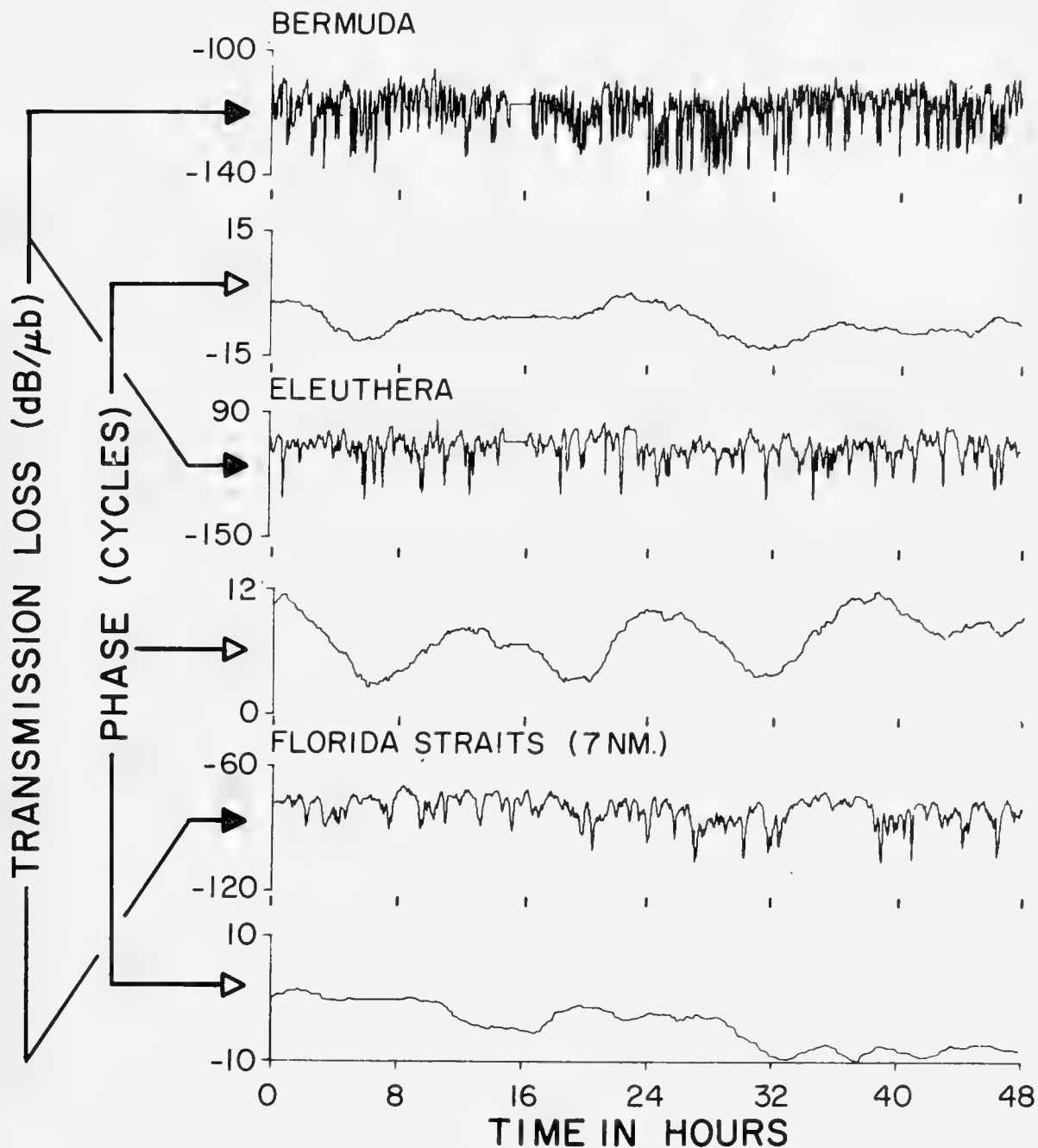


Figure 8. TRANSMISSION LOSS AND PHASE FOR THREE RANGES

Histograms for each of the above time series are shown in Figure 9. They are all about the same with a standard deviation of about 5.5 dB. The essential difference in the three cases is the autocorrelation function. In Figure 10 it is seen that the Bermuda series decorrelates more rapidly than the other two. It appears more noiselike. If we take the decorrelation time to be that value at which the normalized autocorrelation function falls to $1/e$, then we get about 4-1/2 minutes for the Bermuda range, 8-1/2 for Eleuthera and 18 in the Florida Straits.

Another measure is the mean square bandwidth (defined at the top of Figure 11) of the power spectrum of the transmission-loss time series. Figure 11 shows that the more noiselike Bermuda time series has a broader bandwidth.

Now, the characteristics that we have looked at so far are ones which are really consistent from day to day over long periods. But we must be able to differentiate between the fast fading events and the intermediate ones. Figure 12 is a sequence of histograms for a time series of 63 days. Each time series is high pass filtered with a cutoff of 4 cycles/day so the periods of variation are less than 6 hours. All the longer periodicities are removed. Note the spectra day after day are consistent and formally speaking appear to be wide-sense stationary. Figure 13 shows the corresponding autocorrelation functions, again for 63 days. Again these are consistent one after another.

In the above figures, the longer term trends were filtered out. Figure 14 shows variations for periods longer than 5 hours which are significant and I don't think are related to multipath. I can't think of any mechanism for them offhand other than it may just be a complete change in the whole propagation regime. It appears that there are

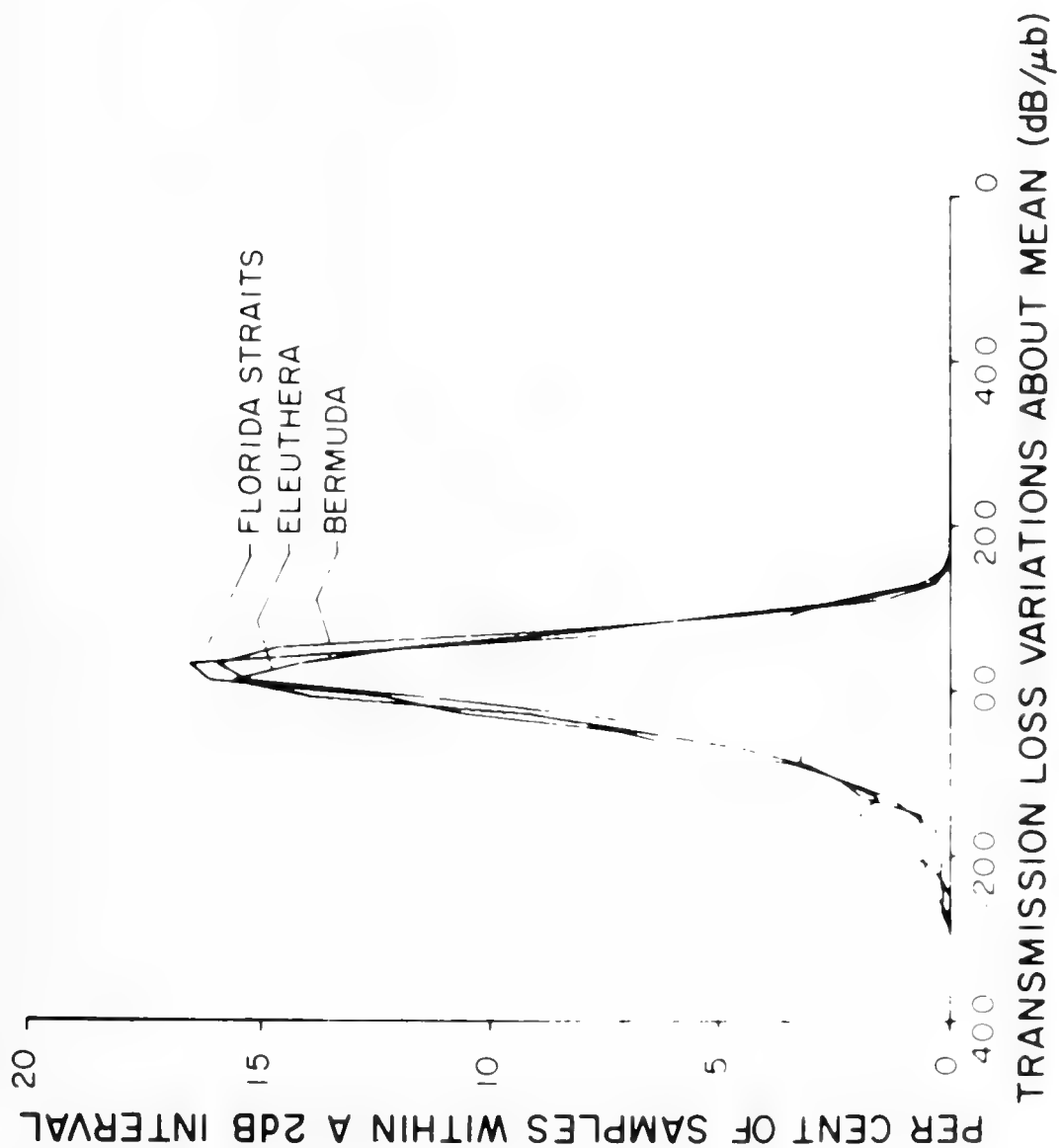


Figure 9. HISTOGRAMS OF C.W. TRANSMISSION LOSS FOR THREE EXPERIMENTAL SITES

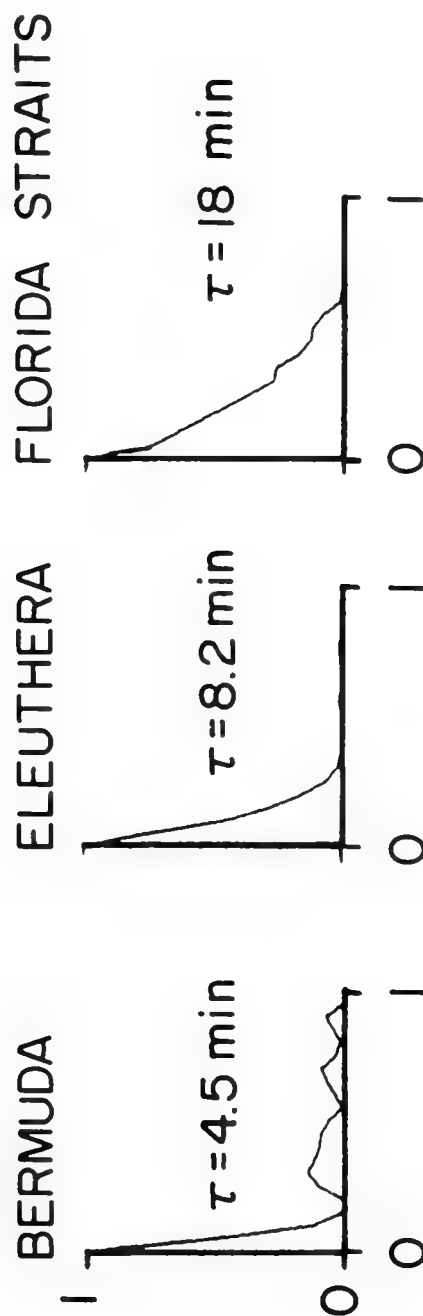


Figure 10. NORMALIZED AUTOCORRELATIONS OF TRANSMISSION
LOSS FOR THREE EXPERIMENTAL SITES

$$\bar{\omega}^2 = \frac{\int_{-\infty}^{\infty} \omega^2 S(\omega) d\omega}{\int_{-\infty}^{\infty} S(\omega) d\omega}$$

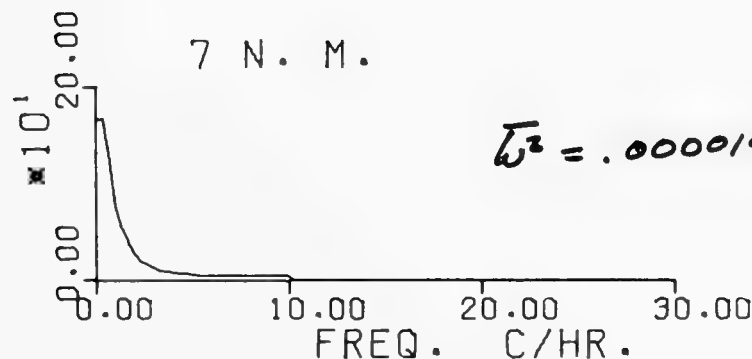
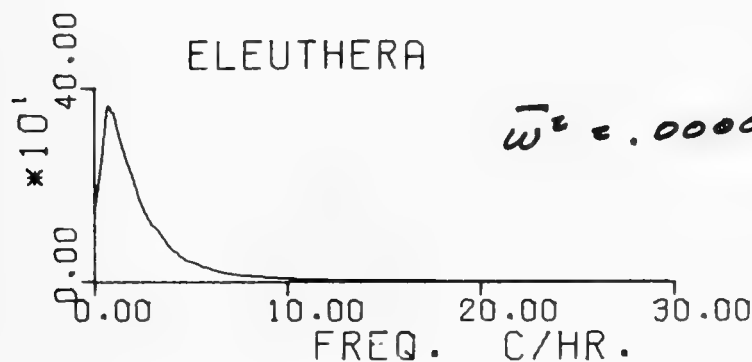
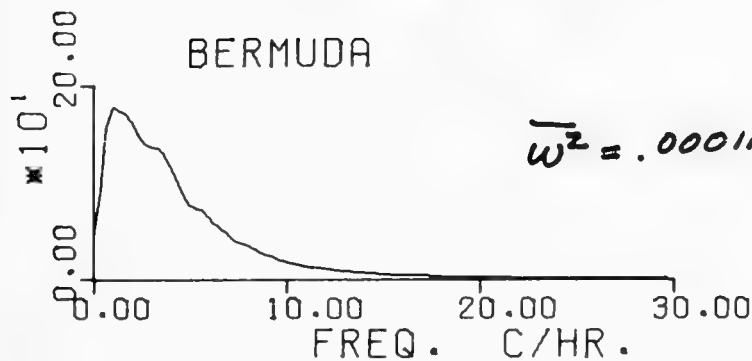


Figure 11. POWER SPECTRA OF THE TRANSMISSION LOSS
FOR THE THREE EXPERIMENTAL RANGES

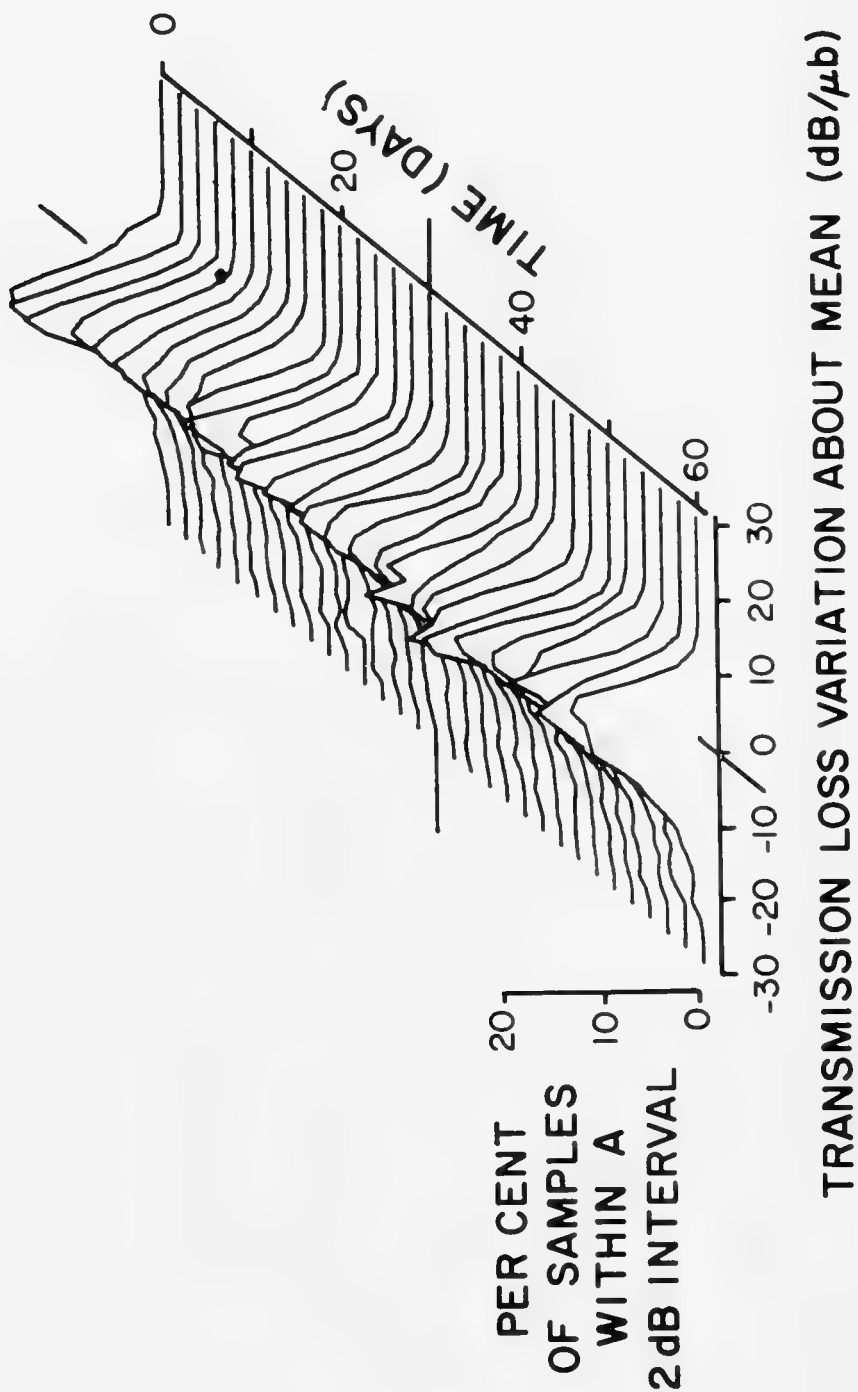


Figure 12. HISTOGRAMS OF C.W. TRANSMISSION LOSS
BERMUDA
(FILTERED H.P. CUTOFF 4 CYC/DAY)

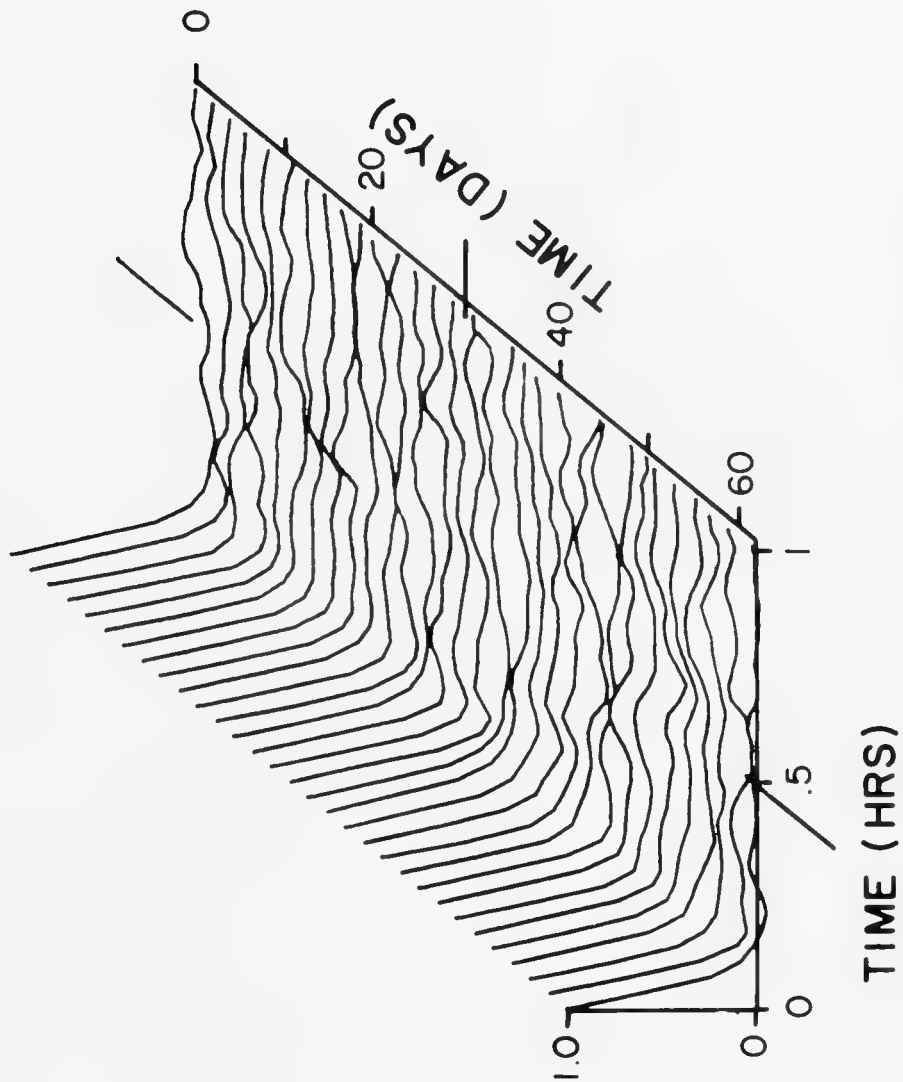


Figure 13. NORMALIZED AUTOCORRELATIONS OF C.W. TRANSMISSION LOSS
BERMUDA
(FILTERED H.P. CUTOFF 4 CYC/DAY)

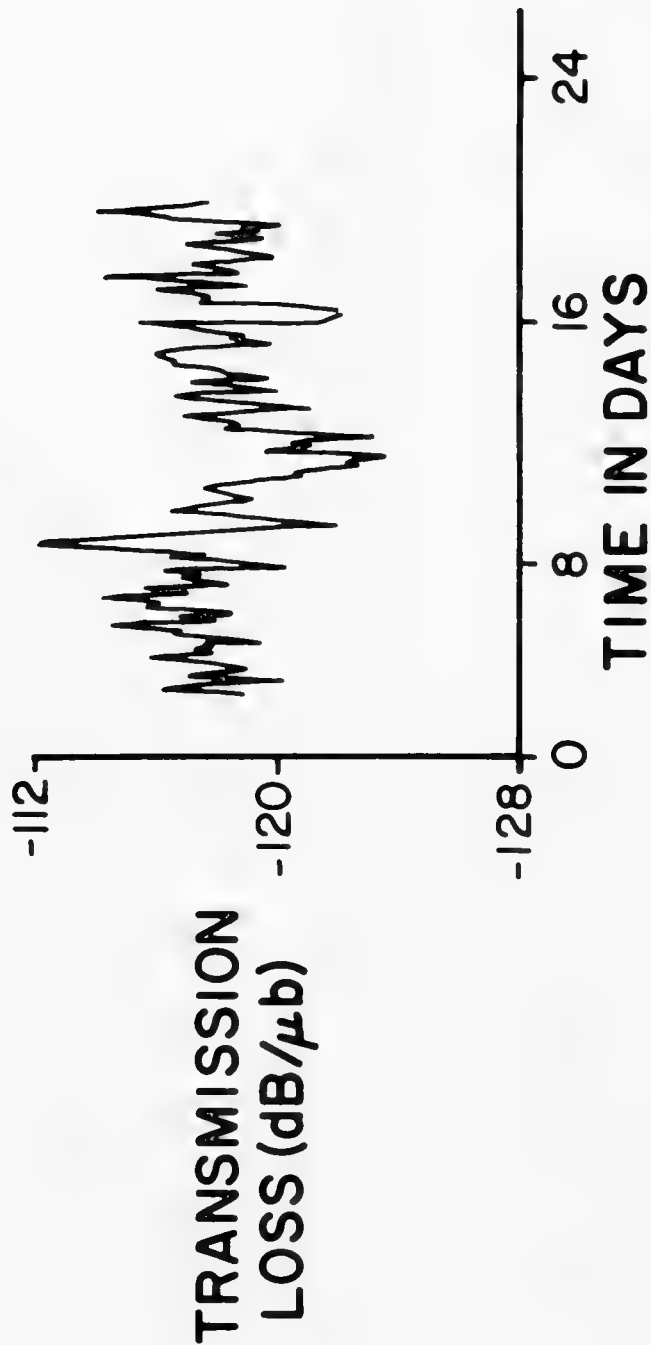


Figure 14. BERMUDA TRANSMISSION LOSS FILTERED LOW PASS CUTOFF .2 cyc/hr

different paths so we may be looking at, say, a twentieth convergence zone sliding back and forth relative to the receiver. There are also significant variations (20-dB or so) on the order of a day which have been omitted for the time being from the study. I don't think they are multipath either.

Figure 15 shows the Bermuda phase record again. The phase has long-term trends in it as well as the tidal component. I have chosen to differentiate this record to look at the rate of change of phase as another variable for comparison. Figure 16 shows these results. Long-term trends have very slow rates of change so they don't contribute very much. One thing that stands out is the large tidal component for both the Eleuthera and the Bermuda ranges. They have about the same average rate of change of phase $\dot{\theta}$, and they have about three or four cycles of change per tidal period. This appears to be a good place to start on some model comparisons.

The first thing that we do with the bilinear profile (shown at the top of Figure 17) is to take a perturbation which is constant with range but varied in time. That is, let the whole profile rise and fall like the first-mode internal tide. The next thing is to adjust the amplitude of the fluctuation so that it gives the right amount of phase shift. However, when we do that, we don't get enough interference. The fades don't come as frequently as they do in the experiment. In fact, there doesn't seem to be any way that you can adjust this profile in this manner to get anything else but the kind of variations shown. The fluctuations that yield large shifts in phase don't give enough amplitude interference, and they decorrelate in about a half hour instead of the four minutes typical of the experiment. This also seems to be true for fluctuations which have a scale larger than the cycle distances of the SOFAR rays. We have tried using an internal tide starting

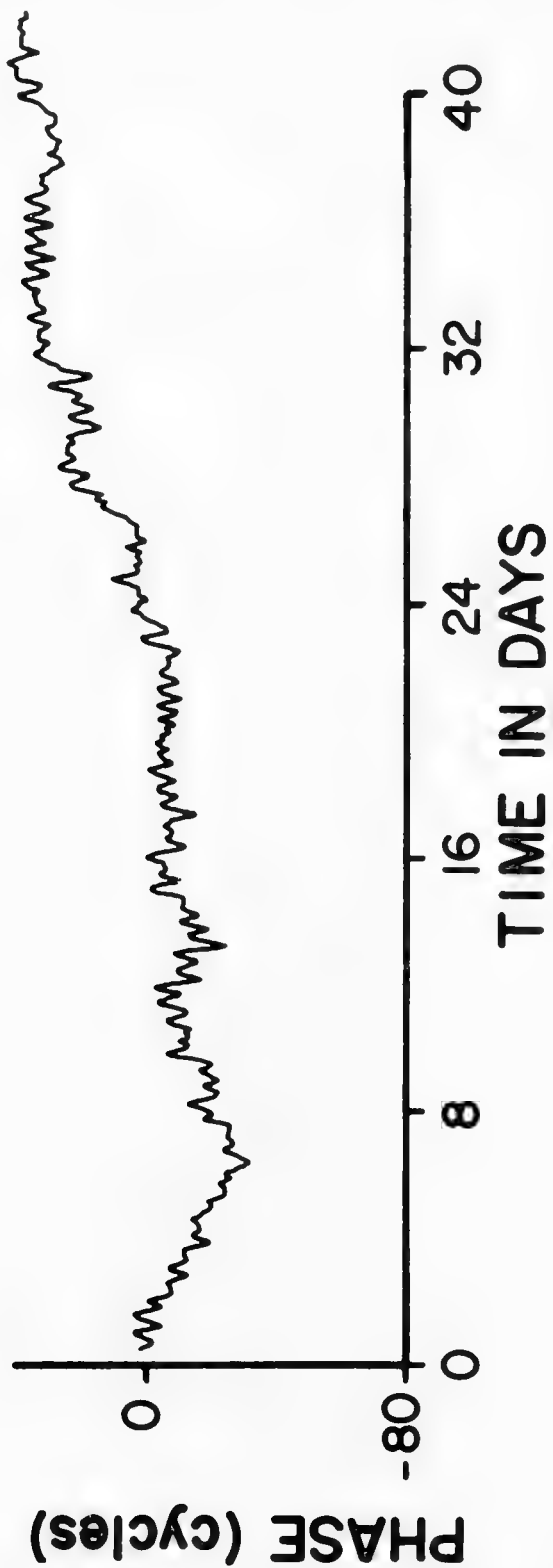


Figure 15. BERMUDA PHASE UNFILTERED

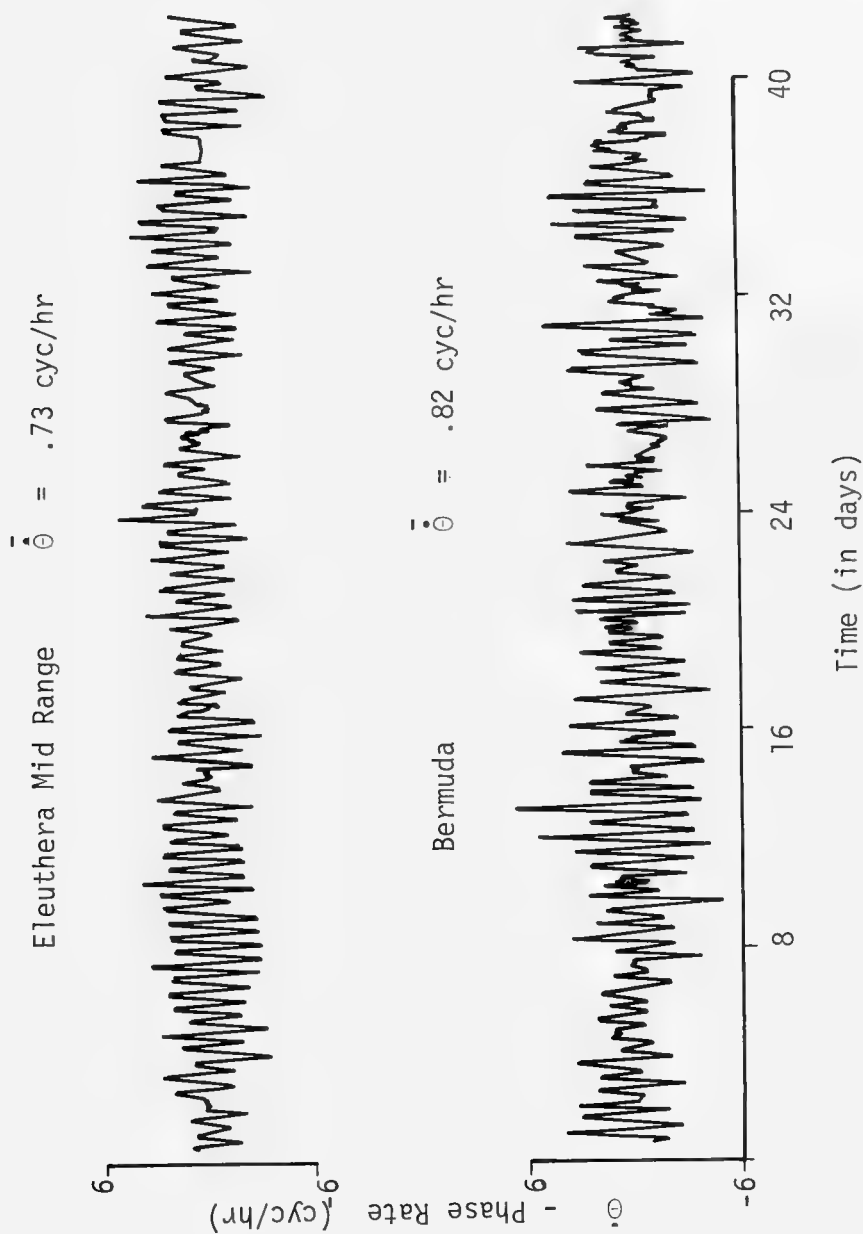


Figure 16. RATE OF CHANGE OF PHASE FOR TWO DEEP OCEAN PATHS

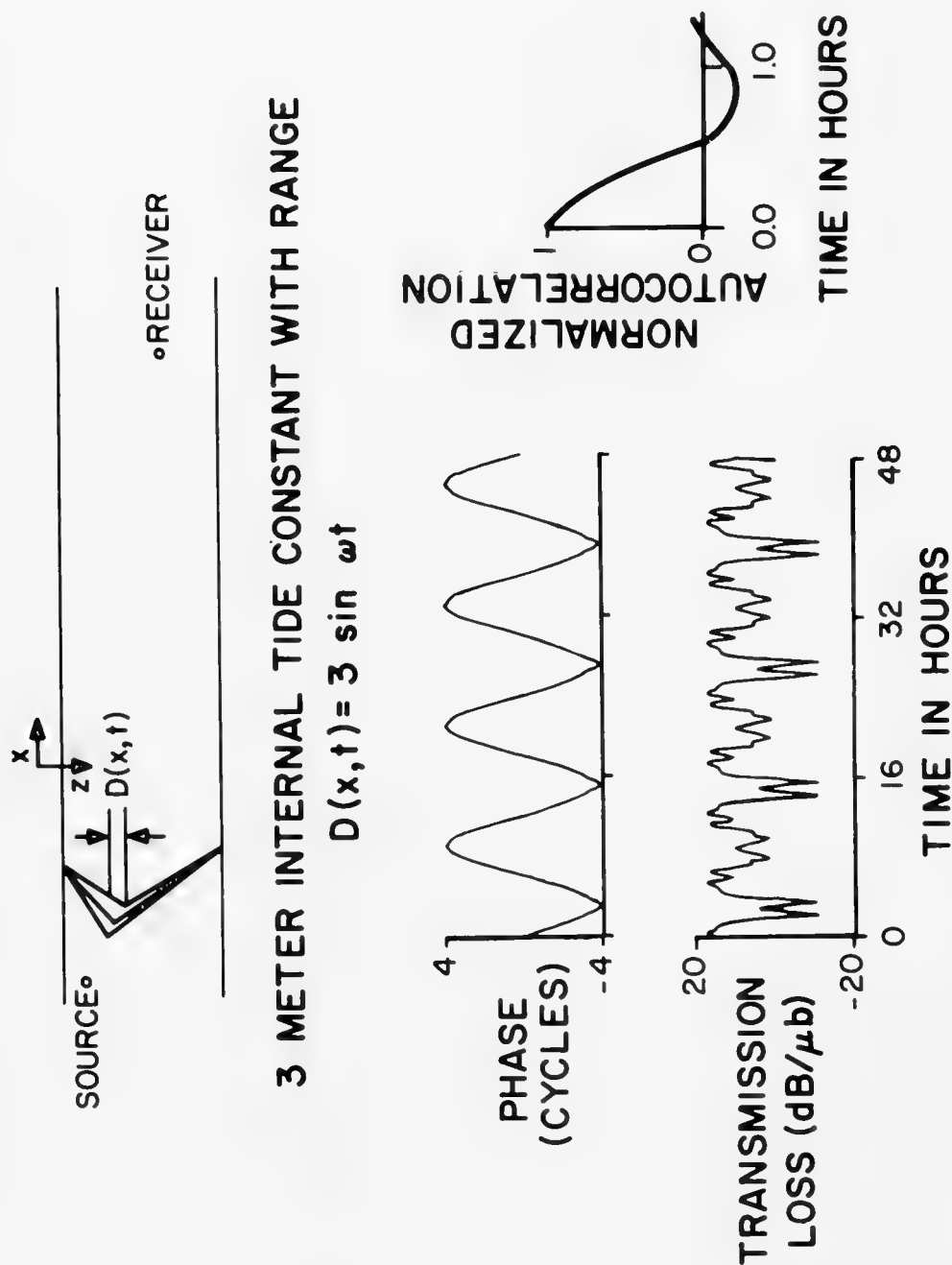


Figure 17. SIMULATED PHASE AND TRANSMISSION LOSS FOR BERMUDA

on the shore and dissipating while propagating seaward. The effect was the same as taking the perturbations and distributing them evenly over the whole range. Basically it provides enough phase shift but not enough interference.

However, using the tidal frequencies and adding a little bit more perturbation to the system we can get the same amount of interference that we see in the experiments. Figure 18 illustrates the procedure where a 4-meter random internal-wave component is added to the decaying tide. It adds no significant contribution to the phase (see middle graph) other than the same jitter. However, the jitter introduces more fades (bottom graph). Each ray basically interacts with fluctuation components of comparable cycle distances. Hence they select the appropriate component from the internal-wave spectrum.

There are a lot of other modes that could be added to the perturbation but all I have put in are tidal-like frequencies. I have broken it up spatially, and it seems to be enough.

The fades that we see are not strictly continuous wave -- that is they have some bandwidth associated with them. One way to measure it is to transmit a broadband signal, a pulse and look at the received time series. Figure 19 illustrates the result of transmitting a 20 millisecond pulse. The signal that arrived was about 100 milliseconds wide representing the superposition of many pulses with slightly different travel times corresponding to different RBR rays. Also a lower level group is seen which appears from the model studies to be an SRBR arrival.

Figure 20 illustrates the behavior of such pulses during the time that a CW signal is fading. The top figure shows the CW amplitude

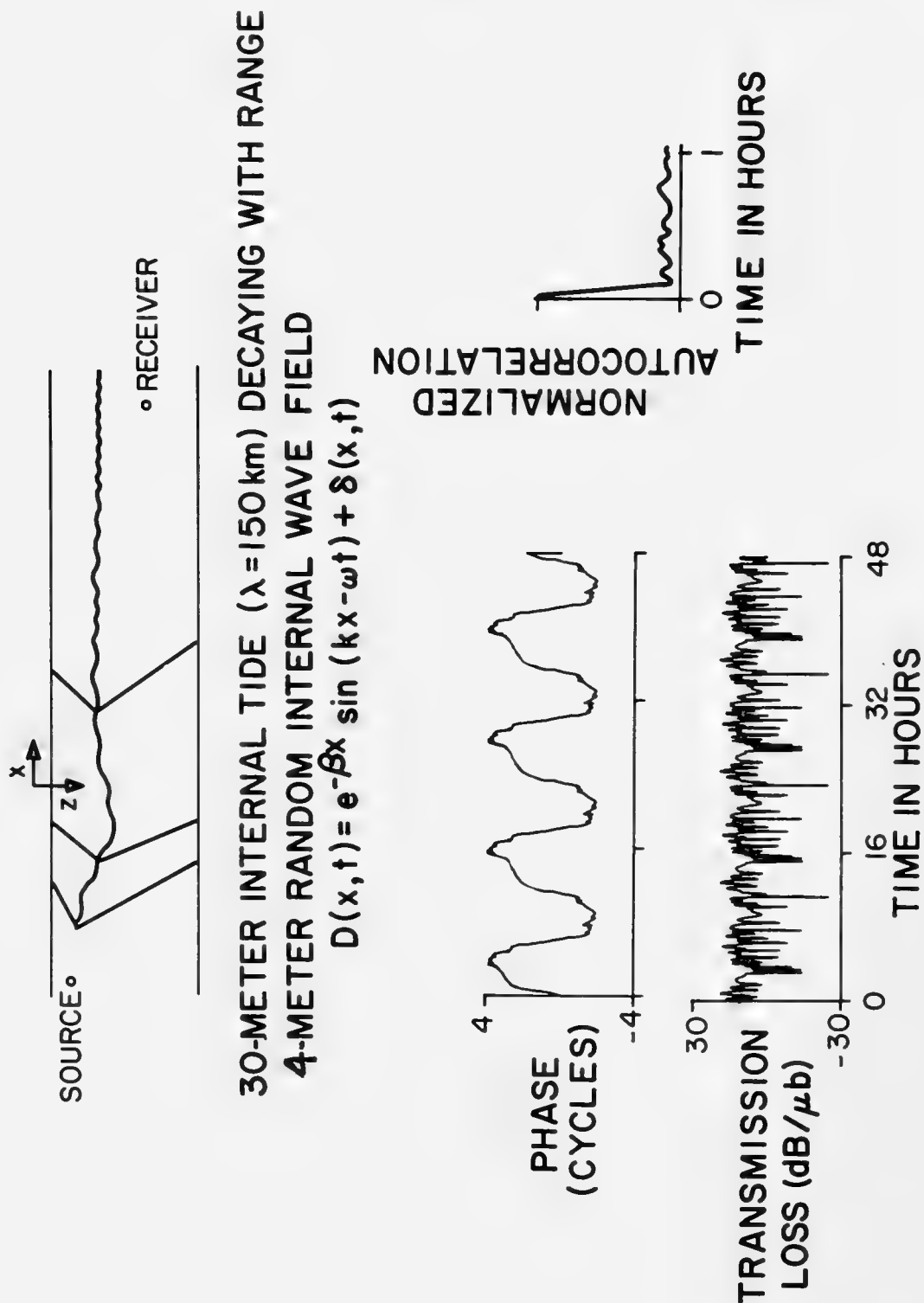


Figure 18. SIMULATED PHASE AND TRANSMISSION LOSS FOR BERMUDA

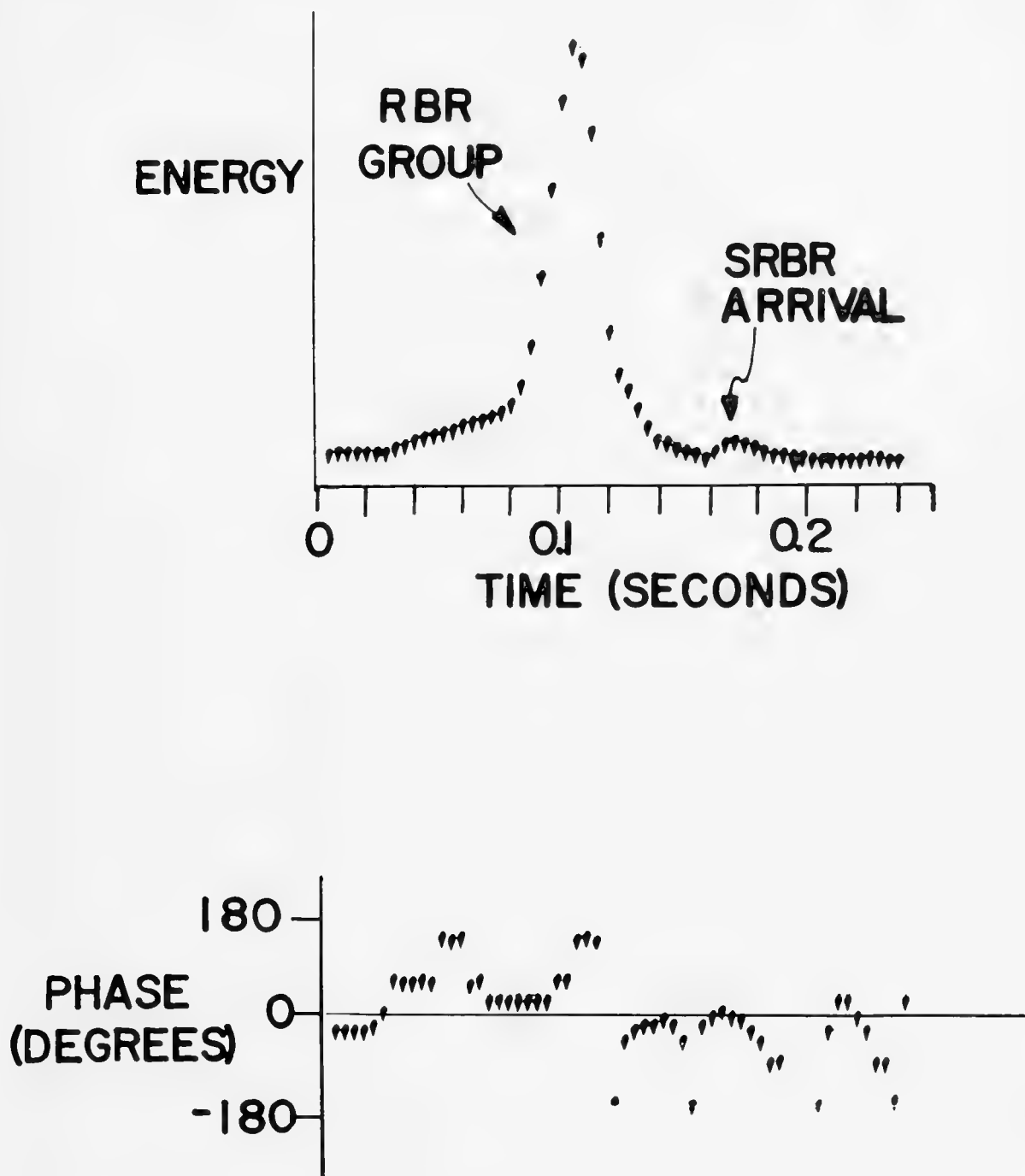


Figure 19. TIME SERIES OF ENERGY AND PHASE
FOR 20 MILLISECOND PULSE

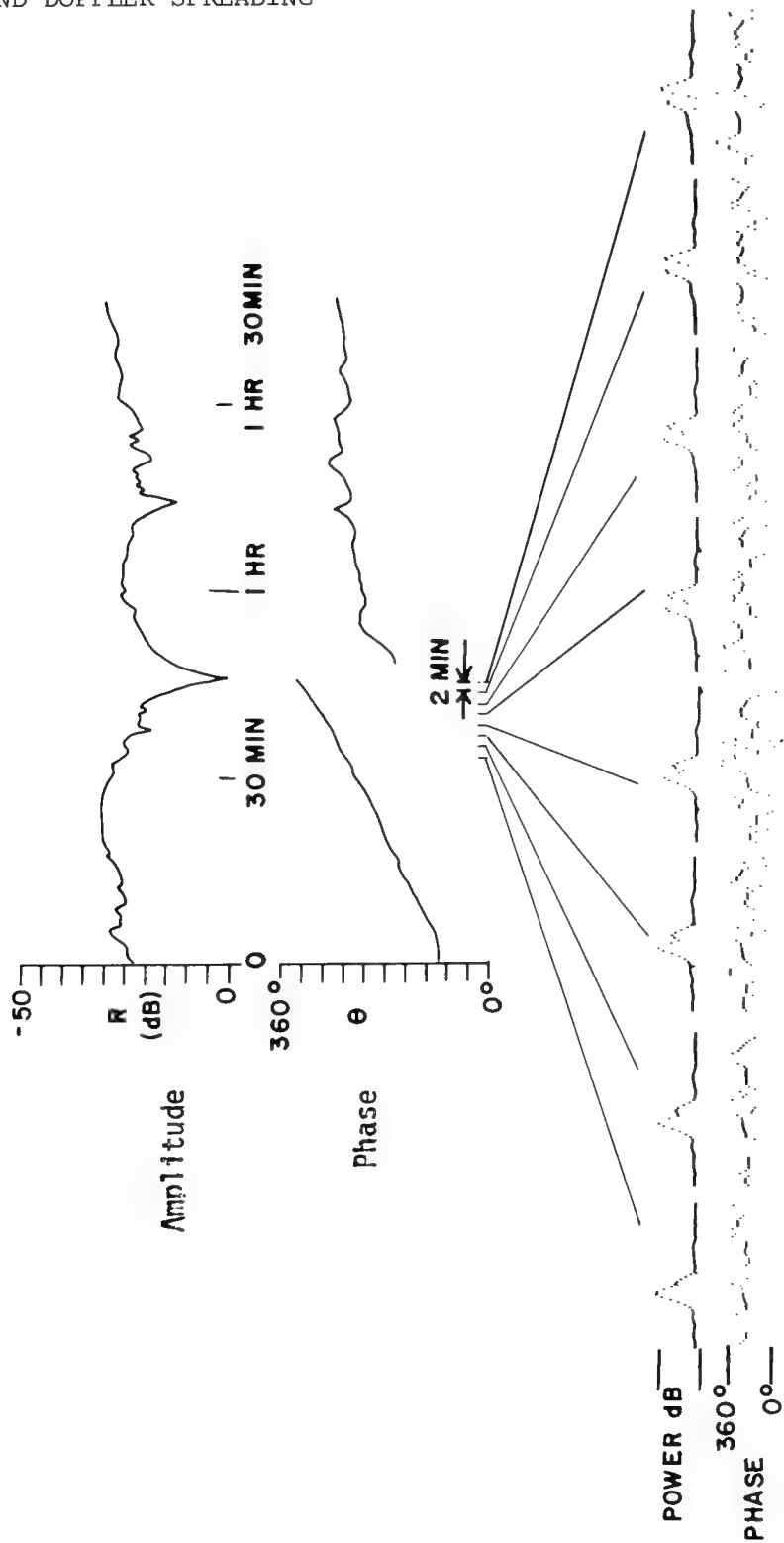


Figure 20. TIME EVOLUTION OF A PULSE DURING A CW FADE

which exhibits a deep fade. The phase of the signal (shown below) goes through a 180-degree phase jump at the fade. For the pulse (bottom figure) a small notch forms on the right side of the pulse which slides across the pulse with increasing time. Precisely in the middle of the CW fade the pulse power is also very low. Traveling with the notch is a 180-degree phase jump.

What this says about the CW fade is that at the instant of the deepest part of the fade, the energy is equally split into two components which are 180 degrees out of phase with each other and hence cancel. On the other side of the fade the resultant vector shows up 180 degrees reversed from before the fade. The only way this can happen is if the perturbation that's causing it is causing all the arrivals -- there are 15 arrivals in the pulse -- to slide relative to each other. So it appears to be a broad-scale process rather than a localized fluctuation.

Figure 21 shows a model simulation where the gradient shifts slowly with time. The pulse response is in the left column and the phase is in the right column. A small notch forms in the pulse and slides across the pulse, notching it out. Traveling with the notch is a 180-degree phase shift. These results contain 15 arrivals each with slightly different travel times.

An alternate representation of this fading is shown in Figure 22 in terms of a series of measured power spectra of successive pulses. The carrier is the center line at 420 Hz. What happens here in time is that we are going through a CW fade. Transmission is falling off and coming back up again on the carrier. For the full spectrum it is apparent that the fade slides across the band resulting in selective fading.

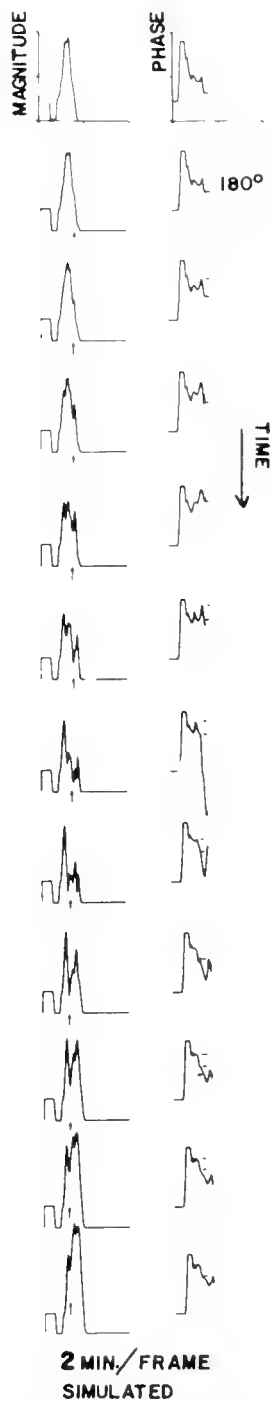


Figure 21. MODEL SIMULATION OF PULSE EVOLUTION FOR
SLOWLY VARYING SOUND-SPEED GRADIENT

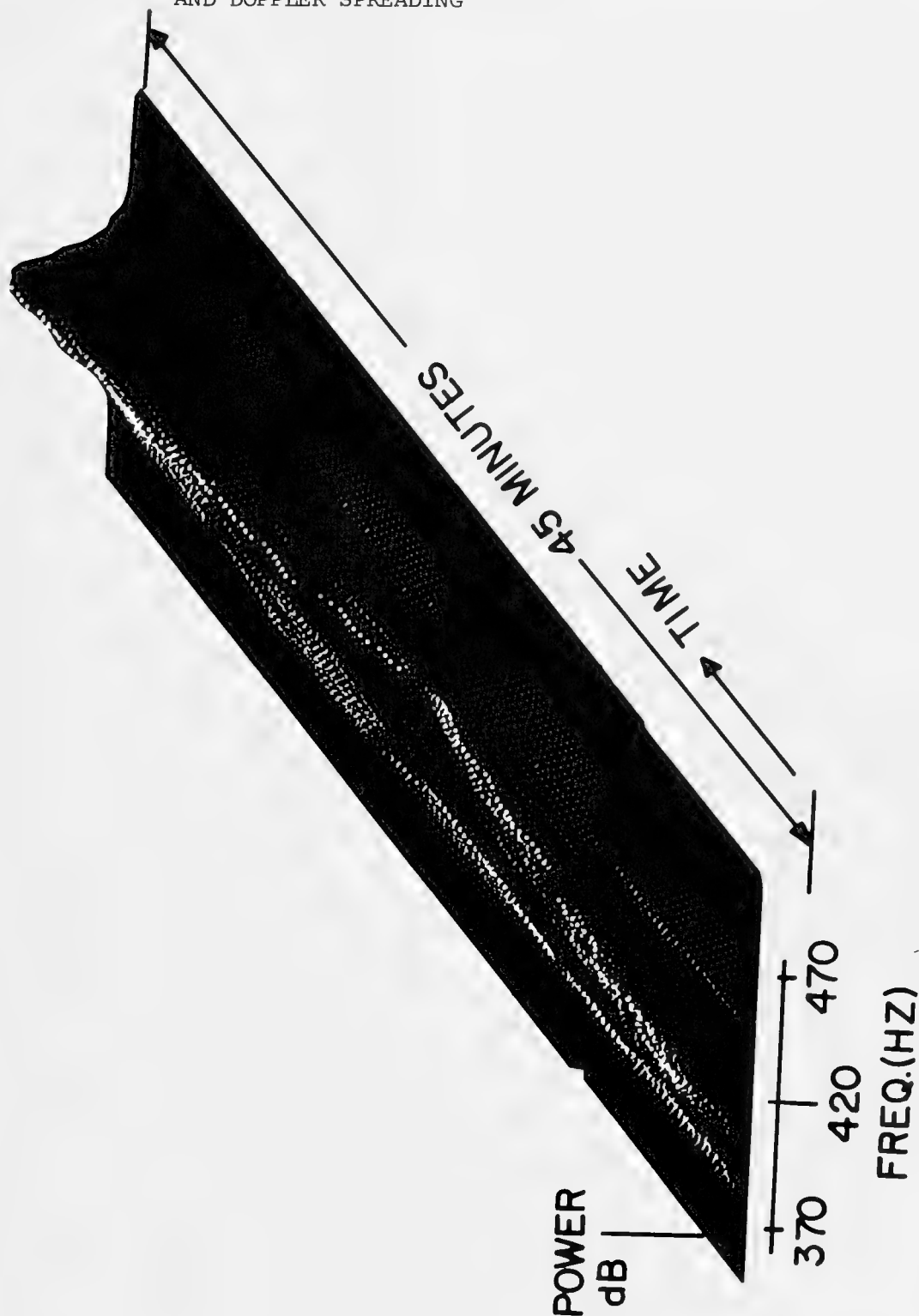


Figure 22. POWER SPECTRA VARYING IN TIME

Figure 23 illustrates a modeled case for a typical sound-speed profile measured in the Florida Straits with a small perturbation added to it. On the left is an amplitude-frequency-time plot and on the right is a phase-frequency-time plot. Note the two fades at early times. As time goes on they slide across the band. Traveling with the deep fade is a 180-degree fade shift. The other fade isn't quite as deep and its phase shift is somewhat less than 180 degrees.

While no one would claim to be able to predict when these fades will occur, certain features are predictable, notably the bandwidth. The bandwidth depends on average characteristics, not on the detailed fluctuations in the sound-speed profile. The precise time of the fade is determined by extremely small changes in the profile and hence is not predictable.

The models not only predict the frequency response but can also simulate spatial processing; for example, a coherent summation at several points. The modeled fade cells as shown in Figure 24 are small and isolated at 100 Hz. One of the few advantages of ray theory is once you make this computation you can change the frequency and easily consider several frequencies. Figure 25 is the same kind of plot for 200 Hz. (Note: there's a scaling of a hundred to one from range to depth so these contours are actually very elongated. The contour interval is 5 dB.) Figure 26 is the same thing at 420 Hz.

I would now like to present some Doppler-spread data. Figure 27 is a typical Doppler spectrum I measured in the Florida Straits. The carrier line at 420 Hz has been suppressed to emphasize the sidebands. The sidebands are characteristically asymmetric and differ by 3 to 6 dB almost always. The spectrum appears to be a replica of the surface-wave spectrum.

$$\begin{aligned} g_1 &= 0.145 \pm 0.015 \quad 1/\text{SEC} \\ g_2 &= 0.385 \quad 1/\text{SEC} \\ D_1 &= 85 \text{ M} \\ C_1 &= 1487 \text{ M/SEC} \end{aligned}$$

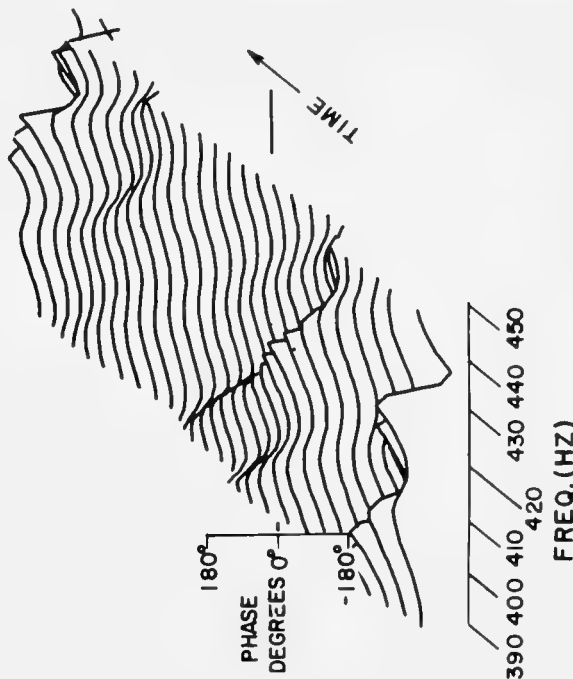
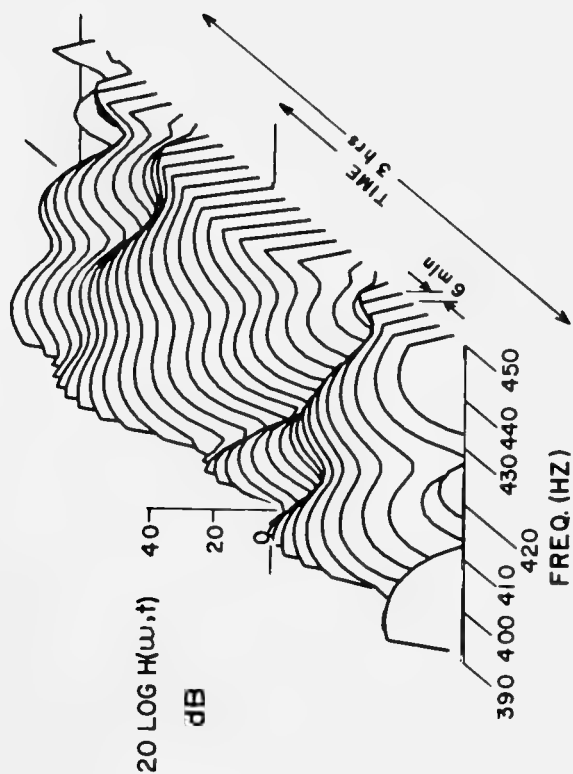


Figure 23. MODELED POWER SPECTRA EVOLUTION FOR FLORIDA STRAITS

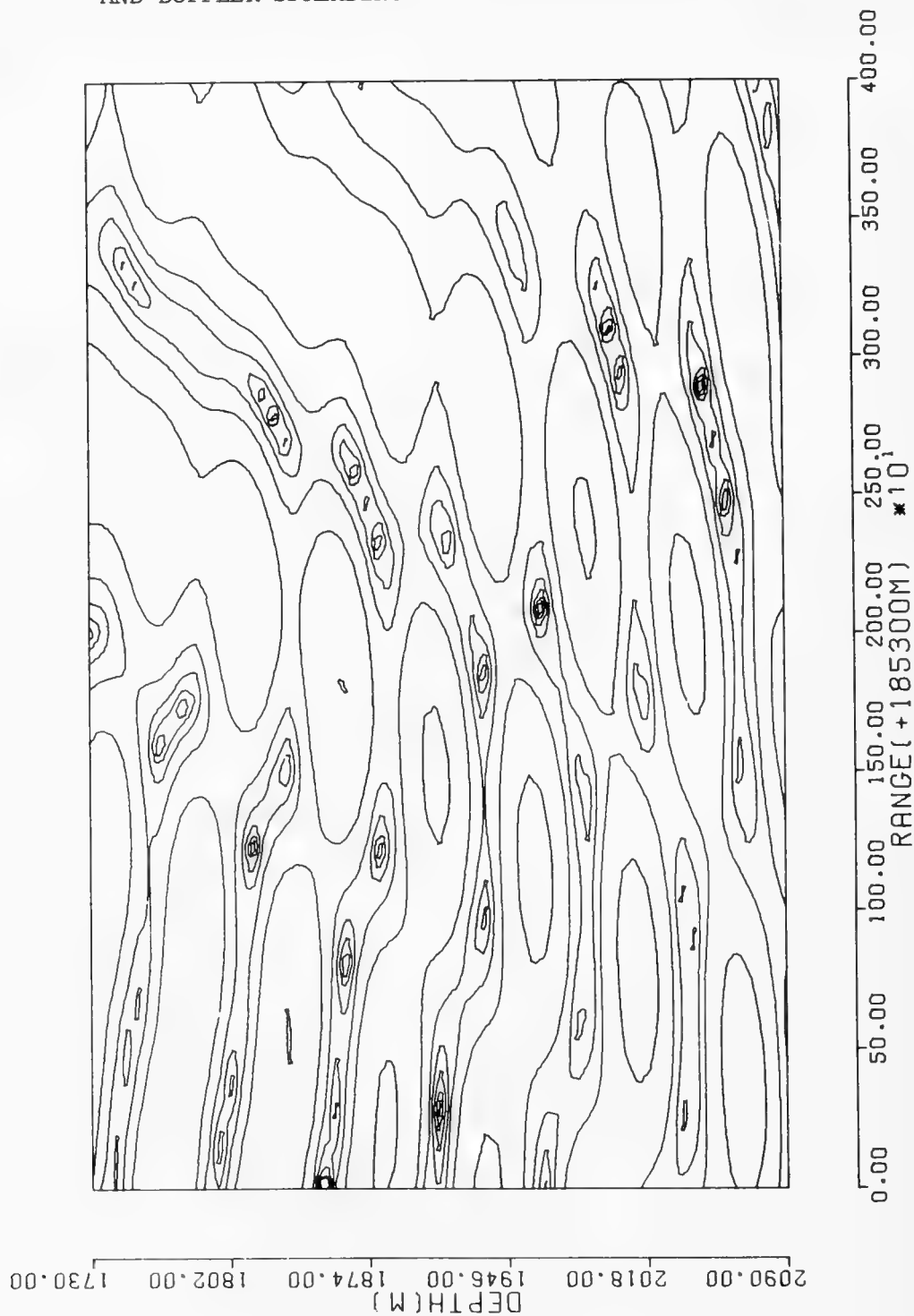


Figure 24. TRANSMISSION LOSS CONTOUR AT 100 Hz.

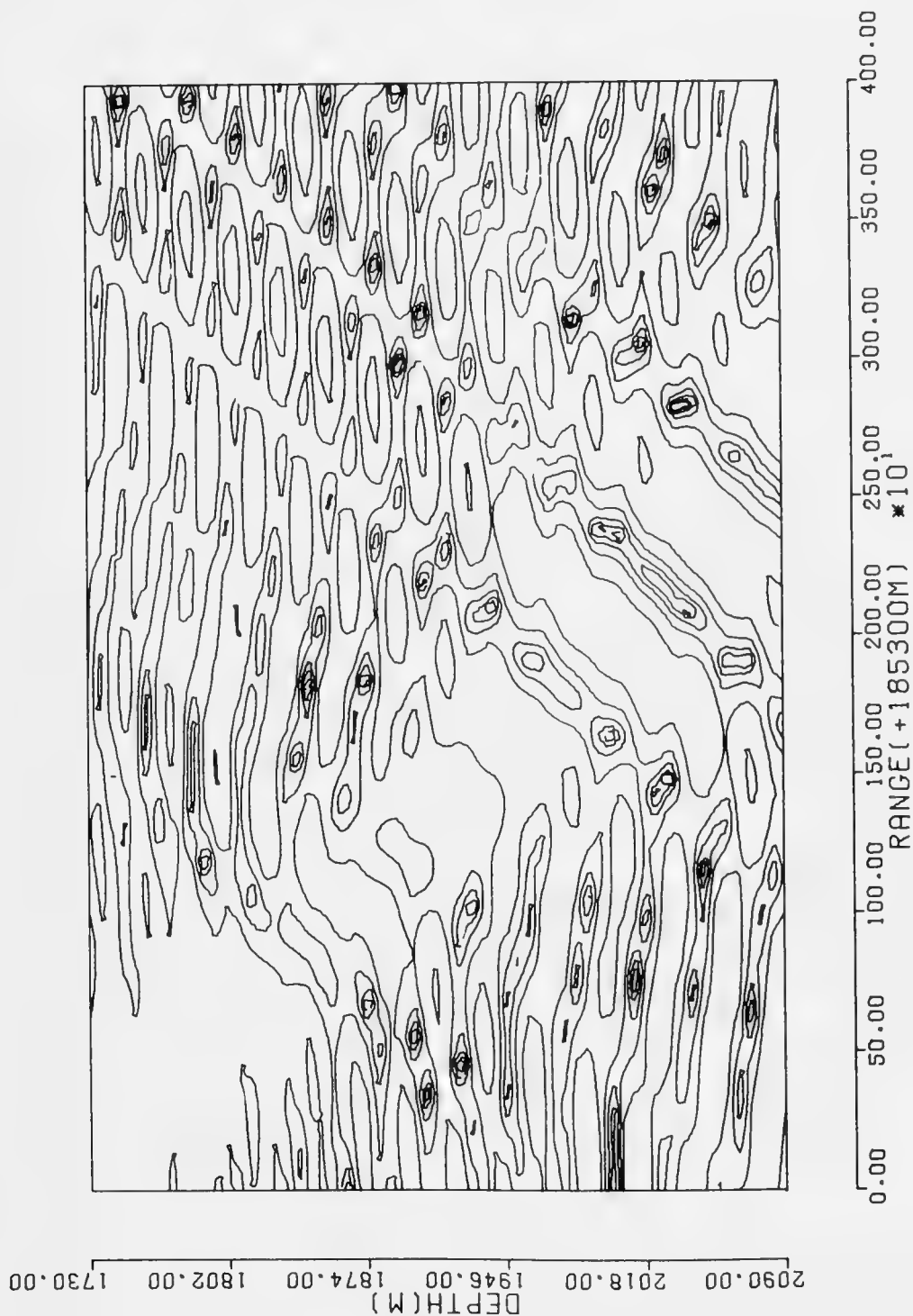


Figure 25. TRANSMISSION LOSS CONTOUR AT 200Hz.

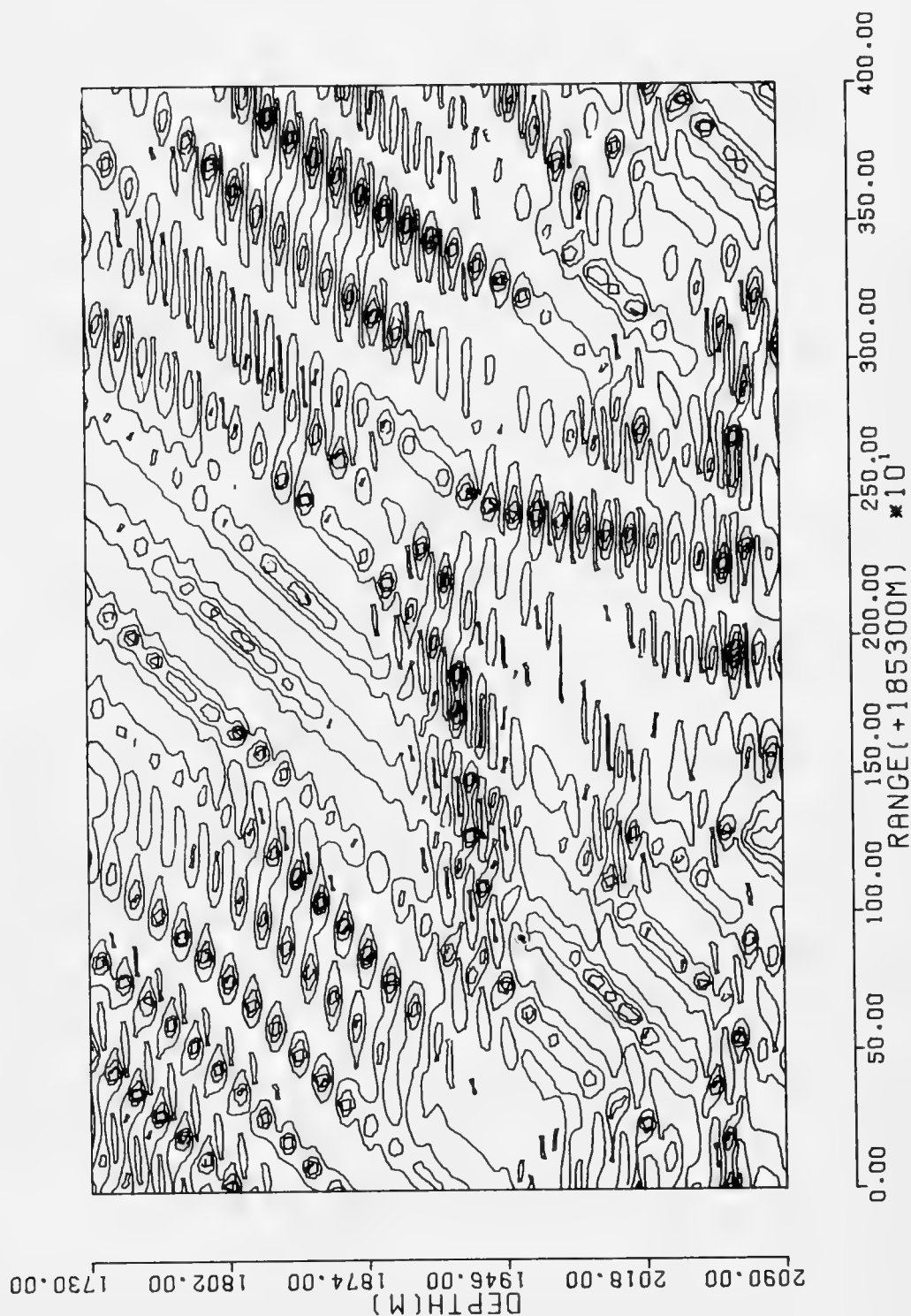


Figure 26. TRANSMISSION LOSS CONTOUR AT 420Hz.

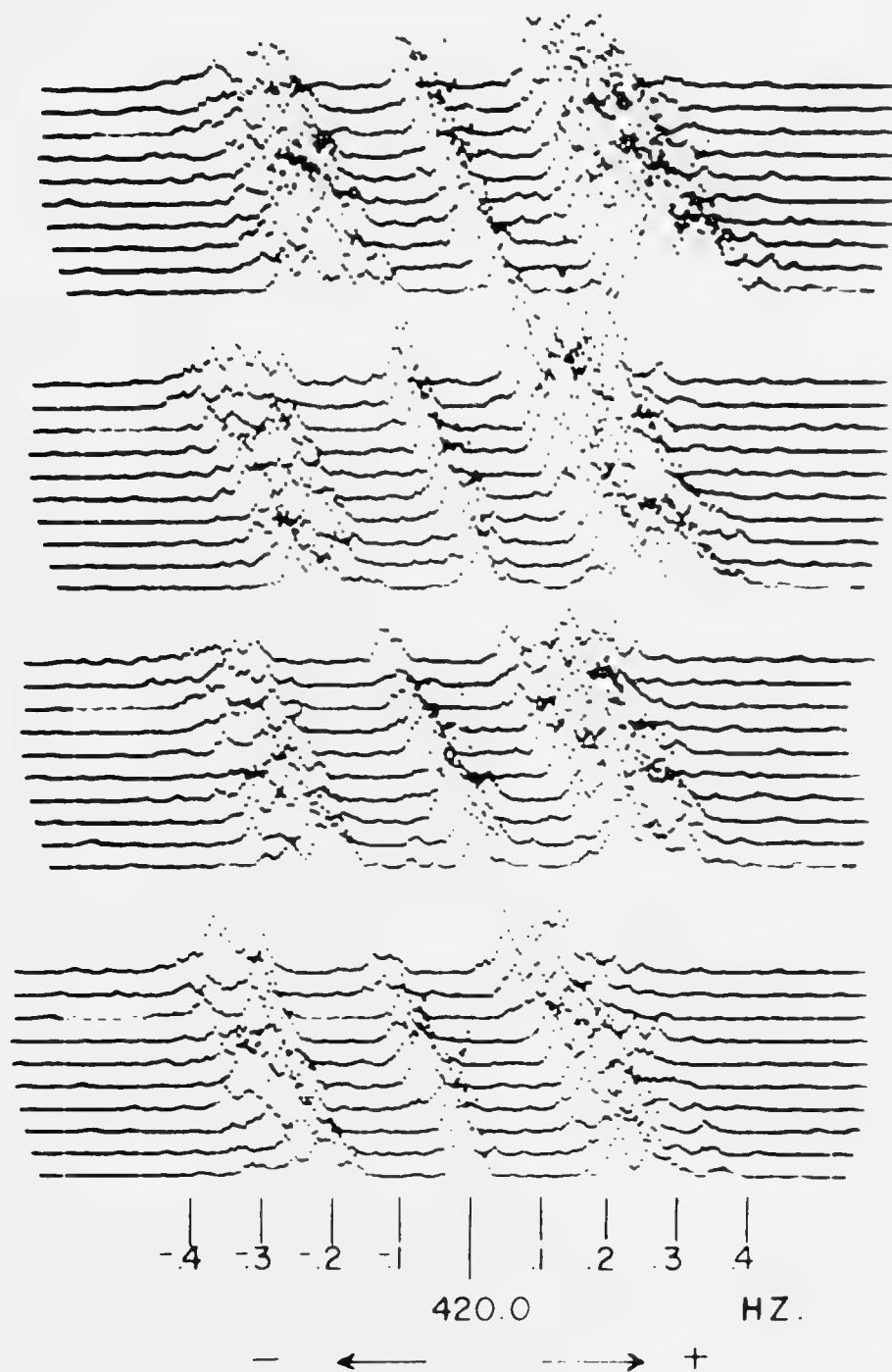


Figure 27. MEASURED DOPPLER SPECTRA IN FLORIDA STRAITS

One of the things I wanted to do in the model work was to include all possible scattered arrivals as well as the specular paths and to look at the resulting distribution for a pulse both in time and frequency. Figure 28 shows the modeled results for levels as a function of time. The top line represents the RBR rays with their characteristic buildup as they stay closer and closer to the bottom. Successive arrivals have one additional bounce. SRBR arrivals (second line) tend to spread out because they are traveling up and down and each order has a significantly greater travel time. They have a little spreading-loss anomaly in the beginning, and then drop in amplitude as a result of the surface interactions.

The model predicts that the Doppler-shifted energy is going to come in and peak out somewhere behind the main RBR group. The first SRBR doesn't have any arrivals that get there at about the same time. The later ones have one or two. Then they peak out with four or five. The surface bounces then start to take over.

Figure 29 is a measurement of this process. The Doppler spectrum has been measured for each successive part of the received signal for a transmitted pulse. Repetitive pulses are actually used to obtain these data. They come in just the way the model says at about the right intensity.

These computations gave me enough confidence in the model to attempt the deep ocean case. Figure 30 corresponds to the 700-nautical-mile case. The bottom line shows the refracted-refracted (RR) rays coming in with various intensities. The top two lines show the RBR rays and SRBR arrivals. The third and fourth lines show the up- and down-Doppler scattered arrivals, respectively. Our model keeps track of all these arrivals, and the Doppler spectrum is predicted to be asymmetric.

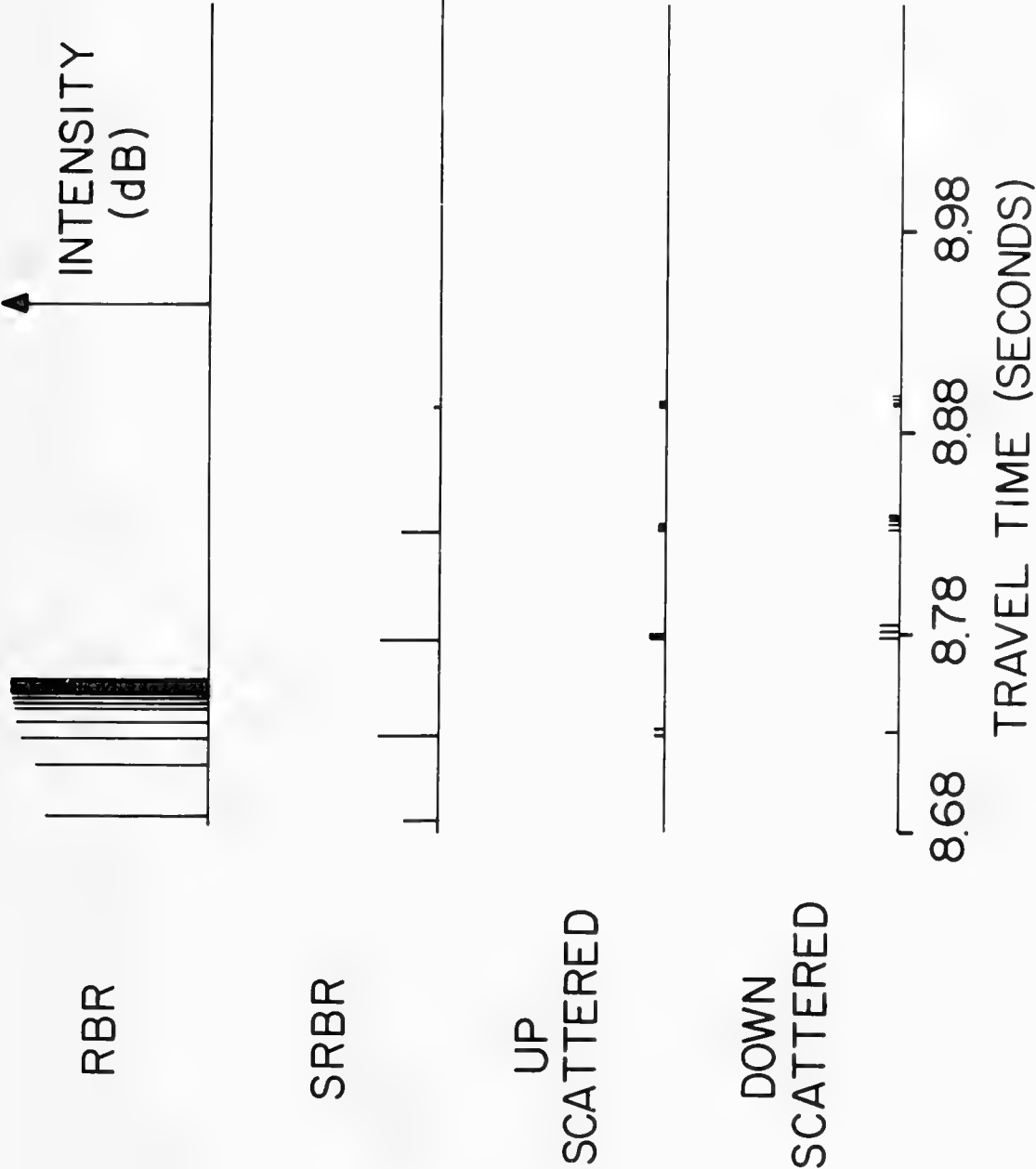


Figure 28. ARRIVAL TIMES & LOSSES

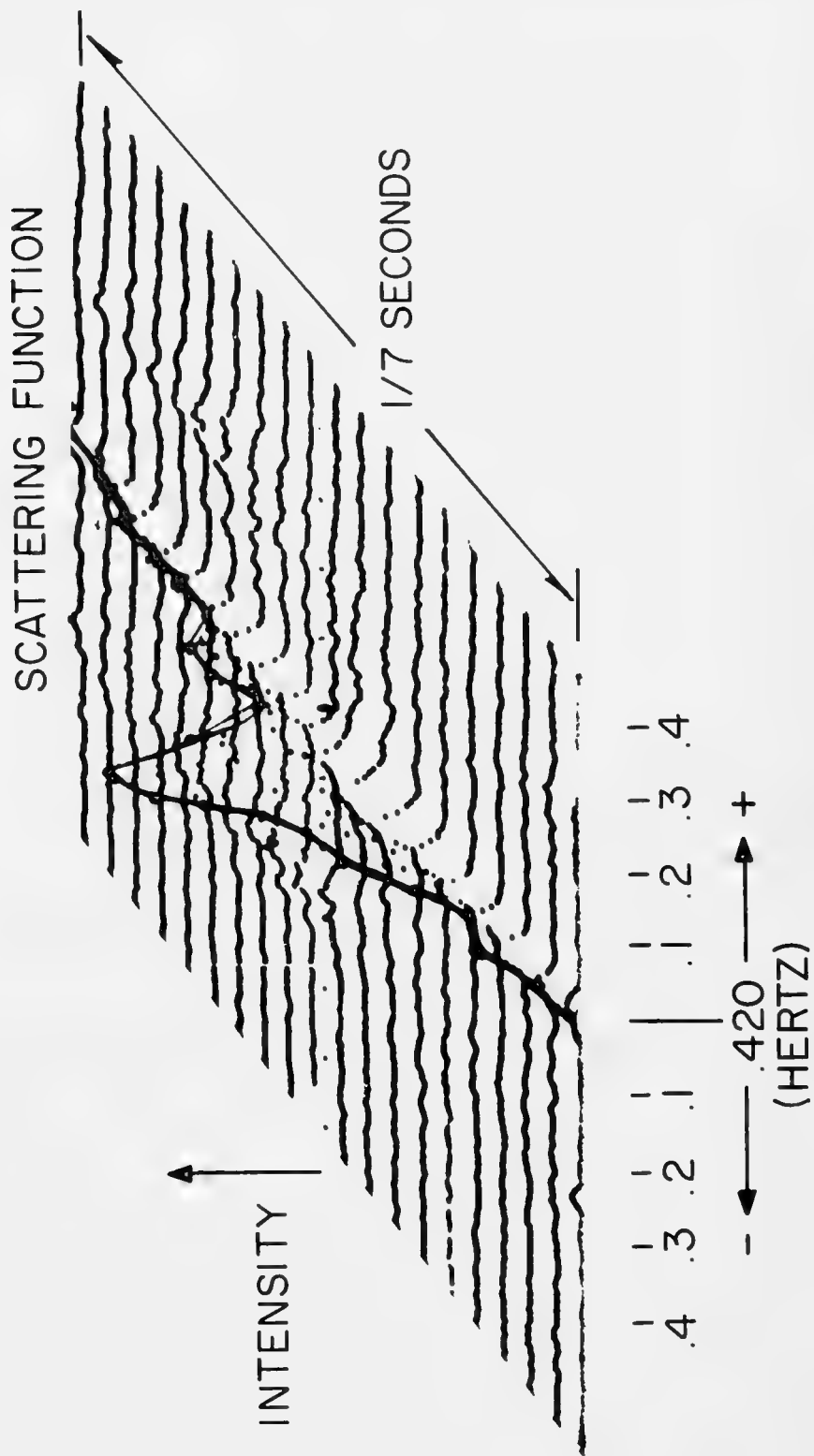


Figure 29. MEASURED DOPPLER SPECTRA EVOLUTION

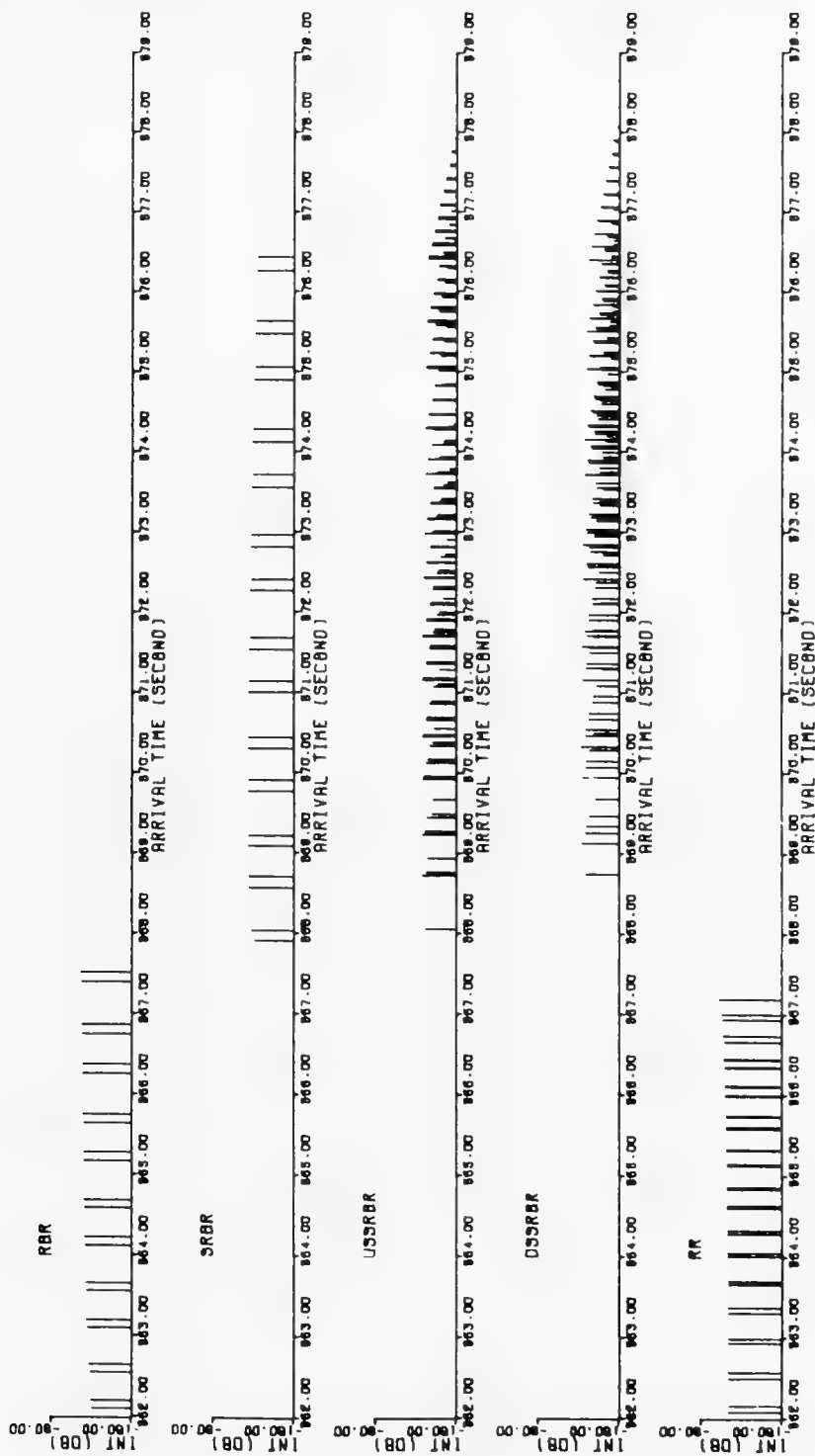


Figure 30. ARRIVAL STRUCTURE FOR DEEP OCEAN CASE

I would like to go back now and look at one specular arrival and the family of scattered arrivals that have the same number of surface interactions. Figure 31 illustrates the SRBR structure plotted in terms of the intensity versus arrival time for the same total number of surface reflections (25). The number next to each arrival indicates the number of specular bounces it had made prior to emitting the scattered ray which happens to hit the receiver. The one marked "24" made 24 specular bounces before it emitted the ray. Note that the rays which scatter at the ends (either near the source or near the receiver) suffer the least loss.

The same information can be expressed in terms of the grazing angle that the arrivals make with the bottom after scattering (Figure 32). All the arrivals that interact in the last half of the received pulse have a significantly lower grazing angle, about 5 to 10 degrees, than all those that are in the first half. Also the first half are all upscattered, whereas the second half are all downscattered. The difference in the bottom loss with these different grazing angles is enough to cause the consistent 3 to 6 dB sideband asymmetry.

Figure 33 is the predicted Doppler spectrum (or more properly the transfer function which must be multiplied by the surface-wave spectrum to get the Doppler spectrum). Note the 3 dB difference in the side bands. The scattering event itself is symmetric. Because of the differences caused by: (1) the angle at which the ray is emitted from the surface and (2) the requirement that the ray hit the receiver, the upscattered paths have significantly less loss than the downscattered paths. These results are quite consistent with what is observed in measured data.

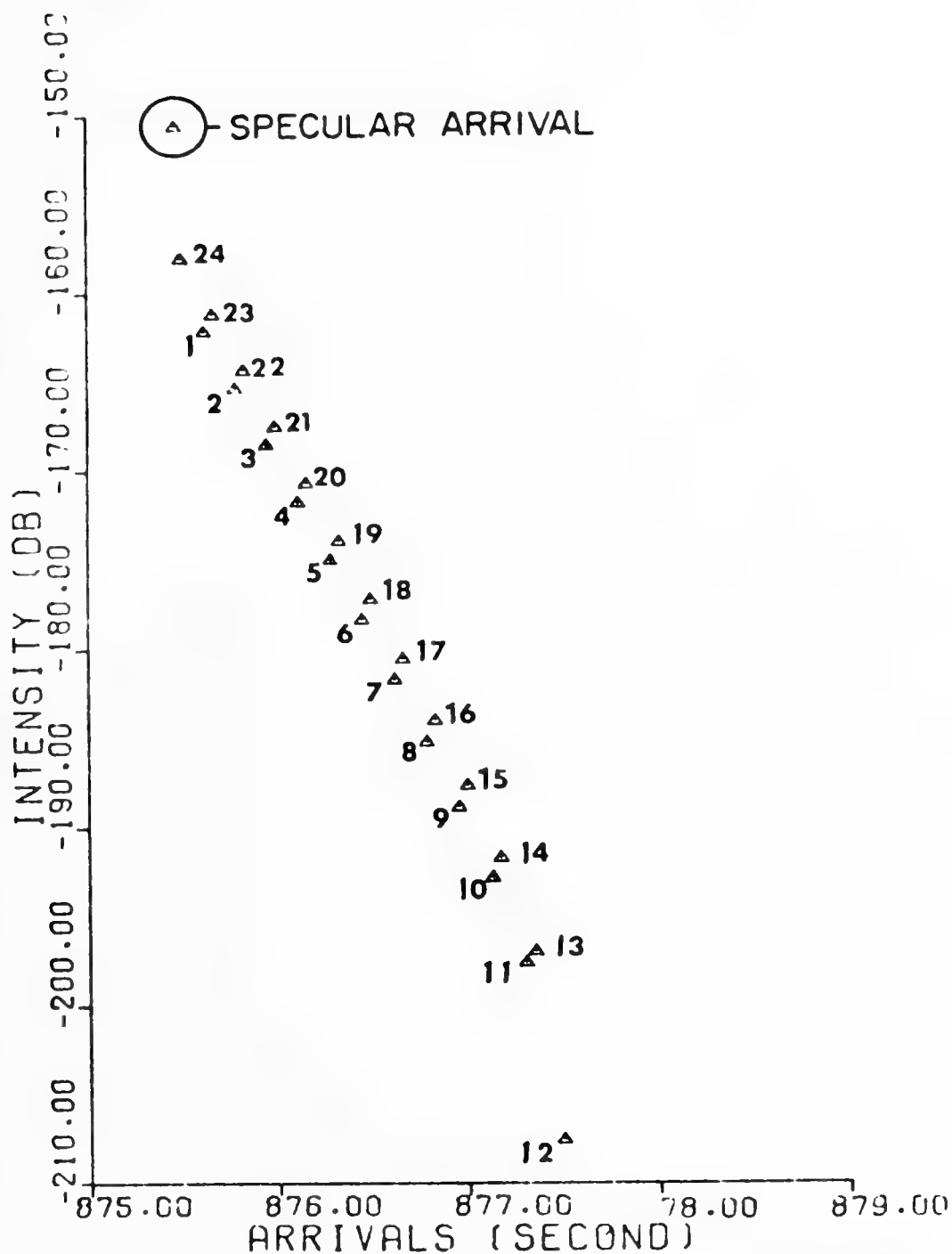


Figure 31. SCATTERED-SRBR ARRIVALS VS TRAVEL TIME

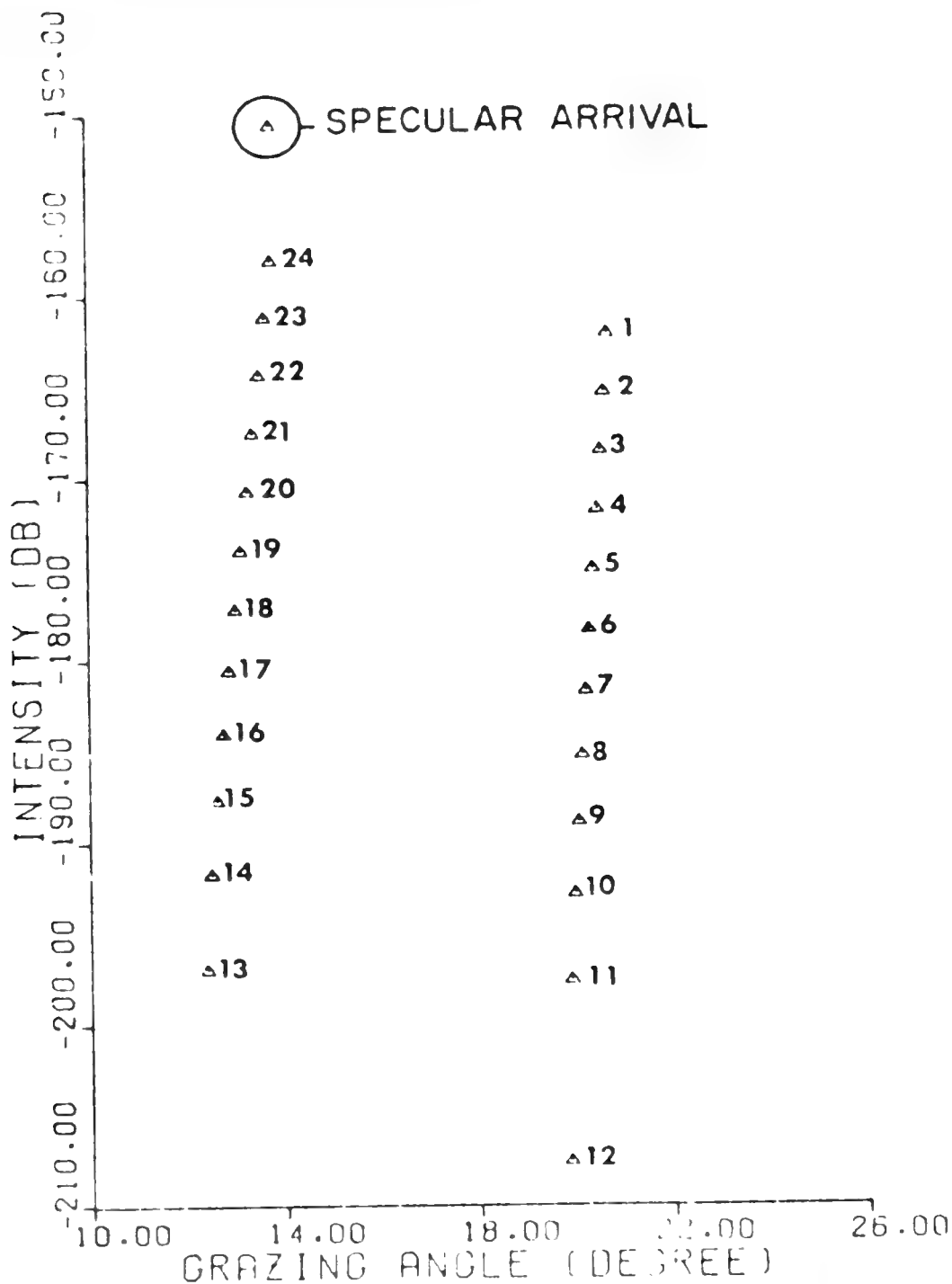


Figure 32. SCATTERED-SRBR ARRIVALS VS SOURCE ANGLE

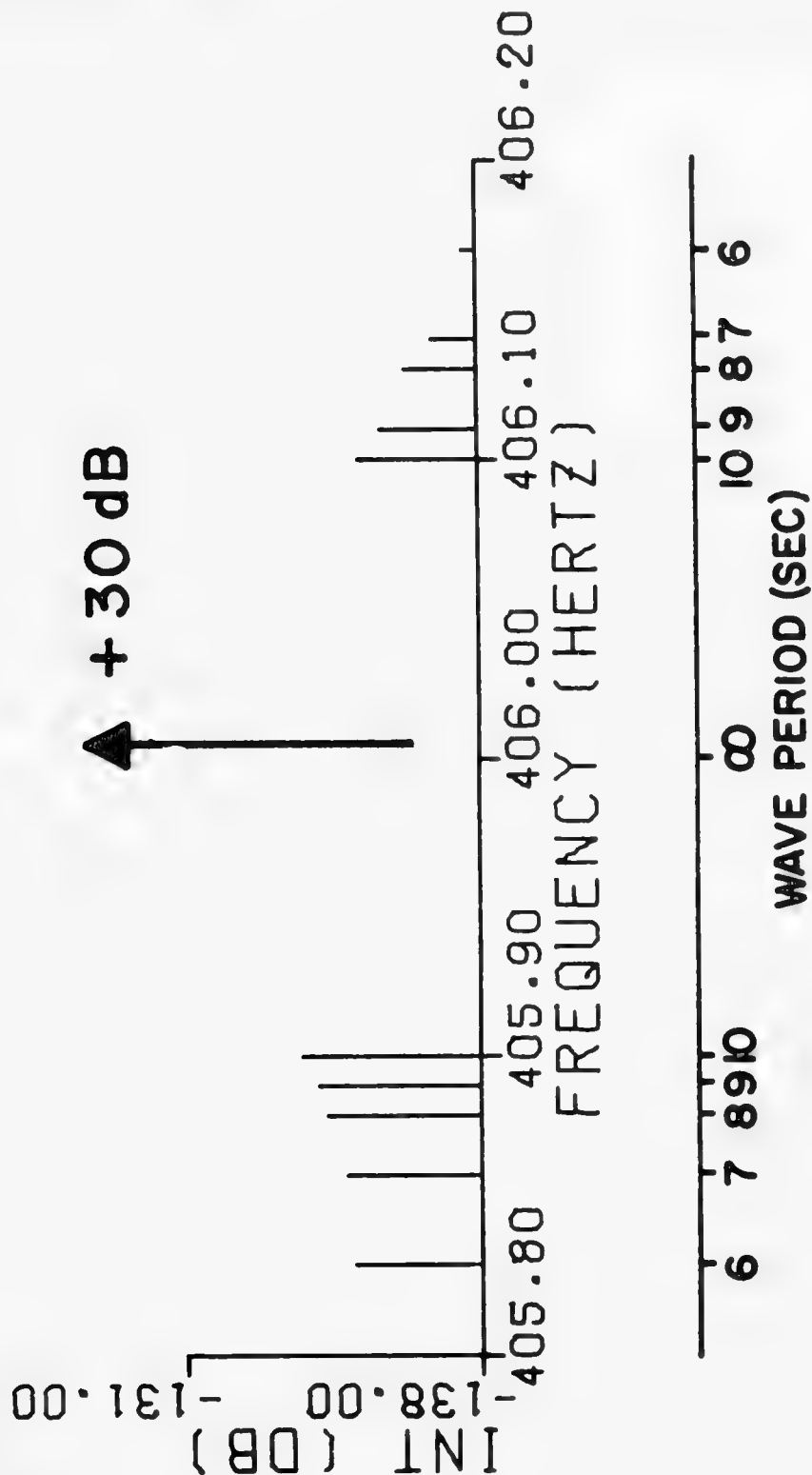


Figure 33. PREDICTED DOPPLER SPECTRUM

DESIGN OF TRANSMISSION LOSS EXPERIMENTS

J. S. Hanna

Office of Naval Research
Code AESD

The conceptual design of transmission loss measurements is discussed. The concern here is not with the hardware implementation of a desired measurement, but with the definition of what is to be measured given everything we know about the medium, the acoustic sources, and the available processing techniques.

The cyclical effort of the past in which models were used to interpret data, and the data in turn used to refine models, is drawn upon to illustrate some general properties of the impulse response of the ocean. Given these general properties, the following topics are addressed:

- 1) The nature of sound sources (impulsive and continuous wave) and the limitations each imposes upon our ability to measure the spectrum of the ocean's impulse response
- 2) The selection of a signal processing scheme (analog or digital), given the expected nature of the impulse response and the properties of the sound sources
- 3) Examples of measurements which, in some cases have and in others have not permitted meaningful interpretation of the results; these examples illustrate common problems and the way they can be avoided.

INTRODUCTION

The objective of any transmission loss experiment is to measure a particular property of the ocean environment, namely its effect on the transmission of an arbitrary signal between two points. This seemingly obvious statement is worth making because some measurements have been conducted in a way which has inextricably confused the properties of our measurement system (source and signal processor) with those of the medium.

If one could determine the impulse response of the ocean between any two points, then, in principle, one can predict what will happen to any signal which propagates between these two points. As a practical matter, however, one can only aspire to measure a band-limited version of this impulse response. If it is furthermore realized that the modelers are interested in not just an experimental determination of the impulse response, but in its interpretation through physical properties of the environment, it becomes clear that measurement planning must consider: 1) the expected properties of the impulse response, and 2) the limitations imposed by signal sources and processors upon the measurement of this impulse response. In the course of this paper, both these topics will be considered.

THE IMPULSE RESPONSE

For the purpose of illustrating some properties of the impulse response, it will be assumed that the medium is not dispersive (that is, the medium simply attenuates the amplitude equally at all frequencies and introduces at most a phase reversal upon reflection from the ocean surface). Consider, then, the hypothetical, idealized impulse response of Figure 1 which consists of four arrivals time-delayed according to the history in the upper right-hand corner. There are two pairs of arrivals separated by a time Δt . The total history is assumed to correspond to the four arrivals of a single order for some source-receiver geometry. For the sake of example the two time differences and amplitudes were selected as shown and the spectrum of the resulting impulse response displayed in the figure.

By way of interpretation, the 40 Hz periodicity corresponds to the time delay Δt while the 2 Hz periodicity corresponds to the time delay ΔT . For a more complicated arrival structure there will be a

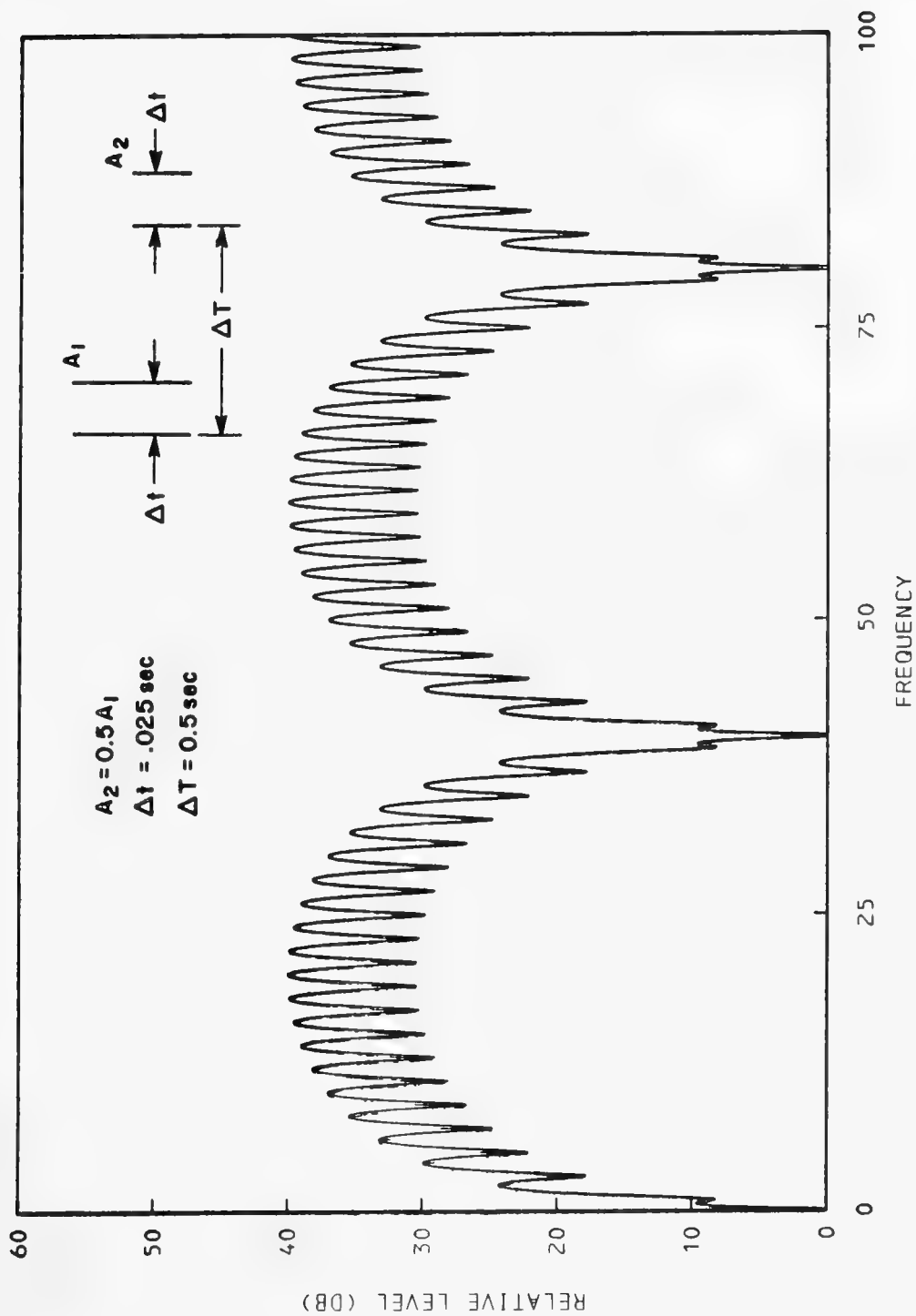


Figure 1. EXAMPLE OF AN IMPULSE RESPONSE FUNCTION

periodicity in the spectrum corresponding to each pairwise time delay in the time history. (It will become apparent shortly that, depending upon the desired characterization of the transmission loss, it is necessary to anticipate the relative time history of arrivals and, thereby, the general structure of the spectrum of the impulse response.) Further elaboration of the model to include such features as frequency dependent absorption and frequency independent phase shifts (such as produced by caustics) will cause details of the spectrum to change; however, the basic periodicities induced by the travel-time differences will remain. It is these periodicities which will drive our later concerns.

SOME COMPLICATIONS

Limitations of Impulsive Sources

The desire to measure the spectrum of the impulse response between any two points runs rapidly into some practical difficulties. To measure a spectrum, such as shown in Figure 1, requires a source of energy with a flat, featureless spectrum over the frequency domain of interest. In general, such sources can only be approximated, often poorly. The most widely used impulsive source in Navy measurement work is the explosive charge. However, because of the presence of bubble pulses, these explosives themselves have a rich spectrum which may rival that of the ocean's impulse response.

Examples of these spectra for 1.8-pound charges of TNT detonated at 60 and 800 feet are shown in Figures 2 and 3, respectively. In Figure 2 the rapid (~ 6 Hz) variation is the bubble pulse frequency while the slower (~ 80 Hz) variation is caused by the surface-reflected arrival. (Both spectra shown in Figures 2 and 3 are low-pass filtered at 300 Hz.) It is quite possible to produce a 6 Hz period in the

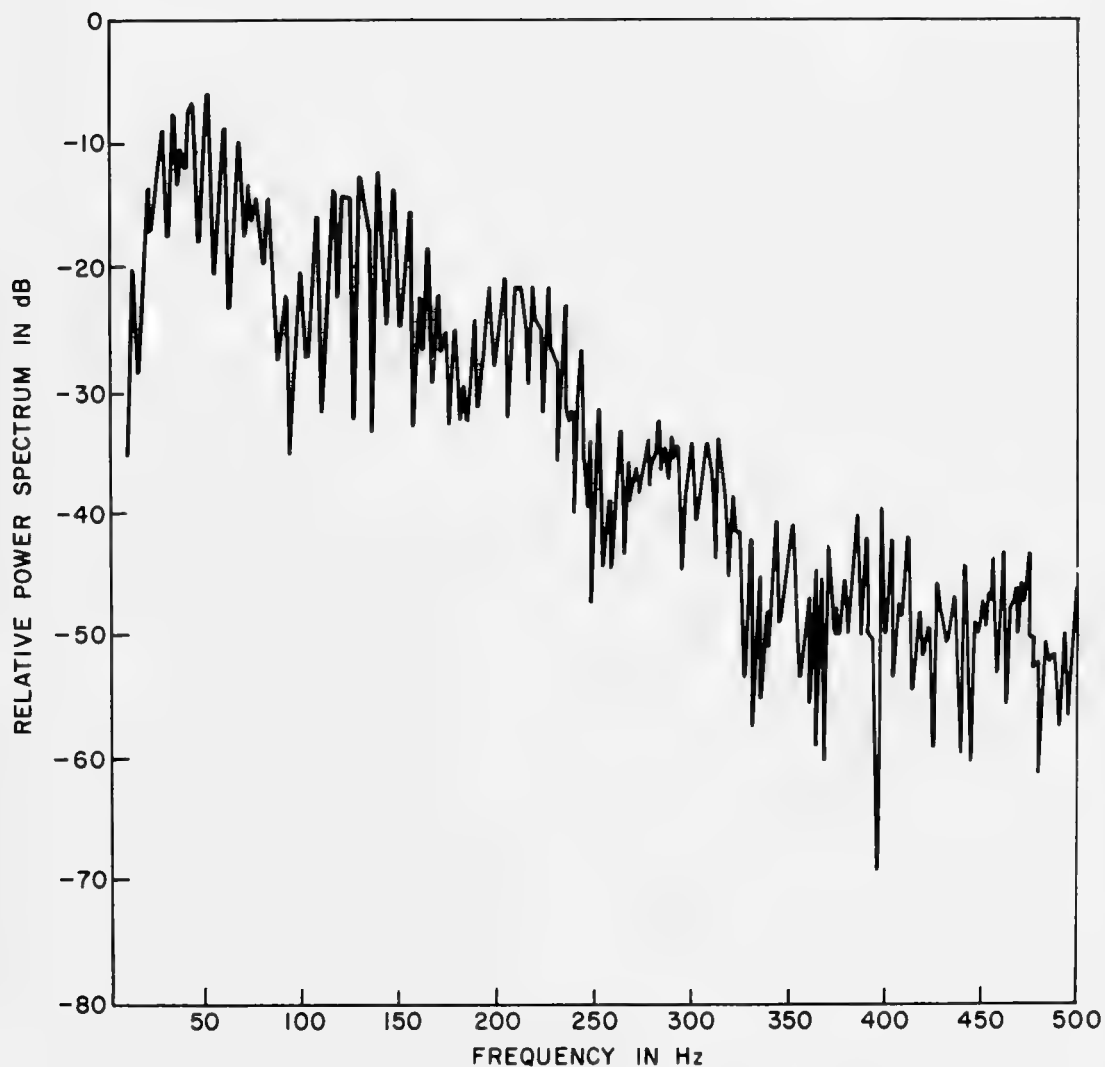


Figure 2. SPECTRUM OF THE DIRECT ARRIVAL AND SURFACE REFLECTION FROM A 1.8-POUND CHARGE DETONATED AT 60 FEET

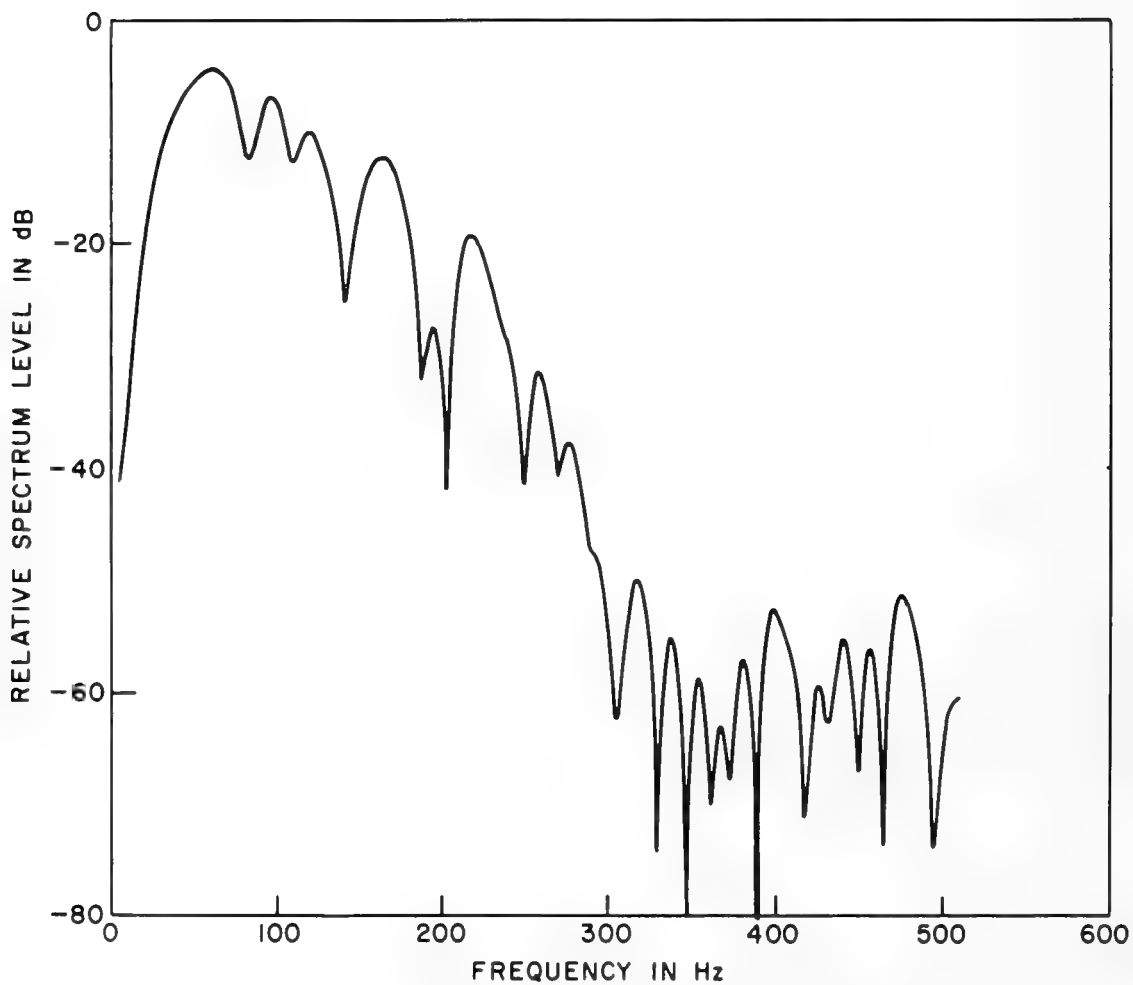


FIGURE 3. SPECTRUM OF A 1.8-POUND CHARGE
DETONATED AT 800 FEET

spectrum of the impulse response discussed earlier, with an appropriate choice of receiver depth (about 800 feet in this case), which would be indistinguishable from that caused by the bubble pulse of the source at 60 feet. Similarly, referring now to Figure 3, the source at 800 feet has a bubble pulse frequency of approximately 50 Hz (the surface reflected path has been gated out in the time domain) and, again, a particular receiver depth could induce a comparable periodicity in the spectrum of the impulse response.

The first point to be made, then, regarding measurement of the impulse response of the ocean is the nature of the limitation induced by our attempt to produce a source with a flat spectrum. The rule of thumb which follows from this point is that a source should be chosen (or tailored) such that its distinct spectral features are very different from those features of interest in the spectrum of the impulse response.

A second potential difficulty may arise in the choice of a signal processing scheme. If it is desired to measure the spectrum of the impulse response in detail over a wide band, then a natural choice of processing is digitization of the data and FFT spectrum analysis. Even though this processing permits very narrowband analysis, some frequency average of the spectrum will be desirable for at least one of two reasons: 1) it may be necessary to average over spectral variations of the source which are not strictly repeatable from event to event (such as the 6 Hz variation in Figure 2), and 2) it may be necessary to average over certain fine structure of the spectrum of the impulse response itself which is known (or expected) to change rapidly from measurement to measurement. These factors are further explored by Hanna and Parkins (1974). This frequency average can be selected only with knowledge of the detailed structure of both the source and impulse response spectra.

For reasons of economy, or for the sake of real-time processing, it may be desirable to do the necessary frequency average by band-pass filtering the received signal before processing. The factors affecting this choice are the same as those mentioned above. However, the penalty for error is higher in this case: in the absence of permanent broadband recordings, the measurement cannot be redone.

An example of an experiment in which the source and signal processing choices proved well matched to the desired measurement concerns the measured spectrum of an impulse response as shown in Figure 4. The event was a 3-pound charge dropped at a range of 300 nm and detonated at a depth of 60 feet. At this range the total received signal consisted of the arrivals from a single convergence zone. The 5 to 6 Hz variation is caused by the bubble pulses of the shot and the 220 Hz variation by the interference of the direct and surface-reflected paths at the source. The received signals were filtered through 1/3-octave filters at 25, 50 and 100 Hz; these filters were wide enough to average out the bubble pulse effect, but narrow enough to properly sample the surface image effect.

It is clear from Figure 4 that the received level will be about 10 dB lower (and, thus, the transmission loss will be 10 dB higher) at 25 Hz than at 100 Hz. This expectation is borne out in Figure 5 which compares the measured transmission losses at these two frequencies over the 500 nm range of the event.

Limitations of CE Sources

So far the discussion has been limited to the consideration of broadband sources; these sources are well suited to measuring the

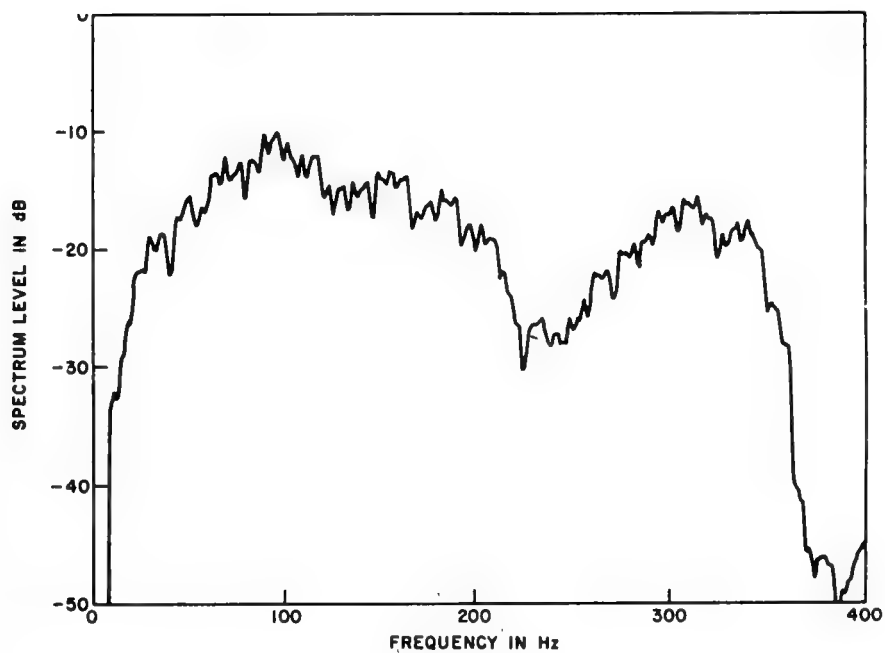


Figure 4. MEASURED SPECTRUM OF IMPULSE RE-
SPONSE FOR CONVERGENCE ZONE AT
300 NM

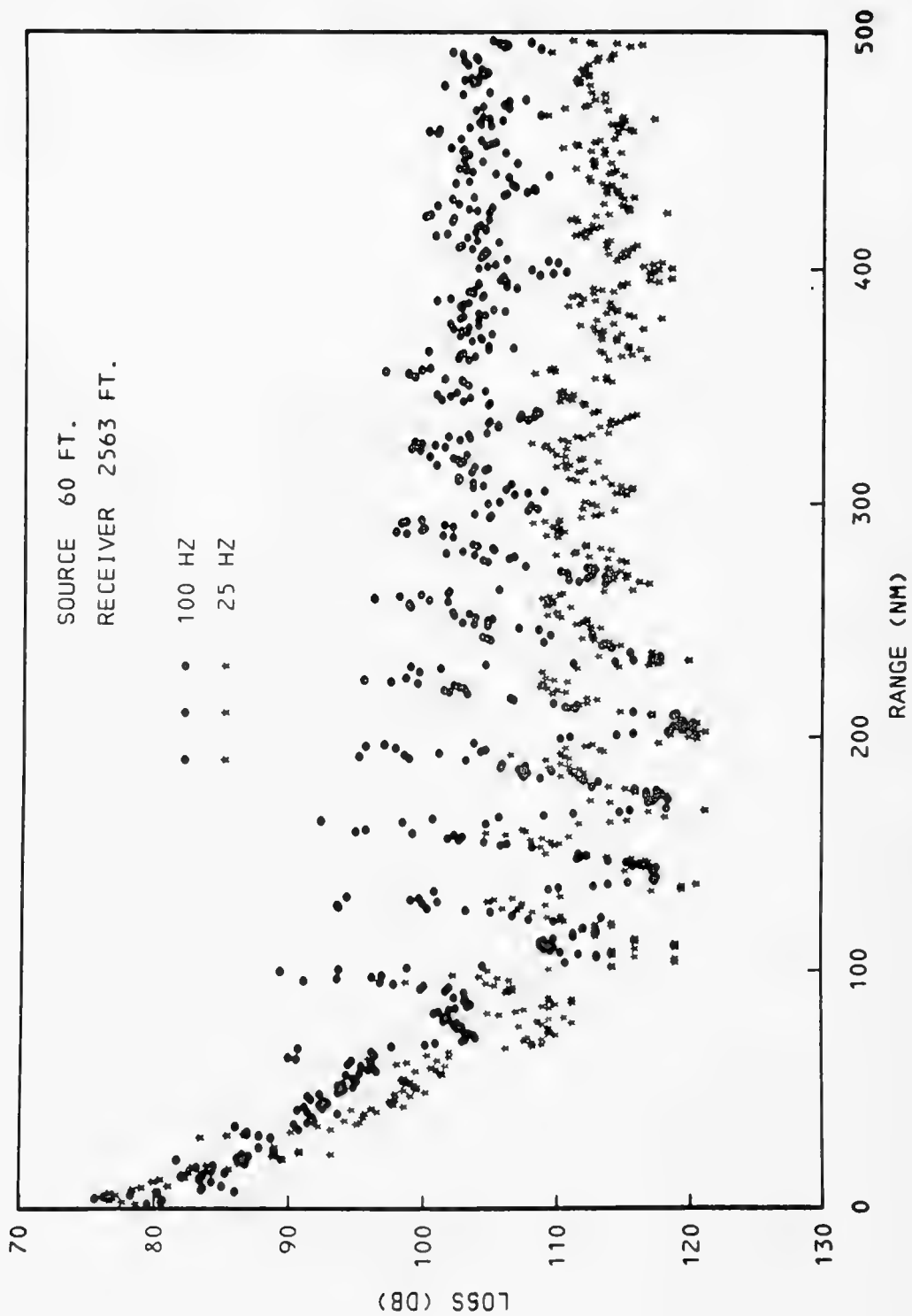


Figure 5. TRANSMISSION LOSS VERSUS RANGE

impulse response spectrum for discrete source-receiver geometries. There is much interest, however, in the behavior of a CW signal radiated by a continuously moving source; the behavior is determined most directly by the use of towed CW projectors. In this case, the spectrum of the impulse response is sampled at a single frequency (with some narrowband resolution) as a function of the changing source-receiver geometry. Even though the narrowband sampling may be produced continuously in time (as, say, the output of an analog filter), the practical question arises as to how often [in time] should this output be sampled to give transmission loss as a function of changing geometry. The answer is simple and obvious: often enough to adequately represent the underlying continuous curve. If, however, one must set up an automatic sampling system, it is necessary to estimate in advance the character of the transmission loss as a function of changing geometry, just as in the case of impulsive sources it is necessary to estimate the spectrum of the impulse response.

This point is illustrated in the next two figures. First, in Figure 6 are shown an estimated transmission loss curve and its experimentally determined counterpart for nearly axis-to-axis propagation in the Mediterranean. The calculation was performed using the parabolic equation program as implemented at the Acoustic Environmental Support Detachment; this calculation was carried out with a range resolution of 0.1 nm which was adequate to sample the rapid variations of the loss with range. The data were taken at approximately 5 nm intervals using a time average equivalent to a range interval of 0.05 nm. Although the data are not inconsistent with the calculation (and, thus, suggest that the real-world transmission loss has character comparable to that of the estimated loss), it is clear that the dependence of the actual transmission loss on

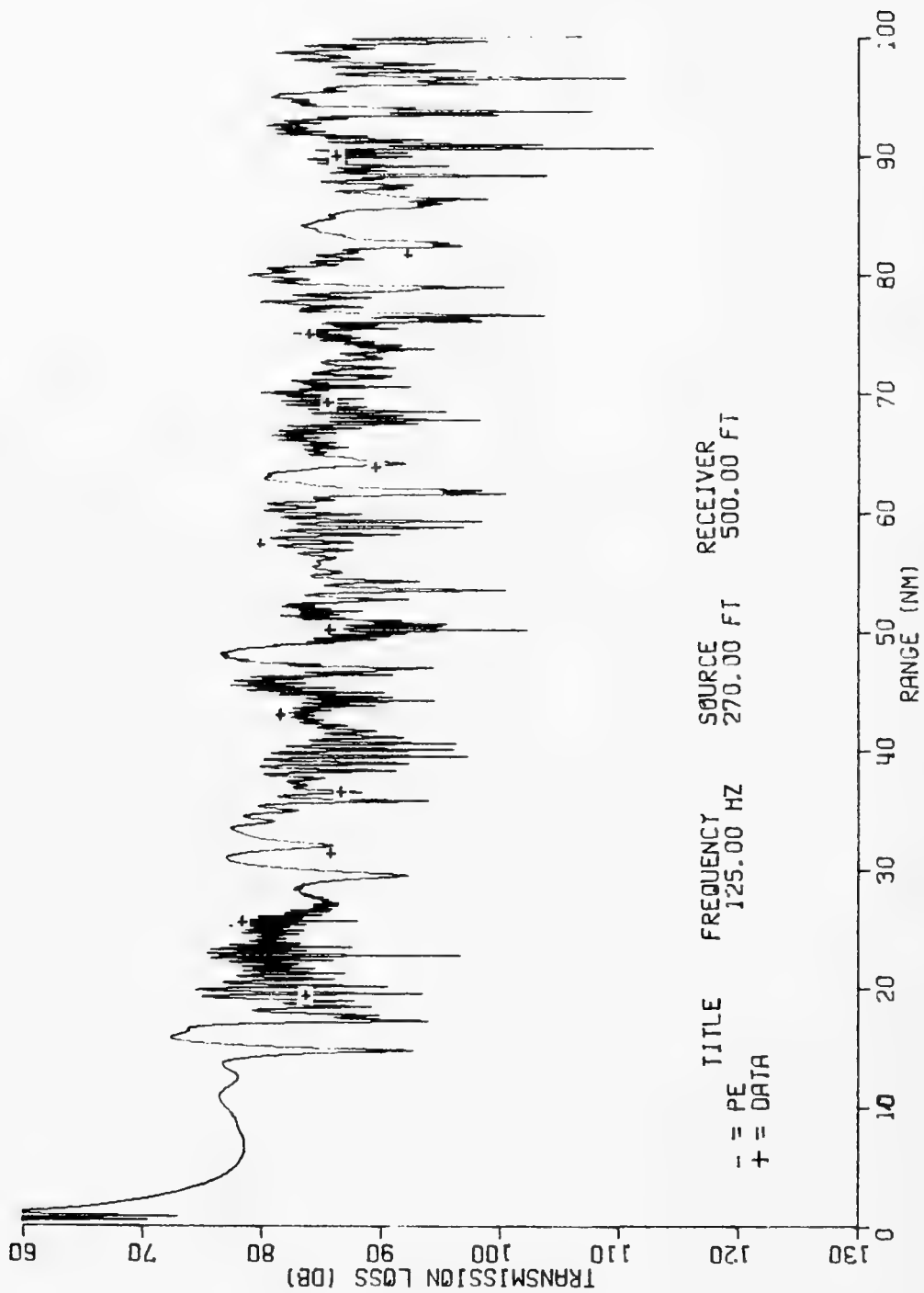


Figure 6. CW CALCULATION VS DATA

range is grossly underdetermined. Second, consider the comparison of Figure 7 which also presents both measured CW data and a parabolic equation calculation. In this case the calculation was done with a resolution of 150 feet in range while the data were taken with a time average corresponding to a range interval of 30 feet. Although different in detail, both curves have comparable structure; the important point is not the level of agreement or disagreement between the curves, but that both represent adequate spatial sampling of the underlying transmission loss and that the model calculation could have been used to set the experimental sampling intervals.

The chief advantage of a CW source is that it permits experimental determination of the behavior of narrowband signals. A significant disadvantage is that it seldom permits a path-by-path analysis of the transmission loss. When properly used, the CW and impulsive sources can provide information on complementary questions regarding the nature of propagation. The impulsive source is suited for measurements of the spectrum of the impulse response of the medium for fixed source and receiver locations (with a frequency average imposed by the nature of the source and, perhaps, even the medium). The CW source is suited for measurements of the spectrum of the impulse response at one frequency for continuously varying source and receiver locations.

The Message

The central point in the above discussion is that proper design of a transmission loss experiment demands *a priori* estimation of the nature of the loss characteristic to be measured. The present state of acoustic models, both ray and wave, certainly permits making these estimates with high confidence in many cases. Historical precedent is no longer a sufficient (or even necessary) reason for using any signal source or processing technique.

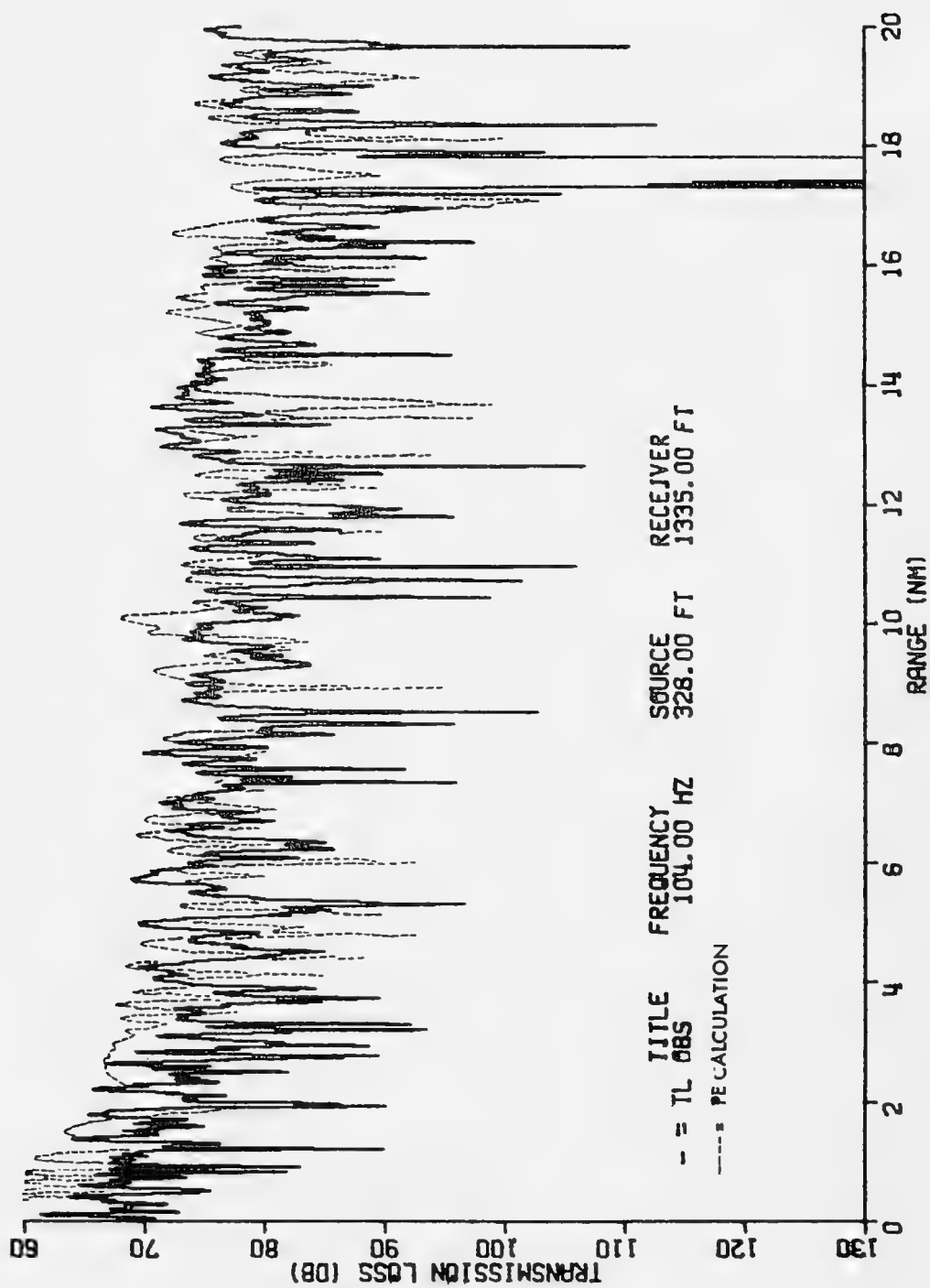


Figure 7. DETAILED CW DATA

A CASE HISTORY: THE CRITIQUE OF A BOTTOM LOSS MEASUREMENT

Introduction

The Naval Oceanographic Office (NOO) and the Naval Air Development Center (NADC) have conducted many measurements over the past several years aimed at determining the bottom reflection loss at low frequencies (less than 1,000 Hz). Although different in detail, the two programs have employed similar experimental techniques. They both tend to use sources and receivers within some hundreds of feet of the ocean surface; in this geometry transmission loss is measured, compared with estimates of the spreading loss through the water, and bottom loss is inferred. A consistent, and surprising, result of most of those measurements is the apparent evidence of negative losses at low frequencies for low grazing angles. This result has serious implications for predicted transmission loss using present models; in the remainder of this discussion the experimental design employed in these measurements will be examined, along with its impact upon the inferred reflectivity.

An Example

The case study here assumes a Pacific profile for the water column and a sound velocity gradient in the upper few hundred feet of bottom sediment of 1.0 sec^{-1} (see Figure 8). This assumed velocity structure for the unconsolidated sediment of the bottom is supported by numerous independent experiments including those being considered here. No discontinuity of the sound velocity into the bottom has been assumed, although there is evidence that a discontinuity of a few percent often exists. Its absence here is of no material consequence for the points to be developed.

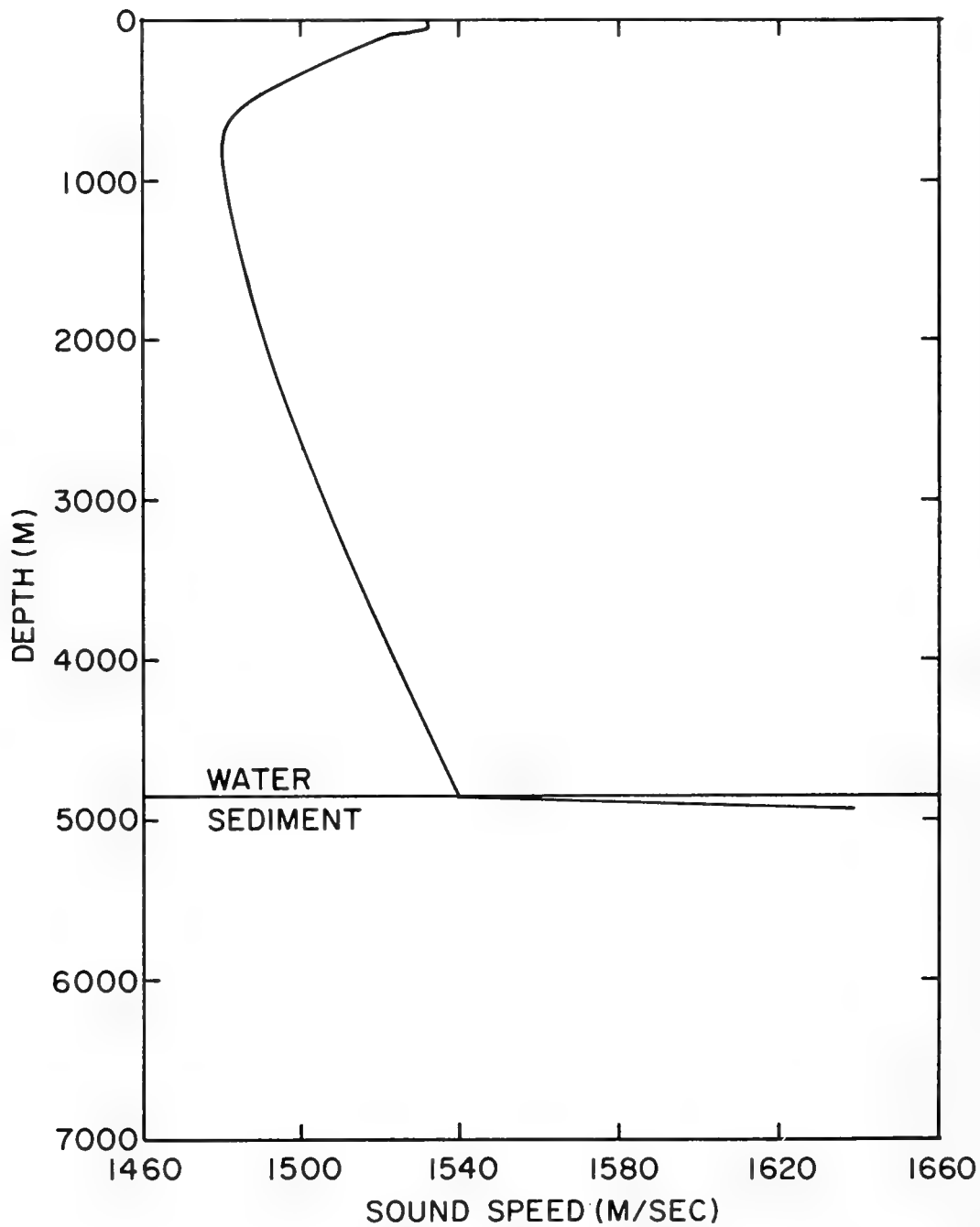


Figure 8. PACIFIC PROFILE

The schematic ray trace of Figure 9 shows a typical source-receiver geometry and the four ray-paths belonging to the family of rays having one bottom interaction. Explosive charges are used as sources and the experimental design assumes that these four paths are isolated by the signal processing. The basic analysis uses the following relationship applied to these paths:

$$RL = SL - TL - BL$$

where

RL = received level,

SL = source level,

TL = transmission loss,

BL = bottom loss.

The received level and source level are measured, the transmission loss (excluding bottom loss) for the paths is estimated and bottom loss is subsequently inferred. For the moment, it will be assumed that there is no uncertainty in the measured received level or source level (although the problem of source level measurements will be touched upon later).

Transmission Loss Estimates

Bottom-refracted Paths

The examination here begins with the assumed transmission loss model. In their data reduction, both organizations have assumed that 1) all four paths are of equal intensity at all ranges, and 2) the contributions from all four paths combine on a power basis to yield the total intensity. Based upon these assumptions, the total spreading loss along the four paths is just 6 dB less than the loss along any single path. Assumption 1) above is acceptable except for ranges corresponding to small grazing angles on the bottom; at these

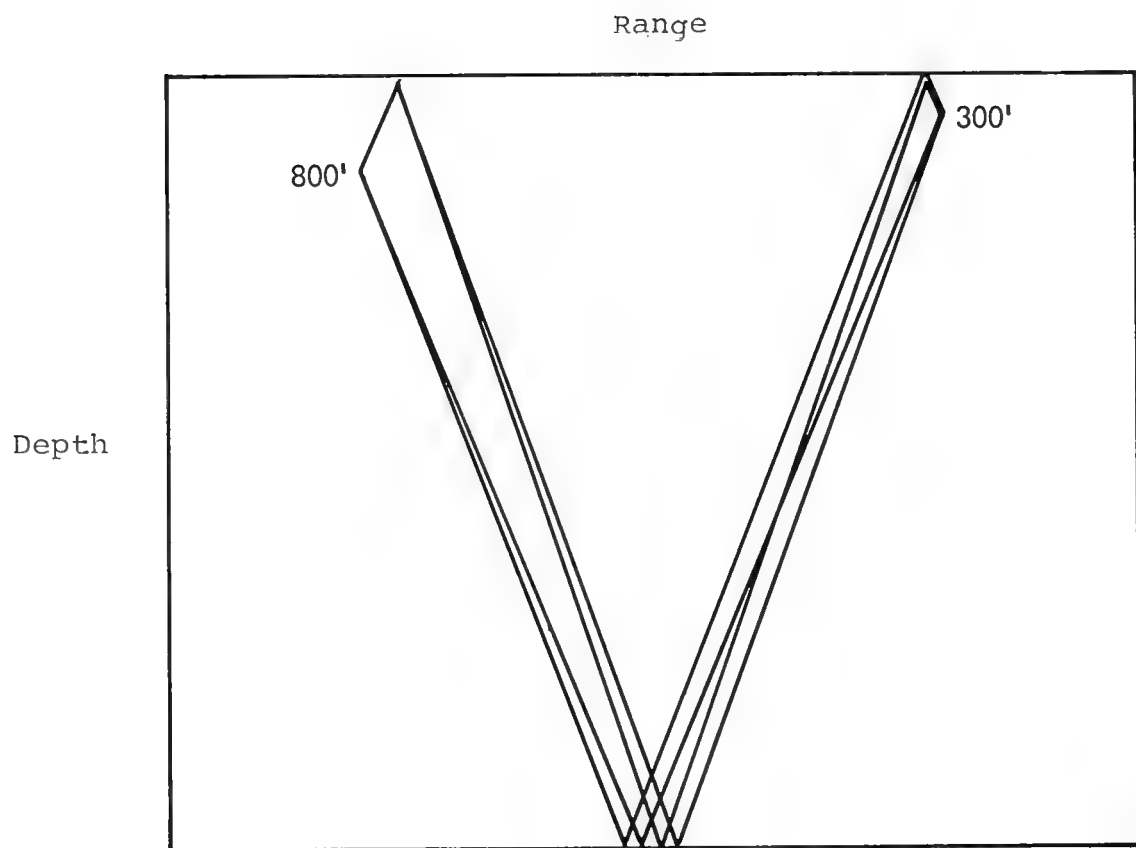


FIGURE 9. SCHEMATIC RAY TRACE

ranges the paths begin to drop off in intensity at significantly different rates. Thus, the total loss estimated from a single path will be different at low grazing angles, depending upon which of the four paths is used.

The second assumption above can lead to more serious difficulties than the first. Based upon the earlier considerations of this paper, whether any set of paths is combined in the signal processing on an rms basis or not depends upon the details of the processing. In the experiments of interest here the received signal was filtered in a 1/3-octave band at several center frequencies. To assess whether assumption 2) is reasonable, estimates of the spectrum of the impulse response for the four paths of Figure 9 were made; these estimates were based upon the computed amplitudes and arrival times for the paths. The relative arrival times as a function of range are shown in Figure 10 for the paths which refract through the sedimentary layer in the sound speed profile shown earlier. (The minimum range corresponds to a path incident upon the bottom at an angle of 20° with respect to the horizontal.) Figure 11 shows the computed spectrum for a range of 14 nm; the 9 Hz variation is caused by the up-and-down-going pair of paths at 800 feet, while the 27 Hz variation is caused by the up-and-down-going pair of paths at 300 feet. At 35 Hz, for example, a 1/3-octave filter is about 8 Hz wide at its 3 dB down points; a filter of this width clearly will not yield the rms sum of the features of this figure. Figure 12 shows the computed spectrum at a range of 29.5 nm; all the travel time differences have decreased with corresponding increases in the frequencies of the variations in the spectrum. Again, the filter at 35 Hz will not yield the rms sum of these variations.

Figure 13 compares the transmission loss for these four paths based upon 1) the rms sum, 2) a 1/3-octave result at 35 Hz, and 3) a 1/3-octave result at 100 Hz. In the portion of the figure above

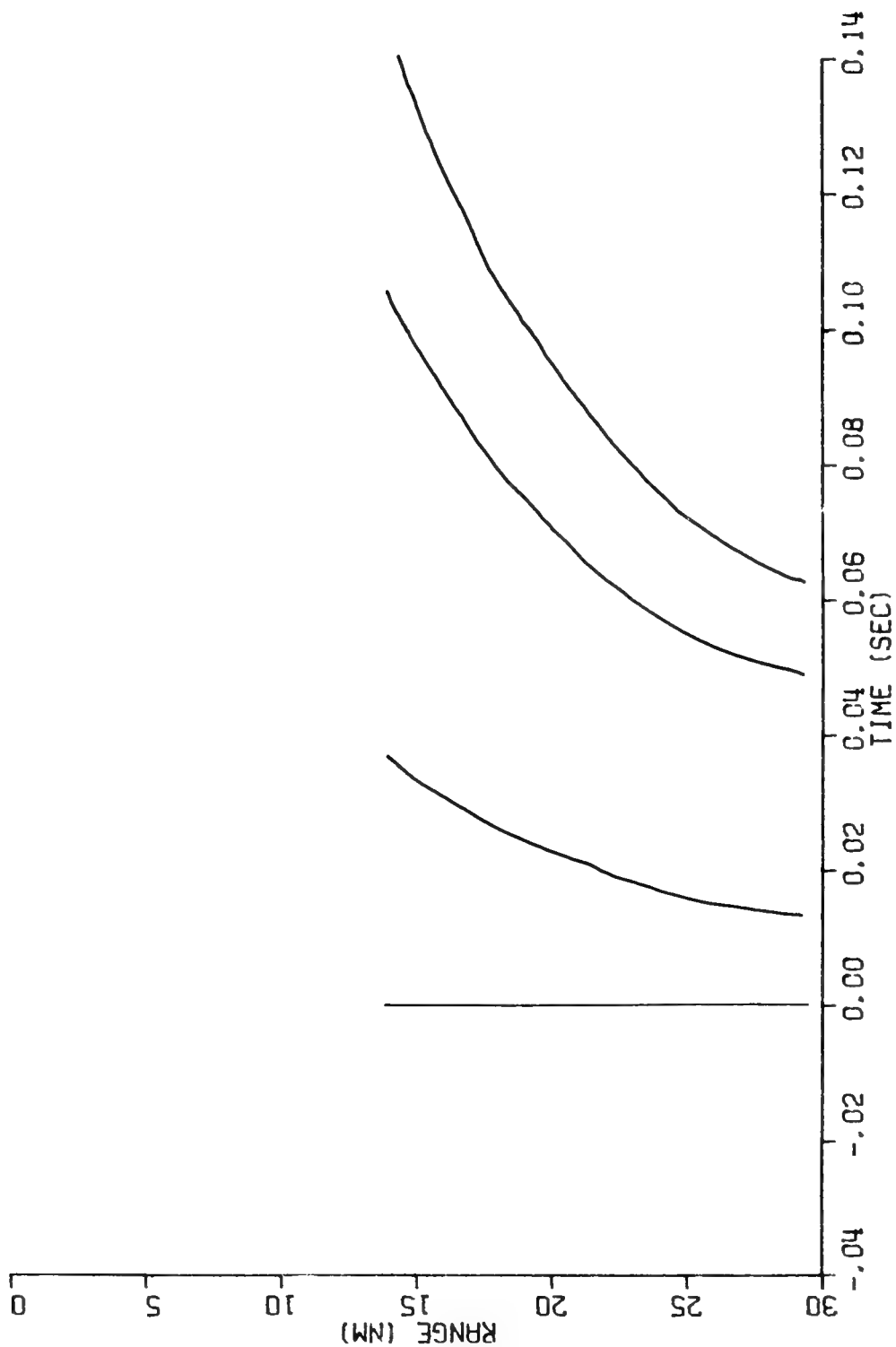


Figure 10. RELATIVE ARRIVAL TIME STRUCTURE
FOR BOTTOM - REFRACTED PATHS

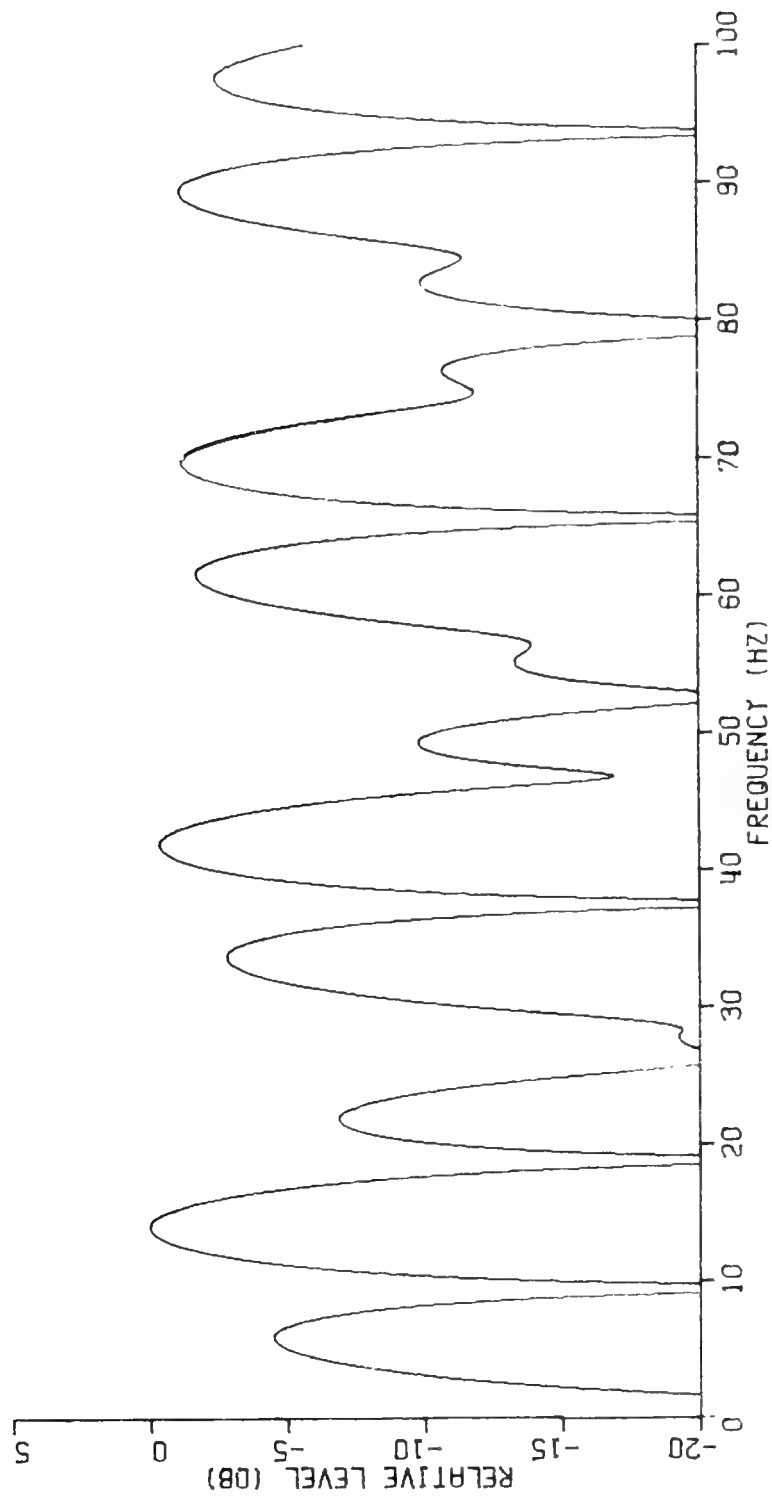


Figure 11. CALCULATED SPECTRUM OF IMPULSE RESPONSE
AT 14 NM FOR BOTTOM-BOUNCE PATHS

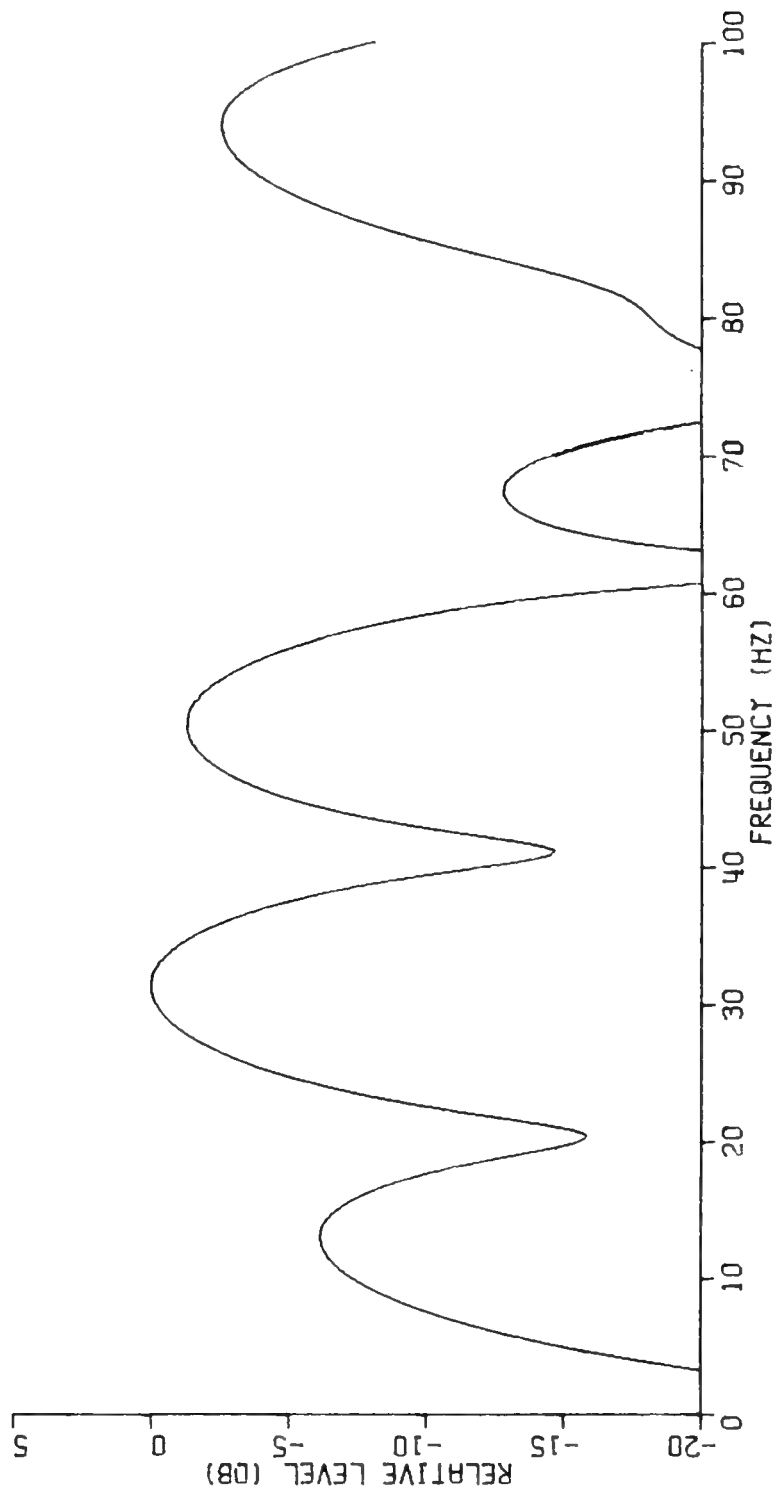


Figure 12. CALCULATED SPECTRUM OF IMPULSE RESPONSE
AT 29.5 NM FOR BOTTOM-BOUNCE PATHS

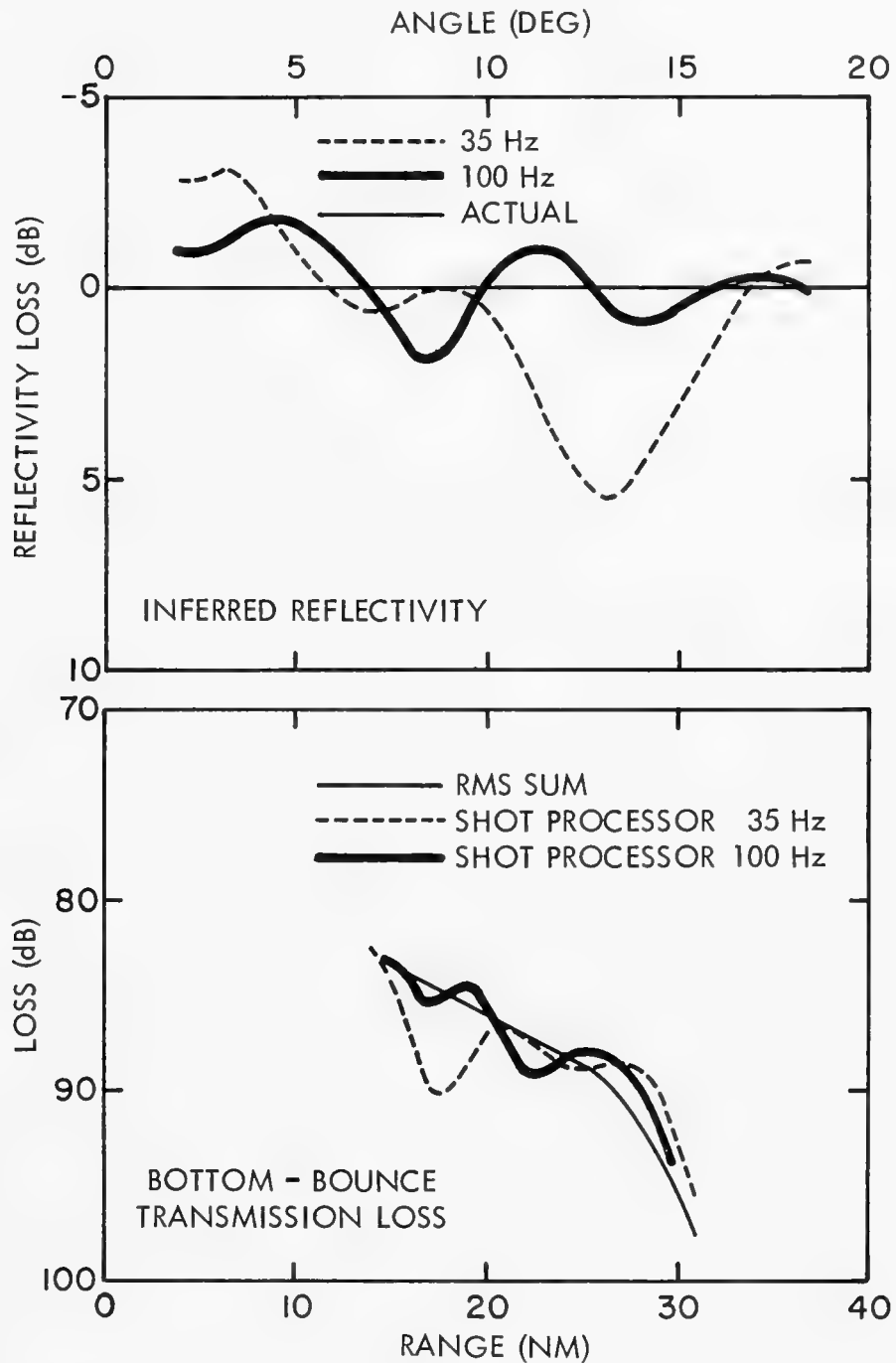


Figure 13. REFLECTIVITY AND TRANSMISSION LOSS FOR STRUCTURE OF FIGURE 9

the transmission loss, the inferred reflectivity is plotted assuming that the measured loss is either the 35 or 100 Hz filtered result while the computed loss is the rms sum. There are two important points to be made here: 1) the inaccurate transmission loss model (viz., the rms sum) induces spurious character into the inferred reflectivity which is not only frequency dependent, but source-receiver geometry dependent; 2) the inferred reflectivity loss is consistently negative for angles less than 6 to 7 degrees.

Water-refracted Paths

Up to this point it has been assumed that the four bottom-interacting paths can be resolved from all other paths in the problem. This is not always the case for ranges corresponding to low grazing angles. To demonstrate this fact, consider first the ray plot of Figure 14 where are shown the rays from a source at 800 feet which arrive in the range-depth window from 25 to 35 nm and 0 to 300 meters. Those paths which reflect from the surface are distinguished according to whether they interact with the bottom or belong to the RSR family; also shown are the RR rays. Consider the rays which intersect the receiver depth at 300 feet: the last bottom-interacting path arrives at a range of 31 nm, yet even the ray-trace shows non-bottom-interacting paths arriving in the overlapping range from 29.5 to 31 nm. In reality, however, the refracting paths make their influence felt before 29.5 nm in the form of the shadow zone field of the RR caustic. The relative travel time between the refracted field and the bottom interacting field is sufficiently small so as to not be resolved by 1/3-octave processing at low frequencies. Thus, attempts to measure the bottom-interacting field at these ranges may be thwarted by the additional influence of the refracting field.

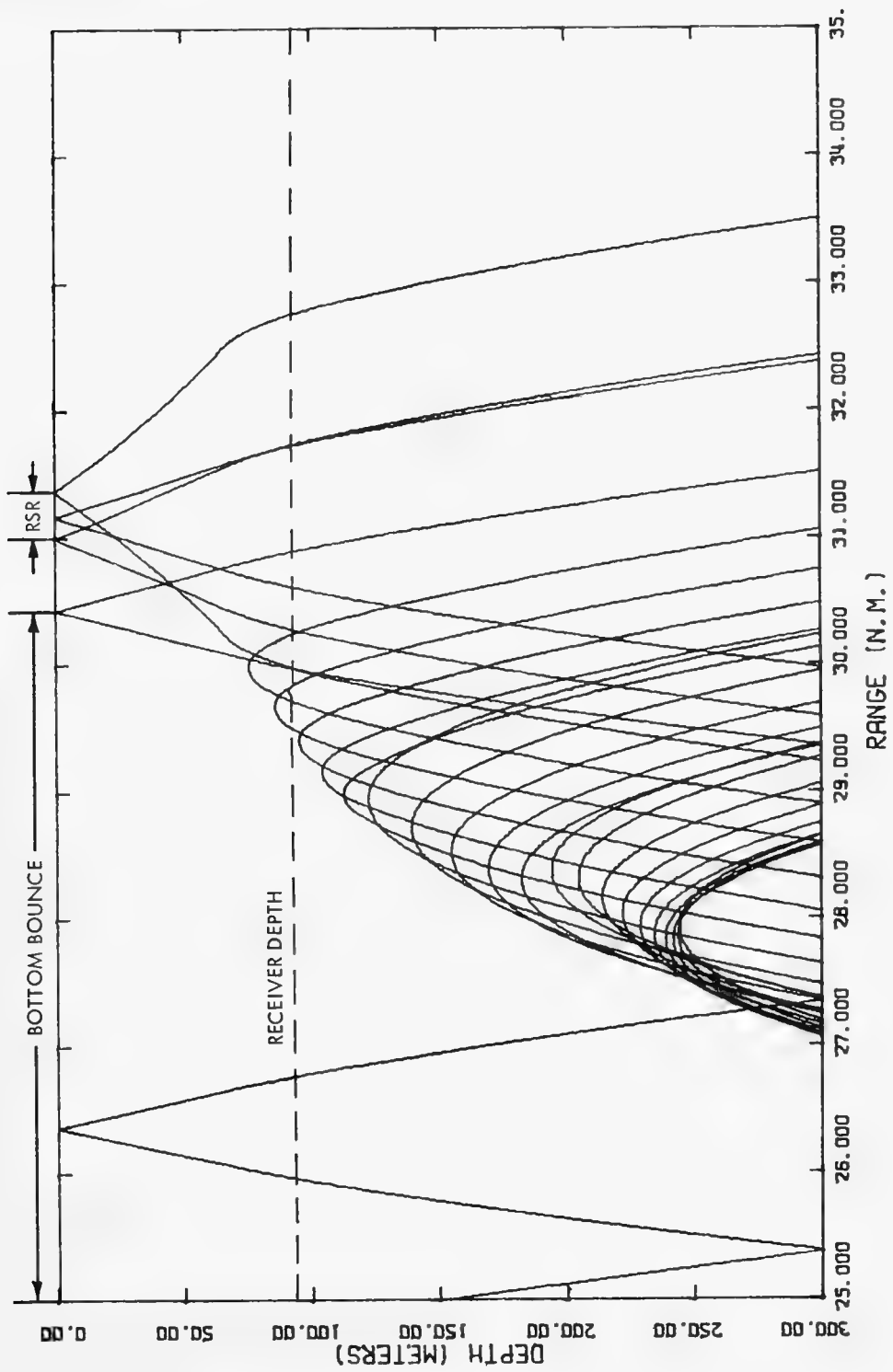


Figure 14. RAY-TRACE AT FIRST CONVERGENCE ZONE

To estimate this effect, a wave model which properly treats caustic fields (the parabolic equation model mentioned earlier) was run, including both the bottom-interacting and refracted fields, and averaged in frequency over 1/3-octave at 35 Hz. The results of these calculations are shown in Figure 15 with the rms sum, again, as the estimated transmission loss. The inferred reflectivity is shown at the top of the figure; it follows the earlier 35 Hz curve down to about 5 degrees, below which it goes even further into negative values than before. The significant point here is that even if the proper summation of the bottom-interacting paths were used as the estimated transmission loss, negative reflectivity losses would be obtained at low grazing angles because of the refracted contribution to the field. The effect of the refracted field will depend upon frequency, geometry and depth excess.

To summarize the analysis at this point, it has been shown that certain features of the low frequency bottom loss measurements made by NOO and NADC, especially apparent negative bottom losses, could be induced by 1) an over-simplified transmission loss model, and 2) inseparable bottom-interacting and refracted fields at ranges corresponding to low grazing angles.

Bottom-reflected paths

So far the attention has focused on the model for propagation in the water. Consider for a moment the diagram of Figure 16 which shows not only a path refracting through the bottom, but one reflecting from the boundary as well (some of the NOO data show the presence of both paths). In general, if the incident amplitude is A and that of the reflected path is αA , then the amplitude of the reflected path is $(1 - \alpha)A$ (neglecting reflection back into the bottom of the emerging refracted ray). When these paths recombine in the water, their

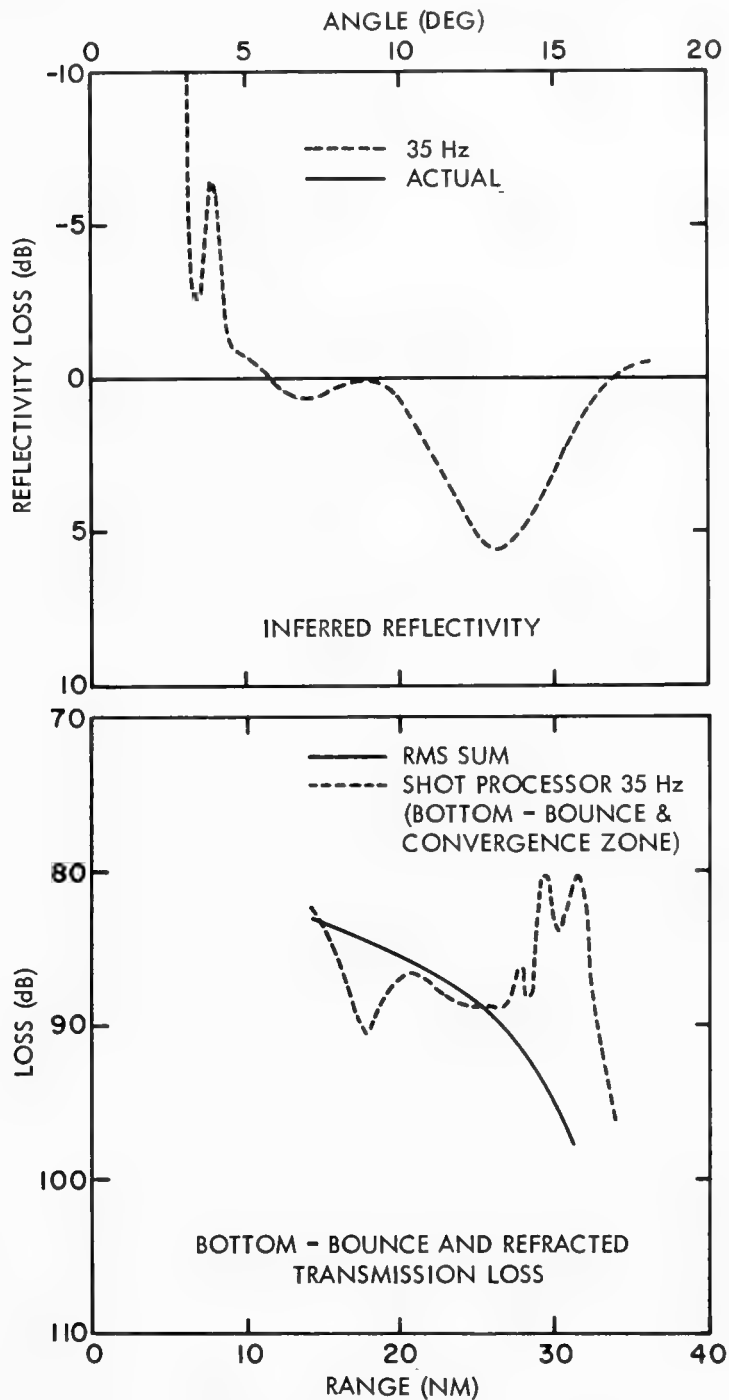


Figure 15. REFLECTIVITY AND TRANSMISSION LOSS FOR STRUCTURE OF FIGURE 14

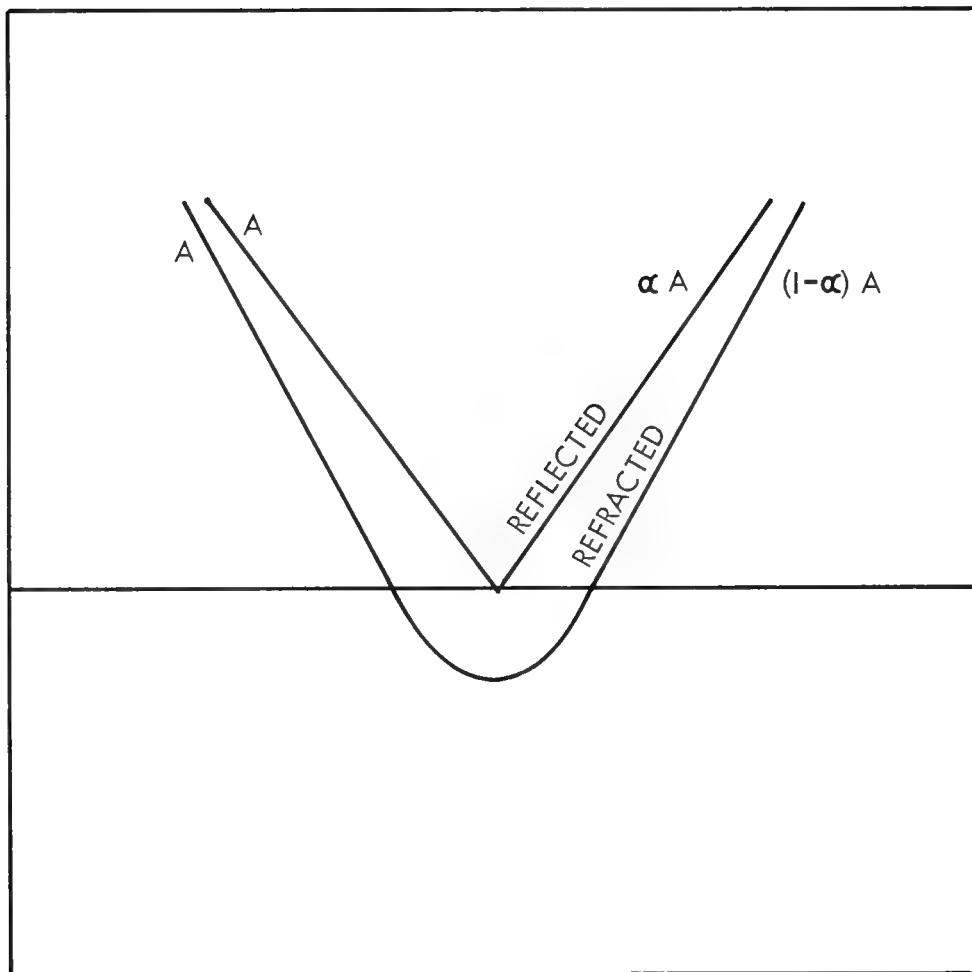


Figure 16. INTENSITY OF RECOMBINED SPLIT PATH

amplitude can be at most A (neglecting spreading losses) and, thus, will not exceed the energy of a path for the case where only one of these two is present. Such a mechanism, then, cannot give rise to negative reflectivity.

While the above argument concludes that the presence of both bottom-refracted and bottom-reflected paths cannot produce apparent negative reflectivities, their simultaneous presence will certainly produce interference patterns in the reflectivity as a function of frequency. Figure 17 shows the relative arrival time structure for the bottom-refracted and bottom-reflected paths for the case being discussed here. Note that the reflected counterpart of each refracted path arrives earlier; the fact that these paths arrive simultaneously at maximum range is a direct consequence of no velocity discontinuity at the bottom. The maximum travel-time difference between these paths is about 15 msec for the geometry considered here; the period of the corresponding variation with frequency of the reflectivity will be 66 Hz or greater. Thus, the 1/3-octave filters discussed above will give essentially the coherent combination of these paths.

Finally, note that the need for dealing with four inseparable paths could be avoided by getting the source and receiver away from the ocean boundaries, but this in general will increase the interference of refracting fields. Conversely, the influence of the refracting fields diminishes near the ocean surface, but the need to deal with the four paths increases. This qualitative trade-off suggests that low grazing angle measurements may always pose a significant problem.

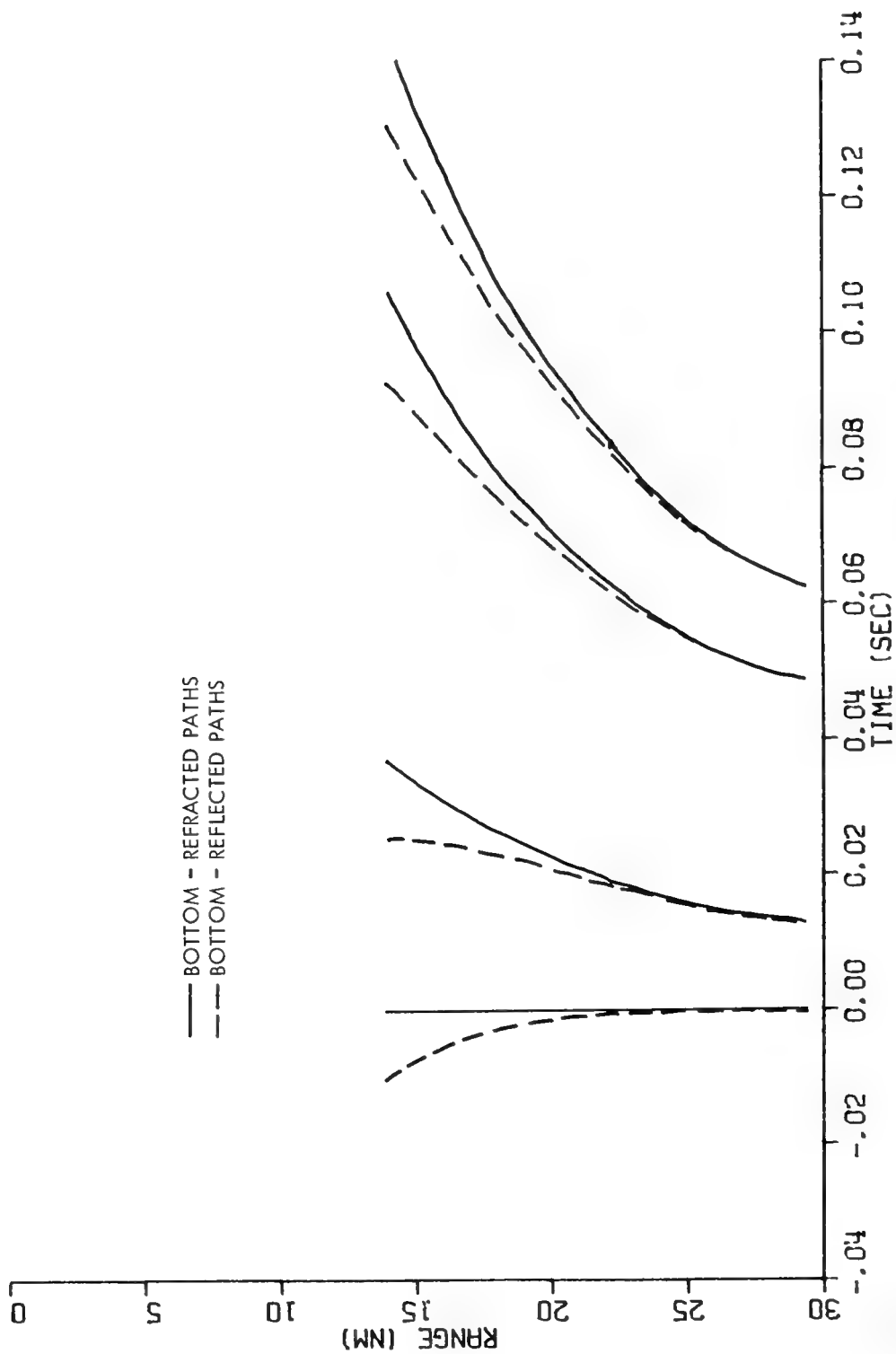


Figure 17. RELATIVE ARRIVAL TIME STRUCTURE

Source Level Errors

Errors in the calibration of the source will directly affect the inferred reflectivity. Worse, variations in the spectrum level of the source from event to event will induce point-to-point errors in the estimates of reflectivity. When pressing to get meaningful values of reflectivity to accuracies of a few dB, it is obvious that all measured or estimated qualities entering the computations must be known to accuracies consistent with that desired in the result. Concerns expressed elsewhere in these proceedings regarding measured source levels for explosives have serious implications for measurements, such as those here, which rely on absolute source levels.

CONCLUSION

This paper has attempted to develop a particular approach to the design of transmission loss measurements based upon the use of existing acoustic models to estimate the nature of the loss in advance. Examples were presented to illustrate common pitfalls which can be avoided with this approach.

REFERENCES

Hanna, J. S., and B. E. Parkins, "Some considerations in choosing an explosive source and processing filter for the measurement of transmission loss," J. Acoust. Soc. Am. 56, 378-386, 1974

DISCUSSION

Dr. J. S. Hanna (Office of Naval Research): What I have here (in Figure 16) is a schematic representation of a path which refracts through the bottom and one which is reflected from the interface. What I intended to have these paths correspond to is essentially what is back at the source and again at the receiver.

The point that I wanted to make here is that even if both of those paths are present in the data, the only thing that they can do to you is produce structure in the bottom reflectivity that you would infer, but they cannot give you reflectivities which are greater than one.

The reason why, I believe, is that if these two paths have amplitude A and they reach this boundary, the reflected path will have some amplitude less than A which I have indicated by αA here. That means that the energy, which is remaining to travel along this path, is essentially $1 - \alpha$ times the original amplitude, and the most that can happen when these two recombine is that you get A back, but not more than that and, in general, perhaps less than that.

So that I don't believe in principle that the combination of those two paths is the problem.

Mr. M. A. Pedersen (Naval Undersea Center): No, that's not quite true, because you have a slope discontinuity there, you are bound to have a caustic down in that bottom medium. There is a slope

discontinuity at the interface because they have different velocity gradients and it bends the right way to cause a caustic.

Dr. Hanna: The implication of that is what?

Mr. Pedersen: Well, that the intensity can be much larger for this one that goes down into the bottom there than that other one. Say, if the original energy that goes into the bottom is less than the reflected ray, you could still get certain convergence regions for that path that goes down next to bottom.

Dr. Hanna: Are you essentially saying that if I began with an amplitude of A incident on the bottom and ran this path through the problem and back out again — well, let me try to simplify the problem just a little by ignoring the reflected path.

Let's say there is no reflection at the boundary and the only thing that happens is that this path goes down, gets refracted and comes out again.

Are you saying, essentially, that if I go to the surface here where the path originates and terminates that I should expect to see a received intensity for this path which may be higher than what corresponds to simply keeping track of spreading loss along that path?

Mr. Pedersen: There is at least one more path. The point of it is whenever you have one gradient, and then you have another slope discontinuity to a steeper gradient, you always get a caustic, if you increase the angle to a steep enough angle.

Mr. C. W. Spofford (Office of Naval Research): Yes, but, Mel, that caustic is occurring way back in range in this problem. John is talking of 5 or 10 degrees, and the caustic was around 25 or 30 degrees.

Mr. J. I. Ewing (Lamont-Doherty Geological Observatory of Columbia University): That's right, too. There is a critical distance involved. In this situation there is a single ray path, but beyond this distance there are two families. At an increased range one family dives deeper into the bottom than the critical ray does, and the other family goes shallower than the other ray does.

Beyond that critical distance you have two distinct paths.

One thing I object to is the neglect of sub-bottom reflections in your treatment. Beyond the low grazing angle you are likely to have rays reflecting off of sub-bottom interfaces at very favorable angles of incidence to return the amount of energy.

Dr. Hanna: Okay, I should make it clear at this point that I have, indeed, not included those possibilities in the problem and I am not suggesting for a moment that they aren't out there in some real case of interest to us.

Mr. Ewing: I agree when you are out there near the 30-mile range you probably only have one refracting ray. The deeper ones have probably already been intersected by either some sedimentary reflector or by the basement rock.

Mr. Pedersen: It depends on where you cut off this positive gradient layer there with your sedimentary bottom. But if you just imagine continuing that on indefinitely, you see that branch has to come back out again in range.

Dr. Hanna: That sounds like almost an academic thing to do, though. That is to say, this sedimentary layer already is 500, 550 fathoms deep and, in any event, I think it is unlikely that any energy that penetrates this deeply, if there is any absorption in the problem, is going to come back to haunt me again, anyway.

Mr. Ewing: Why was the reflected path from that sub-bottom interface terminated where it was? I don't understand that.

Dr. Hanna: I'm sorry, which reflected path? You are talking about the one which reflects at the interface itself?

Mr. Ewing: No, that reflects at the deeper interface.

Dr. Hanna: Oh, down here.

Mr. Ewing: Yes.

Dr. Hanna: In this particular case, they have simply come down reflected and they do return into the problem, but way back in here.

Mr. Ewing: And then what?

Dr. Hanna: Well, for me, and then nothing, because I was interested in these ranges here and those correspond to the very short ranges which I wasn't really discussing at this point.

Let me try to remember another one of Will's slides.

He showed measured transmission loss as a function of range for, I guess it was — wasn't it — the Caribbean?

Mr. W. H. Geddes (Naval Oceanographic Office): That was the Caribbean.

Dr. Hanna: Yes. And if you remember, going from long range into decreasing range there was a very abrupt transition in transmission loss at around — I don't know, it was around this range right here, if I remember correctly, 24, 28 kiloyards, something like that, where the transmission loss abruptly dropped and went on back to the ranges corresponding to this part of the problem here

and there wasn't — at least the way I would read it — any indication of contributions from these paths that might have reflected, let's say, in that deep interface at all.

Dr. C. W. Horton, Sr. (Applied Research Laboratory of the University of Texas at Austin): I think the point is that whether there are two or more rays, your point is still proven. You are wanting to show that you cannot get positive bottom-loss values, and the total reflection, if there is no loss at the bottom, is unity. So where there are two or three rays that add together, you still would only get a total amplitude of unity if they are in base. That is all you set out to establish.

Dr. Hanna: Yes, that's exactly right. It sounds like I have convinced at least one person.

The point I wanted to make is, even if one improved this picture to include for low grazing angles the possibility that some of the incident energy is reflected and not refracted through this layer, that you take that incident energy and send part of it along one path and the remainder along the other path, and that some place in the problem they may come together again. But the most that you can do is get back to the original intensity of that path, less the spreading loss.

Dr. J. B. Hersey (Office of Naval Research): John, have you experimented with nonlinear gradients in the sediment? If there is a second derivative to the gradient, I believe that caustic is guaranteed, right? I can assure you this kind of intensification is seen experimentally and it is very striking indeed. Its explanation is illusive.

Suppose we have two rays that bend together repeatedly, you know, successive rays forming a caustic, there can be intensifications without any violation or conservation of energy or anything like that. It's commonly known as focusing.

All along, you see, we have had experimental evidence for years that there is a strong intensification of an arrival that has to pass through the bottom in some manner and arrive at ranges of the order of 12-14 miles plus, and it continues strong for quite a few miles.

This is the experimental reason why I have believed in the possibility of negative bottom loss. But I have been left very hungry by these various ray analyses, because always it was carefully explained to me that the velocity gradient in the bottom was linear.

Mr. Spofford: I think the point is we are after the plane wave reflection coefficient of the bottom. This is what the models need, this is why we are supposed to be out there measuring reflectivity.

If you go to a range where you think you are observing a 5 degree grazing angle on the bottom and you are really seeing a reflected angle at 5 degrees, plus an angle which is going into the bottom at 20 degrees, transiting through the sediment, and coming up again with a strong focus (which is certainly possible if the sediment is deep enough and the curvature is strong enough) you are not measuring the reflectivity at 5 degrees, you are measuring transmission loss at that point in range.

The point I think John and I are trying to get to is, there is a specific mission in mind for these measurements which is bottom reflectivity. If you put plane waves into the bottom at various angles, you don't observe reflectivities greater than one.

Talking from a very parochial point of view, from the modeling point of view, if you take a negative reflectivity and put it into a propagation model and you go out a few hundred miles, adding in 2 or 3 dB increases of intensity per bounce for the grazing rays, you can get your intensity to arbitrary levels at great range. They are easy to do.

Dr. S. M. Flatte (University of California College of Santa Cruz): Why can't you focus a plane wave?

Mr. Spofford: It will be focused on the bottom, but won't be focused up above.

Dr. Flatte: No, it can be focused up above the bottom. It just won't happen the next time. If you try and say it will do it many times, it won't. But it can be focused the first time.

Mr. Spofford: The definition of the reflection coefficient assumes that in a homogeneous medium we have an incident plane wave of unit amplitude. Now, no matter what you put in the bottom, when it comes out again, if you haven't put any absorption in the bottom, it comes out with unit amplitude.

Dr. Hanna: I have the same concern that Chuck has which is that negative reflectivities are rather difficult for me to accommodate in any of the models I now have. That is not to say those models should not learn how to accommodate to whatever those negative reflectivities are trying to tell us.

The point that I want to make is that there are potential artifacts in some of those inferred bottom reflectivities produced by the assumed transmission loss along the paths involved. I will feel a lot more comfortable about debating the negative reflectivities and

after I think I have done as well as I possibly can toward modeling the part of the propagation that is alledged to take place in the water itself.

Mr. R. L. Martin (Naval Underwater Systems Center, New London Laboratory): In the Labrador Basin, Stan Della has made some measurements of an area of little interest to the Navy for bottom loss because there is so much depth excess, but he has been very careful to separate out a direct path and a bottom reflected path. He has been able to do this successfully down to angles of almost 5 degrees grazing, and starting at 10 degrees he has observed what we call "negative" bottom loss.

Even when you are very careful about your experimental procedure, using shots that are detonated deep in the water column, the receiver deep in the water column, and other factors, you still make that observation of negative bottom loss.

The way models are used today, you can't throw that into a model because every time the ray intersects the bottom, the negative loss is put into that ray. But it does indicate that in those areas where we make that type of observation, that you perhaps have to include the bottom into your model, because it is going to be a function of the point in the water column where you make the measurement.

Dr. H. Weinberg (Naval Underwater Systems Center New London Laboratory): Why don't we just simplify the problem and forget that you even have a bottom. Just consider the ray that goes into a little bottom region with a strong but positive gradient. By changing that gradient, you can get just about any type of answer you want. Clearly, by making that gradient strong enough, you can focus the energy enough to get an increase in the power of its intensity.

I think you are just arguing whether or not you interpret that increase as a negative bottom loss or focusing.

It really doesn't matter what you call it, but it is possible to get the same effect.

Dr. Hanna: The computations of intensity, that is, the rms sum of those four paths that I showed, were made using a ray tracing program which had that strong negative gradient in it. That is how the rays were traced. It was not assumed that the rays reflected from that bottom boundary, they refracted through it in that calculation.

Dr. Weinberg: Maybe in the particular example that you looked at, what you are saying is exactly right. But it's easy enough to construct another example where you can get focusing into that bottom region.

Mr. Ewing: The way I look at it is that you have a gradient in the water, and maybe you change the value of the gradient in the sediment, but I think it can still even be linear, Brackett. The simplest case is not to assume a discontinuity there. Consider an infinitely thick section of sediment that just has a gradient, and for the moment, let's forget about any possibility of reflection here.

I believe it is proper to say that you don't hear anything at your receiver until you get to some critical distance from the source, at which the value of the gradient permits a ray to be bent around and get back to the surface. That happens at some specific depth below the interface.

Then, if you imagine just one step beyond that, what you get is one limiting ray that does not get quite as deep as the first one

did, and you get another ray that goes quite a lot deeper than that, but coming to the same path.

I believe this is, in effect, your lens. When you also introduce reflectors in the sub-bottom, you can, at the right angle of incidence, produce, almost, unit reflectivity.

Dr. P. W. Smith (Bolt, Beranek, and Newman, Inc.): What we are after is tabulated bottom losses for prediction of changes in the environment which are independent of the bottom. We do not want those changes in the environment independent of the bottom to change the parameters by which we classify the bottom. This particular focusing feature is peculiar to the environment. We want a characterization of bottom reflection that will be useful for sampling. The problem is a very complex one. How do we take this apart and get a number that we can usefully use for transmission loss prediction.

Mr. Ewing: I fail to see how the energy that is returned from the sediment is not part of the problem, because it is energy returned into the water. A very large amount of it is returned to the water.

Dr. I. Dyer (Department of Ocean Engineering of Massachusetts Institute of Technology): The analogy might be that if for some reason the model makers forced us to neglect the lower 2,000 meters of the water column, and replaced the lower 2,000 meters of the water column by an effective bottom water reflectivity and we find we have convergent zones and we say, "Ooops! A negative reflection loss."

It seems to me that the problem here is no different. The bottom is part of the column, and any attempt to put an artificial line there and describe it by a simple number in this frequency range is bound to fail.

So, the model makers are going to have to adjust. We can't change the ocean.

Dr. Weinstein: John (Dr. Hanna), concerning another point, you started out by saying, let's assume the source levels are properly taken care of, but in fact they are not, because the measurement of the source level is made at a relatively short range when you are doing this kind of work.

At these ranges you are still in the shock wave region and not in the pseudo-acoustic region. You find that the pressure-time curve changes with range in such a fashion that there is a transfer of energy from the high frequencies to the lows.

This, in itself, would give you an apparent negative bottom loss if you apply spherical spreading as your means of correction, or if you calculate the propagation loss assuming that you have a caustic source.

Dr. Hanna: It is true that the analysis performed on this data is more complicated than only worrying about the estimated loss that you are going to compare to the measured transmission loss.

There is the whole problem of source level. I am not sure that I would agree at this point that it is a mechanism for getting negative reflectivities except if the source level is too high or too low, whichever way it has to be to make that happen.

I would like to make just one more comment about the particular sound velocity structure that I used here and what rays are and are not present at certain ranges in the problem for that particular geometry.

One thing I can say with absolute certainty is that, setting aside for the moment the question of whether you think the constant gradient that I chose in the bottom is at all realistic, if you accept the sound velocity structure, that I outlined above, to trace rays, I can promise that in that particular case for the ranges from 14 to 30 miles, roughly, there is only one path which refracts in that strong gradient then comes back at those ranges.

Now, the thing that I would certainly admit to the possibility of is the following: It may be that for more complicated sound velocity structures and for different values of, say, this initial gradient, and the way that behaves with depth, that you can indeed construct the kind of situations that you mentioned. That is, that at the ranges I considered, you have steeper paths which come back into the problem.

I would not quarrel with the possibility of doing that. The only thing that I would maintain is that with this particular specific example there is only that one path for those ranges.

What that may be telling us is that this example is not really representative of most of the cases that you had in your experience.

Dr. M. Schulkin (Naval Oceanographic Office): You don't have a negative bottom loss going continually out in range. It's just the first one where there is an apparent gain over inverse square spreading, because you have a convergence zone there. Like the other convergent zones that you take for granted in the water column, you have a 3 dB loss the distance level from there on, because you have $10 \log R$ spreading as you continue down the path.

It is no violation of the conservation of energy. If you focus your energy at some points, you lose it at other points in the vertical column, say at that range.

You don't deny this in regard to the series of convergent zones systems?

Dr. Hanna: No. I think the only point I would make here is that the caustic of this convergent zone occurs in the sediment, not back up at the surface.

Dr. Schulkin: No, no. Just like your regular convergent zone. You have got focusing near the surface of the regular convergent zone.

Dr. Hanna: Let me make just one further statement. Whatever focusing is accomplished by this sound velocity structure should be reflected in the ray tracing calculation; that is, the essence of that calculation is to compute the spreading loss along that ray along with whatever focusing the environment creates.

The curves that I showed you were made based on those kinds of computations. So, in my construction, if there is any focusing along that ray from whatever mechanism, it is in the computation.

It is in the curve that I call the rms sum of intensities which was constructed from the computed intensity along each of those paths.

Dr. Schulkin: Phasing is very important and this rms combination of your four rays — that's not what Will does anyway, as far as the analysis goes, except for individual arrivals. I don't know why you did that. The rms summation before arrival is not what Will analyzes in his data.

Dr. Hanna: That is a very important point.

Dr. Hersey: I am going to take a chairman's privilege and suggest that John go on to his next point and say that we have pinpointed a problem with which we had better deal.

Dr. Hanna: I have two things I want to say.

First, the main point that I was really trying to develop throughout this whole discussion — not focusing on this specific example of a kind of transmission loss measurement — is that when you make a measurement of transmission loss and come back with a set of numbers, in the processing of those data you need to think consciously about what it is you believe you are measuring.

I can show examples where that kind of consideration has not been given to the processing of the data, and the inferences drawn from those data are, in fact, quite misleading. That is really the essence of the point that I want to make. It certainly is not profound to ask anybody who is doing something to think about what it is they are doing.

Second, at this particular point, I am reminded of a story which I think summarizes how I feel.

The way the story goes, a chicken and pig were riding in the back of a farmer's truck. The truck was being driven through town. The farmer hit a pothole in the road and the chicken and the pig bounded out into the street. The truck went on, leaving them to their own devices.

The chicken and the pig were strolling down the street at that point and they passed a restaurant with the menu in the window: the menu said, "Ham and eggs, \$1.50."

The chicken looked at the sign, swelled up a bit with pride and said to the pig, "Isn't it marvelous the contribution we make to mankind." The pig looked at the chicken and said, "For you a contribution, for me a personal sacrifice."

Dr. Flatte: I want to tell Chuck that you can't focus a plane wave, you are right.

Mr. Spofford: Thank you.

Mr. Pedersen: I have a few comments to make on the measurement of bottom loss that might help resolve some of these ambiguous situations.

When we make bottom-loss measurements, we perhaps run typically out to the second or third convergent zone. We compare the loss per bounce that we got by way of one bottom bounce, two bottom bounces, and three bottom bounces.

That is, reduce all the data to a common base and then, if these don't agree, you have a self-consistency check right on the spot. That is, you don't have to come back another time to measure to see if it was consistent to the extent that the bottom is uniform over this distance.

You can make these comparisons and any errors in source level always show up as a fixed displacement. That is, sometimes instead of measuring the loss directly, you measure the difference between the second bounce and the third bounce, or something like this. There are certain fixed errors that can be removed in this fashion.

The second point about this is the problem of measuring loss at the low angles as you approach the convergent zone. The relationship of where the bottom reflected angle is intersected by the zone doesn't stay constant from zone to zone. Generally speaking, if you have a case where you just have surface reflected rays, I believe that you can penetrate down to lower angles by going into the, say, third convergent zone than by going into the second zone.

Dr. Hanna: Following on that point, is it not true that Officer, for example, applied exactly that kind of analysis to some of his low frequency bottom reflectivity measurements?

Dr. Hersey: Several reflectivity measurements were made that way.

I think they have a distinct fault, though. I have a funny feeling in my stomach that they simply don't measure bottom loss, and this has been growing on me through the evening. We did it that way for several years.

Dr. Dyer: John, it may be a little late to come back to an opening philosophical point that John made.

You said the motivation for measurements is to better understand the ocean — I applaud that view. You said, also, the motivation for measurement is to better build models — I applaud that view.

Who is going to speak for those poor guys who have to design systems? It's a rather different kind of motivation. And how do you design programs to meet those kinds of needs?

Dr. Hersey: Actually, Ira, I am somewhat disappointed that in the main this first transient of our workshop hasn't addressed that problem more than it has.

There is no question, however, that models based on a rational consideration of the influence of the environment on acoustic propagation and the shaping of the noise field have been applied to estimating the performance of systems that have not been built on analysis of performance of systems that have been built. The results of the latter are very weak in resolving power because of the nature of an operation exercise.

But those models have been able to account accurately — and by accurately I mean the mean discrepancy of the order of a dB — using the type of model we have been talking about so far in the workshop.

However, I have to say that I have no evidence that we have done justice to the systems designer. I guess he is going to have to tell us precisely where he thinks we have fallen down, because we haven't been able to account for the performance of this system.

Mr. Geddes: Regardless of how we process the data, we scale these records. We find an arrival on the records the amplitude of which is the largest thing on the record. It's there, record after record after record.

So that, regardless of the explanation for it, I still have the situation of looking at an arrival which I can look at on the records, I can listen to it, and I can measure its amplitude.

Dr. Hersey: There is only one problem with what you just said, Will. That is what is known as a disallowed area of concern. I disallowed it about 15 minutes ago.

Dr. G. B. Morris (Marine Physical Laboratory, Scripps Institution of Oceanography): I think use of models in planning experiments and comparisons of the models with the experimental data have to be done.

Some of the examples that were shown are sort of extremes in that you compare model data which have a very, very fine resolution with experimental data which have a very long averaging time to very poor resolution. It's the type of example that even experimentalists would not think of doing, comparing a propagation curve that has, say, values every few hundred yards, with another one that might have values every few miles, except in a very gross manner.

I think one thing that we might want to do is to apply some common filter functions to propagation loss models, so that the time averaging used in the experimental data would correspond, say, fairly closely to some sort of averaging in the model of propagation curves.

Dr. Hanna: I don't disagree with what Gerry said, I just make the observation that for the two examples of CW data and CW calculations that I showed, the resolution in range, if you like, was comparable between the data and the calculation in both of those cases.

The first case that I showed represented a problem, if you like, only because there were not enough experimental points with that resolution. If those points had, say, been taken with an equivalent range average of a mile or so, the model could have been run that way and an interesting comparison made. But, unfortunately, given the apparent underlying structure, you are faced with an under-sampled curve and there wasn't a lot which you could do with it.

I don't mean to cast negatively on the experimentalists at that particular point, but just to show that as an example of the kind of difficulty that can arise without anticipating what the function looks like that you are trying to measure.

Dr. Hersey: I should amend my comments, Ira, by saying, of course, the models that we are talking about become considerably modified by the addition to them of the punitive system characteristic. But we have done that.

Dr. Dyer: We haven't talked much about that.

Dr. Hersey: You are dead right, and I am disappointed.

One observation, for example, we do most of our propagation studies — not all, but most — with explosives. We have yet, I think I am right, John — we have yet to model a single explosive transmission event; isn't that correct? Don't we always make a CW model and then sort of imagine that the CW model is like the explosive?

Mr. Spofford: We are doing that.

Dr. Hersey: We have had this as a dream, I know.

Mr. Spofford: Of course with the ray models we can put in the shot characteristics. So I would say at the moment we are a little hard-pressed to come up with them exactly; this is the problem. There is a linearity of something we do with shots.

